BEILSTEIN JOURNAL OF NANOTECHNOLOGY

Physics, chemistry and biology of functional nanostructures II

Edited by Anatolie S. Sidorenko

Imprint

Beilstein Journal of Nanotechnology
www.bjnano.org
ISSN 2190-4286
Email: journals-support@beilstein-institut.de

The *Beilstein Journal of Nanotechnology* is published by the Beilstein-Institut zur Förderung der Chemischen Wissenschaften.

Beilstein-Institut zur Förderung der Chemischen Wissenschaften
Trakehner Straße 7–9
60487 Frankfurt am Main
Germany
www.beilstein-institut.de

BEILSTEIN JOURNAL OF NANOTECHNOLOGY

Physics, chemistry and biology of functional nanostructures II

Anatolie S. Sidorenko

Editorial

Open Access

Address:
Ghitu Institute of Electronic Engineering and Nanotechnologies of ASM, Chisinau, Moldova

Email:
Anatolie S. Sidorenko - Anatoli.sidorenko@kit.edu

Keywords:
nanotechnologies; nanomaterials; sensors

Beilstein J. Nanotechnol. **2014,** *5,* 1218–1219.
doi:10.3762/bjnano.5.134

Received: 26 June 2014
Accepted: 08 July 2014
Published: 06 August 2014

This article is part of the Thematic Series "Physics, chemistry and biology of functional nanostructures II".

Editor-in-Chief: T. Schimmel

Nanotechnology gives to the 21st century the "NANO" logo and covers all domains of human activity ranging from electronics and medicine, to aerospace and agriculture. One of the creators of large-scale nanotechnological implementations Mihail Roco, the initiator of the National Nanotechnology Initiative, a United States federal government program, mentioned that "The accelerating pace of discovery and innovation and its increasingly interdisciplinary nature leads, at times, to the emergence of converging areas of knowledge, capability and investment; nanotechnology is a prime example. It arose from the confluence of discoveries in physics, chemistry, biology and engineering." [1]. Starting in 2000 as the National Nanotechnology R&D Programs, first in the United States, then in Germany, and now in over 60 countries all over the world, nanoscience and nanotechnology gathered impetus and is one of the most rapid developing areas today. The intrinsic logic of that development determines the route of the progress: from a simple, evolutionary reduction of the structure size of single elements (for example, the size of the elementary transistor in a microchip) toward the revolutionary introduction of self-assembling nanostructures and functional nanomaterials.

The self-organization of nanoparticles and nanotubes and the introduction of those in various materials allowed for solutions to problems which have been present for a long time. An example is the problematical increase of the critical current in new MgB_2 superconducting material. This superconductor is very promising for technical applications due to its high critical current of up to 10^7 A/cm^2. However, this critical current is only present in the MgB_2 superconducting material when there is no magnetic field. The external magnetic field very rapidly suppresses the critical current and destroys the superconductivity of magnesium diboride. This issue was successfully resolved by the introduction of self-assembled magnetic nanodots on the MgB_2 surface, which gives rise to a new hybrid material with the desired properties [2].

The conceptual idea of this Thematic Series saw the light of day at the international conference bearing the "NANO" logo, which took place in September 2013 in Chisinau, Moldova (NANO-2013). A variety of technological approaches for the assembly of functional nanostructures and nanomaterials with tailored properties was presented at this conference.

We would like to thank all colleagues who developed new ideas, novel approaches and devices, and submitted their valuable contributions to this Thematic Series. I am convinced that this Thematic Series will attract the attention of researchers and will find many readers! The professional and dependable editorial support by the Editorial Office of the Beilstein-Institut is greatly acknowledged.

Anatolie S. Sidorenko

Chisinau, June 2014

References

1. Roco, M. C.; Mirkin, C. A.; Hersam, M. C. *Nanotechnology Research Directions for Social Needs in 2020;* Springer: Dordrecht, Heidelberg, London, New York, 2011; pp 690 ff.
2. Surdu, A. E.; Hamdeh, H. H.; Al-Omari, I. A.; Sellmyer, D. J.; Socrovisciuc, A. V.; Prepelita, A. A.; Koparan, E. T.; Yanmaz, E.; Ryazanov, V. V.; Hahn, H.; Sidorenko, A. S. *Beilstein J. Nanotechnol.* **2011,** *2,* 809–813. doi:10.3762/bjnano.2.89

License and Terms

Beilstein Journal of Nanotechnology

Controlled synthesis and tunable properties of ultrathin silica nanotubes through spontaneous polycondensation on polyamine fibrils

Jian-Jun Yuan[1], Pei-Xin Zhu[1], Daisuke Noda[1] and Ren-Hua Jin[*2]

Full Research Paper

Open Access

Address:
[1]Synthetic Chemistry Lab., Kawamura Institute of Chemical Research, 631 Sakado, Sakura, 285-0078, Japan and [2]Department of Material and Life Chemistry, Kanagawa University, and JST-CREST 3-27-1 Rokkakubashi, Kanagawa-ku, Yokohama 221-8686, Japan

Email:
Ren-Hua Jin* - rhjin@kanagawa-u.ac.jp

* Corresponding author

Keywords:
biomimetic silicification; polyethyleneimine; silica–carbon nanocomposite; silica nanotubes; template synthesis

Beilstein J. Nanotechnol. **2013,** *4,* 793–804.
doi:10.3762/bjnano.4.90

Received: 16 August 2013
Accepted: 06 November 2013
Published: 25 November 2013

This article is part of the Thematic Series "Physics, chemistry and biology of functional nanostructures II".

Guest Editor: A. S. Sidorenko

Abstract

This paper describes a facile approach to a biomimetic rapid fabrication of ultrathin silica nanotubes with a highly uniform diameter of 10 nm and inner hollow of around 3 nm. The synthesis is carried out through a spontaneous polycondensation of alkoxysilane on polyamine crystalline fibrils that were conveniently produced from the neutralization of a solution of protonated linear polyethyleneimine (LPEI–H^+) by alkali compounds. A simple mixing the fibrils with alkoxysilane in aqueous solution allowed for the rapid formation of silica to produce LPEI@silica hybrid nanotubes. These 10-nm nanotubes were hierarchically organized in a mat-like morphology with a typical size of 1–2 micrometers. The subsequent removal of organic LPEI via calcination resulted in silica nanotubes that keep this morphology. The morphology, the structure, the pore properties and the formation mechanism of the silica nanotubes were carefully investigated with scanning electron microscopy (SEM), transmission electron microscopy (TEM), Brunauer–Emmett–Teller measurements (BET), and X-ray diffraction (XRD). Detailed studies demonstrated that the formation of the nanotubes depends on the molar ratio of [OH]/[CH_2CH_2NH] during the neutralization as well as on the basicity of the alkali compound and on the concentration of the silica source. The synthesis of silica nanotubes established here could be easily applied to a fabrication on the kilogram scale. Silica nanotubes that were obtained from the calcination of hybrid nanotubes of LPEI@silica in an N_2 atmosphere showed a distinct photoluminescence centered at 540 nm with a maximum excitation wavelength of 320 nm. Furthermore, LPEI@silica hybrid nanotubes were applied to create silica–carbon composite nanotubes by alternative adsorption of ionic polymers and subsequent carbonization.

Introduction

Silica nanotubes with a controlled nanostructure (i.e., wall thickness and hollow space) and a tunable chemical composition are important for various applications, such as hydrogen storage [1], healthcare [2] and environmental technology [3]. It is well known that tubular silica structures can be fabricated by using inorganic [4], organic [5] or biological templates [6].

Among them, the utilization of self-assembled organic aggregates as templates for sol–gel reactions has received a great deal of attention, since this method is advantageous for controlling the structure, tuning the chemical composition and accessing surface functionalizations [7]. Shinkai and co-workers [8] reported the pioneering work on the formation of silica nanotubes by using a fibrous organogel as template for the silica deposition in mostly organic solvents. Also, silica nanotubes with helical character have been synthesized by employing chiral organogelating structures for the direct formation of silica [9]. Alternatively, self-assembled aggregates from surfactants or functional small molecules have also been developed for templating the formation of silica nanotubes [10-15]. However, these conventional methods cannot, in principle, avoid a non-templated silica deposition and also need harsh sol–gel conditions, such as long reaction times, elevated temperatures, and extreme pH values: This is partially due to the fact that the template aggregates cannot provide an efficient catalytic site for a selective silicification reaction. In addition, the organic template molecules normally need multiple steps to synthesize and thus are expensive, which limits a wider adoption and large-scale application of silica nanotubes [5,7-15].

In contrast, biosilicification in various biological systems such as diatoms and sponges proceeds in water under ambient conditions and produces siliceous skeletons with precisely controlled nanopatterns, a hierarchical morphology and organic–inorganic hybrid structures [16-18]. It has been demonstrated that the long-chain polyamines (partially combined with proteins) in diatom shells and the silicateins in marine sponges play a vital role in templating the biosilicification [18,19]. Therefore, a number of strategies to design self-assembled organic aggregates has been developed in order to make these organic matrices work as templates/scaffolds/catalysts for a deposition of silica at ambient conditions [20]. Recently, self-assembled fibrils of polypeptides [21-29] or amine-modified polysaccharides [30] have been used as template for the formation of silica nanotubes. For example, Yuwono et al. [23] reported the use of peptide-amphiphile nanofiber templates in order to direct the synthesis of hollow silica nanotubes with outer diameters of 15–23 nm. Pouget et al. [22] synthesized double-walled nanotubes that possess a silica/Lanreotide/silica wall architecture through a unique synergistic growth mechanism. With these methods, which are inspired by biosilicification, silica can be selectively deposited on the template under mild conditions. However, the formation of silica nanotubes needs relatively long reaction times (i.e., several days), and the use of the peptides as templates is costly. In order to achieve a large-scale commercial application of silica nanotubes, a highly efficient low-cost strategy based on simple synthetic chemistry is highly desirable. We are interested in the programmable construction of biomimetic silica nanomaterials by exploiting the crystallization-driven self-assembly of a simple synthetic polyamine, namely linear polyethyleneimine (LPEI) [31-33]. In contrast to branched PEI, LPEI is composed only of secondary amine ($NHCH_2CH_2$, EI unit) and is highly crystalline because of its linear structure [34]. We discovered that, when cooling its hot aqueous solution, LPEI tends to self-assemble into a crystalline nanofilament structure associated with water molecules ($(NHCH_2CH_2)/2H_2O$) [35]. This crystalline nanofilament itself acts as a template that directs the silica morphology as well as a scaffold for the deposition of silica, and as a highly efficient catalyst for promoting the formation of silica. This leads to the facile formation of the one-dimensional LPEI@silica hybrid nanostructure. Further studies indicated that this method of cooling a hot solution normally produced a mixture of nanoribbons and nanofibers with diameters ranging from 30 to 150 nm [36]. A removal of the LPEI core from the nanofibers led to the formation of hollow silica but without control over the final structures. Currently, a facile fabrication of ultrathin (i.e., about 10 nm) high-quality silica nanotubes still remains a challenge.

In contrast to the free base LPEI, which is insoluble in water at room temperature, the protonated LPEI–H^+ is freely soluble in water under ambient conditions. This feature is actually desirable for the self-assembly of LPEI from LPEI–H^+ via a simple neutralization and deprotonation route at ambient temperature. Very recently, we have demonstrated the synthesis of thin films, which consisted of either LPEI@silica hybrid or silica nanotubes. This was achieved through a key step of the neutralization of LPEI–H^+, which was absorbed at the substrate before [37]. That is, the substrate was dipped into an aqueous solution of LPEI–H^+ to adsorb the polymers and then dipped into alkali solution for the neutralization. This self-assembly provided very thin films of LPEI fibrils that allowed for the controlled mineralization of silica, which resulted in hierarchically structured thin coatings composed of LPEI@silica hybrid nanotubes. However, the synthesis of silica nanotube powders through the alkali-induced self-assembly route was not studied systematically. In this paper, we examined the synthesis and the properties of the silica nanostructures in detail. The self-assembly of LPEI was promoted by adding alkali into aqueous solution of LPEI–H^+. The transformation of the soluble protonated LPEI into the insoluble free base led to the growth of crystalline fibrils. These LPEI fibrils acted as template/scaffold/catalysts for the controlled silicification that afforded LPEI@silica hybrid nanotubes, which can be subsequently changed into pure silica nanotubes by removing the organic LPEI. Moreover, we also addressed the possibility to synthesize silica–carbon composite nanotubes by exploiting hybrid chemistry with LPEI@silica nanotubes. We confirmed that a room-tempera-

ture alkali-induced approach to the formation of silica yields highly controlled ultrathin silica nanotubes with uniform diameter of 10 nm and inner hollows of around 3 nm. The hybrid LPEI@silica nanotubes were further applied to create silica/carbon hybridized nanotubes by alternative adsorption of ionic polymers and subsequent carbonization.

Results and Discussion

Silica nanotubes templated by alkali-induced LPEI fibrils. Self-assembled LPEI fibrils were prepared by dropping NaOH solution (1 mL, 5 M) into 5 mL of an aqueous solution of LPEI·HCl (containing 0.5 g) with a molar ratio of [OH]/[EI] = 0.8 at room temperature. The resulting LPEI fibrils were dispersed in 15 mL of water (pH 7.2) and then mixed with 1.5 mL of methyl silicate 51 (MS51) and kept at room temperature for 1 h. The resulting LPEI@silica hybrid nanotubes as well as the products of a calcination at 800 °C were characterized by SEM and TEM. As shown in Figure 1A, two-dimensional silica mats with diameters of ca. 1–2 μm were observed. The high-magnification SEM image indicates that the mat is thin, and composed of very thin one-dimensional nanostructures (Figure 1B). To examine the structure of the nanotubes, the sample was further visualized by TEM. As shown in Figure 1C, the mat is densely knitted from straight one-dimensional nanotubes as the elemental nanostructure. The nanotubes are highly uniform with a diameter of 10 nm and a wall thickness of roughly 3 nm. While self-assembled polypeptides could template the formation of silica nanotubes with uniform diameter, it still remains challenge for the polypeptide template to synthesize stable silica nanotube structures with very small diameters (i.e., 10 nm) [21-27]. Moreover, polypeptides are unsuitable for the large-scale production of silica nanotubes. In contrast, LPEI is one of simplest synthetic polymers and its alkali-induced self-assembly can be easily performed in water at room temperature. According to the recipe to the silica nanotubes shown in Figure 1A–C, we succeeded in the kilogram scale synthesis. To verify the individual characteristic of the alkali-induced self-assembly, the silica formation templated by the LPEI aggregates obtained by cooling a hot LPEI solution procedure was carried out under comparative conditions and the product was subjected to SEM and TEM (see Figure 1D–F). Remarkably, a different silica structure of nanoribbons with a typical width of 100–200 nm was produced. This indicates that large ribbon-like aggregates of LPEI were induced when naturally cooling the hot solution of LPEI because of the relatively slow crystallization. In contrast, the alkali-induced self-assembly of LPEI occurred rapidly because the deprotonation reaction is a fast process. Comparatively, the LPEI fibrils from rapid crystallization-driven self-assembly serve as templates that allow for a well-controlled silicification.

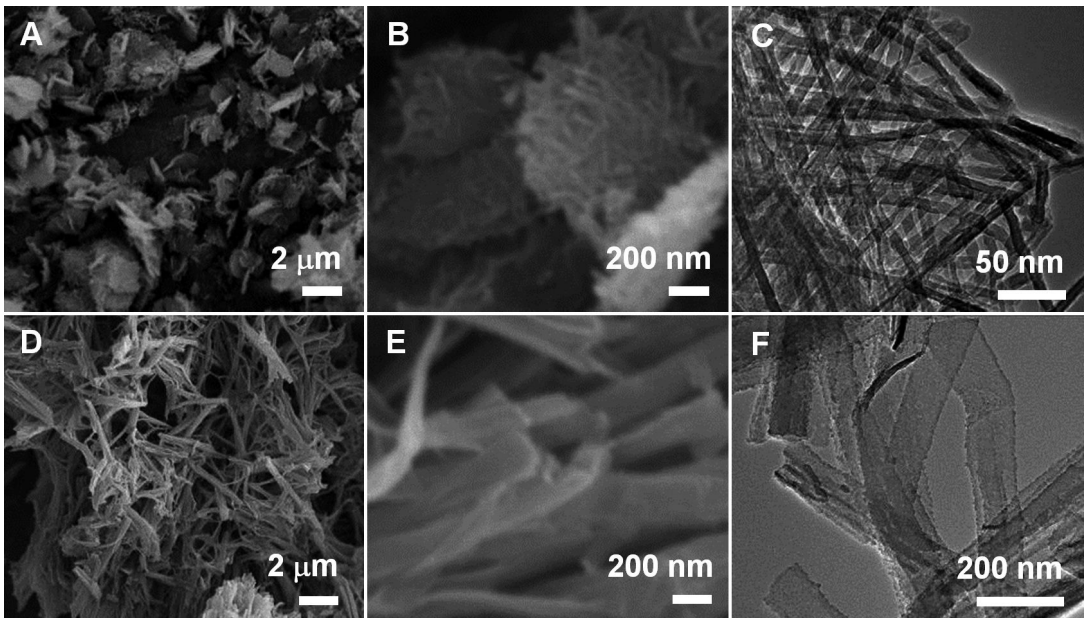

Figure 1: SEM (A, B, D and E) and TEM (C and F) images of silica nanotubes synthesized by alkali-induced room-temperature self-assembly of protonated LPEI (A–C) and silica nanoribbons formed by temperature-induced self-assembly of LPEI (D–F). The LPEI template for the formation of silica nanoribbons was prepared by naturally cooling a 10 mL of hot solution of 3 wt % LPEI. In order to synthesize the silica nanotubes, self-assembled LPEI aggregates were prepared by first dropping 1.0 mL of aqueous NaOH solution (5.0 M) into a mixture of 0.5 g of LPEI·HCl and 5 mL of water, and then washing the crystalline LPEI aggregates to pH 7.0 with centrifugation–redispersion cycles. The silica depositions are the same for the formation of nanotubes and nanoribbons. The latter was performed by adding 1.5 mL of MS51 into 15 mL of aqueous dispersion of LPEI aggregates for 1.0 h at room temperature.

The surface areas and pore size distributions of the silica nanotubes and nanoribbons shown in Figure 1 were characterized with nitrogen adsorption and desorption measurements. As shown in Figure 2A, the BET adsorption–desorption isotherms of both silica nanotubes and nanoribbons can be described as type-IV hysteresis loops, which are indicative of the mesoporous nature of nanotubes and nanoribbons. The BET specific surface areas of the silica nanotubes and nanoribbons were calculated to be 307 m^2/g (run 1 in Table 1) and 404 m^2/g (run 2 in Table 1), respectively. Barrett–Joyner–Halenda (BJH) calculations derived from the adsorption branch showed that there is no peak value observed for silica nanoribbons. This suggests that the size of the mesopores arises from slit-like structures formed by randomly collapsed nanoribbons. In comparison, the silica nanotubes exhibited a narrow pore distribution with a peak value of around 3.5 nm, which corresponds to the hollow inner of nanotube (Figure 2B) [38,39], which is in good agreement with the TEM observations (Figure 1C). This BET result indicates that our silica nanotubes have an excellent thermal stability compared to the conventional mesoporous silica (i.e., M41S), which may collapse upon calcination at temperatures higher than 750 °C [40]. Regarding this, it should be noted that the conventional surfactant-based sol–gel reaction is catalyzed by HCl or NaOH. In this system, the silica sol forms in aqueous solution and then subsequently precipitates within the space of the template to form silica gel. In comparison, in our LPEI aggregate-based silica deposition, the hydrolysis and polycondensation of alkoxysilane occurs simultaneously and selectively on the surface of the LPEI templates. This characteristic hydrolytic polycondensation process gives a homogeneously structured SiO_2 framework. We assume that such silica walls contribute to improve the thermal stability of silica nanotubes.

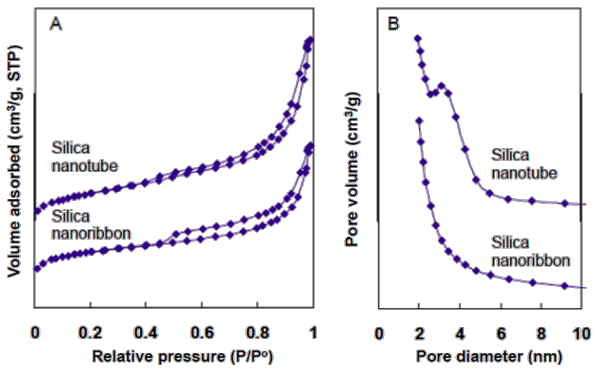

Figure 2: N_2 adsorption/desorption isotherms (A) and BJH pore-size distribution curve obtained from the adsorption branch (B) of silica nanoribbon and silica nanotube. The synthesis conditions are the same to that of the samples shown in Figure 1. The sample was calcined at 800 °C in air for 3 h with at heating rate of 2.5 °C per min.

Silicification reaction time. To evaluate the ability of LPEI fibrils to catalyze the formation of a silica framework, we performed solid-state ^{29}Si CP-MAS NMR measurements of the LPEI@silica nanotubes, which were synthesized with different silicification times ranging from 5 to 240 min. The LPEI fibrils

Table 1: Summary of the molar ratios of [OH]/[EI] for the synthesis of the LPEI templates, the TGA analysis of the composition of LPEI@silica hybrid nanostructures and BET data of the silica nanostructures obtained by calcination of LPEI@silica hybrid at 800 °C at air.[a]

run	ratio of [OH]/[EI] for self-assembly	TG analysis (weight loss %)	BET surface area (m^2/g)	t-plot micropore area (m^2/g)	t-plot external surface area (m^2/g)	BJH desorption cumulative volume of pores (cm^3/g)	maximum of pore width (nm)
1	0.8	30.6	356	61	295	0.673	3.9
2	0.8	24.6	320	82	238	0.558	4.2
3	0.8	23.5	317	91	226	0.533	4.2
4	0.56	19.0	146	33	114	0.395	—
5	3.2	28.68	360	25	335	0.698	3.53
6	0.8	18.9	244	114	130	0.279	—
7	0.8	25.8	387	81	306	0.696	4.2
8	0.8	25.3	294	60	234	0.538	4.3
9	0.8	25.3	419	86	333	0.740	4.2
10	0.8	26.64	477	251	226	0.45	—
11	3.2	29.6	430	162	268	0.625	—

[a]run 1: [NaOH]/[EI] = 0.8, silicification 5 min; run 2: [NaOH]/[EI] = 0.8, silicification 60 min; run 3: [NaOH]/[EI] = 0.8, silicification 240 min; run 4: [NaOH]/[EI] = 0.56, silicification 60 min; run 5: [OH]/[EI] = 3.2, silicification 60 min; run 6: [NaOH]/[EI] = 3.2, [MS-51] = 23.1 wt %, silicification 60 min; run 7: [NaOH]/[EI] = 0.56, [MS-51] = 9.1 wt %, silicification 60 min; run 8: [NaOH]/[EI] = 0.56, [MS-51] = 4.6 wt %, silicification 60 min; run 9: [NaOH]/[EI] = 0.8, [MS-51] = 1.1 wt %, silicification 60 min; run 10: [NH_4OH]/[EI] = 0.8, MS-51/H_2O = 1.5/15 (v/v), silicification 60 min; run 11: [NH_4OH]/[EI] = 3.2, MS-51/H_2O = 1.5/15 (v/v), silicification 60 min.

were prepared by dropping 1.0 mL of NaOH solution (5 M) into an aqueous solution containing 6.0 mL of water and 0.5 g of LPEI·HCl (molar ratio of [OH]/[EI] = 0.8) at room temperature. After water washing, the LPEI fibrils were dispersed into 15 mL of water with pH 7.2. To this dispersion, 1.5 mL of MS51 was added and the mixture was stirred at room temperature for different times. We found that the reaction at 5 min produced a silica framework with Q4/Q3 = 0.88 (no signal of Q2 detectable), indicating that silica with a high degree of polycondensation was produced within a very short time (Figure 3A). When the reaction times were increased up to 60 min and 240 min, the degree of polycondensation increased, which is shown by the ratios Q4/Q3 of 1.30 and 2.1, respectively. After removing the organic LPEI by calcining at 800 °C, the samples were examined by nitrogen adsorption and desorption measurements. It was surprising that only five minutes of the silicification reaction is enough to impart the nanosized hollow structure in the resulting silica, which was evidenced by BJH calculations from adsorption branch that shows a peak value of 3.9 nm corresponding to a nanotubular silica structure (Figure 3B and run 1 in Table 1). We also confirmed that this silica nanotube has the BET specific surface area of 356 m^2/g (run 1 in Table 1 and Figure S1). The silica nanostructures from the hydrolytic condensation reaction times of 60 min and 240 min have the BET specific surface areas of 320 m^2/g (run 2 in Table 1) and 317 m^2/g, respectively (run 3 in Table 1). Their pore size distribution determined by the BJH calculations from adsorption branch has the same peak value of 4.2 nm (Figure 3B) indicating the existence of hollow structure. SEM images demonstrated that the nanotubes synthesized from 5 min, 60 min and 240 min have similar mat morphology (Figure S1 in Supporting Information File 1). Obviously, LPEI fibrils exhibited the high-efficient ability as template/scaffold/catalyst for rapid formation of silica-based wall with high toughness around polymer template via temporally and spatially controlled silicification. This rapid LPEI-mediated silicification would be complete when the reaction time increased longer than 60 min, due to that the catalytic LPEI has been significantly buried into silica matrix so that it became not available for further catalyzing the reaction.

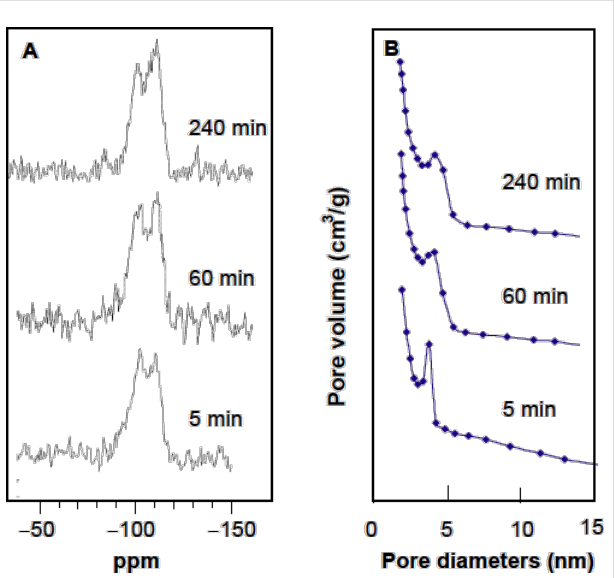

Figure 3: (A) Solid state ^{29}Si CP MAS NMR spectra of LPEI@silica hybrid nanotubes formed after silicification times of 5 min, 60 min and 240 min. The LPEI aggregates were prepared by first dropping 1.0 mL aqueous NaOH solution (5.0 M) into a mixture of 0.5 g of LPEI·HCl and 5 mL of water ([OH]/[EI] = 0.8), then washing the crystalline LPEI aggregates to pH 7.0 with centrifugation–redispersion cycles. The silica deposition was performed by stirring a mixture of 1.5 mL of MS51 and 15 mL of aqueous dispersion of LPEI aggregates at room temperature. (B) BJH pore-size distribution curve obtained from the adsorption branch of the calcined nanotubes of the LPEI@silica hybrid nanotubes shown in (A).

Effect of the molar ratios of [OH]/[EI]. Furthermore, we addressed the dependence of the formation of silica nanotubes on the molar ratios of [OH]/[EI]. Firstly, we prepared self-assembled LPEI aggregates with a decreased molar ratio of [OH]/[EI]. For example, 0.7 mL of NaOH solution (5 M) was dropped into a solution containing 6.0 mL of water and 0.5 g of LPEI·HCl ([OH]/[EI] = 0.56). The mixture was stirred at room temperature for 24 h for LPEI self-assembly before washing and silicification. Silica deposition was performed by mixing 1.5 mL of MS51 and 15 mL of the aqueous dispersion of LPEI aggregates at room temperature for 1 h. As shown in Figure 4A and B, large aggregates composed of two-dimensional films were formed. TEM observation demonstrated that the nanofilm is highly transparent for TEM electron beam (Figure 4C), which suggests that the film is very thin. The BET studies indicated that the nanofilm has a relatively low surface area of 146 m^2/g (run 4 in Table 1 and Figure S2 in Supporting Information File 1) and no peak value was observed in the pore distribution. Different to the silica nanotube formation from a higher molar ratio of [OH]/[EI] (0.8, Figure 1A–C), the decreased molar ratio of [OH]/[EI] induced the formation of nanofilms. This could be attributed to a slower crystallization rate of LPEI, because of insufficient neutralization of the protonated LPEI. On the other hand, when the molar ratio of [OH]/[EI] is higher than 0.8, the self-assembled LPEI fibrils could successfully template the formation of silica nanotubes. Figure 4D–F show typical electron microscopic images of silica nanotubes formed by using a molar ratio of [OH]/[EI] = 3.2. Both SEM (Figure 4D and E) and TEM (Figure 4F) images proved the formation of similar mat-like powders, which consist of silica nanotubes. BET studies showed a surface area of 360 m^2/g and a BJH peak value of 3.5 nm for the tube structures (run 5 in Table 1 and Figure S2 in Supporting Information File 1). These values are similar to those achieved with a molar ratio [OH]/[EI] of 0.8.

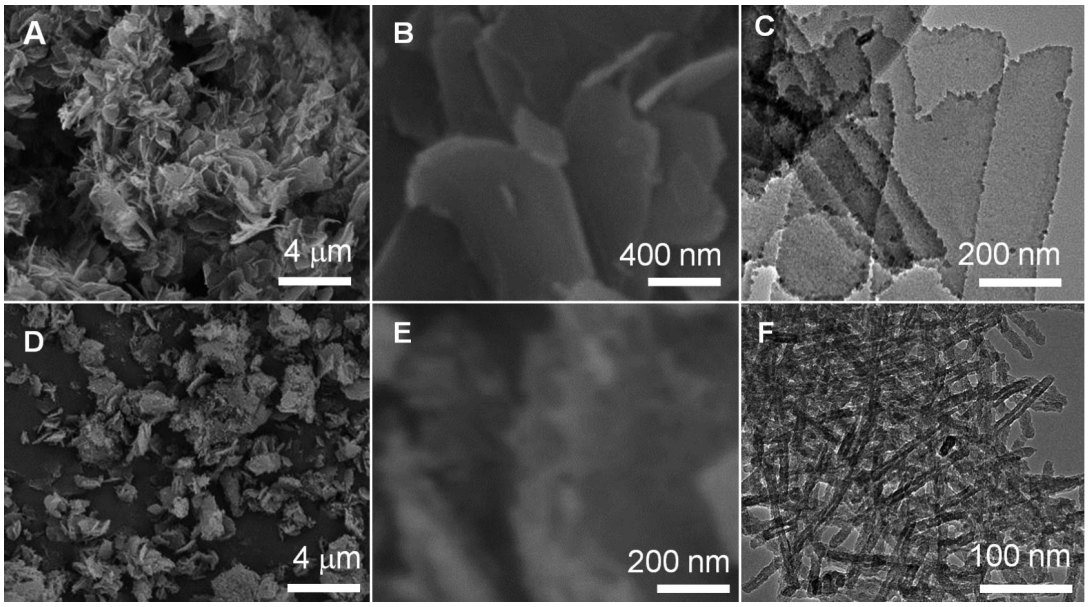

Figure 4: SEM (A, B, D and E) and TEM (C and F) images of silica prepared with molar ratios [OH]/[EI] of 0.56 (A–C) and 3.2 (D–F). The LPEI aggregates were formed first by dropping aqueous NaOH solution into a mixture of 0.5 g of PEI-HCl and 6 mL of water and then washing aggregates with water to pH 7.0. The silicification conditions are the same as described in Figure 1.

XRD measurements were performed in order to investigate the template role of LPEI fibrils for the formation of nanotubes. Three types of LPEI fibrils were prepared with molar ratios of [OH]/[EI] at 0.8, 1.6 and 3.2. The silica depositions were performed with the same conditions as given in Figure 4. We found that the three LPEI samples showed strong diffraction peaks of the crystalline LPEI at 2θ = 23°, 27° and 30° (Figure 5A). After the deposition reaction on the template prepared from the molar ratio of [OH]/[EI] 0.8, the peaks at 2θ = 27° and 30° completely disappeared and the peak at 2θ = 23° became almost undetectable (Figure 5B): This indicated that the crystalline LPEI template has almost disappeared with the silica deposition and the formation of LPEI@silica hybrid tubular walls (Scheme 1). A similar phenomenon is seen well in our previous results, in which the silica deposition was carried out on the same LPEI template but with an extremely diluted silica source. In contrast, when using LPEI fibrils from the [OH]/[EI] molar ratios of 1.6 and 3.2 for silicification, the diffraction peaks due to crystalline LPEI template after silica deposition were obviously detected (Figure 5B). This means that the silicification only partially damaged the crystalline template. We speculate that the higher molar ratios [OH]/[EI] result in LPEI fibrils with an enhanced crystallization structure that can partially survive the silicification reaction. Therefore, it is reasonable to suggest that LPEI fibrils from higher molar ratios of [OH]/[EI] can allow for the formation of hybrid nanostructures that have a crystalline LPEI core and LPEI@silica hybrid wall (Scheme 1). These hybrid structures (Figure 4D–F) will yield nanotubular silica after the LPEI core is removed by calcination.

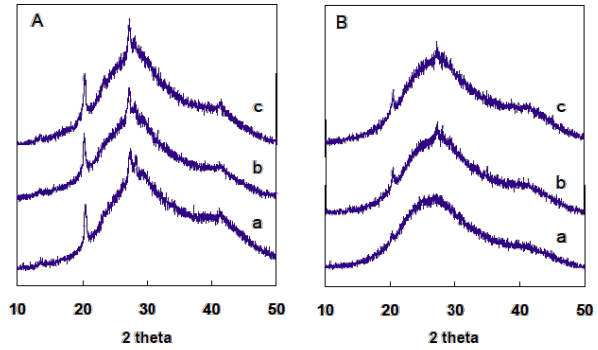

Figure 5: XRD profiles of LPEI aggregates (A) and LPEI@silica hybrid nanostructures (B). The LPEI aggregates were prepared by dropping 5.0 M NaOH solution into a mixture of 0.5 g of LPEI·HCl and 6 mL of water with ratios [OH]/[EI] of 0.8 (a), 1.6 (b) and 3.2 (c). The silica deposition conditions are the same for a, b and c: 1.5 mL of MS51 was added into 15 mL of aqueous dispersion of LPEI aggregates (pH 7.0) and stirred for 1 h at room temperature.

Effect of the silica source concentration. We further found that the silica nanostructure could be controlled by changing the concentrations of the silica source. The LPEI fibrils prepared by using the molar ratio [OH]/[EI] = 0.8 with the same conditions as that used in Figure 1A–C were used in the silica deposition with different MS51 concentrations of 23.1 wt %, 9.1 wt %, 4.6 wt % and 1.1 wt %. SEM observation of the resulted prod-

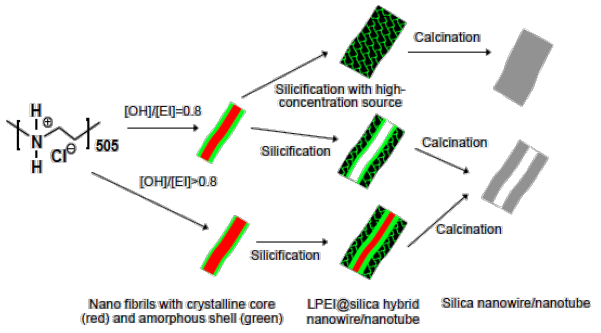

Scheme 1: Proposed formation mechanism of the polyamine-aggregate template for silica nanotubes and nanowires formed by the alkali-induced self-assembly of LPEI.

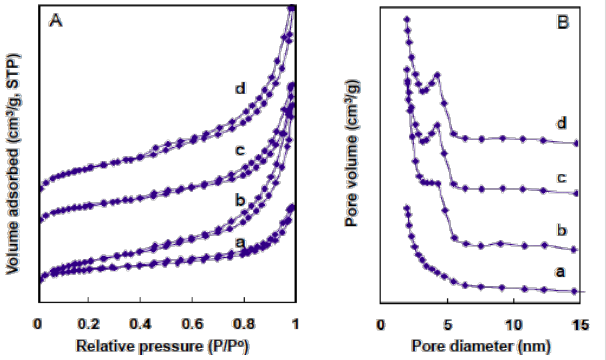

Figure 6: N_2 adsorption/desorption isotherms (A) and BJH pore-size distribution curves obtained from the adsorption branch (B) of silica nanostructures synthesized by using silica source (MS51) concentrations of 23.1 wt % (a), 9.1 wt % (b), 4.6 wt % (c) and 1.1 wt % (d). LPEI aggregates was prepared by first dropping 1.0 mL of aqueous NaOH solution (5.0 M) into a mixture of 0.5 g of LPEI·HCl and 5 mL of water ([OH]/[EI] = 0.8), then washing the crystalline LPEI aggregates to pH 7.0 with centrifugation–redispersion cycles. The silica deposition conditions are the same as described in Figure 1.

ucts demonstrated that all the samples have a mat-like morphology (Figure S3 in Supporting Information File 1), which is similar to the silica nanotubes shown in Figure 1A–C. The N_2 adsorption/desorption measurements provided important information about the difference in the nanostructures synthesized from the different concentrations of MS51. As shown in Figure 6, the silica structures that were synthesized from relatively low MS51 concentrations (9.1 wt %, 4.6 wt % and 1.1 wt %) exhibited BET surface areas from around 290 to 420 m^2/g (runs 7, 8 and 9 in Table 1) with obvious type-IV hysteresis loops (Figure 6A), and peak values of around 4.2–4.3 nm from BJH pore-distribution curves (Figure 6B). This BET study confirmed a silica nanotube formation, which is consistent with that shown in Figure 1A–C. A remarkably different result is that the silica synthesized at high MS51 concentration of 23.1 wt % showed a significantly decreased BET surface area (244 m^2/g, run 6 in Table 1) and a relatively smaller hysteresis loop (Figure 6A) without a peak value in the pore-size distribution (Figure 6B). This indicates the formation of silica as solid nanowires but not nanotubes. Presumably, a too high concentration of the silica source leads to an extremely high rate of hydrolysis and polycondensation of the alkoxysilane around the delicate LPEI fibrils, which could completely damage the crystalline LPEI. The collapsed LPEI then allowed for the silicification reaction to proceed continuously into the core domain of the hybrid nanostructures. Probably, the increased amount of the byproduct MeOH, which can dissolve LPEI aggregates, from this fast hydrolysis of high-concentration of oligomer methoxysilane also accelerates the collapse of the LPEI crystallites.

Effect of the alkali basicity. We also tried to use different alkalies to induce the room-temperature self-assembly of LPEI from the protonated state. The synthesis conditions are similar to that used for the silica formation induced by NaOH. Figure 7 shows the SEM images of silicas prepared by using ammonia solution (NH_4OH) to induce self-assembly of LPEI with molar ratios [OH]/[EI] = 0.6, 0.8 and 3.2. We found that silica nanofilms were formed by using a molar ratio [OH]/[EI] = 0.6 (Figure 7A and Figure 7B), because the LPEI crystallization was delayed due to weak basicity of the ammonia solution and a low degree of deprotonation of LPEI–H^+. This is consistent with the formation of silica nanofilms by using NaOH with low molar ratios [OH]/[EI]. Furthermore, when increasing the molar ratio [OH]/[EI] to 0.8, the templated silicification produced large silica aggregates, which were composed of ribbon-like structures (Figure 7C and D). As shown in Figure S4 (Supporting Information File 1), the BET measurement demonstrated that the N_2 adsorption/desorption isotherm of this silica structure (see run 10 in Table 1) is similar to that synthesized by temperature-induced LPEI self-assembly (Figure 2). No peak value of the pore size distribution was observed (Figure S4 in Supporting Information File 1). To further confirm the effect of ammonia solution on the formation of silica nanostructure, the LPEI self-assembly was performed by using a molar ratio [OH]/[EI] = 3.2. As shown in Figure 7E and Figure 7F, large aggregates composed of a mixture of small silica nanoribbons and nanofibers were formed. The BET study did not show any obvious proof for a uniform formation of nanotube structures (run 11 in Table 1, Figure S4 in Supporting Information File 1).

The formation of this silica nanoribbons from an ammonia-induced LPEI template is dramatically different to the generation of silica nanotubes by NaOH-induced LPEI self-assembly with the same molar ratio of [OH]/[EI]. This could be partially attributed to the relatively weak basicity of ammonia solution compared to NaOH, which might not allow for a sufficient

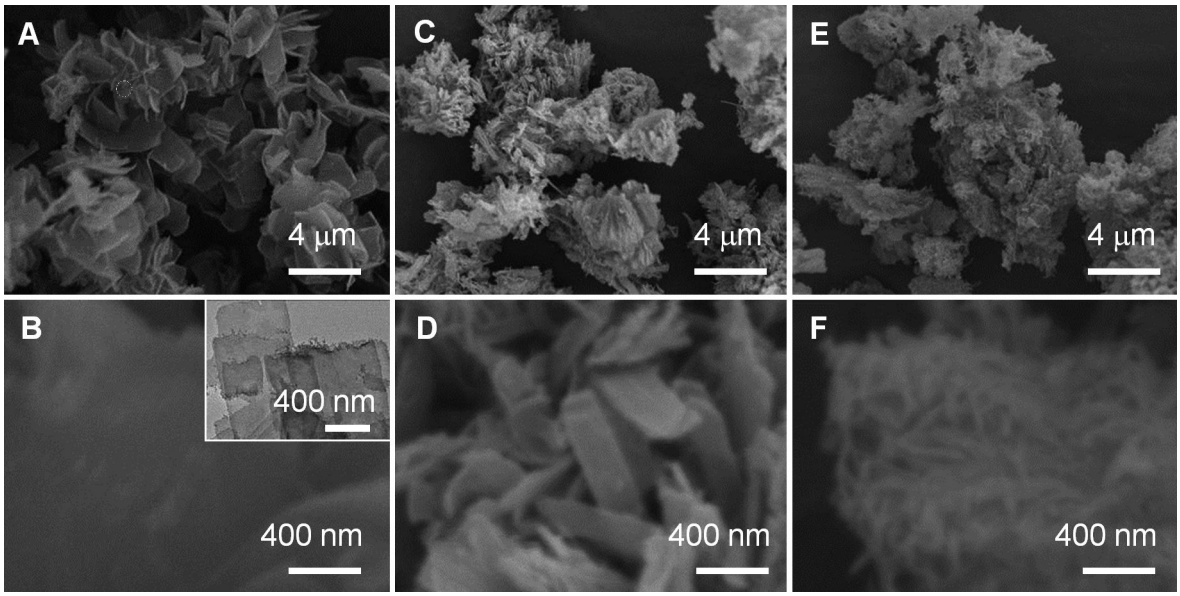

Figure 7: SEM images of silica structures, which were formed by adding different amounts of ammonia solution (NH_4OH) to induce the crystallization-driven self-assembly of LPEI·HCl in water. The ratios of [OH]/[EI] for LPEI self-assembly are 0.6 (A and B), 0.8 (C and D) and 3.2 (E and F). The inset of B is a TEM image of the silica nanofilms. The silica deposition conditions are the same for A, B and C, which was performed by adding 1.5 mL of MS51 into 15 mL of aqueous dispersion of LPEI aggregates (pH 7.0) and stirring for 1 h at room temperature.

deprotonation of LPEI–H^+ to cause the necessary rapid generation of LPEI aggregates. Similar silica nanoribbons were obtained by the use of LPEI aggregates formed from the deprotonation of LPEI–H^+ by using the organic alkali Et_4NOH (Figure S5A–C). In contrast, the utilization of relatively strong alkalies (KOH and LiOH) for the LPEI self-assembly produced the silica nanotube structures (Figure S5D–I). However, it should be noted that well-defined thin films of silica nanotubes could be synthesized even by using ammonia under the comparative conditions with using NaOH [37]. This could be attributed to the extreme excess of ammonia relative to the trace of LPEI–H^+ adsorbed on substrate, which enables a rapid deprotonation reaction of LPEI–H^+ on the substrate.

Photoluminescence. It has been known that silica with a porous structure can be, after annealing, used as material, which emits visible light [41-44]. Although the reason of the silica photoluminescence is not clear, it is mainly attributed to the formation of oxygen defects on the SiO_2 framework [44]. To examine the photoluminescence properties, the LPEI@silica hybrid nanostructures (nanotubes and nanoribbons, synthetic conditions given in Figure 1) were calcined at 1000 °C under N_2 atmosphere. In general, the silica structures prepared from sol–gel procedures emit visible light with wavelengths smaller than 500 nm. However, as shown in Figure 8, a distinct emission centered at 540 nm was observed for the silica nanotubes under a maximum excitation wavelength of 320 nm. In comparison, no obvious emission was observed for the silica nanoribbons

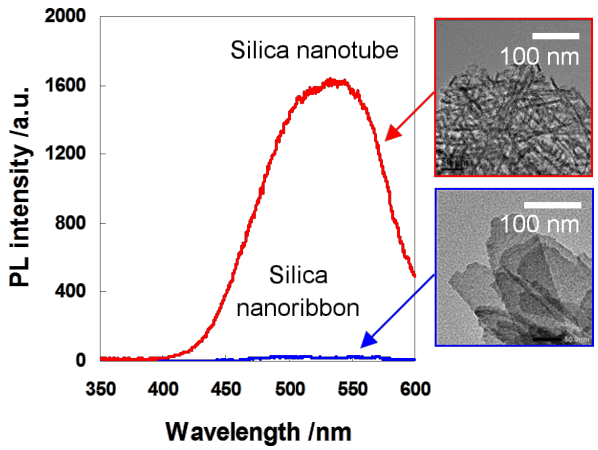

Figure 8: Phosphorescence emission spectra (λ_{Ex} = 320 nm) of silica nanotubes and nanoribbons that were synthesized by calcining the corresponding LPEI@silica hybrid nanotubes (Figure 1A–C) and nanoribbons (Figure 1D–F) under N_2 atmosphere at 1000 °C.

treated under the same N_2-atmosphere pyrolysis conditions. In addition, the pure silica nanotubes calcined under air atmosphere did not show such emission (data not shown).

Although the detailed mechanisms of this special photoluminescent property of silica nanotubes are unknown at present, we expect two factors to be important in our case. One is the unique tubular structure with 3-nm wall and 3-nm inner hollow that would be in favor of generating geometrically stable

photoactive sites, and the other one is the existence of trace carbon in the silica nanotubes (less than 0.9 wt % estimated by TGA) which would be doped into the silica frame to compose the photoactive sites. Probably, these two factors are vital for generating a green emission at over 540 nm. This is an interesting phenomenon and needs further investigation.

Silica nanotube/carbon composite. Silica/carbon composites are potentially applicable for electrochemical devices and selective solar absorber [45,46]. There have been some reports on the carbonization of porous silica–polymer [47] and organosilica/surfactant composites [48,49]. However, the synthesis of silica–carbon composite nanotube materials is still very rare. Liu and co-workers [50] have recently reported the fabrication of silica–carbon nanotubes by carbonization of organosilica nanotubes, which were synthesized by using expensive ethylene- or phenylene-bridged alkoxysilanes through the soft-template assembly method mediated by commercially available P123 in dilute solution.

We found that the direct carbonization of synthesized LPEI@silica hybrid nanotubes under N_2 atmosphere (Figure 1A–C, LPEI content of 29 wt %) produced silica nanotubes with a carbon content of 0.84 wt % ("a" in Figure 9A). In order to increase the carbon content, we performed anionic adsorption of poly(4-styrenesulfonic acid) (PSS) PSS on the LPEI@silica nanotubes, which have a cationic surface because of the hybrid nature of the framework. The carbonization of the sample after the adsorption of one layer of PSS (polymer content: 47.9 wt %) produced silica/carbon composites with a much higher of carbon content (7.9 wt %, "b" in Figure 9A). The network structure of nanofibers of this silica/carbon composite was clearly observed by TEM observation (Figure 10A). The Raman spectrum shows very weak D and G bands at 1350 cm^{-1} and 1580 cm^{-1}, respectively, which is indicative of the formation of disordered carbon in the composite ("b" in Figure 9B). We found that the carbon content in the composites could be further increased to 16.2 wt % ("c" in Figure 9A) by performing a second PSS adsorption (polymer content: 65.9 wt %). The Raman peaks of D and G bands ascribed to amorphous carbon then became stronger ("c" in Figure 9B). In the TEM images, one can still see a fibrous network in a carbon matrix, although the original thin mat of silica nanotubes became thicker (Figure 10B). These results reveal that silica/carbon hybrid nanotubes could be easily synthesized by making use of the hybrid nature of the LPEI@silica nanotubes and the composition of silica and carbon could be precisely controlled by polyelectrolyte adsorption.

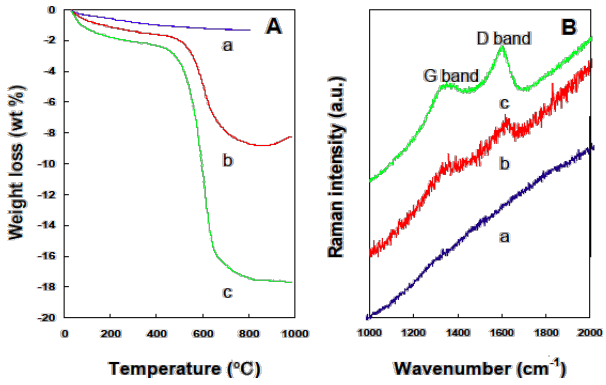

Figure 9: TGA (A) and Raman spectra (B) of silica/carbon composite nanotubes. The samples of a (0.8 wt % carbon), b (7.9 wt % carbon) and c (16.2 wt % carbon) were prepared by calcining LPEI@silica hybrid nanotubes (a), LPEI@silica nanotubes with one layer of adsorbed PSS (b) and two layers of adsorbed PSS (c) under N_2 atmosphere, respectively.

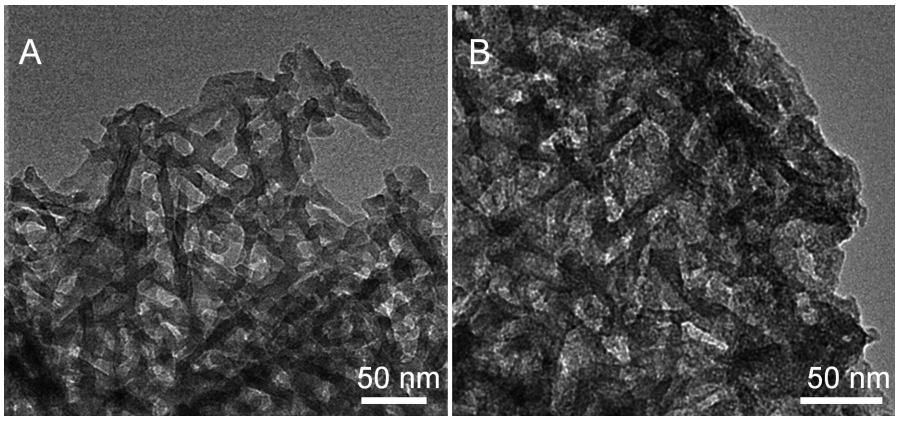

Figure 10: TEM images of silica/carbon composite mats with a nanofibrous network prepared by calcining LPEI@silica nanotubes under N_2 atmosphere after PSS adsorption of one layer (A) and two layers (B).

Conclusion

We have demonstrated that well-defined silica nanotubes of 10 nm diameter could be easily synthesized in solution through a templated silica mineralization on self-assembled LPEI fibrils, which in turn were formed by alkali-induced rapid deprotonation reaction of LPEI–H^+ at room temperature. We demonstrated that a high molar ratio [OH]/[EI], a lower concentration of the silica source and stronger alkalies are important factors for the controlled formation of silica nanotubes. This approach is based on a widely-available low-cost synthetic polyamine and very mild silicification conditions (aqueous media, room-temperature and high efficiency), which could allow for an easy scale-up of silica nanotube fabrication and subsequently for wide technological applications. The silica nanotubes can be tuned to an emitter of visible light through the pyrolysis under N_2 atmosphere. Moreover, silica/carbon composite nanotubes with tunable compositions could be synthesized by adsorption of a polyelectrolyte on LPEI@silica hybrid nanotubes and the subsequent carbonization.

Experimental

Materials. LPEI·HCl with about 500 EI repeating units was synthesized by the hydrolysis of the precursor poly(ethyloxazoline) (M_w = 50,000, M_w/M_n = 1.9, Aldrich) in an aqueous solution of 5 M HCl at 100 °C for 12 h, according to our previous method [35]. After hydrolysis, the white precipitates LPEI·HCl were washed with methanol for 3 times and dried in vacuum at 60 °C. LPEI was prepared by neutralizing LPEI·HCl in water, subsequently washing by water and acetone, and finally drying at 40 °C under vacuum. Poly(4-styrenesulfonic acid) (PSS, M_w = 75000, 18 wt % in water) was purchased from Aldrich. Methyl silicate 51 (MS51, 5-mer of tetramethoxysilane) was purchased from Matsumoto Chemical Co., Japan and was used as received. Other chemicals were used as received. Deionized water was used in all experiments.

Synthesis of silica nanostructure by templating alkali-induced LPEI aggregates. LPEI self-assembly were simply induced by dropping alkali (NaOH, NH_4OH, KOH, LiOH or Et_4NOH) into aqueous solution of LPEI·HCl with various molar ratios of [OH]/[EI] at room temperature. The solid fraction of LPEI aggregates appeared after the neutralized solution was washed with water and centrifuged until the pH of the supernatant reached a neutral value. The silicification was performed by adding MS51 into an aqueous dispersion of LPEI aggregates at room temperature. Specifically, a typical synthesis for silica nanotubes is as follows: 1 mL of an aqueous solution of NaOH (5 M) was dropped into a solution that contained 0.5 g of LPEI·HCl and 5 mL of water with a molar ratio [OH]/[EI] = 0.8. After the formation of self-assembled crystalline aggregates of LPEI, the mixture was washed with water for three cycles of centrifugation–redispersion. To 15 mL of an aqueous dispersion of LPEI aggregates (pH 7.2) was added 1.5 mL of MS51 and the mixture was stirred at room temperature for typically 1 h for the formation of LPEI@silica hybrid nanotubes. After water washing and drying, a white powder was obtained. LPEI@silica hybrid nanotubes were calcined by heating the sample up to 800 °C at a heating rate of 2.5 °C/min, and maintaining this temperature for 4 h under air atmospheres in order to completely remove LPEI and hence obtain pure silica nanotube.

Synthesis of silica nanotube@carbon composite. To increase the carbon content of silica/carbon composite nanotubes, an alternative adsorption of PSS and branched PEI was performed. 0.5 g of LPEI@silica hybrid nanotubes was dispersed into 30 mL of an aqueous solution of PSS (1 wt %), and the mixture was stirred at room temperature for 3 h for the adsorption of PSS. After centrifugation and washing with water, LPEI@silica@PSS (**S**) was obtained. The adsorption of branched PEI on **S** (**SE**) was conducted by dispersing **S** into 30 mL of aqueous solution of branched PEI (1 wt %) for 3 h. After a similar adsorption of PSS, LPEI@silica nanotubes with two PSS layers (**SES**) were finally obtained. The carbonization was performed by heating the samples firstly from room temperature to 900 °C at a heating rate of 2 °C/min and keeping the temperature constant at 900 °C for 8 h. Then the temperature was raised further up to 1000 °C at a rate of 2 °C/min and was held constant for 1 h.

Characterizations. Thermogravimetry analysis was performed on a TG-DTA 6300 instrument (SII Nano technology Inco., Japan). The measurement was conducted by heating LPEI@silica hybrid nanotube powders from 20 °C to 800 °C at a heating rate of 20 °C/min under air atmosphere. The morphology and nanostructure of silica was visualized by using a scanning electron microscope (SEM, Keyence, VE9800, Japan, working at 8 kV). The samples were sputter-coated with a thin layer of Pt prior to observation. Transmission electron microscopy (TEM) studies were conducted on a JEOL JEM-2200FS instrument operating at 200 kV. X-ray diffraction measurements (XRD) were carried out with a Rigaku RINT-TTR II diffractometer (Rigaku Co., Japan), using Cu Kα radiation (λ = 1.54 Å). Nitrogen sorption-isotherm measurements were performed on a Tristar 3000 volumetric adsorption analyzer (Micromeritics). Before the adsorption measurements, the samples were outgassed at 300 °C overnight. The degree of polycondensation (Q4, Q3 and Q2) of the LPEI@silica hybrid nanotube powders were characterized by ^{29}Si CP-MAS NMR spectroscopy, and the spectra were recorded on a JEOL-400 MHz NMR spectrometer. Raman spectra were recorded with a Renishaw Raman imaging microscope. Radiation of 514 nm

from an Ar-ion laser was used as the excitation source. The photoluminescence (phosphorescence) spectra of silica nanostructure were obtained with Hitachi F-4500 fluorescence spectrophotometer, in which the fluorescence emission was cut off electrically.

Supporting Information

Supporting Information features SEM images, charts of N2 adsorption/desorption isotherms and pore size distributions of silica nanotubes synthesized under different conditions. In addition, a TGA profile of the hybrids that consisted of organic and silica nanotubes is given.

Supporting Information File 1

Additional SEM pictures, charts of N2 adsorption/desorption isotherms and pore size distributions, and TGA charts.
[http://www.beilstein-journals.org/bjnano/content/supplementary/2190-4286-4-90-S1.pdf]

References

1. Jung, J. H.; Rim, J. A.; Lee, S. J.; Cho, S. J.; Kim, S. Y.; Kang, J. K.; Kim, Y. M.; Kim, Y. J. *J. Phys. Chem. C* **2007,** *111,* 2679–2682. doi:10.1021/jp066644w
2. Kohli, P.; Harrell, C. C.; Cao, Z.; Gasparac, R.; Tan, W.; Martin, C. R. *Science* **2004,** *305,* 984–986. doi:10.1126/science.1100024
3. Choi, H.; Park, Y. C.; Kim, Y.-H.; Lee, Y. S. *J. Am. Chem. Soc.* **2011,** *133,* 2084–2087. doi:10.1021/ja1101807
4. Lee, S. B.; Mitchell, D. T.; Trofin, L.; Nevanen, T. K.; Soderlund, H.; Martin, C. R. *Science* **2002,** *296,* 2198–2200. doi:10.1126/science.1071396
5. van Bommel, K. J. C.; Friggeri, A.; Shinkai, S. *Angew. Chem., Int. Ed.* **2003,** *42,* 980–999. doi:10.1002/anie.200390284
6. Shenton, W.; Douglas, T.; Young, M.; Stubbs, G.; Mann, S. *Adv. Mater.* **1999,** *11,* 253–256. doi:10.1002/(SICI)1521-4095(199903)11:3<253::AID-ADMA253>3.0.CO;2-7
7. Jung, J. H.; Park, M.; Shinkai, S. *Chem. Soc. Rev.* **2010,** *39,* 4286–4302. doi:10.1039/c002959a
8. Ono, Y.; Nakashima, K.; Sano, M.; Kaneko, Y.; Inoue, K.; Shinkai, S.; Sano, M.; Hojo, J. *Chem. Commun.* **1998,** 1477–1478. doi:10.1039/a802829j
9. Jung, J. H.; Kobayashi, H.; Masuda, M.; Shimizu, T.; Shinkai, S. *J. Am. Chem. Soc.* **2001,** *123,* 8785–8789. doi:10.1021/ja010508h
10. Adachi, M.; Harada, T.; Harada, M. *Langmuir* **1999,** *15,* 7097–7100. doi:10.1021/la9904859
11. Ji, Q.; Iwaura, R.; Kogiso, M.; Jung, J. H.; Yoshida, K.; Shimizu, T. *Chem. Mater.* **2004,** *16,* 250–254. doi:10.1021/cm034356w
12. Kimura, M.; Miki, N.; Suzuki, D.; Adachi, N.; Tatewaki, Y.; Shirai, H. *Langmuir* **2009,** *25,* 776–780. doi:10.1021/la802991g
13. Chen, Y.; Li, B.; Wu, X.; Zhu, X.; Suzuki, M.; Hanabusa, K.; Yang, Y. *Chem. Commun.* **2008,** 4849–4950. doi:10.1039/B810517K
14. Lei, S.; Zhang, J.; Wang, J.; Huang, J. *Langmuir* **2010,** *26,* 4288–4295. doi:10.1021/la9033707
15. Jiang, J.; Wang, T.; Liu, M. *Chem. Commun.* **2010,** *46,* 7178–7180. doi:10.1039/c0cc00891e
16. Currie, H.; Perry, C. C. *Ann. Bot. (Oxford, U. K.)* **2007,** *100,* 1383–1389. doi:10.1093/aob/mcm247
17. Schröder, H.; Wang, C. X.; Tremel, W.; Ushijima, H.; Müller, W. E. G. *Nat. Prod. Rep.* **2008,** *25,* 455–474. doi:10.1039/b612515h
18. Sumper, M.; Brunner, E. *Adv. Funct. Mater.* **2006,** *16,* 17–26. doi:10.1002/adfm.200500616
19. Brutchey, R. L.; Morse, D. E. *Chem. Rev.* **2008,** *108,* 4915–4934. doi:10.1021/cr078256b
20. Patwardhan, S. V. *Chem. Commun.* **2011,** *47,* 7567–7582. doi:10.1039/c0cc05648k
21. Meegan, J. E.; Aggeli, A.; Boden, N.; Brydson, R.; Brown, A. P.; Carrick, L.; Brough, A.; Hussain, R. A.; Ansell, R. J. *Adv. Funct. Mater.* **2004,** *14,* 31–37. doi:10.1002/adfm.200304477
22. Pouget, E.; Dujardin, E.; Cavalier, A.; Moreac, A.; Valery, C.; Marchi-Artzner, V.; Weiss, T.; Renault, A.; Paternostre, M.; Artzner, F. *Nat. Mater.* **2007,** *6,* 434–439. doi:10.1038/nmat1912
23. Yuwono, V. M.; Hartgerink, J. D. *Langmuir* **2007,** *23,* 5033–5038. doi:10.1021/la0629835
24. Holmström, S. C.; King, P. J. S.; Ryadnov, M. G.; Butler, M. F.; Mann, S.; Woolfson, D. N. *Langmuir* **2008,** *24,* 11778–11783. doi:10.1021/la802009t
25. Tarabout, C.; Roux, S.; Gobeauc, F.; Fay, N.; Pouget, E.; Meriadec, C.; Ligeti, M.; Thomas, D.; Ijsselstijin, M.; Besselievre, F.; Buisson, D.-A.; Verbavatz, J.-M.; Petitjean, M.; Valery, C.; Perrin, L.; Rousseau, B.; Artzner, F.; Paternostre, M.; Cintrat, J.-C. *Proc. Natl. Acad. Sci. U. S. A.* **2011,** *108,* 7679–7684. doi:10.1073/pnas.1017343108
26. Altunbas, A.; Sharma, N.; Lamm, M. S.; Yan, C.; Nagarkai, R. P.; Schneider, J. P.; Pochan, D. J. *ACS Nano* **2010,** *4,* 181–188. doi:10.1021/nn901226h
27. Wang, S.; Ge, X.; Xue, J.; Fan, H.; Mu, L.; Li, Y.; Xu, H.; Liu, J. R. *Chem. Mater.* **2011,** *23,* 2466–2474. doi:10.1021/cm2003885
28. Acar, H.; Garifullin, R.; Guler, M. O. *Langmuir* **2011,** *27,* 1079–1084. doi:10.1021/la104518g
29. Shimada, T.; Tamura, Y.; Tirrell, M.; Kuroda, K. *Chem. Lett.* **2012,** *41,* 95–97. doi:10.1246/cl.2012.95
30. Zollfrank, C.; Scheel, H.; Greil, P. *Adv. Mater.* **2007,** *19,* 984–987. doi:10.1002/adma.200601548
31. Jin, R.-H.; Yuan, J.-J. *Chem. Commun.* **2005,** 1399–1401. doi:10.1039/b417351a
32. Yuan, J.-J.; Jin, R.-H. *Adv. Mater.* **2005,** *17,* 885–888. doi:10.1002/adma.200401670
33. Jin, R.-H.; Yuan, J.-J. *Adv. Mater.* **2009,** *21,* 3750–3753. doi:10.1002/adma.200803393
34. Chatani, Y.; Kobatake, T.; Tadokoro, H. *Macromolecules* **1983,** *16,* 199–204. doi:10.1021/ma00236a009
35. Yuan, J.-J.; Jin, R.-H. *Langmuir* **2005,** *21,* 3136–3145. doi:10.1021/la047182l
36. Yuan, J.-J.; Zhu, P.-X.; Fukazawa, N.; Jin, R.-H. *Adv. Funct. Mater.* **2006,** *16,* 2205–2212. doi:10.1002/adfm.200500886
37. Yuan, J.-J.; Jin, R.-H. *J. Mater. Chem.* **2012,** *22,* 5080–5088. doi:10.1039/c2jm15993g
38. Jung, J. H.; Nakashima, K.; Shinkai, S. *Nano Lett.* **2001,** *1,* 145–148. doi:10.1021/nl000190b
39. Wang, X.; Zhuang, J.; Chen, J.; Zhou, K.; Li, Y. *Angew. Chem., Int. Ed.* **2004,** *43,* 2017–2020. doi:10.1002/anie.200353507
40. Pang, J.; Hampsey, J. E.; Hu, Q.; Wu, Z.; John, V. J.; Lu, Y. *Chem. Commun.* **2004,** 682–683. doi:10.1039/b316501a

41. Zhang, M.; Ciocan, E.; Bando, Y.; Wada, K.; Cheng, L. L.; Pirouz, P. *Appl. Phys. Lett.* **2002,** *80,* 491–493. doi:10.1063/1.1434309
42. Nakazaki, Y.; Fujita, K.; Tanaka, K.; Uchino, T. *J. Phys. Chem. C* **2008,** *112,* 10878–10882. doi:10.1021/jp8025368
43. Aboshi, A.; Kurumoto, N.; Yamada, T.; Uchino, T. *J. Phys. Chem. C* **2007,** *111,* 8483–8488. doi:10.1021/jp0718505
44. Banerjee, S.; Datta, A. *Langmuir* **2010,** *26,* 1172–1176. doi:10.1021/la902265e
45. Gavalas, V. G.; Andrews, R.; Bhattacharyya, D.; Bachas, L. G. *Nano Lett.* **2001,** *1,* 719–721. doi:10.1021/nl015614w
46. Mastai, Y.; Polarz, S.; Antonietti, M. *Adv. Funct. Mater.* **2002,** *12,* 197–202. doi:10.1002/1616-3028(200203)12:3<197::AID-ADFM197>3.0.CO;2-A
47. Giunta, P. R.; van de Burgt, L. J.; Stiegman, A. E. *Chem. Mater.* **2005,** *17,* 1234–1240. doi:10.1021/cm040350a
48. Pang, J.; John, V. T.; Loy, D. A.; Yang, Z.; Lu, Y. *Adv. Mater.* **2005,** *17,* 704–707. doi:10.1002/adma.200400873
49. Park, S. S.; Jung, Y.; Xue, C.; Che, R.; Zhao, D.; Ha, C.-S. *Chem. Mater.* **2010,** *22,* 18–26. doi:10.1021/cm901684m
50. Liu, X.; Li, X.; Guan, Z.; Liu, J.; Zhao, J.; Yang, Y.; Yang, Q. *Chem. Commun.* **2011,** *47,* 8073–8075. doi:10.1039/c1cc12136g

License and Terms

Beilstein Journal of Nanotechnology

Energy transfer in complexes of water-soluble quantum dots and chlorin e6 molecules in different environments

Irina V. Martynenko[1], Anna O. Orlova[*1], Vladimir G. Maslov[1], Alexander V. Baranov[1], Anatoly V. Fedorov[1] and Mikhail Artemyev[2]

Full Research Paper

Open Access

Address:
[1]Saint Petersburg National Research University of Information Technologies, Mechanics and Optics, Saint Petersburg, Russia and [2]Institute for Physico-Chemical Problems, Belarussian State University, Minsk, Belarus

Email:
Anna O. Orlova[*] - a.o.orlova@gmail.com

* Corresponding author

Keywords:
chlorin e6; FRET; quantum dots; track membrane

Beilstein J. Nanotechnol. **2013,** *4,* 895–902.
doi:10.3762/bjnano.4.101

Received: 11 September 2013
Accepted: 29 November 2013
Published: 13 December 2013

This article is part of the Thematic Series "Physics, chemistry and biology of functional nanostructures II".

Guest Editor: A. S. Sidorenko

Abstract

The photoexcitation energy transfer is found and investigated in complexes of CdSe/ZnS cationic quantum dots and chlorin e6 molecules formed by covalent bonding and electrostatic interaction in aqueous solution and in porous track membranes. The quantum dots and chlorin e6 molecules form stable complexes that exhibit Förster resonance energy transfer (FRET) from quantum dots to chlorin e6 regardless of complex formation conditions. Competitive channels of photoexcitation energy dissipation in the complexes, which hamper the FRET process, were found and discussed.

Introduction

During the last decade, photophysical properties of the complexes formed by colloidal quantum dots (QDs) and organic molecules, in particular, complexes of QDs and tetrapyrrole compounds, were widely investigated [1-4]. The interest in complexes based on tetrapyrrole compounds has been sparked by their ability to generate singlet oxygen [5]. The singlet oxygen is used in different applications such as photodynamic therapy, blood plasma sterilization and wastewater treatment.

In QD/tetrapyrrole complexes the efficiency of singlet oxygen generation may be significantly increased, as compared with the free tetrapyrroles, due to an efficient photoexcitation energy transfer from the QD to the molecule. QDs have unique optical properties such as a broad absorption spectrum with extremely high extinction coefficient and high quantum yield of photoluminescence with the wavelength controlled by the QD size. It is very attractive to use QDs as an energy donor in complexes

with organic molecules since the conditions for an effective FRET can be quite easily satisfied.

For effective functioning of these complexes as singlet oxygen generators, two conditions should be simultaneously fulfilled: 1) the ability of the tetrapyrrole molecules to generate singlet oxygen upon complex formation should be maintained and 2) the effective intracomplex photoexcitation energy transfer should occur.

In QD–tetrapyrrole complexes, a formation of competitive channels of nonradiative photoexcitation energy dissipation different from FRET may take place for both donor and acceptor [4]. The origin of these energy transfer channels is not completely understood. Several physical mechanisms have been proposed, for example, the photoinduced reversible electron transfer between QD and molecule, and the formation of QD photoluminescence deactivation centers at the place where the molecule is attached to the QD.

Chlorin e6 (Ce6) is one of the tetrapyrrole compounds widely used as a photosensitizer. Photophysical properties of complexes between QDs and chlorin e6 were discussed in [6,7]. For example, FRET in covalently linked QD-Ce6 conjugates in aqueous solution was demonstrated [6]. A strong quenching of the photoluminescence (PL) of Ce6 was also observed together with significant changes of the PL and absorption spectra of complexed Ce6 as compared with those of free Ce6. Similar quenching of the PL of Ce6 with increasing the molar concentration ratio of Ce6 and QDs (n) was also observed in [7]. At the same time, a conservation of photophysical properties of the tetrapyrrole component is extremely important, since the decrease in PL quantum yield (QY) of the tetrapyrroles is usually accompanied by a decrease in efficiency of singlet oxygen generation [4].

In this study we investigate the photophysical properties of QD–Ce6 complexes under variable conditions of formation such as the molar concentration ratio n, the binding type, the ambient environment and the size of the QDs in order to understand the intracomplex photoexcitation energy transfer processes like FRET and other competitive energy transfer mechanisms. Complexes were obtained in two different environments: in aqueous solution and in poly(ethylene terephthalate) track membranes that can be utilized as an element of microfluidic devices [8].

Experimental

Chemicals

Bis-*N*-methyl-D-glucamine salt of chlorin e6 (photosensitizer "Photoditazin") was purchased from VETA Grand Ltd. Photoditazin has a QY of 9% in aqueous solution. Trioctylphosphine oxide (TOPO), cysteamine, 2-(dimethylamino)ethanethiol (DMAET), 1-ethyl-3-(3-dimethylaminopropyl)carbodiimide hydrochloride (EDAC) were purchased from Aldrich. Poly(ethylene terephthalate) (PET) membranes were obtained from FLNR JINR (Dubna, Russia).

Quantum dot synthesis

All semiconductor quantum dots CdSe/ZnS with different core sizes (2.5 nm, 3.5 nm, and 5 nm) were synthesized using similar methods as previously described [9]. All QD samples have a QY of about 20% in hydrophobic solvents and 5–8% in aqueous solutions.

Complex formation in aqueous solutions

To form water-soluble complexes of quantum dots and Ce6 molecules two methods of QD solubilization were used. In the case of covalent binding the hydrophobic CdSe/ZnS/TOPO QDs with a core diameter of 3.5 nm were initially solubilized by L-cysteine. In the second step, the L-cysteine molecules were replaced with molecules of hydroxy-terminated polyethylene glycol (PEG-OH)thiol and amino-terminated polyethylene glycol (PEG-NH_2)thiol with a ratio of 3 to 1. This enables to obtain stable colloidal solutions of quantum dots. Then the covalent binding of the QD surface amino groups with the Ce6 carboxyl functional groups using EDAC as a cross-linking reagent was performed. Using PEG as an additional QD shell resulted in an increase of the average distance between the QD and Ce6 molecules in the complexes to ≈5.5 nm. For the complexes, formed via electrostatic interaction, the hydrophobic CdSe/ZnS/TOPO QDs with a core diameter of 5.0 nm were solubilized with DMAET molecules to provide a positive charge on the QD surface.

Complex formation in the track membranes

The characteristics of PET track membranes are shown in Table 1. An ion-track technique is utilized for fabrication track pore membranes from thin polymer films [10]. Because of the etching, carboxyl groups are produced on the interior surface and in the loosened layer nearby the pore wall. The dissociation of the carboxyl groups in aqueous solutions leads to the appearance of negative charges on the track pore surface [11]. This gives the opportunity to passivate the inner surface of the pores with species that can react with carboxyl groups.

We proposed to utilize these carboxyl groups for a step-by-step formation of the water soluble QD/Ce6 complexes in the membranes. At the first step, positively charged CdSe/ZnS/DMAET QDs with a core size of 2.5 nm were embedded into the membranes due to electrostatic interaction with the carboxyl groups on the inner surface and in the loosened layer on the

Table 1: PET track membranes characteristics.

Pore diameter, *d*	0.5 μm
Thickness, *l*	12 μm
Pore density, *p*	$2.9 \cdot 10^7$ cm^{-2}
Pore direction (relative to the foil surface), φ	90°

track pore wall. Membranes with embedded QDs were impregnated by aqueous solutions of Ce6 for formation of the QDs/Ce6 complexes. In order to study the dependence of the optical properties of the complex components on the Ce6 concentration, the samples were immersed sequentially 10 times into the Ce6 solution for 5 minutes. After each immersion the membranes were removed from the Ce6 solutions, rinsed thoroughly with water and dried, then the static and time-resolved optical measurements were performed.

Since Ce6 molecules have carboxyl groups, these molecules are negatively charged in aqueous solution. Our experiments have shown that the embedding of Ce6 molecules into membranes without QDs does not occur due to the electrostatic repulsion of the carboxyl groups of the membrane and those of the Ce6. We replaced the carboxyl groups on the pore walls by amino groups with EDAC similar as described in [12]. This made it possible to create membranes with positive charges on the pore walls and to embed Ce6 molecules into membranes.

Estimations of the FRET efficiency

In the Förster formalism, a distance dependence of the efficiency of FRET between the donor–acceptor (D–A) pair, Q_{FRET}, is given with [13]:

$$Q_{\mathrm{FRET}} = \frac{R_0^6}{R_0^6 + R^6} \tag{1}$$

where R_0 (Förster radius) is the D–A distance at which the transfer efficiency is 50%, and R is the D–A distance.

R_0 can be calculated using the following equation:

$$R_0^6 = \frac{9000 \cdot \ln 10 \cdot \Phi^2 \cdot \phi_{0D}}{128 \cdot \pi^5 \cdot {n_s}^4 \cdot N} I \tag{2}$$

In this equation, Φ^2 is the orientation factor, Φ_{0D} is the quantum yield of the donor in the absence of quencher; N is the Avogadro number and n_s is the refractive index of the solvent. I is the overlap integral between the donor emission band and the acceptor absorption band:

$$I = \int I_D^H(\nu) \cdot \varepsilon_A(\nu) \cdot \nu^{-4} \cdot d\nu, \tag{3}$$

where $I_D^H(\nu)$ is the normalized PL spectrum of the energy donor; $\varepsilon_A(\nu)$ is the absorption spectrum of the acceptor; ν is the wavenumber. Equation 1 does not take into account a possible appearance of additional nonradiative dissipation channels due to the complex formation. That is why we can use it only for estimation of the upper limit of the FRET efficiency for the donor–acceptor pair in the complexes. The energy transfer efficiency from donor to acceptor, Q_{ET}^{Exp}, can be correctly estimated from the experimental data on the sensitized acceptor emission intensity [14,15], or the PL QY by using the following equation:

$$Q_{ET}^{Exp} = \frac{\phi_{DA}}{\phi_A}, \tag{4}$$

where Φ_{DA} and Φ_A are the PL QY of the acceptor sensitized with QDs and directly excited acceptor emission, respectively. There can be some difficulties in the direct measurement of the Φ_{DA} value, because the contribution of directly excited molecule emission should be correctly accounted for. It also should be noted that the use of Equation 4 is only possible in cases when the molecule does not change its photophysical properties upon binding to a QD. Otherwise, Equation 4 should be modified and the energy transfer efficiency can be estimated from experimental data by using a formula similar to that reported in [16]:

$$Q_{ET}^{Exp} = \frac{I_{AD}\left(\lambda_D^{ex}\right) \cdot D_A\left(\lambda_A^{ex}\right)}{I_A\left(\lambda_A^{ex}\right) \cdot D_{QD}\left(\lambda_D^{ex}\right) \cdot F}, \tag{5}$$

where I_{AD} is the intensity of sensitized acceptor PL, I_A is the intensity of acceptor PL directly excited by light; D_A and D_{QD} are the optical densities of the acceptor and donor at the excitation wavelengths of the PL. λ_D^{ex} and λ_A^{ex} are the wavelengths of the exciting light. The values of λ_A^{ex} and λ_D^{ex} are usually chosen in such a way that a selective excitation of PL either of acceptor or of donor is performed, respectively. F is the efficiency of donor PL quenching:

$$F = 1 - \frac{I}{I_0}, \tag{6}$$

where I and I_0 are the donor PL intensities in presence and in absence of the energy acceptor, respectively.

In the general case, when the complex formation results in appearance of additional nonradiative energy relaxation channels in the donor (QDs) or in a change of the acceptor PL quantum yield as compared to the free acceptor Equation 4 and Equation 5 are more correct for estimation of the energy transfer efficiency than Equation 1. For these equations mechanism of energy transfer from D–A (resulting in donor emission quenching and acceptor emission enhancing) is not strictly important. However, in the case when FRET is the only possible mechanism of energy transfer resulting in acceptor emission enhancing, the utilization of Equation 4 and Equation 5 provides a sufficient estimation of the FRET efficiency.

UV–vis absorption and photoluminescence detection

A spectrophotometer, UV-Probe 3600 (Shimadzu) and a spectrofluorometer, Cary Eclipse (Varian) were used for steady-state absorption and PL measurements, respectively. A 475 nm (λ_D^{ex}) light was used for indirect excitation of the Ce6 PL. At this wavelength there is a local minimum of the Ce6 absorption while the QDs can be efficiently excited by the light. For direct excitation of the Ce6 PL, the light with a wavelength in the spectral range of 640–660 nm (λ_A^{ex}), where a strong Q(I) band of Ce6 is located and the QD absorption is relatively small, was used. Time resolved luminescence measurements were performed with a laser scanning luminescent microscope, Micro Time 100 (Pico Quant), that allows registration of the luminescence decay in the 430–850 nm spectral range with 100 ps time resolution. A 80 ps pulse diode laser operated at 405 nm was used for the PL excitation.

Results and Discussion

Figure 1 shows the PL and absorption spectra of QDs with core diameters of 2.5 nm, 3.5 nm, and 5.0 nm used in this study as well as the PL and absorption spectra of Ce6. In all cases the spectral overlapping of donor (QDs) PL with acceptor (Ce6) absorption needed for the FRET is satisfied.

The quenching of QD PL and sensitization of the Ce6 PL were observed in all prepared QDs–Ce6 complexes. These facts,

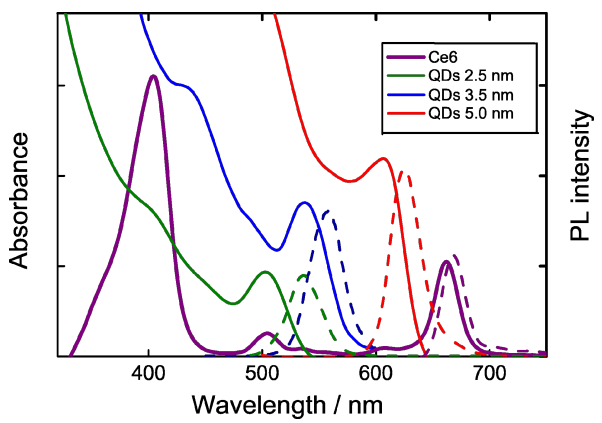

Figure 1: The absorption (solid line) and photoluminescence (dash line) spectra of QDs of different sizes and Ce6. The QD sizes are shown in the legend.

which will be discussed in details below, indicate the presence of intracomplex energy transfer from QDs to molecules. An expected energy transfer efficiency can be easily estimated for the FRET process by using Equation 1 and Equation 2. Table 2 shows the calculated Förster radius (R_0) and FRET efficiency (Q_{FRET}) for various QD–Ce6 pairs using Equation 1 and Equation 2 with $\Phi_{0D} = 1$, $n_s = 1$, and $\Phi^2 = 2/3$ [16]. We suppose that the distance between donor and acceptor is approximately equal to the dot radius, taking into account the size of the QDs, the thickness of the ZnS shell and the length of the solubilizer molecules.

Covalently bonded QDs–Ce6 complexes

The absorption spectrum of QDs–Ce6 complexes, where the Ce6 is covalently bonded to quantum dots, and the spectra of the individual components of the complexes in aqueous solutions are shown in Figure 2.

The absorption spectrum of QDs–Ce6 complexes is not a simple superposition of pure QD and Ce6 absorption spectra at corresponding concentrations. Figure 2 shows that complex formation leads to changes in the absorption spectrum of Ce6 bound to QDs. Most pronounced changes were observed in the

Table 2: Förster distances, R_0 and FRET efficiency, Q_{FRET} for QD–Ce6 complexes with different QD sizes.

Type of bonding	Covalent bonding	Electrostatic interaction in aqueous solution	Electrostatic interaction in PET membrane
QD size *d*, nm	3.5	5.0	2.5
Distance between donor and acceptor *R*, nm	5.5	2.0	1.75
Förster radius R_0, nm	4.6	5.1	4.7
FRET efficiency Q_{FRET}, %	27	98	98

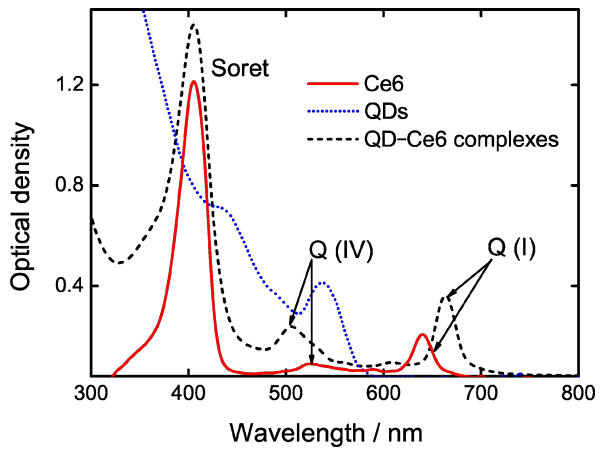

Figure 2: The absorption spectra of Ce6 (solid line), QDs (dotted line) and QD/Ce6 complexes (dashed line) in aqueous solution. The concentration of QDs: $C_{QD} \approx 4 \times 10^{-7}$ mol/L, $n = C_{Ce6}$: $C_{QD} = 20$. Characteristic absorption bands (Soret, Q(IV), and Q(I)) of the Ce6 are marked.

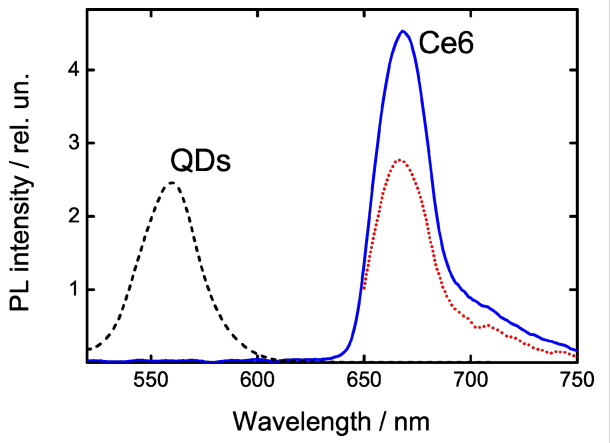

Figure 3: The PL spectra of covalent QDs–Ce6 complexes excited at 475 nm (solid line) and 640 nm (dotted line). The Ce6 PL intensity is normalized to optical density at excitation wavelength. The PL spectrum of QDs excited at 475 nm (dashed line) is shown for comparison.

region of the Ce6 Q(I) band, which demonstrates a bathochromic shift to 662 nm. Also a hypsochromic shift of the Q(IV) of ≈20 nm, and a change in the bandwidth of the Soret band at ~400 nm were observed. Close changes in the Ce6 absorption were already reported for InP/ZnS/Ce6 complexes in dimethylformamide solution [6] and for Ce6 embedded into polyvinylpyrrolidone polymer chains [17]. It was concluded [17,18] that the observed modifications are a typical response to the changes of the Ce6 environment.

To evaluate the efficiency of the energy transfer in the QD–Ce6 complexes using Equation 5, the PL of complexes was excited at two different wavelengths in order to selectively excite PL of either Ce6 or QDs. A 475 nm radiation was used for selective excitation of the QD PL within the QD–Ce6 complex since at this wavelength absorption of QDs was dominant as compared with that of Ce6. On the other hand, 640 nm light was used for selective Ce6 PL excitation to measure the Ce6 PL QY within the complex. For clarification of sensitized PL of Ce6 in these complexes, we normalized the experimental raw spectra to the optical density at the excitation wavelengths, i.e. 475 nm and 640 nm (see Figure 2, dashed line). The PL spectra presented in Figure 3 show that the complex formation results in complete QD PL quenching. At the same time, the Ce6 PL intensity, normalized to the Ce6 optical density at excitation wavelength, is ≈1.5 times higher for 475 nm excitation than for the 640 nm one that indicates a presence of sensibilized Ce6 luminescence. These facts show intracomplex FRET from QD to Ce6.

For this system, the energy transfer efficiency Q_{ET}^{Exp} of 8%, calculated from experimental data with Equation 5, is significantly lower than its expected value Q_{FRET} of 27% estimated using the Förster formula (Equation 1). The relatively low Q_{FRET} value is caused by the large distance between the QD and Ce6 (≈5.5 nm) due to the use of modified polyethylene as a QD solubilizer.

Since the FRET efficiency reaches only 30% of its maximum value, we can assume that quenching of QD PL cannot be explained only by FRET, which is responsible only for 30% of the quenching. Therefore, a presence of competitive channels of a nonradiative photoexcitation energy dissipation in QDs should be taken into account. On the other hand, QY of Ce6 PL in the complexes is about 3 times lower than that in Ce6 bound with PVP [17] and 2 times lower than that for Ce6 in aqueous solutions. Appearance of new channels of Ce6 energy dissipation due to perturbation of the molecule under complexing or aggregation of chlorin e6 [17] on the surface of QDs may be responsible for the QY reduction.

QDs–Ce6 complexing due to electrostatic interaction in aqueous solution

It is known that the FRET efficiency in the QD–molecule complexes may depend on the number of acceptor molecules on the surface of QD [14]. This effect can be studied in case of QD–Ce6 complex formation by electrostatic interaction of oppositely charged solubilizer molecules on the QD surface and carboxyl groups of Ce6. These complexes can be easily formed by simple mixing solutions of the components. Despite the instability of these complexes and their tendency to dissociation, they are supposed to be good model objects to explore the dependencies of FRET efficiency and Ce6 QY on n in the complexes by spectral luminescence methods.

The samples for studies were prepared by stepwise increasing the Ce6 concentration in solution of QD and Ce6, keeping the concentration of QDs constant ($C_{QD} \approx 5 \times 10^{-7}$ mol/L). Band positions in absorption and PL spectra of Ce6 in these complexes coincided with those in covalently bound QDs–Ce6 complexes and did not depend on the Ce6 concentration. An increase of the relative concentration of Ce6 led to quenching QD PL and to appearance of the sensibilized luminescence of Ce6. This is illustrated in Figure 4a where examples of PL spectra of QDs and Ce6 excited at 475 nm are presented. The inset in Figure 4a shows the *n*-dependence of intrinsic Ce6 PL excited at 640 nm. Analysis of these data demonstrates that the intensity of intrinsic Ce6 PL increases slower with increasing *n*, i.e., Ce6 PL QY decreases with growth of *n*, as it shown in Figure 4b. It was found that QD PL lifetimes remained the same upon increasing *n*. This indicates that the binding of QD to the Ce6 molecule leads to total QD PL quenching.

Figure 4b shows that although the FRET efficiency rapidly increases with *n*, its value Q_{ET}^{Exp} calculated using Equation 5 does not exceed 6%. It is significantly lower than the theoretical value of 98% (Table 2) and indicates the presence of energy dissipation channels different from FRET. Similar quenching of Ce6 PL with an increase of *n* was also observed in [7]. The increasing Ce6 concentration in complexes of CdSe/ZnS QD and Ce6 formed by electrostatic interaction led to strong Ce6 PL quenching that allows to suggest a formation of competitive channels of Ce6 energy dissipation.

Origin of the dependencies of the FRET efficiency and QY of Ce6 PL on *n* is not quite clear and requires an additional analysis. When molar ratio *n* varied from 1:0.1 to 1:1, the average number of Ce6 molecules per QD is less than one. It means that the number of complexes with more than one Ce6 molecules is negligible. This excludes an interaction between close Ce6 molecules located on the QD surface as a reason for decreasing of Ce6 QY. As a first approach, we assume that this dependence might be caused by QD aggregation in aqueous solution. To check this assumption QD–Ce6 complexes formed by electrostatic interaction in polymer track membranes were studied.

QDs–Ce6 complexes in track membranes

Aggregation of the quantum dots in solution is one of the possible reason of nonradiative dissipation of the QD excited state [19]. Embedding of cationic quantum dots to a pore wall layer via carboxyl groups of the membrane can prevent spontaneous aggregation of QDs [20]. The described embedding of Ce6 allows the creation of the QD–Ce6 complexes in the track membrane via electrostatic interaction. We found that for such complexes an increase of *n* leads to a complete quenching of QD PL and to a fatal decrease of the PL intensity of Ce6 molecules bound to QDs (Figure 5a). The QD–Ce6 complexes in the track membranes demonstrate the same dependencies of FRET efficiency and QY of Ce6 on *n* as in aqueous solution, i.e., when *n* increases the FRET efficiency increases while Ce6 QY decreases (Figure 5b). It should be noted that for *n* = 1.2 the Ce6 QY reduced nearly to zero.

Summarizing obtained experimental data, we can assume that origin of dependence of FRET efficiency and QY of Ce6 on *n* in QD–Ce6 complexes is irrelevant with aggregation of QDs and Ce6.

The experimental data demonstrate that nonradiative photoexcitation energy dissipation occurs in all types of QD–Ce6

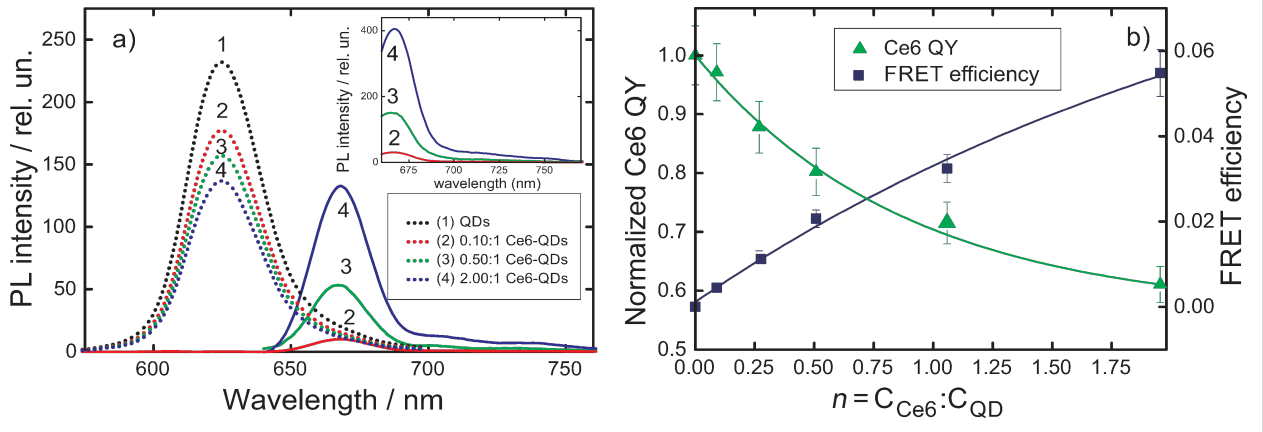

Figure 4: Optical properties of QD–Ce6 complexes formed by electrostatic interactions in aqueous solution as a function of *n*. (a) Evolution of PL spectra of 5 nm QDs (dotted line) and sensibilized luminescence of Ce6 (solid line) extracted from PL spectra of the QD–Ce6 complexes. The PL excitation wavelength is 475 nm. The intensity of the Ce6 emission is multiplied by 2. The inset shows PL spectra of the QD–Ce6 complexes with excitation at 640 nm. (b) FRET efficiency, estimated using Equation 5, and Ce6 QY as a function of *n*.

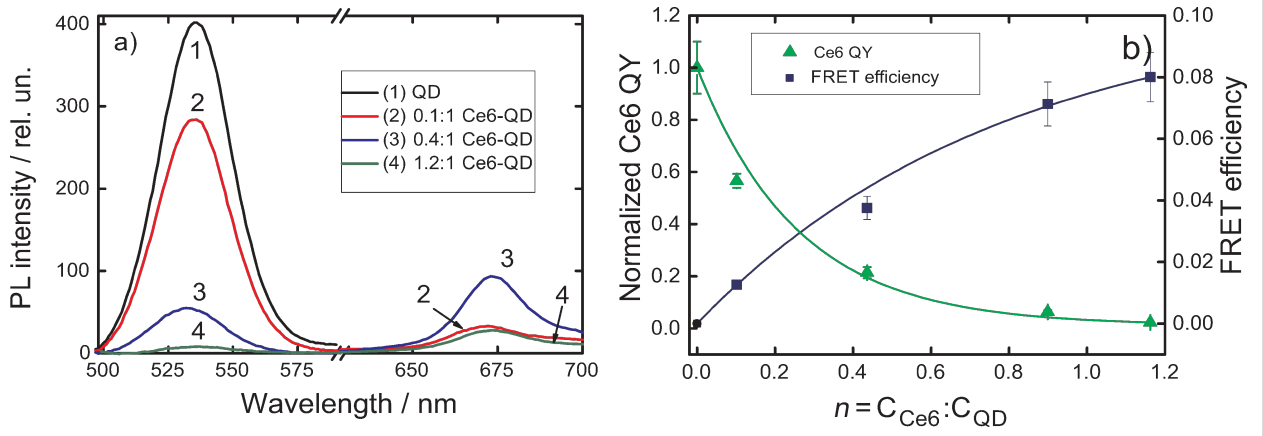

Figure 5: Optical properties of QD–Ce6 complexes formed by electrostatic interaction in the PET membrane as a function of *n*. (a) Evolution of PL spectra of 2.5 nm QDs and Ce6 complexes. PL excitation wavelength is 475 nm. (b) FRET efficiency, estimated using Equation 5 and Ce6 QY as a function of *n*.

complexes and their contribution to the intracomplex energy transfer varies from 70% in covalently bonded complexes to ≈90% in complexes formed by electrostatic interactions and may be responsible for QD and Ce6 PL quenching.

Electron transfer is the other possible mechanism of the QD PL quenching in the QD–organic molecule complexes. This mechanism is efficient if either both LUMO and HOMO or one of these orbitals of the quencher molecule is located within the energy gap of the CdSe QD. In this case the photoexcited electron or hole tunnels from the QD core through the shell and localizes at the LUMO or HOMO of the quenching molecule, respectively. These mechanisms of the tetrapyrrole PL quenching in complexes with QDs have been proposed [21].

The analysis of relative positions of the energy levels of QDs and chlorin e6, presented in Figure 6, shows that in complexes

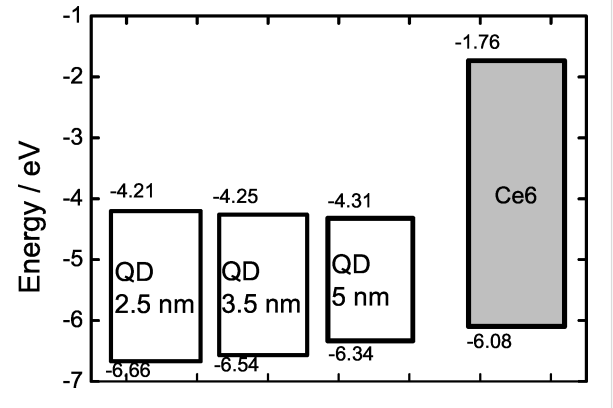

Figure 6: Energy level diagram of CdSe/ZnS QDs used in this work and Ce6 from [22]. The size of QD is shown in corresponding boxes.

with CdSe/ZnS quantum dots a photoinduced electron transfer from Ce6 to the QDs conduction band is possible.

The electron transfer is a more short-range process than FRET because its efficiency drops exponentially with the D–A distance. In the case of the studied covalently linked complexes the D–A distance is too large for effective electron transfer. In agreement with this, FRET contribution to the intracomplex energy transfer in this type of complexes is larger than in complexes with electrostatic interaction (30% and 5% respectively). At the same time, a relatively small FRET contribution in covalently linked complexes, where electron transfer is excluded, indicates the existence of additional channels in QD–Ce6 complexes different from the electron transfer.

Conclusion

The photophysical properties of complexes of CdSe/ZnS cationic quantum dots and chlorin e6 molecules formed by covalent bonding and electrostatic interaction in aqueous solution and PET membranes were investigated. It was found that interactions between quantum dots and chlorin e6 molecules in the QD–Ce6 systems lead to quenching of the quantum dots PL and to sensitizing the chlorin e6 PL. FRET from QDs to Ce6 was observed. Values of the FRET efficiencies estimated from the experimental data for all types of the complexes were low as compared with theoretically predicted for these D–A pairs. This fact and the essential decrease of the Ce6 photoluminescence QY by complex formation indicate that additional channels of nonradiative energy dissipation in QDs and/or in Ce6 should be taken into account. The photoinduced electron transfer from Ce6 to the QDs conduction band was considered as possible mechanism of nonradiative photoexcitation energy dissipation. However, the data analysis also indicated that additional mecha-

nisms of nonraditive energy dissipation, like, e.g., energy transfer from Ce6 to local energy states inside the CdSe bandgap [23], have to be considered to better match our experimental results.

Acknowledgements

The authors gratefully acknowledge the financial support from the Ministry of Education and Science of the Russian Federation (Projects 11.519.11.3026 and 14.B25.31.0002). M.V.A. thanks the Scientific Program "ELECTRONICS".

References

1. Shi, L.; Hernandez, B.; Selke, M. *J. Am. Chem. Soc.* **2006,** *128,* 6278–6279. doi:10.1021/ja057959c
2. Wen, Y.-n.; Song, W.-s.; An, L.-m.; Liu, Y.-q.; Wang, Y.-h.; Yang, Y.-q. *Appl. Phys. Lett.* **2009,** *95,* 143702. doi:10.1063/1.3243979
3. Rakovich, A.; Savateeva, D.; Rakovich, T.; Donegan, J.; Rakovich, Y.; Kelly, V.; Lesnyak, V.; Eychmüller, A. *Nanoscale Res. Lett.* **2010,** *5,* 753–760. doi:10.1007/s11671-010-9553-x
4. Maslov, V. G.; Orlova, A. O.; Baranov, A. V. Combination Therapy: Complexing of QDs with Tetrapyrrols and Other Dyes. In *Photosensitizers in Medicine, Environment, and Security;* Nyokong, T.; Ahsen, V., Eds.; Springer: Netherlands, 2012; pp 351–389. doi:10.1007/978-90-481-3872-2_7
5. Warren, M. J.; Smith, A. G. *Tetrapyrroles: Birth, Life and Death;* Molecular biology intelligence unit; Landes Bioscience, 2009.
6. Charron, G.; Stuchinskaya, T.; Edwards, D. R.; Russell, D. A.; Nann, T. *J. Phys. Chem. C* **2012,** *116,* 9334–9342. doi:10.1021/jp301103f
7. Valanciunaite, J.; Skripka, A.; Streckyte, G.; Rotomskis, R. Complex of water-soluble CdSe/ZnS quantum dots and chlorin e6: interaction and FRET. In *Society of Photo-Optical Instrumentation Engineers (SPIE) Conference Series,* 2010. doi:10.1117/12.871524
8. Orlova, A. O.; Gromova, Yu. A.; Savelyeva, A. V.; Maslov, V. G.; Artemyev, M. V.; Prudnikau, A.; Fedorov, A. V.; Baranov, A. V. *Nanotechnology* **2011,** *22,* 455201. doi:10.1088/0957-4484/22/45/455201
9. Gaponik, N.; Talapin, D. V.; Rogach, A. L.; Hoppe, K.; Shevchenko, E. V.; Kornowski, A.; Eychmüller, A.; Weller, H. *J. Phys. Chem. B* **2002,** *106,* 7177–7185. doi:10.1021/jp025541k
10. Apel, P. *Radiat. Meas.* **2001,** *34,* 559–566. doi:10.1016/S1350-4487(01)00228-1
11. Berezkin, V. V.; Volkov, V. I.; Kiseleva, O. A.; Mitrofanova, N. V.; Sobolev, V. D. *Adv. Colloid Interface Sci.* **2003,** *104,* 325–331. doi:10.1016/S0001-8686(03)00054-X
12. Niemeyer, C. *Bioconjugation Protocols: Strategies and Methods;* Biomed Protocols; Humana Press, 2004.
13. Förster, T. *Delocalized Excitation, Excitation Transfer;* Division of Biology and Medicine: Bulletin; Florida State University, 1965.
14. Clapp, A. R.; Medintz, I. L.; Mauro, J. M.; Fisher, B. R.; Bawendi, M. G.; Mattoussi, H. *J. Am. Chem. Soc.* **2004,** *126,* 301–310. doi:10.1021/ja037088b
15. Zenkevich, E.; Blaudeck, T.; Abdel-Mottaleb, M.; Cichos, F.; Shulga, A.; von Borczyskowski, C. *Int. J. Photoenergy* **2006,** No. 90242. doi:10.1155/IJP/2006/90242
16. Lakowicz, J. *Principles of Fluorescence Spectroscopy;* Springer, 2007.
17. Isakau, H. A.; Parkhats, M. V.; Knyukshto, V. N.; Dzhagarov, B. M.; Petrov, E. P.; Petrov, P. T. *J. Photochem. Photobiol., B: Biol.* **2008,** *92,* 165–174. doi:10.1016/j.jphotobiol.2008.06.004
18. Čunderliková, B.; Kongshaug, M.; Gangeskar, L.; Moan, J. *Int. J. Biochem. Cell Biol.* **2000,** *32,* 759–768. doi:10.1016/S1357-2725(00)00015-7
19. Kagan, C. R.; Murray, C. B.; Bawendi, M. G. *Phys. Rev. B* **1996,** *54,* 8633–8643. doi:10.1103/PhysRevB.54.8633
20. Orlova, A. O.; Gromova, Yu. A.; Maslov, V. G.; Prudnikau, A. V.; Artemyev, M. V.; Fedorov, A. V.; Baranov, A. V. *J. Appl. Phys.* **2013,** *113,* 214305. doi:10.1063/1.4809645
21. Orlova, A. O.; Maslov, V. G.; Baranov, A. V.; Gounko, I.; Byrne, S. *Opt. Spectrosc.* **2008,** *105,* 726–731. doi:10.1134/S0030400X08110131
22. Wang, X.-F.; Kitao, O. *Molecules* **2012,** *17,* 4484–4497. doi:10.3390/molecules17044484
23. Akimov, I. A.; Bentsa, V. M.; Vilesov, F. I.; Terenin, A. N. *Phys. Status Solidi B* **1967,** *20,* 771–776. doi:10.1002/pssb.19670200241

License and Terms

Beilstein Journal of Nanotechnology

Core level binding energies of functionalized and defective graphene

Toma Susi*[1,2], Markus Kaukonen[1,3], Paula Havu[1,4], Mathias P. Ljungberg[5], Paola Ayala[2] and Esko I. Kauppinen[1]

Full Research Paper

Open Access

Address:
[1]Department of Applied Physics, Aalto University School of Science, PO Box 15100, FI-00076 Aalto, Finland, [2]University of Vienna, Faculty of Physics, Strudlhofgasse 4, A-1090 Vienna, Austria), [3]Present address: Helsingin matematiikkalukio, Kuusikkotie 3, 00630 Helsinki, Finland, [4]Present address: Suomen ympäristökeskus, Mechelininkatu 34a, 00260 Helsinki, Finland and [5]LOMA, Université Bordeaux 1, 351 Cours de la Libération, 33405 Talence, France

Email:
Toma Susi* - toma.susi@iki.fi

* Corresponding author

Keywords:
core level; defects; density functional theory; graphene; X-ray photoelectron spectroscopy

Beilstein J. Nanotechnol. **2014,** *5,* 121–132.
doi:10.3762/bjnano.5.12

Received: 15 October 2013
Accepted: 17 January 2014
Published: 03 February 2014

This article is part of the Thematic Series "Physics, chemistry and biology of functional nanostructures II".

Guest Editor: A. S. Sidorenko

Abstract

X-ray photoelectron spectroscopy (XPS) is a widely used tool for studying the chemical composition of materials and it is a standard technique in surface science and technology. XPS is particularly useful for characterizing nanostructures such as carbon nanomaterials due to their reduced dimensionality. In order to assign the measured binding energies to specific bonding environments, reference energy values need to be known. Experimental measurements of the core level signals of the elements present in novel materials such as graphene have often been compared to values measured for molecules, or calculated for finite clusters. Here we have calculated core level binding energies for variously functionalized or defected graphene by delta Kohn–Sham total energy differences in the real-space grid-based projector-augmented wave density functional theory code (GPAW). To accurately model extended systems, we applied periodic boundary conditions in large unit cells to avoid computational artifacts. In select cases, we compared the results to all-electron calculations using an ab initio molecular simulations (FHI-aims) code. We calculated the carbon and oxygen 1s core level binding energies for oxygen and hydrogen functionalities such as graphane-like hydrogenation, and epoxide, hydroxide and carboxylic functional groups. In all cases, we considered binding energy contributions arising from carbon atoms up to the third nearest neighbor from the functional group, and plotted C 1s line shapes by using experimentally realistic broadenings. Furthermore, we simulated the simplest atomic defects, namely single and double vacancies and the Stone–Thrower–Wales defect. Finally, we studied modifications of a reactive single vacancy with O and H functionalities, and compared the calculated values to data found in the literature.

Introduction

X-ray photoelectron spectroscopy (XPS) is commonly used to identify the relative amounts of chemical elements in a sample, and it can provide information about their chemical states, i.e., bonding. Although the method is not local, XPS is able to discern specific atomic defects if they are numerous enough and, furthermore, provide essential statistical information on their concentrations. Typically, XPS has been limited to surface characterization because of the limited escape depth of photoemitted electrons. However, for low-dimensional carbon nanomaterials such as graphene or carbon nanotubes, the escape depth exceeds the size of the system, and this makes XPS in practice a convenient bulk characterization tool.

In order to interpret the binding energies measured by XPS, a reference to which such energies can be compared is needed. Density functional theory (DFT) calculations can be employed to provide such a reference, especially when measurements of known molecular systems are not sufficient. However, because of the computational cost of treating core levels accurately, most calculations up to date have considered either non-periodic (cluster-type) systems or small unit cells. This has made the simulation of extended defects challenging and subject to questionable approximations, and possibly even spurious image–image interaction or finite size effects. Furthermore, the electronic structure of molecular models such as coronenes differs significantly from graphene, which can be an issue.

A prominent recent example of the value of XPS for studying graphene is in chemical functionalization, in which the pristine structure is modified by a known covalent adsorbate or a substitution. Besides substitutional doping, which we will not discuss here, the functionalization of graphene by, e.g., hydrogenation [1,2] and oxygenation [3,4] has been a topic of intense research. These treatments result in –H, –O, or –OH groups bonded to the carbon atoms, the orbital hybridization of which is changed from sp^2 to sp^3. This can lead to a band gap opening [3] and other interesting features [5]. To study such functional groups, along with intrinsic defects, is also vital for the spectroscopic analysis of reduced graphene oxide [6,7], which in turn is a promising avenue to the mass production of graphene.

Several intrinsic defects are relevant for graphene. Of these, the simplest are single (SV) and double vacancies (DV), along with the Stone–Thrower–Wales (STW) bond rotation. All of these have been directly observed [8] in aberration-corrected transmission electron microscopes (TEM). More extended defects (such as the 555-777 and the 5555-6-7777 double vacancy defects [9]) have also been seen, but are likely to be beam-induced. In any case, locally they do not present very different bonding environments, and thus their XPS signatures are unlikely to differ significantly from the simpler cases.

The single vacancy is different from the DV (called V_2(5-8-5) by Banhart et al. [9]) and the STW (SW(555-777) [9]) as by necessity it presents dangling bonds. The removal of a single carbon atom from a graphene lattice leaves the three neighboring atoms with a single dangling bond each, which can be called an unreconstructed single vacancy (uSV). As this is energetically unfavorable, two of the atoms tend to form a bond between themselves and reconstruct to close a pentagon [8] in the Jahn–Teller distortion [10]. We will call this a reconstructed single vacancy, or simply SV (V_1(5-9) [9]). However, the remaining single carbon atom still cannot satisfy its chemically reactive dangling bond, as has been directly observed by scanning tunneling microscopy (STM) in high vacuum [11].

To address these important systems, and the potential shortcomings of previous studies, we have calculated graphene core level binding energies by using density functional theory implemented with real-space grid-based projector-augmented waves in the GPAW code [12]. We applied periodic boundary conditions in large unit cells to avoid spurious image interaction effects. Furthermore, we benchmarked select results against all-electron calculations with the FHI-aims code [13] to ensure that the projector-augmented waves in GPAW described the core levels of these systems accurately.

In addition to pristine graphene, we studied *hydrogen* (-H), *dihydrogen* (2 –H), graphane-like *dihydrogen* (2 –H_{opp}, i.e., two neighboring H adatoms on opposite sides of the graphene sheet [2]) *hydroxide* (–OH), *oxygen* (=O), *dioxygen* (–2O), *epoxide* (>O, [3,4]), and *carboxylic* (–COOH, [14]) functional groups. The defect structures we studied were the single vacancy (SV), double vacancy (DV) and the Stone–Thrower–Wales (STW) defects. Several modifications of the SV site were considered as well, as the dangling bond constitutes a reactive site for the absorption of molecules from the environment. As the absorption of more electronegative atoms can have a large impact on the C 1s binding energy of the neighboring carbon atom, the following adsorbates were considered: *hydrogen* (SV–H), *ketone* (SV=O), *annulene* (SV–O–, [15]), *ketone* + *annulene* (SV=O+–O–), *diketone* (SV=2O, possibly relevant for oxygen splitting [16]), *hydroxide* (SV–OH), and *carboxylic* (SV–COOH) groups.

We found that the projector-augmented results were in excellent agreement with all-electron calculations. In almost all cases, in which data was available, a good agreement for the

C 1s levels with experimental values reported in the literature was also found [4,17-20]. As a further refinement, we considered binding energy contributions arising from up to third nearest neighbors to the functional group or defect, and plotted the resulting line shapes by using experimentally realistic broadenings. In the case of the O 1s level, the line-shape variations of graphene have not been extensively examined in experimental reports, which makes the comparison of the calculated O 1s values to literature data problematic. This is why we have focused our discussion on the C 1s energies. With this caveat, core-hole calculations with the GPAW code are a convenient and valuable tool for simulating the core level binding energies of graphene systems.

Results

Relaxed structures

The relaxed structures are shown in Figure 1, Figure 2, and Figure 3. Note that all systems were allowed to relax with no constraints, which induced a slight curvature into some of the structures to compensate for the strain induced by the local defects. The unreconstructed single vacancy spontaneously reconstructed during the geometry relaxation, by closing a pentagonal carbon ring. The bond lengths and angles of the relaxed structures match closely to what has been reported in the literature [3,4,9,14,16]. The Arabic numerals denote the target atoms of the core-hole calculations discussed below.

Formation energies

The formation energies of the defects were calculated according to Equation 1, found in section “Computational details“ below along with the chemical potentials chosen for the missing carbon atoms and the added functional groups. The formation energy of the STW defect was calculated to be 4.99 eV, in perfect agreement with previous studies [2]. The values for the single (7.21 eV) and double vacancies (7.01 eV) are marginally lower than previously reported, which could be attributed to the unconstrained structural relaxation allowed here. Following Banhart et al. [9], it should be noted that the formation energy per atom is much lower for the double vacancy.

The formation energies of the saturated vacancy structures were calculated with respect to the bare single vacancy. The hydro-

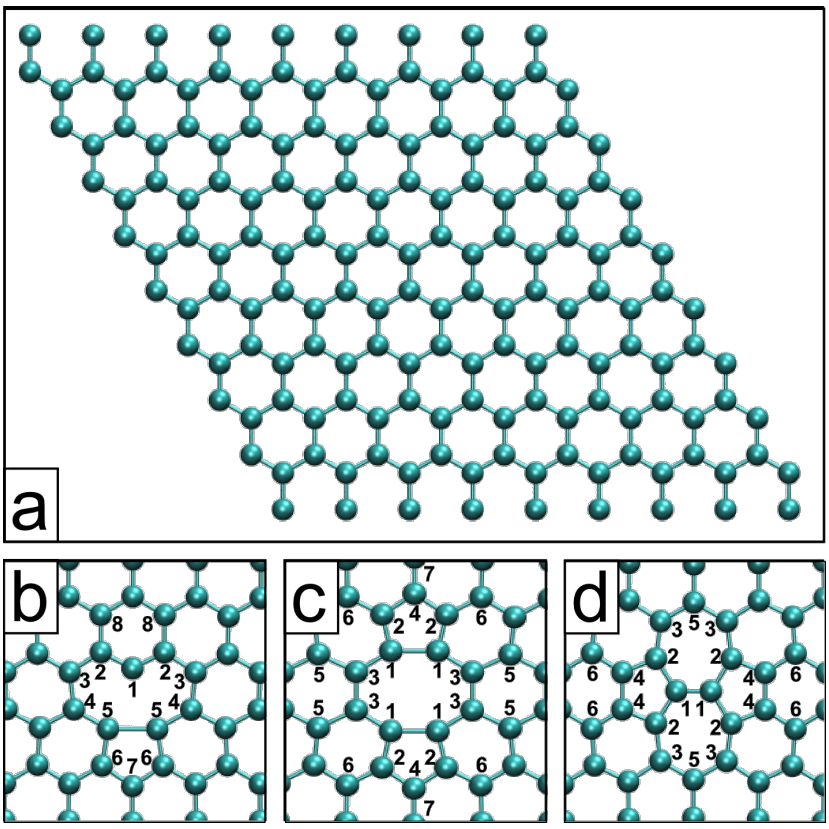

Figure 1: a) The 9 × 9 graphene computational unit cell. Cropped relaxed structures of the b) reconstructed single vacancy (SV), c) the double vacancy (DV), and d) the Stone–Thrower–Wales (STW) defect.

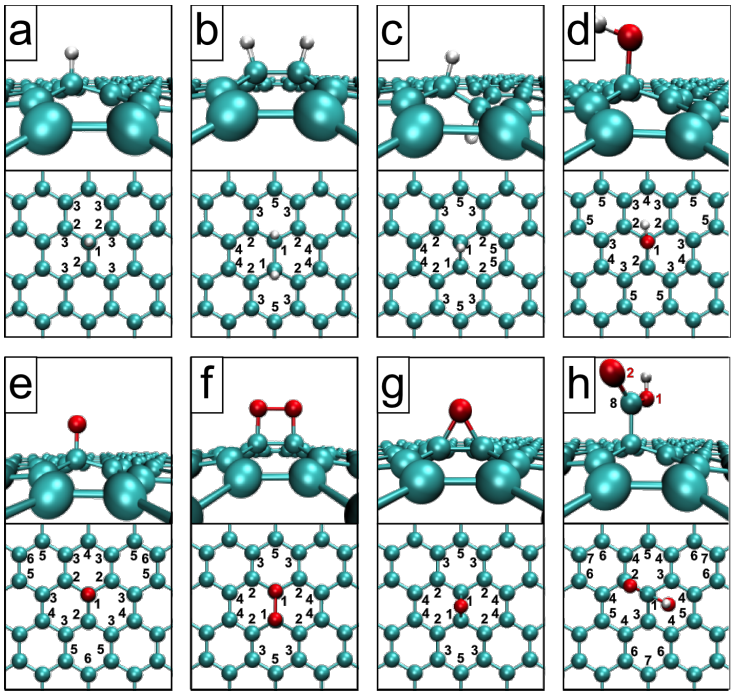

Figure 2: Cropped relaxed structures of functionalized graphene. The a) hydrogen (–H), b) dihydrogen (2 –H), c) graphene-like dihydrogen (2 $–H_{opp}$), d) hydroxide (–OH), e) oxygen (=O), f) dioxygen (–2O), g) epoxide (>O), and h) carboxyl (–COOH) functionalities.

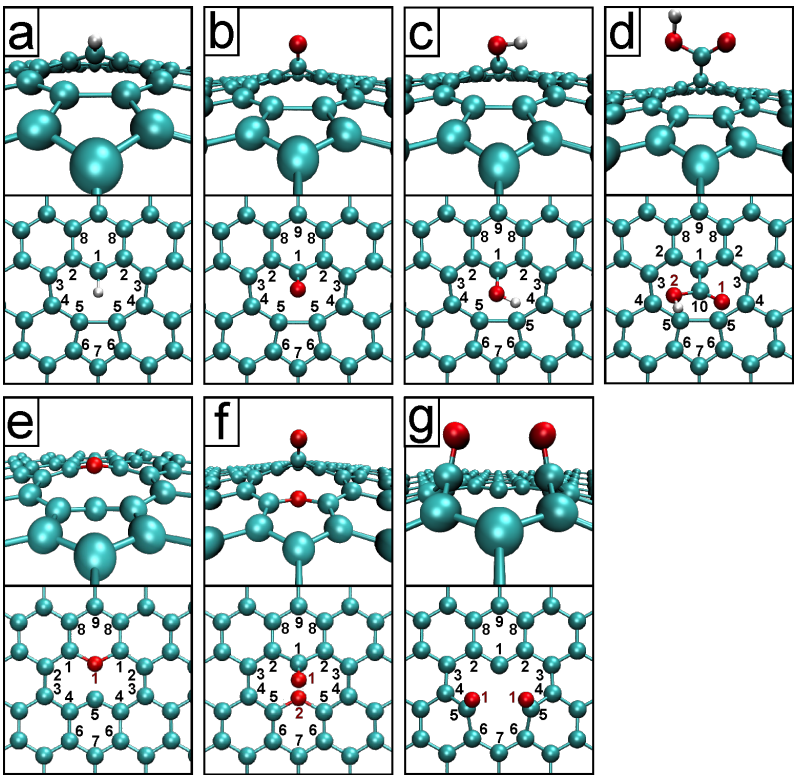

Figure 3: Cropped relaxed saturated single vacancy structures. The single vacancy saturated by a) hydrogen (SV–H), b) oxygen (SV–O), c) hydroxide (SV–OH), d) carboxyl (SV–COOH), e) annulene (SV–O–), f) ketone + annulene (SV=O+–O–), and g) diketone (SV=2O) groups.

genated SV had a formation energy of −2.46 eV due to the saturation of the dangling bond. The lowest formation energies were obtained for the oxygen-saturated structures, with the ketone-saturated (SV=O) vacancy at −4.01 eV, the diketone (=2O) at −4.91 eV, the annulene-bridged vacancy (SV-O-) at –4.00 eV, and finally, the annulene plus ketone vacancy structure (SV=O + -O-), which had by far the lowest value at −8.65 eV. In agreement with a previous calculation, which used a cluster model [14], the carboxyl-saturated vacancy (SV-COOH) has a formation energy −1.62 eV compared to the SV, or 3.12 eV compared to the pristine structure.

The formation energies of the functional groups without vacancies are 1.45 eV for the -H adatom (in good agreement with a previous calculation [21]), 1.70 eV for 2 -H, 2.30 eV for the -OH, 1.20 eV for the =O, 0.74 eV for adjacent =O adatoms, and 2.07 eV for the carboxylic group -COOH. The epoxide group >O had a remarkably low formation energy of 0.3 eV, in line with the thermally reversible oxidation recently observed experimentally by Hossain and co-workers [4].

Core level binding energies

The core level binding energies were calculated according to the delta Kohn–Sham total energy differences method [22,23] as detailed in section “Computational details”. The calculated core level binding energies for the pristine and defected graphene are shown in Table 1, for functionalized graphene in Table 2, and for the saturated vacancy configurations in Table 3. C(*) denotes a carbon atom far away from the defect (“bulk”), and “*” in the column “# of atoms” denotes that the number of such atoms depends on the defect concentration. For each configuration, we calculated the C 1s binding energies (and O 1s, where applicable) for up to third nearest neighbor C atoms from the defect to capture the significant shifts while keeping the computational effort manageable. Target atoms are denoted by Arabic numerals in Figures 1–3 with the same numeral denoting multiple equivalent atoms, and the number of atoms of each type is noted in Tables 1–3.

For the all-electron FHI-aims calculations, we considered the pristine, SV, -H, and 2 -H_{opp} configurations. Although the C 1s energy of pristine graphene had a slightly different absolute value with FHI-aims (283.69 eV vs 283.61 eV), the all-electron calculations gave binding energy shifts within 10 meV of the GPAW results. This demonstrates that the use projector-augmented waves in the GPAW calculations is not a significant source of error.

Line shapes

To help interpret the calculated core level binding energies shown in Tables 1–3, we plotted line shapes for each configur-

Table 1: Calculation results for the pristine and defected graphene structures. The columns show: system identifier; formation energy of the defect; target atom of the calculation (see Figure 1); number of target atoms; calculated 1s binding energy; C 1s BE shift with respect to the calculated C 1s energy of pristine graphene.

ID	E_{form} (eV)	atom	# of atoms	C 1s BE (eV)	BE shift (eV)
gra	0	C (*)	*	283.61	0.00
SV	7.21	C (*)	*	283.32	−0.29
		C (1)	1	281.21	−2.40
		C (2)	2	282.97	−0.64
		C (3)	2	282.87	−0.74
		C (4)	2	283.55	−0.06
		C (5)	2	283.24	−0.37
		C (6)	2	292.91	−0.70
		C (7)	1	282.51	−1.10
		C (8)	2	282.97	−0.64
DV	7.02	C (*)	*	283.39	−0.22
		C (1)	4	283.27	−0.34
		C (2)	4	282.79	−0.82
		C (3)	4	283.58	−0.03
		C (4)	2	282.43	−1.18
		C (5)	4	283.53	−0.08
		C (6)	4	283.21	−0.40
		C (7)	2	283.12	−0.49
S-W	4.99	C (*)	*	283.61	0.00
		C (1)	2	283.10	−0.51
		C (2)	4	283.16	−0.45
		C (3)	4	283.83	0.22
		C (4)	4	282.67	−0.94
		C (5)	2	283.70	0.09
		C (6)	4	283.27	−0.34

Table 2: Calculation results for the functionalized graphene structures. The columns show: system identifier; formation energy of the defect; target atom of the calculation (see Figure 2); number of target atoms; calculated 1s binding energy; C 1s BE shift with respect to the calculated C 1s energy of pristine graphene or the O 1s BE shift with respect to the calculated O 1s energy of epoxide/hydroxide functional groups, where applicable.

ID	E_{form} (eV)	atom	# of atoms	1s BE (eV)	BE shift (eV)
gra	0	C (*)	*	283.61	0.00
-H	1.45	C (*)	*	283.39	−0.22
		C (1)	1	284.10	0.49
		C (2)	3	282.78	−0.83
		C (3)	6	283.35	−0.26
2 -H	1.69	C (*)	*	283.59	−0.02

Table 2: Calculation results for the functionalized graphene structures. The columns show: system identifier; formation energy of the defect; target atom of the calculation (see Figure 2); number of target atoms; calculated 1s binding energy; C 1s BE shift with respect to the calculated C 1s energy of pristine graphene or the O 1s BE shift with respect to the calculated O 1s energy of epoxide/hydroxide functional groups, where applicable. (continued)

		C (1)	2	284.55	0.94
		C (2)	4	283.19	−0.42
		C (3)	4	283.58	−0.03
		C (4)	4	283.55	−0.05
		C (5)	2	283.31	−0.30
2 -H_{opp}	1.30	C (*)	*	283.59	−0.02
		C (1)	2	284.36	0.75
		C (2)	4	283.16	−0.45
		C (3)	4	283.60	−0.01
		C (4)	4	283.53	−0.08
		C (5)	2	283.31	−0.30
-OH	2.30	C (*)	*	283.38	−0.23
		C (1)	1	284.81	1.20
		C (2)	3	282.35	−1.26
		C (3)	6	282.91	−0.70
		C (4)	3	282.83	−0.78
		C (5)	6	283.29	−0.02
		O	1	530.11	0.00
=O	1.20	C (*)	*	283.38	−0.23
		C (1)	1	283.93	0.32
		C (2)	3	282.35	−1.25
		C (3)	6	282.91	−0.70
		C (4)	3	282.83	−0.78
		C (5)	6	283.14	−0.47
		C (6)	3	283.16	−0.45
		O	1	526.36	−3.75
-2O	0.74	C (*)	*	283.53	−0.08
		C (1)	2	285.16	1.55
		C (2)	4	283.00	−0.61
		C (3)	4	283.44	−0.17
		C (4)	4	283.45	−0.16
		C (5)	2	282.83	−0.78
		O	2	530.29	0.18
>O	0.29	C (*)	*	283.57	−0.04
		C (1)	2	285.13	1.52
		C (2)	4	283.16	−0.45
		C (3)	4	283.56	−0.05
		C (4)	4	283.55	−0.07
		C (5)	2	283.30	−0.31
		O	1	530.11	0.00
-COOH	2.07	C (*)	*	283.34	−0.27
		C (1)	1	284.43	0.81
		C (2)	1	282.67	−0.94

Table 2: Calculation results for the functionalized graphene structures. The columns show: system identifier; formation energy of the defect; target atom of the calculation (see Figure 2); number of target atoms; calculated 1s binding energy; C 1s BE shift with respect to the calculated C 1s energy of pristine graphene or the O 1s BE shift with respect to the calculated O 1s energy of epoxide/hydroxide functional groups, where applicable. (continued)

	C (3)	2	282.77	−0.84
	C (4)	6	283.21	−0.40
	C (5)	3	282.89	−0.72
	C (6)	6	282.26	−0.35
	C (7)	3	283.36	−0.25
	C (8)	1	286.07	2.46
	O (1)	1	532.82	2.71
	O (2)	1	530.50	0.39

Table 3: Calculation results for the saturated single vacancy structures. The columns show: system identifier; formation energy of the defect; target atom of the calculation (see Figure 3); number of target atoms; calculated 1s binding energy; C 1s BE shift with respect to the calculated C 1s energy of pristine graphene or the O 1s BE shift with respect to the calculated O 1s energy of epoxide/hydroxide functional groups, where applicable.

ID	E_{form} (eV)	atom	# of atoms	1s BE (eV)	BE shift (eV)
SV[a]	0	—	—	—	—
SV-H	−2.46	C (*)	*	283.30	−0.31
		C (1)	1	282.11	−1.50
		C (2)	2	283.00	−0.61
		C (3)	2	282.96	−0.65
		C (4)	2	283.65	0.04
		C (5)	2	283.24	−0.37
		C (6)	2	282.78	−0.83
		C (7)	1	282.37	−0.24
		C (8)	2	283.09	−0.52
SV=O	−4.01	C (*)	*	283.47	−0.14
		C (1)	1	284.27	0.65
		C (2)	2	282.64	−0.97
		C (3)	2	283.27	−0.34
		C (4)	2	283.65	0.04
		C (5)	2	283.42	−0.19
		C (6)	2	283.01	−0.60
		C (7)	1	282.60	−1.01
		C (8)	2	283.26	−0.35
		C (9)	1	283.05	−0.56
		O	2	528.88	−1.23
SV-OH	−1.53	C (*)	*	283.35	−0.26
		C (1)	1	284.03	0.42
		C (2)	2	282.98	−0.63
		C (3)	2	283.03	−0.58

Table 3: Calculation results for the saturated single vacancy structures. The columns show: system identifier; formation energy of the defect; target atom of the calculation (see Figure 3); number of target atoms; calculated 1s binding energy; C 1s BE shift with respect to the calculated C 1s energy of pristine graphene or the O 1s BE shift with respect to the calculated O 1s energy of epoxide/hydroxide functional groups, where applicable. (continued)

		C (4)	2	283.55	−0.06
		C (5)	2	283.28	−0.33
		C (6)	2	282.79	−0.82
		C (7)	1	282.41	−1.20
		C (8)	2	283.15	−0.46
		C (9)	1	283.13	−0.48
		O	1	531.93	1.82
SV -O-	−4.00	C (*)	*	283.20	−0.41
		C (1)	2	284.40	0.79
		C (2)	2	283.33	−0.28
		C (3)	2	282.80	−0.81
		C (4)	2	282.99	−0.62
		C (5)	1	281.25	−2.06
		C (6)	2	283.05	−0.56
		C (7)	1	283.23	−0.38
		C (8)	2	283.35	−0.26
		C (9)	1	282.92	−0.59
		O	1	532.10	1.99
SV=O + -O-	−8.65	C (*)	*	283.61	0.00
		C (1)	1	284.59	0.98
		C (2)	2	282.98	−0.63
		C (3)	2	283.62	0.01
		C (4)	2	283.75	0.14
		C (5)	2	284.89	1.19
		C (6)	2	283.80	0.19
		C (7)	1	283.54	−0.07
		C (8)	2	283.49	0.12
		C (9)	1	283.25	0.36
		O (1)	1	529.23	−0.78
		O (2)	1	532.57	2.46
SV=2O	−4.91	C (*)	*	283.28	−0.33
		C (1)	1	280.73	−2.88
		C (2)	2	282.55	−1.06
		C (3)	2	282.90	−0.71
		C (4)	2	282.39	−1.22
		C (5)	2	284.26	0.65
		C (6)	2	282.44	−1.17
		C (7)	1	283.32	−0.29
		C (8)	2	282.92	−0.69
		C (9)	1	283.03	−0.58
		O	2	528.29	−1.82
SV-COOH	−1.61	C (*)	*	283.35	−0.26
		C (1)	1	282.38	−1.23
		C (2)	2	283.01	−0.60

Table 3: Calculation results for the saturated single vacancy structures. The columns show: system identifier; formation energy of the defect; target atom of the calculation (see Figure 3); number of target atoms; calculated 1s binding energy; C 1s BE shift with respect to the calculated C 1s energy of pristine graphene or the O 1s BE shift with respect to the calculated O 1s energy of epoxide/hydroxide functional groups, where applicable. (continued)

		C (3)	2	282.97	−0.64
		C (4)	2	283.65	0.04
		C (5)	2	283.24	−0.37
		C (6)	2	282.79	−0.82
		C (7)	1	282.36	−1.25
		C (8)	2	283.08	−0.53
		C (9)	1	283.19	−0.42
		C (10)	1	285.72	2.11
		O (1)	1	529.32	−0.79
		O (2)	1	531.83	1.72

[a]The formation energies in this table are calculated with respect to the single vacancy structure. See Table 1 for the C 1s values of this configuration.

ation in Figure 4. For realistic defect concentrations, most of the atoms in the system – and thus most of the photoemitted signal – will be from atoms in the "bulk" of the system. This was calculated as the C 1s energy of an atom far away from the defect, and shown as the C(*) atoms for each configuration in the tables. Since the energy resolution of most laboratory XPS spectrometers is broader than the narrow deviations that can be obtained from our calculations, we have omitted peaks with shifts less than 0.3 eV from the bulk value determined for each system from the graphical representations of the line shapes below. Thus the line shapes should be used to interpret experimental spectra only after the main C 1s peak has been subtracted. Accordingly, the plots show chemical shifts with respect to the system bulk, with weights equal to the number of atoms of each type.

Once the binding energies for the different configurations are identified, the experimental broadening must be considered. The widths of the components of these XPS peaks are defined by their Voigtian lineshape. These comprise a Gaussian broadening related to the instrumental resolution as well as vibrational effects, and Lorentzian broadening, corresponding to the lifetime of the excited electron. We have set both the Gaussian and Lorentzian amplitude to 0.3 eV in the line shapes below. This can give us a fair picture of the line shapes since this value corresponds to a good resolution and a reasonable average for the lifetimes arising from each bonding environment. In addition, we have provided the Mathematica script used to plot the line shapes as Supporting Information File 1, in which these parameters can be easily varied to match a particular experimental setup.

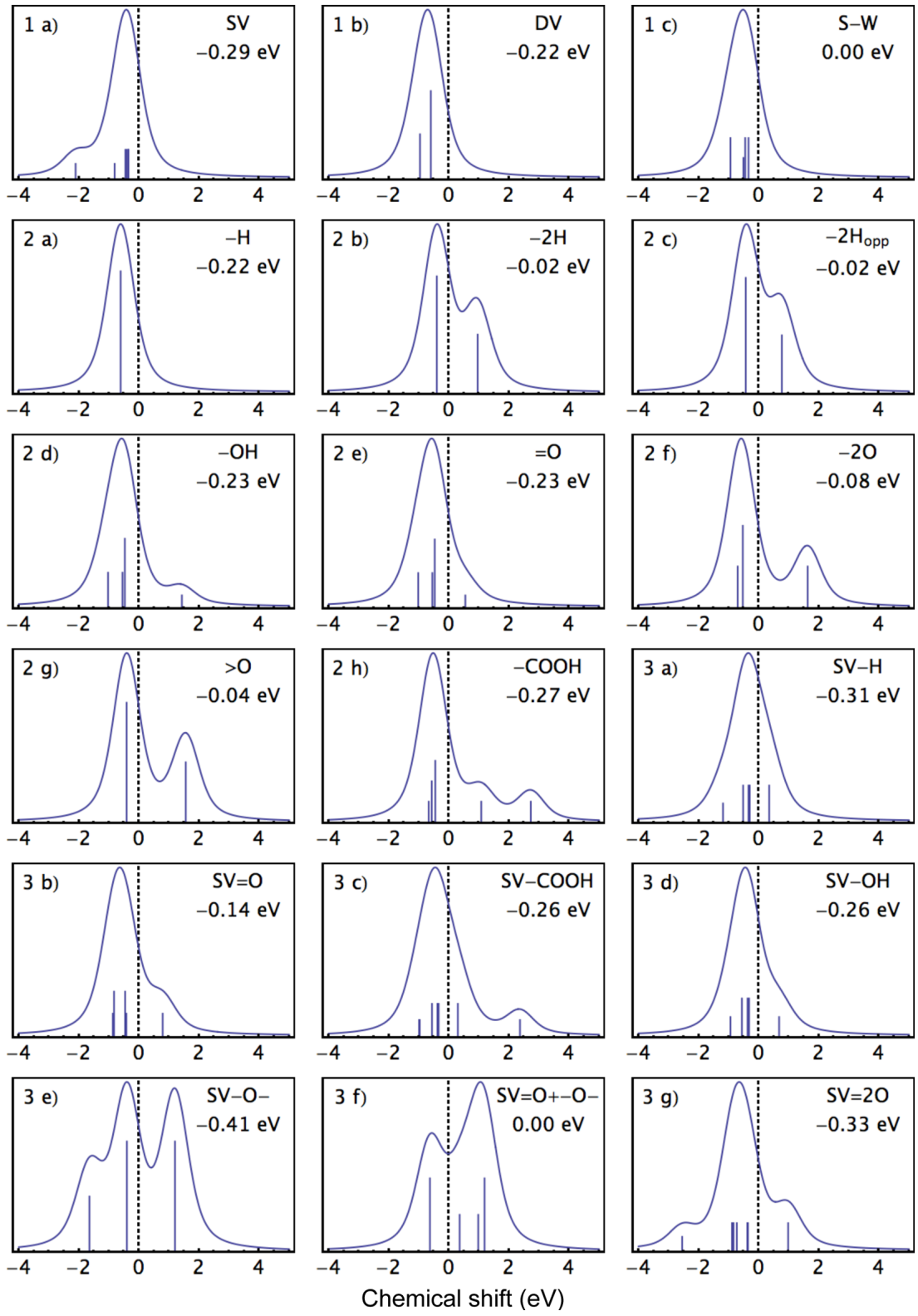

Figure 4: The calculated line shapes, in which peaks with shifts smaller than 0.3 eV from the system bulk value have been suppressed. The identifier in the top left corner of each panel refers to the corresponding structures in Figures 1–3, while the energy inset under the system identifier in the top right corner denotes the shift of the system bulk value compared to that of pristine graphene. The vertical lines represent the shifts of the calculated binding energies with respect to the system bulk value, weighted by the number of atoms for each calculated energy and scaled for clarity.

Discussion

The value of the carbon 1s core level binding energy of graphite is commonly cited to be at 284.4 eV [18,24]. In the case of graphene, however, this value varies according to the substrate, on which graphene is placed or grown. Some authors have measured the C 1s of epitaxial monolayered graphene at a slightly higher value of 284.8 eV, but attribute this to a charge transfer from the SiC substrate [25]. A similar shift has been observed for the Dirac point in this system by angle-resolved photoemission spectroscopy [26]. Other authors have measured the C 1s at 284.15 eV [27] on Ir(111) and 284.2 eV on Au-intercalated Ni(111) [28], but again, charge transfer very likely contributes to the results. Since no conclusive XPS data on free-standing monolayered graphene is available so far, we have chosen to use 284.4 eV as the reference value for the graphene C 1s binding energy.

Looking at the calculated C 1s value of pristine graphene in Table 1, we can see that the computational method underestimates the binding energy by 0.8 eV. As mentioned above, the absolute values for the DFT energies will depend on the functional that was used. Errors on the order of 1 eV compared to the experimental values are typical [23]. A common practice to compare simulations to experiments is to rigidly shift the calculated values to match a well-known experimental value, which allows the prediction of core level binding energies for atomic configurations that are not known experimentally. Thus the experimentally meaningful values are the shifts of the C 1s energy with respect to the graphene bulk value, which are shown as the last column of Tables 1–3. However, it should be noted that the C 1s values for bulk atoms in certain configurations differ from the pristine graphene value by up to 0.4 eV. This shift depends on the computational unit cell size and would certainly be affected by the presence of a substrate. We have thus chosen to list the absolute shifts with respect to the pristine value in Tables 1–3, but use the shifted bulk values in the graphical representations of the line shapes shown above.

First, we must note that the C 1s energies calculated for the intrinsic defects (SV, DV and STW) are lower than the pristine graphene energy. This is only rarely seen in experiments, perhaps because of the spontaneous saturation of such sites under ambient conditions, as suggested by the negative formation energies of the saturated SV structures (Table 3). Speranza et al. [18] measured such negative shifts for irradiated graphite, and speculated that a component shifted by −0.5 eV could be due to an imbalance of electric charge around vacancies. Barinov et al. [17] explicitly calculated the dangling bond atom in the SV to have a downshift of −1.1 eV, while the two atoms in the pentagon have shifts of −0.7 eV. Our calculations give corresponding values of −2.4 and −0.37 eV. However, several other atoms surrounding the vacancy present shifts of around −0.7 eV. The binding energies for the DV and the STW defects present similar downshifts from the pristine value as in the SV case, but not quite as large.

The calculated values for the functionalized graphene systems can be found in Table 2. The C 1s value of the carbon atoms bonded to oxygen in the epoxide configuration (>O) is 1.5 eV higher than the pristine graphene value, in excellent agreement with Barinov et al., who calculated a shift of 1.6 eV [17] (although it should be noted that the experimental shift reported by Hossain et al. is slightly higher at 1.8 eV [4]). However, atoms 2 and 5 present negative shifts of −0.45 and −0.31 eV, respectively, contributing to the overall signature of these groups. For functionalities without vacancies, commonly accepted shifts in the literature [19,20] are 1.3–1.7 eV for a carbon bonded to -OH, 2.5–3.0 eV to =O, and 4.0–4.5 eV to -COOH. Looking at the values in Table 1, we find 1.2 eV for -OH, only 0.32 eV for =O, and 2.5 eV for -COOH. We note that the reference for =O actually comes from benzoquinone, which has =O functionalities at neighboring sites of the benzene ring. Thus we also considered a -2O functionality with oxygen atoms bonded to two adjacent carbon atoms. This gave a C 1s energy shift of 1.6 eV, which is closer to the literature value. However, it should be noted that the systems considered in the references above are different than those considered here, and thus one should not expect a perfect agreement. Looking at Table 2, we see that even when the C atom bonded to the functional group presents a positive shift, this is invariably compensated by negative shifts on neighboring carbons.

The calculated values for the saturated vacancy systems can be found in Table 3. For a single vacancy saturated with oxygen (SV-O), we found a shift of 0.67 eV (smaller than a reported value of 1.4 eV [17]). For the dangling bond atom in the hydroxyl group saturated vacancy (SV-OH) the C 1s is shifted by 0.42 eV, but the carbon atom at the other side of the vacancy close to the H presents a downshift of −0.29 eV, which is small but could still be experimentally observable. The carboxylic group presents large shifts of −1.23 eV for the dangling bond atom, and +2.11 eV for the carbon bonded to the two oxygens. However, considering the relatively high formation energies of the latter two structures, it should be noted that they might not represent stable ground state configurations. The diketone-saturated vacancy (SV=2O) shows a very large downshift of −2.88 eV for the dangling bond atom, and upshifts of 0.65 eV for the atoms bonded to the oxygens. The most stable ketone + annulene saturation presents large upshifts of 0.98 eV for the C bonded to the ketone O and 1.19 eV for the two C bonded to the annulene bridge O. However, atoms 2 also have moderate downshifts of −0.63 eV, complicating the peak signature.

Comparing equivalent functional groups with and without the vacancy, we see that the presence of the vacancy lowers the calculated C 1s energies of the carbon atom that is attached to the functional group significantly. This is likely due to the effect of the missing electron in the p_z orbital of the vacancy.

Concerning the oxygen 1s core level binding energies, we chose in Table 1 to use the calculated binding energy shared by the hydroxide and epoxide functional groups as the reference with which to compare the other O 1s values. For comparing our calculations to experimental values, we will discuss the epoxide configuration, since good recent data from Hossain et al. [4] is available. In their well-characterized graphene samples functionalized with oxygen atoms convincingly in the epoxide configuration, they observed an O 1s peak at 531.9 eV. Looking at Table 1, we calculated this value to be of 530.11 eV. Thus there is a difference of 1.8 eV corresponding to a relative error of around 0.3%, the same as for C 1s. Since the absolute computational error for the O 1s energies is different than for the C 1s energies we cannot use the same shift for the two, and we have much less information about the correct O 1s values in our particular case. However, the relative shifts between our calculated O 1s values are expected to be accurate and useful if an experimental baseline can be established in a specific study.

Conclusion

We have calculated the core level binding energies of both pristine and defective monolayered graphene functionalized with oxygen- and hydrogen-based adsorbates in a large and periodic unit cell. We have shown that the use of the projector-augmented wave method does not introduce significant errors in the treatment of the core electrons compared to all-electron calculations. The computationally efficient and scalable GPAW code is thus well suited for calculating core level binding energy shifts for graphene-based systems. However, higher levels of theory or more advanced functionals could certainly improve the absolute energy values. Because good agreement was obtained with experimental data found in the literature as far as it was available, we envisage that the calculations presented here will be especially useful for predicting the X-ray photoelectron spectroscopy signatures for novel structures for which such data is not available.

Computational details

Density functional theory was used as implemented in the GPAW simulation package [12]. The projector-augmented wave method [29] was used with frozen core electrons, and exchange and correlation was estimated by the Perdew–Burke–Ernzerhof (PBE) generalized gradient approximation [30]. Periodic boundary conditions were applied with a Monkhorst–Pack [31] k-point mesh up to 5 × 5 × 1 k-points.

Convergence checks

First, the pristine graphene lattice distance a_0 and the GPAW grid spacing parameter h were carefully converged with respect to the total energy. The converged parameters were a_0 = 2.443 Å and h = 0.19 Å. Next, the carbon 1s core level binding energy (using total energy differences) of a carbon atom in graphene was converged with respect to the unit cell size. The use of a sufficiently large unit cell is important to avoid spurious interactions with periodic images of the core hole. The maximum unit cell size for which the core-hole calculation could be completed with the available computational resources was 11 × 11. However, the C 1s energy was fully converged already for a 9 × 9 unit cell (a total of 162 atoms) when employing 3 × 3 × 1 k-points in the calculation. This convergence was checked to be valid also for more extended defects. A vacuum distance of 8 Å in the direction perpendicular to the graphene plane was sufficient to ensure convergence in all cases, including the highly non-planar -COOH functional group. All structures were allowed to fully relax so that the maximum forces reached less than 0.01 eV/atom. The all-electron projected density of states of the pristine graphene system reproduced all of the expected features of graphene, including the Dirac cones and the semi-metallic nature of a graphene monolayer. Similarly for FHI-aims, the convergence of both the total energies and the studied core level binding energies with respect to the computational parameters was ensured.

Formation energies

The formation energies E_{form} of the various configurations were calculated as

$$E_{\text{form}} = -\left(E_{\text{gra}} + E_{\text{ads}}\right) + \left(E_{\text{def}} + nE(\text{C})\right), \qquad (1)$$

where E_{gra} is the total energy of pristine graphene (for functional groups and vacancies) or the total energy of graphene with a single vacancy (for saturated single vacancies), E_{def} is the total energy of the system with a defect, E(C) is the energy for each of the n removed carbon atoms (equal to E_{gra}/N, where N is the number of atoms; in this case 162), and E_{ads} is the energy of the adsorbants.

The energies of missing carbon atoms were calculated as the energy of the pristine graphene sheet divided by the number of atoms, 1492.312 eV / 162 = 9.212 eV. The energies of added hydrogen and oxygen atoms were determined with respect to the chemical potentials of H_2 and O_2 molecules, which we calculated at 6.755 eV / 2 = 3.377 eV for hydrogen, and 9.137 eV / 2 = 4.569 eV for oxygen. For the COOH functionalities, we calculated the energy of a HCOOH molecule in vacuum by using the same unit cell and parameters as in the graphene

calculations [14], which yielded an energy of 30.213 eV, and subtracted half the H_2 molecule energy. In order to calculate the formation energies of the OH functionalities, we used $E_{OH} = E_{H2O} - E_{H2}/2$ [32], with the energy of the H_2O molecule calculated to be 14.336 eV.

GPAW core-hole calculation

The total energy of a system before photoemission is a sum of the energy of the X-ray photon, $h\nu$, and the energy of the target system in its initial state, E_i. After the photoemission, the total energy is equal to the kinetic energy of the emitted photelectron, E_k, plus that of the ionized system in its final state, E_f. We thus have $h\nu + E_i = E_k + E_f$. The binding energy, E_b, of the 1s electron is given by the difference between the energies of the X-ray photon and the emitted photelectron: $E_b = h\nu - E_k$, which leads to $E_b = E_f - E_i$, the difference between final and initial energies of the target system.

For the DFT calculations, we used the real-space grid-based projector-augmented wave (GPAW) code [12]. Recently, core-hole calculations that utilize a delta Kohn–Sham (ΔK–S) total energy differences method were implemented into GPAW by Ljungberg et al. [22,23], and into SIESTA by García-Gil et al. [33]. The core-hole setup (similar to a pseudo-potential) is created by using a spin-paired atomic calculation with the occupation of the core orbital decreased by one and held fixed. This setup is used to replace the target atom in a system of interest in the calculation. To obtain correct exchange–correlation effects, the 1s core spin densities are scaled to make the hole confined to spin up, which is an approximation that works very well for the case of small atomic number elements such as carbon and oxygen with only one core state, but requiring a spin-polarized calculation for the system of interest. A similar methodology, however employing pseudo-potentials [17], was previously used to study oxidized graphene.

The energy of the core level excitation was determined in the ΔK–S procedure, in which the total energy difference between the ground state and the first core ionized state is calculated. The core electron is removed from the 1s state and introduced into the valence band to ensure the neutrality of the unit cell. For metallic systems this is a very reasonable approach since the screening of the core hole is very efficient and the extra electron would be introduced at the Fermi level; however, for systems with large band gaps, this procedure could lead to large errors. Although the energy will depend on the exchange–correlation functional being used, the method should give consistent results for all atoms of the same kind. Since the C 1s level of graphite is well known experimentally, a rigid shift of the calculated energy scale to match it for the pristine defect-free system is applied to all C 1s energies calculated, which allows for a comparison of the results to experimental measurements. For O 1s, no unambiguous reference energy is present in all samples that could be used to shift the calculated O 1*s* energies.

FHI-aims all-electron calculations

Finally, to confirm that the use of the projectors did not introduce errors in the treatment of the core level energies, we performed additional calculations for selected systems using the all-electron code FHI-aims [13], also with the PBE functional, and compared the C 1s energy values to the corresponding GPAW calculation. The core level energies were calculated by comparing the relaxed total energies of a system with or without a core hole – described by an explicitly empty 1*s* core orbital in the case of FHI-aims – on an atom of interest.

Supporting Information

Supporting Information File 1

Mathematica script used for plotting the line shapes shown in Figure 4.
[http://www.beilstein-journals.org/bjnano/content/supplementary/2190-4286-5-12-S1.zip]

Acknowledgements

We thank Jani Kotakoski, Jussi Enkovaara, Arkady Krasheninnikov, Duncan Mowbray and Georgina Ruiz-Soria for helpful discussions.. T.S. was supported by the Austrian Science Fund (FWF) through grant M 1497-N19, by the Finnish Cultural Foundation, and by the Walter Ahlström Foundation. Generous computational resources from CSC–IT Center for Science in Espoo, Finland are gratefully acknowledged.

References

1. Elias, D. C.; Nair, R. R.; Mohiuddin, T. M. G.; Morozov, S. V.; Blake, P.; Halsall, M. P.; Ferrari, A. C.; Boukhvalov, D. W.; Katsnelson, M. I.; Geim, A. K.; Novoselov, K. S. *Science* **2009,** *323,* 610–613. doi:10.1126/science.1167130
2. Sofo, J. O.; Chaudhari, A. S.; Barber, G. D. *Phys. Rev. B* **2007,** *75,* 153401. doi:10.1103/PhysRevB.75.153401
3. Leconte, N.; Moser, J.; Ordejon, P.; Tao, H.; Lherbier, A. I.; Bachtold, A.; Alsina, F.; Sotomayor Torres, C. M.; Charlier, J.-C.; Roche, S. *ACS Nano* **2010,** *4,* 4033–4038. doi:10.1021/nn100537z
4. Hossain, M. Z.; Johns, J. E.; Bevan, K. H.; Karmel, H. J.; Liang, Y. T.; Yoshimoto, S.; Mukai, K.; Koitaya, T.; Yoshinobu, J.; Kawai, M.; Lear, A. M.; Kesmodel, L. L.; Tait, S. L.; Hersam, M. C. *Nat. Chem.* **2012,** *4,* 305–309. doi:10.1038/nchem.1269
5. Leconte, N.; Soriano, D.; Roche, S.; Ordejon, P.; Charlier, J.-C.; Palacios, J. J. *ACS Nano* **2011,** *5,* 3987–3992. doi:10.1021/nn200558d
6. Wei, Z.; Wang, D.; Kim, S.; Kim, S.-Y.; Hu, Y.; Yakes, M. K.; Laracuente, A. R.; Dai, Z.; Marder, S. R.; Berger, C.; King, W. P.; de Heer, W. A.; Sheehan, P. E.; Riedo, E. *Science* **2010,** *328,* 1373–1376. doi:10.1126/science.1188119

7. Gómez-Navarro, C.; Meyer, J. C.; Sundaram, R. S.; Chuvilin, A.; Kurasch, S.; Burghard, M.; Kern, K.; Kaiser, U. *Nano Lett.* **2010,** *10,* 1144–1148. doi:10.1021/nl9031617
8. Meyer, J. C.; Kisielowski, C.; Erni, R.; Rossell, M. D.; Crommie, M. F.; Zettl, A. *Nano Lett.* **2008,** *8,* 3582–3586. doi:10.1021/nl801386m
9. Banhart, F.; Kotakoski, J.; Krasheninnikov, A. V. *ACS Nano* **2011,** *5,* 26–41. doi:10.1021/nn102598m
10. El-Barbary, A. A.; Telling, R. H.; Ewels, C. P.; Heggie, M. I.; Briddon, P. R. *Phys. Rev. B* **2003,** *68,* 144107. doi:10.1103/PhysRevB.68.144107
11. Ugeda, M. M.; Brihuega, I.; Guinea, F.; Gómez-Rodríguez, J. M. *Phys. Rev. Lett.* **2010,** *104,* 096804. doi:10.1103/PhysRevLett.104.096804
12. Mortensen, J. J.; Hansen, L. B.; Jacobsen, K. W. *Phys. Rev. B* **2005,** *71,* 035109. doi:10.1103/PhysRevB.71.035109
13. Blum, V.; Gehrke, R.; Hanke, F.; Havu, P.; Havu, V.; Ren, X.; Reuter, K.; Scheffler, M. *Comput. Phys. Commun.* **2009,** *180,* 2175–2196. doi:10.1016/j.cpc.2009.06.022
14. Al-Aqtash, N.; Vasiliev, I. *J. Phys. Chem. C* **2009,** *113,* 12970–12975. doi:10.1021/jp902280f
15. Felten, A.; Bittencourt, C.; Pireaux, J. J.; Van Lier, G.; Charlier, J. C. *J. Appl. Phys.* **2005,** *98,* 074308. doi:10.1063/1.2071455
16. Allouche, A.; Ferro, Y. *Carbon* **2006,** *44,* 3320–3327. doi:10.1016/j.carbon.2006.06.014
17. Barinov, A.; Malcioglu, O. B.; Fabris, S.; Sun, T.; Gregoratti, L.; Dalmiglio, M.; Kiskinova, M. *J. Phys. Chem. C* **2009,** *113,* 9009–9013. doi:10.1021/jp902051d
18. Speranza, G.; Minati, L.; Anderle, M. *J. Appl. Phys.* **2007,** *102,* 043504. doi:10.1063/1.2769332
19. Yumitori, S. *J. Mater. Sci.* **2000,** *35,* 139–146. doi:10.1023/A:1004761103919
20. Sherwood, P. M. A. *J. Electron Spectrosc. Relat. Phenom.* **1996,** *81,* 319–342. doi:10.1016/0368-2048(95)02529-4
21. Boukhvalov, D. W.; Katsnelson, M. I.; Lichtenstein, A. I. *Phys. Rev. B* **2008,** *77,* 035427. doi:10.1103/PhysRevB.77.035427
22. Ljungberg, M. P. Theoretical modeling of X-ray and vibrational spectroscopies applied to liquid water and surface adsorbates. Ph.D. Thesis, Department of Physics, Stockholm University, Stockholm, 2010.
23. Ljungberg, M. P.; Mortensen, J. J.; Pettersson, L. G. M. *J. Electron Spectrosc. Relat. Phenom.* **2011,** *184,* 427–439. doi:10.1016/j.elspec.2011.05.004
24. Emtsev, K. V.; Speck, F.; Seyller, T.; Ley, L.; Riley, J. D. *Phys. Rev. B* **2008,** *77,* 155303. doi:10.1103/PhysRevB.77.155303
25. Hibino, H.; Kageshima, H.; Nagase, M. *J. Phys. D: Appl. Phys.* **2010,** *43,* 374005. doi:10.1088/0022-3727/43/37/374005
26. Zhou, S. Y.; Gweon, G. H.; Fedorov, A. V.; First, P. N.; de Heer, W. A.; Lee, D. H.; Guinea, F.; Castro Neto, A. H.; Lanzara, A. *Nat. Mater.* **2007,** *6,* 770–775. doi:10.1038/nmat2003
27. Lizzit, S.; Zampieri, G.; Petaccia, L.; Larciprete, R.; Lacovig, P.; Rienks, E. D. L.; Bihlmayer, G.; Baraldi, A.; Hofmann, P. *Nat. Phys.* **2010,** *6,* 345–349. doi:10.1038/nphys1615
28. Haberer, D.; Giusca, C. E.; Wang, Y.; Sachdev, H.; Fedorov, A. V.; Farjam, M.; Jafari, S. A.; Vyalikh, D. V.; Usachov, D.; Liu, X.; Treske, U.; Grobosch, M.; Vilkov, O.; Adamchuk, V. K.; Irle, S.; Silva, S. R. P.; Knupfer, M.; Büchner, B.; Grüneis, A. *Adv. Mater.* **2011,** *23,* 4497–4503. doi:10.1002/adma.201102019
29. Blöchl, P. E. *Phys. Rev. B* **1994,** *50,* 17953–17979. doi:10.1103/PhysRevB.50.17953
30. Perdew, J. P.; Burke, K.; Ernzerhof, M. *Phys. Rev. Lett.* **1996,** *77,* 3865–3868. doi:10.1103/PhysRevLett.77.3865
31. Monkhorst, H. J.; Pack, J. D. *Phys. Rev. B* **1976,** *13,* 5188–5192. doi:10.1103/PhysRevB.13.5188
32. Boukhvalov, D. W.; Katsnelson, M. I. *J. Am. Chem. Soc.* **2008,** *130,* 10697–10701. doi:10.1021/ja8021686
33. García-Gil, S.; García, A.; Ordejón, P. *Eur. Phys. J. B* **2012,** *85,* 239. doi:10.1140/epjb/e2012-30334-5

License and Terms

Beilstein Journal of Nanotechnology

Charge and spin transport in mesoscopic superconductors

M. J. Wolf, F. Hübler, S. Kolenda and D. Beckmann*

Full Research Paper

Open Access

Address:
Karlsruher Institut für Technologie (KIT), Institut für Nanotechnologie, P.O. Box 3640, D-72021 Karlsruhe, Germany

Email:
D. Beckmann* - detlef.beckmann@kit.edu

* Corresponding author

Keywords:
spintronics; superconductor–ferromagnet hybrids

Beilstein J. Nanotechnol. **2014,** *5,* 180–185.
doi:10.3762/bjnano.5.18

Received: 28 November 2013
Accepted: 23 January 2014
Published: 17 February 2014

This article is part of the Thematic Series "Physics, chemistry and biology of functional nanostructures II".

Guest Editor: A. S. Sidorenko

Abstract

Background: Non-equilibrium charge transport in superconductors has been investigated intensely in the 1970s and 1980s, mostly in the vicinity of the critical temperature. Much less attention has been paid to low temperatures and the role of the quasiparticle spin.

Results: We report here on nonlocal transport in superconductor hybrid structures at very low temperatures. By comparing the nonlocal conductance obtained by using ferromagnetic and normal-metal detectors, we discriminate charge and spin degrees of freedom. We observe spin injection and long-range transport of pure, chargeless spin currents in the regime of large Zeeman splitting. We elucidate charge and spin transport by comparison to theoretical models.

Conclusion: The observed long-range chargeless spin transport opens a new path to manipulate and utilize the quasiparticle spin in superconductor nanostructures.

Introduction

The investigation of spin-polarized transport in hybrid structures was pioneered in the 1970s with the discovery of spin-dependent tunneling into thin-film superconductors with a large Zeeman splitting by Tedrow and Meservey [1,2]. While much of the related basic physics such as tunneling magnetoresistance (TMR) [3] and non-equilibrium spin injection [4] was observed subsequently, spin-polarized transport did not attract much attention until the discovery of the giant magnetoresistance (GMR) [5-7] and its technical applications.

In superconductors, electrons are bound in Cooper pairs, which usually have a singlet structure and therefore carry only charge

but no spin. The quasiparticle excitations, however, may carry both charge and spin. Non-equilibrium charge transport in superconductors has been investigated intensely in the 1970s and 1980s, mostly in the vicinity of the critical temperature [8-10] and more recently also in the low-temperature regime [11-13]. In contrast, only few experiments on quasiparticle spin transport [14] have been reported, and the subject remains poorly understood. For example, both anomalously short [15] and anomalously long [16] spin relaxation times have been reported in superconducting aluminum.

In this paper, we summarize some of our recent experimental results on non-equilibrium charge and spin transport in nanoscale superconductors [12,17,18], and perform additional numerical analysis to obtain more insight into the physical mechanisms.

Results and Discussion

Figure 1 shows a typical sample layout and measurement scheme. A central superconducting aluminum wire is contacted by several normal-metal (copper) or ferromagnetic (iron) electrodes attached via thin tunnel barriers. A dc bias voltage V_{inj} with a small superimposed low-frequency ac excitation is applied to one junction (injector), and the resulting current I_{inj} flowing into the junction is measured to determine the local differential conductance $g_{loc} = dI_{inj}/dV_{inj}$. Simultaneously, the current I_{det} flowing out of a nearby detector junction is measured to obtain the nonlocal conductance $g_{nl} = dI_{det}/dV_{inj}$. The nonlocal conductance was measured for different contact distances d, and different material combinations, for which both injector and detector could be either normal (N) or ferromagnetic (F). These configurations will be labeled by AISIB, where A and B denote the injector and detector contacts, respectively. Two examples (NISIN and NISIF) are indicated in Figure 1.

The measurements were carried out in a dilution refrigerator at temperatures down to about 50 mK, and with a magnetic field B applied along the substrate plane parallel to the copper or iron wires. The thickness of the aluminum films was t_{Al} = 12–30 nm, and for the thinnest films, critical fields exceeding 2 T were observed.

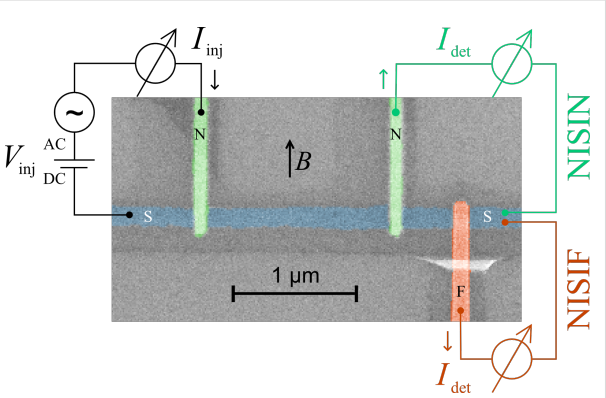

Figure 1: False color scanning electron microscopy image of one of our samples, together with the measurement scheme. The samples consist of a central superconducting wire (S), with normal-metal (N) and/or ferromagnetic (F) wires attached to it via tunnel contacts [18].

Before we discuss the spin signal observed by using ferromagnetic detector junctions, we analyze the charge imbalance signal observed in an NISIN configuration. The aluminum film thickness of this sample was t_{Al} = 30 nm, with a critical field B_c = 0.53 T. Here, the effect of the applied field is mostly orbital pair breaking, and the Zeeman splitting of the density of states does not play a significant role. In Figure 2a, we show the nonlocal conductance g_{nl} of a pair of contacts at low temperature and for bias voltages above the energy gap $\Delta \approx 200$ µeV of the superconductor. By fitting g_{nl} at a given bias voltage for

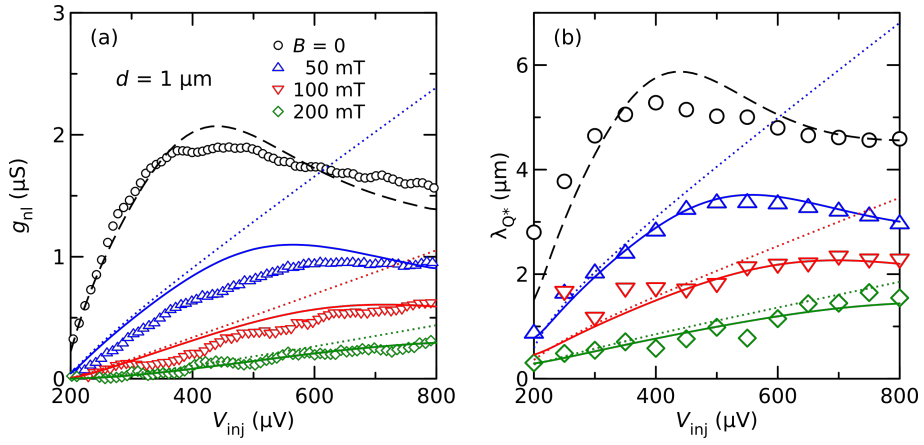

Figure 2: (a) Nonlocal conductance of one contact pair of an NISIN sample with d = 1 µm as a function of the injector bias V_{inj} for different magnetic fields B. (b) Charge imbalance relaxation length λ_{Q^*}. Data taken from [12], the lines are various model predictions explained in the text.

different contact distances to an exponential decay, we can obtain a bias-dependent charge relaxation length λ_{Q^*} (see [12] for details). The corresponding results are shown in Figure 2b.

Since we are interested here mostly in the behavior at finite magnetic fields, where Green's function methods are most appropriate, we model the data with the linearized kinetic equation derived by Schmid et al. [19]. A simple analytical approximation that neglects the cooling of the quasiparticles (see Supporting Information File 1) yields the charge-imbalance relaxation length at low temperature

$$\lambda_{Q^*} = \xi\sqrt{\frac{N_1^2 + N_2^2}{2N_2}}\,, \tag{1}$$

where N_1 is the density of states in the superconductor, N_2 is the real part of the anomalous Green's function, $\xi = \sqrt{\hbar D_N / \Delta}$ is the dirty-limit coherence length, and D_N is the normal-state diffusion coefficient. The nonlocal conductance due to charge imbalance within the same approximation is

$$g_{nl}^{CI} = G_{inj}G_{det} \times \int \frac{N_1^2}{N_1^2 + N_2^2}\frac{\rho_N \lambda_{Q^*}}{2\mathcal{A}} e^{-d/\lambda_{Q^*}} f_0'\left(E - eV_{inj}\right)dE\,, \tag{2}$$

where $f_0'(E)$ is the derivative of the Fermi function, ρ_N is the normal-state resistivity of the superconductor, and $\mathcal{A}$ is the cross-section area of the superconducting wire.

In Figure 2, we compare the model predictions to the experimental data. We proceeded by first fitting λ_{Q^*} at finite magnetic fields with the simple "no-cooling" approximation Equation 1. Here, we assume that the pair-breaking strength follows the relation $\zeta = (B/B_c)^2/2$ for a magnetic field applied parallel to a thin film, and use the diffusion coefficient D_N as the single free fit parameter for all curves. These fits are shown as dotted lines in Figure 2b. As can be seen, a good fit can be made for the initial slope of the data, and we obtain $D_N = 70$ cm^2/s from the fit, a value somewhat larger than the independent estimate (40 cm^2/s) from the resistivity. Without additional fitting, we can then plot the predictions for the nonlocal conductance according to Equation 2 in Figure 2a. For large bias, the experimental data (both g_{nl} and λ_{Q^*}) deviate downward from the fits. Full numerical simulations that include cooling, with the characteristic inelastic scattering time τ_E as the only remaining fit parameter, are shown as solid lines in Figure 2. Excellent agreement with the experimental data for λ_{Q^*} can be achieved for $\tau_E = 12$ ns. The agreement for the nonlocal conductance is not as good as for λ_{Q^*}, but still satisfactory. We finally attempted to fit the data at zero field, i.e., for $\zeta = 0$. The predictions exceeded the experimental data by about a factor of two, both for g_{nl} and λ_{Q^*} (not shown). We attribute this discrepancy to the fact that at zero applied field, any small additional source of pair breaking, such as gap anisotropy, magnetic impurities, spatial profile of the gap due to quasiparticle injection, etc., may contribute to charge relaxation [20]. A reasonable fit (dashed lines) could be obtained by setting $\zeta = 8 \times 10^{-4}$ to account for all these pair-breaking perturbations. At zero field, we find a relaxation length of a few micrometers, which corresponds to characteristic time scales of a few nanoseconds. Recently, some experiments reported shorter time scales (sometimes by orders of magnitude) under similar conditions [21,22]. In contrast, our results are quantitatively consistent with the "old" knowledge obtained from experiments close to the critical temperature [23-25], as well as more recent low-temperature experiments on the spatial decay of charge imbalance in thin wires [11,13]. Both experimentally and theoretically, we find that the charge relaxation length decreases with increasing magnetic field, and is smallest at energies just above the gap. This is the parameter range where the spin signal is observed by the ferromagnetic detectors described below. Also, in this parameter regime we can use the analytical "no-cooling" approximation (Equation 2) to describe the charge imbalance.

In Figure 3 we compare the nonlocal conductance for an FISIN (a) and NISIF (b) configuration, while using the same pair of contacts, but reversing the roles of injector and detector. We plot here the normalized nonlocal conductance $\hat{g}_{nl} = g_{nl}/G_{inj}G_{det}$, where G_{inj} and G_{det} are the normal-state conductances of the injector and detector junctions, respectively. In the FISIN configuration, the nonlocal conductance is negligible at bias voltages below the gap. At bias voltages above the gap, the signal initially increases almost linearly, and then the slope decreases except for the highest magnetic fields. The signal is an even function of the bias and can be attributed to charge imbalance, as described above, since the normal-metal detector is not sensitive to spin accumulation. The lines are fits to Equation 2.

For the NISIF configuration, shown in Figure 3b, a similar signal is observed at $B = 0$. Upon increasing the field, however, two additional peaks appear near the gap edge, with opposite sign for opposite bias polarity. These features can be attributed to spin injection into the Zeeman-split density of states of the superconductor [17,18,22,26], which is probed by the ferromagnetic detector in this configuration. Spin-polarized tunneling can be described by two independent conductances $g_\downarrow$ and $g_\uparrow$ for the two spin orientations. The conductance is then given by the sum $g_\downarrow + g_\uparrow$, whereas the spin current is proportional to the

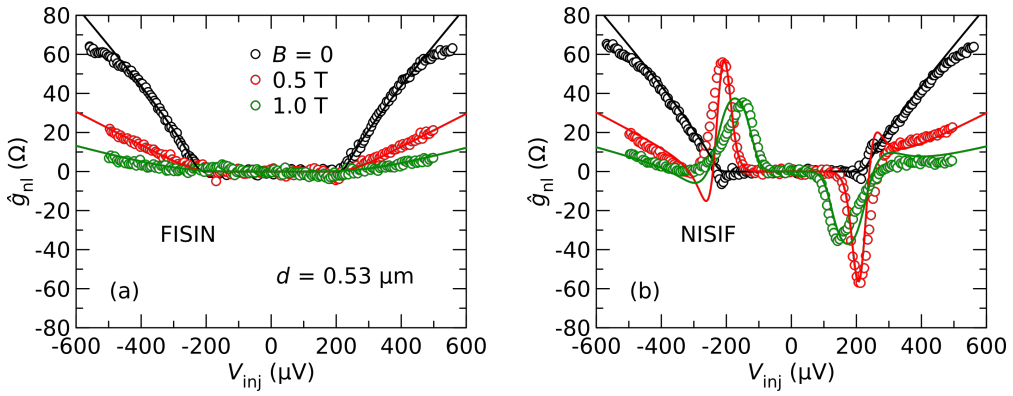

Figure 3: Normalized nonlocal conductance of one contact pair in an FISIN (a) and NISIF (b) configuration as a function of V_{inj} for different magnetic fields B. Symbols are experimental data [18], lines are fits explained in the text.

difference $g_\downarrow - g_\uparrow$. The lines in Figure 3b are the sum of the charge-imbalance contribution shown in Figure 3a and an additional contribution $g_{nl}^S \propto (g_\downarrow - g_\uparrow)$ to account for the spin signal. For the latter, we use parameters that we obtained from fits of the local conductance of the injector junctions, which leaves only the overall signal amplitude as a free fit parameter. As can be seen, the reasonable fit can be obtained over the entire bias range.

In Figure 4, we compare the lengths of charge and spin relaxation of several samples with similar properties of the aluminum film as a function of the normalized magnetic field B/B_c. The samples have different numbers of ferromagnetic and normal-metal junctions, as indicated in the figure. In Figure 4a, we plot the charge relaxation length λ_{Q^*} obtained at a bias voltage of about 2Δ, for which λ_{Q^*} is usually largest at zero field (compare Figure 2). λ_{Q^*} is typically a few micrometers at zero field, and then quickly drops. The lines are fits to Equation 1. The spin relaxation length λ_S is found by fitting the area A of the spin-signal peaks as a function of contact distance to an exponential decay [17,18]. At small fields, λ_S is similar to λ_{Q^*}, but then strongly increases with increasing field. At present, no theoretical model for high-field spin diffusion and relaxation in superconductors is available, therefore only a tentative interpretation is possible. The normal-state spin diffusion length in the samples is typically less than 500 nm, which means a tenfold increase in the superconducting state. A possible relaxation mechanism could be a two-stage process of spin-flip scattering and recombination, which has been considered theoretically in a different context [27,28]. A generalization of existing models for the non-equilibrium transport in superconductors [19,29] to the case of large Zeeman splitting, treating both charge and spin degrees of freedom on an equal footing, would be highly desirable.

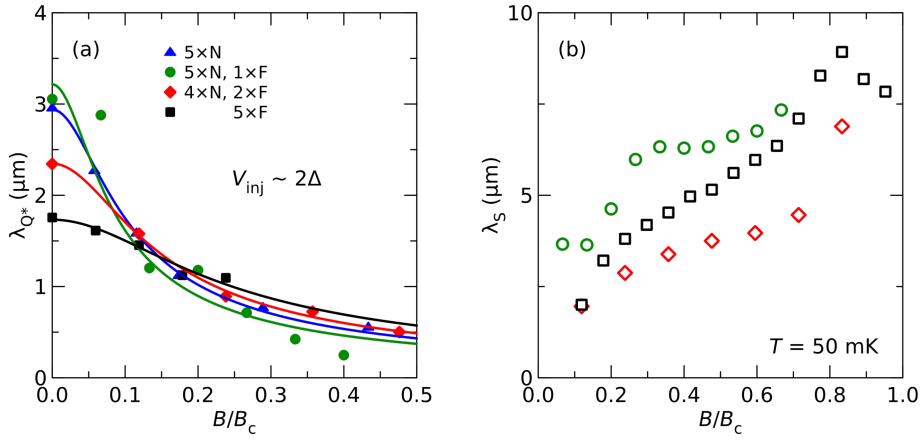

Figure 4: Charge relaxation length λ_{Q^*} at a bias voltage of about 2Δ (a) and spin diffusion length λ_S (b) for different samples as a function of normalized magnetic field B/B_c. The samples have different number of ferromagnetic (F) and normal-metal (N) contacts, as indicated in the legend. Symbols are experimental data [17,18], lines are fits explained in the text.

Figure 5 shows the evolution of the spin relaxation length λ_S and the amplitude A of the spin signal as a function of the temperature. λ_S is independent of the temperature within the accuracy of the experiment, similar to λ_{Q^*} in the same temperature range [12]. In contrast, the signal amplitude decreases with increasing temperature. The spin-injection rate proportional to $g_\downarrow - g_\uparrow$ inferred from the local conductance does not change appreciably in this temperature range, except for thermal broadening, which should not affect the overall peak area A. Thus, since neither injection nor relaxation cause the signal change, the decrease of signal amplitude must be related to the detection process. A simple model based on the tunnel Hamiltonian yields [17]

$$I_{\mathrm{det}} \propto S = \sum_{\sigma} \sigma \int N_{1\sigma}(E)\left[f_\sigma(E) - f_0(E)\right] dE\,, \qquad (3)$$

where S is the net spin accumulation, $f_\sigma(E)$ is the quasiparticle distribution for spin σ in the superconductor, and f_0 denotes the Fermi distribution in the ferromagnetic detector junction. As can be seen, the detector signal is proportional to the difference of the distribution functions in the superconductor and ferromagnet. The former is determined by spin injection, whereas the latter can be assumed to be (nearly) at equilibrium at the bath temperature. Therefore, we can expect the spin signal to decrease as the bath temperature is raised. A very simple model to describe this drop can be obtained by assuming that non-equilibrium injection raises the effective temperature of the quasiparticles inside the superconductor to about 1 K, as we have found in similar structures with normal-metal junctions [30], and that most quasiparticles have an energy close to the energy gap E_g, which is typically around 0.5–0.75 × Δ_0 at the fields of the experiments. Then, the spin signal should be proportional to $f_0(E_g, 1\ \mathrm{K}) - f_0(E_g, T)$. Fits to this model are shown in Figure 5b. As can be seen, the agreement is quite good, despite the oversimplification of the model. We note that, usually, the current through an NIS junction does not depend on the temperature of the normal metal due to particle–hole symmetry. This is no longer true if a spin-dependent density of states in the superconductor is combined with a spin-dependent tunnel conductance, as it is the case in our experiment. For this case, large thermoelectric effects driven by the temperature difference between superconductor and ferromagnet have been predicted recently [31,32].

Conclusion

We have presented an analysis of our recent experiments on spin and charge transport in nanoscale superconductors at very low temperatures and high magnetic fields. We find that charge imbalance can be described surprisingly well with existing models, despite the fact that they were initially developed for experiments close to the critical temperature. Charge relaxation is very fast at energies just above the gap. This is the bias regime, in which we observe long-range spin transport in the presence of a Zeeman splitting of the density of states. By comparing the relaxation lengths for charge and spin, we can conclude that spin currents in this regime are nearly chargeless. While no detailed model of spin transport and relaxation is available yet, we find that simple models based on the tunnel Hamiltonian explain the dependence of spin injection and detection on bias, magnetic field and temperature. The ability to create and transport pure spin currents in superconductors may be useful for future superconducting spintronics devices. Further, our analysis of the temperature dependence hints at the importance of new thermoelectric effects in nanoscale superconductor-ferromagnet hybrids.

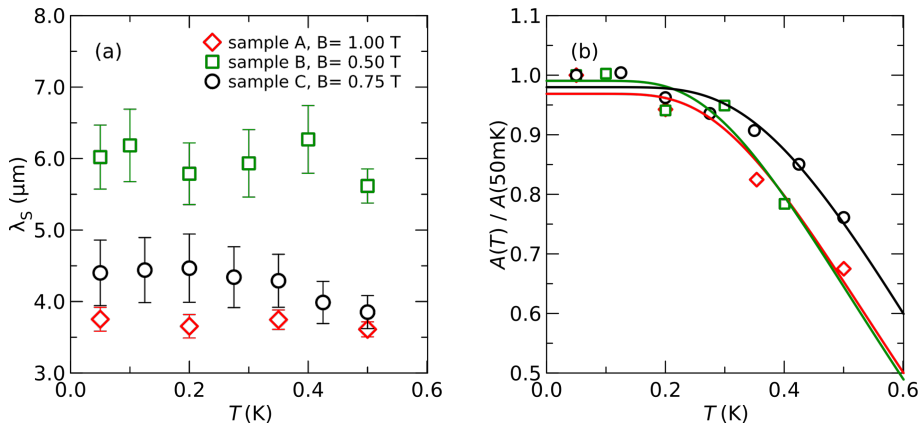

Figure 5: Spin relaxation length λ_S (a) and amplitude A of the spin signal (b) for different samples as a function of the temperature T. Symbols are experimental data [17,18], lines are fits explained in the text.

Supporting Information

Supporting Information File 1

Details of the theoretical model.
[http://www.beilstein-journals.org/bjnano/content/supplementary/2190-4286-5-18-S1.pdf]

Acknowledgements

We acknowledge financial support by DFG grant BE-4422/1-1 and the competence network “Functional Nanostructures” of the Baden-Württemberg-Stiftung, and W. Belzig and M. Eschrig for stimulating discussions.

References

1. Tedrow, P. M.; Meservey, R. *Phys. Rev. Lett.* **1971,** *26,* 192. doi:10.1103/PhysRevLett.26.192
2. Meservey, R.; Tedrow, P. M. *Phys. Rep.* **1994,** *238,* 173. doi:10.1016/0370-1573(94)90105-8
3. Julliere, M. *Phys. Lett. A* **1975,** *54,* 225. doi:10.1016/0375-9601(75)90174-7
4. Johnson, M.; Silsbee, R. H. *Phys. Rev. Lett.* **1985,** *55,* 1790. doi:10.1103/PhysRevLett.55.1790
5. Baibich, M. N.; Broto, J. M.; Fert, A.; Nguyen Van Dau, F.; Petroff, F.; Etienne, P.; Creuzet, G.; Friederich, A.; Chazelas, J. *Phys. Rev. Lett.* **1988,** *61,* 2472. doi:10.1103/PhysRevLett.61.2472
6. Binasch, G.; Grünberg, P.; Saurenbach, F.; Zinn, W. *Phys. Rev. B* **1989,** *39,* 4828. doi:10.1103/PhysRevB.39.4828
7. Žutić, I.; Fabian, J.; Das Sarma, S. *Rev. Mod. Phys.* **2004,** *76,* 323. doi:10.1103/RevModPhys.76.323
8. Clarke, J. *Phys. Rev. Lett.* **1972,** *28,* 1363. doi:10.1103/PhysRevLett.28.1363
9. Tinkham, M.; Clarke, J. *Phys. Rev. Lett.* **1972,** *28,* 1366. doi:10.1103/PhysRevLett.28.1366
10. Langenberg, D. N.; Larkin, A. I., Eds. *Nonequilibrium Superconductivity;* North-Holland: Amsterdam, New York, 1986.
11. Yagi, R. *Phys. Rev. B* **2006,** *73,* 134507. doi:10.1103/PhysRevB.73.134507
12. Hübler, F.; Camirand Lemyre, J.; Beckmann, D.; v. Löhneysen, H. *Phys. Rev. B* **2010,** *81,* 184524. doi:10.1103/PhysRevB.81.184524
13. Arutyunov, K. Yu.; Auraneva, H.-P.; Vasenko, A. S. *Phys. Rev. B* **2011,** *83,* 104509. doi:10.1103/PhysRevB.83.104509
14. Johnson, M. *Appl. Phys. Lett.* **1994,** *65,* 1460. doi:10.1063/1.112015
15. Poli, N.; Morten, J. P.; Urech, M.; Brataas, A.; Haviland, D. B.; Korenivski, V. *Phys. Rev. Lett.* **2008,** *100,* 136601. doi:10.1103/PhysRevLett.100.136601
16. Yang, H.; Yang, S.-H.; Takahashi, S.; Maekawa, S.; Parkin, S. S. P. *Nat. Mater.* **2010,** *9,* 586. doi:10.1038/nmat2781
17. Hübler, F.; Wolf, M. J.; Beckmann, D.; v. Löhneysen, H. *Phys. Rev. Lett.* **2012,** *109,* 207001. doi:10.1103/PhysRevLett.109.207001
18. Wolf, M. J.; Hübler, F.; Kolenda, S.; v. Löhneysen, H.; Beckmann, D. *Phys. Rev. B* **2013,** *87,* 024517. doi:10.1103/PhysRevB.87.024517
19. Schmid, A.; Schön, G. *J. Low Temp. Phys.* **1975,** *20,* 207. doi:10.1007/BF00115264
20. Lemberger, T. R. *Phys. Rev. B* **1984,** *29,* 4946. doi:10.1103/PhysRevB.29.4946
21. Kleine, A.; Baumgartner, A.; Trbovic, J.; Golubev, D. S.; Zaikin, A. D.; Schönenberger, C. *Nanotechnology* **2010,** *21,* 274002. doi:10.1088/0957-4484/21/27/274002
22. Quay, C. H. L.; Chevallier, D.; Bena, C.; Aprili, M. *Nat. Phys.* **2013,** *9,* 84. doi:10.1038/nphys2518
23. Chi, C. C.; Clarke, J. *Phys. Rev. B* **1979,** *19,* 4495. doi:10.1103/PhysRevB.19.4495
24. Stuivinga, M.; Ham, C. L. G.; Klapwijk, T. M.; Mooij, J. E. *J. Low Temp. Phys.* **1983,** *53,* 633. doi:10.1007/BF00683998
25. Mamin, H. J.; Clarke, J.; Van Harlingen, D. J. *Phys. Rev. B* **1984,** *29,* 3881. doi:10.1103/PhysRevB.29.3881
26. Giazotto, F.; Taddei, F. *Phys. Rev. B* **2008,** *77,* 132501. doi:10.1103/PhysRevB.77.132501
27. Grimaldi, C.; Fulde, P. *Phys. Rev. Lett.* **1996,** *77,* 2550. doi:10.1103/PhysRevLett.77.2550
28. Grimaldi, C.; Fulde, P. *Phys. Rev. B* **1997,** *56,* 2751. doi:10.1103/PhysRevB.56.2751
29. Morten, J. P.; Brataas, A.; Belzig, W. *Phys. Rev. B* **2004,** *70,* 212508. doi:10.1103/PhysRevB.70.212508
30. Kolenda, S.; Wolf, M. J.; Golubev, D. S.; Zaikin, A. D.; Beckmann, D. *Phys. Rev. B* **2013,** *88,* 174509. doi:10.1103/PhysRevB.88.174509
31. Machon, P.; Eschrig, M.; Belzig, W. *Phys. Rev. Lett.* **2013,** *110,* 047002. doi:10.1103/PhysRevLett.110.047002
32. Ozaeta, A.; Virtanen, P.; Bergeret, F. S.; Heikkilä, T. T. **2013**. Huge thermoelectric effects in ferromagnet-superconductor junctions in the presence of a spin-splitting field, arXiv:1307.4672, Condensed Matter - Superconductivity, 2013.

License and Terms

Beilstein Journal of Nanotechnology

En route to controlled catalytic CVD synthesis of densely packed and vertically aligned nitrogen-doped carbon nanotube arrays

Slawomir Boncel[*1], Sebastian W. Pattinson[2], Valérie Geiser[2], Milo S. P. Shaffer[3] and Krzysztof K. K. Koziol[*2]

Full Research Paper

Open Access

Address:
[1]Department of Organic Chemistry, Biochemistry and Biotechnology, Silesian University of Technology, Krzywoustego 4, 44-100 Gliwice, Poland, [2]Department of Materials Science and Metallurgy, University of Cambridge, 27 Charles Babbage Road, Cambridge CB3 0FS, United Kingdom and [3]Imperial College London, Department of Chemistry, London SW7 2AZ, United Kingdom

Email:
Slawomir Boncel[*] - slawomir.boncel@polsl.pl; Krzysztof K. K. Koziol[*] - kk292@cam.ac.uk

* Corresponding author

Keywords:
carbon nanotubes; catalytic chemical vapour deposition; crystallinity; nitrogen doping; vertically aligned nanotube arrays

Beilstein J. Nanotechnol. **2014,** *5,* 219–233.
doi:10.3762/bjnano.5.24

Received: 29 November 2013
Accepted: 05 February 2014
Published: 03 March 2014

This article is part of the Thematic Series "Physics, chemistry and biology of functional nanostructures II".

Guest Editor: A. S. Sidorenko

Abstract

The catalytic chemical vapour deposition (c-CVD) technique was applied in the synthesis of vertically aligned arrays of nitrogen-doped carbon nanotubes (N-CNTs). A mixture of toluene (main carbon source), pyrazine (1,4-diazine, nitrogen source) and ferrocene (catalyst precursor) was used as the injection feedstock. To optimize conditions for growing the most dense and aligned N-CNT arrays, we investigated the influence of key parameters, i.e., growth temperature (660, 760 and 860 °C), composition of the feedstock and time of growth, on morphology and properties of N-CNTs. The presence of nitrogen species in the hot zone of the quartz reactor decreased the growth rate of N-CNTs down to about one twentieth compared to the growth rate of multi-wall CNTs (MWCNTs). As revealed by electron microscopy studies (SEM, TEM), the individual N-CNTs (half as thick as MWCNTs) grown under the optimal conditions were characterized by a superior straightness of the outer walls, which translated into a high alignment of dense nanotube arrays, i.e., 5×10^8 nanotubes per mm^2 (100 times more than for MWCNTs grown in the absence of nitrogen precursor). In turn, the internal crystallographic order of the N-CNTs was found to be of a 'bamboo'-like or 'membrane'-like (multi-compartmental structure) morphology. The nitrogen content in the nanotube products, which ranged from 0.0 to 3.0 wt %, was controlled through the concentration of pyrazine in the feedstock. Moreover, as revealed by Raman/FT-IR spectroscopy, the incorporation of nitrogen atoms into the nanotube walls was found to be proportional to the number of deviations from the sp^2-hybridisation of graphene C-atoms. As studied by XRD, the temperature and the [pyrazine]/[ferrocene] ratio in the feedstock affected the composition of the catalyst particles, and hence changed the growth mechanism of individual N-CNTs into a 'mixed base-and-tip' (primarily of the base-type) type as compared to the purely 'base'-type for undoped MWCNTs.

Introduction

The doping of carbon nanotubes (CNTs) with boron [1,2], nitrogen [3,4] or phosphorus [5] atoms has been frequently used to enhance or tune their physicochemical properties. Among the elemental dopants, nitrogen emerges as of particular interest in electronics since N-CNTs should be characterized by a higher electrical conductivity (n-doping). Consequently, the significance of N-CNTs in a variety of electrical engineering applications has been continuously growing [6,7]. The enhancement of other properties of N-CNTs, including the chemical reactivity [8], the dispersibility in a variety of solvents/matrices [9], the structural strength [10] or the thermal conductivity [11] has been also reported. The field emission characteristics of N-CNTs have also been demonstrated to be superior to that of pristine CNTs [12]. Moreover, N-CNTs emerged as material of an improved capability to anchor metal nanoparticles through nitrogen coupling [13,14] and to form catalytically active centres, e.g., for the reduction of nitrogen oxides (N_xO_y) emission in exhausts [15]. A high degree of vertical alignment in the nanotube films (also called 'carpets' or 'forests') is a key aspect in numerous applications that gain from anisotropy, i.e., supercapacitors [16], counter electrodes [17], structural composites of enhanced thermal and electrical conductivity [18,19], superhydrophobic surfaces [20], separation membranes [21] and sensors [22]. As for aligned N-CNT arrays, to mention the most recent and prominent applications, they have shown to be suitable catalysts for the reduction of oxygen in alkaline fuel cells [23] or paracetamol sensors [24].

Nitrogen atoms can be incorporated into the CNT lattice trough either in situ or post-treatment strategies [25]. The former techniques are dominant and comprise primarily catalytic chemical vapour deposition (c-CVD) and its variations, which include bias or plasma enhancements, with typical parameters of the synthesis being the selection of the nitrogen source and/or the catalyst, and temperature. The literature survey (Table 1) shows that the N-doping of CNTs usually induced lattice deformations, i.e., the formation of regular and irregular compartments that replace or accompany the multi-wall structure. Those defects, e.g., 'bamboo'-and 'nanobell'-morphologies could translate further into twists and corrugations, and as a consequence, into a lesser degree of alignment of the arrays. Additionally, the incorporation of nitrogen atoms was found to be the driving force in the formation of defect sites in the carbon sp^2-network [26].

We have previously reported that control over *chirality* of individual nanotube walls can be achieved by the selection of the nitrogen source, which is related to the stability of Fe_3C nanoparticles as nucleation sites of the nanotubes growth in c-CVD process [48-51]. Here, we track how the parameters of a c-CVD synthesis, which employs pyrazine (Pz) as the precursor of nitrogen-based compounds, affect growth and properties of N-CNTs on the macro-, nano- and atomic scales. The growth kinetics, the morphology, and the areal density, and physical/spectral properties of the N-CNT products were studied as a function of the growth time, the temperature and the composition of the supply injected to the quartz-tube reactor.

Results and Discussion

Synthesis of N-CNTs (and MWCNTs). The synthesis of different types of N-CNT was carried out by using a horizontal injection c-CVD furnace (Figure 1, see 'Experimental' for full experimental data).

The conditions of the synthesis were analogous to those applied for the catalytic growth of pristine MWCNT arrays (which were also synthesized here for comparison and referred to as *Ref. Synthesis*, Scheme 1), except that Pz, – the additional heteroaromatic nitrogen precursor, which decomposes into acetylene, hydrogen cyanide and cyanoacetylene [52-56] at 760 °C – was introduced into the feedstock. Pz was an immediate selection since it is well-soluble (85 g/100 g at room temperature) in toluene (PhMe, the primary carbon source), and has a boiling point (bp) of 115 °C, which is just 5 °C above the bp of PhMe. N-CNTs (and MWCNTs) grew both on the quartz substrates inserted into the centre of the furnace as well as on the internal wall of the quartz reactor.

Optimising the conditions. In order to establish conditions for a high growth rate of N-CNTs and the highest achievable alignment as well as a high density of the N-CNTs arrays, temperature and composition of the feedstock were scanned as variable parameters (Table 2). The parameters used were set progressively according to the emerging results. The starting point in the optimisation (*Synthesis I*) was based on the most suitable conditions for the synthesis of MWCNT carpets, i.e., 860 °C and [$FeCp_2$] = 2 wt %. In case of the synthesis of N-CNTs, PhMe was partially replaced by Pz to 19.6 wt %. Then, temperature and [$FeCp_2$] were kept constant, while [Pz] was gradually decreased (*Synthesis II*, *III*). Based on the SEM analysis (qualitative inspection of the alignment and purity of the product), parameters from *Synthesis II* were selected as the most appropriate for the further synthesis of aligned N-CNT arrays free from carbonaceous particles. Therefore next, temperature and [Pz] were left unchanged, while [$FeCp_2$] was increased to 9.6 wt % (*Synthesis IV*). At those settings, the synthesis yielded clean and thinner nanotubes, but not dense arrays. Hence at a [Pz] value of 5 wt % and a [$FeCp_2$] value of

Table 1: Literature overview of representative synthetic pathways toward N-CNTs.

method	C/N feedstock	catalyst (precursor)	*T*, °C	product	N content, wt %	ref.
arc discharge	graphite, melamine	Ni–Y	—	N-SWCNT	1.0	[27]
arc discharge	graphite, N_2	Fe–Ni–Co	—	N-CNT	4.6–13.7	[28]
arc discharge	graphite, N_2	Fe_2O_3, Co_2O_3, NiO	—	N-CNT	unknown	[29]
high-pressure CO conversion (HiPCO)	graphite, N_2	-	1300	N-CNT, nanofibers	3.0–13.0	[30]
c-CVD	CH_3CN	Co–Mo/MgO	700	bamboo-like N-CNT	12.0	[31]
c-CVD	CH_3CN $CH_3CN + H_2$	Fe–MgO	850	bamboo-like N-CNT bamboo-like N-CNT	0.94 2.62	[32]
c-CVD	ethylenediamine	Co, $FeCp_2$	780 860 980 1080	irregular N-CNT pearl-like nanobells bamboo-like N-CNT bamboo-like N-CNT	24.45 22.42 19.56 18.77	[33]
c-CVD	NH_3	iron(II) phthalate, SiO_2	850	aligned bamboo-like N-CNT	9.0	[34]
c-CVD	C_2H_2, NH_3	$Fe(CO)_5$	750 850 950	bamboo-like N-CNT	2.8 4.2 6.6	[35]
c-CVD	CH_3CN	Co–Ni/SiO_2	800	twisted bundles N-MWNT	3.0	[36]
c-CVD	THF, CH_3CN	$Fe(acac)_3$	950	bamboo-like N-MWNT	16.0–20.0	[37]
c-CVD	1. propylene, 2. CH_3CN 1. CH_3CN, 2. propylene	Al_2O_3	800	aligned N-CNT	3.2 3.5	[38]
c-CVD	C_2H_2, NH_3	Fe/SiO_2	850	bamboo-like N-CNT	0.4–2.4	[39]
c-CVD	CH_4, NH_3 C_2H_2, NH_3	Fe/Si	900 1000 1100	bamboo-like N-CNT	2.0–6.0	[40]
c-CVD	CH_3CN	Al_2O_3	800	aligned N-CNTs within Al_2O_3 pores	unknown	[41]
c-CVD	pyridine pyrimidine	$FeCp_2$	600–900	aligned bamboo-like N-CNT	1.0–2.0 3.2	[42]
c-CVD	CH_4, NH_3, N_2	Ni–Fe	720–810	bamboo-like CNT with graphene sheets	0–4	[43]
bias CVD	CH_4, N_2	Fe–Ni	500	bamboo-like N-CNT	≈15	[44]
plasma CVD	CH_4, NH_3	SiO_2/Si	450	N-SWCNT	0–4	[45]
plasma CVD	graphite, N_2	Ni	650	aligned bamboo-like N-CNT	20.0–30.0	[46]
magnetron sputtering	SWNTs, N_2^+	—	—	→ N-SWCNT → amorphous	450 ppm	[25]
low-energy ion irradiation	MWNTs, N_2^+	—	—	N-MWCNTs	0.58	[47]

9.6 wt %, the temperature was lowered to 760 °C (*Synthesis V*). Here, the nanotubes were visually purer as compared to the previous batch and the density of the N-CNT arrays was very high. Eventually, the temperature was set to remain unchanged, whereas [$FeCp_2$] was decreased again to 2 wt % (*Synthesis VI*). Under these conditions, the obtained nanotube arrays were characterized by a higher alignment and a high areal density. Further, [Pz] was increased gradually (*Synthesis VII, VIII*), which led to the compromise between a high alignment and a high areal density. In a control experiment at 660 °C, in which [$FeCp_2$] was also increased (*Synthesis IX*), no nanotubes could be identified as the product.

Macroscopic properties and elemental composition. The observation of the N-CNTs at the macroscopic level revealed them as a harder and more brittle material as MWCNTs, which suggested either alterations in the structure of the catalyst nanoparticles and/or of the nanotube themselves. Nevidomskyy

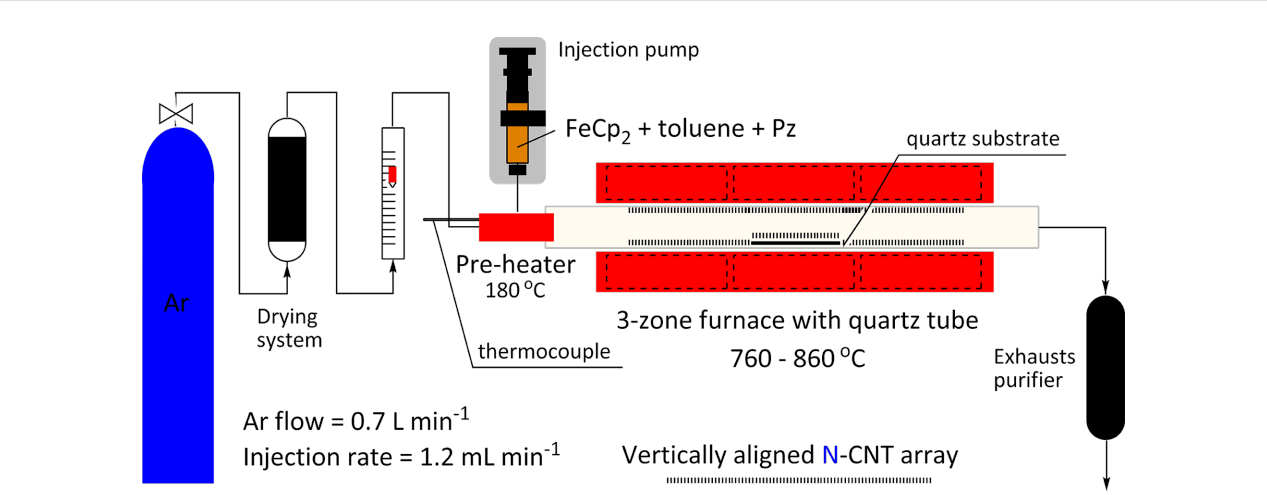

Figure 1: Injection c-CVD furnace and constant parameters for the synthesis of aligned N-CNT arrays.

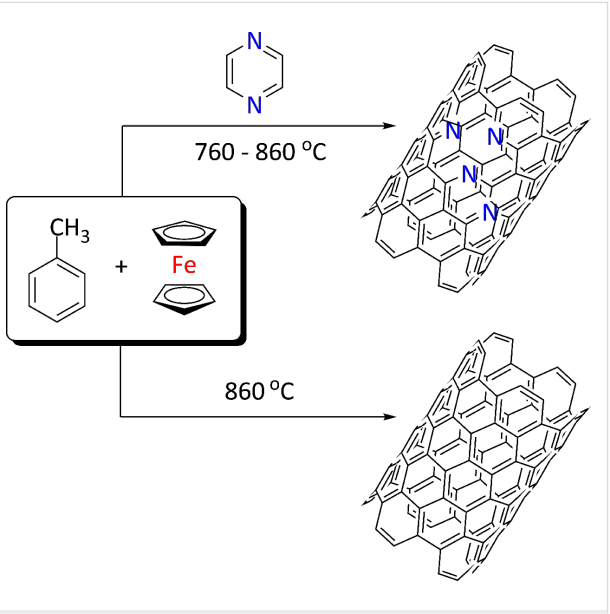

Scheme 1: Schematic reactions in the synthesis of N-CNTs and MWCNTs; for clarity only the outer nanotube walls are shown.

Table 2: Composition of the feedstock and growth temperatures in the syntheses of N-CNTs. The growth time was equally 4 h in all of the syntheses.

no.	*T*, °C	[PhMe], wt %	[Pz], wt %	[$FeCp_2$], wt %
I	860	78.4	19.6	2.0
II	860	93.2	4.8	2.0
III	860	97.0	1.0	2.0
IV	860	85.2	5.2	9.6
V	760	85.4	5.0	9.6
VI	760	93.0	5.0	2.0
VII	760	68.0	30.0	2.0
VIII	760	53.0	45.0	2.0
IX	660	56.0	40.0	4.0
Ref.	860	95.4	—	5.6

et al. reported in their ab-initio studies that nitrogen incorporation into SWCNTs could cause the formation of covalent junctions between neighbouring tubes if the nitrogen atoms were opposed to each other [57]. Therefore, if the density of inter-tube bonds is sufficiently high, a tightly-packed bundle of covalently cross-linked nanotubes (analogous to the cross-linking of polymer chains) with substantially changed mechanical properties, compared to MWCNT arrays, could be synthesized. The aligned MWCNT arrays were soft and could be easily peeled off from the quartz reactor in large pieces by using a razor blade, whereas the N-CNTs were peeled off as powder. Also, a drastic increase in the adhesion of N-CNT arrays to the quartz substrates as compared to pristine MWCNT films was noticeable because of changes in the structure and composition of the catalyst nanoparticles.

The contents of C, H, N and Fe, and empirical formulae (calculated per 1000 atoms) that were derived from the elemental analysis of the CNTs, as well as the respective feedstock compositions are presented in Table 3. The Fe content was determined from the amount of Fe_2O_3, which was found to be the sole residual material after the combustion in air after completion of the TG analysis. The iron content in the N-CNT product was higher than in the MWCNTs, apart from *Syntheses I–III*. The overall conversion of the initial carbon (in all carbon-bearing starting reactants) into carbon in nanotubes was different for MWCNTs and N-CNTs and was found to depend upon: 1) [$FeCp_2$] as a crucial catalyst for the growth of nanotubes, and 2) [Pz] as the source of nitrogen compounds that

Table 3: Elemental composition of the feedstock vs N-CNT products from *Syntheses I-VIII* in a comparison with MWCNTs.

no.	*T*, °C	feedstock, wt %				N-CNT product, wt %				formula
		C	H	N	Fe	C	H	N	Fe	
I	860	84.6	7.9	6.9	0.6	97.8	0.4	0.8	1.0	$C_{947}H_{46}N_7$
II	860	89.3	8.4	1.7	0.6	97.0	0.4	0.2	2.4	$C_{951}H_{47}N_2$
III	860	90.5	8.6	0.3	0.6	97.9	0.4	0.0	1.7	$C_{953}H_{47}$
IV	860	87.1	8.2	1.8	2.9	91.3	0.3	0.0	8.4	$C_{962}H_{38}$
V	760	87.1	8.2	1.8	2.9	84.1	0.3	0.4	15.2	$C_{955}H_{41}N_4$
VI	760	89.2	8.4	1.8	0.6	92.0	0.3	0.6	7.1	$C_{957}H_{37}N_6$
VII	760	81.4	7.5	10.5	0.6	91.5	0.3	1.4	6.8	$C_{950}H_{37}N_{13}$
VIII	760	76.7	7.0	15.7	0.6	91.1	0.3	3.0	5.6	$C_{937}H_{37}N_{26}$
Ref.	860	90.8	8.6	0	0.6	96.5	0.3	0	3.2	$C_{964}H_{36}$

stabilize the iron carbide phase. For these two extreme cases, the yield of nanotubes per amount of carbon was 8.9 and 36.6% for N-CNTs (*Synthesis VII*, [Pz] = 30%, [$FeCp_2$] = 2%, [PhMe] = 68%) and MWCNTs, respectively. The other yields lie in this range, e.g., for *Synthesis V* ([Pz] = 5%, [$FeCp_2$] = 9.6%, [PhMe] = 85.4%) the yield per amount of carbon was 27.1%.

The nitrogen content of the N-CNTs was found to correlate with that in the feedstock, both at 760 °C and 860 °C (Figure 2). Note that the higher incorporation of nitrogen into the nanotube lattice occurred at the lower temperature. Also noteworthy is a similar hydrogen content in all N-CNTs and MWCNT. All nanotube products contained 0.3–0.4 wt % H, which is assumed to be in a form of nanotube H-terminations and other possible C–H functions localized at structural defects.

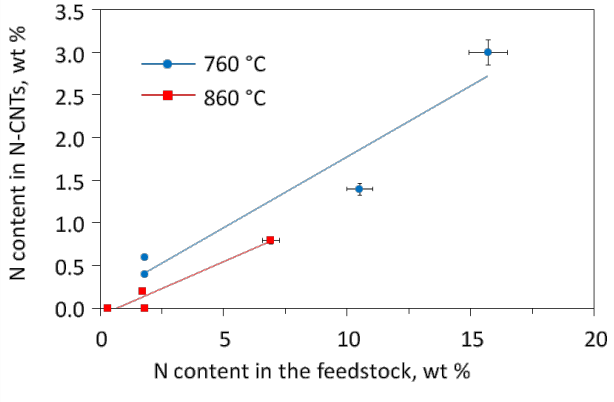

Figure 2: Relationship between the nitrogen content in the N-CNTs products and in the feedstock.

Morphology of N-CNTs. Raw products from each of the N-CNTs syntheses were examined with respect to the degree of alignment and areal density of the nanotubes, the purity (presence/absence of carbonaceous particles), the structure of the individual nanotubes (with a special emphasis on their straightness), and the quantitative analysis of the outer and inner diameters (OD, ID) of the nanotubes. Although the raw products were analysed, practically no amorphous carbon was observed for all of the N-CNT arrays of high quality. SEM images of the products from *Syntheses I–IX* are shown in Figure 3. In general, N-CNT films of different thicknesses were obtained depending on the concentration of the nitrogen species in the hot zone, which act as growth inhibitors. *Synthesis I* and *III* furnished nanotubes of small diameters that were twisted around the thicker ones. A lower degree of alignment, with abundant entangled nanotubes at the surface of the films in the products from *Synthesis I–IV* was evident. In the N-CNTs from *Synthesis V* the degree of alignment was higher, but some spiral and entangled nanotubes were also present (see Figure S1, Supporting Information File 1). In this case the nanotubes were nevertheless densely packed and of a narrow range of diameters. Eventually, it was confirmed that *Synthesis V* yielded the most dense N-CNT arrays of 5×10^8 nanotubes per mm^2 while the highest value of areal density of MWCNTs reported up-to-date was 4.9×10^8 nanotubes per mm^2 [58]. However, this value was found for the hydrogen-assisted growth from ethylene with an Fe/Al_2O_3 catalyst that was pre-treated with hydrogen. This synthesis yielded nanotubes whose thickness was about half to a third the thickness of the CNTs synthesized here. Nonetheless, it must be emphasized that the value of 5×10^8 nanotubes per mm^2 that cover 27% of the accessible area is still below the theoretically achievable areal density of the nanotubes (91%). In turn, SWCNT arrays as less geometrically restricted 'forests' can be grown up to 1.64×10^{11} nanotubes per mm^2 [59]. Moreover, for the N-CNTs grown in *Synthesis V* the highest Fe content was found, and in the SEM imaging (in which pre-ultrasonication was not required) the catalyst nanoparticles can be still seen as 'corks' in the 'elephant trunks'. An image of such a magnified bottom-view of the most dense N-CNT arrays from *Synthesis V* is an inset in Figure 3 in the corresponding window.

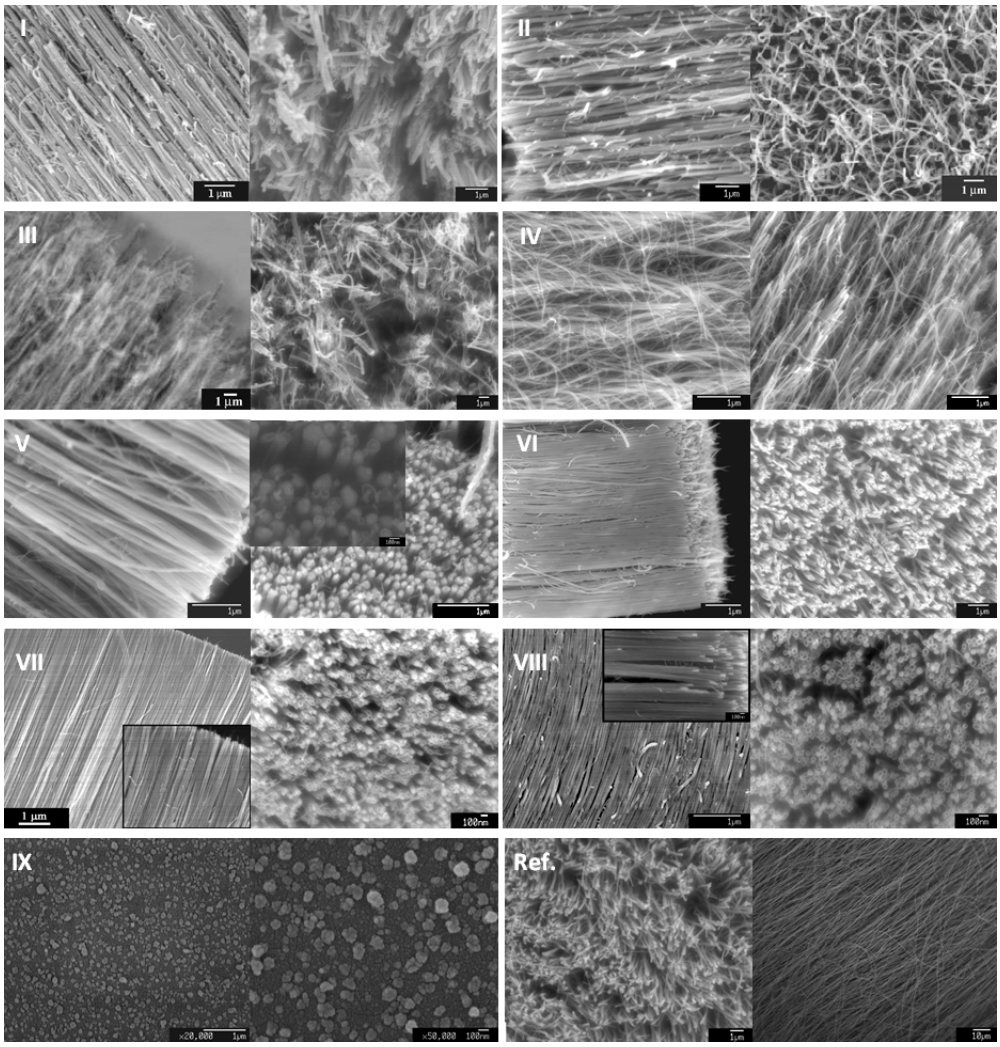

Figure 3: SEM examination of the N-CNTs from *Syntheses I–IX* and MWCNT from *Ref. Synthesis*.

Synthesis VI resulted in well-aligned nanotubes with a narrow range of diameters and clearly visible open nanotube tips. *Synthesis VII* and *VIII* yielded densely packed (up to 5×10^7 nanotubes per mm^2), well-developed nanotubes with the highest degree of alignment. For comparison, for MWCNT arrays of ca. 5×10^6 nanotubes per mm^2 were found, and the misalignment was significantly higher. As mentioned earlier, when the temperature of the growth process was reduced (*Synthesis IX*), N-CNTs could not be detected and only catalyst particles of different heights and diameters were found as bright spots ('seeds') on the quartz substrate. In conclusion, the highest 'quality' of the nanotube arrays, i.e., no waviness, and a high density of nanotubes was found in the products from *Syntheses VII* and *VIII*. One hundred different nanotubes that were randomly selected from the TEM micrographs were measured. Different growth temperatures and concentrations of the feedstock ingredients influenced the average outer diameters (OD_{av}) of N-CNTs, which ranged from 26 to 161 nm. The summary of the OD measurements is compiled in Table 4.

At 860 °C, and constant and low [$FeCp_2$], OD_{av} of N-CNTs was found to be between 84 and 161 nm. A significant decrease in OD_{av} was observed after increasing [$FeCp_2$] while keeping the temperature of growth at 860 °C. In *Syntheses IV* and *V* one can observe that decreasing the temperature from 860 to 760 °C caused a drop of OD_{av} from 34 to 26 nm. Lowering [$FeCp_2$] from 9.6 to 2.0 wt % at 760 °C caused an increase in OD_{av} from 26 to 43 nm. No obvious relationship between the concentration of nitrogen in the feedstock and the value of OD_{av} of the nanotubes was found. The medium values of OD_{av} for N-CNTs from *Syntheses VI–VIII* were around 45 nm, which is about half of those of pure MWCNTs (83 nm). The distribution of the outer diameters of the N-CNTs is presented in Figure 4. As can be seen, it was found to be broad at higher temperatures but it is

Table 4: Summary of the results from measurements of OD N-CNTs' from *Syntheses I–VIII* and MWCNTs from *Ref. Synthesis*.

Synthesis	*I*	*II*	*III*	*IV*	*V*	*VI*	*VII*	*VIII*	*Ref.*
T, °C	860	860	860	860	760	760	760	760	860
[Pz], wt %	19.6	4.8	1.0	5.2	5.0	5.0	30.0	45.0	0.0
[FeCp2], wt %	2.0	2.0	2.0	9.6	9.6	2.0	2.0	2.0	2.0
N content, wt %	0.8	0.2	0.0	0.0	0.4	0.6	1.4	3.0	0.0
min. OD, nm	20	10	13	10	5	7	5	12	45
max. OD, nm	236	224	461	61	64	93	95	99	127
OD_{av}, nm	102 ± 48	84 ± 44	161 ± 105	34 ± 13	26 ± 15	43 ± 21	43 ± 22	49 ± 19	83 ± 19

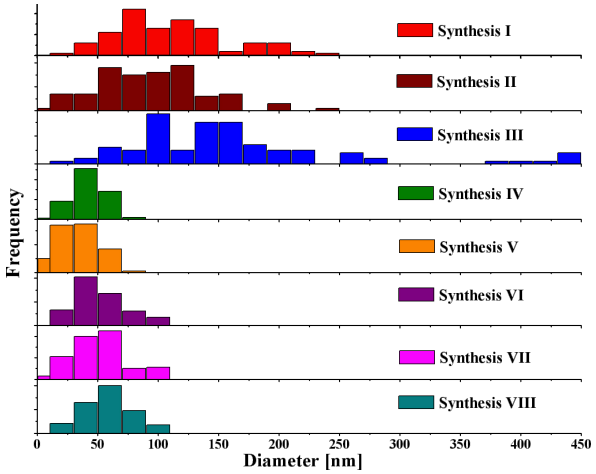

Figure 4: Histograms of the outer diameters of N-CNTs from *Syntheses I–VIII*.

narrowed down when increasing [$FeCp_2$] in the feedstock and decreasing the temperature.

It has been reported that higher temperatures of the nanotube growth increased both the OD_{av} of the nanotubes as well as the range of the ODs [60,61]. In the case of undoped carbon nanotubes, increasing [$FeCp_2$] resulted in an increase of the diameter of the MWCNTs [55]. This phenomenon is related to Ostwald ripening [62-64]. However, the opposite was found in N-CNTs, which could indicate a different mechanism of growth, which will be discussed further below. Also, the inner diameters of the nanotubes from *Syntheses VI–VIII* was measured based on TEM. The average value was 22 ± 5 nm, which is larger than that of pure MWCNTs (10 ± 4 nm). The increased ID of N-CNTs must be related to a larger size of the catalyst particles, which are located at the growth end of the nanotubes. Additionally, N-CNTs have fewer walls. Typically about 30 walls are present in the nitrogen tubes compared to around 100 in the pure MWCNTs. N-CNTs produced in *Syntheses VII* and *VIII* were found to be smoother (Figure 5) as compared to MWCNTs. A feature exclusive for N-CNTs is that their inner core is not continuously hollow as it is in MWCNTs, but is separated by discrete layers of distorted graphene across the core perpendicular to the tube axis.

No significant kinks in the nanotube walls could be observed in the TEM images of N-CNTs from *Synthesis VII* (Figure 5, upper panel). The outer walls were typically smooth (just a few wavy nanotubes among hundreds were found). A careful look at the magnified images reveals that the nanotube cores are characterized by a periodic internal morphology, i.e., 'bamboo'-like (or cone-like) of a distinctive regularity. Unlike pristine MWCNTs, which have iron particles encapsulated inside the core, the channels of the N-CNTs were free from metal nanoparticles suggesting that, for instance, a partial removal of the catalyst residues could occur while removing N-CNTs from the quartz surface. Representative TEM images of N-CNTs from *Synthesis VIII* are shown in the middle panel of Figure 5. Numerous characteristic graphene layers, which divide the nanotube core into densely distributed compartments, could be observed here. The N-CNTs were grown as straight as in the case of nanotubes from *Synthesis VII*. In this case however, larger metal catalyst nanoparticle residues (dark spots) can be visible at the nanotube ends. It must be emphasized that Fe_3C is a brittle material, which can be easily withdrawn from the nanotube tips during ultrasonication, and also possibly in other mechanical operations. Moreover, there are a few smaller particles on the outer surface of the nanotubes, which are not likely to take part in the nanotube growth. Also, catalyst nanoparticles were found to be embedded in between the nanotube wall filaments. The removal of the catalyst particles either during scraping off the nanotubes from the substrate surface or during the TEM sample preparation in the ultrasonic bath left a wedge shaped cavity at the nanotube end. This behavior has never been

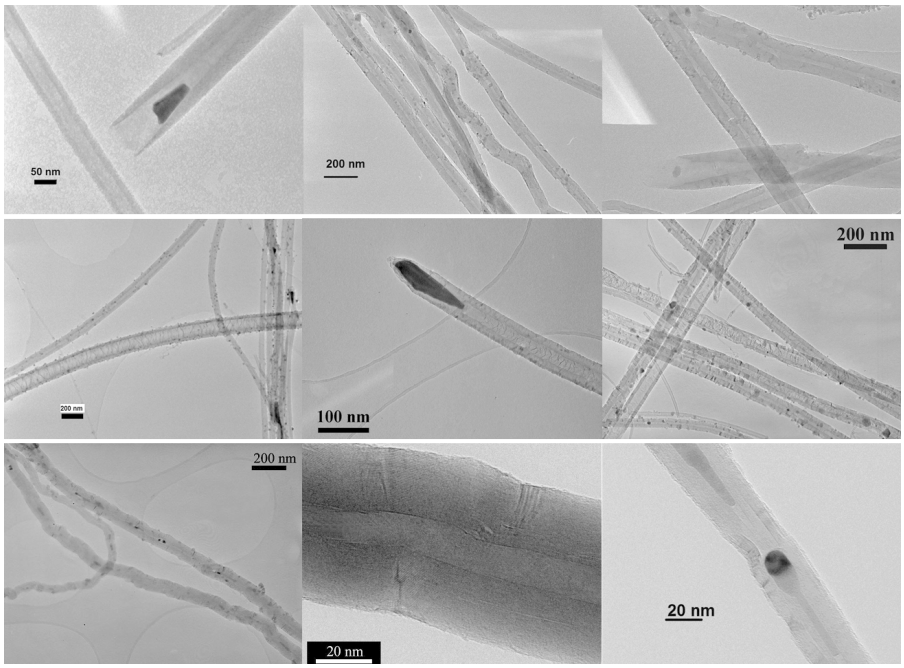

Figure 5: TEM images of: N-CNTs from *Synthesis VII* (**upper panel**) – straight N-CNTs; magnified views reveal 'bamboo'-like (cone-like) periodic structures; N-CNTs from *Synthesis VIII* (**middle panel**) – straight N-CNTs of a compartmental ('membrane'-like) morphology and bearing large catalyst nanoparticle residues at the nanotube ends and smaller ones on the outer walls, occasionally embedded in between the wall filaments; MWCNTs from *Ref. Synthesis* (**lower panel**) – nanotubes composed of irregular walls full of corrugations and kinks with a core discontinuously filled with metallic nanoparticles.

observed for MWCNTs. A summary of representative and dominating nanotube morphologies from *Synthesis VII* and *Synthesis VIII* with the corresponding models is presented in Figure 6.

Growth rate of N-CNT arrays. In order to analyse the growth rate of N-CNTs four runs were carried out with different times of synthesis, and with high [Pz] as the growth-retardant and the lowest concentration of catalyst precursor; namely 1, 2, 3 and 4 h at 760 °C, and at the following composition of the feedstock: [PhMe] = 68.0, [Pz] = 30.0, and [$FeCp_2$] = 2.0 wt.%. In this kinetic experiment it was demonstrated that for the period of 4 h the growth rate of N-CNTs remained linear at approximately 10 ± 1 μm·h^{-1} (Figure 7).

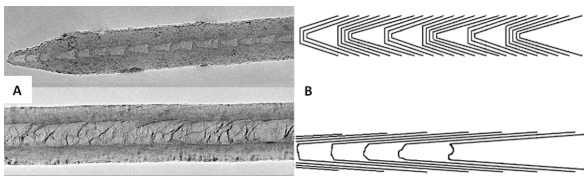

Figure 6: (**A**) TEM micrograph comparing two distinguishable types of nanotube morphologies: *top* – 'bamboo'-like (*Synthesis VII*) and *bottom* – 'membrane'-like (*Synthesis VIII*); and (**B**) graphical representations thereof.

The overall growth of nanotubes was substantially inhibited by the presence of nitrogen compounds in the growth zone, with the growth rate for pristine MWCNTs being about 20 times higher under otherwise equivalent conditions. Obviously, the growth rates of other N-CNT arrays lie in the range depicted above, which confirms [Pz] and [$FeCp_2$] to be the critical parameters for the growth rate of nanotube arrays. The linear fit function passes through the point of origin, which suggests a short time of nucleation.

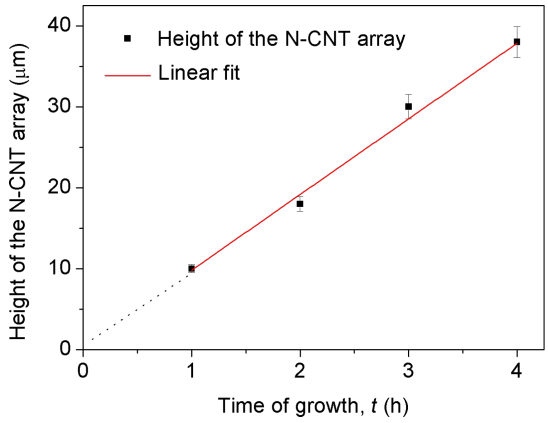

Figure 7: The height of the N-CNTs array vs time of growth.

Thermal stability. Thermogravimetric analysis (TGA) showed that all N-CNTs (for the sake of clarity, only *Synthesis V* and *VII* are presented here) were less thermally stable in air than their undoped counterparts (Figure 8).

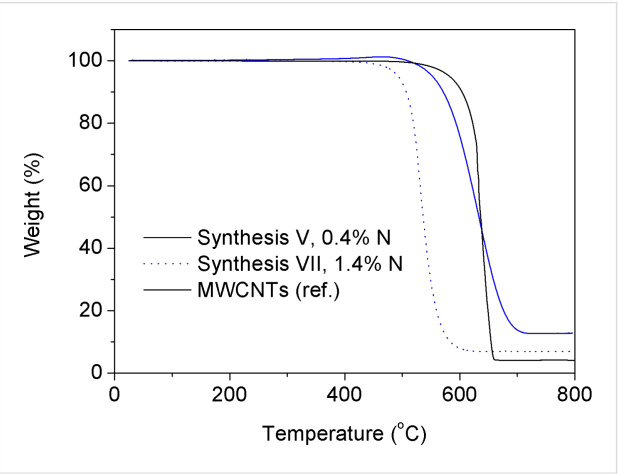

Figure 8: Overlaid TGA curves recorded in air for N-CNTs (*Synthesis V* and *VII*) and MWCNTs (*Ref. Synthesis*).

Referring back to the TEM images, a higher number of disordered graphitic layers (not fully graphitized) could explain this behavior. There are a few factors that are possibly responsible for a lower thermal stability of the N-CNTs as compared to pristine CNTs. The main point seems to be related to the defected morphology of the walls of the N-CNTs. A number of defects found in the N-CNTs by using Raman spectroscopy indicated that N-CNTs are less crystalline structures. Therefore, defect-inducing C–N bonds could generate a higher number of reactivity centres ('hot-spots') that are more susceptible to thermal cleavage and attack of oxygen. The higher number of 'nanogrooves', which translates into a higher surface area, could additionally enhance the accessibility of the outer nanotube walls. Moreover, the thermal resistivity in air was found to be inversely proportional to the nitrogen content in the N-CNTs. The maximum rate of combustion was found at 630 °C for both MWCNTs and N-CNTs (0.4% N), but for the latter oxidation initiated at ca. 20 °C earlier, and already at 530 °C for N-CNTs with 1.4% N. Furthermore, it must be emphasized that only single peaks were found in the DTA curves for N-CNTs whereas multiplets were recorded for MWCNTs indicating that the latter material was composed of more than one phase (see Figure S2, Supporting Information File 1). It was also noticeable that in the N-CNTs there was a fraction of iron more accessible to air, and therefore a slight increase in weight of the sample could be observed before the oxidation of the C-sp^2 atoms has started. The residue left after completion of the analysis was composed of pure red Fe_2O_3, the weight of which enabled the determination of the Fe content in the nanotubes. These values were found to be in agreement with the elemental analysis discussed earlier.

Spectral properties of N-CNTs. FT-IR was applied to characterize the functional groups in the N-CNTs. Figure 9 shows the FT-IR spectra of MWCNTs and N-CNTs (*Synthesis VIII*) with main peaks at 1645, 2949 and 1244, 1580 and 2937 cm^{-1}, respectively.

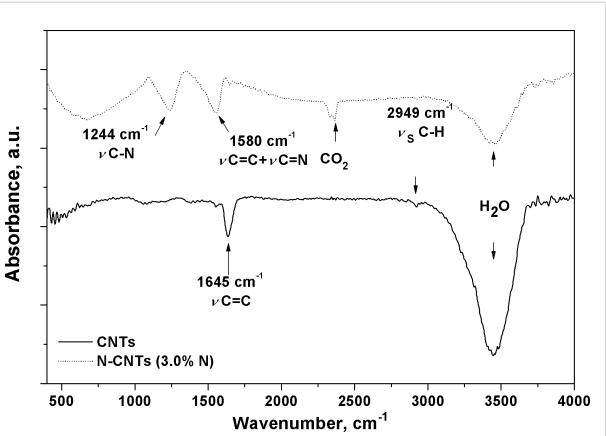

Figure 9: FT-IR spectra of CNTs and N-CNTs (*Synthesis VIII*).

For MWCNTs the absorption band at 1645 cm^{-1} was assigned to the stretching of C=C bonds in the graphene layers (νC=C). The peak at 2949 cm^{-1} corresponds to the symmetric stretching of C–H bonds in carbonaceous material (ν_sC–H). A similar signal for N-CNTs was absent, which indicated the lack of such impurities bound to the surface of the N-CNTs. In turn, the presence of C–N bonds could be identified by an intensive signal at 1244 cm^{-1}, which possibly derived from the stretching of C–N bonds (νC–N). The incorporation of N-atoms into the graphitic lattice could be confirmed by a signal at 1580 cm^{-1} from a mixed stretching mode of C=N and C=C (νC=N + C=N), which was shifted to lower wavenumbers as compared to the signal from aromatic C=C bonds. These findings are in accordance with the previous reports [65-68], which demonstrated that the substitution of carbon atoms with nitrogen atoms in the sp^2-networks induces a strong IR activity. Consequently, the absorption in the 1200–1600 cm^{-1} region would be expected if N-atoms were covalently bonded into the carbon network.

Raman spectroscopy was used to determine a degree of crystallinity (graphitisation) of N-CNTs. It must be emphasized here that the ratio I_D/I_G not only reflects of the presence of amorphous carbon (i.e., 'cauliflowers') but, particularly in our case, corresponds to the degree of graphitisation. In general, the ratio I_D/I_G reflects a number of structural defects, the concentration of amorphous carbon and it is sensitive to doping. In the case of

N-CNTs, the D-peak originates not only from structural defects but also from the covalent heteroatomic doping of the nanotubes. Firstly, changes in the positions of critical G- and D-peaks were found for N-CNTs (3% N) (ω_G = 1585 cm^{-1}, ω_D = 1354 cm^{-1}) as compared to MWCNTs (ω_G = 1576 cm^{-1}, ω_D = 1351 cm^{-1}). However, the critical changes appeared in the intensities of D-bands. The presence of nitrogen-based compounds during the growth of nanotubes affected their structure, which can be seen as an increase in the D-peak intensity. The relationship between the ratio I_D/I_G and the nitrogen content in the N-CNTs is presented in Figure 10.

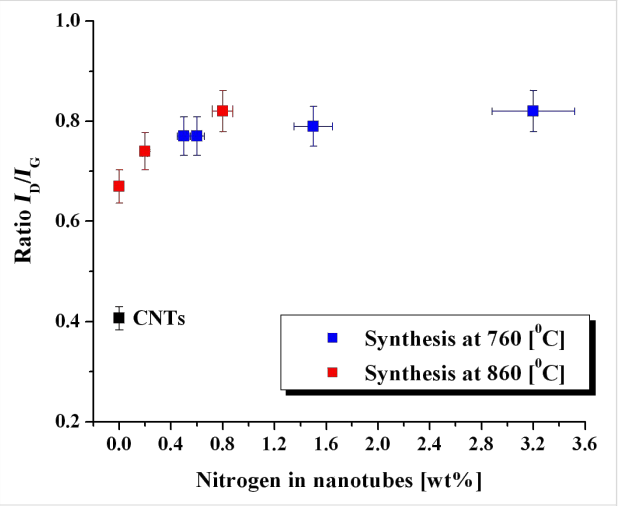

Figure 10: The ratio I_D/I_G vs the level of N-doping at 760 and 860 °C, as compared to pristine MWCNTs.

Importantly, in *Syntheses III* and *IV* also an increase in the I_D/I_G ratio was found, although no nitrogen was detected by elemental analysis. This fact is of a great significance and it means that it is the presence of nitrogen species, which affects the growth of N-CNTs and, further, their morphology. Additionally, I_D/I_G ratios increase with an increased N-doping at higher temperature. Continuing our insights into the mechanism of N-CNTs growth, we have investigated particular stages of the synthesis from the kinetic experiment. Raman spectra acquired from different stages of the N-CNTs synthesis confirmed that that N-CNTs preserve their chemical structure and morphology throughout the whole course of the synthesis since no significant changes, either in intensities or Raman shifts, were observed (see Table S1, Supporting Information File 1).

XRD analysis and growth mechanism. Analysing the XRD patterns of N-CNTs (Figure 11), it was possible to identify peaks that correspond to the graphitic lattice. (002), (100) and (004) XRD reflections from pristine MWCNTs and N-CNTs match the values of graphite (see Table S1, Supporting Information File 1). Furthermore, there were other peaks observed for N-CNTs, which were absent in the XRD patterns acquired from pristine MWCNTs. By comparing 2θ values for those peaks with the reference XRD data [69], several iron based compounds could be assigned as phases accompanying the nanotubes. The most intensive reflections at 2θ = 42.9, 44.7 and 49.9° could be assigned to α-Fe (110) and γ-Fe (111, 200), respectively. The peak at 2θ = 35°, of the second highest intensity, matches several iron oxides, i.e., FeO, Fe_2O_3 and Fe_3O_4. The iron oxides in all of their possible crystallographic structures have nearly identical XRD patterns and match well with the peaks marked as A, B, C and D. Likewise, FeSiC, Fe_8Si_2C and FeSiO match with the peaks A and B. These compounds also have several peaks in the region of C, D and E. The XRD peaks of Fe_3C overlap with the (002) reflection of graphite and also match with the B, C and E region. Most of the reflections were found to be relatively broad, hence they could originate from different phases. It is not possible to unequivocally identify those phases solely by analysing the XRD patterns.

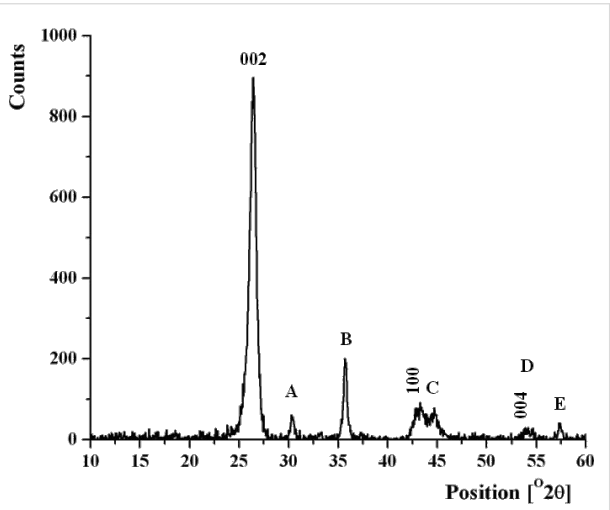

Figure 11: XRD pattern of N-CNTs (*Synthesis VIII*). The numbers are the hkl indices of the highest intensity peaks of graphite that coincide with the peaks from N-CNTs. The other peaks possibly refer to iron-based compounds.

Based on the combination of TEM and XRD analysis, a model of MWCNT and N-CNT that contain nanoparticles of the catalyst was proposed (Figure 12, upper panel). For MWCNT, the metal particles were always encapsulated in the core of the nanotubes. It is most likely that the particles in the core of the nanotube are composed of pure iron and iron carbide. As XRD analysis revealed these particles were not oxidized because of the shielding from the carbon shell. The particle at the growth surface is an active catalyst particle ('base' growth mechanism) [70] and it is an iron silicon carbide phase. In case of N-CNTs, the catalyst particles found just underneath the nanotube surface

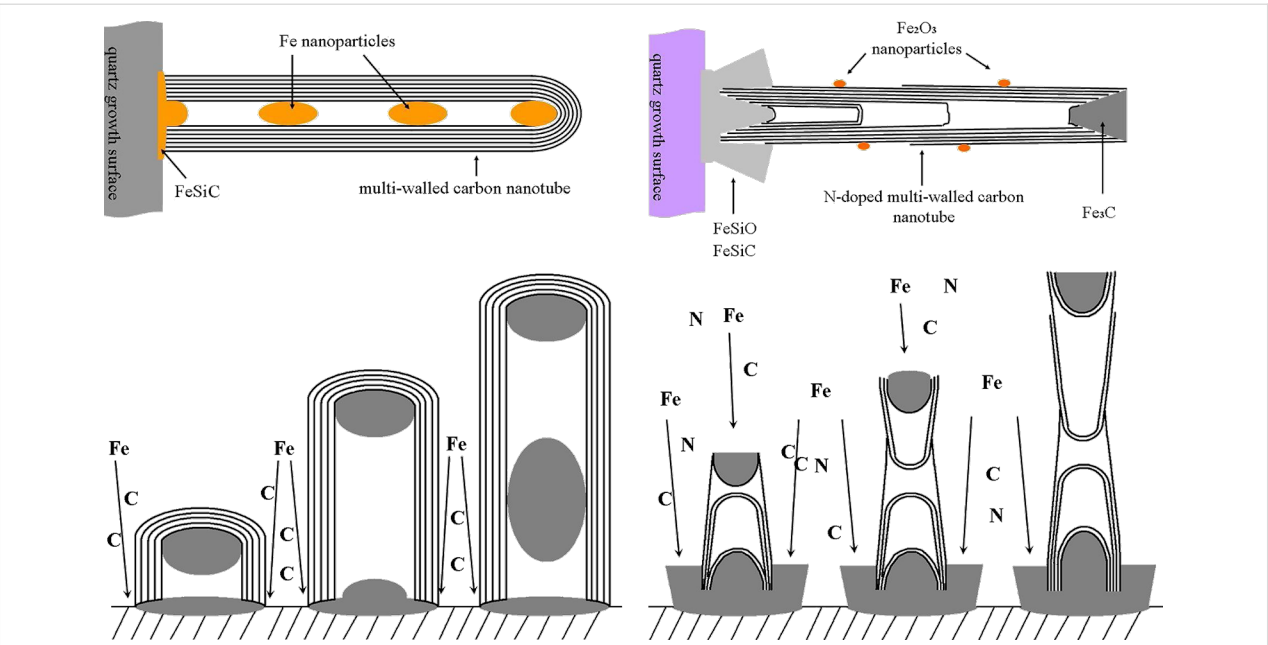

Figure 12: Models of MWCNT (left) and N-CNT (right) with metal particles differently distributed along the nanotube core (upper panel) and schematic presentation of a possible growth model for 'base' growth mechanism of MWCNTs and 'mixed base and tip' growth mechanism of N-CNTs (lower panel).

are α-Fe (if encapsulated by few graphene layers) or Fe_xO_y (if the metal particle was not entirely protected by a graphene shell, and once exposed to air it was oxidized). The catalyst particle at the nanotube tip is probably Fe_3C due to the catalytic growth of nanotubes and mainly carbon diffusion through the metal particle. The particle at the base (growth substrate) of the nanotube is likely to be iron silicon carbide and iron silicon oxide since it was in the contact with the silica quartz substrate.

In the nitrogen-assisted growth of nanotubes, the mechanism is more complicated than the 'base' growth of N-CNTs (Figure 12, lower panel). Since iron particles were observed at both the bottom and the top of individual nanotubes and no signal from iron was recorded from the middle part of the nanotubes, N-CNTs must grow in a mixed 'base and tip growth' mechanism, although primarily in a base-type growth [49]. We have already presented a direct evidence for the partial tip mechanism of the growth of N-CNTs [49]. We showed there that shape and position of the catalyst in the final N-CNT product can be explained with the following stages of the nanotube growth: (1) a formation of graphite nucleus and then a 'carbon belt', which fully encircles the catalyst nanoparticle, (2) as the 'N-CNT belt' grows, it stretches the catalyst particle (the catalyst is continuously replenished from the bottom) to form into the shape of a 'sand clock', (3) the catalyst particle divides and the growth continues from both sides, (4) the new layers are then formed internally and these break off, cap-wise, from the growing and receding catalyst particles to yield the interconnected webs in core of the nanotube, and (e) the final shapes of catalyst residues at the tip and at the bottom of the nanotube are witnesses and remains of the growth process. It must be also emphasized here that catalyst particles were absent in the MWCNT tips.

Based on results from FT-IR and Raman spectroscopy, and TG measurements, some important premises on the molecular structure of N-CNTs can be suggested. As it was shown, the interstitial nitrogen in graphite lattice leads to the development of defects. Even a difference of 0.5% between the C–C and C–N bond lengths in nanotubes (0.1422 nm and 0.1429 nm, respectively) leads to deformations and bending of the sp^2-layers [30]. Partial deformations of the graphene walls were found to be caused by the formation of 5- and 7-membered rings in MWCNTs. This effect will be even more distinct for N-doped CNTs since 5- and 7-membered rings that contain nitrogen are thermodynamically more stable their C-homoatomic analogues [71]. The most probable ways of N-incorporation into graphene walls, including substitutions and substitutions with a simultaneous formation of vacancies structures, are presented in Figure 13. The presence of nitrogen or 5- and 7-member-ring defects is crucial for the formation of the cone structure of the N-CNTs. The vacancies also provide geometrical degrees of freedom to the structure of N-CNTs, which allows for the fulfilment of the crystallographic matching criteria (–ABAB–) between the layers. This is geometrically impossible in the case of MWCNTs.

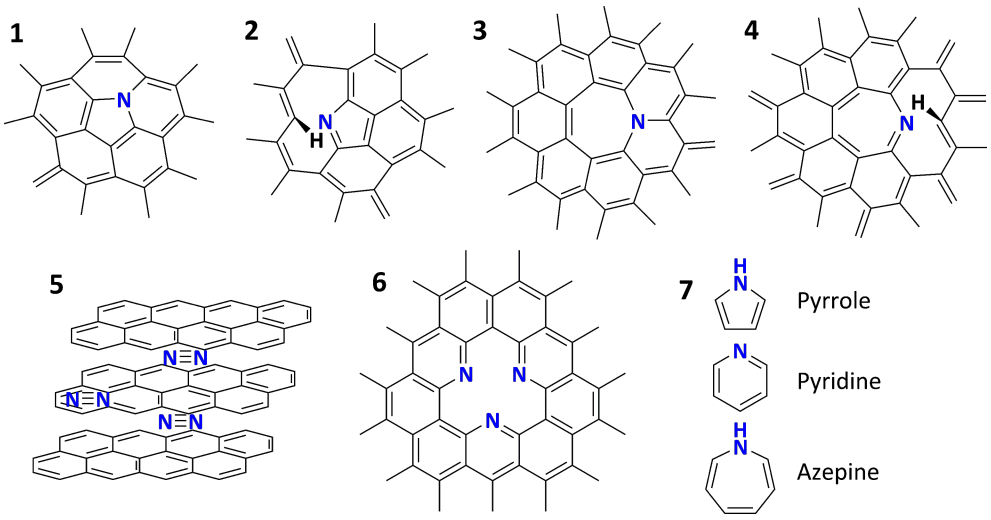

Figure 13: Examples of how nitrogen atoms can be incorporated into the graphene layer: (1) and (3) deformational substitutions; (2) and (4) deformational substitutions with a vacancy; (6) "nitrogen gap" (three 'pyridinic'-like nitrogen atoms, that all lead to a higher degree of freedom of the lattice); (5) molecules of nitrogen entrapped between adjacent graphene layers. The types of nitrogen-doping can be referred to 'pyridinic-', 'pyrrolic-' and 'azepinic-like' in analogy to the nomenclature of simple heterocyclic molecules.

Conclusion

N-CNTs were synthesized via an injection c-CVD method. With the intension to grow the most aligned and dense arrays of N-CNTs, we have studied the parameters of the N-CNTs growth to find the concentration of pyrazine in the toluene/ferrocene solution and temperature as the critical parameters. The most dense and aligned N-CNTs were obtained when [Pz] of 30 and 45 wt % were used in a mixture with toluene and ferrocene. The nanotubes, grown via a 'mixed base-and-tip' growth mechanism at 760 °C, exhibited 'bamboo-' or 'membrane'-like (compartmental) morphology and a narrow diameter distribution of 43 ± 22 and 49 ± 19 nm. The highest areal density of up to 5×10^8 N-CNTs per mm^2 in the array was gained for nanotubes of OD equal to 26 ± 15 nm grown at [Pz] = 5 wt % and [$FeCp_2$] = 9.6 wt %. These results make N-CNTs the perfect construction material for separation membranes of tuneable permeability. N-CNTs of a high N-doping level can be used as high surface area electrodes. Apart from this, the 'bamboo'-like N-CNTs obtained here could provide a new opening in drug delivery systems due to their rigid 'needle-like' morphology. These N-CNTs with a high content of ferromagnetic nanoparticles could potentially serve as magnetically steerable drug carriers for the enhanced penetration of target cells in anticancer therapies [72,73].

Experimental

Synthesis. The synthesis setup was composed of a pre-heater, a furnace, a quartz reaction tube, injection pump with a syringe, an inert gas flow-meter and an exhausts purifier. The pre-heater was assembled with a T-junction shape quarter inch quartz tube (Cambridge Glassblowing Ltd.) wrapped by a heating tape (electrothermal HT9, Fisher Scientific) made of resistive wires covered in a glass fibre fabric. The heating tape was operated with a digital controller (electrothermal, MC810). The temperature of the pre-heater was maintained at 180 °C and in order to avoid heat loss, it was insulated by a ceramic fibre cloth. The function of the pre-heater was to evaporate the carbon feedstock injected by a 50-mL gas-tight Hamilton syringe, which then was taken by pre-dried argon as the carrier gas (Air products, 99.995 %), into the reaction tube. The syringe was operated by the injection pump (Linton instrumentation, KD Scientific). A fused quartz reaction tube (silica, 99.99 %) of following dimensions: length 2000 mm, OD 17 mm, ID 14 mm was introduced into the furnace (Lenton Thermal Designs CSC12, split 3-zone tube furnace). The exhausts from the reaction tube were directed through a bottle containing activated carbon and another one with silicon oil.

Characterisation. The elemental analyses of dried samples (atmospheric pressure desiccator containing silica gel) were performed by using an Exeter Analytical CE-440 CHN Elemental Analyzer. A JEOL 6340F FEG SEM was used with an accelerating voltage of 5 kV. A secondary electron imaging (SEI) detector was used in all cases. TEM imaging of nanotube samples was performed on JEOL 200CX (tungsten filament, operated at 200 kV), JEOL 2000FX (LaB6 electron source, operated at 200 kV), FEI Tecnai F20-G2 (field emission gun, operated at 200 kV) and JEOL 4000EX-II (LaB_6 electron source, operated at 400 kV) transmission electron microscopes depending on characterization requirements. Prior to imaging

the samples were dispersed in diethyl ether in an ultrasonication bath and dropped onto 400 mesh copper grids covered with a holey carbon film. The nanotube samples were investigated by using a RM1000 (Ramascope-1000 system) Raman microscope with a spectral resolution of 0.1 cm^{-1} and a spatial resolution of the X/Y/Z stage of 1 μm. An argon ion laser (green, λ = 514.5 nm) was used in all cases. FT-IR analyses were performed by using a Perkin Elmer spectrometer in the range from 0.44 eV (2778 nm, 3600 cm^{-1}) to 0.1 eV (12500 nm, 800 cm^{-1}) from KBr pellets. TGA analyses were carried out in air at a heating rate of 10 °C·min^{-1} by using a TGA Q500. XRD studies were performed on a Philips GEN4 diffractometer at 40 kV and 40 mA, which covered the 2θ angles from 8 to 60°. Cu Kα radiation (λ = 0.154 nm) was used. The nanotube powder sample was supported by a single crystal silicon holder.

Supporting Information

Supporting Information File 1

Additional experimental data.
[http://www.beilstein-journals.org/bjnano/content/supplementary/2190-4286-5-24-S1.pdf]

Acknowledgements

Krzysztof K.K. Koziol thanks the Royal Society for funding. Slawomir Boncel thanks the Foundation for Polish Science (FNP-DS-402-7410/2012/Kf, 'Kolumb' program), National Science Centre ('Sonata' program, 2012/05/D/ST5/03519) and Ministry of Science and Higher Education ('Iuventus Plus' program, IP2012003572), both Poland, for the financial support.

References

1. Wiltshire, J. G.; Li, L.-J.; Herz, L. M.; Nicholas, R. J.; Glerup, M.; Sauvajol, J.-L.; Khlobystov, A. N. *Phys. Rev. B* **2005,** *72,* 205431. doi:10.1103/PhysRevB.72.205431
2. Yokomichi, H.; Matoba, M.; Fukuhara, T.; Sakima, H.; Sakai, F.; Maezawa, K. *Phys. Status Solidi B* **1998,** *207,* R1–R2. doi:10.1002/(SICI)1521-3951(199805)207:1<R1::AID-PSSB99991>3.0.CO;2-D
3. Ewels, C. P.; Glerup, M. *J. Nanosci. Nanotechnol.* **2005,** *5,* 1345–1363. doi:10.1166/jnn.2005.304
4. Koós, A. A.; Dillon, F.; Obraztsova, E. A.; Crossley, A.; Grobert, N. *Carbon* **2010,** *48,* 3033–3041. doi:10.1016/j.carbon.2010.04.026
5. Cruz-Silva, E.; Cullen, D. A.; Gu, L.; Romo-Herrera, J.; Muñoz-Sandoval, E.; López-Urías, F.; Sumpter, B. G.; Meunier, V.; Charlier, J.-C.; Smith, D. J.; Terrones, H.; Terrones, M. *ACS Nano* **2008,** *2,* 441–448. doi:10.1021/nn700330w
6. Dekker, C. *Phys. Today* **1999,** *52,* 22–28. doi:10.1063/1.882658
7. Krstić, V.; Rikken, G. L. J. A.; Bernier, P.; Roth, S.; Glerup, M. *EPL* **2007,** *77,* 37001. doi:10.1209/0295-5075/77/37001
8. van Dommele, S.; Romero-Izquirdo, A.; Brydson, R.; de Jong, K. P.; Bitter, J. H. *Carbon* **2008,** *46,* 138–148. doi:10.1016/j.carbon.2007.10.034
9. van Dommele, S.; de Jong, K. P.; Bitter, J. H. *Chem. Commun.* **2006,** 4859–4861. doi:10.1039/b610208e
10. Tang, C.; Golberg, D.; Bando, Y.; Xu, F.; Liu, B. *Chem. Commun.* **2003,** 3050–3051. doi:10.1039/b311807j
11. Choi, Y.-M.; Lee, D.-S.; Czerw, R.; Chiu, P.-W.; Grobert, N.; Terrones, M.; Reyes-Reyes, M.; Terrones, H.; Charlier, J.-C.; Ajayan, P. M.; Roth, S.; Carroll, D. L.; Park, Y.-W. arXiv:cond-mat/0204249 [cond-mat] 2002.
12. Srivastava, S. K.; Vankar, V. D.; Sridhar Rao, D. V.; Kumar, V. *Thin Solid Films* **2006,** *515,* 1851–1856. doi:10.1016/j.tsf.2006.07.016
13. Zamudio, A.; Elías, A. L.; Rodríguez-Manzo, J. A.; López-Urías, F.; Rodríguez-Gattorno, G.; Lupo, F.; Rühle, M.; Smith, D. J.; Terrones, H.; Díaz, D.; Terrones, M. *Small* **2005,** *2,* 346–350. doi:10.1002/smll.200500348
14. Jiang, K.; Eitan, A.; Schadler, L. S.; Ajayan, P. M.; Siegel, R. W.; Grobert, N.; Mayne, M.; Reyes-Reyes, M.; Terrones, H.; Terrones, M. *Nano Lett.* **2003,** *3,* 275–277. doi:10.1021/nl025914t
15. Huang, M.-C.; Teng, H. *Carbon* **2003,** *41,* 951–957. doi:10.1016/S0008-6223(02)00436-0
16. Hughes, M.; Shaffer, M. S. P.; Renouf, A. C.; Singh, C.; Chen, G. Z.; Fray, J.; Windle, A. H. *Adv. Mater.* **2002,** *14,* 382–385. doi:10.1002/1521-4095(20020304)14:5<382::AID-ADMA382>3.0.CO;2-Y
17. Lee, K. S.; Lee, W. J.; Park, N.-G.; Kim, S. O.; Park, J. H. *Chem. Commun.* **2011,** *47,* 4264–4266. doi:10.1039/c1cc10471c
18. Boncel, S.; Koziol, K. K. K.; Walczak, K. Z.; Windle, A. H.; Shaffer, M. S. P. *Mater. Lett.* **2011,** *65,* 2299–2303. doi:10.1016/j.matlet.2011.04.065
19. Koziol, K. K. K.; Boncel, S.; Shaffer, M. S. P.; Windle, A. H. *Compos. Sci. Technol.* **2011,** *71,* 1606–1611. doi:10.1016/j.compscitech.2011.07.007
20. Boncel, S.; Walczak, K. Z.; Koziol, K. K. K. *Beilstein J. Nanotechnol.* **2011,** *2,* 311–317. doi:10.3762/bjnano.2.36
21. Srivastava, A.; Srivastava, O. N.; Talapatra, S.; Vajtai, R.; Ajayan, P. M. *Nat. Mater.* **2004,** *3,* 610–614. doi:10.1038/nmat1192
22. Tang, Y.; Allen, B. L.; Kauffman, D. R.; Star, A. *J. Am. Chem. Soc.* **2009,** *131,* 13200–13201. doi:10.1021/ja904595t
23. Gong, K.; Du, F.; Xia, Z.; Durstock, M.; Dai, L. *Science* **2009,** *323,* 760–764. doi:10.1126/science.1168049
24. Tsierkezos, N. G.; Othman, S. H.; Ritter, U. *Ionics* **2013,** *19,* 1897–1905. doi:10.1007/s11581-013-0930-1
25. Yamamoto, K.; Kamimura, T.; Matsumoto, K. *Jpn. J. Appl. Phys.* **2005,** *44,* 1611–1614. doi:10.1143/JJAP.44.1611
26. Misra, A.; Tyagi, P. K.; Singh, M. K.; Misra, D. S. *Diamond Relat. Mater.* **2006,** *15,* 385–388. doi:10.1016/j.diamond.2005.08.013
27. Glerup, M.; Steinmetz, J.; Samaille, D.; Stephan, O.; Enouz, S.; Loiseau, A.; Roth, S.; Bernier, P. *Chem. Phys. Lett.* **2004,** *387,* 193–197. doi:10.1016/j.cplett.2004.02.005
28. Droppa, R., Jr.; Hammer, P.; Carvalho, A. C. M.; dos Santos, M. C.; Alvarez, F. *J. Non-Cryst. Solids* **2002,** *299–302,* 874–879. doi:10.1016/S0022-3093(01)01114-0
29. Cui, S.; Scharff, P.; Siegmund, C.; Schneider, D.; Risch, K.; Klötzer, S.; Spiess, L.; Romanus, H.; Schawohl, J. *Carbon* **2004,** *42,* 931–939. doi:10.1016/j.carbon.2003.12.060

30. Blank, V. D.; Polyakov, E. V.; Batov, D. V.; Kulnitskiy, B. A.; Bangert, U.; Gutiérrez-Sosa, A.; Harvey, A. J.; Seepujak, A. *Diamond Relat. Mater.* **2003,** *12,* 864–869. doi:10.1016/S0925-9635(02)00378-3
31. Lim, S. H.; Elim, H. I.; Gao, X. Y.; Wee, A. T. S.; Ji, W.; Lee, J. Y.; Lin, J. *Phys. Rev. B* **2006,** *73,* 045402. doi:10.1103/PhysRevB.73.045402
32. Yan, H.; Li, Q.; Zhang, J.; Liu, Z. *Chem. Phys. Lett.* **2003,** *380,* 347–351. doi:10.1016/j.cplett.2003.09.031
33. Liang, E. J.; Ding, P.; Zhang, H. R.; Guo, X. Y.; Du, Z. L. *Diamond Relat. Mater.* **2004,** *13,* 69–73. doi:10.1016/j.diamond.2003.08.025
34. Wang, X.; Liu, Y.; Zhu, D.; Zhang, L.; Ma, H.; Yao, N.; Zhang, B. *J. Phys. Chem. B* **2002,** *106,* 2186–2190. doi:10.1021/jp013007r
35. Lee, C. J.; Lyu, S. C.; Kim, H.-W.; Lee, J. H.; Cho, K. I. *Chem. Phys. Lett.* **2002,** *359,* 115–120. doi:10.1016/S0009-2614(02)00655-3
36. Kudashov, A. G.; Okotrub, A. V.; Yudanov, N. F.; Romanenko, A. I.; Bulusheva, L. G.; Abrosimov, O. G.; Chuvilin, A. L.; Pazhetov, E. M.; Boronin, A. I. *Phys. Solid State* **2002,** *44,* 652–655. doi:10.1134/1.1470550
37. Glerup, M.; Castignolles, M.; Holzinger, M.; Hug, G.; Loiseau, A.; Bernier, P. *Chem. Commun.* **2003,** 2542–2543. doi:10.1039/b303793b
38. Xu, W.; Kyotani, T.; Pradhan, B. K.; Nakajima, T.; Tomita, A. *Adv. Mater.* **2003,** *15,* 1087–1090. doi:10.1002/adma.200304752
39. Jang, J. W.; Lee, C. E.; Lyu, S. C.; Lee, T. J.; Lee, C. J. *Appl. Phys. Lett.* **2004,** *84,* 2877–2879. doi:10.1063/1.1697624
40. Lee, Y. T.; Kim, N. S.; Bae, S. Y.; Park, J.; Yu, S.-C.; Ryu, H.; Lee, H. J. *J. Phys. Chem. B* **2003,** *107,* 12958–12963. doi:10.1021/jp0274536
41. Hawelek, L.; Brodka, A.; Dore, J. C.; Honkimäki, V.; Kyotani, T.; Yang, Q. H.; Burian, A. *Acta Phys. Pol., A* **2010,** *117,* 302–306.
42. Liu, J.; Czerw, R.; Carroll, D. L. *J. Mater. Res.* **2005,** *20,* 538–543. doi:10.1557/JMR.2005.0069
43. Kurt, R.; Bonard, J. M.; Karimi, A. *Thin Solid Films* **2001,** *398–399,* 193–198. doi:10.1016/S0040-6090(01)01462-6
44. Ma, X.; Xu, G.; Wang, E. *Sci. China, Ser. E: Technol. Sci.* **2000,** *43,* 71–76. doi:10.1007/BF02917139
45. Min, Y.-S.; Bae, E. J.; Asanov, I. P.; Kim, U. J.; Park, W. *Nanotechnology* **2007,** *18,* 285601. doi:10.1088/0957-4484/18/28/285601
46. Cao, L. M.; Zhang, X. Y.; Gao, C. X.; Wang, W. K.; Zhang, Z. L.; Zhang, Z. *Nanotechnology* **2003,** *14,* 931–934. doi:10.1088/0957-4484/14/8/316
47. Morant, C.; Andrey, J.; Prieto, P.; Mendiola, D.; Sanz, J. M.; Elizalde, E. *Phys. Stat. Sol. (a)* **2006,** *203,* 1069–1075. doi:10.1002/pssa.200566110
48. Koziol, K.; Shaffer, M.; Windle, A. *Adv. Mater.* **2005,** *17,* 760–763. doi:10.1002/adma.200401791
49. Koziol, K. K. K.; Ducati, C.; Windle, A. H. *Chem. Mater.* **2010,** *22,* 4904–4911. doi:10.1021/cm100916m
50. Pattinson, S. W.; Diaz, R. E.; Stelmashenko, N. A.; Windle, A. H.; Ducati, C.; Stach, E. A.; Koziol, K. K. K. *Chem. Mater.* **2013,** *25,* 2921–2923. doi:10.1021/cm401216q
51. Pattinson, S. W.; Ranganathan, V.; Murakami, H. K.; Koziol, K. K. K.; Windle, A. H. *ACS Nano* **2012,** *6,* 7723–7730. doi:10.1021/nn301517g
52. Hore, N. R.; Russell, D. K. *J. Chem. Soc., Perkin Trans. 2* **1998,** 269–275. doi:10.1039/a706731c
53. Kiefer, J. H.; Zhang, Q.; Kern, R. D.; Yao, J.; Jursic, B. *J. Phys. Chem. A* **1997,** *101,* 7061–7073. doi:10.1021/jp970211z
54. Doughty, A.; Mackie, J. C.; Palmer, J. M. In *Twenty-Fifth Symposium (International) on Combustion,* The Combustion Institute, 1994; pp 893–900.
55. Kiefer, J. H.; Zhang, Q.; Kern, R. D.; Chen, H.; Yao, J.; Jursic, B. In *Twenty-Sixth Symposium (International) on Combustion,* The Combustion Institute, 1996; pp 651–658.
56. Crow, W. D.; Wentrup, C. *Tetrahedron Lett.* **1968,** *9,* 3115–3118. doi:10.1016/S0040-4039(00)89566-0
57. Nevidomskyy, A. H.; Csányi, G.; Payne, M. C. *Phys. Rev. Lett.* **2003,** *91,* 105502. doi:10.1103/PhysRevLett.91.105502
58. Nessim, G. D.; Hart, A. J.; Kim, J. S.; Acquaviva, D.; Oh, J.; Morgan, C. D.; Seita, M.; Leib, J. S.; Thompson, C. V. *Nano Lett.* **2008,** *8,* 3587–3593. doi:10.1021/nl801437c
59. Zhong, G.; Warner, J. H.; Fouquet, M.; Robertson, A. W.; Chen, B.; Robertson, J. *ACS Nano* **2012,** *6,* 2893–2903. doi:10.1021/nn203035x
60. Sinnott, S. B.; Andrews, R.; Qian, D.; Rao, A. M.; Mao, Z.; Dickey, E. C.; Derbyshire, F. *Chem. Phys. Lett.* **1999,** *315,* 25–30. doi:10.1016/S0009-2614(99)01216-6
61. Singh, C.; Shaffer, M. S.; Windle, A. H. *Carbon* **2003,** *41,* 359–368. doi:10.1016/S0008-6223(02)00314-7
62. Hasegawa, K.; Noda, S. *Carbon* **2011,** *49,* 4497–4504. doi:10.1016/j.carbon.2011.06.061
63. Sakurai, S.; Nishino, H.; Futaba, D. N.; Yasuda, S.; Yamada, T.; Maigne, A.; Matsuo, Y.; Nakamura, E.; Yumura, M.; Hata, K. *J. Am. Chem. Soc.* **2012,** *134,* 2148–2153. doi:10.1021/ja208706c
64. Börjesson, A.; Bolton, K. *ACS Nano* **2011,** *5,* 771–779. doi:10.1021/nn101214v
65. Wixom, M. R. *J. Am. Ceram. Soc.* **1990,** *73,* 1973–1978. doi:10.1111/j.1151-2916.1990.tb05254.x
66. Kaufman, J. H.; Metin, S.; Saperstein, D. D. *Phys. Rev. B* **1989,** *39,* 13053. doi:10.1103/PhysRevB.39.13053
67. Yap, Y. K.; Kida, S.; Aoyama, T.; Mori, Y.; Sasaki, T. *Appl. Phys. Lett.* **1998,** *73,* 915–917. doi:10.1063/1.122036
68. Lai, S. H.; Chen, Y. L.; Chan, L. H.; Pan, Y. M.; Liu, X. W.; Shih, H. C. *Thin Solid Films* **2003,** *444,* 38–43. doi:10.1016/S0040-6090(03)01091-5
69. International Centre for Diffraction Data (ICDD®).
70. Terrones, M. *Int. Mater. Rev.* **2004,** *49,* 325–377. doi:10.1179/174328004X5655
71. Zhao, M.; Xia, Y.; Lewis, J. P.; Zhang, R. *J. Appl. Phys.* **2003,** *94,* 2398–2402. doi:10.1063/1.1593798
72. Carrero-Sánchez, J. C.; Elías, A. L.; Mancilla, R.; Arrellín, G.; Terrones, H.; Laclette, J. P.; Terrones, M. *Nano Lett.* **2006,** *6,* 1609–1616. doi:10.1021/nl060548p
73. Boncel, S.; Müller, K. H.; Skepper, J. N.; Walczak, K. Z.; Koziol, K. K. K. *Biomaterials* **2011,** *32,* 7677–7686. doi:10.1016/j.biomaterials.2011.06.055

Beilstein Journal of Nanotechnology

Near-infrared dye loaded polymeric nanoparticles for cancer imaging and therapy and cellular response after laser-induced heating

Tingjun Lei[1,2], Alicia Fernandez-Fernandez[1,3], Romila Manchanda[1,4], Yen-Chih Huang[1] and Anthony J. McGoron[*1]

Full Research Paper

Open Access

Address:
[1]Biomedical Engineering Department, Florida International University, 10555 West Flagler Street, Miami, FL 33174, USA, [2]Cirle, 1951 NW 7th Ave, Suite 13016, Miami, FL, 33136, USA, [3]Physical Therapy Department, Nova Southeastern University, 3200 S. University Dr., Fort Lauderdale, FL 33328, USA and [4]Department of Basic and Applied Sciences, Galgotias University, UP, 201308, India

Email:
Anthony J. McGoron[*] - mcgorona@fiu.edu

* Corresponding author

Keywords:
hypoxia-inducible factor-1; IR820; nanoparticle; poly(glycerol malate co-dodecanedioate) (PGMD); vascular endothelial growth factor

Beilstein J. Nanotechnol. **2014,** *5,* 313–322.
doi:10.3762/bjnano.5.35

Received: 22 November 2013
Accepted: 21 February 2014
Published: 18 March 2014

This article is part of the Thematic Series "Physics, chemistry and biology of functional nanostructures II".

Guest Editor: A. S. Sidorenko

Abstract

Background: In the past decade, researchers have focused on developing new biomaterials for cancer therapy that combine imaging and therapeutic agents. In our study, we use a new biocompatible and biodegradable polymer, termed poly(glycerol malate co-dodecanedioate) (PGMD), for the synthesis of nanoparticles (NPs) and loading of near-infrared (NIR) dyes. IR820 was chosen for the purpose of imaging and hyperthermia (HT). HT is currently used in clinical trials for cancer therapy in combination with radiotherapy and chemotherapy. One of the potential problems of HT is that it can up-regulate hypoxia-inducible factor-1 (HIF-1) expression and enhance vascular endothelial growth factor (VEGF) secretion.

Results: We explored cellular response after rapid, short-term and low thermal dose laser-IR820-PGMD NPs (laser/NPs) induced-heating, and compared it to slow, long-term and high thermal dose heating by a cell incubator. The expression levels of the reactive oxygen species (ROS), HIF-1 and VEGF following the two different modes of heating. The cytotoxicity of NPs after laser/NP HT resulted in higher cell killing compared to incubator HT. The ROS level was highly elevated under incubator HT, but remained at the baseline level under the laser/NP HT. Our results show that elevated ROS expression inside the cells could result in the promotion of HIF-1 expression after incubator induced-HT. The VEGF secretion was also significantly enhanced compared to laser/NP HT, possibly due to the promotion of HIF-1. In vitro cell imaging and in vivo healthy mice imaging showed that IR820-PGMD NPs can be used for optical imaging.

Conclusion: IR820-PGMD NPs were developed and used for both imaging and therapy purposes. Rapid and short-term laser/NP HT, with a low thermal dose, does not up-regulate HIF-1 and VEGF expression, whereas slow and long term incubator HT, with a high thermal dose, enhances the expression of both transcription factors.

Introduction

The synthesis and development of novel polymers and their use for nanoparticle (NP) synthesis has been an important focus of materials science research in the past decade. NPs delivery systems are useful for in vivo applications because their small size (≈100 nm) allows them to escape reticuloendothelial system (RES) uptake, resulting in prolonged plasma circulation times. Moreover, they are able to stabilize and protect their cargo from degradation, including drugs and other types of biomolecules [1,2]. NPs have also proven to be useful in overcoming multidrug resistance (MDR) by preventing the direct interaction of drug exporter pumps with their substrates once encapsulated in NPs [3]. An additional advantage of NPs is that they are passively targeted to tumor sites because of the enhanced permeability and retention (EPR) effect. This effect occurs as a result of a combination of factors, including increased pore sizes of tumor vasculature, fast tumor angiogenesis from increased secretion of vascular endothelial growth factor (VEGF), and poor lymphatic clearance from tumor sites [4]. Because of these advantages, we synthesized a new formulation of polymeric NPs for image-guided therapy based on the polymer poly(glycerol malate co-dodecanedioate) (PGMD) developed in our lab. The work described in this manuscript is based on experiments completed as a partial fulfillment of the requirements for Tingjun Lei's PhD thesis [5]. Biocompatible and biodegradable PGMD polymers were synthesized through the thermal condensation method by mixing glycol, malic acid and 1,12-dodecanedioic acid (DDA). Following the synthesis of PGMD polymer, PGMD NPs were also successfully formulated.

Optical imaging has several advantages over more traditional imaging techniques (MRI, PET, CT, etc.), such as high spatial resolution, real time imaging, and systems that are usually smaller and less expensive. Near-infrared imaging dyes (wavelength 700–900 nm) are promising for in vivo imaging because light at these wavelengths has minimal absorption by tissue [6,7]. Moreover, some NIR dyes such as indocyanine green (ICG) can be used as both imaging agents and heat generators due to their unique photothermal properties. However, ICG has a plasma half-life of about 3 min and a poor stability in aqueous solution, which complicates the timing of imaging and hyperthermia (HT) [8]. In our previous work, we investigated the commercially available cyanine dye IR820 and proposed that it could be an alternative for ICG. Our studies have shown that IR820 can be used in lieu of ICG in imaging and hyperthermia applications. Three-minute laser exposure (power at 1440 J/cm^2) with 5 μM IR820 or ICG can elevate the temperature of cell culture media from 37 °C to 42 °C or from 37 °C to 46 °C, respectively [9]. Despite the fact that IR820 has a lower fluorescence yield and results in a lower temperature increase after laser exposure compared to ICG, we have found that either 5 μM IR820 or ICG can be used successfully for in vitro and in vivo optical imaging, and the increased temperature created by IR820 laser exposure is still within the range (usually 41–45 °C) needed for killing cancer cells. More importantly, IR820 has improved in vitro and in vivo stability compared to ICG. The in vitro IR820 degradation half-time is about twice that of ICG. In vivo, the plasma distribution half-life of IR820 is about 15 min, which is 5 times that of ICG; with an elimination half-life of over 30 h for IR820 compared to approximately 2 h for ICG [8]. Based on these advantages we chose IR820 as our near-infrared agent and we synthesized and characterized IR820-PGMD NPs for cancer imaging and HT applications.

HT is used clinically as an adjuvant treatment with chemotherapy and radiotherapy. HT achieves therapeutic benefits by damaging cancer cell proteins and structures as a result of an increase in cell temperature. However, one of the potential problems is that hypoxia-inducible factor-1 (HIF-1) could be up-regulated by HT [10,11]. An overexpression of HIF-1 has often been correlated to a poor therapeutic outcome, since HIF-1 could circumvent the anticancer drug effect by protecting cells from drug-induced apoptosis [12-14]. Moreover, tumor angiogenesis occurs partly by activating the expression of VEGF, which is partially regulated by HIF-1 [15-17]. Given the importance of HIF-1, studies of the effect of HT on this protein are very relevant for therapeutic HT applications in cancer. Goyal et al. and Chandel et al. reported that elevated reactive oxygen species (ROS) levels in cells stabilize HIF-1 expression [18,19]. On the other hand, ROS was also reported to induce mRNA accumulation for heat shock protein 70 (HSP70) [20], which is able to minimize the effect of heat on cells during heat exposure by inducing cells' thermotolerance [21,22]. Our previous study investigated the effect of HT on cancer cells in a thermal dose-dependent manner, and the results showed that HSP70 was inhibited by indocyanine green (ICG)-induced rapid heating after exposure to laser, so that the thermal protective mechanism of the cells was not initiated [23]. This was compared to the increased expression of HSP70 under slower but longer term heat accumulation by using a cell culture incu-

bator. The results indicated that the promotion of HSP70 was minimized during rapid heating.

As mentioned before, ROS can activate the expression of HSP70. The inhibition of HSP70 during rapid-rate and low thermal dose heating could possibly mean the abolishment of ROS generation, or abolishment of ROS-induced expression of HSP70. It would be important to investigate if laser-IR820-PGMD NP (laser/NP)-induced HT could result in ROS generation and trigger an overexpression of HIF-1. We hypothesized that rapid, short-term and low-dose heat accumulation after laser exposure to IR820-PGMD NPs within cancer cells will not activate ROS production and trigger HIF-1 and VEGF expression. Whereas slow and long-term incubator HT, with high thermal dose, will activate ROS production and result in the promotion of HIF-1 and VEGF expression. The study of cell killing and the cellular response of ROS, HIF-1 and VEGF expression in cancer cells after laser exposure are very important in determining the effect of the heating rate and the amount of thermal dose in the treatment of cancer cells. We used incubator-induced HT to mimic the application of whole-body HT, since the heating process is slow, thus taking a fairly long time to reach the targeted temperature (39–43 °C). Therefore, the comparison between incubator HT and laser/NP HT may provide important information on the effects of different modes of HT used in cancer therapy.

In a previous publication, we described the in vivo pharmacokinetics and biodistribution of IR820-PGMD NPs [24]. The present manuscript concentrates primarily on the in vitro response of cancer cells after hyperthermia. Therefore, this paper focuses not only on the cancer imaging and therapy capabilities of IR820-PGMD NPs, but also on exploring the cellular response following two different HT modes. We first investigated the potential application of IR820-PGMD NPs on cancer imaging and therapy and compared the therapeutic effect to incubator HT. Next, we performed cell-based assays to study ROS, HIF-1 and VEGF expression under these two different heating methods.

Results

Characterization of the PGMD polymer and IR820-PGMD NPs

The MW of PGMD polymers measured by GPC column is around 3000 Da. The glass transitional temperature (T_g) is measured to be approximately 42 °C, which is within the range of the IR820 temperature increase after laser exposure. The diameters of void PGMD NPs and IR820-PGMD NPs (see dynamic light scattering (DLS) measurements in Figure S1, Supporting Information File 1) are 90 ± 18.2 nm, and 108 ± 7.4 nm (mean ± SD) respectively. The shape and size of IR820-PGMD NPs were also confirmed with scanning electron microscopy (SEM) imaging (see SEM images in Supporting Information File 1, Figure S2). Polydispersity (PDI) is 0.142 ± 0.007 (mean ± SD), zeta potential is −28.3 ± 6.4 mV (mean ± SD), and the dye loading efficiency is 8.2 ± 0.6 (wt/wt %) (mean ± SD). These results were obtained from ten different NP batches.

Subcellular localization

Figure 1 shows images of cells treated with 5 μM free IR820 or 0.05 mg/mL IR820-PGMD NPs (equivalent to 5 μM IR820), and illustrates that the localization of the agents within the cells is similar. Free IR820 is widely spread throughout the cytoplasm, most likely due to interaction with intracellular proteins such as ligandin [25]. In the case of the NP formulation, IR820

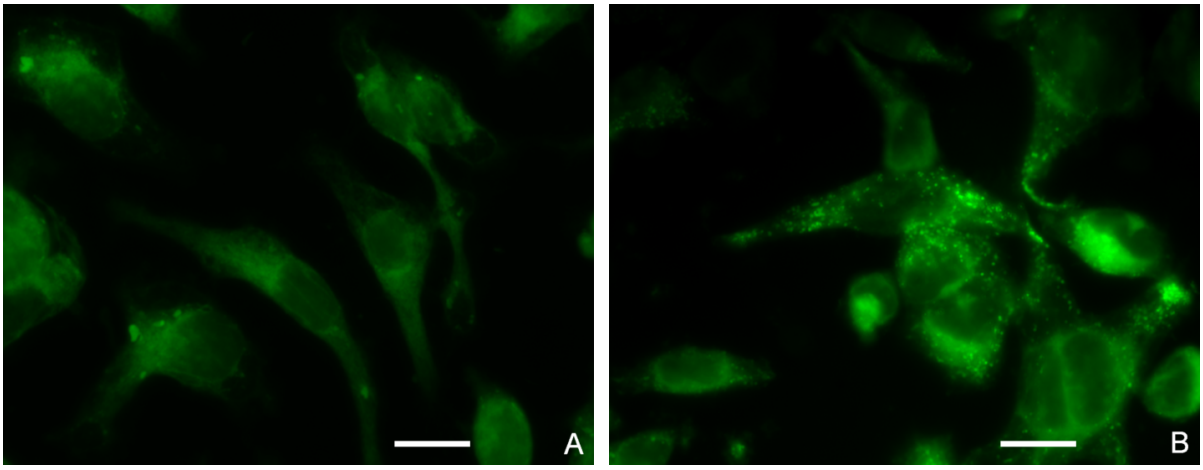

Figure 1: Subcellular localization of free IR820 (A) and IR820-PGMD NPs (B) in SKOV-3 after 24-hour incubation. Scale bar represents 20 μm.

released from the NPs should exhibit identical behavior as free IR820, whereas IR820 still within the NPs is expected to be located in endosomes/lysosomes. Lysotracker Blue was used to identify that PGMD NPs were taken up by the cells through an endocytosis pathway (Supporting Information File 1, Figure S5). Calculated image ratio values, R, from the fluorescence microscope images show that the NP formulation produces a higher intracellular fluorescence intensity ($R = 3.75 \pm 0.54$) (mean ± SD) than the free dye ($R = 2.89 \pm 0.23$) (mean ± SD) after 24 h of incubation, although the difference is not statistically significant, possibly due to the small sample size ($n = 3$ for each group).

HT thermal dose calculation

The temperature curves during 1 h incubator HT and 3 min laser/NP HT are shown in Figure S3 and S4 (Supporting Information File 1). A much slower temperature increase curve was observed in incubator HT compared to the temperature increase in laser/NP exposure. The thermal doses given in these two treatments were calculated according to the CEM_{43} model developed by Sapareto et al. [26] with a slight modification to accommodate for the utilization at 42 °C (CEM_{42}) with a smaller empirical value R = 0.25. Laser/NP HT for 3 min with 5 μM IR820-PGMD NPs produced a much lower thermal dose (CEM_{42} = 3.06 min) as compared to the 42 °C incubator HT treatment (CEM_{42} = 25.98 min) over 1 h.

Cytotoxicity study

Our group previously described the thermal effects of IR820 in cells exposed to 808 nm laser at a power density of 1440 J/cm^2. Specifically, exposure to 5 μM IR820 and a 3-minute laser treatment under these conditions produces temperature increases of 5 °C from a baseline of 37 °C [9]. Based on this finding, we used a concentration of 0.05 mg/mL IR820-PGMD NPs (containing approximately 5 μM IR820) in the current study and compared it to the incubator treatment. Figure 2 shows the results of the cytotoxicity study in MES-SA and Dx5. As seen in the figure, laser exposure without concomitant exposure to IR820 did not significantly impact cell growth. It is also noteworthy that NP concentrations equivalent to 5 μM IR820 had a slight cell growth inhibition effect on MES-SA cells. This is in line with our previous observations on the cytotoxicity effects of free IR820 on MES-SA, and seems to be related to the fact that drug-sensitive MES-SA cells are more readily affected by environmental changes and exposure to foreign substances than their drug-resistant counterpart Dx5. Both incubator HT and laser/NP-induced HT killed cancer cells due to the HT effect ($p < 0.05$). Laser/NP HT cause greater cell killing compared to incubator HT ($p < 0.05$), probably because thermotolerance and cell protective mechanisms were not triggered [27].

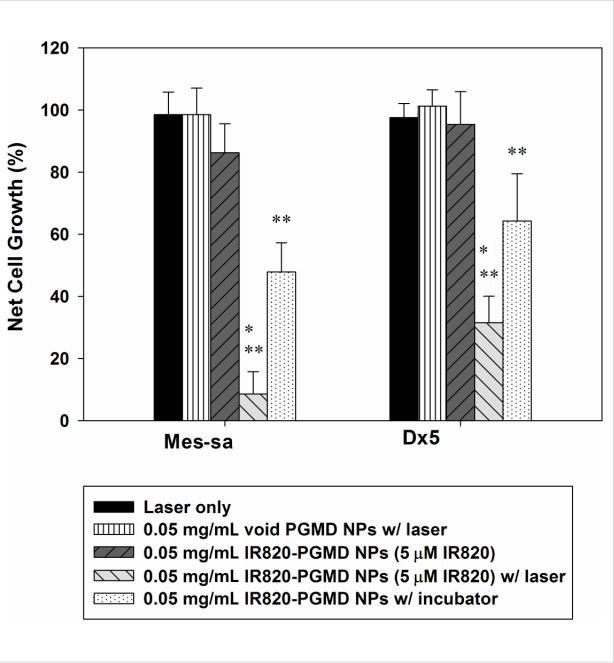

Figure 2: 24-hour cytotoxicity profile of IR820-PGMD NPs with laser and incubator exposure in MES-SA and Dx5 cells; $n = 3$, 4 wells/treatment. * $p < 0.05$ (by ANOVA) between laser/NP HT and incubator/NP HT, indicating laser/NP HT results in significantly improved cytotoxicity compared to incubator HT. ** $p < 0.05$ (by ANOVA) between HT and without HT group in both cell lines, indicating significantly higher cancer cell killing was achieved due to HT.

ROS production after HT treatment

ROS production after the two different modes of HT is shown in Figure 3. Incubator HT at 42 °C for 1 h induced production of ROS in both MES-SA and Dx5 cells, whereas ROS production after 3 min of 5 μM laser/NP HT was not different from the control cells that were incubated in a 37 °C incubator probably because much less thermal dose was used, and/or the rapid heating rate does not initiate the ROS production.

HIF-1 expression

As expected, incubator HT induced significantly elevated HIF-1 expression as compared to control ($p < 0.05$), while laser/NP HT did not result in significant changes in HIF-1 expression as shown in Figure 4. These results suggest that rapid laser/NP HT did not up-regulate HIF-1 expression either as a result of the rapid heating or low thermal dose or both.

VEGF expression

VEGF expression is shown in Figure 5. It is not surprising to observe that VEGF secretion was enhanced after incubator HT, since HIF-1 expression was elevated after incubator HT and VEGF is one of the downstream target genes of HIF-1. Accordingly, we did not observe significant changes in VEGF expression after laser/NP HT, given that laser/NP HT did not have any effect on HIF-1 expression.

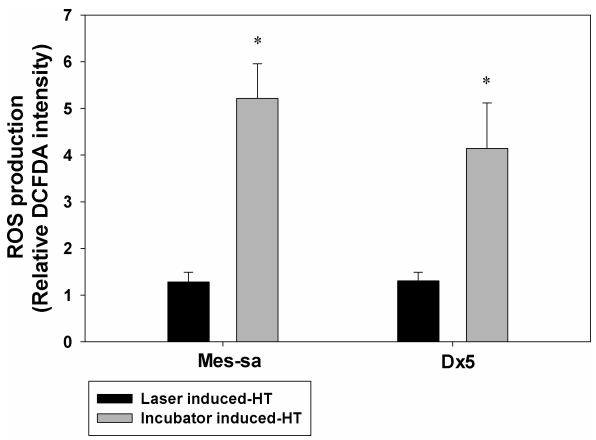

Figure 3: HT-induced ROS production following laser/NPs and incubator was measured in MES-SA and Dx5 cells. Fluorescent dye CM-H2DCFDA was used to measure the fluorescence intensity and normalized to values obtained from the control group (37 °C). *$p < 0.05$ indicates significant ROS production was observed in incubator induced-HT as compared to control. Laser/NP induced-HT did not result in enhanced ROS production as compared to control. Data presented as mean ± SD, $n = 3$.

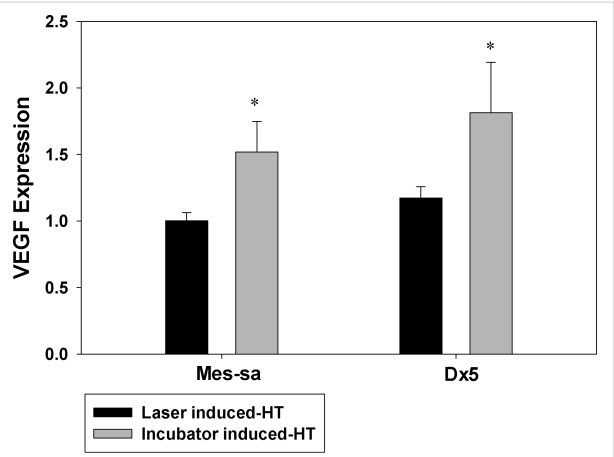

Figure 5: HT-induced VEGF expression after laser/NP and incubator was measured in MES-SA and Dx5 cells. VEGF secretion was measured by using VEGF ELISA. The obtained VEGF expression amount was normalized to SRB value as an indicator of cellular protein amount. All the values measured were then normalized to the controls. * $p < 0.05$ indicates significant VEGF expression was observed in incubator HT as compared to control. Laser/NP HT did not result in enhanced VEGF expression. Data presented as mean ± SD, $n = 3$.

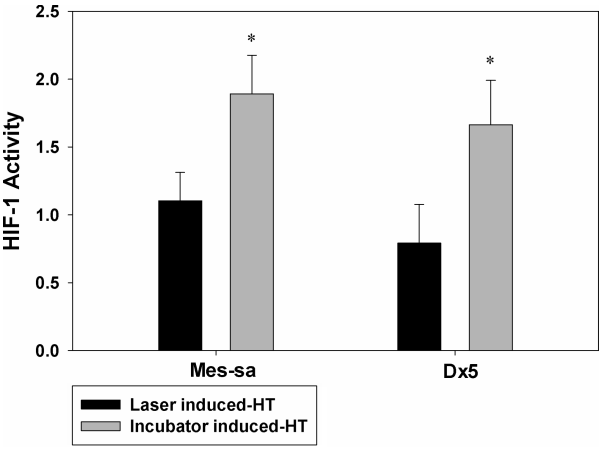

Figure 4: HT-induced HIF-1 expression after laser/NPs and incubator was measured in MES-SA and Dx5 cells. HIF-1 activity was assayed by using HIF-1 ELISA. All measured values were normalized to the mean value of the treatment at 37 °C. * $p < 0.05$ indicates significant HIF-1 expression was observed in incubator induced-HT as compared to control. Laser/NP induced-HT did not result in promoted HIF-1 expression compared to control. Data presented as mean ± SD, $n = 3$.

In vivo imaging studies

In vivo imaging was performed for multiple time points as described in the Experimental section. Images taken at 15 min and 24 h are shown in Figure 6A and Figure 6B, respectively. These images show that the biodistribution of IR820-PGMD NPs is initially very similar to free IR820, as both were processed rapidly through hepatobiliary excretion and start to accumulate in the liver within the first 15 min. After 24 h, it seems that both free dye and NPs were mainly located in the liver. Our previous organ studies showed that considerable IR820 content was also found in the kidneys and the lungs, indicating uptake by RES [24]. However, the IR820 content in kidneys and lungs is lower with NP formulation than in their free form, possibly indicating less RES uptake of NPs, especially in the case of the kidneys. These differences were not statistically significant, probably due to the small sample size and individual variance. The NPs allow for longer image collection times. R values show that NPs have significantly higher fluorescence intensity ($R = 2.37 \pm 0.70$) (mean ± SD) than does the dye in free form ($R = 1.42 \pm 0.19$) (mean ± SD) 24 h after injection ($p < 0.05$). Additionally, our previous pharmacokinetic analysis of plasma samples showed that IR820 plasma concentration 24 h after injection was significantly higher when administered in NP form compared to the free form [24]. Our release kinetics and pharmacokinetics study results [24] seem to indicate that the NP formulation stabilizes IR820, protecting it from degradation and allowing for longer detection windows.

Discussion

The MW of PGMD polymer is 3000 Da, which is expected for polymers synthesized by polycondensations of these MW monomers of glycerol, malic acid and DDA [24,28]. The size of the IR820-PGMD NPs is around 100 nm, which allows them to escape RES uptake, and as a result, to have reduced plasma clearance rates [2]. The loading of IR820 is equivalent to 5 μM IR820 in 0.05 mg/mL IR820-PGMD NPs, which is sufficient to induce HT. IR820 is amphiphilic and has both hydrophilic and hydrophobic properties, whereas PGMD is hydrophobic. Therefore, there are hydrophobic-hydrophobic

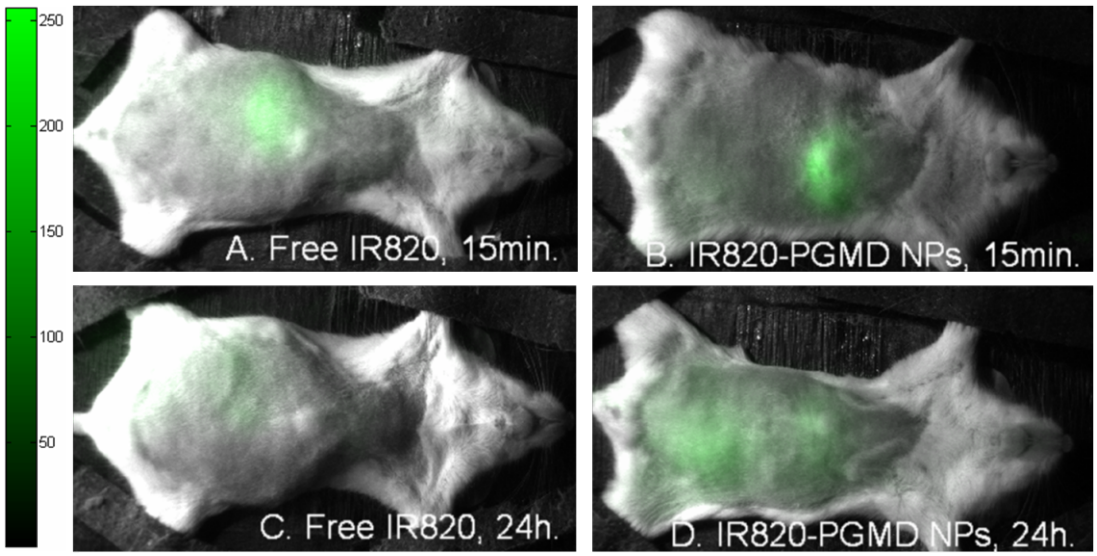

Figure 6: In vivo imaging of free IR820 and IR820-PGMD NPs. Figure 6A and 6B 15 min in vivo imaging. Figure 6C and 6D 24 h in vivo imaging.

interactions between IR820 and PGMD, and IR820 is encapsulated inside the PGMD polymer matrix. Void PGMD NPs do not have any cytotoxicity effect at this concentration. Optical imaging of cancer cells and mice showed that the use of the NP formulation resulted in a stronger fluorescence signal 24 h after injection. This is consistent with the literature reporting that nanoformulations can result in improved plasma circulation time and protect the loading agent from degradation, which would explain the higher intensities observed in vivo when comparing the NP form with the free dye [29,30]. Our pharmacokinetics study showed that IR820-PGMD NPs administration results in significantly increased IR820 plasma concentration 24 h after injection compared to free IR820. In addition, our biodistribution studies showed that kidney IR820 dye content was lower in NP form than in free IR820 form, which means less IR820 was excreted through the renal system when in NP form. This is consistent with kidney excretion being limited to very small particles and small molecules.

The cytotoxicity studies showed that laser/NP induced HT caused significantly higher cell killing than incubator HT, although a much lower thermal dose was given to the cells. In the commonly used CEM_{43} model for thermal dose calculation, which normalizes the thermal dose to cumulative equivalent minutes at 43 °C [26], the temperature and the duration of heating can be used to define thermal damage. Our previous paper and other groups' reports indicate that the rate of photothermal treatment might also affect the HT outcome, because under rapid heating the cells are not able to initiate protective mechanisms by inducing the expression of proteins of the heat shock family to reduce DNA damage [23,31]. Although the laser/NP HT produced approximately 9 times less thermal dose than incubator HT, it still resulted in significantly higher cytotoxicity than incubator HT, thus confirming the importance of the heating rate. Note that the final temperature reached in both modes of HT was identical.

Madamanchi's group reported that ROS can up-regulate HSP70 protein levels by binding signal transducers and activators of transcription (STATs) to the HSP70 promoters in vascular smooth muscle cells (VSMCs) [32]. This group exposed VSMCs to H_2O_2 and found that the cytoplasmic janus tyrosine kinase 2 (JAK2)/STAT pathway can up-regulate HSP70 and minimize oxidative stress effects on the cells. The inhibition of HSP70 expression under laser/NP HT probably means no enhancement of ROS production within the cells. Our ROS detection experiments support this hypothesis, showing that no significant ROS was produced inside the cells after laser/NP HT compared to controls. However, when incubator HT was used to mimic conditions more similar to whole body HT, we observed significant intracellular ROS production. This result is consistent with Moon et al. reporting that ROS was activated when a slow water bath HT was applied to cells. HT can activate the ERK pathway and increase NADPH oxidase activity, which leads to the production of ROS [10]. Based on our results, it seems that the application of rapid laser/NP HT to cells will not induce an increase of ROS. However, the specific mechanism of ROS abolishment within cells after laser/NP HT has to be studied further.

Following the inhibition of ROS production in laser/NP HT treatment, we did not observe enhanced HIF-1 expression.

However, HIF-1 up-regulation was observed in slow and longer term HT, probably because ROS production was activated in the heating process. Other groups have also suggested that the presence of ROS is able to up-regulate HIF-1 expression [18,33]. HIF-1 is very important as a therapeutic target [34]. Traditional HT with slow and long-term heating appears beneficial as an adjuvant therapy for radiotherapy and chemotherapy since it can hinder DNA damage repair mechanisms and increase drug delivery by enhancing its diffusion into the tumor [35,36]. However, this heating modality is also able to induce up-regulation of HIF-1, and the overexpression of HIF-1 could compromise the therapeutic effect by increasing drug resistance by an up-regulation of p-glycoprotein and by reducing cancer cells drug senescence [37,38]. Our results showed that VEGF secretion was also elevated along with the up-regulation of HIF-1, which could potentially result in enhanced tumor angiogenesis. The combination of HT and other therapies could elevate the HIF-1 expression to an even higher extent than single therapy, which could alter tumor cell behavior and promote the aggression of cells. Therefore, it is important to review the possible molecular effects of HT in considering its application as an adjuvant therapy, as other groups have reported that HIF-1 can also be up-regulated by radiotherapy and chemotherapy [39-41]. Based on our study, IR820-PGMD NPs could be used for HT applications without inducing the adverse effects of HIF-1. The HT therapeutic effect might be determined more by the temperature and the heating rate and perhaps less by the total thermal dose. Due to the usage of laser/NP HT we did not observe enhancement of HIF-1 and VEGF expression, but an improved therapeutic outcome was still achieved compared to incubator HT. Despite these promising results for laser/NP HT, further studies have to be performed to determine treatment parameters, such as how to efficiently deliver these NPs and the timing for HT treatment.

Conclusion

In summary, we successfully developed IR820-PGMD NPs, which are promising as theranostic agents with multifunctional imaging and HT capabilities. These NPs, when tested in vitro and in vivo, are able to yield higher fluorescence intensity than free IR820 24 h after incubation or 24 h after i.v. injection of equivalent dye concentrations, allowing for longer imaging collection times and potentially widening the window for HT applications. We also proved in our study that the use of IR820-PGMD NPs and laser/NP HT will neither activate ROS expression, nor induce HIF-1 and VEGF expression, which could yield a beneficial therapeutic outcome. This study is an extension of the current knowledge of delivery of HT in NP form, and we believe it will have a significant impact on the application of nanotechnology on cancer imaging and therapy.

Experimental

Chemicals and cell-based assays

The following materials were purchased from Sigma-Aldrich (St. Louis, MI): Malic acid, 1,12-dodecanedioic acid (DDA), dimethylsulfoxide (DMSO > 99.9%, reagent grade), pluronic F-127, Dulbecco phosphate-buffered saline (DPBS), phosphate buffered saline (PBS), IR820, penicillin-streptomycin solution, tetrahydrofuran (THF) and trypsin-EDTA. Glycerol was purchased from MP Biomedical (MP Biomedical, LLC, Solon OH). 5-(and-6)-chloromethyl-2′,7′-dichlorodihydrofluorescein diacetate, acetyl ester (CM-H2DCFDA) was purchased from Invitrogen, (Invitrogen, NY), human/mouse total HIF-1 alpha cell-based ELISA and human VEGF quantikine ELISA kit were purchased from R & D systems (R & D Systems, MN).

Synthesis and characterization of PGMD polymer

This procedure has been previously described by our group [24]. Briefly, a mixture of glycerol, DDA and malic acid (7:3 DDA:malic acid; 1:1 glycerol:DDA/malic acid) was heated to 120 °C for 48 h. Malic acid allows us to control the degree of hydrophilicity and in turn the glass transition temperature (T_g). Characterization was performed by differential scanning calorimetry (for glass transition temperature) and gel permeation chromatography (for molecular weight, based on a calibration curve of polysterene standards).

Synthesis and characterization of IR820-PGMD NPs

IR820-PGMD NPs were prepared by using an oil-in-water emulsification solvent evaporation technique followed by centrifugation at 5000 rpm for 5 min, and dialysis at MWCO 1000 Da to remove any free IR820 residue. After preparation, the particles were freeze-dried and lyophilized for 48 h. To measure the IR820-PGMD NP size distribution, 100 μL IR820-PGMD NPs were resuspended in 3 mL deionized (DI) water. Then, the solution was measured for average size, size distribution plot based on intensity plot, polydispersity, and zeta potential with a Malvern Zetasizer (Malvern Instruments, Worcestershire, United Kingdom). The size of the particles was measured by determining a correlation function and fitting a polynomial to the correlation function. We used the cumulant analysis as a fitting model for the correlation function in our study. The average particle size, polydispersity, and zeta potential were determined from 10 different NP batches. The DLS intensity plot was obtained from one batch of void PGMD NPs and IR820-PGMD NPs. Scannning Electron Microscopy (SEM, JEOL-JEM) was also used to characterize the NPs shape and size. The loading of IR820 in NP's was evaluated by using a Cary WinUV spectrophotometer (Varian/Agilent Technologies, Switzerland).

In vitro studies of NPs

Cancer cells MES-SA, Dx5, and SKOV3 were purchased from American Type Culture Collection (Manassas, VA) along with McCoy's 5A medium and fetal bovine serum. Cell culture supplies were purchased from Fisher Scientific (Pittsburg, PA), and penicillin was purchased from Sigma-Aldrich. Cell culture conditions were as described in our previous publication [24], with 1% penicillin and 10% fetal bovine serum supplementation.

Subcellular localization of the NPs

SKOV-3 cells were plated in a 24-well tissue culture plate at densities of 4×10^4 cells per well. After overnight incubation to allow for attachment and confluence, we replaced the medium with the test solutions, namely 5 μM free IR820 or 0.05 mg/mL IR820-PGMD NPs (equivalent to 5 μM IR820). Plates were kept at physiological temperature in the dark inside an incubator. Subcellular localization of the IR820-PGMD NPs was identified by incubating 5 μM Lysotracker Blue (Invitrogen, NY) with cells for 10 min at the end of the experiment, followed by 3 × wash with PBS, and fixation with 4% (vol/vol) formaldehyde. Fluorescence images were obtained by using a 60 × water merged objective and a CCD camera, with fluorescence filters of λ_{ex} = 775 nm, λ_{em} = 845 nm for IR820, and λ_{ex} = 355 nm, λ_{em} = 420 nm for LysoTracker Blue. After processing to add pseudo color (IPLab, Qimaging, Canada), the images were imported into Matlab (MathWorks, Massachusetts) and analyzed to determine the intensity ratio *R*. First, the intensity of each pixel was background-subtracted, and the region of interest was defined as being composed of any pixels with above-background intensity values (defined as an intensity of at least 2 out of a 255 scale after background subtraction). The ratio *R* was then determined by normalizing the total pixel intensity of this region of interest to its total area.

HT treatment

Two different heating modes, namely (1) an incubator and (2) a laser/NP HT delivery system, were used for in vitro studies. Detailed descriptions of the heating systems and the temperature calibration for both heating modes were provided in our previous paper [23]. Note that when incubator HT was used, cells were incubated with the same concentration of IR820-PGMD NPs as used in laser/NP HT in order to eliminate the effect of NPs by themselves.

Cytotoxicity assessment

Cell viability after five different treatments (laser only, void PGMD NPs w/ laser, IR820-PGMD NPs, IR820-PGMD NPs w/ laser, incubator HT w/ IR820-PGMD NPs) was measured with the Sulforhodamine B colorimetric (SRB) assay 24 h post-treatment, as previously described in our publications [24,42]. The effect of each treatment on cell growth was normalized to the growth of the control group, which did not receive any treatment.

Cell-based assays for the detection of ROS, HIF-1 and VEGF expression

Study of ROS expression

Intracellular ROS level was measured by using the fluorescent dye CM-H2DCFDA, which is converted into a nonfluorescent derivative (H2DCF) by cellular esterases after uptake by cells. Then, H2DCF can be oxidized to highly fluorescent 2′,7′-dichlorofluorescein (DCF) in the presence of ROS. After HT (either 1 h incubator HT or 3 min laser HT), cells were washed with PBS and collected by incubating with trypsin for 5 min. The same number of cells were counted and incubated with CM-H2DCFDA in the dark. After 30 min, cells were briefly washed with PBS, and the intensity of DCF was measured by a flow cytometer (BD Accuri C6, NJ).

Study of HIF-1 expression

To investigate HIF-1 expression in both incubator HT and laser/NP HT, a human/mouse enzyme-linked immunosorbent assay (ELISA) was used to detect the expression of HIF-1 by using specific HIF-1 antigen. Basal level HIF-1 expression was identified in cells incubated at normal temperature (37°C). HIF-1 expression was measured immediately after HT by reading the plate with a fluorescence plate reader (GENios, TECAN, CA) with an excitation at 540 nm and an emission at 600 nm to measure the amount of total HIF-1 in the cells. Then, the plate was read with an excitation at 360 nm and an emission at 450 nm to measure the amount of total cytochrome c in the cells. Finally, the HIF-1 amount was normalized to the amount of cytochrome c and expressed as HIF-1 activity.

Study of VEGF expression

Cancer cell culture medium was collected 6 h after HT. After centrifuging cell culture media for 10 min at 14000 rpm, 200 μL of supernatant was added into a 96-well plate provided in a human quantikine VEGF ELISA kit. VEGF levels were quantified following the kit protocol, and a sulforhodamine B (SRB) assay (Invitrogen, NY) was used to determine the amount of cellular protein in each well. Subsequently, the measured VEGF amount was normalized to SRB value and the calculated results were normalized to controls.

In vivo optical imaging

Animal studies were performed following the regulations of the Institutional Animal Care and Use Committee. Twenty-four Nd4 Swiss Webster mice (25–30 grams, 9 weeks old) were purchased from Harlan (Indianapolis, IN), and randomly distributed into 8 different experimental groups based on two

factors: time elapsed between injection and data collection (15 min, 30 min, 60 min, and 24 h), and solution injected (0.2 mL of either free IR820 or IR820-PGMD NPs in PBS). Injected solution concentration was matched to an IR820 dose of 0.24 mg/kg of body weight [43]. The in vivo biodistribution of the NPs was recorded with a CCD camera (Qimaging, Canada) coupled with a NIR filter (λ_{ex} = 785 nm, λ_{em} = 820 nm). Later, the images were processed with Matlab to calculate the image fluorescence intensity ratio R as described above.

Statistical analysis

Statistically significant ($p < 0.05$) differences in responses between the treatment groups and control groups was analyzed by ANOVA or t-test (SPSS, Chicago, Illinois).

Supporting Information

Supporting Information File 1

Additional experimental details.
[http://www.beilstein-journals.org/bjnano/content/supplementary/2190-4286-5-35-S1.pdf]

Acknowledgements

This work was conducted using the facilities of the Biomedical Engineering Department at Florida International University (FIU), and funded in part by NIH grant 1R15CA167571-01A1. We also thank AMERI in FIU for taking the SEM images.

References

1. Panyam, J.; Labhasetwar, V. *Adv. Drug Delivery Rev.* **2003,** *55,* 329–347. doi:10.1016/S0169-409X(02)00228-4
2. Moghimi, S. M.; Hunter, A. C.; Murray, J. C. *Pharmacol. Rev.* **2001,** *53,* 283–318.
3. Lei, T. J.; Srinivasan, S.; Tang, Y.; Manchanda, R.; Nagesetti, A.; Fernandez-Fernandez, A.; McGoron, A. J. *Nanomed. Nanotechnol.* **2011,** *7,* 324–332. doi:10.1016/j.nano.2010.11.004
4. Maeda, H. *Adv. Enzyme Regul.* **2001,** *41,* 189–207. doi:10.1016/S0065-2571(00)00013-3
5. Lei, T. Multifunctional nanoparticles in cancer: In vitro characterization, in vivo distribution, and cellular response after laser-NIR dye-induced heating. *ProQuest ETD Collection for FIU.* **2013**, Paper AAI3567295. http://digitalcommons.fiu.edu/dissertations/AAI3567295.
6. Simpson, C. R.; Kohl, M.; Essenpreis, M.; Cope, M. *Phys. Med. Biol.* **1998,** *43,* 2465–2478. doi:10.1088/0031-9155/43/9/003
7. Weissleder, R.; Tung, C.-H.; Mahmood, U.; Bogdanov, A., Jr. *Nat. Biotechnol.* **1999,** *17,* 375–378. doi:10.1038/7933
8. Fernandez-Fernandez, A.; Manchanda, R.; Carvajal, D. A.; Lei, T.; McGoron, A. J. Covalent IR820-PEG diamine conjugates: characterization and in vivo biodistribution. In *Reporters, Markers, Dyes, Nanoparticles, and Molecular Probes for Biomedical Applications V,* Achilefu, S.; Raghavachari, R., Eds.; SPIE: Bellingham, WA, USA, 2013; pp 859605 ff. doi:10.1117/12.2004869
9. Fernandez-Fernandez, A.; Manchanda, R.; Lei, T.; Carvajal, D. A.; Tang, Y.; Kazmi, S. Z.; McGoron, A. J. *Mol. Imaging* **2012,** *11,* 99–113.
10. Moon, E. J.; Sonveaux, P.; Porporato, P. E.; Danhier, P.; Gallez, B.; Batinic-Haberle, I.; Nien, Y. C.; Schroeder, T.; Dewhirst, M. W. *Proc. Natl. Acad. Sci. U. S. A.* **2010,** *107,* 20477–20482. doi:10.1073/pnas.1006646107
11. Du, F.; Zhu, L.; Qian, Z.-M.; Wu, X.-M.; Yung, W.-H.; Ke, Y. *Biochim. Biophys. Acta, Mol. Basis Dis.* **2010,** *1802,* 1048–1053. doi:10.1016/j.bbadis.2010.06.013
12. Yokoi, K.; Fidler, I. J. *Clin. Cancer Res.* **2004,** *10,* 2299–2306. doi:10.1158/1078-0432.CCR-03-0488
13. Kilic, M.; Kasperczyk, H.; Fulda, S.; Debatin, K.-M. *Oncogene* **2007,** *26,* 2027–2038. doi:10.1038/sj.onc.1210008
14. Dong, Z.; Wang, J. Z.; Yu, F.; Venkatachalam, M. A. A. J. *Pathol.* **2003,** *163,* 663–671. doi:10.1016/S0002-9440(10)63693-0
15. Ferrara, N.; Davis-Smyth, T. *Endocr. Rev.* **1997,** *18,* 4–25. doi:10.1210/edrv.18.1.0287
16. Carmeliet, P.; Dor, Y.; Herbert, J.-M.; Fukumura, D.; Brusselmans, K.; Dewerchin, M.; Neeman, M.; Bono, F.; Abramovitch, R.; Maxwell, P.; Koch, C. J.; Ratcliffe, P.; Moons, L.; Jain, R. K.; Collen, D.; Keshet, E. *Nature* **1998,** *394,* 485–490. doi:10.1038/28867
17. Forsythe, J. A.; Jiang, B. H.; Iyer, N. V.; Agani, F.; Leung, S. W.; Koos, R. D.; Semenza, G. L. *Mol. Cell. Biol.* **1996,** *16,* 4604–4613.
18. Goyal, P.; Weissmann, N.; Grimminger, F.; Hegel, C.; Bader, L.; Rose, F.; Fink, L.; Ghofrani, H. A.; Schermuly, R. T.; Schmidt, H. H. H. W.; Seeger, W.; Hänze, J. *Free Radical Biol. Med.* **2004,** *36,* 1279–1288. doi:10.1016/j.freeradbiomed.2004.02.071
19. Chandel, N. S.; McClintock, D. S.; Feliciano, C. E.; Wood, T. M.; Melendez, J. A.; Rodriguez, A. M.; Schumacker, P. T. *J. Biol. Chem.* **2000,** *275,* 25130–25138. doi:10.1074/jbc.M001914200
20. Nishizawa, J.; Nakai, A.; Matsuda, K.; Komeda, M.; Ban, T.; Nagata, K. *Circulation* **1999,** *99,* 934–941. doi:10.1161/01.CIR.99.7.934
21. Li, G. C.; Mivechi, N. F.; Weitzel, G. *Int. J. Hyperthermia* **1995,** *11,* 459–488. doi:10.3109/02656739509022483
22. Hildebrandt, B.; Wust, P.; Ahlers, O.; Dieing, A.; Sreenivasa, G.; Kerner, T.; Felix, R.; Riess, H. *Crit. Rev. Oncol. Hematol.* **2002,** *43,* 33–56. doi:10.1016/S1040-8428(01)00179-2
23. Tang, Y.; McGoron, A. J. *J. Photochem. Photobiol., B: Biol.* **2009,** *97,* 138–144. doi:10.1016/j.jphotobiol.2009.09.001
24. Lei, T.; Manchanda, R.; Huang, Y.-C.; Fernandez-Fernandez, A.; Bunetska, K.; Milera, A.; Sarmiento, A.; McGoron, A. J. Near-infrared imaging loaded polymeric nanoparticles: in vitro and in vivo studies. In *Reporters, Markers, Dyes, Nanoparticles, and Molecular Probes for Biomedical Applications V,* Achilefu, S.; Raghavachari, R., Eds.; SPIE: Bellingham, WA, USA, 2013; pp 859607 ff. doi:10.1117/12.2005563
25. Kaplowitz, N.; Kuhlenkamp, J.; Clifton, G. *Exp. Biol. Med.* **1975,** *149,* 234–237. doi:10.3181/00379727-149-38779
26. Sapareto, S. A.; Dewey, W. C. *Int. J. Radiat. Oncol., Biol., Phys.* **1984,** *10,* 787–800. doi:10.1016/0360-3016(84)90379-1
27. Tang, Y.; McGoron, A. J. *Int. J. Hyperthermia* **2013,** *29,* 145–155. doi:10.3109/02656736.2012.760757
28. Padilla De Jesús, O. L.; Ihre, H. R.; Gagne, L.; Fréchet, J. M. J.; Szoka, F. C., Jr. *Bioconjugate Chem.* **2002,** *13,* 453–461. doi:10.1021/bc010103m
29. Li, S.-D.; Huang, L. *Mol. Pharmaceutics* **2008,** *5,* 496–504. doi:10.1021/mp800049w
30. Moghimi, S. M.; Hunter, A. C.; Andresen, T. L. *Annu. Rev. Pharmacol. Toxicol.* **2012,** *52,* 481–503. doi:10.1146/annurev-pharmtox-010611-134623

31. Dewhirst, M. W.; Viglianti, B. L.; Lora-Michiels, M.; Hanson, M.; Hoopes, P. J. *Int. J. Hyperthermia* **2003,** *19,* 267–294. doi:10.1080/0265673031000119006
32. Madamanchi, N. R.; Li, S.; Patterson, C.; Runge, M. S. *Arterioscler., Thromb., Vasc. Biol.* **2001,** *21,* 321–326. doi:10.1161/01.ATV.21.3.321
33. Mansfield, K. D.; Guzy, R. D.; Pan, Y.; Young, R. M.; Cash, T. P.; Schumacker, P. T.; Simon, M. C. *Cell Metab.* **2005,** *1,* 393–399. doi:10.1016/j.cmet.2005.05.003
34. Semenza, G. L. *Nat. Rev. Cancer* **2003,** *3,* 721–732. doi:10.1038/nrc1187
35. Nevaldine, B.; Longo, J. A.; Hahn, P. J. *Int. J. Hyperthermia* **1994,** *10,* 381–388. doi:10.3109/02656739409010282
36. Jain, R. K. *Cancer Res.* **1988,** *48,* 2641–2658.
37. Sullivan, R.; Paré, G. C.; Frederiksen, L. J.; Semenza, G. L.; Graham, C. H. *Mol. Cancer Ther.* **2008,** *7,* 1961–1973. doi:10.1158/1535-7163.MCT-08-0198
38. Wartenberg, M.; Gronczynska, S.; Bekhite, M. M.; Saric, T.; Niedermeier, W.; Hescheler, J.; Sauer, H. *Int. J. Cancer* **2005,** *113,* 229–240. doi:10.1002/ijc.20596
39. Harada, H.; Kizaka-Kondoh, S.; Li, G.; Itasaka, S.; Shibuya, K.; Inoue, M.; Hiraoka, M. *Oncogene* **2007,** *26,* 7508–7516. doi:10.1038/sj.onc.1210556
40. Brown, L. M.; Cowen, R. L.; Debray, C.; Eustace, A.; Erler, J. T.; Sheppard, F. C. D.; Parker, C. A.; Stratford, I. J.; Williams, K. J. *Mol. Pharmacol.* **2006,** *69,* 411–418. doi:10.1124/mol.105.015743
41. Song, X.; Liu, X.; Chi, W.; Liu, Y.; Wei, L.; Wang, X.; Yu, J. *Cancer Chemother. Pharmacol.* **2006,** *58,* 776–784. doi:10.1007/s00280-006-0224-7
42. Tang, Y.; Lei, T. J.; Manchanda, R.; Nagesetti, A.; Fernandez-Fernandez, A.; Srinivasan, S.; McGoron, A. J. *Pharm. Res.* **2010,** *27,* 2242–2253. doi:10.1007/s11095-010-0231-6
43. Rajagopalan, R.; Uetrecht, P.; Bugaj, J. E.; Achilefu, S. A.; Dorshow, R. B. *Photochem. Photobiol.* **2000,** *71,* 347–350. doi:10.1562/0031-8655(2000)071<0347:SOTOTA>2.0.CO;2

License and Terms

Beilstein Journal of Nanotechnology

Fullerenes as adhesive layers for mechanical peeling of metallic, molecular and polymer thin films

Maria B. Wieland[1], Anna G. Slater[2,3], Barry Mangham[2], Neil R. Champness[2] and Peter H. Beton[*1]

Full Research Paper

Open Access

Address:
[1]School of Physics & Astronomy, University of Nottingham, Nottingham, NG7 2RD, UK, [2]School of Chemistry, University of Nottingham, Nottingham, NG7 2RD, UK and [3]Present address: Department of Chemistry, University of Liverpool, Crown St, Liverpool, L69 7ZD, UK

Email:
Peter H. Beton[*] - peter.beton@nottingham.ac.uk

* Corresponding author

Keywords:
polymerisation; porphyrin; surface; thin film; transfer

Beilstein J. Nanotechnol. **2014,** *5,* 394–401.
doi:10.3762/bjnano.5.46

Received: 13 January 2014
Accepted: 10 March 2014
Published: 02 April 2014

This article is part of the Thematic Series "Physics, chemistry and biology of functional nanostructures II".

Guest Editor: A. S. Sidorenko

Abstract

We show that thin films of C_{60} with a thickness ranging from 10 to 100 nm can promote adhesion between a Au thin film deposited on mica and a solution-deposited layer of the elastomer polymethyldisolaxane (PDMS). This molecular adhesion facilitates the removal of the gold film from the mica support by peeling and provides a new approach to template stripping which avoids the use of conventional adhesive layers. The fullerene adhesion layers may also be used to remove organic monolayers and thin films as well as two-dimensional polymers which are pre-formed on the gold surface and have monolayer thickness. Following the removal from the mica support the monolayers may be isolated and transferred to a dielectric surface by etching of the gold thin film, mechanical transfer and removal of the fullerene layer by annealing/dissolution. The use of this molecular adhesive layer provides a new route to transfer polymeric films from metal substrates to other surfaces as we demonstrate for an assembly of covalently-coupled porphyrins.

Introduction

The mechanical removal of thin films, molecular layers and nanostructured semiconductors from the substrates on which they are grown has been developed over several decades for applications in photonics, sensing and flexible electronics. In early work the focus was on the formation of ultra-smooth metal surfaces [1-6] for the study of thiolate self-assembled monolayers (SAMs). This is achieved by applying epoxy to the top surface of a gold thin film grown on a mica substrate. The combined epoxy/gold layer can then be detached by mechanical peeling, and the roughness of the resulting free surface is comparable with that of the mica substrate. In a variation of this approach Rogers and co-workers demonstrated that nano- and

microstructured semiconductors could not only be removed from a substrate, but also transferred to more technologically relevant surfaces [7,8]. The transfer of molecular films from a metal to a dielectric substrate has also been demonstrated for cross-linked self-assembled monolayers (SAM) using a polymeric 'glue' to first peel off a Au/SAM/polymer layer, followed by an etch process to remove the gold, thus isolating the SAM/polymer film for subsequent processing [9]. Most recently, the transfer and removal of monolayer films has been widely adopted by graphene researchers through exfoliation [10] and, for samples grown by chemical vapour deposition, by etching the underlying metal thin film or foil used as a growth substrate [11-13].

In a complementary strand of research the formation of two-dimensional molecular arrays on surfaces which are stabilised by hydrogen bonding, metal co-ordination and covalent bonds has attracted great interest over the past decade [14-17]. There have been significant advances in the understanding of the growth and formation of such arrays, but their application in a functional form has so far been limited by their formation on substrates which are not compatible with potential applications. This is of particular relevance to the growing interest in the formation of polymers through on-surface synthesis using Ullmann-type, and other coupling reactions [18-28]. This approach has been used to form one-dimensional polymers [19] and graphene nanoribbons [20] with lengths up to ≈40 nm, small domains of multiply-connected molecules [18,20,21,25,28] and more extended two-dimensional arrays in some cases continuously covering macroscopic areas of a sample surface [29]. The scientific investigations of such polymers have provided new insights into charge transport in molecular systems [19], but many properties of potential interest, particularly those related to optical and electronic properties, cannot be easily investigated while the structures remain on a metallic substrate (the common choice for catalysing the relevant coupling reaction). For the case of graphene nanoribbons direct mechanical transfer has been demonstrated [20] but the process remains relatively uncontrolled.

The development of a systematic process for the transfer of functional monolayers analogous to template stripping is thus highly desirable, but many of the layers of potential interest are likely to be chemically and mechanically fragile and are therefore unlikely to be compatible with the application of conventional adhesives and, in addition, have unknown solubilities in solvents which might be used to remove the adhesive layers in subsequent process steps. Furthermore, the application of adhesive layers is not easily compatible with the controlled environments, such as ultra-high vacuum, under which many on-surface polymerisation studies are performed.

In this paper we demonstrate that a sublimed layer of organic molecules provides unexpected adhesive properties which may be used to remove thin metallic films from a mica substrate by mechanical peeling. We focus in particular, but not exclusively, on the adhesive properties of the fullerene C_{60}, and show that films with a thickness greater than 10 nm can be used for this application. The use of a sublimed C_{60} adhesion layer also ensures high chemical purity, is compatible with formation under ultra-high vacuum (UHV) conditions and is known, even for thicknesses down to 3 nm, to provide effective protection for buried 'UHV-clean' surfaces on exposure to atmosphere [30]. In addition, small organic molecules, such as C_{60}, are readily soluble in a range of solvents offering a flexible approach to the selective removal of the adhesion layers in subsequent process steps.

Results and Discussion

The transfer process is shown schematically in Figure 1, in which a porphyrin/C_{60}/PDMS layer (Figure 1a) is formed on a gold surface. The overall aim of our approach is to remove the organic layer (the porphyrin thin film (or monolayer)) from the gold, but we consider first the adhesion of the C_{60} in the absence of such a layer.

In our experiments we start with a gold thin film deposited on mica (provided commercially by Georg Albert GmbH). Pieces with typical dimensions of 1 × 1 cm^2 were loaded into a UHV system (base pressure 10^{-10} mbar) and prepared by repeated cycles of sputtering and annealing until a clear herringbone reconstruction pattern could be observed on the Au(111) surface using scanning tunnelling microscopy (STM). See the Experimental section for more details.

Fullerene films with thickness ranging from 5 nm to 100 nm were deposited via sublimation onto the gold using a deposition rate of 1 nm/min. The samples were subsequently removed from UHV and a support layer of polydimethylsiloxane (PDMS) with a thickness of ≈1 mm was deposited from solution onto the samples (see the Experimental section). Mechanical peeling of the PDMS layer removes the gold from the mica as depicted in Figure 1b. For control samples, where the PDMS was directly deposited onto a clean Au(111) sample, the PDMS is peeled off leaving the gold layer intact on the mica, indicating that the adhesive properties arise from the fullerene layer. Similar results are obtained using a Ag thin film on mica.

For C_{60} layers with thickness <10 nm the gold remains partially on the mica substrate. The peeling is also less reliable for films with thickness >70 nm although this has been studied less systematically due to the significant consumption of C_{60} involved. A fullerene thickness of 15 nm was therefore used as

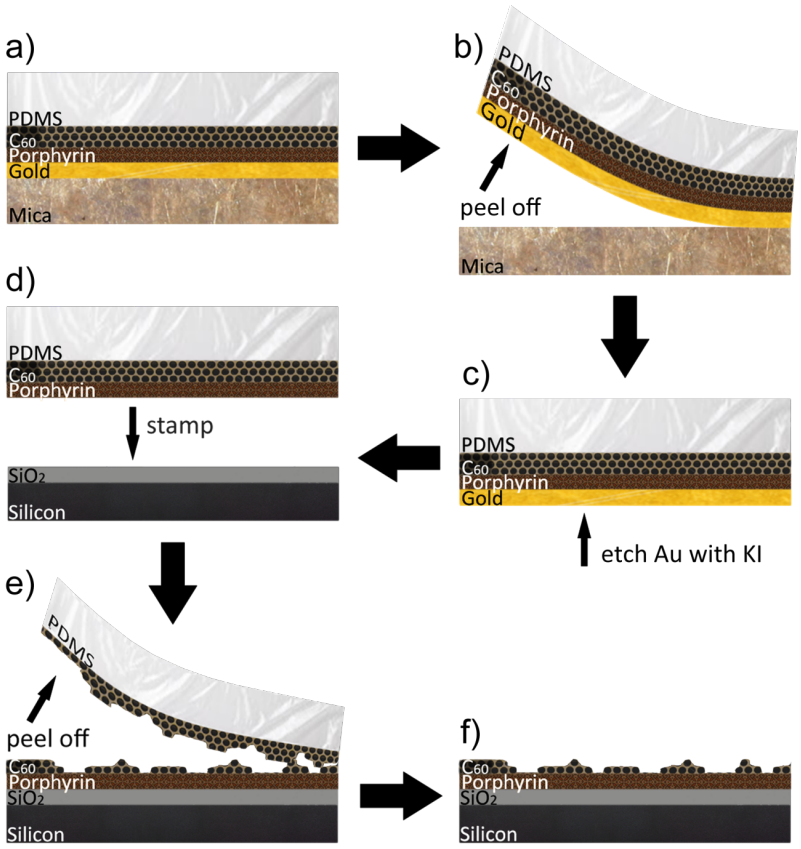

Figure 1: Schematic process for the transfer of porphyrin using C_{60} as an adhesive and protection layer.

a standard in subsequent experiments. A similar effect was obtained when substituting perylene tetracarboxylic acid (PTCDI) for the fullerene although the results are less reproducible for this choice of molecule.

The gold may be subsequently etched using an aqueous potassium iodide solution (see the Experimental section and schematic in Figure 1c), leaving the fullerene layer exposed (C_{60} is insoluble in gold etchant). The presence of the fullerene was verified by Raman and fluorescence spectroscopy (see the Experimental section). The fullerene layer was then mechanically transferred onto a SiO_2 surface (thickness 90 nm, grown on a Si wafer and supplied commercially). SiO_2 was chosen for its well defined Raman spectrum and very low background intensity at high wave numbers. This is achieved through gentle manual pressure in a stamping process in which the PDMS layer was peeled away to expose the fullerene layer remaining on the SiO_2.

The Raman [31,32] and fluorescence [33,34] spectra of the transferred C_{60} are very similar to the spectra of C_{60} sublimed directly onto SiO_2 (see Figure 2). The transferred fullerene layer can be readily removed from the SiO_2 by annealing the sample at 300 °C under vacuum conditions, or by dissolving the C_{60} in toluene or carbon disulfide.

To utilize these adhesive properties of fullerene as a means to transfer organic material, test layers of porphyrin thin films down to monolayer level were introduced between the gold and fullerene layer as depicted in Figure 1a. Films of thicknesses ranging from one monolayer up to 5 nm of tetra(4-bromophenyl)porphyrin (TBPP) or tetra(4-bromophenyl)porphyrinato zinc (Zn-TBPP) do not impair the peeling process. These molecules were chosen as a target for transfer since they undergo on-surface polymerisation and may be readily characterised optically.

The transfer process has been implemented with (non-polymerised) porphyrin layers with thickness varying from 0.5 nm to 5 nm, and a 15 nm overlayer of fullerene. For control purposes porphyrin thin films covered by varying thicknesses of fullerene layers were directly deposited onto SiO_2/Si samples via sublimation. The presence of porphyrin under the fullerene layer after transfer to SiO_2, and also for the control samples, is

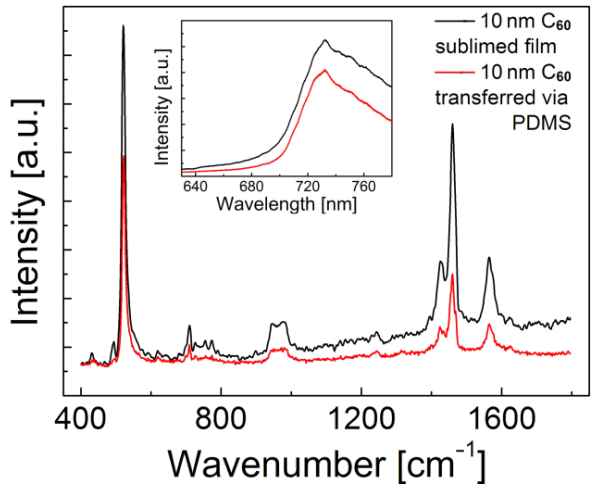

Figure 2: Raman spectrum of C_{60} on SiO_2/Si; the features at 520 and 900–1000 cm^{-1} correspond to the Si substrate, the peak at 720 cm^{-1} and the region between 1400 and 1600 cm^{-1} with the relatively sharp line at around 1470 cm^{-1} are characteristic for C_{60}; [31,32] insert: fluorescence emission spectrum (excitation wavelength = 532 nm) of the same samples with the characteristic broadened emission band at about 740 nm from excited singlet and triplet states of C_{60} [33,34].

verified via fluorescence spectroscopy (Figure 3). The lowest two curves show the spectrum from a control sample, a sublimed layer of porphyrin in which the characteristic double peak in the Q-band region at 656 ± 1 nm and 722 ± 1 nm [35,36] (655 ± 1 nm and 720 ± 1 nm for Zn-TBPP) can be observed. These peaks are also clearly observed for a porphyrin layer of 3 nm on which a 5 nm layer of C_{60} has been deposited. However, for a sample with 20 nm of fullerene the second porphyrin peak (Por2) is obscured by the characteristic broadened spectral peak at approximately 740 nm from the excited singlet and triplet states of C_{60} [33,34] and the first porphyrin peak (Por1) may only just be resolved.

The spectrum from the transferred sample (uppermost curve in Figure 3) shows the porphyrin peak at 656 ± 1 nm and the C_{60} peak at 740 nm. From a comparison with the spectra of control samples with sublimed layers of C_{60} we conclude that the porphyrin layer, together with more than 5 nm but less than 20 nm C_{60}, has been successfully stamped onto a SiO_2 surface. The desorption and solubility properties of porphyrin monomers are similar to C_{60}, thus removal of the fullerene layer results in simultaneous desorption or dissolution of the porphyrin layer, for example by immersion in toluene.

We now consider the transfer of porphyrin polymers onto a target dielectric substrate. An extended covalently linked network of TBPP was prepared by sublimation onto a heated substrate as described in the Experimental section.

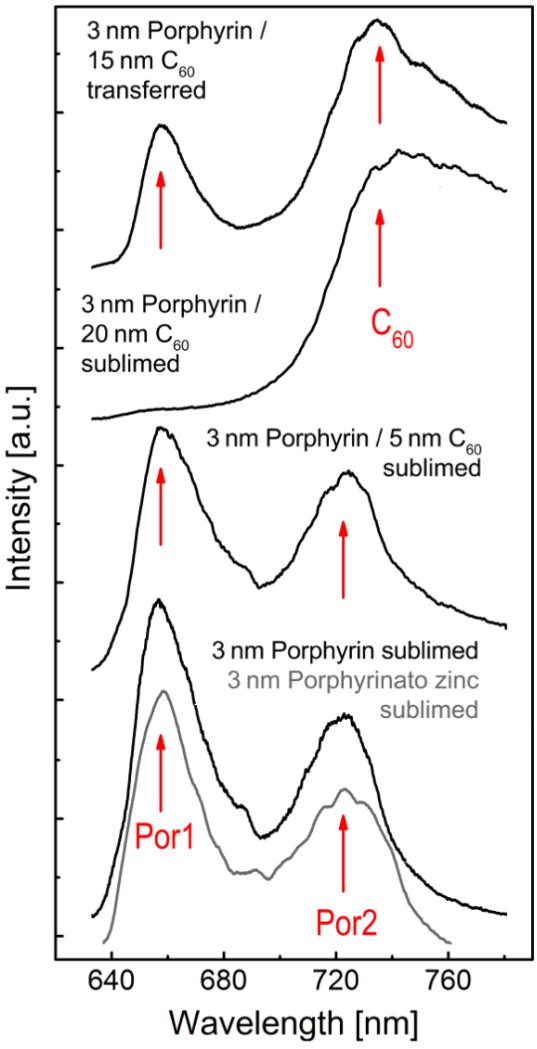

Figure 3: Normalised fluorescence emission spectra (excitation wavelength = 532 nm) of sublimed and transferred porphyrin on SiO_2/Si substrates with C_{60} cover layers of varying thickness; the characteristic double peak at 656 ± 1 nm and 722 ± 1 nm (655 ± 1 nm and 720 ± 1 nm for Zn-TBPP) corresponds to the porphyrin Q band region [31-33], the broadened emission band at about 740 nm corresponds to the excited singlet and triplet states of C_{60}.

An STM image of the resulting surface (Figure 4) shows small regions of local square order with lateral dimensions ≈5 nm within a disordered polymeric matrix. The ordered regions are very similar to those originally reported by Grill et al. [18] for this molecule, and are formed through an Ullmann-type coupling of molecules via the phenyl sidegroups, which is mediated by the catalytically-induced breaking of carbon-bromine bonds. If the molecules are deposited with sub-monolayer coverage on a substrate held at room temperature, followed by annealing, small disconnected islands in which monomers are connected in an arrangement with square

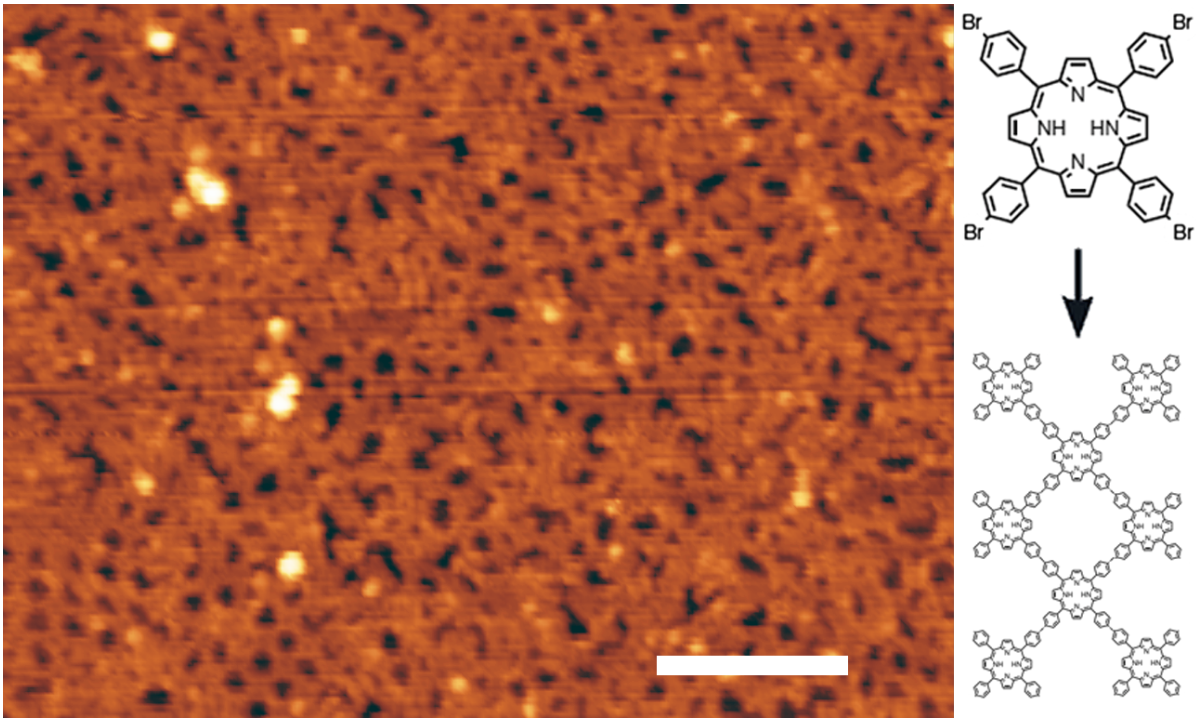

Figure 4: STM image of extended polymerized TBPP (−1.7 V, 0.03 nA, scale bar: 10 nm); schematic: structure of a TBPP monomer and the resulting polymeric structure.

symmetry are observed. In our previous work on the polymerisation of tri(bromphenyl)benzene (TBPB) [22] we have shown that a continuously connected polymer may be formed by subliming at very low rates (<1 monolayer/h) onto a heated substrate. We have used an analogous preparative procedure to form the extended polymeric network shown in Figure 4.

For the transfer experiments a 15 nm thick layer of C_{60} is deposited on a porphyrin polymer derived from Zn-TBPP and the network is transferred to SiO_2 by peeling, gold etching and mechanical transfer as described earlier. In order to demonstrate the effective transfer of the porphyrin polymer/C_{60} layers, fluorescence spectra were obtained of the surfaces before and after annealing to remove C_{60}. In Figure 5 we show maps of the fluorescence intensity at wavelengths corresponding to one of the porphyrin peaks (Por1; Figure 5a and 5d) or the peak around 740 nm associated with the C_{60} (Figure 5b and 5e). These maps, taken over macroscopic areas of 0.5 × 0.5 mm^2 confirm that porphyrin, together with C_{60}, is transferred over large areas of the sample. Prior to annealing we observe a variation in intensity of the Por1 peak (Figure 5a) across the surface which we attribute to the attenuating effect of a residual C_{60} layer of varying thickness across the surface. This hypothesis is consistent with a comparison of spectra taken at positions A and B (see Figure 5c) with spectra taken from control samples of C_{60} films of varying thicknesses (Figure 3), implying that during the transfer the C_{60} layer is broken apart irregularly.

Due to the thermal stability of the covalent bonds linking neighbouring porphyrins, the residual C_{60} can be removed by annealing without removing the polymeric network (note that a similar annealing treatment applied to non-polymerised porphyrins results in complete removal of the molecular thin film). After annealing the sample for 30 min at 300 °C fluorescence maps are re-acquired (Figure 5d and 5e) and show that porphyrin is still present on the surface with near homogenous intensity, while the fullerene has been almost completely removed from the surface. The characteristic double peak (Por1 at 655 ± 1 nm, Por2 at 720 ± 1 nm) in the fluorescence spectra of the polymerised porphyrin (Figure 5f) is present across over 90% of the mapped area.

The spectra of transferred porphyrin two-dimensional polymers are similar in shape to those of transferred or sublimed porphyrin monomer monolayers; the peaks are observed at, within experimental error, the same wavelength as the monomer. These observations are consistent with previous studies of arrays of porphyrins coupled by phenyl groups [37]. The very

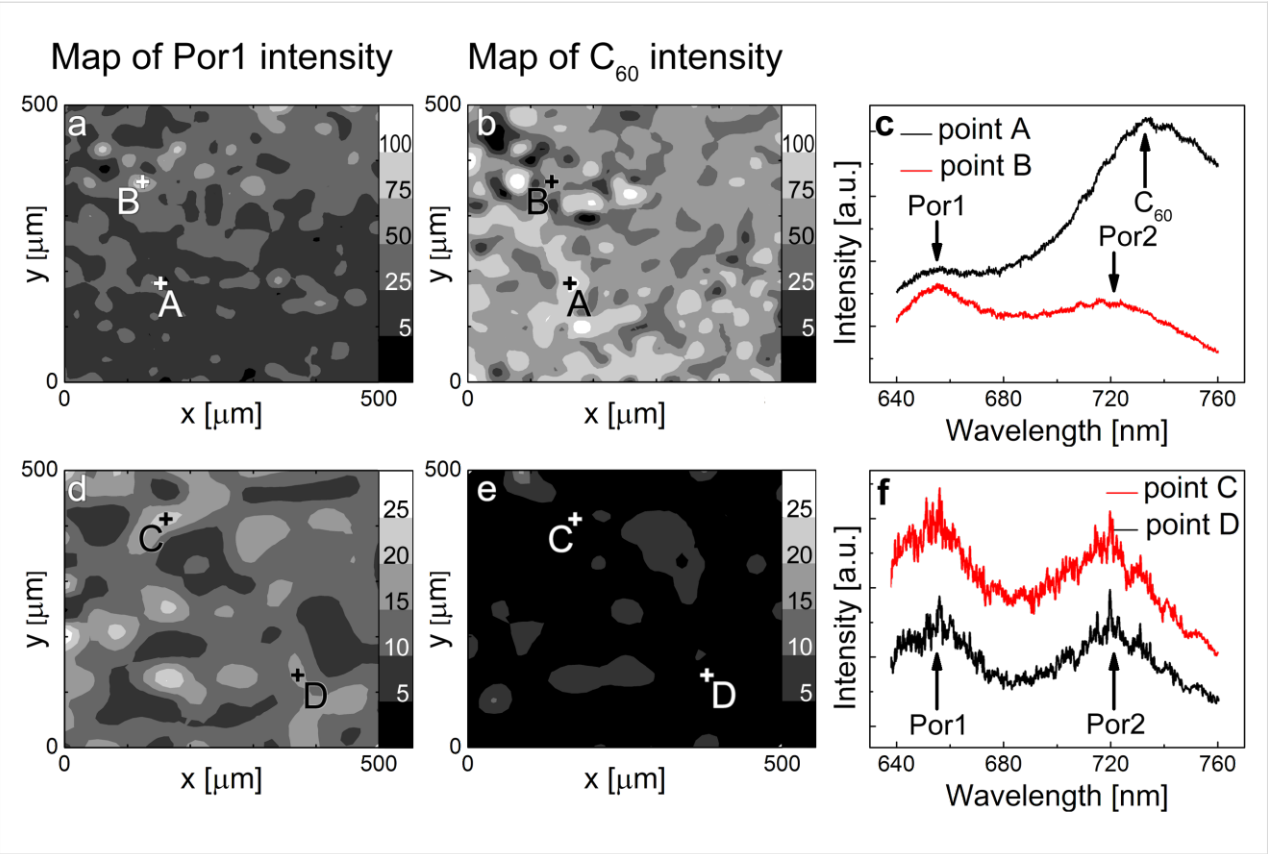

Figure 5: Fluorescence emission spectroscopy maps over 0.25 mm^2 (excitation wavelength = 532 nm) and selected spectra of transferred polymerised TBPP-Zn networks before (a–c) and after (d–f) thermal desorption of the fullerene layer.

weak coupling of neighbouring porphyrins has been attributed to the rotation of the phenyl linker groups [38], which are not in the same plane as the porphyrin macrocycle, inhibiting extended π-conjugation.

Conclusion

In conclusion we have shown that C_{60} shows an unexpected mechanical adhesion which is sufficiently strong to promote the removal of a metal film from a mica substrate. Furthermore this route may be used to remove molecular thin films from a metal substrate through a process of mechanical removal followed by etching, and also to transfer them to a dielectric surface. The method is demonstrated for a SiO_2 substrate but is expected to be compatible with other dielectrics. The process is effective for films with thickness as small as a monolayer and has been demonstrated as route to isolate two dimensional polymers formed by on-surface synthesis, allowing an investigation of their functional properties.

Experimental

The ultra-high vacuum system in which we perform the sublimation of organic thin films and house the STM has a base pressure of 10^{-10} mbar. Commercially supplied (111) terminated gold films on mica (Georg Albert, Physical Vapor Deposition) are used as substrates and prepared via Ar-sputtering for 30 min at 0.8 keV and 10^{-5} mbar Ar-pressure, followed by annealing at 400 °C for 1 h using a piece of highly doped silicon under the gold/mica sample as a heater. The sputter-anneal-cycle is repeated until the herringbone reconstruction is clearly observed in STM images.

TBPP and Zn-TBPP monomer layers, prepared by literature methods [18], are sublimed from a Knudsen cell at rates of 0.2 nm/min onto samples at room temperature. Polymerised covalent networks of TBPP and Zn-TBPP are formed via sublimation at rates of 0.07 ML/h onto samples held at 200 °C, followed by annealing at 250 °C for 3 h. C_{60} is deposited from a Knudsen cell at 1 nm/min.

PDMS is prepared from 9 parts 184 silicon elastomer base and 1 part 184 silicon elastomer curing agent (commercially supplied by Dow Corning), applied to the sample, and cured at 150 °C for 15 min. After the mica is removed, the gold is etched using commercial gold etchant (supplied by Sigma Aldrich), an aqueous KI solution, for 3 to 5 min. Subsequently the samples are rinsed with de-ionised water to remove excess KI.

Raman and fluorescence spectra are taken using a Horiba LabRAM HR Raman Spectroscopy System with an excitation wavelength of 523 nm. To avoid beam damage, spectra are acquired over 10 s to 30 s integration time at 10% to 1% laser power. Fluorescence maps are taken over 500 × 500 μm^2 areas, consisting of 10 × 10 to 20 × 20 single spectra.

Acknowledgements

N.R.C. gratefully acknowledges the receipt of a Royal Society Wolfson Merit Award. We thank the UK Engineering and Physical Sciences Research Council for funding under grant EP/H010432/1.

References

1. Wagner, P.; Hegner, M.; Guentherodt, H.-J.; Semenza, G. *Langmuir* **1995,** *11,* 3867–3875. doi:10.1021/la00010a043
2. Hegner, M.; Wagner, P.; Semenza, G. *Surf. Sci.* **1993,** *291,* 39–46. doi:10.1016/0039-6028(93)91474-4
3. Ederth, T. *Phys. Rev. A* **2000,** *62,* 062104. doi:10.1103/PhysRevA.62.062104
4. Diebel, J.; Löwe, H.; Samorí, P.; Rabe, J. P. *Appl. Phys. A: Mater. Sci. Process.* **2001,** *73,* 273–279. doi:10.1007/s003390100935
5. Mosley, D. W.; Chow, B. Y.; Jacobson, J. M. *Langmuir* **2006,** *22,* 2437–2440. doi:10.1021/la052650s
6. Banner, L. T.; Richter, A.; Pinkhassik, E. *Surf. Interface Anal.* **2009,** *41,* 49–55. doi:10.1002/sia.2977
7. Khang, D.-Y.; Jiang, H.; Huang, Y.; Rogers, J. A. *Science* **2006,** *311,* 208–212. doi:10.1126/science.1121401
8. Kim, D.-H.; Ahn, J.-H.; Choi, W. M.; Kim, H.-S.; Kim, T.-H.; Song, J.; Huang, Y. Y.; Liu, Z.; Lu, C.; Rogers, J. A. *Science* **2008,** *320,* 507–511. doi:10.1126/science.1154367
9. Turchanin, A.; Beyer, A.; Nottbohm, C. T.; Zhang, X.; Stosch, R.; Sologubenko, A.; Mayer, J.; Hinze, P.; Weimann, T.; Gölzhäuser, A. *Adv. Mater.* **2009,** *21,* 1233–1237. doi:10.1002/adma.200803078
10. Novoselov, K. S.; Geim, A. K.; Morozov, S. V.; Jiang, D.; Zhang, Y.; Dubonos, S. V.; Grigorieva, I. V.; Firsov, A. A. *Science* **2004,** *306,* 666–669. doi:10.1126/science.1102896
11. Yu, Q.; Lian, J.; Siriponglert, S.; Li, H.; Chen, Y. P.; Pei, S.-S. *Appl. Phys. Lett.* **2008,** *93,* 113103. doi:10.1063/1.2982585
12. Kim, K. S.; Zhao, Y.; Jang, H.; Lee, S. Y.; Kim, J. M.; Kim, K. S.; Ahn, J.; Kim, P.; Choi, J.; Hong, B. H. *Nature* **2009,** *457,* 706–710. doi:10.1038/nature07719
13. Li, X.; Cai, W.; An, J.; Kim, S.; Nah, J.; Yang, D.; Piner, R.; Velamakanni, A.; Jung, I.; Tutuc, E.; Banerjee, S. K.; Colombo, L.; Ruoff, R. S. *Science* **2009,** *324,* 1312–1314. doi:10.1126/science.1171245
14. Bartels, L. *Nat. Chem.* **2010,** *2,* 87–95. doi:10.1038/nchem.517
15. Barth, J. V.; Costantini, G.; Kern, K. *Nature* **2005,** *437,* 671–679. doi:10.1038/nature04166
16. Kudernac, T.; Lei, S.; Elemans, J. A. A. W.; De Feyter, S. *Chem. Soc. Rev.* **2009,** *38,* 402–421. doi:10.1039/b708902n
17. Slater (née Phillips), A. G.; Beton, P. H.; Champness, N. R. *Chem. Sci.* **2011,** *2,* 1440–1448. doi:10.1039/c1sc00251a
18. Grill, L.; Dyer, M.; Lafferentz, L.; Persson, M.; Peters, M. V.; Hecht, S. *Nat. Nanotechnol.* **2007,** *2,* 687–691. doi:10.1038/nnano.2007.346
19. Lafferentz, L.; Ample, F.; Yu, H.; Hecht, S.; Joachim, C.; Grill, L. *Science* **2009,** *323,* 1193–1197. doi:10.1126/science.1168255
20. Cai, J.; Ruffieux, P.; Jaafar, R.; Bieri, M.; Braun, T.; Blankenburg, S.; Muoth, M.; Seitsonen, A. P.; Saleh, M.; Feng, X.; Müllen, K.; Fasel, R. *Nature* **2010,** *466,* 470–473. doi:10.1038/nature09211
21. Bieri, M.; Nguyen, M.-T.; Gröning, O.; Cai, J.; Treier, M.; Aït-Mansour, K.; Ruffieux, P.; Pignedoli, C. A.; Passerone, D.; Kastler, M.; Müllen, K.; Fasel, R. *J. Am. Chem. Soc.* **2010,** *132,* 16669–16676. doi:10.1021/ja107947z
22. Blunt, M. O.; Russell, J. C.; Champness, N. R.; Beton, P. H. *Chem. Commun.* **2010,** *46,* 7157–7159. doi:10.1039/c0cc01810d
23. Lipton-Duffin, J. A.; Ivasenko, O.; Perepichka, D. F.; Rosei, F. *Small* **2009,** *5,* 592–597. doi:10.1002/smll.200801943
24. Abel, M.; Clair, S.; Ourdjini, O.; Mossoyan, M.; Porte, L. *J. Am. Chem. Soc.* **2011,** *133,* 1203–1205. doi:10.1021/ja108628r
25. Gutzler, R.; Walch, H.; Eder, G.; Kloft, S.; Heckl, W. M.; Lackinger, M. *Chem. Commun.* **2009,** 4456–4458. doi:10.1039/b906836h
26. Gao, H.-Y.; Wagner, H.; Zhong, D.; Franke, J.-H.; Studer, A.; Fuchs, H. *Angew. Chem., Int. Ed.* **2013,** *52,* 4024–4028. doi:10.1002/anie.201208597
27. Russell, J. C.; Blunt, M. O.; Garfitt, J. M.; Scurr, D. J.; Alexander, M.; Champness, N. R.; Beton, P. H. *J. Am. Chem. Soc.* **2011,** *133,* 4220–4223. doi:10.1021/ja110837s
28. Eder, G.; Smith, E. F.; Cebula, I.; Heckl, W. M.; Beton, P. H.; Lackinger, M. *ACS Nano* **2013,** *7,* 3014–3021. doi:10.1021/nn400337v
29. Blunt, M.; Lin, X.; Gimenez-Lopez, M. D. C.; Schröder, M.; Champness, N. R.; Beton, P. H. *Chem. Commun.* **2008,** 2304–2306. doi:10.1039/b801267a
30. Cotier, B. N.; Upward, M. D.; Jones, F. H.; Moriarty, P.; Beton, P. H. *Appl. Phys. Lett.* **2001,** *78,* 126. doi:10.1063/1.1336553
31. Bethune, D. S.; Meijer, G.; Tang, W. C.; Rosen, H. J. *Chem. Phys. Lett.* **1990,** *174,* 219–222. doi:10.1016/0009-2614(90)85335-A
32. Akers, K. L.; Douketis, C.; Haslett, T. L.; Moskovits, M. *J. Phys. Chem.* **1994,** *98,* 10824–10831. doi:10.1021/j100093a025
33. Reber, C.; Ye, L.; McKiernan, J.; Zink, J. I.; Williams, R. S.; Tong, W. M.; Ohlberg, D. A. A.; Whetten, R. L.; Diederich, F. *J. Phys. Chem.* **1991,** 2127–2129. doi:10.1021/j100159a011
34. Guss, W.; Feldmann, J.; Göbel, E. O.; Taliani, C.; Mohn, H.; Müller, W.; Häussler, P.; ter Meer, H.-U. *Phys. Rev. Lett.* **1994,** *72,* 2644–2647. doi:10.1103/PhysRevLett.72.2644
35. Fonda, H. N.; Gilbert, J. V.; Cornier, R. A.; Sprague, J. R.; Kamioka, K.; Connolly, J. S. *J. Phys. Chem.* **1993,** *97,* 7024–7033. doi:10.1021/j100129a017
36. Dorough, G. D.; Miller, J. R.; Huennekens, F. N. *J. Am. Chem. Soc.* **1951,** *73,* 4315–4320. doi:10.1021/ja01153a085
37. Hsiao, J.; Krueger, B. P.; Wagner, R. W.; Johnson, T. E.; Delaney, J. K.; Mauzerall, D. C.; Fleming, G. R.; Lindsey, J. S.; Bocian, D. F.; Donohoe, R. J. *J. Am. Chem. Soc.* **1996,** *118,* 11181–11193. doi:10.1021/ja961612f
38. Pawlicki, M.; Morisue, M.; Davis, N. K. S.; McLean, D. G.; Haley, J. E.; Beuerman, E.; Drobizhev, M.; Rebane, A.; Thompson, A. L.; Pascu, S. I.; Accorsi, G.; Armaroli, N.; Anderson, H. L. *Chem. Sci.* **2012,** *3,* 1541–1547. doi:10.1039/c2sc00023g

Beilstein Journal of Nanotechnology

Preparation of poly(*N*-vinylpyrrolidone)-stabilized ZnO colloid nanoparticles

Tatyana Gutul[1], Emil Rusu[*1], Nadejda Condur[1], Veaceslav Ursaki[1], Evgenii Goncearenco[2] and Paulina Vlazan[3]

Full Research Paper

Open Access

Address:
[1]Institute of Electronic Engineering and Nanotechnologies D. Ghitu, Academy of Sciences of Moldova, 3 Academiei str., Chisinau, MD-2028, Moldova, [2]State University of Republic of Moldova, 60 Alexe Mateevici str., Chisinau MD-2009, Moldova and [3]National Institute of Electrochemistry and Condensed Matter, 144 Dr. A. Paunescu Podeanu str., Timisoara 300569, Romania

Email:
Emil Rusu[*] - rusue@nano.asm.md

* Corresponding author

Keywords:
colloidal solutions; nanocomposite; poly(*N*-vinylpyrrolidone); sol–gel; zinc oxide

Beilstein J. Nanotechnol. **2014,** *5,* 402–406.
doi:10.3762/bjnano.5.47

Received: 30 December 2013
Accepted: 12 March 2014
Published: 03 April 2014

This article is part of the Thematic Series "Physics, chemistry and biology of functional nanostructures II".

Guest Editor: A. S. Sidorenko

Abstract

We propose a method for the synthesis of a colloidal ZnO solution with poly(*N*-vinylpyrrolidone) (PVP) as stabilizer. Stable colloidal solutions with good luminescence properties are obtained by using PVP as stabilizer in the synthesis of ZnO nanoparticles by a sol–gel method assisted by ultrasound. Nanoparticles with sizes of 30–40 nm in a PVP matrix are produced as a solid product. The colloidal ZnO/PVP/methanol solution, apart from the most intense PL band at 356 nm coming from the PVP, exhibits a strong PL band at 376 nm (3.30 eV) which corresponds to the emission of the free exciton recombination in ZnO nanoparticles.

Introduction

Zinc oxide is widely used in various applications such as gas sensors, solar cells, antireflection coatings, varistors, surface acoustic wave devices, light emitting diodes and random lasers [1-4]. Among different processing methods, the sol–gel technique has various advantages such as cost-efficient processing, low-temperature sintering capability, the possibility of coating large and complex surfaces, and the capability to produce high quality coatings with a wide range of easily controlled thicknesses [5]. Preparation of ZnO nanoparticles by a colloidal method in the form of hydrosols was widely investigated in recent years in connection with a possible employment in biology [6]. ZnO nanoparticles have been synthesized in conjunction with different polymers such as polyethylene glycol (PEG) and poly(*N*-vinylpyrrolidone) (PVP). Nanoparticles of various morphologies were formed, and the photoluminescence intensity was increased because of the passivation of surface defects in the nanoparticles [7].

Nanohybrid films with resistivity of 10^8 Ω·cm were obtained by using PVP with molar mass of 400,000 at various Zn^{2+}/PVP ratios [8]. Colloidal solutions of ZnO are obtained by different methods. For instance, a nano-colloid has been synthesized

using a top-down wet chemistry method with bulk ZnO powder with grain size of 1–2 mm as starting material [9]. Stearic or oleic acids have been used as capping agents in the stabilization technique to prevent agglomeration of the ZnO nanoparticles [9-11]. Colloidal ZnO solutions with nanoparticle sizes of 2–6 nm were also obtained with a method employing lasers [12]. The mechanism of nano-colloidal solution formation was previously investigated [13], while the production of colloidal solutions stabilized by polyvinylpyrrolidone was not previously described. In this context, the investigation of mechanisms for the formation of colloidal solutions and solid phases of ZnO nanoparticles by a colloidal method in the presence of poly(*N*-vinylpyrrolidone) (PVP) is of great interest. We propose in our work a method for the synthesis of colloidal ZnO solutions with PVP as stabilizer.

Experimental

Synthesis of colloidal ZnO solutions and nanocomposites

The following chemical were used in the synthesis processes: zinc acetate $Zn(Ac)_2{\cdot}H_2O$ (Aldrich, 99%); KOH (Aldrich, 99.0%); poly(*N*-vinylpyrrolidone) PVP10, M_S = 10,000 (Aldrich, 99%); methanol 99.9%; ethanol anhydrous (Sigma Aldrich); hexane (Aldrich, 99%); acetone (Sigma 99%). We have modified the typical synthesis of ZnO colloidal solutions [13]. Zinc acetate dihydrate ($Zn(OAc)_2{\cdot}2H_2O$) powder (0.439 g) was added to a KOH solution (0.02–0.04 M). Poly(*N*-vinylpyrrolidone) PVP was dissolved in methanol under stirring at room temperature and the ZnO solution was added to set various ratios of Zn:PVP (from 1:0.1 to 1:0.5 wt %). The prepared mixture was put into an Erlenmeyer flask and heated to 60 °C for 4 h under continuous stirring in an ultrasonic bath. In order to remove impurities from the white powder, it was precipitated and washed with absolute ethanol several times after cooling to room temperature. The excess surfactant, unreacted precursor, and high-boiling point solvents were removed by means of a solvent containing hexane, anhydrous ethanol, and acetone in the proportion of 2:1:5 [14]. Centrifugation with a solvent containing acetone and hexane was carried out for site-selective precipitation. Finally, the powder was dried at 150 °C overnight and characterized with regards to its structural, morphological and optical properties (sample 1). An amount of 100 mg of the prepared powder in the form of ZnO/PVP nanoparticles was resuspended in 30 mL of methanol and put in an Erlenmeyer flask and held at room temperature for 2 h under continuous magnetic stirring. The produced colloidal ZnO/PVP solution (sample 2) is stable for 3 months.

Characterization methods

Powder X-ray diffraction (XRD) and infrared absorption spectroscopy (FTIR) were used to characterize the size, shape, structure, and composition of the colloidal solution and nanocrystals. The XRD analysis of products was determined by powder X-ray diffraction (XRD) PW 3040/60 X'Pert PRO diffractometer system, using Cu Ka radiation with (λ = 1.5418 Å) in the range of 2θ = 10–80° at room temperature. FTIR absorption spectra were measured with a PerkinElmer Spectrum100 FTIR spectrometer in the spectral range of 650–4000 cm^{-1} with a resolution of 2 cm^{-1} at a close-to-normal light incidence on the substrate at room temperature. Photoluminescence (PL) spectra of the ZnO nanoparticles in methanol were measured at room temperature with an MDR-23 spectrometer. The samples were excited by a nitrogen laser with wavelength of 337.1 nm.

Results and Discussion

The image of a cell with ZnO colloidal solution is shown in Figure 1. A bright luminescence is observed under the excitation of the solution with a HBO-103W/2 mercury lamp.

Figure 1: Photograph of colloidal ZnO /PVP nanoparticles (a), and luminescence under UV excitation with a HBO-103W/2 lamp (b).

The PL spectrum of sample 1 compared to the spectrum of bulk ZnO crystals is presented in Figure 2. Apart from the emission band at 356 nm, which comes from the PPV shell, the spectrum of sample 1 exhibits ZnO near-bandgap luminescence with a maximum at 376 nm, which coincides with that observed in high-quality ZnO bulk crystals and is related to the recombination of free excitons. The observation of efficient free exciton emission at room temperature, as well as the weak visible emission observed at 550 nm is indicative of high-quality of ZnO nanoparticles in this sample, i.e., the PPV shell effectively passivates the surface defects of ZnO nanoparticles.

The photoluminescence spectra of the components of a colloidal ZnO/PVP/methanol solution are shown in Figure 3. The methanol exhibits a broad luminescence ranging from 350 to

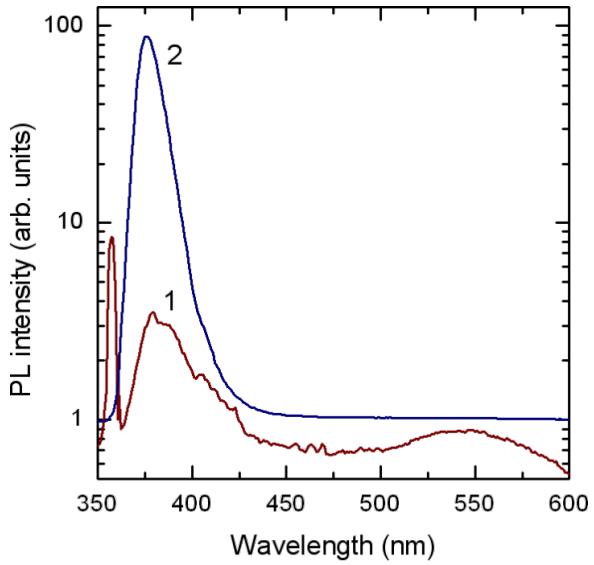

Figure 2: PL spectrum of PVP-capped ZnO nanoparticles (sample 1, curve 1) and PL spectra of ZnO bulk crystal (curve 2).

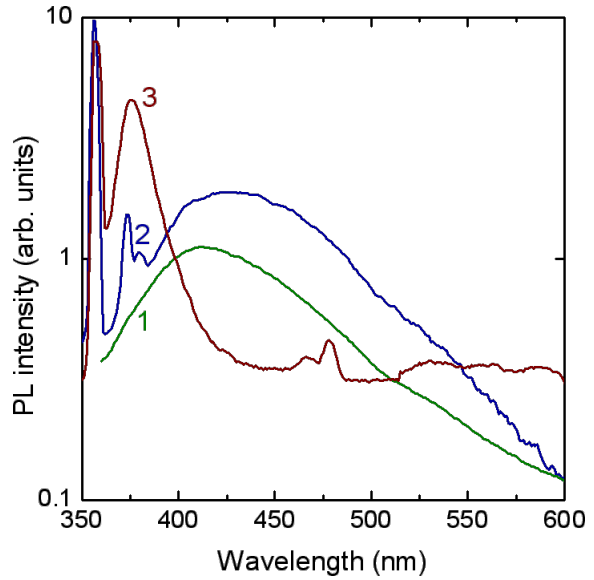

Figure 3: PL spectrum of methanol (1), PVP (2) and colloidal ZnO/PVP/methanol (3) at 300 K (Sample 1).

600 nm. Two luminescence bands at 356 nm and 373 nm dominate the PL spectrum of PVP apart from a broad PL band with the maximum around 430 nm. A luminescence band around 370 nm has been previously found from PVP molecules [15], while a strong PL band was observed at around 350 nm in PVP-protected gold atomic clusters [16], and a broad luminescence band centered at 440 nm was found in PVP-capped ZnS nanoparticles [17]. The colloidal ZnO/PVP/methanol solution, apart from the most intense PL band at 356 nm coming from the PVP, exhibits a strong PL band at 376 nm (3.30 eV), which corresponds to the emission from the free exciton recombination in ZnO nanoparticles. The position of this emission band coincides with the one related to free exiton recombination in ZnO microwires [18]. Note, that if we will add the value of the free exciton binding energy of 60 meV to the position of this PL band (3.30 eV) we will obtain the value of the bulk ZnO bandgap at room temperature (3.36 eV). On the one hand, this is an indication for the high quality of the produced ZnO nanoparticles, since free exciton luminescence is observed only in highly pure material with a high structural quality. On the other hand, this hints at the absence of quantum confinement in the produced ZnO nanoparticles. The absence of quantum confinement effects is due to the relatively large size of the ZnO nanoparticles as compared to the exciton Bohr radius of around 2 nm in ZnO [19], as discussed below on the basis of XRD analysis. Note also that the emission in the visible spectral range, which is usually associated with structural defects, is practically absent from ZnO/PVP nanoparticles.

The XRD pattern of the powder material is shown in Figure 4. The diffraction peaks for 2θ = 31.71°, 34.40°, 36.42°, 47.58°, 56.84°, 63.12°, 66.52°, 68.12°, 69.18°, 72.58°, and 77.08° are observed, which correspond to the hexagonal phase of ZnO nanoparticles (space group $P6_3mc$, a = 3.249 Å, c = 5.206 Å).

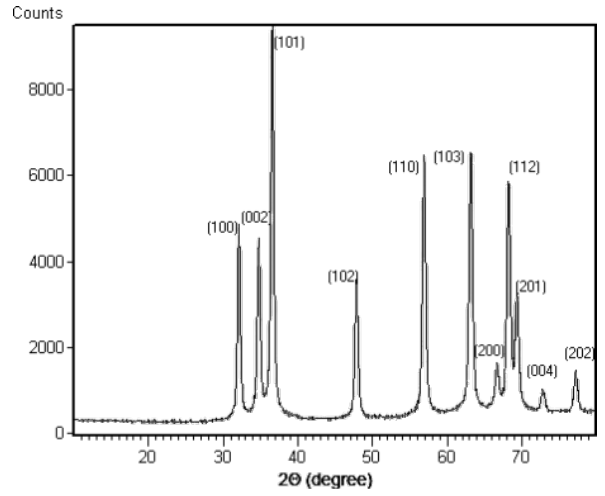

Figure 4: Typical powder diffraction pattern of ZnO/PVP NPs.

The size d of ZnO particles was estimated from the width of the most intense peak according to the Scherrer formula $d = k \cdot \lambda / (\beta \cdot \cos\theta)$, where k is a constant, λ is the X-ray radiation wavelength (1.5418 Å), β is the full width at half maximum (FWHM), and θ is the diffraction angle. The particle size calculated from X-ray diffraction line width is around 30–40 nm.

FTIR spectrum of ZnO nanoparticles (Figure 5) shows significant absorption peaks at 3377.6 cm^{-1}, 1448.2 cm^{-1}, and 882.2 cm^{-1}. The band near 1448.2 cm^{-1} is assigned to H–O–H bending vibration mode due to the adsorption of moisture. The absorption band at 452 cm^{-1} assigned to Zn–O stretching vibrations, which was described in [20], was not observed in our experiments because of the limited capacities of the instrument.

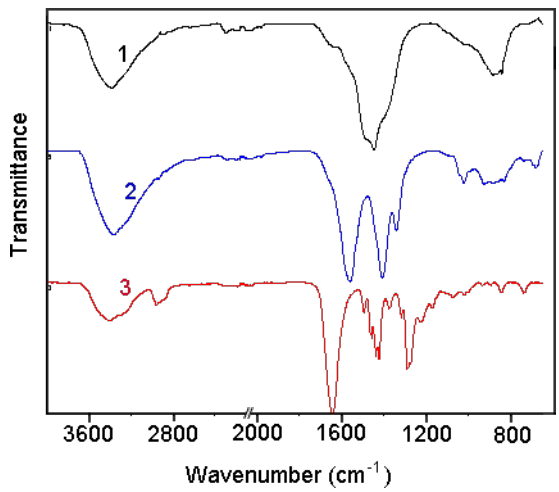

Figure 5: FTIR spectra of pure ZnO nanoparticles (1), ZnO/PVP composite (2), and pure PVP (3).

The presence of various chemical functional groups in PVP (M_S = 10,000) is indicated by FTIR spectra as shown in Figure 5 (curve 3). The broad absorption band at 3399.6 cm^{-1} is due to O–H stretching vibrations of adsorbed water at the surface of particles. A peak at 1645 cm^{-1} is assigned to the stretching vibration of the C=O. The absorption peak at 1373.6 cm^{-1} is due to the C–H bond in PVP [21]. Other important peaks at 1287.6 cm^{-1} and the doublet at 1437.8 cm^{-1}, 1422.4 cm^{-1} are assigned to the C–N stretching vibrations and the attachment of CH_2 groups in the pyrrole ring of PVP [22,23]. A comparison of the spectra of the prepared ZnO/PVP nanoparticles (Figure 5, curve 2) and pure PVP reveals similar absorption bands in regions of 3600–2400 cm^{-1} and 1650–650 cm^{-1}. The peak observed in pure PVP at 1645 cm^{-1}, which is due to C=O bonds, is red-shifted to 1559.6 cm^{-1} as a result of the interaction of the carbonyl oxygen with the zinc ion [23]. As concerns the absorption in the region of 1500–1200 cm^{-1}, an overlap of absorption bands of PVP with bands of the hydrated zinc oxide, as well as interaction between them occurs. As a result, we observe a wide band with the maximum at 1406.5 cm^{-1} and a peak at 1341.3 cm^{-1}. The first of these bands is related to the peak observed in ZnO nanoparticles at 1448.2 cm^{-1}, which stems from the hydrated zinc oxide, but is shifted to 1406.5 cm^{-1}, while the peak at 1341.3 cm^{1} is apparently attributed to the occurrence of covalent bonds of PVP with ZnO nanoparticles. Thus, our FTIR studies show that chemical reaction occur between the zinc oxide nanoparticles and polymeric stabilizer, by coordination of the zinc oxide particles with the nitrogen and oxygen atoms in PVP, as evidenced in [24].

Conclusion

The usage of poly(*N*-vinylpyrrolidone) as a stabilizer in the synthesis of ZnO nanoparticles by an ultrasound-assisted sol–gel method allowed for the obtainment of stable colloidal solutions with good luminescence properties. The solid product consist of nanocomposite-encapsulated nanoparticles with sizes of 30–40 nm in a PVP matrix. The colloidal ZnO/PVP/methanol solution, apart from the most intense PL band at 356 nm coming from the PVP, exhibits a strong PL band at 376 nm (3.30 eV) which corresponds to the emission from the free exciton recombination in ZnO nanoparticles.

Acknowledgements

This work was supported financially by the Supreme Council for Research and Technological Development of the Academy of Sciences of Moldova under the Project 10.820.05.20RoF.

References

1. Zhang, Q.; Park, K.; Cao, G. *Material Matters* **2010,** *5,* 32–39.
2. Hsu, C.-L.; Chen, K.-C.; Tsai, T.-Y.; Hsueh, T.-J. *Sens. Actuators, B* **2013,** *182,* 190–196. doi:10.1016/j.snb.2013.03.054
3. Singh, P.; Sinha, O. P.; Srivastava, R.; Srivastava, A. K.; Thomas, S. P.; Sood, K. N.; Kamalasanan, M. N. *J. Nanopart. Res.* **2013,** *15,* 1758–1763. doi:10.1007/s11051-013-1758-3
4. Ursaki, V. V.; Zalamai, V. V.; Burlacu, A.; Fallert, J.; Klingshirn, C.; Kalt, H.; Emelcenko, G. A.; Redkin, A. N.; Gruzintsev, A. N.; Rusu, E. V.; Tiginyanu, I. M. *J. Phys. D: Appl. Phys.* **2009,** *42,* 095106. doi:10.1088/0022-3727/42/9/095106
5. Lee, J.; Easteal, A. J.; Pal, U.; Bhattachayya, D. *Curr. Appl. Phys.* **2009,** *9,* 792–796. doi:10.1016/j.cap.2008.07.018
6. Hsu, S.-H.; Lin, Y. Y.; Huang, S.; Lem, K. W.; Nguyen, D. H.; Lee, D. S. *Nanotechnology* **2013,** *24,* 475102. doi:10.1088/0957-4484/24/47/475102
7. Rajamanickam, N.; Rajashabala, S.; Ramachandran, K. *J. Lumin.* **2014,** *146,* 226–233. doi:10.1016/j.jlumin.2013.09.074
8. Guo, L.; Yang, S.; Yang, C.; Yu, P.; Wang, J.; Ge, W.; Wong, G. K. L. *Appl. Phys. Lett.* **2000,** *76,* 2901–2903. doi:10.1063/1.126511
9. Sharma, S.; Tran, A.; Nalamasu, O.; Duttas, P. S. *J. Electron. Mater.* **2006,** *35,* 1237–1240. doi:10.1007/s11664-006-0247-1
10. Xiong, H.-M. *J. Mater. Chem.* **2010,** *20,* 4251–4262. doi:10.1039/b918413a
11. Patra, M.; Manzoora, K.; Manoth, M.; Choudhry, V. S. R.; Vadera, S.; Kumar, N. *J. Optoelectron. Adv. Mater.* **2008,** *10,* 2588–2591.
12. Ismail, R. A.; Ali, A. K.; Ismail, M. M.; Hassoon, K. I. *Appl. Nanosci.* **2011,** *1,* 45–49. doi:10.1007/s13204-011-0006-3
13. Fu, Y.-S.; Du, X.-W.; Kulinich, S. A.; Qiu, J.-S.; Qin, W.-J.; Li, R.; Sun, J.; Liu, J. *J. Am. Chem. Soc.* **2007,** *129,* 16029–16033. doi:10.1021/ja075604i

14. Todosiciuc, A.; Nicorici, A.; Gutsul, T.; Gramm, F.; Braginsky, L.; Shklover, V. *Romanian J. Inf. Sci. Technol.* **2010,** *13,* 84–97.
15. Tachikawa, S.; Noguchi, A.; Tsuge, T.; Hara, M.; Odawara, O.; Wada, H. *Materials* **2011,** *4,* 1132–1143. doi:10.3390/ma4061132
16. González, B. S.; Rodríguez, M. J.; Blanco, C.; Rivas, J.; López-Quintela, M. A.; Gaspar-Martinho, J. M. *Nano Lett.* **2010,** *10,* 4217–4221. doi:10.1021/nl1026716
17. Mohan, R.; Sankarrajan, S.; Santham, P. *Int. J. Recent Sci. Res.* **2013,** *4,* 420–424.
18. Chai, G. Y.; Lupan, O.; Rusu, E. V.; Stratan, G. I.; Ursaki, V. V.; Şontea, V.; Khallaf, H.; Chow, L. *Sens. Actuators, A* **2012,** *176,* 64–71. doi:10.1016/j.sna.2012.01.012
19. Fonoberov, V. A.; Alim, K. A.; Balandin, A. A.; Xiu, F.; Liu, J. *Phys. Rev. B* **2006,** *73,* 165317. doi:10.1103/PhysRevB.73.165317
20. Hong, R. Y.; Li, J. H.; Chen, L. L.; Liu, D. Q.; Li, H. Z.; Zheng, Y.; Ding, J. *Powder Technol.* **2009,** *189,* 426–432. doi:10.1016/j.powtec.2008.07.004
21. Ghosh, G.; Naskar, M. K.; Patra, A.; Chatterjee, M. *Opt. Mater.* **2006,** *28,* 1047–1053. doi:10.1016/j.optmat.2005.06.003
22. Han, T. Y.-J.; Worsley, M. A.; Baumann, T. F.; Satcher, J. H., Jr. *J. Mater. Chem.* **2011,** *21,* 330–333. doi:10.1039/c0jm03204b
23. Sudha, M.; Rajarajan, M. *IOSR J. Appl. Chem.* **2013,** *3,* 45–53. doi:10.9790/5736-0334553
24. Ilegbusi, O. J.; Trakhtenberg, L. *J. Mater. Eng. Perform.* **2013,** *22,* 911–915. doi:10.1007/s11665-012-0336-7

License and Terms

Beilstein Journal of Nanotechnology

Nanoscale particles in technological processes of beneficiation

Sergey I. Popel*[1,2], Vitaly V. Adushkin[1,2] and Anatoly P. Golub'[1]

Full Research Paper

Open Access

Address:
[1]Institute for Dynamics of Geospheres of the Russian Academy of Sciences, Leninsky pr. 38, bldg. 1, 119334 Moscow, Russia and [2]Moscow Institute of Physics & Technology, 141700 Dolgoprudny, Moscow region, Russia

Email:
Sergey I. Popel* - s_i_popel@mtu-net.ru

* Corresponding author

Keywords:
cavitation disintegration; gold ore; nano- and microparticles; polymineral and monomineral fractions

Beilstein J. Nanotechnol. **2014,** *5,* 458–465.
doi:10.3762/bjnano.5.53

Received: 05 January 2014
Accepted: 20 March 2014
Published: 11 April 2014

This article is part of the Thematic Series "Physics, chemistry and biology of functional nanostructures II".

Guest Editor: A. S. Sidorenko

Abstract

Background: Cavitation is a rather common and important effect in the processes of destruction of nano- and microscale particles in natural and technological processes. A possible cavitation disintegration of polymineral nano- and microparticles, which are placed into a liquid, as a result of the interaction of the particles with collapsed cavitation bubbles is considered. The emphasis is put on the cavitation processes on the interface between liquid and fine solid particles, which is suitable for the description of the real situations.

Results: The results are illustrated for the minerals that are most abundant in gold ore. The bubbles are generated by shock loading of the liquid heated to the boiling temperature. Possibilities of cavitation separation of nano- and microscale monomineral fractions from polymineral nano- and microparticles and of the use of cavitation for beneficiation are demonstrated.

Conclusion: The cavitation disintegration mechanism is important because the availability of high-grade deposits in the process of mining and production of noble metals is decreasing. This demands for an enhancement of the efficiency in developing low-grade deposits and in reprocessing ore dumps and tailings, which contain a certain amount of noble metals in the form of finely disseminated fractions. The cavitation processes occuring on the interface between liquid and fine solid particles are occasionally more effective than the bulk cavitation processes that were considered earlier.

Introduction

At present, significant attention is being paid to the study of properties and processes of formation of mineral nano- and microsize particles [1,2]. The investigation of nanosize structures in nature can provide new information about the interstellar substance [3], deflation of the rock mass, etc. Nanosize components are the main structural elements in solid-state chemistry [4]. However, in many situations, physical processes such as cavitation are of paramount importance in the formation of nano- and microsize structures. For example, more than thirty years ago, Galimov [5] predicted the possibility of diamond synthesis through a cavitation process. In 2003, this possibility was confirmed in experiments [6]. The particles formed in the cavitation process were an aggregation of nanosize crystallites. The diamond crystals were 10–30 nm in size. The idea of the cavitation mechanism of diamond formation is the following [5]: A narrow canal cavity of varying cross section is formed as a result of the fast motion of fluid going up from the mantle to the surface of the Earth. When the canal cavity dilates or opens up, the pressure decreases, resulting in phase separation of the fluid, which stratifies into an essentially liquid phase and a gas phase existing in the form of gas bubbles. When the fluid goes into the narrowing of the canal cavity, the pressure is reestablished and the bubbles collapse. The pressure inside the collapsing bubbles, which are filled with carbon-containing gas is sufficient for the synthesis of diamonds.

The mechanism of cavitation melting was discussed in [7] while explaining the origin of microscopic globules found in cavities and fractures of vein quartz from mesothermal gold deposits. Adushkin et al. [8-10] developed an internally consistent theory that describes the formation of mineral nano- and microspherules through a cavitation mechanism that takes into account typical dimensions of cavitation bubbles and their evolution along with the dynamics of particle heating in cavitation bubbles. On the basis of this theory, the maximum dimensions of cavitation bubbles were estimated, as well as the size of globules generated due to the melting of particles of different mineral composition under cavitation effects in hydrothermal fluids. It was shown that the cavitation mechanism may bring about the formation of mineral and metallic nanospherules in hydrothermal fluids. The formation of nano- and microspherules with regard to the depth of host rock was also investigated.

In [11] the possible cavitation disintegration of polymineral microparticles placed into a liquid as a result of the interaction of particles with collapsing cavitation bubbles was shown for the minerals most abundant in gold ore. This disintegration mechanism is important because the availability of high-grade deposits in the process of mining and production of noble metals is decreasing. This demands for an enhancement of the efficiency in developing low-grade deposits and in reprocessing ore dumps and tailings, which contain a certain amount of noble metals in the form of finely disseminated fractions. The recovery of disseminated metals from fractions no more than 100 μm in size is a complicated problem, which can be solved with the use of the cavitation mechanism of disintegration of microscale particles.

The proposed method of cavitation disintegration is the following: Ore microparticles that contain finely disseminated fractions of noble metals are placed into a cavitation chamber (Figure 1) filled with a liquid (water) heated up to the boiling temperature. It is known that, in the process of heterogeneous boiling, the bubbles in a liquid nucleate and grow mostly on foreign inclusions: dust particles, roughnesses of the vessel walls, etc. Therefore, ore microparticles will serve as natural centers of cavitation bubble nucleation. If the pressure in the cavitation chamber rises abruptly, for instance, owing to shock loading by a plunger (press), the cavitation bubbles will collapse. Compression and collapse of a cavitation bubble is commonly accompanied by an abrupt local rise in temperature and pressure that can induce melting of an ore microparticle attached to the bubble and lead to its subsequent separation into monomineral fractions. The monomineral fractions obtained by cavitation melting may afterward be divided using standard techniques, e.g., gravity or chemical separation.

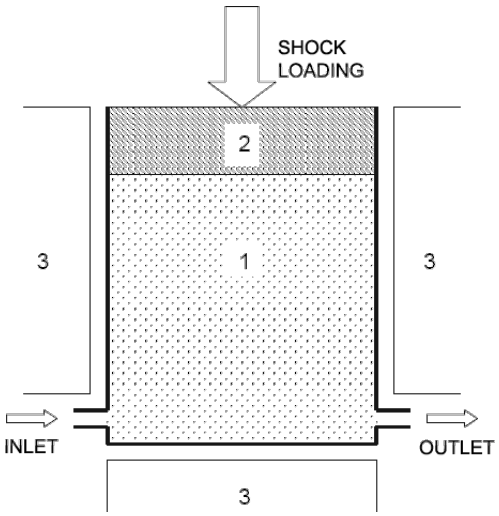

Figure 1: A conceptual design of a device for cavitation separation of gold-bearing particles. (1) Cavitation chamber with liquid (water) containing ore microparticles; (2) plunger providing shock loading (an abrupt rise in pressure in the chamber to 10–15 bar); (3) thermostat maintaining a temperature T_0 = 373 K in the cavitation chamber.

In [8-11] a one-dimensional spherically symmetric model, in which the nano- or microscale particle is placed in the center of the cavitation bubble is given. In general, this model does not describe the real situations when the bubbles are formed on foreign inclusions: dust particles, roughnesses of the vessel walls, etc. Here, we provide insights into the separation of polymineral microparticles into monomineral fractions in the process of interaction of the particles with collapsing cavitation bubbles. In contrast to [8-11], we propose the consideration of the cavitation processes on the interface between liquid and fine solid particles (or roughness of vessel wall), which is more suitable for the description of the real situations.

Model

We numerically investigate the cavitation melting of mineral microparticles and the possibility of their destruction while using physical parameters of the minerals from gold ore. The mineral and chemical compositions of ores at large gold deposits, such as Cripple Creek (United States), Bagio (Philippines), and Pueblo Viejo (Dominican Republic), and at gold deposits in Russia are fairly complex [12], although the number of major minerals is relatively low. Native gold often occurs together with quartz and is always associated with iron, copper, antimony, lead, and zinc sulfides. Quartz, barite, and carbonates are the major gangue minerals. In addition to native gold, the primary ores contain pyrite, arsenopyrite, sphalerite, and galena. Several of the most abundant and important minerals of gold ore were chosen for the numerical analysis of the cavitation melting effect. Their physical parameters (density ρ, thermal diffusivity χ, and melting temperature T_m) necessary for calculations are given in the Table 1.

Table 1: Physical parameters of the minerals from gold ore.

mineral	formula	ρ, g/cm^3	χ, cm^2/s	T_m, K
gold	Au	19.3	1.3	1336
silver	Ag	10.5	1.73	1235
quartz	SiO_2	2.14	0.042	1883
pyrite	FeS_2	4.9	0.15	1461
galena	PbS	7.3	0.23	1387
calcite	$Ca(CO_3)$	2.71	0.017	1885
stibnite	Sb_2S_3	4.6	0.145	819

The dynamics of a cavitation bubble in response to an abrupt rise of pressure P_0 in the cavitation chamber due to shock loading was calculated with a numerical method by using a model, which has the main features described below. The cavitation processes on the interface between liquid and fine solid particles (or roughnesses of the vessel walls) result in an appearance of cavitation bubbles of mushroom-like form. The size of the bubbles, the time of their presence on the solid surface, the rate of detachment from the surface, etc. depend on local variations of wettability, roughness of the surface, its bending, and other random actions, which cannot be taken into account. Under the steady-state conditions the bubble is stable, the gas pressure inside the bubble is equalized by the external pressure (in the liquid surrounding the bubble). If the pressure in the liquid becomes larger than the gas pressure inside the bubble then the equilibrium is violated, the liquid presses forward to the solid surface, and leads to a collapse of the bubble. Pressure and temperature of the gas inside the bubble increase as the volume reduces. If the pressure in the liquid increases slowly and becomes higher than the pressure of saturated vapor (at the temperature equal to the temperature of liquid) then the bubble disappears. In case of a sufficiently rapid increase of the pressure, the vapor in the bubble does not have enough time to be condensed. The pressure inside the bubble increases so that the liquid head is restrained and the liquid itself retreats back. Rapid compression of the bubble results in very high magnitudes of density, pressure, and temperature of vapor, which are independent from the initial volume and geometric shape of the bubble. The motion of vapor inside the bubble remains subsonic. Gas dynamic processes dominate over those of thermal conductivity. Since the vapor temperature is significantly higher than that of the liquid and the phase equilibrium is violated, it is necessary to take into account the heat exchange between vapor and liquid due to phase transformation. Furthermore, imperfection of dense gas in the bubble may be an important factor in determining the dynamics of the bubble compression.

The dynamics of cavitation bubble was calculated under the following assumptions to simplify the problem: (1) The liquid, water, is incompressible with a density of ρ_l = 1 g/cm^3 and the boiling temperature T_0 = 373 K. (2) The cavitation bubbles do not interact with each other. The bubble shape is hemispherical with the center placed on the interface between liquid and fine solid particle. As the volume of the bubble changes, its geometric shape is maintained. (3) The bubble dynamics, the vapor motion, as well as liquid heating are described within the corresponding spherically symmetric model. The state of the vapor in the bubble is described by the van der Waals equation with the critical parameters T_{cr} = 647 K and P_{cr} = 225 bar. When calculating the gas dynamic processes inside the bubble, the heat exchange between the vapor and fine solid particles is neglected in comparison with the much more intensive (accompanied by a phase transition) heat exchange between the vapor and liquid. (4) The polymineral nature of the fine solid particle is taken into account in the following manner: The real geometrical shape of the particle is not considered, only its characteristic linear size (the diameter of the particle of nearly spherical

shape or the thickness of the particle of some flat shape) and the characteristic linear dimension of its noble-metal core are introduced. Processes of heating and melting of the fine solid particle in its interaction with the bubbles are described within the framework of one-dimensional (plane) problem of thermal conductivity for the corresponding three-layer incompressible body, in which the noble metal is placed between two layers of mineral.

In this case, the dynamics of the bubble compression is described by the Rayleigh–Plesset equation [13]:

$$r_{\rm b}\frac{d^2r_{\rm b}}{dt^2}+\frac{3}{2}u_{\rm b}^2+\frac{1}{\rho_{\rm l}}\left(p_\infty-q_{\rm pw}+\frac{2\sigma}{r_{\rm b}}+\frac{4\eta u_b}{r_{\rm b}}\right)=0\,, \quad (1)$$

where t is time coordinate, $r_{\rm b}$ is the radius of the bubble, $u_{\rm b}$ is the speed of the bubble edge, p_∞ is the pressure in the liquid far from the bubble, $q_{\rm pw}$ is the momentum flux density on the edge of the bubble from the side of the vapor, and η and σ are the viscosity and surface tension of the liquid, respectively. The set of equations of gas-dynamics, which is solved together with the van der Waals equation of state describes the vapor motion as well as the pressure, the temperature, and the internal energy inside the bubble. The change in the liquid temperature is determined by the set of thermal conductivity equations that, in particular, takes into account the heat exchange with the vapor. The liquid velocity is determined by the continuity equation for the incompressible liquid.

The set of gas-dynamics and thermal conductivity equations describing the vapor dynamics inside the bubble is:

$$\begin{gathered}
\rho r^2\frac{\partial r}{\partial m}=1\,,\ \frac{\partial u}{\partial t}=-r^2\frac{\partial p}{\partial m}\,,\\
\frac{\partial e}{\partial t}+p\frac{\partial(r^2u)}{\partial m}+\frac{\partial F}{\partial m}=0\,,\ F=-r^2\lambda\frac{\partial T}{\partial r}\,,\\
u=0\ \text{ and }\ \frac{\partial T}{\partial r}=0\quad\text{if}\quad m=0\,,\\
p=p(\rho,T)\,,\ e=e(\rho,T)\,,\ \lambda=\lambda(\rho,T)\,,\\
\rho=\rho_0,\ T=T_0,\ p=p_0,\ u=0\,,\\
r_b=r_{b0},\ \text{and}\ m_w=m_{w0}\quad\text{if}\quad t=0\,,\\
0\le r\le r_b(t)\,,\ 0\le m\le m_w(t)\quad\text{if}\quad t\ge 0\,,
\end{gathered} \quad (2)$$

where r is the radius (Eulerian coordinate), m is Lagrangian (mass) coordinate, $m_{\rm w}(t)$ is the vapor mass inside the bubble per unit solid angle, u is the speed, ρ is the density, p is the pressure, e is the specific internal energy, T is the temperature, F is the energy flux transferred by the thermal conduction mechanism, λ is the thermal conductivity coefficient. The interface between the gas and the fine particle corresponds to the values of $m = 0$ and $r = 0$ while that between the vapor and the liquid fits the equations $m = m_{\rm w}$ and $r = r_{\rm b}$. The subscript "0" denotes the values at $t = 0$.

The equation of state and the thermal equation for the vapor, which is considered to be a van der Waals gas, take the following form under the condition of the local thermal dynamics equilibrium:

$$\begin{gathered}
\left(p+a\rho^2\right)\left(1-b\rho\right)=\rho RT\,,\\
e=c_{\rm v}T-a\rho=\frac{3}{2}RT+e_{\rm int}-a\rho\,,
\end{gathered} \quad (3)$$

where a and b are constants characterizing the van der Waals gas, $c_{\rm v}$ is the specific heat capacity for a constant volume, $e_{\rm int}(T)$ is the energy of the unit of gas mass related to the internal degrees of freedom of molecules, $R = k/M$ is the universal gas constant, M is the molecule mass, and k is Boltzmann constant.

The liquid temperature variations are determined by the set of thermal conductivity equations:

$$\begin{gathered}
c_{\rm l}\frac{\partial T_{\rm l}}{\partial t}+\frac{\partial F_{\rm l}}{\partial m_{\rm l}}=0\,,\ F_{\rm l}=-r^2\lambda_{\rm l}\frac{\partial T_{\rm l}}{\partial r}\,,\ \frac{\partial m_{\rm l}}{\partial r}=\rho_{\rm l}r^2\,,\\
T_{\rm l}(t=0,m_{\rm l})=T_0\,,F_{\rm l}=0,T_{\rm l}=T_0\quad\text{if}\quad m\to+\infty,\\
F_{\rm l}(t,m_{\rm l}=m_w+0)=F_{\rm lw}\,,\ m_{\rm l}>m_{\rm w}\,,\ r>r_{\rm b}\quad\text{if}\quad t\ge 0\,,
\end{gathered} \quad (4)$$

where $m_{\rm l}$ is the Lagrangian (mass) coordinate in the region of the presence of the liquid. $T_{\rm l}$, $c_{\rm l}(T_{\rm l})$, and $\lambda_{\rm l}(T_{\rm l})$ are the temperature, the specific heat capacity, and the coefficient of the thermal conductivity of the liquid, respectively. $F_{\rm lw}$ is the energy flux due to the thermal conductivity mechanism.

The distribution of the liquid velocity $u_{\rm l}$ over the radius r is determined by the continuity equation for incompressible liquid under the condition of spherical symmetry:

$$\begin{gathered}
u_{\rm l}=u_{\rm b}\frac{r_{\rm b}^2}{r^2},\ r>r_{\rm b}\quad\text{if}\quad t\ge 0\,,\\
u_{\rm b}=0\quad\text{if}\quad t=0\,,
\end{gathered} \quad (5)$$

where the pressure p_l inside the liquid satisfies the Euler equation:

$$\frac{\partial u_l}{\partial t} = -r^2 \frac{\partial p_l}{\partial m_l}. \quad (6)$$

If the temperature T_{lw} of the liquid at the edge with the vapor is less than the critical temperature T_{cr} of the van der Waals gas then the phase transition takes place at the bubble surface. Considering the edge of the bubble as a hydrodynamical discontinuity (a wave of phase transition) we use the relationships of continuity of the fluxes of mass, momentum, and energy on the surface of the discontinuity:

$$\frac{dm_w}{dt} = -r_b^2 \rho_w (u_w - u_b), \quad p_{lw} = q_{pw} \equiv p_w + \rho_w (u_w - u_b)^2,$$
$$F_{lw} - \frac{dm_w}{dt}(c_l T_{lw} - Q_v) = F_w - \frac{dm_w}{dt}\left(e_w + \frac{p_w}{\rho_w} + \frac{(u_w - u_b)^2}{2}\right), \quad (7)$$

where the subscript "w" characterizes the values on both sides of the wave of phase transition, $\rho_w << \rho_l$, p_{lw} is the pressure on the edge of the bubble, and $Q_v(T_{lw})$ is the specific steam heat.

If the liquid temperature at the interface with the vapor is higher than (or equal to) the critical temperature then the phase transition is absent and the relationships in Equation 7 are fulfilled at the interface ($m_l = m_w$) under the condition

$$u_w = u_b, \quad \text{if} \quad T_{lw} \geq T_{cr}. \quad (8)$$

At the surface of the bubble there are two competing processes, namely, surface evaporation and surface condensation. We assume that the vapor is in local thermodynamic equilibrium over the whole volume of the bubble with the exception of the Knudsen layer (of the thickness of several mean free paths of molecules) adjacent to the liquid surface. In this layer, the distribution of the molecules over the speeds can differ substantially from the local equilibrium Maxwell distribution. Since the radius of the bubble is much larger than the mean free path of the gas molecules, the Knudsen layer can be considered as quasistationary thin flat area, which is a part of the wave of phase transformation. Furthermore, since the convective transport dominates over thermal conductivity, the convective flows of mass, momentum and energy are conserved when passing the Knudsen layer under the condition of the violation of the phase equilibrium. The structure of the Knudsen layer and the magnitudes of the gas-dynamics variables in the vicinity of the evaporating surface of the liquid are determined by the equations of the kinetics of phase transitions where we take into account substantially subsonic nature of the flow of gas in the bubble.

Results

Here, we present some examples of numerical calculations. We assume that a bubble of the radius r_{b0} = 0.5 cm located on a microparticle is in water with the pressure of $p_0 = 10^5$ Pa and the temperature of T_0 = 373 K (boiling temperature of water). At the initial moment of time the pressure in the liquid (far from the bubble) increases abruptly to a value of $p_\infty = 15\,p_0$. Figure 2 shows the time-dependence of the following values: the ratio of the radius of the bubble to its initial value r_b/r_{b0}, the ratio betwenn the vapor mass inside the bubble and the initial vapor mass m_w/m_{w0}, the vapor temperature at the border with the solid surface of the microparticle T_c, the liquid temperature at the border of the bubble T_{lw}; the vapor pressure in the bubble p_c. It is evident that the bubble motion has oscillatory character with successive stages of compression and expansion up to a time t_m = 14 ms. These oscillations are damped because of heating of the liquid surrounding the bubble. During the first compression of the bubble, its radius and the vapor mass are lowered by factors equal to 8 and 1.4, respectively, while the vapor pressure inside the bubble increases and reaches $4200p_0$, the vapor temperature T_c increases up to the value of 3100 K, which is 1.4 times higher than the corresponding value obtained

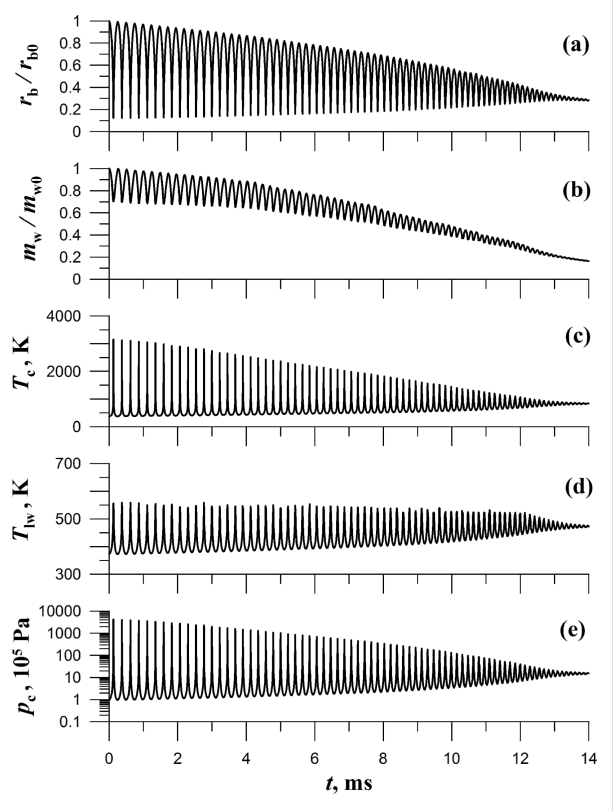

Figure 2: Time dependencies r_b/r_{b0}, m_w/m_{w0}, T_c, T_{lw}, and p_c in a pulsating cavitation bubble. Initial parameters are the bubble radius r_{b0} = 0.5 cm, the pressure inside the bubble $p_0 = 10^5$ Pa, the vapor temperature T_0 = 373 K. The pressure in the liquid far from the bubble is $p_\infty = 15p_0$.

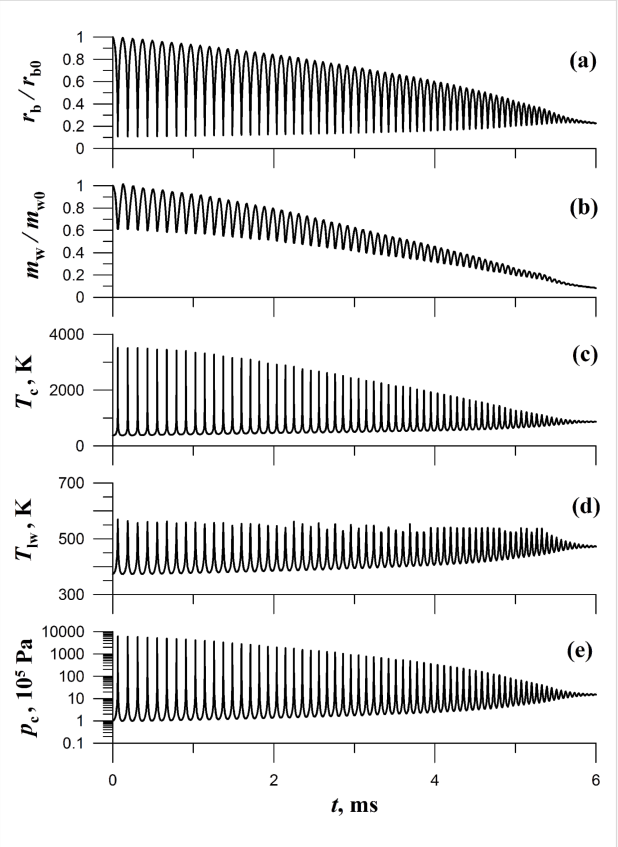

Figure 3: Time dependencies r_b/r_{b0}, m_w/m_{w0}, T_c, T_{lw}, and p_c in a pulsating cavitation bubble. Initial parameters are the bubble radius r_{b0} = 0.25 cm, the pressure inside the bubble $p_0 = 10^5$ Pa, the vapor temperature T_0 = 373 K. The pressure in the liquid far from the bubble is $p_\infty = 15p_0$.

under the assumptions of the model in [8-11], which takes into account adiabatic compression of the vapor but does not take into account the phase transformation liquid–vapor. Thus the model described in the present paper shows that the cavitation processes occurring on the interface are occasionally more effective than the bulk cavitation processes [8-11].

When the initial radius of the cavitation bubble is reduced, the influence of the surface processes, namely condensation, evaporation, and heat transfer between the vapor and liquid, on the bubble dynamics increases, while the pulsation time t_m decreases. For example, if r_{b0} = 0.25 cm (Figure 3) then the pulsation time is t_m = 6 ms. The vapor mass in the bubble is lowered by a factor equal to 1.6 in the state corresponding to the first maximum compression, the vapor temperature reaching 3500 K, and the vapor pressure in the bubble attaining the magnitude of $p_c = 6250p_0$. For r_{b0} = 0.1 cm (Figure 4) the pulsation time is t_m = 2 ms, the first maximum compression fits a 2.1 times decrease in the vapor mass, the temperature increases up to the value of 4400 K, and the vapor pressure grows up to $p_c = 13800p_0$.

The microparticle, on which the bubble is located, is melted if the vapor temperature becomes higher than the melting point $(T_m)_p$ of the substance of the microparticle, e.g., for quartz $(T_m)_p$ = 1883 K, for gold $(T_m)_p$ = 1336 K). Each bubble compression results in the extrusion of melt (formed during this compression) out of the bubble. A bubble works like a borer. We calculate the thickness $(X_{mt})_1$ of the melt which is extruded out of the bubble after the first compression as well as the total melt thickness over during the whole time of the bubble pulsations, X_{mt} of the microparticle, i.e., the layer of the microparticle, which is melted and removed out of the particle if the particle size is larger than X_{mt}. Otherwise, if the particle size is smaller than X_{mt} then the particle is melted and, finally, completely destroyed. For the quartz particle we obtain $(X_{mt})_1$ = 2.6 μm and X_{mt} = 62 μm if r_{b0} = 0.5 cm, $(X_{mt})_1$ = 1.9 μm and X_{mt} = 60 μm if r_{b0} = 0.25 cm, and $(X_{mt})_1$ = 0.88 μm and X_{mt} = 55 μm if r_{b0} = 0.1 cm. For the gold particle we have $(X_{mt})_1$ = 23 μm and X_{mt} = 924 μm if r_{b0} = 0.5 cm, $(X_{mt})_1$ = 16 μm and X_{mt} = 694 μm if r_{b0} = 0.25 cm, and $(X_{mt})_1$ = 8.8 μm and X_{mt} = 465 μm if r_{b0} = 0.1 cm.

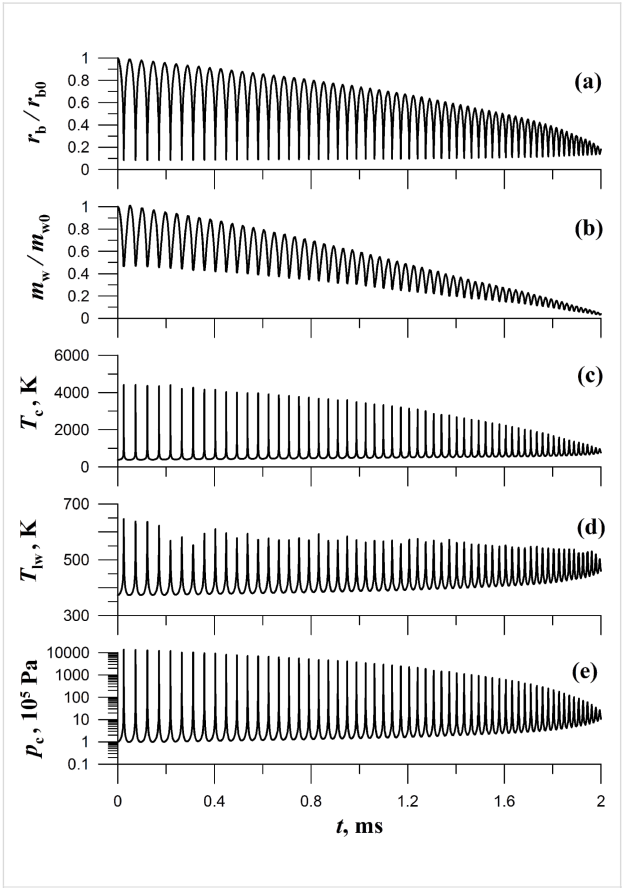

Figure 4: Time dependencies r_b/r_{b0}, m_w/m_{w0}, T_c, T_{lw}, and p_c in a pulsating cavitation bubble. Initial parameters are the bubble radius r_{b0} = 0.1 cm, the pressure inside the bubble $p_0 = 10^5$ Pa, the vapor temperature T_0 = 373 K. The pressure in the liquid far from the bubble is $p_\infty = 15p_0$.

Consider the situation when a gold particle is located inside a larger quartz particle. Figure 5 shows the dependence of the maximum thickness $X_{Au,max}$ of the molten layer of gold on the thickness X_{SiO2} of the quartz layer which screens the gold off the heating from the pulsating cavitation bubble. The calculations show that quartz layers with thicknesses above 54 μm completely shield the gold from melting.

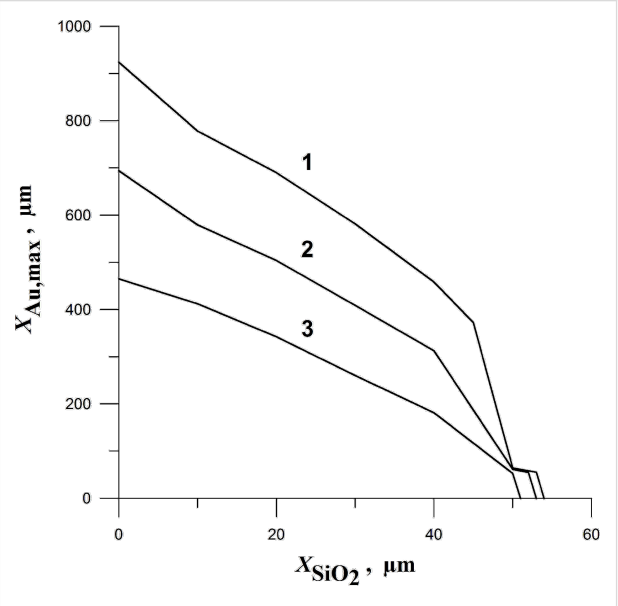

Figure 5: The maximum thickness $X_{Au,max}$ of the molten layer of gold versus the thickness X_{SiO2} of the quartz layer. Curves 1, 2, and 3 correspond to the initial bubble radii of r_{b0} = 0.5 cm, 0.25 cm, and 0.1 cm, respectively. The initial parameters are $p_0 = 10^5$ Pa and T_0 = 373 K. The pressure in the liquid far from the bubble is $p_\infty = 15p_0$.

Discussion

In [11] it has been shown that, in the process of melting, the density of gold decreases from ρ_s = 19.3 g/cm^3 to ρ_l = 17.31 g/cm^3, i.e., the volume of the gold particle changes by a factor of $\rho_s/\rho_l = 1.12$. If the melted particle is incorporated into quartz and its expansion is impossible, its internal pressure will be increased corespondingly. The pressure that arises during the melting of a gold particle incorporated into quartz may be estimated, by using the coefficient of volumetric expansion of gold, K = 2.2 Mbar, from the formula

$$P_m = K\left(1-\frac{\rho_l}{\rho_s}\right) = 0.24 \text{ Mbar}. \quad (9)$$

Such a high pressure, several times higher than the strength of quartz (90 kbar), results in the breakup of quartz and separation of the polymineral particle into monomineral fractions. This mechanism works in the case of polymineral nano- and microscale particles considered here when the cavitation processes occur on the interface between liquid and fine solid particles. However, it only occurs for the thicknesses of quartz layer less than 54 μm (Figure 5 which determines the maximum thickness of the molten layer of gold), i.e., when the gold placed inside the quartz particle can be melted.

Conclusion

The calculations performed in this report show that cavitation melting of microparticles with sizes less than several dozens of micrometers, composed of minerals characteristic of gold deposits, can be realized under shock loading of water. This means, when the pressure in water, which is heated up to the boiling temperature, increases abruptly to a value of p_∞ = 15 bar. As a result of the cavitation melting, the interaction of polymineral microparticles with collapsing cavitation bubbles may lead to breakup and fragmentation of microparticles into monomineral fractions. The cavitation disintegration mechanism can be important in technological processes of beneficiation because it can provide the recovery of disseminated metals from microscale fractions, with sizes of dozens of micrometers, which are obtained when developing the low-grade deposits and reprocessing the ore dumps and tailings.

Acknowledgements

This study was supported by the Division of Earth Sciences, Russian Academy of Sciences (the basic research program No. 5 “Nanoscale Particles: Conditions of Formation, Methods of Analysis and Recovery from Mineral Raw”).

References

1. Roco, M. C.; Williams, R. S.; Alivisatos, P., Eds. *Nanotechnology Research Directions: Vision for Nanotechnology, R&D in the Next Decade;* Kluwer Academic Publishers: Dordrecht, 2000.
2. Banfield, J. E.; Navrotsky, A., Eds. *Nanoparticles and the Environment;* Reviews in Mineralogy and Geochemistry, Vol. 44; Mineralogical Society of America: Washington DC, 2001.
3. Popel, S. I.; Kopnin, S. I.; Yu, M. Y.; Ma, J. X.; Huang, F. *J. Phys. D: Appl. Phys.* **2011,** *44,* 174036. doi:10.1088/0022-3727/44/17/174036
4. Sergeev, G. B.; Klabunde, K. J. *Nanochemistry,* 2nd ed.; Elsevier: Amsterdam, 2013.
5. Galimov, E. M. *Nature* **1973,** *243,* 389–391. doi:10.1038/243389a0
6. Galimov, E. M.; Kudin, A. M.; Skorobogatskii, V. N.; Plotnichenko, V. G.; Bondarev, O. L.; Zarubin, B. G.; Strazdovskii, V. V.; Aronin, A. S.; Fisenko, A. V.; Bykov, I. V.; Barinov, A. Y. *Dokl. Phys.* **2004,** *49,* 150–153. doi:10.1134/1.1710678
7. Novgorodova, M. I.; Gamyanin, G. N.; Zhdanov, Y. Y. *Geochem. Int.* **2003,** *41,* 76–85.
8. Adushkin, V. V.; Andreev, S. N.; Popel, S. I. *Geol. Ore Deposits (Transl. of Geol. Rudn. Mestorozhd.)* **2004,** *46,* 313–320.
9. Adushkin, V. V.; Andreev, S. N.; Popel, S. I. *Dokl. Earth Sci.* **2004,** *399,* 1153–1155.

10. Adushkin, V. V.; Andreev, S. N.; Popel, S. I. *Geol. Ore Deposits (Transl. of Geol. Rudn. Mestorozhd.)* **2006,** *48,* 237–243. doi:10.1134/S1075701506030056
11. Adushkin, V. V.; Andreev, S. N.; Popel, S. I. *Geol. Ore Deposits (Transl. of Geol. Rudn. Mestorozhd.)* **2007,** *49,* 201–207. doi:10.1134/S1075701507030038
12. Nekrasov, I. Y. *Geochemistry, Mineralogy, Genesis of Gold Deposits;* CRC Press: Boca Raton, FL, 1996.
13. Margulis, M. A. *Phys.-Usp.* **2000,** *43,* 259–282. doi:10.1070/PU2000v043n03ABEH000455

Beilstein Journal of Nanotechnology

Plasma-assisted synthesis and high-resolution characterization of anisotropic elemental and bimetallic core–shell magnetic nanoparticles

M. Hennes[*1], A. Lotnyk[1] and S. G. Mayr[*1,2,3]

Full Research Paper

Open Access

Address:
[1]Leibniz-Institut für Oberflächenmodifizierung e.V., Permoserstr. 15, 04318, Leipzig, Germany, [2]Translationszentrum für Regenerative Medizin, Universität Leipzig, 04103 Leipzig, Germany and [3]Fakultät für Physik und Geowissenschaften, Universität Leipzig, 04103 Leipzig, Germany

Email:
M. Hennes[*] - marcel.hennes@iom-leipzig.de; S. G. Mayr[*] - stefan.mayr@iom-leipzig.de

* Corresponding author

Keywords:
bimetallic magnetic nanoparticle; core–shell; magnetron sputtering; plasma gas condensation

Beilstein J. Nanotechnol. **2014,** *5,* 466–475.
doi:10.3762/bjnano.5.54

Received: 22 November 2013
Accepted: 17 March 2014
Published: 14 April 2014

This article is part of the Thematic Series "Physics, chemistry and biology of functional nanostructures II".

Guest Editor: A. S. Sidorenko

Abstract

Magnetically anisotropic as well as magnetic core–shell nanoparticles (CS-NPs) with controllable properties are highly desirable in a broad range of applications. With this background, a setup for the synthesis of heterostructured magnetic core–shell nanoparticles, which relies on (optionally pulsed) DC plasma gas condensation has been developed. We demonstrate the synthesis of elemental nickel nanoparticles with highly tunable sizes and shapes and Ni@Cu CS-NPs with an average shell thickness of 10 nm as determined with scanning electron microscopy, high-resolution transmission electron microscopy and energy-dispersive X-ray spectroscopy measurements. An analytical model that relies on classical kinetic gas theory is used to describe the deposition of Cu shell atoms on top of existing Ni cores. Its predictive power and possible implications for the growth of heterostructured NP in gas condensation processes are discussed.

Introduction

Due to their size, novel physical properties and the possibility of contactless manipulation, magnetic nanoparticles can be employed as powerful nanotools in many areas of biology, biophysics and medicine [1]. Possible applications include their use as contrast agents for cell tracking via magnetic resonance imaging (MRI) [2], as colloidal mediators in cancer therapy (hyperthermia) [3] or as nanocarriers for targeted drug delivery [4]. Unfortunately, many ferromagnetic materials are prone to strong oxidation (thereby losing their magnetic properties over time) and turn out to be highly cytotoxic, a knock-out criterion for any application in life sciences. The synthesis of well designed nanoalloys [5], combining two and more metals at the nanoscale, might circumvent this problem. Core–shell nanoparticles (CS-NPs) that are composed of an inert metallic layer of

several nanometer thickness covering a magnetic core, can prohibit the latter from oxidation and prevent the release of toxic ions in solution. While a plethora of wet-chemical methods has been designed for the synthesis of heterostructured magnetic particles [6], less is known about possible issues of methods that are based on inert-gas condensation, in which nanoparticles grow out of a supersaturated metal vapor. Yet, gas phase techniques possess several advantages over their chemical counterparts: the high purity of the resulting samples, high throughput in continuous operating mode, and easy integration into other UHV manufacturing/analysis steps. Although early experiments used inert gas condensation in combination with thermal evaporation [7], magnetron sputtering at high pressures soon emerged as a superior technique for the production of large amounts of nanoparticles with very narrow size distribution, a unique advantage for further fundamental and applied research [8,9]. Nevertheless, relatively few studies dealing with the precise tailoring of heterostructured particles in plasma gas condensation setups have been performed yet [10-12], and many publications remain mostly focused on the tuning of size and shape of selected elemental particles [13-19].

When concentrating on the synthesis of CS-NPs in the gas phase, two general approaches are practicable. On the one hand, self organizational properties of matter at the nanoscale can be exploited. Immiscibility of the involved components combined with pronounced differences in surface energies can result in CS structures through a single step process relying on the creation of a bimetallic metal vapor [11,20]. Nevertheless, it is doubtful that this approach will be employable for arbitrary binary alloys with miscibility gap. Indeed, extensive computational studies reveal that equilibrium segregation patterns of immiscible metallic components only seldom result in rotationally symmetric CS-structures [21-23]. Immiscibility was even predicted to be entirely suppressed in NPs [24,25]. The second approach, a two step synthesis process in which the core is produced first and subsequently covered by the vapor atoms of a second metal species therefore seems a promising alternative.

For systematic experimental studies of these scenarios, Cu/Ni constitutes an interesting model system with a moderate miscibility gap in the bulk solid phase (T_c = 630 K) [26] and a moderate difference in the surface energies between Cu and Ni (γ_{Cu} = 1.78 J/m^2 and γ_{Ni} = 2.37 J/m^2) [27]. Recent studies have put Cu/Ni nanoparticular phase diagrams under scrutiny: Thermodynamic equilibrium configurations of nanoclusters were predicted to depend on concentration and structure, and no indications for rotationally symmetric CS configurations were found [22,23]. In addition, the properties of the Cu/Ni system compare reasonably well with the Au/Ni system, which –when in the shape of magnetic core/inert shell nanoclusters– is highly promising as easily functionalized carrier in biomedical environments. Although our studies, at the present stage, are targeted at a fundamental physical understanding, they also can be regarded as a testbed to link to highly attractive future applications. Unfortunately, experimental studies on Cu/Ni or other bimetallic particles with weak miscibility gap are not available to date.

Here, without loss of generality, we therefore explore the capacity of a plasma gas condensation setup to produce out-of-equilibrium CS structures. After presenting experimental details in the first section, we will focus on several key aspects of gas phase synthesis of nanoparticles in the second part. The third and fourth part of this paper are devoted to the presentation and discussion of our results. The last section will consist of a summary and a conclusion.

Experimental

UHV setup and operating conditions

A sketch of the UHV setup used in the present study can be found in Figure 1. The apparatus is divided into three main regions: a condensation vessel (A), a coating stage (B) and a transfer chamber (C), connected by two nozzles n_1 and n_2. Argon 5.0 (99.999%) is used as inert gas and additionally cleaned with an O_2 purifier (Air Liquide) so that the final oxygen content in the stream falls below 0.1 ppm, the partial pressure of contaminants therefore being roughly the same order of magnitude as the initial concentration in the evacuated vessels. Ar flow into A is controlled manually by a leak valve v_1 (Balzers 135) while an additional valve v_2 (MKS 248) regulates the stream into vessel B. The pressure in these two chambers can therefore be adjusted separately. The gas transport is maintained by differential pumping using two turbo molecular pumps (Varian TV 301) with a pumping capacity of 300 L/s. Two gate valves are employed to switch between gas flow configurations that enable pumping towards base pressures $p \approx 10^{-7}$ mbar (v_3 and pv_1 open, pv_2 closed) and particle transport to C (v_3 and pv_1 closed, pv_2 open). In chamber C the substrate is mounted on a rotating sample holder allowing for multiple deposition within one run without venting the chamber. The pressure in the chambers is monitored with the help of cold cathodes at pressures below 10^{-3} mbar (Pfeiffer IKR 251) and capacitance manometers (MKS Baratron 122A and 220BHS) when working in the mbar regime. Metal vapors are generated with the help of two 2-inch DC magnetron sputtering guns (AJA A-320) that can be operated up to pressures as high as 2 mbar. Both magnetron guns have additionally been equipped with a welded bellow to allow for a displacement of the sputter gun under UHV conditions. All particles generated with the present setup were analyzed after transport through air. Scanning electron microscopy (SEM) studies were performed

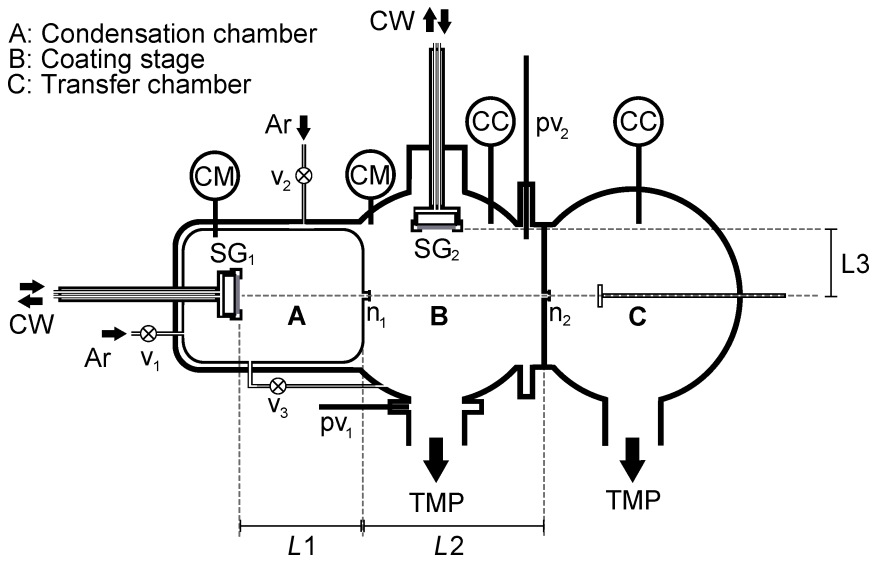

Figure 1: Schematic drawing of the home-built UHV setup used in the present study. CM: capacitance manometers, CC: cold cathode, TMP: turbo molecular pump, CW: cooling water, v: valve, pv: gate valve, SG: sputter gun, n: nozzle.

with a Zeiss Ultra 55 (acceleration voltage U = 15 kV). High resolution transmission electron microscopy (HRTEM) investigation was done using a probe-Cs corrected FEI Titan3 G2 60-300 microscope operating at 300 kV acceleration voltage. Energy dispersive X-ray (EDX) analysis was performed by using a FEI SuperX detector with high visibility low-background FEI holder. The data was collected and evaluated with Bruker software. For EDX measurements, the microscope was set to STEM mode. The beam current was 200 pA. The nanoparticles were directly deposited on Cu grids covered by lacey carbon.

Particle synthesis

Sputtering of the target material in chamber A leads to the ejection of metal atoms with typical mean energies in the eV range for the setup presented here. Subsequent thermalization in the buffer gas is fast and has been predicted to occur after few collisions, as shown analytically and with the help of Monte-Carlo (MC) simulations [28]. The cooling of the metal vapor is dependent on the background gas pressure. In our experiment, atoms are expected to be thermalized after less than a millimeter in chamber A, and less than a centimeter in chamber B, thus in a region close to the target with regard to chamber dimensions. When the metal vapor reaches sufficient supersaturation, the growth of small nuclei occurs. Following classical nucleation theory, these nuclei have to overcome a critical size to become thermodynamically stable and then further grow while moving through the condensation chamber towards the nozzle. The NPs can additionally get covered by a supplementary coating layer in chamber B, while traveling through the metallic vapor generated by SG_2, which is carefully kept below supersaturation. Finally, particles are extracted in C, where they are deposited onto a Si substrate or TEM grids for further analysis.

Gas dynamics and NP transport

Particle synthesis and growth is inherently connected to gas dynamics in the chamber. Indeed, as described above, the Ar background gas serves a threefold purpose: it is used as ionizable species for sputtering, as thermal reservoir for generation of the supersaturated metal vapor and finally, for convective particle transport. Working in the millibar-range allows for the application of standard continuum gas dynamics equations, as the mean free path of the gas is found well below chamber dimensions. With pressure differences between subsequent chambers exceeding the critical ratio of 0.487, the flow will be choked, which facilitates the calculation of Ar mass flow by using [29]

$$\dot{m} = \frac{\alpha A_{\mathrm{n}} P \sqrt{m}}{\sqrt{kT}} \tag{1}$$

with k being the Boltzmann constant, T the temperature, m the mass of the Ar atoms, A_{n} the cross sectional area of the nozzle, P the upstream pressure and α, a numerical coefficient derived from

$$\alpha = \sqrt{\gamma \left(\frac{2}{\gamma+1} \right)^{\frac{\gamma+1}{\gamma-1}}},$$

where γ is the ratio of heat capacities and equals 5/3 for the gas used herein. For our experimental setup, the total mass flow was calculated to be equal to $\dot{m}_{tot} = 1.3 \cdot 10^{-5}$ mol/s ($r_{n2} = 1.25$ mm, $P_A = 1.51$ mbar, $P_B = 0.35$ mbar, $T = 300$ K). The use of mass conservation permits the calculation of the convective velocity of the gas [13]

$$v = \frac{\alpha A_n \sqrt{kT}}{\sqrt{m} A_c} \tag{2}$$

with A_c being the cross sectional vessel area ($A_c = 3.1 \cdot 10^{-2}\ m^2$). For our setup, resulting approximate travel velocities between 1.5 and 3.0 cm/s for chamber A and B, respectively, have been calculated.

Although playing a major role in sputtering, the influence of the plasma is usually neglected in the analysis of particle growth and transport as the degree of ionization is expected to be low in the operating regime described in the present paper. In contrast, an eventual heating of the gas through thermalization of the metal vapor has to be considered [16,19]. A simple thermodynamic analysis of energy fluxes in the chamber can be used to find out whether Ar heating will be prominent or not. Assuming steady state conditions to be reached and neglecting energy loss at the chamber walls, the following identity can be derived

$$T_{chamber} = \frac{\dot{m}^{Ar} C^{Ar} T_{in} + IY\bar{E}/e^{-}}{\dot{m}^{Ar} C^{Ar} + \dot{m}^{metal} C^{metal}} \tag{3}$$

with I being the electrical current and Y the sputter yield, $\bar{E}$ the average energy of the sputtered metal atoms and C the heat capacity of a monoatomic gas. Interestingly, the calculation of the above temperature yields erroneously high values contrasting with the measured pressure increase in chamber A observed when switching on the magnetron gun (Figure 2).

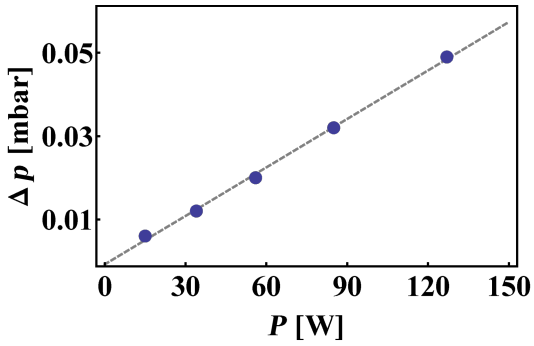

Figure 2: Measured linear pressure increase in chamber A as a function of magnetron power.

This quantity hardly exceeds 5%, even at high powers and might be considered a measure for overall gas heating in vessel A. This suggests that a) full thermalization of the sputtered species, especially of high energy metal atoms is not achieved and/or b) one is eventually overestimating the sputter yield by assuming that Ar ions get fully accelerated by the applied voltage. Indeed, energy loss mechanisms, such as elastic collisions and charge transfer during sputtering, might play a crucial role in our setup, in which the mean free path of gas atoms can drop well below the extension of the cathode dark space. This will again play a role in the discussion part of the present work.

Results

Elemental Ni particles

Continuous operation mode

Elemental magnetic Ni NPs have been generated for various values of pressure and current as well as growth distances by solely using SG_1 in continuous mode. As seen in Figure 3a,

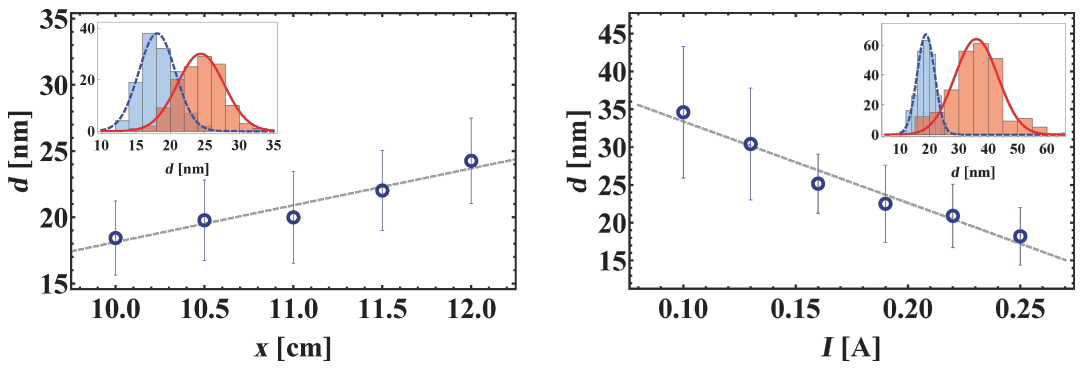

Figure 3: Elemental Ni NP diameter dependency on a) aggregation length $L1$ and b) electrical current of the sputter gun SG_1. Several hundred particles imaged with SEM have been analyzed by hand to gain satisfactory statistics. Interestingly, particle distributions are close to Gaussian and show little resemblance with log-normal size distributions that have been predicted theoretically.

when varying the aggregation length, a clear increase of the particle diameter was found with sizes evolving roughly from 18 to 24 nm at constant pressure. Surprisingly, we observed that crossing a minimum value of x, the particle flow ceased abruptly. This has also been reported in earlier studies [13], but the origin of this effect remains unclear to date. In addition to the mean diameter, the particle size distribution has been analyzed. It was found to be close to Gaussian and only slightly skewed, which stands in contrast to results gained with other inert gas condensation techniques like thermal evaporation, for which log-normal size distributions are usually reported [7]. The influence of the gun current on the particle diameter at fixed condensation pressure and aggregation length is presented in Figure 3b. In contrast to previous studies on Ni NPs [13], the latter is found to decrease monotonously with increasing gun current, with maximum average sizes reached in the present study around 35 nm, while raising the current up to 0.25 A results in particles as small as 18 nm. Finally, EDX measurements hint at a small amount of Fe impurities, which could be traced back to undesirable sputtering of the target holder at elevated pressures in chamber A.

Target morphology and intermittent mode

Inhomogeneous depletion of the sputtered material in magnetron sputtering sources is known to result in pronounced circular trenches in the target (racetracks), as depicted in Figure 4b. In the present study, this undesirable side-effect was found to have a dramatic influence on the size as well as the morphology of the particles. Indeed, as shown in Figure 5, NPs produced with a strongly used target exhibit typical radii increased by almost an order of magnitude with respect to particles obtained with a planar target at moderate powers ($P < 60$ W).

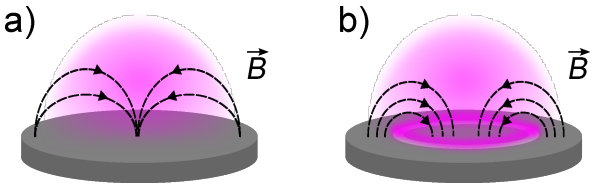

Figure 4: Erosion of the target is found to affect particle sizes and structure. Schematic of the sputtering target a) fresh planar target, b) eroded target eventually generating an increase in plasma density, sputter yield and temperature in the vicinity of the racetrack.

While the latter typically possess a polycrystalline structure (as will be shown in a later part of this work), larger particles are mostly single crystalline with truncated cubic and cuboctahedral crystal shapes reminiscent of Wulff-construction structures (Figure 5b). When operating the magnetron gun in a high-power ($P > 400$ W) intermittent mode [18] with low-frequency pulses and pauses of the order of 10^{-1} Hz, the particle morphology

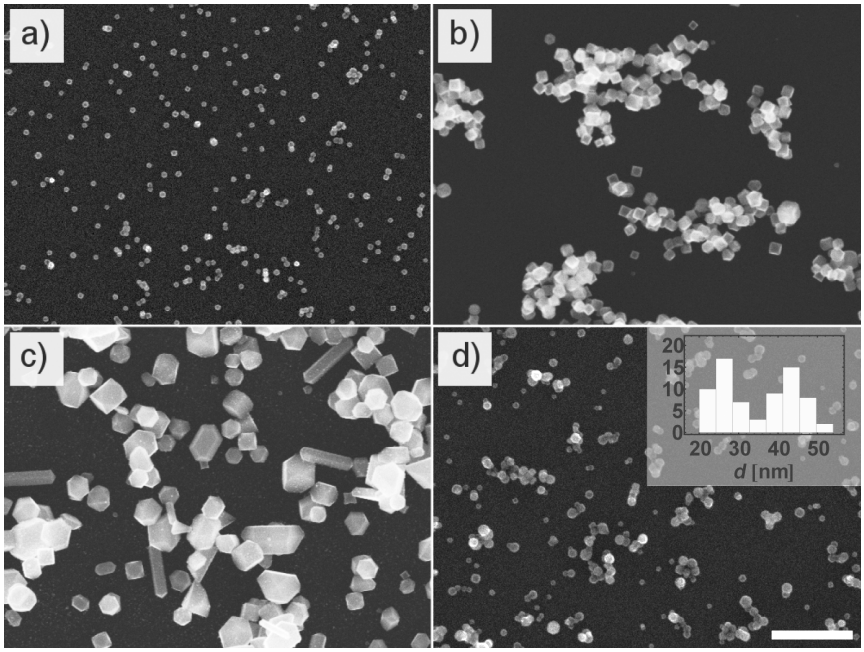

Figure 5: SEM pictures of particles generated with our plasma gas condensation setup. a) Polycrystalline Ni NPs (continuous mode), b) single crystalline Ni NPs produced with strongly eroded target (continuous mode), c) Large sub-micron particles synthesized with strongly eroded target (intermittent mode), d) Ni@Cu CS particles produced by simultaneously using SG_1 and SG_2 (continuous mode). All pictures have been taken at the same magnification. The length of the scale bar is 500 nm. (lower right).

was found to change dramatically and resulted in a population composed of various sub-micron crystals like rods, triangular plates, pyramids and cubes. While this reminds of earlier studies reporting accurate morphology tuning of Cu crystals by pre-seeded sputtering [18], we stress that present results turned out to be intrinsically linked to the target morphology. Using a planar target in combination with pulsed sputtering did not result in the structures described above. On the contrary, a population of very small particles with radii <10 nm was gained, which again hints at a strong correlation between the target morphology and the growth mechanism of the NP.

Bimetallic Ni@Cu particles

In order to ensure a good reproducibility and to avoid eventual shortcomings induced by a missing knowledge of the exact target morphology, all bimetallic particles generated in the following study have been produced using planar, non-eroded targets with the magnetron gun operated in continuous mode. Figure 5 shows SEM pictures of a sample generated by using solely SG_1 in direct comparison with NPs obtained by operating SG_1 and SG_2 simultaneously (see Table 1 for operation parameters).

While in Figure 5a, the NPs exhibit a well defined narrow Gaussian size distribution, analysis of the sizes in Figure 5d on the contrary results in a bimodal distribution. It is also noteworthy that elemental Ni particles possess a rougher surface while all particles with $d \geq 30$ nm exhibit a more regular and rather smooth contour in the SEM micrographs. In order to assess the relative concentration of the components, SEM-EDX spectra (not shown herein) over areas of approximately 100 μm^2 have been recorded, which yielded values between $Cu_{67}Ni_{33}$ and $Cu_{49}Ni_{51}$, depending on the position on the sample. TEM inspection of the particles yields the same binodal size distribution as previously observed with SEM, which becomes apparent in Figure 6. TEM bright field images show that all analyzed NPs present a darker core and brighter halo surrounding the latter. This halo is found to be more pronounced for larger particles and has a typical thickness of 4–5 nm (Figure 7).

To gain quantitative information about the atomic structure of the nanoparticles, lattice plane separations in individual particles were assessed by analysing the FFT of HRTEM micro-

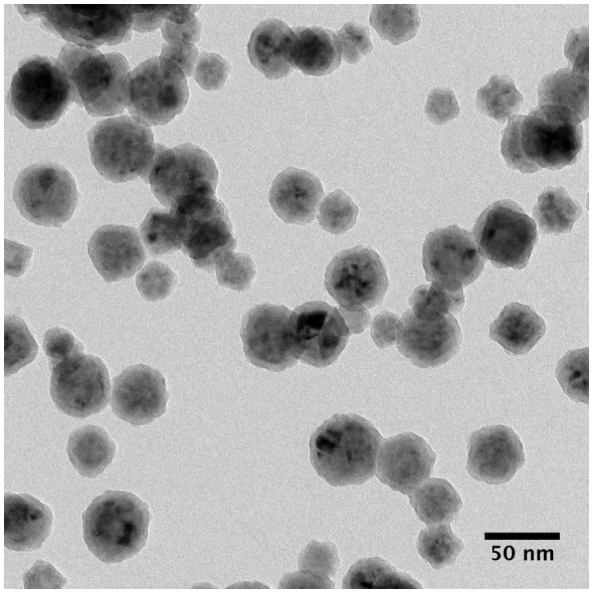

Figure 6: CS-NP deposited on a TEM grid coated with lacey carbon. The same bimodal size distribution as observed in SEM is retrieved.

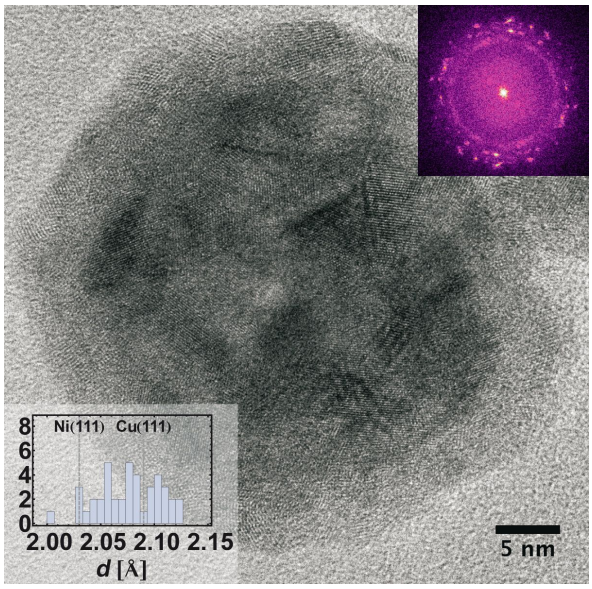

Figure 7: Single CS-NPs exhibit a polycrystalline core as confirmed by FFT analysis (inset upper right) surrounded by an oxidized layer of several nanometers thickness. All particles investigated with HRTEM are found consistent with Cu and Ni fcc phases with a slight systematic shift towards higher values, when compared to bulk plane separations (inset lower left for Cu(111) and Ni(111)).

Table 1: Optimized operating conditions and synthesis parameters used for the production of CS-NPs described in the present study.

P_A [mbar]	P_B [mbar]	$\dot{m}_{tot}$ [mol/s]	I_{SG1} [mA]	I_{SG2} [mA]	U_{SG1} [V]	U_{SG2} [V]
1.52	0.34	$1.3 \cdot 10^{-5}$	150	90	368	270

graphs. In a first step, only the core of individual particles was taken into consideration. It was found to be polycrystalline and yielded results in agreement with Cu and Ni fcc phases (JCPDS: 04-0836 a = 0.3615 nm and JCPDS: 04-0850 a = 0.3523 nm). Although a systematic spread of lattice spacings beyond bulk values was observed, it remained within the estimated uncertainty of the TEM (1.5%). A closer look at the brighter regions surrounding the particles shows that these are composed of small crystallites with typical sizes of a few nm (Figure 7). A FFT of the grains yields lattice spacings that were attributed to Cu_2O (JCPDS: 05-0667 a = 0.4252 nm), although the analysis is seriously impeded by pronounced distortions, small grain sizes and boundaries as well as surface effects.

Conclusive evidence for the successful synthesis of CS structures is ultimatively provided by EDX mapping as shown in Figure 8. While smaller particles almost exclusively contain Ni, larger NPs present a typical concentric pattern, with a Cu rich shell of approximately 10 nm thickness. Closer analysis shows that this shell consists of an oxygen-rich outer part of several nanometers thickness, which is in agreement with previous HRTEM bright field image results. Finally, the long-term stability of the samples has been analyzed. CS-NPs have therefore been stored for 12 months under ambient air conditions. Subsequent HRTEM and EDX spectra analysis demonstrated the stability of the heterostructured particles, which remained in a CS configuration and showed no indication for enhanced oxidation.

Discussion

Elemental particles

Several studies have put under scrutiny the growth mechanisms of elemental NP in plasma gas condensation sources [13,16,19]. Unfortunately, the analysis is often hindered by the lack of information concerning relevant synthesis parameters that are difficult to assess experimentally and can only, if at all, be inferred indirectly. Results found in literature therefore remain contradictory and lack comparability. While some authors found increasing nanoparticle sizes with increasing electrical current of the magnetron gun [13], the results gained with our setup show the opposite trend. Similar findings have been reported recently for the synthesis of niobium NPs [19], in which the temperature profile inside the condensation chamber was taken into account. Local heating of the inert gas through thermalization of the sputtered atoms was argued to be responsible for a nucleation delay, increasing the gun power thereby resulted in a decrease of cluster size. Still, it remains unclear to what extent this explanation is applicable to our setup. Indeed, as described in a previous section, the overall rise of pressure in the condensation chamber measured in the present experiments is small, even at high powers. If inert gas heating through metal vapor thermalization is responsible for this effect, it must be restricted to a region close to the target in order to leave the overall gas temperature nearly constant. Then, its pronounced impact on particle size remains puzzling. Other mechanisms giving rise to a decrease of particle size with increasing gun current are also conceivable. It is known for example from wet-chemistry synthesis of NPs that the degree of supersaturation can be used to tune particle sizes and size distribution. At high supersaturation ratios, fast nucleation rates are attained and the ensuing rapid consumption of the elemental species (nucleation burst) results in a high number of seeds and a fast drop below the nucleation barrier, thus a large number of small particles with narrow size distribution. On the other hand, low supersaturation manifests in a low nucleation rate, larger particles and broader distributions. In this scenario, particle growth would be limited by the available local amount of metal vapor in the particle coordinate system. Unfortunately, it is unknown to date, whether NP production in a cluster source has to be considered a highly localized phenomenon, and additional assumptions concerning the homogeneity of the metal vapor distribution are often plugged ad-hoc into existing growth models. An additional problem that comes into play and has already been discussed in literature [16,19] is the extent of metal vapor loss at the chamber walls. Indeed, although thermalization is believed to be carried out rapidly with regard to typical chamber dimen-

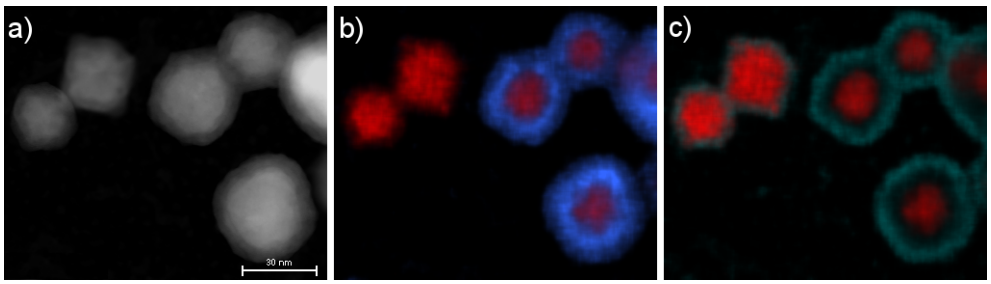

Figure 8: Quantitative EDX mapping revealing the underlying CS-structure: a) HAADF-STEM micrograph, b) Cu (blue) and Ni (red) distribution, c) O (green) and Ni (red) distribution. The length of the scale bar is 30 nm.

sions, diffusion of metal vapor in the background gas can take place on much shorter time scales than convective transport in the stream. Assuming sticking coefficients close to one, one has to consider the vessel walls as a sink for metal vapor atoms with considerable impact on the resulting steady state vapor density, as will be argued below. Again, a quantitative description of this effect has not yet been achieved.

The dependency of nanoparticle size on increasing growth distance has generated, at least qualitatively, less disagreement. All studies known to us report an increasing particle size with increasing growth distance, in accord with our findings. Nevertheless, robust quantitative analysis of the phenomenon remains difficult. Indeed, all studies have at some point to commit to a specific growth mechanism. Hihara et al. [13] compared growth through collisions via a Smoluchowski equation with addatom growth in Ni particle synthesis and found the latter to be better suited for description of their data. Quesnel et al. [16] also sticked to addatom growth to determine Cu cluster size distributions. While yielding good results for clusters with sizes of several nm, their model failed when applied to NPs with greater average diameters. NPs generated in the present experiments are roughly one order of magnitude larger than those described in the studies mentioned above. This might be traced back to significantly lower particle velocities in the growth region, when comparing to available data. Unfortunately, this severely impedes the description of the NP growth. As it becomes clear from the present TEM results, Ni particles shown herein are highly polycrystalline, suggesting that, at least in later growth stages, collisions and sintering of smaller clusters play a significant role. On the other hand, early growth stages will eventually rely on nuclei growth through deposition of single atoms. This gives rise to additional parameters (like the crossover time τ_c from single atom deposition to coagulation driven growth) that would be needed for modeling but cannot be assessed with the present setup. This impedes any reasonable analytical description of growth processes in the condensation chamber.

Our results also clearly highlight the influence of target morphology on particle growth. As was shown in earlier studies, shaping the plasma above the target by manipulation of the magnetic field can have a strong effect on particle structure and phase [30]. Here, a similar trend is observed, although additional mechanisms might play a role. Indeed, the appearance of a profound racetrack might not only change the magnetic field configuration and thereby induce an increase in plasma density near the target (Figure 4). The creation of a curved surface can also dramatically enhance the sputter yield, which is known to be severely affected by the incidence angle of the impinging Ar ions, an effect which has been shown to influence the size of NPs generated in plasma condensation sources [31]. Further experimental investigation is needed to clarify the exact correlation of target shape and produced NPs.

Bimetallic nanoparticles

Despite all the shortcomings described before, metallic shell addatom growth onto particles traveling through the gas phase seems to be, in principle, amenable to analytical modeling. As long as nucleation of the shell species is avoided, expressions for the size evolution of CS-NPs in the coating chamber can be derived by using classical kinetic gas theory, as the particle size is well below the typical mean free path of the background gas atoms. Assuming the traveling velocity of the NPs to be identical to the gas stream velocity, the growth of a shell onto an existing core can be described by [32]:

$$\frac{di}{dt} = v\frac{di}{dx} = \sigma v_{\text{th}} n_0 \beta \tag{4}$$

Here, i represents the number of shell atoms, x the traveling distance through the coating chamber B, $v_{\text{th}} = \sqrt{8kT/(\pi\tilde{m})}$ the thermal velocity in the gas phase with $\tilde{m}$ the reduced mass of the collision partners, $\sigma = \pi\,(r_p + r_{Cu})^2$ the interaction cross section of a particle with radius r_p with a Cu atom with radius r_{Cu} and finally n_0 the density of thermalized Cu atoms in the gas phase. A possible re-evaporation of deposited shell atoms is taken into account by the factor β and plays a major role in initial stages of cluster growth, as the large heat of condensation of metals can significantly reduce the sticking rate of impinging atoms on small clusters [13,32]. Nevertheless, in the present study, due to the rather large size of the Ni core, evaporation rates will be assumed close to zero, setting β equal to one. Additionally, the following approximations are used: $\tilde{m} \approx m_{Cu}$ and $r_p + r_{Cu} \approx r_p$. This yields

$$\frac{di}{dt} = \pi n_0 \left(\frac{3a^3 i}{16\pi} + r_c^3\right)^{2/3} \cdot \left(\frac{8kT}{\pi m_{Cu}}\right)^{1/2} \tag{5}$$

This differential equation is easily solved by using appropriate boundary conditions. Unfortunately, the vapor density is a crucial parameter that can only be determined indirectly. It has recently been proposed to use a simple balance equation for the calculation of n_0 [16]. Equating the incoming metal atom flux from the sputter gun with the outflowing metal vapor yields

$$n_0 = \frac{IY}{vAe^-},$$

where I denotes the electrical current of the sputter gun, Y the sputter yield of the Cu target, v the mean convective velocity of the gas, A the average area of the vessel B and e^- the electron

charge. Applying this to our setup (Y = 1.2, I = 0.09 A, v = 0.028 m·s^{-1}, A = 3.1·10^{-2} m^2) yields $n_0 \approx 7.5 \cdot 10^{20}$ m^{-3}. On the other hand, the vapor density can also be deduced from the effective shell thickness by using the above equation ($a = 0.362 \cdot 10^{-9}$ m, v = 0.028 m·s^{-1}, $r_c = 12.5 \cdot 10^{-9}$ m, x = 0.2 m), which results in: $n_0 \approx 1.5 \cdot 10^{18}$ m^{-3}. This large discrepancy clearly illustrates the shortcomings of modeling NP growth. Lower metal vapor densities allow two interpretations. Either our setup faces a large loss of metal vapor at the chamber walls, an assumption which is supported by calculations of Cu diffusivity in buffer Ar by using the Chapman–Enskog theory [33], or the sputter rate is incorrectly determined by neglecting collisional processes of Ar-ions on their way to the target. This shows that, in order to gain a better quantitative understanding of heterostructured NP growth, direct assessment of metal vapor densities is a crucial requirement. Experiments aiming at a determination of n_0 are currently underway.

With respect to the structure of the CS particles, several things are noteworthy. No elemental Cu particles were found in the present experiments. This was realized by carefully working at sufficiently low pressures and demonstrates the possibility of a complete suppression of homogeneous nucleation of the shell species in the gas phase. Unfortunately, the presence of shadowed or blind zones in the vessel, where Ni core particles can pass without encountering sufficient Cu atoms lead to a significant amount of uncoated NPs. This can in principle be avoided by an improved design of the coating chamber.

Finally, as discussed above, oxidation of the NPs surface was observed, but restricted to a thin layer of few nanometers thickness, for CS as well as for elemental particles. This can be either attributed to the presence of residual oxygen in the chamber, which would require the usage of even higher gas purities in order to avoid contamination, or the transport of the particles through air for further analysis. Future studies will aim at circumventing this problem by using a noble metal as the shell material.

Conclusion

We set up a plasma gas-condensation apparatus for the synthesis of nanoparticles and demonstrated the successful production of highly tunable elemental and CS-structured magnetic nanoparticles. In contrast to earlier studies, in which a shell thickness of only several monolayers was reached [10], the present experiments demonstrate the capacity of plasma gas condensation to synthesize CS-NPs with much larger shell dimensions. Deposition of a 10 nm layer of Cu atoms on Ni cores was explicitly shown by using HRTEM and EDX. Repetition of the measurements showed that particle structures remained stable under ambient air conditions for a period of more than 12 months. A description of the shell growth by using simple kinetic gas theory arguments was undertaken and demonstrated the importance of an exact knowledge of metal vapor densities in the chamber to understand addatom deposition. By using the particles as local probes, the gas phase density, n_0, was assessed and shown to differ dramatically from results gained from simple flux calculations. This might be attributed to a) oversimplifying assumptions concerning the sputter rates or b) significant losses of metal vapor at the chamber walls. Finally, we emphasize that, although the present study was restricted to Cu/Ni as a material system, the growth of fine tuned shells by using gas-phase magnetron deposition is generalizable to any sputterable material, thus paving the way for synthesis of novel multifunctional NPs.

Acknowledgements

We thank A. M. Jakob for fruitful discussions as well as Prof. Dr. Dr. h.c. Bernd Rauschenbach for general support. This project is funded by the Deutsche Forschungsgemeinschaft (DFG) via Schwerpunktprogramm 1681 “Feldgesteuerte Partikel-Matrix-Wechselwirkungen: Erzeugung, skalenübergreifende Modellierung und Anwendung magnetischer Hybrid-Materialien”. Financial support of the European Union and the Free State of Saxony (LenA project; project no. 100074065) is also greatly acknowledged.

References

1. Pankhurst, Q. A.; Connoly, J.; Jones, S. K.; Dobson, J. *J. Phys. D: Appl. Phys.* **2003,** *36,* R167. doi:10.1088/0022-3727/36/13/201
2. Ferreira, L.; Karp, J. M.; Nobre, L.; Langer, R. *Cell Stem Cell* **2008,** *3,* 136–146. doi:10.1016/j.stem.2008.07.020
3. Duguet, E.; Vasseur, S.; Mornet, S.; Devoisselle, J.-M. *Nanomedicine* **2006,** *1,* 157–168. doi:10.2217/17435889.1.2.157
4. Alexiou, C.; Arnold, W.; Klein, R. J.; Parak, F. G.; Hulin, P.; Bergemann, C.; Erhardt, W.; Wagenpfeil, S.; Lübbe, A. S. *Cancer Res.* **2000,** *60,* 6641–6648.
5. Ferrando, R.; Jellinek, J.; Johnston, R. L. *Chem. Rev.* **2008,** *108,* 845–910. doi:10.1021/cr040090g
6. Liu, J. P.; Fullerton, E.; Gutfleisch, O.; Sellmyer, D. J., Eds. *Nanoscale Magnetic Materials, Applications;* Springer: Boston, 2009.
7. Granqvist, C. G.; Buhrman, R. A. *J. Appl. Phys.* **1976,** *47,* 2200–2219. doi:10.1063/1.322870
8. Hahn, H.; Averback, R. S. *J. Appl. Phys.* **1990,** *67,* 1113–1115. doi:10.1063/1.345798
9. Haberland, H.; Karrais, M.; Mall, M.; Thurner, Y. *J. Vac. Sci. Technol., A* **1992,** *10,* 3266–3271. doi:10.1116/1.577853
10. Bai, J.; Wang, J.-P. *Appl. Phys. Lett.* **2005,** *87,* 152502. doi:10.1063/1.2089171
11. Krishnan, G.; Verheijen, M. A.; ten Brink, G. H.; Palasantzas, G.; Kooi, B. J. *Nanoscale* **2013,** *5,* 5375–5383. doi:10.1039/C3NR00565H
12. Llamosa Pérez, D.; Espinosa, A.; Martínez, L.; Román, E.; Ballesteros, C.; Mayoral, A.; García-Hernández, M.; Huttel, Y. *J. Phys. Chem. C* **2013,** *117,* 3101–3108. doi:10.1021/jp310971f

13. Hihara, T.; Sumiyama, K. *J. Appl. Phys.* **1998,** *84,* 5270–5276. doi:10.1063/1.368776
14. Yamamuro, S.; Sumiyama, K.; Suzuki, K. *J. Appl. Phys.* **1999,** *85,* 483–489. doi:10.1063/1.369476
15. Gracia-Pinilla, M.; Martínez, E.; Silva Vidaurri, G.; Pérez-Tijerina, E. *Nanoscale Res. Lett.* **2009,** *5,* 180–188. doi:10.1007/s11671-009-9462-z
16. Quesnel, E.; Pauliac-Vaujour, E.; Muffato, V. *J. Appl. Phys.* **2010,** *107,* 054309. doi:10.1063/1.3310420
17. Ayesh, A. I.; Thaker, S.; Qamhieh, N.; Ghamlouche, H. *J. Nanopart. Res.* **2011,** *13,* 1125–1131. doi:10.1007/s11051-010-0104-2
18. Werner, R.; Höche, T.; Mayr, S. G. *CrystEngComm* **2011,** *13,* 3046–3050. doi:10.1039/C1CE00002K
19. Bray, K. R.; Jiao, C. Q.; DeCerbo, J. N. *J. Appl. Phys.* **2013,** *113,* 234307. doi:10.1063/1.4811448
20. Xu, Y.-H.; Wang, J.-P. *Adv. Mater.* **2008,** *20,* 994–999. doi:10.1002/adma.200602895
21. Baletto, F.; Mottet, C.; Ferrando, R. *Phys. Rev. Lett.* **2003,** *90,* 135504. doi:10.1103/PhysRevLett.90.135504
22. Hennes, M.; Buchwald, J.; Mayr, S. G. *CrystEngComm* **2012,** *14,* 7633–7638. doi:10.1039/C2CE25817J
23. Wang, Y.; Hou, M. *J. Phys. Chem. C* **2012,** *116,* 10814–10818. doi:10.1021/jp302260b
24. Christensen, A.; Stoltze, P.; Norskov, J. K. *J. Phys.: Condens. Matter* **1995,** *7,* 1047. doi:10.1088/0953-8984/7/6/008
25. Xiao, S.; Hua, W.; Luo, W.; Wu, Y.; Li, X.; Deng, H. *Eur. Phys. J. B* **2006,** *54,* 479–484. doi:10.1140/epjb/e2007-00018-6
26. an Mey, S. *CALPHAD: Comput. Coupling Phase Diagrams Thermochem.* **1992,** *16,* 255–260. doi:10.1016/0364-5916(92)90022-P
27. Tyson, W. R. *Surf. Sci.* **1977,** *62,* 267–276. doi:10.1016/0039-6028(77)90442-3
28. Bogaerts, A.; van Straaten, M.; Gijbels, R. *J. Appl. Phys.* **1995,** *77,* 1868–1874. doi:10.1063/1.358887
29. Hagena, O. F. *Surf. Sci.* **1981,** *106,* 101–116. doi:10.1016/0039-6028(81)90187-4
30. Qiu, J.-M.; Wang, J.-P. *Appl. Phys. Lett.* **2006,** *88,* 192505. doi:10.1063/1.2202130
31. Ganeva, M.; Pipa, A. V.; Hippler, R. *Surf. Coat. Technol.* **2012,** *213,* 41–47. doi:10.1016/j.surfcoat.2012.10.012
32. Knauer, W. *J. Appl. Phys.* **1987,** *62,* 841–851. doi:10.1063/1.339688
33. Cussler, E. L. *Diffusion: Mass Transfer in Fluid Systems,* 2nd ed.; Cambridge University Press: New York, 1997.

License and Terms

Beilstein Journal of Nanotechnology

DNA origami deposition on native and passivated molybdenum disulfide substrates

Xiaoning Zhang, Masudur Rahman, David Neff and Michael L. Norton*

Full Research Paper

Open Access

Address:
Department of Chemistry, Marshall University, One John Marshall Drive, Huntington, West Virginia 25755, United States

Email:
Michael L. Norton* - norton@marshall.edu

* Corresponding author

Keywords:
atomic force microscopy (AFM); DNA origami; molybdenum disulfide (MoS_2); pyrene; 1-pyrenemethylamine; surface modification

Beilstein J. Nanotechnol. **2014,** *5,* 501–506.
doi:10.3762/bjnano.5.58

Received: 21 December 2013
Accepted: 03 April 2014
Published: 22 April 2014

This article is part of the Thematic Series "Physics, chemistry and biology of functional nanostructures II".

Guest Editor: A. S. Sidorenko

Abstract

Maintaining the structural fidelity of DNA origami structures on substrates is a prerequisite for the successful fabrication of hybrid DNA origami/semiconductor-based biomedical sensor devices. Molybdenum disulfide (MoS_2) is an ideal substrate for such future sensors due to its exceptional electrical, mechanical and structural properties. In this work, we performed the first investigations into the interaction of DNA origami with the MoS_2 surface. In contrast to the structure-preserving interaction of DNA origami with mica, another atomically flat surface, it was observed that DNA origami structures rapidly lose their structural integrity upon interaction with MoS_2. In a further series of studies, pyrene and 1-pyrenemethylamine, were evaluated as surface modifications which might mitigate this effect. While both species were found to form adsorption layers on MoS_2 via physisorption, 1-pyrenemethylamine serves as a better protective agent and preserves the structures for significantly longer times. These findings will be beneficial for the fabrication of future DNA origami/MoS_2 hybrid electronic structures.

Introduction

Since it was first proposed and implemented by Rothmund in 2006 [1], DNA origami has offered a promising pathway for the construction of precisely programmed molecular architectures [2]. Through programmed, specific oligonucleotide recognition and hybridization, these DNA nanostructures can be used to combine, and therefore expand, the functional diversity of other materials [3]. The nanopatterning technologies of DNA origami structures allow for the lithographic transfer of a wide range of spatial information to other surfaces [3], enable the organized placement of nanoparticles [4] and receptors for the capture of proteins [5,6], and act as templates for the organization of carbon nanotubes [6-9]. This bottom-up process offers a tremendous advantage over photolithography, because is enables the patterning of surfaces with feature sizes less than

20 nm [10]. However, some materials may interfere with the base pairing responsible for origami structure formation and maintenance and are therefore unsuitable substrates for DNA origami deposition and patterning. For example, the folded structures are lost when they are deposited onto a graphene surface, because of π–π stacking between the single-stranded DNA and the graphene flakes [11]. In contrast, several materials have been found that enable the deposition of DNA origami structures while maintaining their structural integrity. These materials include mica [12], silicon dioxide [13], gold [14], and graphene oxide [2]. The ideal substrate surface must be atomically smooth to enable optimal patterning and imaging through atomic force microscopy (AFM) because the origami structures are very thin and conformal. A final substrate property that needs to be considered for maximal utility is that the material should possess conductive or semiconductive electronic properties, so as to enable complex and diverse circuit designs, thereby providing functionality essential for the construction of sensing biodevices with extraordinary sensitivity, rapid readout and good stability.

As a layered two-dimensional (2D) material, molybdenum disulfide (MoS_2) exhibits robust mechanical properties and superior electrical performance [15]. Compared to the zero bandgap of graphene, the bandgap of MoS_2 is adjustable. With decreasing the thickness, the gap progressively shifts from 1.29 eV to over 1.90 eV [16], which makes it a promising material for transistor, optoelectronic and energy harvesting applications [17]. Compared to conventional semiconductor materials such as silicon, MoS_2 is readily processed as a prototypical nanomaterial. MoS_2 nanosheets, nanofibers, and nanorods have been prepared [15], which means the material could readily be used to construct electronic devices with nanoscale dimensions. Several recent studies have examined the interaction of DNA with MoS_2 [15,18]. However, the adsorption of DNA origami structures on MoS_2 surfaces has not previously been explored. The behavior of DNA origami structures on this "S–Mo–S" sandwich structured compound is reported below for the first time. An unanticipated observation was that DNA origami structures decompose on contacting the MoS_2 surface. However, the shape of DNA origami constructs can be preserved with the aid of an adhesion layer composed of either pyrene or 1-pyrenemethylamine. It is expected that this method will be helpful in the development of future applications for the DNA origami/MoS_2 hybrid system in nanoelectronics, optoelectronics and sensing.

Results and Discussion

Cross-like DNA origami structures were first constructed by using the protocols of Liu [19]. A schematic representation of such a tile is shown in Figure 1a. The key feature of this DNA origami structure is that the tile is composed of two rectangular domains (97 nm × 38 nm for each domain), one stacked above the other. Further experimental details are included in

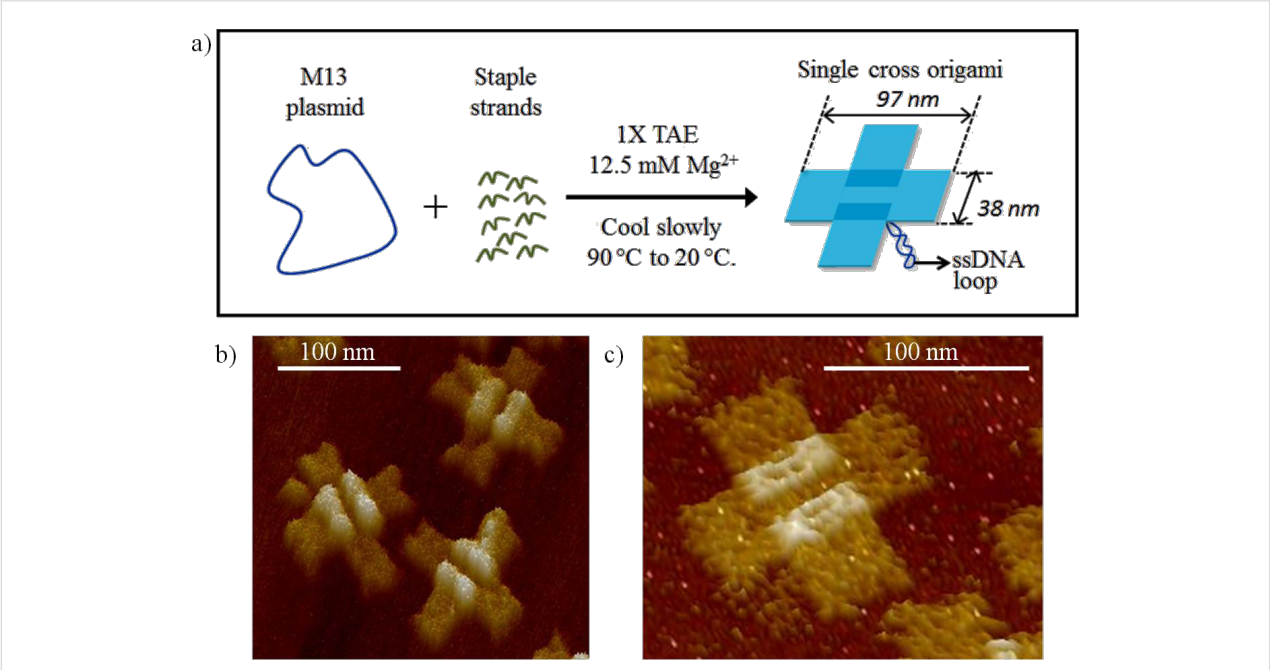

Figure 1: Schematic illustration representing (a) self-assembly of M13 plasmid (dark blue) and staple strands (deep green) to form cross shaped DNA origami (light blue); (b) and (c) represent AFM 3D images of formed DNA origami on mica. Each of the tiles forms the cross-like structure shown in (a). The 3D images of the cross-shaped DNA origami emphasize the overlap of the two domains.

Supporting Information File 1. High-resolution AFM images of the cross-like DNA origami structure on a mica surface are shown in Figure 1b and Figure 1c.

The surface morphology and surface roughness of the MoS_2 mineral sample were investigated by using AFM. As anticipated, the newly cleaved pristine MoS_2 surface was very smooth, featureless, and homogenous (Figure 2a). For optimal AFM imaging, the roughness of the surface should be kept as low as possible in order to avoid additional noise in the imaging of these very thin (about 2 nm) objects. Based on measurements taken over a 5 μm × 5 μm area similar to that shown in Figure 2a, the root mean square roughness (RMS) of the MoS_2 surface was found to be 0.92 Å, indicating that MoS_2 presents an ideal physical surface for the deposition of flat DNA nanostructures.

Importantly, AFM imaging reveals that shape and structure of the DNA origami constructs tended to be lost (Figure 2b) when the DNA origami was incubated on the MoS_2 surface for only 10 s. This observation suggests that the complementary DNA double strands inside the origami structures are denatured due to the interaction with the MoS_2 surface. The deposition time was also expanded to 30 s in order to gain some level of insight into the kinetics of the surface-driven denaturation reaction. Comparison with the images resulting from 30 s of incubation, shown in Figure 2c, suggests that the denaturation process appears to be complete in 10 s, since no significant changes with regard to the morphology of the DNA origami were observed. Although the extra staples present in the synthesis solution were removed via dialysis, debris is observed in the background of these images and is attributed to small quantities of additional staple DNA released from the DNA origami structures. It may be observed that these ssDNA staples adsorbed to the pristine MoS_2 surface adopt many different structures, most likely originating partially from intra-strand base pairing and partially from the strong interaction between DNA bases and the MoS_2 surface [11].

Recent studies indicate that the MoS_2 surfaces have high polarity and hydrophilicity [20], which lead DNA to adsorb through van der Waals forces between the four nitrogenous nucleobases and the basal plane of MoS_2 [18]. For example, in the report of Maddocks et al. [21], guanine, one of the four DNA bases, was observed, by using scanning tunneling microscopy (STM), to form a stable two-dimensional ordered array. These results are of crucial importance, as they support the hypothesis that the van der Waals interaction between MoS_2 and the DNA in the origami is of sufficient strength to destabilize the hydrogen bonds as well as the π–π stacking interactions in the relatively short duplex regions within the DNA origami constructs. This leads to denaturation of these complexes. The transition from double-stranded DNA to single-stranded DNA would be expected to require an expansion of the size (footprint) of the origami, however if the interaction between the bases of the DNA origami structure and the MoS_2 substrate are of sufficient strength, further dispersion/equilibration in two dimensions would not be anticipated. This is consistent with the observation that the structures do not evolve significantly between 10 and 30 s of incubation.

Surface modification using 1-pyrenemethylamine and pyrene

1-pyrenemethylamine has been employed as a linker to bind DNA to graphene and carbon nanotube surfaces [3,22]. Here, we adopted a similar approach by treating the MoS_2 surface with 1-pyrenemethylamine, a bifunctional bridging compound, and then exposing the substrate to a solution of DNA origami constructs. While the surface roughness increased significantly to 5.3 Å after surface modification (Figure 3a), we found that DNA nanostructures remained intact in the presence of the 1-pyrenemethylamine adhesion layer (Figure 3b–d), in contrast to the DNA nanostructures deposited on the bare MoS_2 surface. This is readily understood in the context of a model, in which the pyrenyl group in 1-pyrenemethylamine is bound to the highly planar, polar, and polarizable MoS_2 surface by van der Waals forces and forms an adhesion layer. Conversely, the

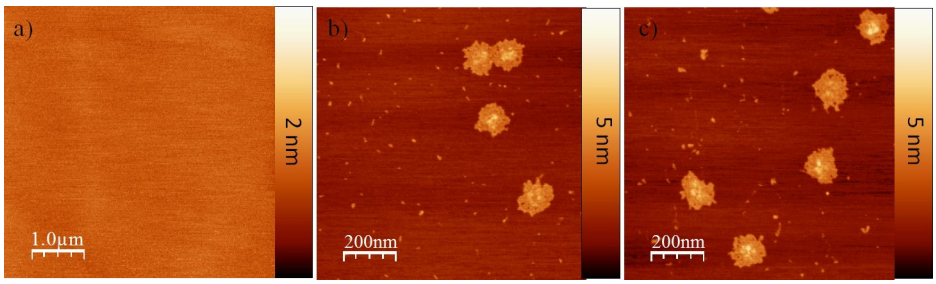

Figure 2: Representative AFM images of the pristine MoS_2 substrate before (a) and after the DNA origami solution was deposited onto it with different incubation times: 10 s (b) and 30 s (c).

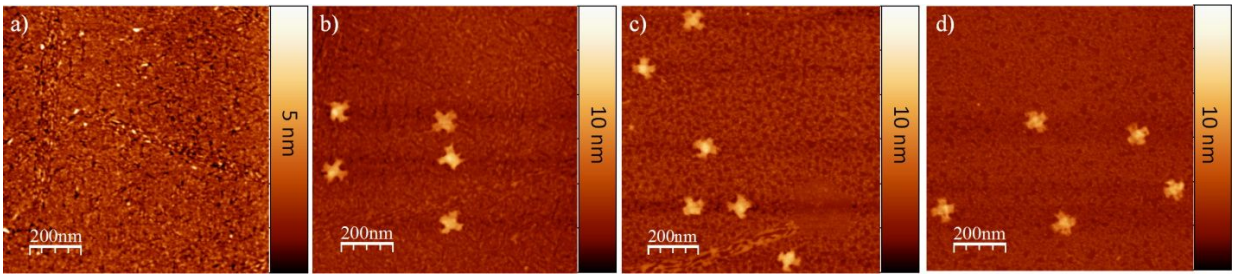

Figure 3: (a) AFM image of the MoS_2 basal plane after exposure to 0.5 mM 1-pyrenemethylamine methanol solution for 5 min. (b) DNA origami with a cross shape imaged immediately after deposition onto pre-modified MoS_2 substrates. (c) AFM images of DNA origami adsorbed on the MoS_2 after 24 h and (d) 48 h.

amine group in 1-pyrenemethylamine interacts electrostatically with the phosphate group of the DNA origami constructs, binding them to the surface through formation of salt bridges. Pre-adsorption of 1-pyrenemethylamine molecules serves to mask the MoS_2 surface and to sufficiently reduce the van der Waals interaction between MoS_2 and the double stranded DNA in the origami constructs, thereby preserving their original structure.

It is known that MoS_2 readily adsorbs water molecules from the atmosphere [20]. Because DNA origami structures are unstable and easily degraded in a pure H_2O environment [11], it was necessary to perform a variable-time study to investigate any morphological changes in the DNA origami structure on the modified MoS_2 surface in ambient environment. No significant changes were noted after 24 h and 48 h, respectively (Figure 3c and Figure 3d), indicating that the 1-pyrenemethylamine layer does not experience significant water accumulation from the atmosphere. The morphology after 120 h was also studied (see Supporting Information File 1, Figure S2). AFM imaging indicated a good retention of the structure of the DNA origami constructs. This relatively stability over a relatively long time is favorable for future construction of DNA origami-based MoS_2 sensing devices.

Since the pyrene moiety, a primary functional component group of 1-pyrenemethylamine, is known to interact with MoS_2 as an intercalant [23], pyrene was also studied in this research. Using the same conditions for surface film fabrication, a MoS_2 substrate was dipped into a pyrene–methanol solution, followed by the deposition of DNA origami constructs onto the treated substrate. Apparently, the surface coverage of pyrene on the MoS_2 was not as smooth as that of 1-pyrenemethylamine (Figure 4a), which might be partially caused by the lower polarity of the pyrene molecules. Although initial images (Figure 4b) indicated a retention of the origami structures, AFM images of DNA origami constructs deposited on the pyrene-modified MoS_2 surface recorded at 24 h (Figure 4c) and 48 h (Figure 4d) after deposition demonstrated a progressive decomposition of the DNA origami structures.

Although this might be attributed to the accumulation of H_2O molecules on the MoS_2 surface caused by the limited surface coverage of pyrene, other mechanisms for disruption of the structure, including the strong van der Waals interactions with pyrene or even pyrene intercalation into the DNA [24-27], may be active. Additionally, a control experiment was performed to confirm that methanol, or a methanol impurity, was not possibly contributing to the preservation of the DNA origami structures

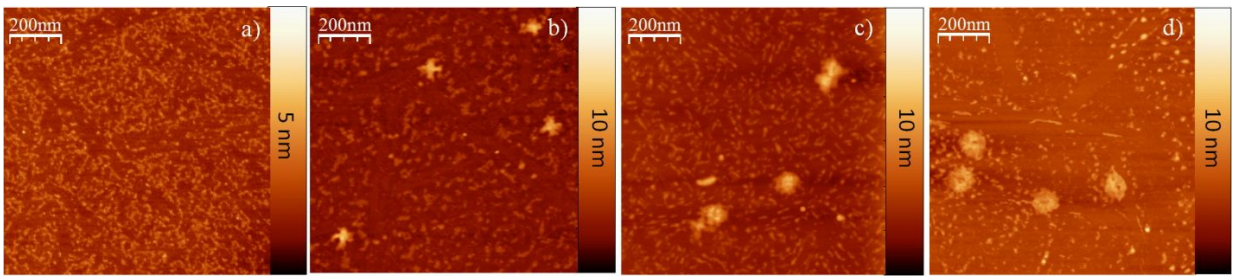

Figure 4: (a) MoS_2 substrate incubated with a 0.5 mM pyrene–methanol solution for 5 min. (b) Cross-shaped DNA origami nanostructures deposited on MoS_2 pre-treated with pyrene and immediately imaged by AFM in air. The AFM images were also recorded after 24 h (c) and 48 h (d). The observed DNA origami structure degrades over time.

(see Supporting Information File 1 for full experimental data). In summary, although both 1-pyrenemethylamine and pyrene can prevent immediate DNA origami structural disruption caused by interaction with the MoS_2 substrate, the protective effect of the 1-pyrenemethylamine surface layer is much greater than that of pyrene.

Conclusion

MoS_2 has a great potential as a transducer material in future biosensor applications. In this work, the behavior of DNA origami structures on a MoS_2 surface was studied for the first time. Our results revealed that DNA origami nanostructures are not stable when in direct contact with the MoS_2 surface. This can be attributed to the van der Waals interaction between nucleobases and the basal plane of MoS_2, which destabilizes the double-stranded structure of the DNA origami constructs. However, it was found that DNA origami structures retain their structures for a relatively long time when adsorbed onto MoS_2 surfaces that have first been treated to generate a 1-pyrenemethylamine surface adhesion layer. The structure-preserving properties of a pyrene protective layer were compared with those of a 1-pyrenemethylamine layer. It was found that 1-pyrenemethylamine provides much better protection of the DNA origami structure than the pyrene layer. Although the microscopic mechanism was not determined in this work, it is possible that the methyl spacer in 1-pyrenemethylamine is sufficient to disrupt the van der Waals interaction between pyrene and DNA, which enables the origami to retain its base complementarity and therefore its shape. This model, in which the pyrenyl moiety of the 1-pyrenemethylamine molecule enables it to physisorb on to the MoS_2 surface while the amine functionality enables the electrostatic tethering of the 1-pyrenemethylamine to the DNA, is consistent with the reported intercalation of pyrene into MoS_2 [23] and the known use of amines to efficiently bind DNA to surfaces [23]. This method will benefit research involving biomolecular sensing on MoS_2 in general, and the use of DNA origami to generate nanostructures on MoS_2 surfaces specifically.

Experimental

MoS_2 was obtained from Ward's (Rochester, N.Y.). Methanol, pyrene, and 1-pyrenemethylamine hydrochloride were obtained from Sigma-Aldrich. We used M13mp18 ssDNA plasmid (7249 bp) and short complementary DNA staple strands to program the cross-shaped DNA origami (the details are provided in Supporting Information File 1). To remove the excess staple strands, the DNA origami solutions were dialyzed with Amicon Ultra Centrifugal Filter Devices (100,000 molecular weight cutoff) for 30 min; 1 × TAE with 12.5 mM Mg^{2+} was used as the buffer solution. After dialysis, the solution of DNA origami structures was recovered from the dialysis tubing and prepared for imaging. M13mp18 single stranded phage DNA was purchased from Bayou Bio-Labs, while the short DNA staple strands were purchased from Integrated DNA Technologies (IDT). DI water (Millipore, 18 MΩ·cm) was used to prepare all buffer solutions.

To deposit DNA nanostructures onto the modified MoS_2, freshly cleaved MoS_2 samples were first dipped into 0.5 mM 1-pyrenemethylamine/pyrene–methanol solution for 5 min, then washed with 400 µL of pure methanol and gently dried in an argon stream. Subsequently, 5 µL of dialyzed DNA origami in 1 × TAE/12.5 mM $MgCl_2$ buffer was dispensed on the top of the treated MoS_2 surface. Ten seconds later, the DNA drop was blown dry with an argon stream, and then washed with 400 µL of Milli-Q water in order to remove excess salts from the surface. Next, the morphologies of the DNA origami on the substrates were determined by using a Bruker Multimode AFM with Nanoscope VI controller in SCANASYST-AIR mode. All steps were performed at room temperature. All AFM images were processed and rendered by using the software WSxM [28].

Supporting Information

Supporting Information features additional information about the formation of self-assembled DNA origami nanostructures and a study of the effect of methanol on the preservation of DNA origami structures.

Supporting Information File 1

Additional experimental data.
[http://www.beilstein-journals.org/bjnano/content/supplementary/2190-4286-5-58-S1.pdf]

Acknowledgements

We thank the following grants for support of this research: ARO awards: W911NF-08-1-0109, W911NF-09-1-0218, W911NF-11-1-0024 and NSF Cooperative Agreement Number EPS-1003907.

References

1. Rothemund, P. W. K. *Nature* **2006,** *440,* 297–302. doi:10.1038/nature04586
2. Yun, J. M.; Kim, K. N.; Kim, J. Y.; Shin, D. O.; Lee, W. J.; Lee, S. H.; Lieberman, M.; Kim, S. O. *Angew. Chem., Int. Ed.* **2012,** *51,* 912–915. doi:10.1002/anie.201106198
3. Jin, Z.; Sun, W.; Ke, Y.; Shih, C.-J.; Paulus, G. L. C.; Wang, Q. H.; Mu, B.; Yin, P.; Strano, M. S. *Nat. Commun.* **2013,** *4,* No. 1663. doi:10.1038/ncomms2690
4. Sharma, J.; Chhabra, R.; Cheng, A.; Brownell, J.; Liu, Y.; Yan, H. *Science* **2009,** *323,* 112–116. doi:10.1126/science.1165831

5. Rinker, S.; Ke, Y.; Liu, Y.; Chhabra, R.; Yan, H. *Nat. Nanotechnol.* **2008,** *3,* 418–422. doi:10.1038/nnano.2008.164
6. Mangalum, A.; Rahman, M.; Norton, M. L. *J. Am. Chem. Soc.* **2013,** *135,* 2451–2454. doi:10.1021/ja312191a
7. Eskelinen, A.-P.; Kuzyk, A.; Kaltiaisenaho, T. K.; Timmermans, M. Y.; Nasibulin, A. G.; Kauppinen, E. I.; Törmä, P. *Small* **2011,** *7,* 746–750. doi:10.1002/smll.201001750
8. Zhao, Z.; Liu, Y.; Yan, H. *Org. Biomol. Chem.* **2013,** *11,* 596–598. doi:10.1039/c2ob26942b
9. Maune, H. T.; Han, S.-p..; Barish, R. D.; Bockrath, M.; Goddard, W. A., III; Rothemund, P. W.; Winfree, E. *Nat. Nanotechnol.* **2010,** *5,* 61–66. doi:10.1038/nnano.2009.311
10. Pearson, A. C.; Pound, E.; Woolley, A. T.; Linford, M. R.; Harb, J. N.; Davis, R. C. *Nano Lett.* **2011,** *11,* 1981–1987. doi:10.1021/nl200306w
11. Husale, B. S.; Sahoo, S.; Radenovic, A.; Traversi, F.; Annibale, P.; Kis, A. *Langmuir* **2010,** *26,* 18078–18082. doi:10.1021/la102518t
12. Shen, W.; Zhong, H.; Neff, D.; Norton, M. L. *J. Am. Chem. Soc.* **2009,** *131,* 6660–6661. doi:10.1021/ja901407j
13. Albrecht, B.; Hautzinger, D. S.; Krüger, M.; Elwenspoek, M.; Müller, K. M.; Korvink, J. G. Adsorption studies of DNA origami on silicon dioxide. In *Proceedings of the 21st Micromechanics and Micro systems Europe Workshop,* Enschede, The Netherlands, Sept 26–29, 2010; Abelmann, L.; Groenland, H.; van Honschoten, J.; Verputten, H., Eds.; University of Twente, Transducers Science and Technology: Enschede, The Netherlands; pp 153–156.
14. Ding, B.; Wu, H.; Xu, W.; Zhao, Z.; Liu, Y.; Yu, H.; Yan, H. *Nano Lett.* **2010,** *10,* 5065–5069. doi:10.1021/nl1033073
15. Goswami, N.; Giri, A.; Pal, S. K. *Langmuir* **2013,** *29,* 11471–11478. doi:10.1021/la4028578
16. Mak, K. F.; Lee, C.; Hone, J.; Shan, J.; Heinz, T. F. *Phys. Rev. Lett.* **2010,** *105,* 136805. doi:10.1103/PhysRevLett.105.136805
17. Radisavljevic, B.; Radenovic, A.; Brivio, J.; Giacometti, V.; Kis, A. *Nat. Nanotechnol.* **2011,** *6,* 147–150. doi:10.1038/nnano.2010.279
18. Zhu, C.; Zeng, Z.; Li, H.; Li, F.; Fan, C.; Zhang, H. *J. Am. Chem. Soc.* **2013,** *135,* 5998–6001. doi:10.1021/ja4019572
19. Liu, W.; Zhong, H.; Wang, R.; Seeman, N. C. *Angew. Chem., Int. Ed.* **2011,** *50,* 264–267. doi:10.1002/anie.201005911
20. Li, Y.; Xu, C.-Y.; Zhen, L. *Appl. Phys. Lett.* **2013,** *102,* 143110. doi:10.1063/1.4801844
21. Heckl, W. M.; Smith, D. P.; Binnig, G.; Klagges, H.; Hänsch, T. W.; Maddocks, J. *Proc. Natl. Acad. Sci. U. S. A.* **1991,** *88,* 8003–8005. doi:10.1073/pnas.88.18.8003
22. Xin, H.; Woolley, A. T. *J. Am. Chem. Soc.* **2003,** *125,* 8710–8711. doi:10.1021/ja035902p
23. Bissessur, R.; Wagner, B. D.; Brüning, R. *J. Mater. Sci.* **2004,** *39,* 119–125. doi:10.1023/B:JMSC.0000007735.51684.75
24. Cai, Y.; Zheng, H.; Ding, S.; Kropachev, K.; Schwaid, A. G.; Tang, Y.; Mu, H.; Wang, S.; Geacintov, N. E.; Zhang, Y.; Broyde, S. *Chem. Res. Toxicol.* **2013,** *26,* 1115–1125. doi:10.1021/tx400156a
25. Kropachev, K.; Kolbanovskiy, M.; Liu, Z.; Cai, Y.; Zhang, L.; Schwaid, A. G.; Kolbanovskiy, A.; Ding, S.; Amin, S.; Broyde, S.; Geacintov, N. E. *Chem. Res. Toxicol.* **2013,** *26,* 783–793. doi:10.1021/tx400080k
26. Mu, H.; Kropachev, K.; Chen, Y.; Zhang, H.; Cai, Y.; Geacintov, N. E.; Broyde, S. *Biochemistry* **2013,** *52,* 5517–5521. doi:10.1021/bi4009177
27. Cai, Y.; Ding, S.; Geacintov, N. E.; Broyde, S. *Chem. Res. Toxicol.* **2011,** *24,* 522–531. doi:10.1021/tx1004002
28. Horcas, I.; Fernández, R.; Gómez-Rodríguez, J. M.; Colchero, J.; Gómez-Herrero, J.; Baro, A. M. *Rev. Sci. Instrum.* **2007,** *78,* 013705. doi:10.1063/1.2432410

License and Terms

The definitive version of this article is the electronic one which can be found at:
doi:10.3762/bjnano.5.58

Beilstein Journal of Nanotechnology

CoPc and $CoPcF_{16}$ on gold: Site-specific charge-transfer processes

Fotini Petraki, Heiko Peisert*, Johannes Uihlein, Umut Aygül and Thomas Chassé

Full Research Paper

Open Access

Address:
Institute of Physical and Theoretical Chemistry, University of Tübingen, Auf der Morgenstelle 18, 72076 Tübingen, Germany

Email:
Heiko Peisert* - heiko.peisert@uni-tuebingen.de

* Corresponding author

Keywords:
Auger parameter; charge transfer; interfaces; organic semiconductors; photoemission; phthalocyanines; polarization screening

Beilstein J. Nanotechnol. **2014,** *5,* 524–531.
doi:10.3762/bjnano.5.61

Received: 04 February 2014
Accepted: 10 April 2014
Published: 25 April 2014

This article is part of the Thematic Series "Physics, chemistry and biology of functional nanostructures II".

Guest Editor: A. S. Sidorenko

Abstract

Interface properties of cobalt(II) phthalocyanine (CoPc) and cobalt(II) hexadecafluoro-phthalocyanine ($CoPcF_{16}$) to gold are investigated by photo-excited electron spectroscopies (X-ray photoemission spectroscopy (XPS), ultraviolet photoemission spectroscopy (UPS) and X-ray excited Auger electron spectroscopy (XAES)). It is shown that a bidirectional charge transfer determines the interface energetics for CoPc and $CoPcF_{16}$ on Au. Combined XPS and XAES measurements allow for the separation of chemical shifts based on different local charges at the considered atom caused by polarization effects. This facilitates a detailed discussion of energetic shifts of core level spectra. The data allow the discussion of site-specific charge-transfer processes.

Introduction

In order to develop and improve the performance of organic-based electronic devices an extended and comprehensive understanding of the basic physics appearing at the interface between organic and metallic materials is required. Molecules from the family of metal phthalocyanines have already been extensively applied to numerous molecular devices. In particular, opto-electronic devices such as light-emitting diodes, field-effect transistors, solar cells, and spintronic devices have been in the focus of research [1-4]. For several transition metal phthalocyanine (TMPc) layers on noble metal surfaces (e.g., Au and Ag) a charge transfer toward the central metal atom has been reported previously [5-13]. This affects the electronic and magnetic properties of the organic–metal interface and thus the performance of the molecular device. In the case of CoPc the open shell structure of Co can be easily affected by the presence of free electrons donated from a metallic substrate (e.g., Au, Ag) [6,7]. A complete description of the electronic situation and the energy level alignment at these interfaces must not only consider the observed metal-to-molecule charge transfer, but also other processes such as an adsorption-induced geometric

distortion of the molecules, a possible molecule-to-metal back transfer, or a combination of these two [13,14].

The fluorination of phthalocyanines represents an ideal route for the tuning of the ionization potential (IP), a basic electronic parameter which can significantly affect the interface dipole and thus the energy level alignment [15,16]. In the context of applications, perfluorinated counterparts of Pcs have demonstrated a high performance and stability in air and are used as n-type channels in electronic devices [17,18]. It is interesting to see whether and how the fluorination of the molecules affects possible charge-transfer (or back-transfer) processes occurring at interfaces to metallic substrates. For the perfluorinated phthalocyanine $ZnPcF_{16}$ on gold no evidence for a charge transfer between the central metal atom of the molecule and the substrate was observed, even if a charge-transfer screening of the Zn LMM Auger final state evidences an overlap of the wave functions of Zn with those of the Au substrate [19]. On the other hand, for perfluorinated $CoPcF_{16}$ on Au(100) or Ag(111) an adsorption induced charge transfer including the central metal atom of the Pc is reported, pointing to a more complex interaction mechanism [13,20]. The aim of the present work is a more comprehensive study of the interfacial charge transfer between CoPc or $CoPcF_{16}$ and metals by using core level X-ray photoemission spectroscopy (XPS), X-ray excited Auger electron spectroscopy (XAES), valence band ultraviolet photoemission spectroscopy (UPS) as well as X-ray absorption spectroscopy (XAS). Combined XPS and XAES measurements can be employed as a tool to study the contribution of the polarization energy to chemical shifts at interfaces. XAS gives valuable information about the unoccupied electronic structure and the hybridization of molecular levels at the interface (see, e.g., [21]).

Results and Discussion

Charge transfer to the central metal atom of the Pc

First we discuss Co $2p_{3/2}$ XPS core level spectra of $CoPcF_{16}$ on polycrystalline Au as a function of the film thickness (Figure 1). The spectra on single crystalline Au(100) are very similar (see Supporting Information File 1). A distinct difference of the shape of the line is observed going from the interface to the bulk. A new peak appears at the low binding energy side at low coverage, the energy shift of which is about 2.3 eV with respect to the peaks for thicker, more bulk-like films. In addition, the shape of the spectrum changes for coverage in the monolayer range. In general, the shape of the Co 2p spectrum is determined by satellite features at higher binding energies arising from multiplet splitting due to the interaction of unpaired electrons in the photoemission final state. Therefore, a change of the spectral shape can be attributed to (i) an electron transfer from the metal surface, leading to a reduction of the Co(II) ion to Co(I), (ii) by a redistribution of the d-electrons, or both (i) and (ii). Both the appearance of an interface component and the change of the satellite structure at the interface were previously observed for the CoPc and related compounds on several metal surfaces [6,7,12,22]. Both phenomena reveal a change of the electronic configuration of the Co atoms at the interface by charge-transfer mechanisms. Taking into account a comparison of, e.g., CoPc on Au(100) and Ag(111), the detailed electronic situation might depend on the substrate under consideration [7]. In all cases the results indicate that an electron is transferred from the substrate to the Co atom of CoPc or $CoPcF_{16}$.

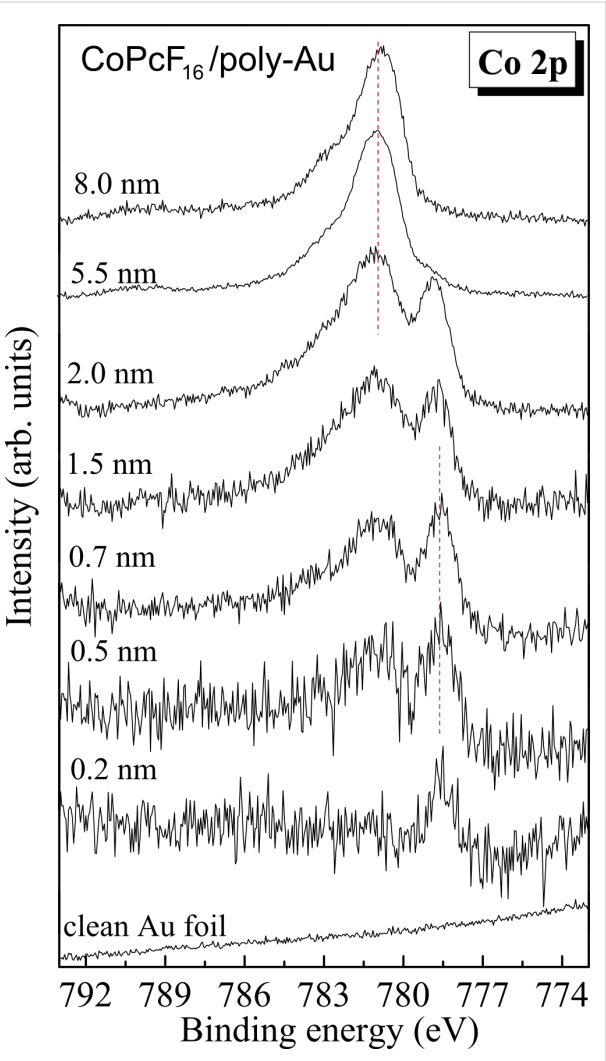

Figure 1: $CoPcF_{16}$ on polycrystalline (poly-) Au: Co 2p core-level photoemission spectra (XPS, Al Kα) with increasing $CoPcF_{16}$ film thickness on gold foil.

Polarization effects at the interface

Generally, the underlying reasons for energetic shifts in photoemission are complex. It is important to distinguish between a

variation of the local charge at the considered atom and a different ability for a polarization screening of the environment. Combined X-ray photoemission spectroscopy (XPS) and X-ray excited Auger electron spectroscopy (XAES) can be used as a tool to study the screening mechanism of holes at organic interfaces [19,23-25]. The different final states in XPS (one hole) and XAES (two holes) cause different binding energy (E_B) shifts. Frequently, for the analysis of these shifts the change of the modified Auger parameter α' is monitored according to $\Delta\alpha' = \Delta E_B(\text{XPS}) + \Delta E_{kin}(\text{XAES})$ (E_{kin} corresponds to the kinetic energy). On the other hand, the modified Auger parameter α' is correlated to the dynamical or one-hole relaxation energy R_D ($\Delta\alpha' \approx 2 \cdot \Delta R_D$) and thus to the electronic polarization P. We note, however, that the discovery is hindered for the central metal atom of the TMPcs due to (i) an extra-molecular charge transfer within the time scale of the Auger-process or (ii) the change of the multiplet structure of the spectrum caused by charge-transfer processes in the initial state [5,19]. On the other hand, in case of fluorinated Pcs the absence of a local charge transfer process at the fluorine atom allows the estimation of the polarization screening via the corresponding Auger parameter [19].

In Figure 2 we discuss F 1s core level spectra (Figure 2a) and F KLL Auger spectra (Figure 2b) for different film thicknesses of $CoPcF_{16}$ on Au foil. Whereas the F 1s XPS core level spectra in Figure 2a show almost no change in the spectral shape and energetic position (+/− 0.1 eV) with increasing film thickness, the corresponding Auger spectra (Figure 2b) exhibit a significant energetic shift of about 0.7 eV toward lower kinetic energies. This points to the presence of polarization effects at the interface even if the photoemission spectrum shows no change. For a more detailed analysis the modified Auger parameter α´ for fluorine ($\alpha' = E_B(\text{F 1s}) + E_K(\text{F KLL})$) during the formation of the interface is plotted in Figure 3. Up to 5.5 nm a change of α´of about 0.7 eV (+/− 0.2 eV) occurs, which corresponds to ΔR_D = 0.35 eV (+/− 0.1 eV). According to a previous study, where a dielectric continuum model for $ZnPcF_{16}$ was applied [19], such values of the relaxation energy are reasonable for the first few organic layers and can be understood by polarization screening [26]. Thus, a small shift (0.3–0.4 eV) toward lower binding energies might be expected for all core levels at the interface compared to the bulk value. The question therefore arises why an energetic shift of F 1s to lower binding energies at the interface to Au is hardly observable.

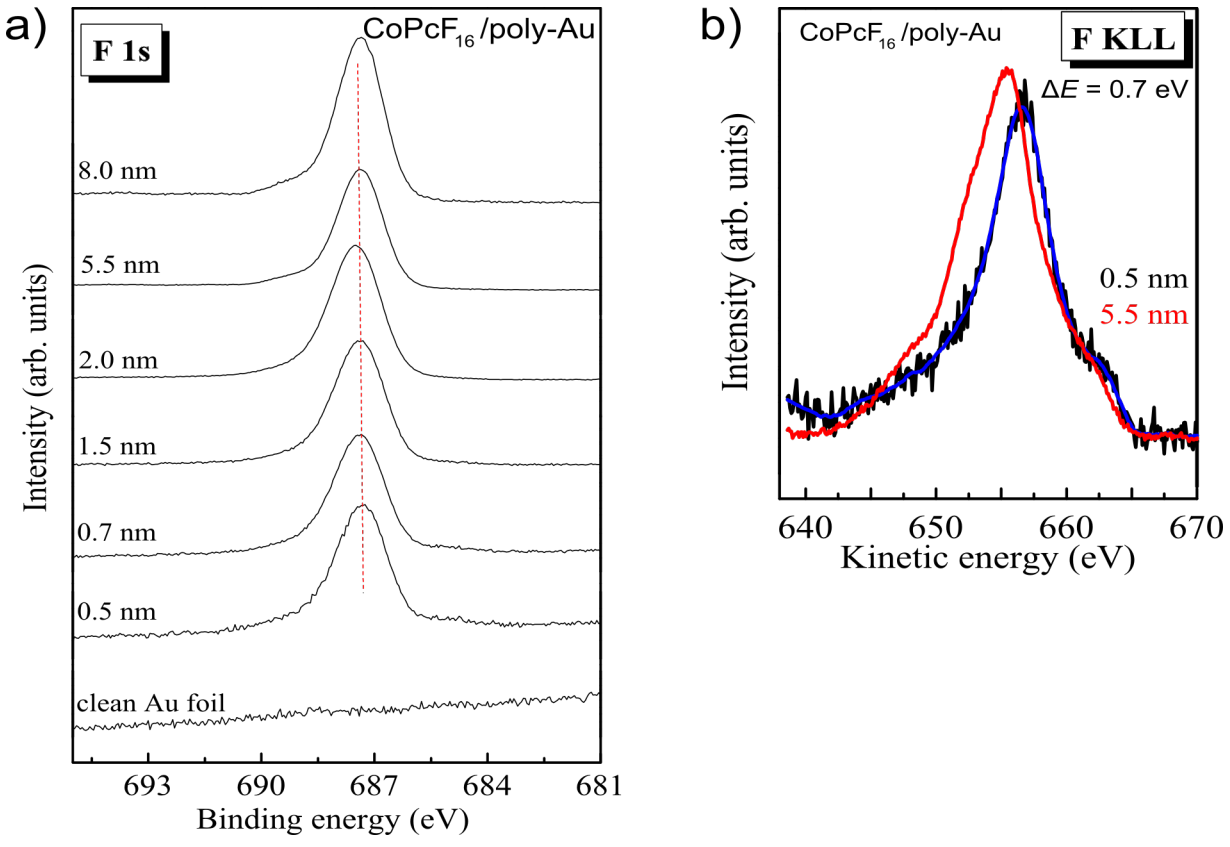

Figure 2: $CoPcF_{16}$ on polycrystalline (poly-) Au: (a) F 1s core level spectra and (b) F KLL Auger spectra during the interface formation.

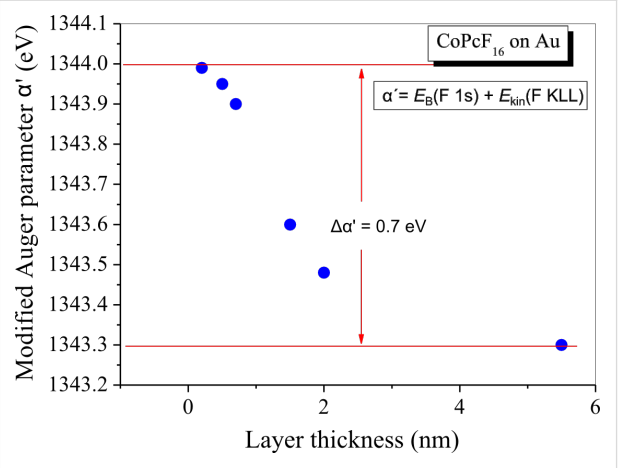

Figure 3: $CoPcF_{16}$ on polycrystalline Au: Modified Auger parameter α' for fluorine.

Bidirectional charge transfer

In order to understand the polarization and charge-transfer processes for the $CoPcF_{16}$ macrocycle at the interface to poly-Au in more detail, we analyzed the energetic shifts of all core level lines of F 1s, N 1s and C 1s in Figure 4. The data were compared to CoPc/Au. Generally, only small changes of less than 0.4 eV could be observed for a $CoPcF_{16}$ coverage of up to 2 nm. This might be expected for a polarization screening at the interface. On the other hand, it is visible from this figure that the core level spectra of different atoms directly at the interface (and up to 2 nm of film thickness) are shifted by different amounts. A shift of about 0.2 eV to a higher binding energy (E_B) from the interface (about monolayer) to 2 nm thickness may be observed for the electronegative fluorine and nitrogen in $CoPcF_{16}$, while the carbon peak shift <0.1 eV is hardly recognizable. With increasing film thickness the N 1s shift increases to ≈0.3 eV, while both F 1s and C 1s exhibit total shifts of only ≈0.1 eV. This unequal behavior can be explained by (i) a different polarization screening for each atom at the interface or (ii) a superposition of chemical shifts and polarization screening at the interface. A different polarization screening may arise from a bending of the molecule at the interface accompanied with different distances for each atom from the substrate surface as suggested for $CuPcF_{16}$ on Cu(111) and Ag(111) [27]. However, the increase of the distance of fluorine on these systems is less than 0.03 nm and thus the expected change of the polarization screening is rather small (less than 0.08 eV [19]). Also, we rule out radiation damage since the shape of the Carbon 1s XPS spectrum is independent on the radiation exposure and film thickness. Thus, we conclude that chemical shifts toward higher binding energies compensate (partly) the expected (physical) shifts toward lower binding energies due to polarization screening. The chemical shift to higher binding energies, most clearly visible for F and C, implies that the phthalocyanine macrocycle is positively charged compared to molecules in the bulk. This means, while we observe an electron transfer to Co of $CoPcF_{16}$, an opposite charge transfer is observed between the macrocycle of the molecule and the substrate, i.e., the charge transfer is bidirectional as observed for related systems [12,14,28]. Moreover, from the different energetic shifts we can conclude that the negative charge resides in the inner part of the molecule, whereas positive charges are observed primarily in the outer part – in the case of fluorine, the atoms are "less negatively" charged compared to the bulk.

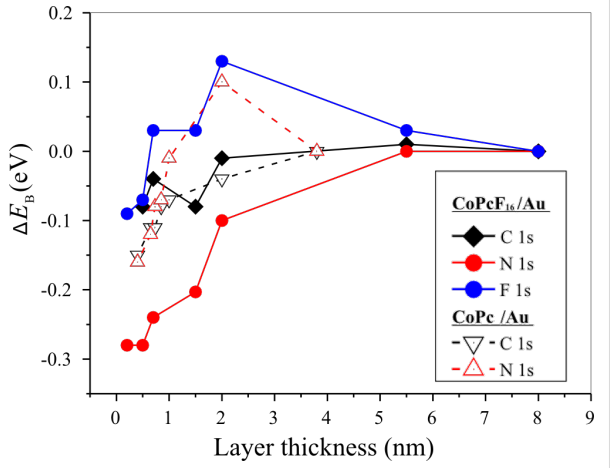

Figure 4: Comparison of energetic core level shifts as a function of the organic film thickness for $CoPcF_{16}$ and CoPc on polycrystalline Au.

For a strongly related system, namely $CoPcF_{16}$ on Au(100), X-ray absorption spectroscopy measurements at the fluorine K-edge show that the electron density can change at the fluorine site. Since XAS probes transitions from occupied into unoccupied valence states information about the unoccupied electronic structure is accessible. In Figure 5 we compare F K-edge spectra for two different film thicknesses acquired at a grazing and at a normal incidence of radiation. From N K absorption spectra (data not shown) we conclude that the molecules are flat lying on the substrate surface, thereby being in good agreement with related phthalocyanine films on single crystalline metal surfaces (see, e.g., [29]). Consequently, we observe transitions in the molecular plane at a normal incidence and transitions perpendicular to the molecular plane are probed at a grazing incidence (out of plane). The assignment of the two prominent features at photon energies of about 688 and 693 eV is complicated. It was reported that resonances in π* orbitals overlap in energy with σ* resonances at only slightly higher energies but with a much larger intensity. This results in a reversed linear dichroism of F K-edge XAS spectra compared to N or C K-edge spectra [30]. The presence of angular dependent π* and σ* transitions indicates that fluorine atoms partici-

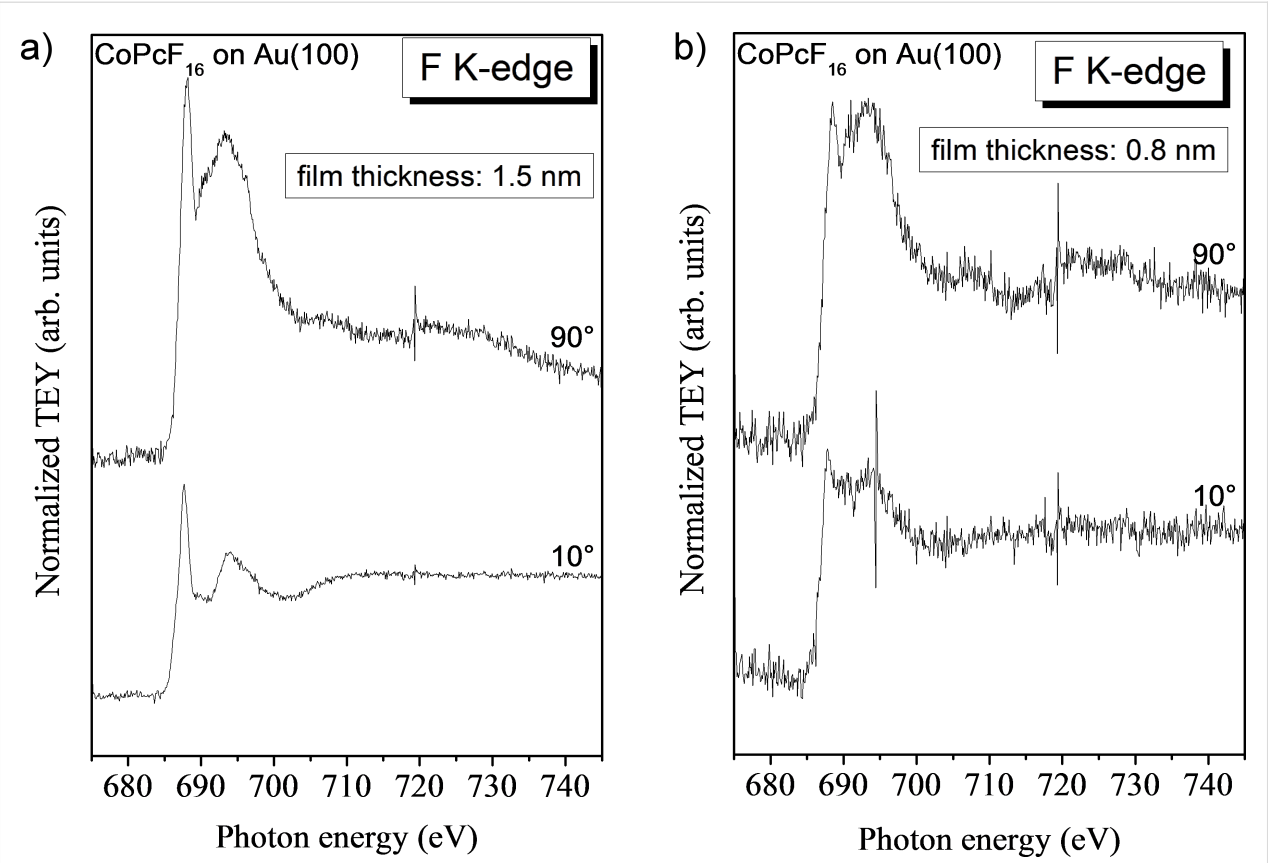

Figure 5: Angle dependent F K-edge XAS spectra for (a) 1.5 nm $CoPcF_{16}$ on Au(100) and (b) 0.8 nm $CoPcF_{16}$on Au(100). The different peak shape in both cases indicates a different electron distribution at the interface.

pate in the conjugated π system. Comparing spectra from the thick film in Figure 5a to spectra at a lower coverage of about 0.8 nm (approximately 2 monolayers, Figure 5b), it is clearly visible that the shape of the spectra is changed, indicating a different electron distribution at the fluorine atom at the interface.

The results show that only the consideration of several charge-transfer processes resulting in an inhomogeneous distribution of transferred charges may sufficiently explain "macroscopic" electronic interface properties such as the size of dipoles. The formation of interface dipoles can be monitored by work function (Φ) measurements, where a change of Φ at the interface indicates the formation of an interface dipole. Figure 6 displays the development of the work function determined by using UPS as a function of the $CoPcF_{16}$ thickness on gold. The corresponding values for the CoPc–Au interface studied previously [6] were added for comparison. A strong decrease of the work function occurs for the very first steps of the deposition on both interfaces, relating to coverage in the monolayer range. Such potential drops at the interface can be attributed to a modification of the work function of gold upon adsorption of molecules due to the push back of the electron cloud of the metallic substrate. The extent of the changes of the work function caused by an adsorption of molecules (often also called Pauli repulsion or pillow effect) is considered a controversial issue, but for several systems values in the order of ≈0.3 eV are found [31-34]. Therefore, it seems that further processes contribute to the potential change at the interface, including charge transfer across the interface and intramolecular charge transfer. These effects seem to be remarkably similar for both types of molecules in the initial stage of adsorption. For thicker layers beyond ≈1 nm the behavior of the work function between the two interfaces changes, and with the development of bulk-like PC films beyond ≈2 nm (Δ) approaches to saturation levels. In the case of CoPc a total decrease of the work function of approximately 1.1 eV leads to a work function equal to 4.20 ± 0.1 eV for a thick (about 4 nm) CoPc layer. In case of $CoPcF_{16}$ after the monolayer coverage there is a tendency of the work function toward higher values, reaching a plateau at about 5.50 ± 0.1 eV. Recently calculated energy level diagrams predict molecular HOMO (LUMO) energies of about −5.3 eV (−3.1 eV) and −6.7 eV (−4.5 eV) for CoPc and $CoPcF_{16}$, respectively [35]. The difference of, e.g., calculated HOMO energies of 1.4 eV

fits well to the observed work function difference of 1.3 eV. This implies that the related energy shifts with respect to the Au Fermi level are driven by the adjustment of chemical potentials to equilibrium at the interface between the metal substrate and the formed phthalocyanine film. A downward (upward) energy shift arises at the interface due to the location of the E_F or the midgap energy for free molecules above (below) the Fermi level of the metal substrate [35]. Therefore, a corresponding negative (positive) vacuum level shift strongly sustains an electron flow from the molecule (substrate) to the substrate (molecule) for CoPc/Au ($CoPcF_{16}$/Au). We conclude that there is a positive total charge on CoPc at the established gold interface, whereas there only is a rather weak negative charge on the organic side in the case of $CoPcF_{16}$ on Au. However, taking into account the charge transfer from gold to Co (see above), the macrocycle of the Pc must be positively charged in both cases: For $CoPcF_{16}$ the dipoles related to positive (macrocycle) and negative charge transfer (Co) virtually compensate, whereas in the case of CoPc the positive charge transfer even exceeds the negative charge transfer. This is also reflected in the shifts of the binding energy of the respective core levels in Figure 4. In general, the observed binding energy shifts for C 1s and F 1s at the interface are lower than expected hinting at a positively charged macrocycle in both cases (see above). The binding energy of N 1s for $CoPcF_{16}$ is decreased by about 0.3 eV matching the expectations of the polarization screening. In the case of CoPc the shift of N 1s is partly overwhelmed by a chemical shift due to a positive charge transfer. This points to a higher positive charge at the N sites in the case of CoPc.

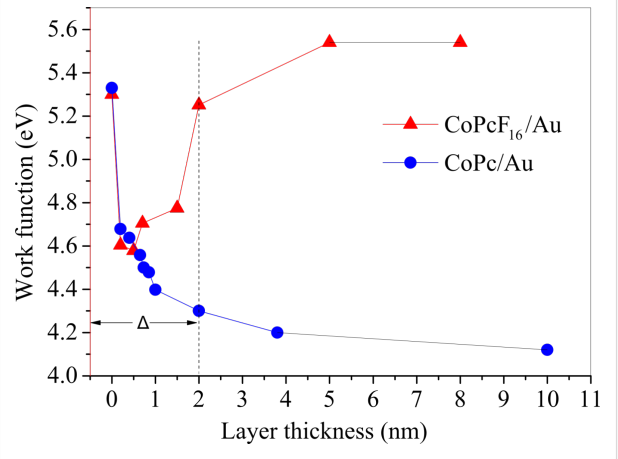

Figure 6: Energetic shift of the work function determined from the high binding energy cut-off in UPS spectra as a function of the film thickness for $CoPcF_{16}$ and CoPc on polycrystalline Au. The observed shift is attributed to the formation of an interfacial dipole Δ.

The development of the work function as a function of the film thickness for CoPc and $CoPcF_{16}$ on Au as well as the energy level alignment is in remarkable agreement to other Pcs such as CuPc/$CuPcF_{16}$ [16] or ZnPc/$ZnPcF_{16}$ [19] even if the charge transfer to the respective central metal atom is clearly different (no charge transfer was observed for ZnPc/$ZnPcF_{16}$ [19]). It seems that the charge on the macrocycle of the Pc can compensate possible local charge transfer processes between the central metal atom of the Pc and the substrate adjusting the interface energetics.

Conclusion

Combined photoemission spectroscopy and X-ray excited Auger electron spectroscopy was used as a tool to study the screening mechanism of holes at organic interfaces. This allows for the discrimination between chemical shifts due to a different local charge at the considered atom and polarization effects, thereby facilitating a detailed discussion of the energetic shifts of core level spectra. The Co 2p XPS spectral change reveals a strong charge donation from the underlying metal to the Co-atoms of the phthalocyanine. On the other hand, binding energy shifts of core level spectra representative for the Pc macrocycle point to an opposite charge transfer. The detailed analysis indicates that the positive charge is differently distributed over the Pc macrocycle. Together with UPS data we have shown that a bidirectional charge transfer determines the interface energetics for CoPc and $CoPcF_{16}$ on Au.

Experimental

X-ray photoemission spectroscopy (XPS), ultraviolet photoemission spectroscopy (UPS) and X-ray excited Auger electron spectroscopy (XAES) measurements were performed by using a multichamber UHV-system (base pressure 2×10^{-10} mbar), equipped with a Phoibos 150 cylindrical hemispherical analyzer (SPECS), a monochromatic Al Kα source, and a high-flux He discharge lamp (UVS 300, SPECS). The energetic resolution determined from the width of the Fermi edge for XPS and UPS was about 400 meV and 100 meV, respectively. The binding energy (E_B) scale of the spectra was calibrated to reproduce the E_B of Au $4f_{7/2}$ (84.0 eV), Ag $3d_{5/2}$ (368.3 eV) and Cu $2p_{3/2}$ (932.5 eV). The cleanliness of the Au substrate was checked by XPS. Thin films of $CoPcF_{16}$ (purchased from Aldrich) were thermally evaporated on the substrate in an ultra-high vacuum (base pressure $<1 \times 10^{-8}$ mbar) from a temperature-controlled evaporation cell. The thickness of the organic films ranged from sub-monolayer to about 100 Å and was determined by the attenuation of the intensity of the Au 4f substrate peaks in photoemission.

X-ray absorption (XAS) measurements were carried out at the third generation synchrotron radiation source BESSY II (Berlin) by using the Optics-beamline and the end-station SurICat. XAS spectra were acquired in total-electron yield (TEY) mode.

Supporting Information

Supporting Information File 1

Co 2p core-level photoemission spectra.
[http://www.beilstein-journals.org/bjnano/content/supplementary/2190-4286-5-61-S1.pdf]

Acknowledgements

The work was supported by the German Research Council Ch 132/20-2. We thank A. Vollmer (BESSY II) for valuable discussion and W. Neu (University Tübingen) as well as M. Bauer (BESSY II) for technical support. We acknowledge the Helmholtz Zentrum Berlin GmbH, Elektronenspeicherring BESSY II for providing synchrotron radiation at the Optics beamline. Financial travel support by the Helmholtz Zentrum Berlin GmbH is gratefully acknowledged.

References

1. Walzer, K.; Maennig, B.; Pfeiffer, M.; Leo, K. *Chem. Rev.* **2007,** *107,* 1233–1271. doi:10.1021/cr050156n
2. Martínez-Díaz, M. V.; de la Torre, G.; Torres, T. *Chem. Commun.* **2010,** *46,* 7090–7108. doi:10.1039/c0cc02213f
3. Cinchetti, M.; Heimer, K.; Wüstenberg, J.-P.; Andreyev, O.; Bauer, M.; Lach, S.; Ziegler, C.; Gao, Y.; Aeschlimann, M. *Nat. Mater.* **2009,** *8,* 115–119. doi:10.1038/nmat2334
4. Bogani, L.; Wernsdorfer, W. *Nat. Mater.* **2008,** *7,* 179–186. doi:10.1038/nmat2133
5. Petraki, F.; Peisert, H.; Biswas, I.; Aygül, U.; Latteyer, F.; Vollmer, A.; Chassé, T. *J. Phys. Chem. Lett.* **2010,** *1,* 3380–3384. doi:10.1021/jz101395s
6. Petraki, F.; Peisert, H.; Biswas, I.; Chassé, T. *J. Phys. Chem. C* **2010,** *114,* 17638–17643. doi:10.1021/jp104141s
7. Petraki, F.; Peisert, H.; Latteyer, F.; Aygül, U.; Vollmer, A.; Chassé, T. *J. Phys. Chem. C* **2011,** *115,* 21334–21340. doi:10.1021/jp207568q
8. Petraki, F.; Peisert, H.; Aygül, U.; Latteyer, F.; Uihlein, J.; Vollmer, A.; Chassé, T. *J. Phys. Chem. C* **2012,** *116,* 11110–11116. doi:10.1021/jp302233e
9. Petraki, F.; Peisert, H.; Hoffmann, P.; Uihlein, J.; Knupfer, M.; Chassé, T. *J. Phys. Chem. C* **2012,** *116,* 5121–5127. doi:10.1021/jp211445n
10. Betti, M. G.; Gargiani, P.; Frisenda, R.; Biagi, R.; Cossaro, A.; Verdini, A.; Floreano, L.; Mariani, C. *J. Phys. Chem. C* **2010,** *114,* 21638–21644. doi:10.1021/jp108734u
11. Gargiani, P.; Rossi, G.; Biagi, R.; Corradini, V.; Pedio, M.; Fortuna, S.; Calzolari, A.; Fabris, S.; Cezar, J. C.; Brookes, N. B.; Betti, M. G. *Phys. Rev. B* **2013,** *87,* 165407. doi:10.1103/PhysRevB.87.165407
12. Lindner, S.; Treske, U.; Knupfer, M. *Appl. Surf. Sci.* **2013,** *267,* 62–65. doi:10.1016/j.apsusc.2012.06.104
13. Toader, M.; Shukrynau, P.; Knupfer, M.; Zahn, D. R. T.; Hietschold, M. *Langmuir* **2012,** *28,* 13325–13330. doi:10.1021/la302792z
14. Romaner, L.; Heimel, G.; Brédas, J.-L.; Gerlach, A.; Schreiber, F.; Johnson, R. L.; Zegenhagen, J.; Duhm, S.; Koch, N.; Zojer, E. *Phys. Rev. Lett.* **2007,** *99,* 256801. doi:10.1103/PhysRevLett.99.256801
15. Peisert, H.; Knupfer, M.; Fink, J. *Surf. Sci.* **2002,** *515,* 491–498. doi:10.1016/S0039-6028(02)01967-2
16. Peisert, H.; Knupfer, M.; Schwieger, T.; Fuentes, G. G.; Olligs, D.; Fink, J.; Schmidt, T. *J. Appl. Phys.* **2003,** *93,* 9683–9692. doi:10.1063/1.1577223
17. Brinkmann, H.; Kelting, C.; Makarov, S.; Tsaryova, O.; Schnurpfeil, G.; Wöhrle, D.; Schlettwein, D. *Phys. Status Solidi A* **2008,** *205,* 409–420. doi:10.1002/pssa.200723391
18. Ling, M.-M.; Bao, Z. *Org. Electron.* **2006,** *7,* 568–575. doi:10.1016/j.orgel.2006.09.003
19. Peisert, H.; Kolacyak, D.; Chassé, T. *J. Phys. Chem. C* **2009,** *113,* 19244–19250. doi:10.1021/jp9057548
20. Lindner, S.; Treske, U.; Grobosch, M.; Knupfer, M. *Appl. Phys. A* **2011,** *105,* 921–925. doi:10.1007/s00339-011-6648-x
21. Uihlein, J.; Peisert, H.; Glaser, M.; Polek, M.; Adler, H.; Petraki, F.; Ovsyannikov, R.; Bauer, M.; Chassé, T. *J. Chem. Phys.* **2013,** *138,* 081101. doi:10.1063/1.4793523
22. Lukasczyk, T.; Flechtner, K.; Merte, L. R.; Jux, N.; Maier, F.; Gottfried, J. M.; Steinrück, H.-P. *J. Phys. Chem. C* **2007,** *111,* 3090–3098. doi:10.1021/jp0652345
23. Kaindl, G.; Chiang, T.-C.; Eastman, D. E.; Himpsel, F. J. *Phys. Rev. Lett.* **1980,** *45,* 1808–1811. doi:10.1103/PhysRevLett.45.1808
24. Moretti, G. *Surf. Sci.* **2013,** *618,* 3–11. doi:10.1016/j.susc.2013.09.009
25. Kolacyak, D.; Peisert, H.; Chassé, T. *Appl. Phys. A* **2009,** *95,* 173–178. doi:10.1007/s00339-008-5003-3
26. Helander, M. G.; Greiner, M. T.; Wang, Z. B.; Lu, Z. H. *Phys. Rev. B* **2010,** *81,* 153308. doi:10.1103/PhysRevB.81.153308
27. Gerlach, A.; Schreiber, F.; Sellner, S.; Dosch, H.; Vartanyants, I. A.; Cowie, B. C. C.; Lee, T.-L.; Zegenhagen, J. *Phys. Rev. B* **2005,** *71,* 205425. doi:10.1103/PhysRevB.71.205425
28. Huang, Y. L.; Wruss, E.; Egger, D. A.; Kera, S.; Ueno, N.; Saidi, W.; Bucko, T.; Wee, A. T. S.; Zojer, E. *Molecules* **2014,** *19,* 2969–2992. doi:10.3390/molecules19032969
29. Peisert, H.; Biswas, I.; Knupfer, M.; Chassé, T. *Phys. Status Solidi B* **2009,** *246,* 1529–1545. doi:10.1002/pssb.200945051
30. de Oteyza, D. G.; Sakko, A.; El-Sayed, A.; Goiri, E.; Floreano, L.; Cossaro, A.; Garcia-Lastra, J. M.; Rubio, A.; Ortega, J. E. *Phys. Rev. B* **2012,** *86,* 075469. doi:10.1103/PhysRevB.86.075469
31. Peisert, H.; Knupfer, M.; Fink, J. *Appl. Phys. Lett.* **2002,** *81,* 2400–2402. doi:10.1063/1.1509472
32. Yamane, H.; Yoshimura, D.; Kawabe, E.; Sumii, R.; Kanai, K.; Ouchi, Y.; Ueno, N.; Seki, K. *Phys. Rev. B* **2007,** *76,* 165436. doi:10.1103/PhysRevB.76.165436
33. Vázquez, H.; Dappe, Y. J.; Ortega, J.; Flores, F. *J. Chem. Phys.* **2007,** *126,* 144703. doi:10.1063/1.2717165
34. Betti, M. G.; Kanjilal, A.; Mariani, C.; Vázquez, H.; Dappe, Y. J.; Ortega, J.; Flores, F. *Phys. Rev. Lett.* **2008,** *100,* 027601. doi:10.1103/PhysRevLett.100.027601
35. Toader, M.; Gopakumar, T. G.; Shukrynau, P.; Hietschold, M. *J. Phys. Chem. C* **2010,** *114,* 21548–21554. doi:10.1021/jp1078295

Beilstein Journal of Nanotechnology

An ultrasonic technology for production of antibacterial nanomaterials and their coating on textiles

Anna V. Abramova*[1], Vladimir O. Abramov[1], Aharon Gedanken[2], Ilana Perelshtein[2] and Vadim M. Bayazitov[1]

Full Research Paper

Open Access

Address:
[1]Institute of general and inorganic chemistry of the Russian Academy of Sciences, Leninskiy prospect 31, Moscow, 119991, Russian Federation and [2]Department of Chemistry, Bar Ilan University, Ramat-Gan, 52900, Israel

Email:
Anna V. Abramova* - anna_v_abramova@mail.ru

* Corresponding author

Keywords:
antibacterial textile; cavitation; electrical discharge in liquid; nanoparticle; ultrasound

Beilstein J. Nanotechnol. **2014,** *5,* 532–536.
doi:10.3762/bjnano.5.62

Received: 02 December 2013
Accepted: 14 March 2014
Published: 28 April 2014

This article is part of the Thematic Series "Physics, chemistry and biology of functional nanostructures II".

Guest Editor: A. S. Sidorenko

Abstract

A method for the production of antibacterial ZnO nanoparticles has been developed. The technique combines passing an electric current with simultaneous application of ultrasonic waves. By using high-power ultrasound a cavitation zone is created between two zinc electrodes. This leads to the possibility to create a spatial electrical discharge in water. Creation of such discharge leads to the depletion of the electrodes and the formation of ZnO nanoparticles, which demonstrate antibacterial properties. At the end of this reaction the suspension of ZnO nanoparticles is transported to a specially developed ultrasonic reactor, in which the nanoparticles are deposited on the textile. The nanoparticles are embedded into the fibres by the cavitation jets, which are formed by asymmetrically collapsing bubbles in the presence of a solid surface and are directed towards the surface of textile at very high velocities. Fabrics coated with ZnO nanoparticles by using the developed method showed good antibacterial activity against *E. coli*.

Introduction

Currently, the problem of nosocomial (acquired in hospitals) infections becomes more and more urgent. About 5–10% of all patients in hospitals are affected by them. Hospital-acquired infections are one of the ten most frequent causes of death. The economic loss caused by nosocomial infections is significant. In the Russian Federation it may reach 10–15 billion RUB per year (conservative estimation). For comparison, the annual economic impact of nosocomial infections in Europe is around 7 billion EUR and in the US about 6.5 billion USD. Hospital-acquired infections significantly reduce the life quality of the patients of life and lead to a loss of reputation for the hospital [1]. In order to reduce the hospital acquired infections, the staff sterilizes surfaces, employs hygiene measures and minimizes contacts between patients. However, reusable textiles such as the patients linen or the doctor robes remain a significant source of infection. To ameliorate the problem one could replace reusable

textiles with disposable items. But this is quite expensive. Another more promising approach is to use antibacterial textiles. In this case it is very important to ensure the preservation of the antibacterial properties after washing. Antimicrobial textiles can be produced by coating textiles with antibacterial nanoparticles (NPs). NPs such as zinc oxide NPs are known to have antibacterial properties due to $OH^{\bullet}$ radicals, which result from defects in their crystal structure [2].

In the case of power ultrasound, cavitation bubbles emerge when the cavitation threshold is exceeded. A sonochemical reaction happening upon the collapse of the acoustic bubble yields a product having nanometric size. The rapidly moving surface of the cavitation bubble, the dynamics of which determines the main characteristics of the coating process, accelerates the nanoparticles. Due to the asymmetric collapse of the bubble and the formation of liquid jets in the presence of a solid surface, the formed jets push the nanoparticles towards the surface at very high velocities (larger than 500 m/s). Scientists at Bar Ilan University [3] demonstrated this deposition technique for the first time by coating submicron silica spheres with Ni nanoparticles. Using this technique antibacterial ZnO or other metallic oxide NPs can be embedded into the textile. The nanoparticles can be produced in a sonochemical reaction described elsewhere [2,3], but on an industrial scale this method requires large amounts of ethanol, whose vapours are dangerous to people and the environment. Thus the goal of the current research is to produce an aqueous suspension of ZnO NPs directly before their introduction into the fibres, deposit them on textile samples and analyse the antibacterial properties of the samples comparing their antibacterial activity and the antibacterial activity of samples coated with industrially produced NPs.

In the research described in this paper we produced a suspension of zinc oxide NPs in water by using a sonoplasma discharge between two Zn electrodes in water. Preliminary experiments have shown that if ultrasonic vibrations are applied to an electrode while an arc discharge is created in polar fluids a new form of an electrical discharge, a spatial sonoplasma discharge, is formed [4,5]. It is a form of a quasi-spatial discharge in liquid, formed in the gap between the electrodes where the ultrasonic vibrations lead to the formation of cavitation bubbles. If certain parameters of the electrical circuit and certain intensity of the ultrasonic field are achieved, the plasma discharge can be formed in the whole volume of the bubbly liquid between the electrodes. The experiments also revealed that the sonoplasma discharge is characterized by a glow in the whole volume of the liquid and an increasing current–voltage characteristic, which is typical for the abnormal glow discharge. Arc discharges in aqueous electrolytes, which are widely used in the industry, are the best known type of a stationary plasma discharge in liquids [6]. Currently this discharge is applied in physical and chemical studies and in the synthesis of different materials, but due to small effective volume of the discharge zone the rate of the processes is quite low. The use a spatial sonoplasma discharge can accelerate the speed of this process.

The current paper reports on the experimental production of ZnO NPs by oxidation of the Zn electrodes induced by the sonoplasma discharge. In continuation of this research a sonication machine for the treatment of textiles in a roll-to-roll mode [7] of operation was used to coat cotton fabrics with ZnO NPs. The testing results of the antibacterial activity of the coated fabric samples are reported and compared with the antibacterial activity of the fabric coated by using the same ultrasonic method [2,7-9] with industrially produced ZnO NPs.

Experimental

We have built the experimental setup [10] shown in Figure 1 to study the possibility of producing ZnO NPs in a sonoplasma discharge in water. The setup contained a reactor (1) with a working volume of 1 LS. Zinc electrodes (2) were introduced into the reactor. The upper electrode was simultaneously an emitter of the oscillation system, which contained also a waveguide and an ultrasonic transducer. An ultrasonic generator (4) powered the transducer. The electrodes were connected to the power supply of the sonoplasma discharge (5). The setup also contained rod electrodes (3) to initiate the arc discharge, which were connected to their own power supply (7). Gaseous reaction products were accumulated in a special gas collector (6).

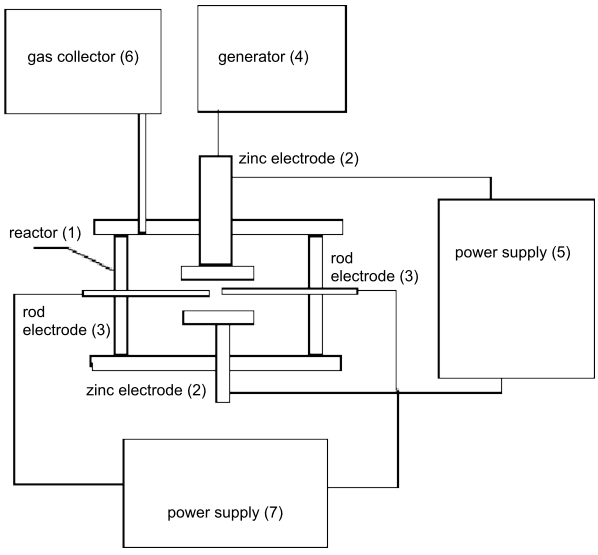

Figure 1: Block diagram of the experimental setup for the production of ZnO NPs in a sonoplasma discharge.

The output of acoustical power of the system was 2.0 kW, the working frequency of the transducer and waveguide was 18 kHz. The parameters of acoustical equipment allowed for reaching an intensity of ultrasonic radiation of 10 W/cm^2 in the liquid. We have used a capacitor C_1 as the power supply of the sonoplasma discharge. The discharge was initiated by a high voltage pulse in the secondary winding of the transformer TH1. The pulse was initiated by a controlled discharge of the capacitor C_2, which was connected to the primary winding of the transformer. The capacitor C_2 was charged by a voltage of 5–10 kV, the transformer ratio of TH1 was 4:1. We have used a heat exchanger to maintain the operating temperature of 60 °C. The experimental production of ZnO NPs was done as follows: We switched on the ultrasonic generator to create a cavitation zone between the electrodes. Then we switched on the discharger that commutes capacitor C_2 to the primary winding of the pulse transformer. The voltage pulse occurring on the secondary winding induced an electrical discharge in the gap between the electrodes in the reactor. The induced discharge was maintained by the capacitor C_1 charged to a voltage of 400 V. During such work of the setup we produced a suspension of ZnO NPs in the reactor.

We have studied the morphology of the structure, the chemical and phase composition of the settled NPs using an electron microscope (CAM SCAN S2) and an X-ray spectral microanalyzer. Studies of the particle size distribution were carried out by using DLS measurements. X-ray diffraction was performed on the diffractometer "AMUR-K". The instrument was equipped with a one-coordinate position-sensitive detector OD2 for the fixed wavelength λ equal to 0.1542 nm and a Kratky collimation system. The cross-section of the X-ray beam was 0.2 × 8 mm, the area of scattering angles corresponded to the scattering-vector range of $0.1 < s < 5.0$ nm^{-1} ($s = (4\pi \sin\theta)/\lambda$, with 2θ being the scattering angle). Samples of the particles were placed in a test cell of polyethylene terephthalate film with a thickness of 20 μm. The measurement procedure was performed using a certified methodology approved for the machine "AMUR-K" [11].

We have used the reactor described in [7] to produce antimicrobial textiles coated with nanoparticles. Ultrasonic vibrations were introduced into the reactor through two magnetostrictive transducers with an operating frequency of 19 kHz, one of which was located above the moving fabric, and the other one below it. Magnetostrictive transducers were welded onto rectangular steel plates to increase the surface area for irradiation. The vibrations of the plates were transmitted directly into the reaction zone. The power of each transducer was 2.5 kW, which was enough to initiate cavitation in the reactor. The speed of the textile (which was 100% cotton) was 1.5 m/min. We have produced two sets of coated fabrics. The first set was coated with industrial NPs (ZnO NPs dispersion in H_2O, Sigma Aldrich). An aqueous suspension with the concentration of 1.125 g ZnO per litre of distilled water was prepared. In the second set the suspension produced by the sonoplasma discharge was immediately used to impregnate the textile. The same concentration of ZnO NPs was used in both experiments. The antibacterial activity of the two sample sets against *E. coli* was tested by using the standard method BS EN ISO 20743:2007 [12]. We have calculated the antibacterial activity according to the following formula:

$$A = F - G,$$

where F is the growth rate of bacteria in the control sample ($\log_{10}$ CFU/mL after incubation − $\log_{10}$ CFU/mL before incubation), G is the growth rate of bacteria on the coated samples.

Results and Discussion

In order to produce a suspension of ZnO NPs in water we have initiated a sonoplasma discharge with the described above parameters in the experimental setup. An X-ray diffraction analysis of the obtained suspension confirmed that ZnO NPs were produced. Figure 2 shows the X-ray diffraction pattern. The reflections were indexed according to the diffraction pattern of hexagonal wurtzite-type ZnO.

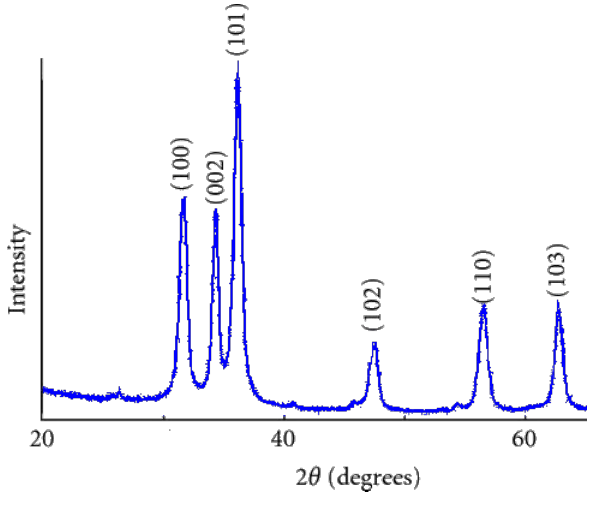

Figure 2: XRD pattern of the produced particles. The reflections were indexed according to the diffraction pattern of hexagonal wurtzite-type ZnO.

We have investigated the morphology and particle size by electron microscopy. Figure 3 shows the SEM image of the product. The SEM image shows that the produced particles have a cylin-

drical shape and confirms that their radius is about 10 nm. The length of these rods is about 50 nm.

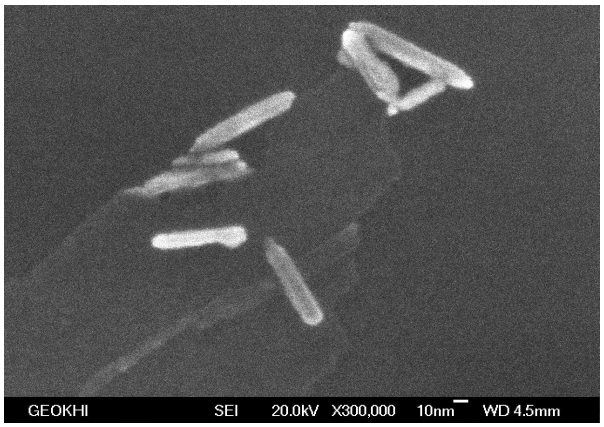

Figure 3: SEM image of ZnO NPs produced in a sonoplasma discharge. The scale bar is 10 nm.

We have obtained the size distribution of the zinc oxide particles produced in the sonoplasma discharge by using DLS measurements (Figure 4). The results confirm that a stable monodispersed suspension of ZnO NPs can be produced by using a sonoplasma discharge. A narrow size distribution of particles with an average size of 10 nm is obtained from the DLS measurements, which is in good agreement with the SEM data.

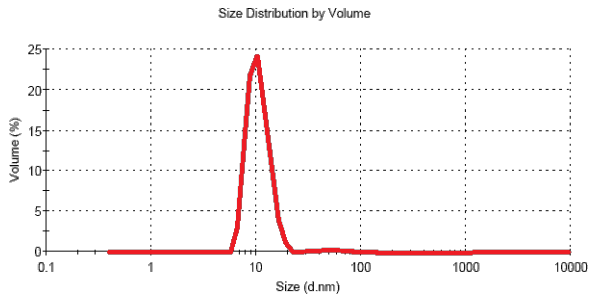

Figure 4: Size distribution of the zinc oxide particles produced in the sonoplasma discharge.

It was relevant for the coating process that the suspension produced in the sonoplasma discharge was used for coating immediately after production. Otherwise the nanoparticles formed agglomerates with the average size of 1–5 μm. This fact was confirmed by using SEM imaging. Figure 5 shows a SEM image of the agglomerates that appeared in the suspension after 1 h.

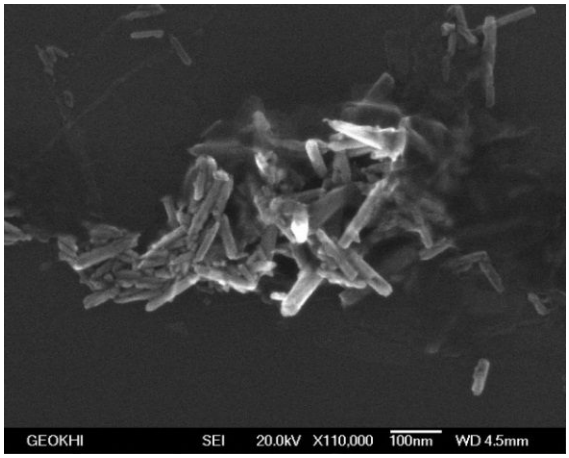

Figure 5: A SEM image of the agglomerates of ZnO NPs in the suspension 1 h after the discharge. The scale bar is 100 nm.

Two sets of fabric, one coated with industrial nanoparticles and the second one with nanoparticles fabricated in the sonoplasma discharge, were produced. Figure 6 shows a SEM image of the coated fabric. The sample shown was coated with commercial nanoparticles. It is clearly visible that the commercial nanoparticles can reach up to 1000 nm.

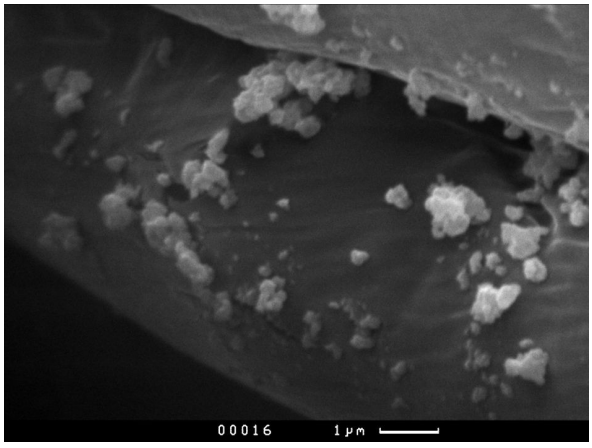

Figure 6: A SEM image of the coated textile fibres. The scale bar is 1 μm.

We have tested the antibacterial activity against *E. coli* of the two sets of fabrics. Figure 7 shows the results of these tests. It is clearly visible that the antibacterial activity of the textile coated by the sonoplasma particles against *E. coli* is higher than the fabric coated with industrial NP's. This might be explained as the result of the small ZnO NPS obtained by the sonoplasma synthesis. We have repeatedly shown that the biocidal effect is size dependent and particles with smaller size kill bacteria better. It is also advantageous that the suspension is continu-

ously exposed to an ultrasonic field, which prevents the particles from forming agglomerates.

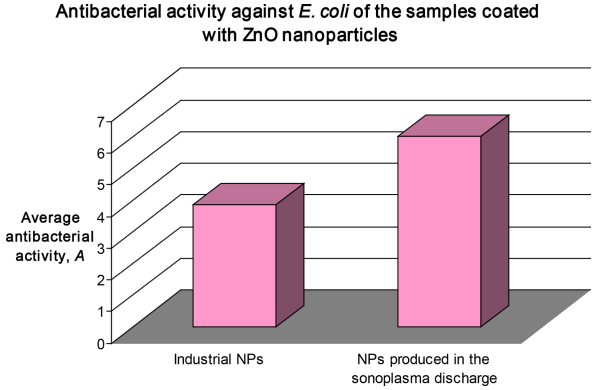

Figure 7: Antibacterial activity against *E. coli* of the samples coated with ZnO nanoparticles.

Conclusion

A method for the production of antibacterial ZnO nanoparticles has been developed. By using high power ultrasound a sonoplasma discharge is created between two zinc electrodes. Cylindrical rod-shaped ZnO nanoparticles with dimensions of 10–50 nm are formed in such a discharge. If the suspension of nanoparticles obtained in the sonoplasma reactor is immediately transported to a special reactor for coating of textiles with nanoparticles, antibacterial textiles can be produced. This coated textiles show better antibacterial activity against *E. coli* than textiles that were coated in the same reactor with industrially produced nanoparticles.

Acknowledgements

A part of this research was carried out as part of the activities of the SONO Consortium, Contract No. NMP-2008-1.2-1 - 228730. SONO is an IP Project of the 7th EC program.

References

1. Nosocomial infections: problems and solutions (in Russian). http://www.zdrav.ru/articles/practice/detail.php?ID=76435 (accessed Aug 28, 2013).
2. Abramov, O. V.; Gedanken, A.; Koltypin, Y.; Perkas, N.; Perelshtein, I.; Joyce, E.; Mason, T. J. *Surf. Coat. Technol.* **2009,** *204,* 718–722. doi:10.1016/j.surfcoat.2009.09.030
3. Ramesh, S.; Koltypin, Y.; Prozorov, R.; Gedanken, A. *Chem. Mater.* **1997,** *9,* 546–551. doi:10.1021/cm960390h
4. Abramov, V. O.; Andriyanov, Y. V.; Kisterev, E. V.; Gradov, O. M.; Shechtman, A. V.; Klassen, N. V.; Bulychev, H. A. *Inghenernaya fizika* **2009,** *8,* 34.
5. Abramov, O. V.; Abramov, V. O.; Andriyanov, Yu. V.; Gradov, O. M.; Mullakaev, M. S.; Bulychev, N. A. *Materialovedenie* **2009,** *2,* 53–67.
6. Yasnogorodskiy, I. Z. *Heat of metals and alloys in an electrolyte (in Russian);* Mashgiz: Moscow, 1949.
7. Abramova, A.; Gedanken, A.; Popov, V.; Ooi, E.-H.; Mason, T. J.; Joyce, E. M.; Beddow, J.; Perelshtein, I.; Bayazitov, V. *Mater. Lett.* **2013,** *96,* 121–124. doi:10.1016/j.matlet.2013.01.041
8. Ghule, K.; Ghule, A. V.; Chen, B.-J.; Ling, Y.-C. *Green Chem.* **2006,** *8,* 1034–1041. doi:10.1039/b605623g
9. Perelshtein, I.; Applerot, G.; Perkas, N.; Grinblat, J.; Hulla, E.; Wehrschuetz-Sigl, E.; Hasmann, A.; Guebitz, G.; Gedanken, A. *ACS Appl. Mater. Interfaces* **2010,** *2,* 1999–2004. doi:10.1021/am100291w
10. Abramova, A. V.; Abramov, V. O.; Eldarhanov, A. S. A sonoplasma method of hydrogen production. In *Proceedings of the international scientific-practical conference "Innovative technologies in industry, science and education,* Grozniy, Russia, 2010.
11. Severgun, D. I.; Feigin, L. A. *Small-angle X-ray and neutron scattering (in Russian);* Nauka: Moscow, 1986.
12. BS EN ISO 20743:2007, British Standards Institution, London, 2007.

License and Terms

Beilstein Journal of Nanotechnology

Chemi- vs physisorption in the radical functionalization of single-walled carbon nanotubes under microwaves

Victor Mamane[*1], Guillaume Mercier[2], Junidah Abdul Shukor[3], Jérôme Gleize[4], Aziz Azizan[3], Yves Fort[1] and Brigitte Vigolo[*2]

Full Research Paper

Open Access

Address:
[1]Laboratoire SRSMC UMR CNRS 7565, Université de Lorraine, 54506 Vandoeuvre-les-Nancy, France, [2]Institut Jean Lamour, CNRS-Université de Lorraine, BP 70239, 54506 Vandœuvre-lès-Nancy, France, [3]School of Materials and Mineral Resources Engineering, Universiti Sains Malaysia, 14300 Nibong Tebal, Penang, Malaysia and [4]Laboratoire de Chimie Physique-Approche Multi-échelle de Milieux Complexes-Université de Lorraine, 1 Bd Arago, 57078 Metz, France

Email:
Victor Mamane[*] - victor.mamane@univ-lorraine.fr; Brigitte Vigolo[*] - Brigitte.Vigolo@univ-lorraine.fr

* Corresponding author

Keywords:
carbon nanotubes; covalent functionalization; grafting; microwaves; physisorption

Beilstein J. Nanotechnol. **2014,** *5,* 537–545.
doi:10.3762/bjnano.5.63

Received: 15 January 2014
Accepted: 28 March 2014
Published: 29 April 2014

This article is part of the Thematic Series "Physics, chemistry and biology of functional nanostructures II".

Guest Editor: A. S. Sidorenko

Abstract

The effect of microwaves on the functionalization of single-walled carbon nanotubes (SWNTs) by the diazonium method was studied. The usage of a new approach led to the identification of the strength of the interaction (physical or chemical) between the functional groups and the carbon nanotube surface. Moreover, the nature (chemical formula) of the adsorbed/grafted functional groups was determined. According to thermogravimetric analysis coupled with mass spectrometry and Raman spectroscopy, the optimal functionalization level was reached after 5 min of reaction. Prolonged reaction times can lead to undesired reactions such as defunctionalization, solvent addition and polymerization of the grafted functions. The strength (chemi- vs physisorption) of the bonds between the grafted functional groups and the SWNTs is discussed showing the occurrence of physical adsorption as a consequence of defunctionalization after 15 min of reaction under microwaves. Several chemical mechanisms of grafting could be identified, and it was possible to distinguish conditions leading to the desired chemical grafting from those leading to undesired reactions such as physisorption and polymerization.

Introduction

Carbon nanotubes (CNTs) are recognized to have a huge potential in a variety of applications such as electronics, composite materials, energy storage and medicine [1-4]. From bulk synthesis method, CNTs are often entangled contingent upon the production process. They have a high tendency to remain aggregated and are difficult to process if no particular treatment is used to maintain them in a dispersed state. Covalent functionalization is the attachment of a chemical group able to disperse, compatibilize or induce a particular activity to the CNTs. It is recognized to be an efficient way to confer specific surface properties [5]. However, the methods generally used for the covalent functionalization of CNTs often require long reaction times (from several hours to days) [6]. The reaction times can be considerably reduced to a few minutes by using microwave-induced heating [7] as shown by the increasing number of publications in the past years [8]. Microwave irradiation has been efficiently used to assist CNT functionalization by cycloaddition [9-14], aryl radical addition [15-18], oxidation [19], bromination [20] and alkylation [21,22]. Control of the CNT functionalization level is of crucial importance in order to achieve the best benefit of CNT properties in materials and devices. High functionalization levels might lead to both a strong damage of the CNT structure and a disruption of the conjugated π system of CNTs thereby having a negative impact on their intrinsic properties (conductivity, mechanical properties) [23-25]. Low functionalization levels are indisputably preferred for CNT based composites [26].

As a consequence of the fast reaction times achieved under microwave heating, a careful control of the functionalization level has to be performed. Indeed, although the debate on the "microwave effect" in organic chemistry is still open, Kappe et al. have demonstrated that the temperature in the microwave vessel was often underestimated [27].

Therefore, high temperatures and prolonged reaction times can induce a detachment of the functional groups from the CNT surface [15,28,29] or allow the removal of metallic and amorphous carbon impurities resulting in the efficient primary purification of CNTs [30].

With the aim of optimizing a CNT functionalization approach based on microwave-assisted diazonium chemistry [31,32], chlorophenyl groups were grafted at the CNT surface and the functionalization level was followed by thermogravimetric analysis coupled with mass spectrometry (TGA–MS) (Scheme 1).

The present work highlights the importance of controlling the reaction times under microwave heating. Because of the locally high temperatures attained in the microwave reactor, we show that undesired reactions can occur after prolonged reaction times such as the addition of the solvent xylene, partial functional group detachment, and polymerization by adding diazonium to the functional groups already present at the CNT surface.

Results and Discussion

Occurrence of the functionalization. The functionalization was carried out by treating the raw SWNTs with 4-chloroben-

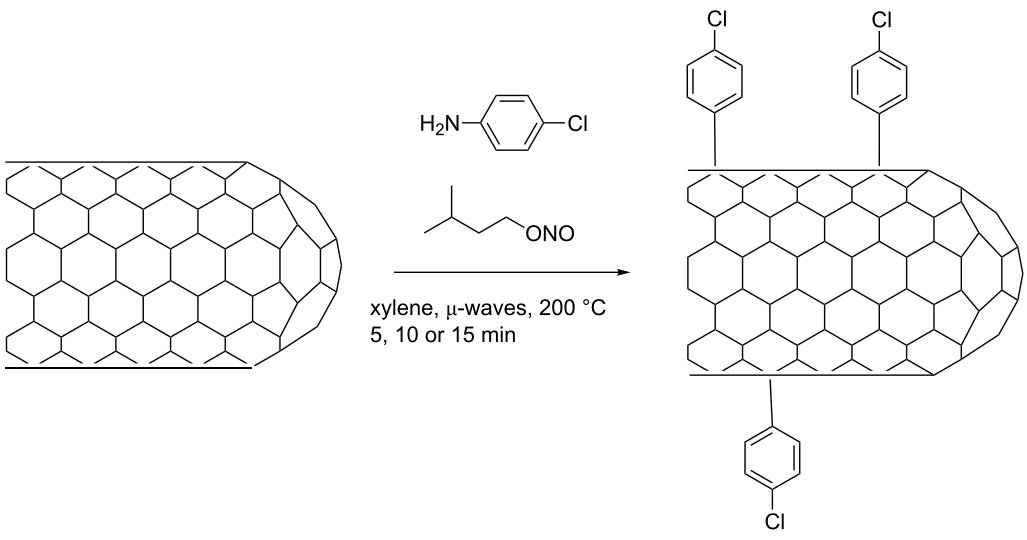

Scheme 1: SWNT functionalization by diazonium addition under microwave heating.

zenediazonium (in situ formed by reacting 4-chloroaniline with isoamyl nitrite) under microwaves at 200 °C for 5 min, 10 min and 15 min (Scheme 1). After treatment, the obtained functionalized samples (f-SWNT-5min, f-SWNT-10min and f-SWNT-15min) were analyzed by dispersion tests, high resolution transmission electron microscopy (HRTEM), Raman spectroscopy, and TGA–MS. Figure 1 shows photographs of the dispersions of the f-SWNTs in tetrahydrofuran (THF).

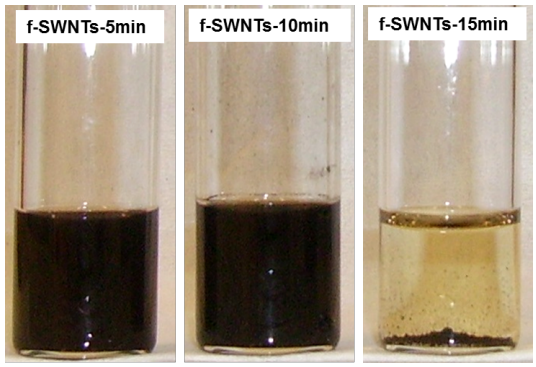

Figure 1: Photographs of f-SWNT-5min, f-SWNT-10min and f-SWNT-15min dispersed in THF 1 week after their preparation.

The SWNTs functionalized under 5 min or 10 min of microwaves could be well dispersed leading to dark solutions. As the functionalization duration was increased to 15 min, f-SWNT-15min was very poorly dispersed as a consequence of a rapid aggregation and separation from the solvent. Beyond 10 min of reaction time, the affinity of the f-SWNT surface and the solvent was strongly reduced. THF is a polar aprotic solvent which can lead to the formation of weak bonds with polar surface groups such as chlorophenyl. The observed modification of affinity for f-SWNT-15min means that the SWNTs behaved differently during the reaction than those that were functionalized with shorter times.

Raman spectroscopy is a widely used technique to follow the modification of the SWNTs upon a chemical treatment since the D band is sensitive to the introduction of defects in the SWNT sp^2 structure [31,33]. Figure 2a shows typical Raman spectroscopy spectra of the raw SWNTs (black curve), f-SWNT-5min (red curve) and f-SWNT-10min (green curve).

The recorded signal of f-SWNT-15min shows an intense broad fluorescence band in the domain of interest, so that Raman features could not be observed for this sample. For the two other functionalized samples, the D band intensity is increased after the functionalization reaction due to the induced break of the conjugated structure of the SWNTs in accordance with the expected functionalization mechanism. The I_D/I_G ratio increases

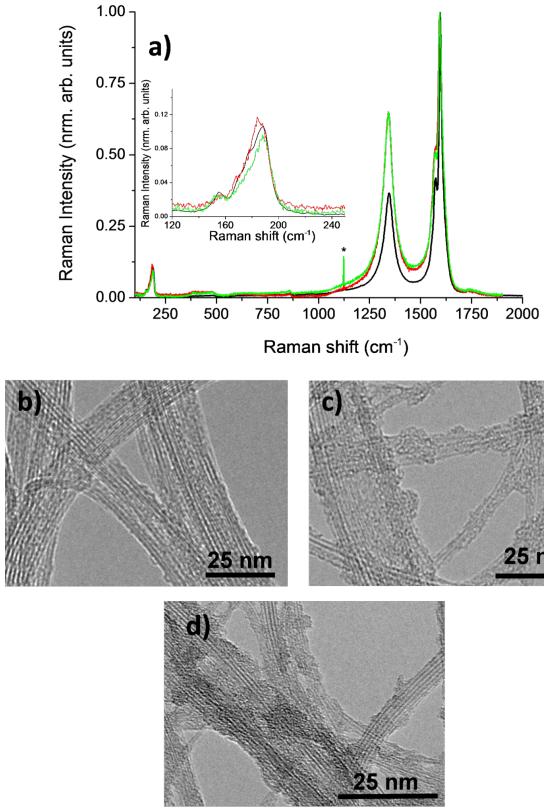

Figure 2: Raman spectra of the starting and functionalized SWNTs and typical HRTEM images. a) Raman spectrum of raw SWNTs (black curve), f-SWNT-5min (red curve) and f-SWNT-10min (green curve).* mercury peak of a reference neon light. HRTEM images of the raw SWNTs (b), f-SWNT-10min (c), and f-SWNT-15min (d).

from 0.82 for the raw SWNTs to 1.09 and 1.07 for f-SWNT-5min and f-SWNT-10min, respectively.

The Raman spectra of these two functionalized samples are indeed relatively similar. This could be attributed to none or only a little increase of the functionalization level for f-SWNT-10min compared to that of f-SWNT-5min. The RBM band is only slightly modified after functionalization, and the main contribution located around ω_{RBM} = 185 cm^{-1} is observed for all three samples. The corresponding SWNT diameter d_t was deduced from

$$\omega_{RBM} = \frac{A}{d_t} + B \quad (1)$$

where A = 234 nm·cm^{-1} and B = 10·cm^{-1} [34]. Following Equation 1 the SWNT diameter d_t is 1.34 nm as expected for arc-discharge produced SWNTs.

The modification of the SWNT structure caused by functionalization is also revealed in the HRTEM images shown in

Figure 2. For the raw sample, the walls of the SWNTs exhibit a low defect level (Figure 2b) and appear undamaged. After functionalization (Figure 2c and 2d), SWNT walls whose damages are difficult to identify in the images are observed. No significant difference between the three functionalized samples (including f-SWNT-5min, not shown in Figure 2) could be evidenced by using HRTEM.

Functionalization levels and nature of the created bonds. The recorded weight losses of raw, chemically functionalized samples with three different reaction times and phys-SWNT during heating under helium are shown in Figure 3a. The new sample, phys-SWNT, prepared by mixing the SWNTs with chlorobenzene for 30 min under sonication, was used in order to confirm the covalent nature of the bonds between SWNTs and the chloroaryl group. The derivative representation in Figure 3b helps to position the main weight loss ranges. Consequently, no particular feature is visible in dTG for raw SWNTs (not shown).

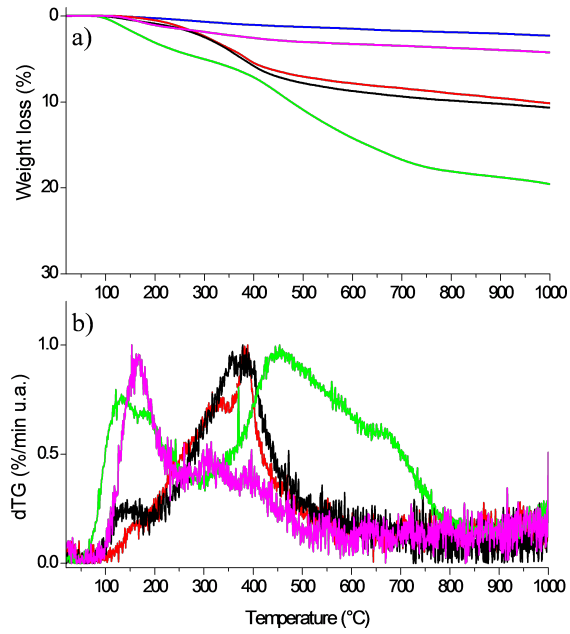

Figure 3: TGA weight loss under helium of raw SWNTs (blue curve), phys-SWNT (violet curve), f-SWNT-5min (red curve), f-SWNT-10min (black curve), and f-SWNT-15min (green curve).

For the phys-SWNT, the weight loss regularly increased above 300 °C identical to the weight loss of the raw SWNTs and is 4.2 wt % at 1000 °C. At a lower temperature, around 174 °C, a more pronounced loss of about 1.5 wt % is attributed to species which are physically adsorbed on the SWNT surface. f-SWNT-5min and f-SWNT-10min show a comparable behavior with a weight loss of 10.1 and 10.7 wt % centered at 380 and 360 °C as the reaction time is increased from 5 to 10 min. The difference between the two samples is a marginal loss (about 1.0 wt %) between 100 and 200 °C only visible for f-SWNT-10min. The TGA profile of f-SWNT-15min is different from the two other functionalized samples. The total weight loss recorded of 19.4 wt % at 1000 °C is almost twice as high. The curve clearly shows two main losses: at a low temperature in range of 100−200 °C and in the range of 400–700 °C with the weight loss being 5.0 and 12.0 wt %, respectively. The sum of the weight losses of these two temperature ranges does not necessarily correspond to the total weight loss recorded at 1000 °C since each of them directly corresponds to the loss recorded in the related temperature range. The lower and upper bounds of the temperature ranges were also determined by means of mass spectrometry data (see Figure 4). As expected, the raw SWNTs bear very few surface groups and thus progressively lost 2.2 wt % during heating under helium.

Table 1 recalls the weight losses corresponding to i) the low temperature range (below 200 °C) assigned to the departure of the groups physisorbed at the sample surface, and ii) the high temperature range (above 200 °C) which typically involves the detachment of covalently functional groups. For the latter, the corresponding functionalization level n considering the exclusive grafting of chlorophenyl groups was determined by using Equation 2:

$$n = \frac{M_{PhCl}}{M_C}\left(\frac{100}{WL} - 1\right) \quad (2)$$

where M_C and M_{PhCl} are the mass of a carbon atom (M_C = 12 g/mol) and chlorophenyl (M_{PhCl} = 111.5 g/mol), respectively. WL (wt %) is the weight loss regarding only the chemisorbed groups. n corresponds to the number of carbon atoms for one functional group.

The functionalization level determined for f-SWNT-5min (n = 114) is slightly lower than that obtained for f-SWNT-10min (n = 107) since the weight loss recorded for the latter is higher. The mass spectrometer coupled with the TGA system allows for the examination of the nature of the groups that are detached from the sample surface upon heating. Chlorophenyl groups can be followed by detection of the main fragments expected for pure chlorobenzene, i.e., *m*/*z* 112, 77, 114, 51, 50 with their relative intensity decreasing from 112 to 50. The masses 112 and 114 correspond to the fragments containing chlorine ^{35}Cl and ^{37}Cl, respectively, whereas the masses 77, 51 and 50 correspond to the fragmentation of the phenyl group from chlorophenyl. Figure 4 shows the detected intensity for the main masses expected for chlorobenzene for f-SWNT-5min (Figure 4a), f-SWNT-10min (Figure 4b), f-SWNT-15min (Figure 4c) and phys-SWNT (Figure 4d).

Table 1: Weight loss, temperature ranges for the physisorbed and chemisorbed functional groups, and the corresponding functionalization level.

sample	Total weight loss at 1000 °C /wt %	Chemisorbed functional groups				Physisorbed functional groups	
		Temperature range /°C	Main temperature /°C	Weight loss /wt %	Functionalization level /n	Main temperature /°C	Weight loss /wt %
Raw SWNTs	2.2	—	—	—	—	—	—
f-SWNT-5min	10.1	175–600	380	7.5	114	—	0.0
f-SWNT-10min	10.7	223–586	360	8.0	107	190	1.0
f-SWNT-15min	19.4	325–750	550	12.0	68	190	5.0
Phys-SWNTs	4.2	—	—	—	—	174	1.5

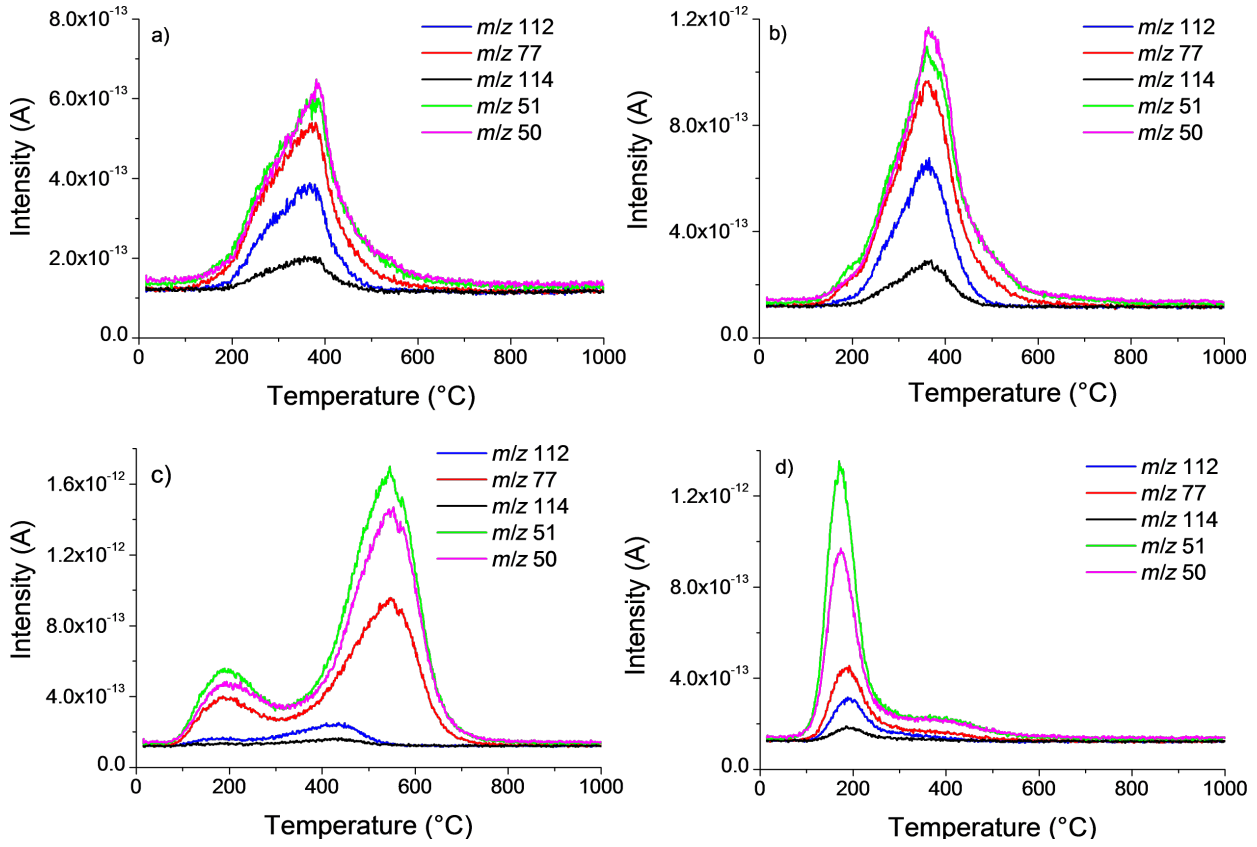

Figure 4: Mass spectrometry intensities for the main *m*/*z* corresponding to chlorobenzene. a) f-SWNT-5min, b) f-SWNT-10min, c) f-SWNT-15min, d) phys-SWNT.

For the four samples, the *m*/*z* of the expected fragments for chlorobenzene could be detected, and as the intensity profile of each mass is comparable they can be considered without ambiguity as the signature of chlorophenyl groups grafted at the sample surface. Clearly, their departure occurs according to a one-step mechanism for f-SWNT-5min and in two distinct steps for f-SWNT-15min. The behavior of f-SWNT-10min mainly follows a one-step mechanism, but for the most intense masses (77, 51, 50) a low temperature bump begins to appear. For phys-SWNT, the main intensity is located at low temperatures

as expected for non-covalently grafted functional groups. Traces of chlorobenzene could also be detected at high temperatures. Still, the intensity of *m/z* 112 is less than 1×10^{-13} A. For comparison, it is 3.9×10^{-13} A for f-SWNT-5min, 6.5×10^{-13} A for f-SWNT-10min, and goes down to 2.4×10^{-13} A for f-SWNT-15min. For all samples, the relative intensity of the recorded *m/z* of chlorobenzene turned out to be different from our expectations with intensities for the fragments containing chlorine (*m/z* 112 and 114) being less intense than those from the phenyl part (*m/z* 50 and 51) [6]. It is noteworthy that this difference is more pronounced for f-SWNT-15min.

Over-reactions under microwaves and chemical mechanisms. The main fragments for pure xylene (*m/z* 91, 106 and 105) which has been used as the solvent for the reaction were clearly detected for f-SWNT-15min (Figure 5a).

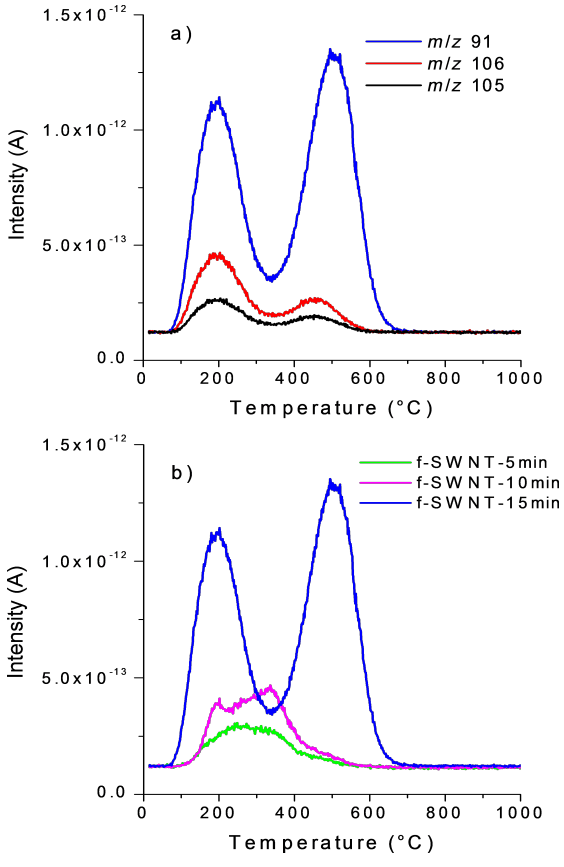

Figure 5: Mass spectrometry intensities for xylene. a) main *m/z* of xylene for f-SWNT-15min, b) *m/z* 91 for f-SWNT-5min (pink curve), f-SWNT-10min (green curve), and f-SWNT-15min (blue curve).

The most intense mass for xylene, *m/z* 91, is, as expected, superimposed for the three functionalized samples (Figure 5b). Whereas a broad weak peak appears around 300 °C for f-SWNT-5min, as the reaction time is increased, the intensity of *m/z* 91 is amplified and significantly more structured. In particular, this holds true for a contribution emerging at high temperature around 550 °C. Raman and TGA–MS data clearly evidence the covalent functionalization of the chlorophenyl groups at the SWNT surface after a reaction time of 5 min. I_D/I_G is indeed increased after functionalization due to the opening of the C=C bonds by a radical reaction. From Raman and TGA–MS data, it appears that the level of functionalization is almost identical between a reaction time of 5 and 10 min.

The functional groups grafted at the surface of SWNTs are mainly covalently bonded chlorophenyl groups. However, after 10 min, a small amount of physisorbed chlorophenyl and xylyl groups can be detected. The large temperature range for xylene departure suggests a possible solvent addition as previously observed with toluene during the reaction of arylhydrazines with SWNTs under conventional thermal conditions. The longer reaction time under microwave heating can either induce defunctionalization [15] or it can facilitate the debundling of the SWNTs. The latter ultimately results in the removal of physisorbed functional groups which were trapped in the bundles and therefore not visible in the TGA–MS of sample f-SWNT-5min. After 15 min of reaction, these additional processes (defunctionalization/debundling and xylene addition) are more pronounced. Indeed, in TGA–MS of f-SWNT-15min, the peaks around 200 °C related to physisorbed chlorophenyl and xylyl groups are significantly increased. Another feature of the f-SWNT is the apparent increase of the functionalization level, since one function each 68C can be calculated from the TGA curve for f-SWNT-15min. However, a careful analysis of the TGA–MS profiles for the detachment of the chlorophenyl groups reveals that most of the groups are detected between 350 and 700 °C. The same observation can be made for the detachment of xylyl groups. In this case, however, half of the groups are detected in the range of 100–200 °C and the other half between 350 and 700 °C. These large temperature ranges can be explained by the progressive detachment of functional groups from a polymeric structure. Indeed, under the reaction conditions, the aryl radicals can give rise to the growth of aryl chains at the SWNT surface [35].

All these possible over-reaction processes are summarized in Scheme 2. The proposed polyaromatic structure for f-SWNT-15min sample can explain the intense broad fluorescence band observed during the Raman experiments as well as the poor dispersion ability in THF compared to f-SWNT-5min and f-SWNT-10min. Moreover, it can explain the much lower detection of *m/z* 112 and 114 compared to *m/z* 50 and 51 in TGA–MS of sample f-SWNT-15min. Indeed, the analysis of mass spectra of several dichloro-biphenyles revealed that *m/z* 50

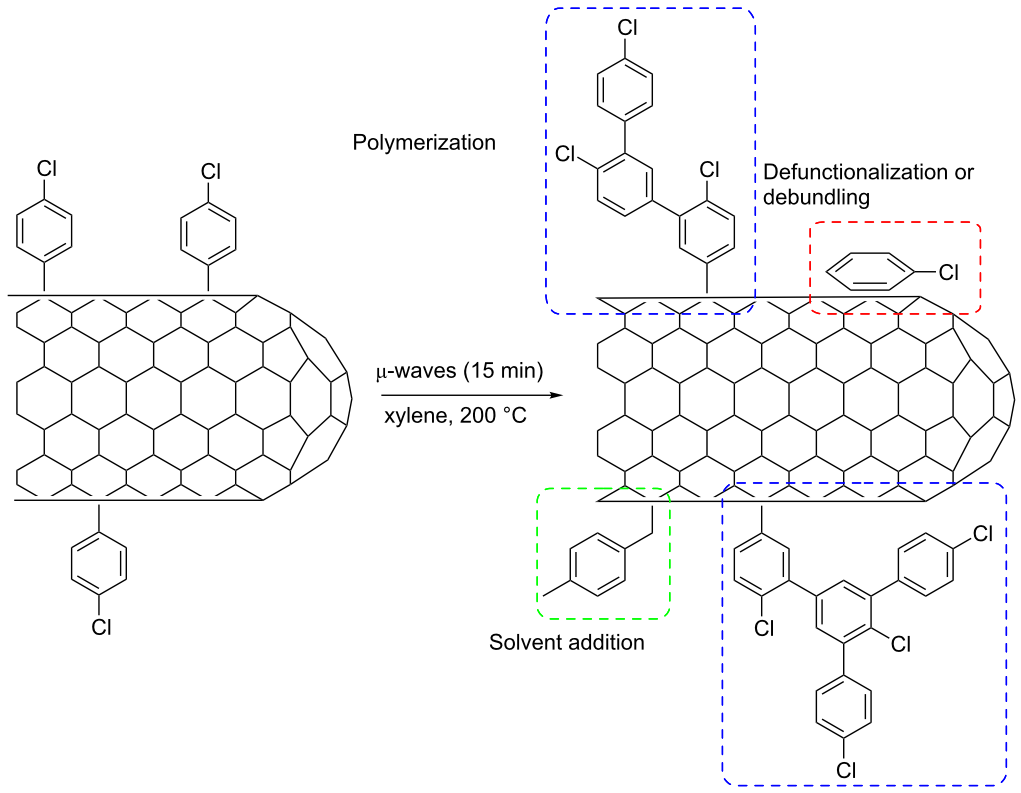

Scheme 2: Over-reactions after 15 min under microwaves.

and 51 are higher compared to *m*/*z* 112 and 114, whereas it is vice versa for chlorobenzene [36].

Conclusion

SWNTs were efficiently functionalized under microwaves by aryl radical addition. The functionalization level and more importantly the nature of the functional groups could be controlled by performing the reaction in very short time. The chlorophenyl groups covalently grafted at the SWNT surface were detected by TGA-–MS after only 5 min of reaction. The TGA-MS technique also showed that after 15 min of reaction, the functionalization level was increased but the nature of the functional groups as well as the interaction between the functional groups and SWNTs (chemi- vs physisorption) were evolved. Given the reported reaction conditions, longer reaction times under microwaves caused three undesired processes: defunctionalization, solvent addition, and polymerization of the grafted functions.

Experimental

Reagents. Single-walled carbon nanotubes (SWNTs) were obtained by means of a home-made reactor using conventional experimental conditions [37]. SWNTs are used without any purification process because common purification treatments may introduce additional defects on the SWNT surface. 4-Chloroaniline and isoamyl nitrite were purchased from Sigma-Aldrich and used as received. Xylene (mixture of isomers) was purchased from Carlo-Alba and used as received.

Functionalization procedure. The microwave device was a CEM discover System. In a 10 mL glass tube, SWNTs (15 mg) were mixed with 4-chloroaniline (300 mg) in xylene (2.5 mL). The mixture was gently sonicated for 10 min until it was visually homogenous. Isoamyl nitrite (0.45 mL) was added and the glass tube was sealed with a Teflon cap. A set of reactions was carried out in the microwave oven at 200 W with different reaction times (5 min, 10 min and 15 min) under cooling conditions to obtain a constant temperature of 200 °C and a pressure of 17 bar during the reaction. After the reaction, the nanotubes were filtered on a FG filter (pore size 0.2 μm) and washed with dimethylformamide (DMF) and methanol several times until the solvent became colorless. Modified SWNTs were dried in vacuum at 80 °C overnight. The obtained samples functionalized with 5, 10 and 15 min of microwaves were named f-SWNT-5min, f-SWNT-10min and f-SWNT-15min.

Characterizations. For the dispersion tests, functionalized SWNTs in a powder state were added to tetrahydrofuran (THF)

and the mixture was dispersed by using a sonication bath during 15 min. The solutions were allowed to settle for one week. Raman spectra were collected at room temperature (300 K) with a LabRAM HR 800 micro-Raman spectrometer. The incident light from a 514.5 nm laser was focused on the samples with a x50 microscope objective with a power density of 0.25 mW/μm^2. Three spectra were recorded for the same sample. The main Raman features are the Radial Breathing Modes (RBM) in the 150–300 cm^{-1} range. At higher frequency, the D band, which is located in the 1320–1350 cm^{-1} range, and the G band in the 1500–1600 cm^{-1} range correspond to the C=C bond vibrations of the nanotubes. The D band was fitted with a Lorentzian curve and the G band was fitted with three Lorentzian curves: the G$^-$ band around 1570 cm^{-1}, the G$^+$ band at about 1594 cm^{-1} and the G* band at around 1614 cm^{-1}. The G area is obtained from the sum of the areas of the 3 corresponding components. The calculated areas of the D and G band are used to obtain the intensity ratio I_D/I_G. For the sake of clarity in the figure, the intensities of the spectra were normalized with respect to the maximum of the G$^+$ band. For high resolution transmission electron microscopy (HRTEM) observations, SWNTs were dispersed in ethanol in a sonication-bath for a few minutes and deposited on a holey carbon copper grid (300 mesh). A Philips CM 200 apparatus was used at an operating voltage of 200 kV. About 10 zones were observed for each sample in order to obtain a statistical view, and we show one typical image for each sample. A SetaramSetsys evolution 1750 Thermal Gravimetric Analyser coupled with a Pfeiffer GSD 301C Vacuum OmniStar mass spectrometer (TGA–MS) was used for the detection of the detached functions from the SWNT surface. About 5 mg of raw or functionalized sample were placed in an alumina crucible in the TGA chamber, and the temperature was increased from room temperature up to 1000 °C under a helium Alphagaz 2 flux of 20 mL/min at a rate of 3 °C/min. Derivative data (dTG) were obtained by deriving the weight loss with respect to time. The parameters we used for the mass spectrometer ensure that most of the species undergo single ionization, that is, $z = 1$ for the detected m/z. Thus, m/z and mass will be interchangeably employed in the text.

Acknowledgments

We acknowledge the help of P. Franchetti in Raman measurements. We would like to thank L. Aranda for technical assistance in TGA measurements and J. Ghanbaja for TEM observations.

References

1. Ajayan, P. M. *Chem. Rev.* **1999,** *99,* 1787–1800. doi:10.1021/cr970102g
2. Rao, C. N. R.; Satishkumar, B. C.; Govindaraj, A.; Nath, M. *ChemPhysChem* **2001,** *2,* 78–105. doi:10.1002/1439-7641(20010216)2:2<78::AID-CPHC78>3.0.CO;2-7
3. Dai, H. *Acc. Chem. Res.* **2002,** *35,* 1035–1044. doi:10.1021/ar0101640
4. Van Noorden, R. *Nature* **2011,** *469,* 14–16. doi:10.1038/469014a
5. Tasis, D.; Tagmatarchis, N.; Bianco, A.; Prato, M. *Chem. Rev.* **2006,** *106,* 1105–1136. doi:10.1021/cr050569o
6. Lejosne, J.; Mercier, G.; Mamane, V.; Fort, Y.; Marêché, J.-F.; McRae, E.; Valsaque, F.; Vigolo, B. *Carbon* **2011,** *49,* 3010–3018. doi:10.1016/j.carbon.2011.03.019
7. de la Hoz, A.; Diaz-Ortiz, Á.; Moreno, A. *Chem. Soc. Rev.* **2005,** *34,* 164–178. doi:10.1039/b411438h
8. Vázquez, E.; Prato, M. *ACS Nano* **2009,** *3,* 3819–3824. doi:10.1021/nn901604j
9. Brunetti, F. G.; Herrero, M. A.; de M. Muñoz, J.; Giordani, S.; Díaz-Ortiz, A.; Filippone, S.; Ruaro, G.; Meneghetti, M.; Prato, M.; Vázquez, E. *J. Am. Chem. Soc.* **2007,** *129,* 14580–14581. doi:10.1021/ja077927k
10. Li, J.; Grennberg, H. *Chem.–Eur. J.* **2006,** *12,* 3869–3875. doi:10.1002/chem.200501314
11. Guryanov, I.; Toma, F. M.; López, A. M.; Carraro, M.; Da Ros, T.; Angelini, G.; D'Aurizio, E.; Fontana, A.; Maggini, M.; Prato, M.; Bonchio, M. *Chem.–Eur. J.* **2009,** *15,* 12837–12845. doi:10.1002/chem.200901408
12. Rubio, N.; Herrero, M. A.; de la Hoz, A.; Meneghetti, M.; Prato, M.; Vázquez, E. *Org. Biomol. Chem.* **2010,** *8,* 1936–1942. doi:10.1039/b925227d
13. Wang, Y.; Iqbal, Z.; Mitra, S. *Carbon* **2005,** *43,* 1015–1020. doi:10.1016/j.carbon.2004.11.036
14. Delgado, J. L.; de la Cruz, P.; Langa, F.; Urbina, A.; Casado, J.; López Navarrete, J. T. *Chem. Commun.* **2004,** 1734–1735. doi:10.1039/b402375g
15. Liu, J.; Rodriguez i Zubiri, M.; Vigolo, B.; Dossot, M.; Fort, Y.; Ehrhardt, J.-J.; McRae, E. *Carbon* **2007,** *45,* 885–891. doi:10.1016/j.carbon.2006.11.006
16. Liu, J.; Rodriguez i Zubiri, M.; Vigolo, B.; Dossot, M.; Humbert, B.; Fort, Y.; McRae, E. *J. Nanosci. Nanotechnol.* **2007,** *7,* 3519–3523. doi:10.1166/jnn.2007.819
17. Brunetti, F. G.; Herrero, M. A.; de M. Muñoz, J.; Díaz-Ortiz, A.; Alfonsi, J.; Meneghetti, M.; Prato, M.; Vázquez, E. *J. Am. Chem. Soc.* **2008,** *130,* 8094–8100. doi:10.1021/ja801971k
18. Karousis, N.; Economopoulos, S. P.; Iizumi, Y.; Okazaki, T.; Liu, Z.; Suenaga, K.; Tagmatarchis, N. *Chem. Commun.* **2010,** *46,* 9110–9112. doi:10.1039/c0cc04108d
19. Wang, Y.; Iqbal, Z.; Mitra, S. *J. Am. Chem. Soc.* **2006,** *128,* 95–99. doi:10.1021/ja053003q
20. Colomer, J.-F.; Marega, R.; Traboulsi, H.; Meneghetti, M.; Van Tendeloo, G.; Bonifazi, D. *Chem. Mater.* **2009,** *21,* 4747–4749. doi:10.1021/cm902029m
21. Xu, Y.; Wang, X.; Tian, R.; Li, S.; Wan, L.; Li, M.; You, H.; Li, Q.; Wang, S. *Appl. Surf. Sci.* **2008,** *254,* 2431–2435. doi:10.1016/j.apsusc.2007.09.081
22. Wan, L.; Wang, X.; Li, S.; Li, Q.; Tian, R.; Li, M.; Cheng, J. *Chin. J. Chem.* **2009,** *27,* 359–364. doi:10.1002/cjoc.200990058
23. Garg, A.; Sinnott, S. B. *Chem. Phys. Lett.* **1998,** *295,* 273–278. doi:10.1016/S0009-2614(98)00969-5
24. Byrne, M. T.; Gun'ko, Y. K. *Adv. Mater.* **2010,** *22,* 1672–1688. doi:10.1002/adma.200901545
25. Bose, S.; Khare, R. A.; Moldenaers, P. *Polymer* **2010,** *51,* 975–993. doi:10.1016/j.polymer.2010.01.044

26. Vigolo, B.; Mamane, V.; Valsaque, F.; Le, T. N. H.; Thabit, J.; Ghanbaja, J.; Aranda, L.; Fort, Y.; McRae, E. *Carbon* **2009,** *47,* 411–419. doi:10.1016/j.carbon.2008.10.024
And references cited therein.
27. Kappe, C. O.; Pieber, B.; Dallinger, D. *Angew. Chem., Int. Ed.* **2013,** *52,* 1088–1094. doi:10.1002/anie.201204103
28. Lin, W.; Moon, K.-S.; Zhang, S.; Ding, Y.; Shang, J.; Chen, M.; Wong, C.-p. *ACS Nano* **2010,** *4,* 1716–1722. doi:10.1021/nn901621c
29. Cabana, J.; Lavoie, S.; Martel, R. *J. Am. Chem. Soc.* **2010,** *132,* 1389–1394. doi:10.1021/ja908729y
30. Chajara, K.; Andersson, C.-H.; Lu, J.; Widenkvist, E.; Grennberg, H. *New J. Chem.* **2010,** *34,* 2275–2280. doi:10.1039/c0nj00087f
31. Dyke, C. A.; Tour, J. M. *J. Am. Chem. Soc.* **2003,** *125,* 1156–1157. doi:10.1021/ja0289806
32. Price, K. B.; Tour, J. M. *J. Am. Chem. Soc.* **2006,** *128,* 12899–12904. doi:10.1021/ja063609u
33. Martinez, M. T.; Calleja, M. A.; Benito, A. M.; Cochet, M.; Seeger, T.; Ansón, A.; Schreiber, J.; Gordon, C.; Marhic, C.; Chauvet, O.; Fierro, J. L. G.; Maser, W. K. *Carbon* **2003,** *41,* 2247–2256. doi:10.1016/S0008-6223(03)00250-1
34. Jorio, A.; Pimenta, M. A.; Souza Filho, A. G.; Saito, R.; Dresselhaus, G.; Dresselhaus, M. S. *New J. Phys.* **2003,** *5,* 139. doi:10.1088/1367-2630/5/1/139
35. Marcoux, P. R.; Hapiot, P.; Batail, P.; Pinson, J. *New J. Chem.* **2004,** *28,* 302–307. doi:10.1039/b309509f
36. Mass-spectrometry database from NIST Chemistry WebBook.
37. Mercier, G.; Gleize, J.; Ghanbaja, J.; Marêché, J.-F.; Vigolo, B. *J. Phys. Chem. C* **2013,** *117,* 8522–8529. doi:10.1021/jp400890n

License and Terms

Beilstein Journal of Nanotechnology

In vitro toxicity and bioimaging studies of gold nanorods formulations coated with biofunctional thiol-PEG molecules and Pluronic block copolymers

Tianxun Gong[1,2], Douglas Goh[1], Malini Olivo[1,3] and Ken-Tye Yong[*2]

Full Research Paper

Open Access

Address:
[1]Bio-Optical Imaging Group, Singapore Bioimaging Consortium (SBIC), Agency for Science Technology and Research (A*STAR), 11 Biopolis Way, 138667 Singapore, [2]School of Electrical and Electronic Engineering, Nanyang Technological University, 639798 Singapore and [3]School of Physics, National University of Ireland, Galway, Ireland

Email:
Ken-Tye Yong[*] - ktyong@ntu.edu.sg

* Corresponding author

Keywords:
cancer cells; dark-field imaging; gold nanorods; PEG-SH; PEO–PPO–PEO

Beilstein J. Nanotechnol. **2014,** *5,* 546–553.
doi:10.3762/bjnano.5.64

Received: 18 October 2013
Accepted: 31 March 2014
Published: 30 April 2014

This article is part of the Thematic Series "Physics, chemistry and biology of functional nanostructures II".

Guest Editor: A. S. Sidorenko

Abstract

In this work, we investigated the cytotoxicity, colloidal stability and optical property of gold nanorods before and after functionalizing them with thiolated PEG and Pluronic triblock copolymer (PEO–PPO–PEO) molecules. The morphology of functionalized gold nanorods was characterized by UV–visible absorption spectroscopy, transmission electron microscopy, and dynamic light scattering. Solution phase synthesis of gold nanorods has remained the method of choice for obtaining varying shapes and aspect ratios of rod nanoparticles. This method typically involves the use of cetyltrimethylammonium bromide (CTAB) surfactants as directing agents to grow gold nanorods in the solution phase. The as-synthesized gold nanorods surfaces are terminated with CTAB molecules and this formulation gives rise to adverse toxicity in vitro and in vivo. To employ the gold nanorods for biological studies, it is important to eliminate or minimize the exposure of CTAB molecules from the gold nanorods surface to the local environment such as cells or tissues. Complete removal of CTAB molecules from the gold nanorods surface is unfeasible as this will render the gold nanorods structurally unstable, causing the aggregation of particles. Here, we investigate the individual use of thiolated PEG and PEO–PPO–PEO as capping agents to reduce the cytotoxicity of gold nanorods formulation, while maintaining the optical, colloidal, and structural properties of gold nanorods. We found that encapsulating gold nanorods with the thiolated PEG or PEO–PPO–PEO molecules guarantees the stability and biocompatibility of the nanoformulation. However, excessive use of these molecules during the passivation process leads to a reduction in the overall cell viability. We also demonstrate the use of the functionalized gold nanorods as scattering probes for dark-field imaging of cancer cells thereby demonstrating their biocompatibility. Our results offer a unique solution for the future development of safe scattering color probes for clinical applications such as the long term imaging of cells and tissues.

Introduction

Gold nanorods (AuNRs) have been widely adopted for biological applications due to their unique plasmonic properties. One of the most important characteristics of AuNRs is that as light interacts with them, localized surface plasmon resonance (LSPR) is excited and locally oscillates around the particle [1]. LSPRs are electromagnetic modes associated with the collective oscillations of the free electrons confined to the nanoscale size. AuNRs have the unique ability to enhance the electromagnetic field within sub-wavelength regions adjacent to their surfaces under resonance excitation. The optical cross section of AuNRs is comparable to gold nanospheres and nanoshells, but the smaller effective dimension of AuNRs makes them useful for the targeted delivery into biological cells. AuNRs with larger aspect ratios and smaller effective radii are excellent photo-absorbing nanoparticles, while those with a larger effective radius have a higher scattering contrast signal [2]. These remarkable absorption and scattering capabilities make AuNRs promising candidates for bioimaging and biosensors [3,4].

AuNRs possess two SPR absorption peaks. One peak is located at the shorter wavelength (transverse plasmon peak) where light is transmitted across the transverse direction. The second peak can be found at the longer wavelength (longitudinal plasmon peak) where light is transmitted along the longitudinal direction [5]. The location of the longitudinal plasmon peak is highly dependent on the size, shape and aggregation state of the AuNRs. By carefully adjusting the length and diameter of AuNRs particle, one is able to manipulate their longitudinal absorption peak within the range from 600 to 1500 nm [6]. It is well recognized that near infrared (NIR) light is able to penetrate the human tissue up to a few centimeters since water and blood cells absorb light only minimally at this region. AuNRs can be designed to absorb light specifically in the NIR region so that heat is generated to damage cells and tissues. This property renders them useful for photothermal therapy and imaging of cancer [7,8]. In addition, the AuNRs surface can be functionalized with ligands for targeted drug delivery to support cancer therapy in vitro and in vivo [9]. Furthermore, it is well reported that AuNRs are often used for surface enhanced Raman spectroscopy (SERS) biosensing applications. This is based on the observation that a gold rod-like particle has a higher electric field at both ends of the rod [10,11] where it is particularly useful for enhancing the signals from Raman tags.

Over the past few years, the seed-mediated growth method proposed by Murphy and El-Sayed's group has been commonly used for synthesizing AuNRs formulations [6,12,13]. Cetyltrimethylammonium bromide (CTAB) molecules are used as structure directing agents to support the formation of gold rod-like particles in the aqueous medium. The issue with CTAB, however, is that it forms a tightly bound cationic bilayer on the surface of the AuNR with the cationic trimethylammonium head group exposed to the external environment. The presence of CTAB on the AuNRs surface poses a threat to many biological systems as they are toxic to cells and tissues. As a result, CTAB-coated AuNRs are not suitable to be used for biomedical applications [14,15]. CTAB can be partially removed from the AuNRs surface by centrifugation, but the majority of the CTAB molecules remains on the particle surface and continues to exhibit toxicity to cells. On the other hand, repeated centrifugations results in structurally unstable AuNRs and causes them to aggregate and precipitate in solution. Also, CTAB-coated AuNRs are not suitable for in vitro and in vivo applications because they do not allow antibodies or antigens to be linked to their surface for targeted delivery and imaging [16,17]. More importantly, one is not able to use CTAB-coated AuNRs as a carrier for drug delivery of water insoluble anti-cancer agents (e.g., doxorubicin, paclitaxel) to the cancerous area since their surface is hydrophilic and positively charge [18,19]. Therefore, a surface functionalization platform is needed to furnish a AuNR surface with a biocompatible polymer-coating for reducing their cytotoxicity while maintaining colloidal stability and allowing them to be conjugated for biomedical applications. Bio functional thiol-poly(ethylene glycol) (PEG-SH) molecules and Pluronic block copolymers (PEO–PPO–PEO) (see chemical formula of PEG-SH and Pluronic (PEO–PPO–PEO) in Supporting Information File 1, Figure S1) are commonly used to prepare non-ionic polymer encapsulated AuNRs with a stealth property for in vivo studies [20-23]. It is noteworthy that these PEG polymers can even be modified with additional functional groups such as a carboxyl and an amino group for the conjugation of targeting ligands. It is known that the CTAB bilayers on a AuNRs surface can be removed and replaced with PEG-SH molecules by means of the chemisorption process between the thiol moiety and the gold particle surface [24,25]. Pluronic is a commercially available triblock copolymer with a hydrophobic segment of poly(propylene oxide) (PPO) polymer sandwiched between two hydrophilic segments of PEO. In our previous study, we found that the hydrophobic PPO segment from the Pluronic block copolymer is able to bind to the hydrophobic part of CTAB molecules on AuNRs and form stable CTAB-polymer complexes [26,27].

Upon functionalizing AuNRs with either PEG-SH or PEO–PPO–PEO molecules, many physicochemical property of a gold nanoparticles formulation will be affected and this may impact their applications in sensing, imaging and targeted delivery. Thus, it is essential for the nanoparticle community to understand the effects of functionalizing PEG-SH or PEO–PPO–PEO molecules on the AuNRs surface and their

corresponding impact on biological systems. In this work, we systematically study the cytotoxicity, colloidal stability, and optical property of AuNRs before and after functionalizing them with PEG-SH and PEO–PPO–PEO molecules. These AuNRs formulations were characterized by using UV–vis spectroscopy, transmission electron microscopy (TEM), cell viability assay, dynamic light scattering (DLS), and dark-field imaging microscopy. The non-specific uptake of these AuNRs by cells was also studied under dark-field microscopy. Our work demonstrates that the coating of AuNRs surfaces with PEG-SH or PEO–PPO–PEO molecules significantly improved the colloidal and optical stability of the gold nanoformulation. No aggregation is found even a few weeks after the preparation. More importantly, the cell viability and dark-field imaging studies indicate that the AuNRs functionalized with PEG-SH or PEO–PPO–PEO molecules have minimal cytotoxicity and they can be used for long term in vitro and in vivo imaging study.

Experimental

Materials: Hydrogen tetrachloroaurate(III) trihyrate ($HAuCl_4 \cdot 3H_2O$), cetylmethylammonium bromide (CTAB), sodium borohydride ($NaBH_4$), silver nitrate ($AgNO_3$), L-ascorbic acid, trisodium citrate ($Na_3C_6H_5O_7$), Pluronic F127, and the cell counting kit (CCK8) were purchased from Sigma-Aldrich. PEG-SH (CH_3O–PEG-SH) was purchased from Rapp Polymere. Dulbecco's modified Eagles's medium (DMEM) and 1× phosphate buffer sulphate (PBS) were prepared in-house. Fetal bovine serum (FBS) and penicillin/streptomycin (Pen Strep) were purchased from Gibco®. The clean-mount solution for fixing a glass cover slip over 8-chamber slides was purchased from electron microscopy sciences.

AuNRs synthesis and characterization: Synthesis of AuNRs was adapted from Nikhoobakt et al. [6]. As described in [27], 5 mL of 0.5 mM $HAuCl_4$ was added to 5 mL of 200 mM CTAB to obtain an amber colored solution. 600 µL of 10 mM $NaBH_4$ was then added to the solution and stirred vigorously for a minute. A light brown seed solution was obtained. AuNRs were synthesized by a seed-mediated method, and 5 mL of 1 mM $HAuCl_4$ was added to 5 mL of 200 mM CTAB and stirred. 350 µL of 4 mM $AgNO_3$ was then added. 70 µL of 78.8 mM of L-ascorbic acid was added, and a colorless solution was formed. 18 µL of the seed solution was injected into the growth solution and left to form AuNRs for an hour at room temperature. The AuNRs solution was centrifuged at 10,000 rpm for 10 min and suspended in water. This washing step was repeated 3 times to remove excess CTAB. For AuNRs encapsulation, after three centrifugations, the supernatant were taken out and the AuNRs pellet was left in the centrifuge tube without suspending them in water. A transmission electron microscope (TEM) was used with JEOL JEM-1010 to characterize the shapes and sizes of the AuNRs. The TEM specimens were prepared on 200 mesh nickel-coated grids. UV–vis absorption spectra of AuNRs were obtained by using a Hitachi U-2900 with a double-beam optical system and a spectral bandpass of 1.5 nm over the spectrophotometric with a wavelength range of 400 to 1100 mm. The specimen was placed in a quartz cuvette for measurement and deionized water was used as a reference.

Functionalization of AuNRs with PEG-SH or Pluronic molecules: In a similar way as described in [27], 1 mL of Pluronic F127 or PEG-SH solution of various concentrations (10 nM, 100 nM, 1 µM, 10 µM, 100 µM and 1 mM) was added to the AuNRs pellet. The resultant solutions were left to be incubated for 1 h and then centrifuged once to remove excess Pluronic or PEG-SH solution. The functionalized AuNRs were then resuspended in water. Concentrations of the AuNRs solutions were fixed at an optical density of 1.5 for our studies.

Cell culture and cell viability: As described in [27], oral squamous cell carcinoma (OSCC) cell line was cultured in DMEM containing 10% FBS with Pen Strep. All cultures were kept at 37 °C with 5% CO_2. 5,000 cells were seeded in a 96-well plate for 24 h before loading each well with 10 µL of AuNRs solution (concentrations of all the solutions were fixed at an optical density of 1.5 with a UV–vis spectrophotometer). After a further incubation of the cells for 24 h, 10 µL of CCK8 was added to each well followed by another incubation of 4 h in the dark at 37 °C with 5% (v/v) CO_2. Cell population absorbance was performed with the SpectraMax 384 Plus spectral analyzer. The absorbance from the tetrazolium dye in CCK8 was measured at 450 nm excitation.

In vitro dark-field imaging study: As described in [27], 5,000 cells suspended in media were seeded in each well of the 8-well chamber glass slide and allowed to be confluent. Media was then removed and the slide was rinsed with PBS. Media was replenished in the wells. The corresponding synthesized substances were loaded and allowed to incubate for four hours at room temperature and pressure in the dark. The media and synthesized substances were removed and rinsed with PBS again, and the cells were fixed with 4% paraformaldehyde for 10 min. Thereafter, 4% paraformaldehyde was removed and rinsed with PBS. The well was removed and a cover slip was fastened with a layer of clean-mount on the slide. Dark-field imaging was performed with a Nikon Eclipse 80i at 100× magnification.

Results and Discussion

We used a seed-mediated approach to synthesize AuNR particles with a longitudinal SPR at 750 nm. During the formation of the AuNRs, the head group of CTAB molecules preferentially

binds to specific crystallographic faces of gold. Thus the gold atoms are directed to deposit on selective faces of gold and attain anisotropic nanoparticles in the solution medium [6,28,29]. In this process, CTAB forms a tightly bound cationic bilayer on the surface of AuNRs and CTAB-coated particles are known to be cytotoxic. We found that a major fraction of the CTAB molecules can be removed from the gold particle surface by multiple centrifugation steps. However, the washing steps affect the stability of the AuNRs and cause them to aggregate into precipitates in the solution. CTAB molecules are known to serve as surfactants for passivating the particles surface and maintaining the colloidal stability of the particles. The disruption and removal of CTAB from the gold particle surface results in large attractive interparticle forces, so that the particles form aggregates. To better understand this process UV–vis absorption spectra were measured for AuNR formulations before and after different treatments with washing steps. Figure 1 shows the normalized absorption spectra of AuNRs at different stages of washing treatments. A comparison of the absorption spectrum of as-synthesized AuNRs and treated AuNRs revealed that every round of washing caused a slight blue shift of the longitudinal SPR peak and an increase in the intensity of the transverse SPR peak starting from the third round of washing treatment. As the longitudinal SPR peak is determined by the aspect ratio of the AuNRs, the blue shift of this peak indicates that the aspect ratio of the AuNRs decreases as nanoparticles start to form large aggregates in the solution. To determine the morphology of AuNR particles at various stages, we performed TEM analysis on as-synthesized AuNRs and AuNRs after four rounds of washing treatment. The TEM image in Figure 2a shows that more than 90% of the as-synthesized AuNR particles are rod-like in dimension. Figure 2b indicates that a large fraction of AuNRs formed larger spherical aggregates, accounting for less than 50% rod-like particles.

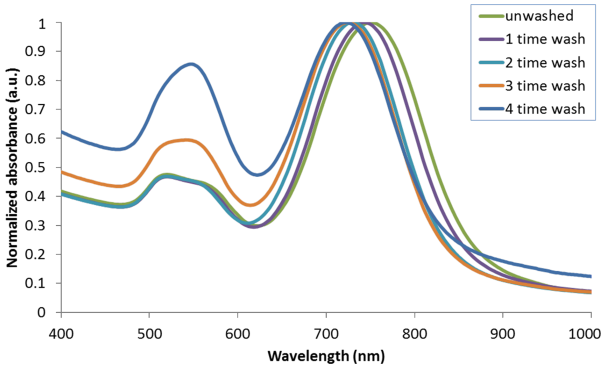

Figure 1: Normalized UV–vis absorption spectra of as-synthesized AuNRs and AuNRs washed one, two , three and four times by centrifugation.

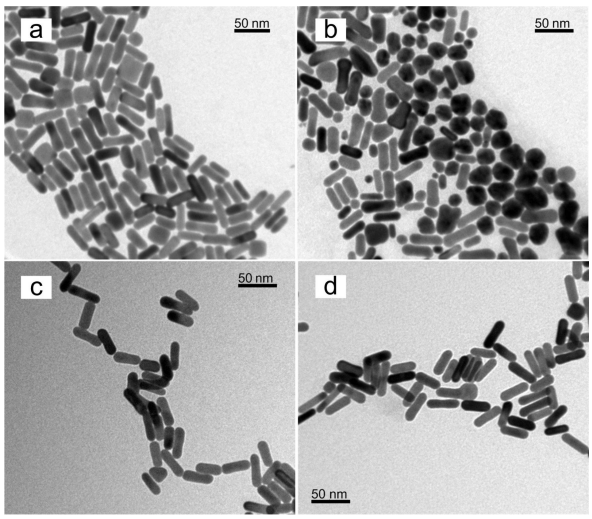

Figure 2: TEM images of (a) as-synthesized AuNRs, (b) AuNRs washed 4 times by centrifugation, (c) PEGylated AuNRs and (d) PEO–PPO–PEO encapsulated AuNRs.

To improve the compatibility of AuNRs for biological applications, we functionalized the particles with PEG-SH or PEO–PPO–PEO molecules. Hydrophobic PPO chains of Pluronic copolymer are able to bind to the hydrophobic tails of CTAB molecules, so that PEO–PPO–PEO molecules on the surface of CTAB-coated AuNRs are passivated. The hydrophilic PEO chains of the copolymer are then favorably interacting with the aqueous phase thereby maintaining the overall colloidal solubility of the AuNRs passivated by the Pluronic copolymer. Pluronic F127 was chosen as it has PPO and PEO chains of comparable length. Therefore, the advantages of these two block copolymers are combined to provide a better surface passivation on the particles and a better colloidal stability [30-32]. PEG-SH and Pluronic encapsulated AuNRs were prepared by retrieving particles after the third round of the washing treatment. Figure 2c and Figure 2d show the TEM images of AuNRs functionalized with PEG-SH and PEO–PPO–PEO molecules, respectively. In comparison to Figure 2a, the overall size and shape of AuNRs functionalized with either PEG-SH or PEO–PPO–PEO molecules remain the same, thus demonstrating that these two polymer molecules are suitable to be utilized in engineering the particle surface in way that maintains the optical and colloidal stability of AuNRs.

To systematically study the cytotoxicity of these functionalized AuNRs formulations, different concentrations of PEG-SH and PEO–PPO–PEO were used to react with CTAB-coated AuNRs and thereby producing AuNR formulations with a different surface coverage of PEG-SH and PEO–PPO–PEO molecules. The cytotoxicity between the as-synthesized AuNRs and AuNRs after varying times of washing treatment was also

compared. As shown in Figure 3, the as-synthesized AuNR formulation has excess CTAB molecules not only on the particle surface but also in the solution. This formulation exhibits a high toxicity to the cells. The cell viability of OSCC cells is maintained around 10% at 24 h post-treatment. Upon treating the OSCC cells with AuNRs after three rounds of washing, we were able to observe a significant increase in the cell viability to up to 70%. This demonstrates that the toxicity of the formulation was drastically reduced by removing CTAB surfactants from the particle suspension. However, further washing treatments to the AuNRs is infeasible because the particles will become unstable in the absence of CTAB surfactants in the suspension. The cell viability of AuNRs functionalized by different concentrations of PEG-SH or PEO–PPO–PEO surfactants is shown in Figure 4. It is clear that functionalizing the AuNRs surface with PEG-SH and PEO–PPO–PEO molecules can dramatically reduce the cytotoxicity of the formulation. This can be observed from the cell viability assay where the percentage is maintained at nearly 90% with concentrations of PEG-SH and PEO–PPO–PEO ranging from 10 nm to 1 mM. However, we observed that there is a concentration of PEG-SH and PEO–PPO–PEO molecules used for synthesizing AuNRs which yields the lowest cytotoxicity. We found that the use of 1 μM PEG-SH or 100 μM PEO–PPO–PEO to treat CTAB-coated AuNRs is able to produce a highly biocompatible particles formulation for in vitro applications. The reaction of CTAB-coated AuNRs with higher concentrations of PEG-SH and PEO–PPO–PEO molecules resulted in decreased cell viabilities. This may be caused by the impact of forming a thicker coating layer on the AuNRs surface [33]. Many groups have reported on the encapsulation of AuNRs with other polymer coatings to improve the biocompatibility of the rod nanoparticle formulations. For example, Alkilany et al. demonstrated the use of polyacrylic acid (PAA) and polyelectrolyte poly(allylamine) hydrochloride (PAH) to coat AuNRs surface. The coating was performed on as-synthesized CTAB-coated AuNRs after a washing treatment by centrifugation [15]. The CTAB-coated AuNRs solution was found to reduce cell viability by 30%, while both PAA-coated AuNRs and PAH-PAA-coated AuNRs were found to be non-toxic with a cell viability of about 90%. It was also found that the effective hydrodynamic diameter of PAA-coated AuNRs and PAH-PAA-coated AuNRs increases from 20 nm (CTAB-coated AuNRs) to 25 nm and 30 nm, respectively, indicating the successful coating of a polymer layer on the AuNRs surface. Wang et al. also reported the cytotoxicity of AuNRs under different conditions [34]. They found that the as-synthesized AuNRs formulation was highly toxic and a very low cellviability result (≈10%) was observed for this formulation. However, after 3 washing treatments by centrifugation, the cytotoxicity of CTAB-coated AuNRs was found to decrease, even though not to the extent which allows their usage for biological studies. Similar observations were made in our study.

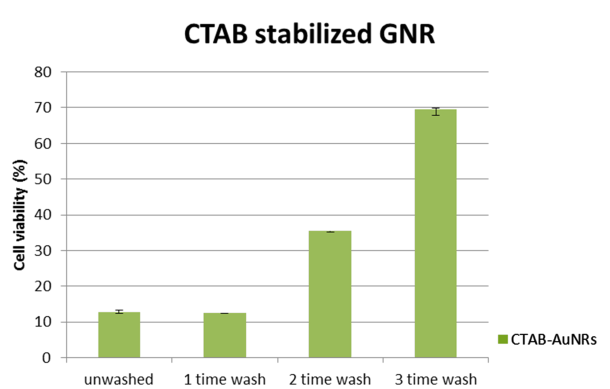

Figure 3: Relative cell viability of OSCC cells 24 h post-treatment. The cells were treated with as-synthesized AuNRs and AuNRs after different rounds of washing treatments.

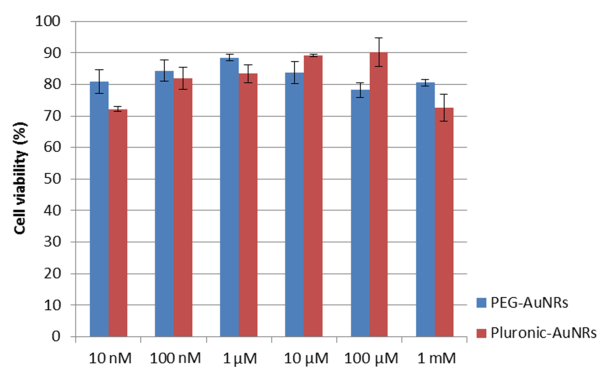

Figure 4: Cell viability of AuNRs encapsulated with different concentrations of PEG-SH or Pluronic triblock copolymer. The concentration of PEG-SH and Pluronic adopted for encapsulation ranges from 10 nM to 1 mM.

DLS experiments were performed in our study to determine the hydrodynamic diameter and the colloidal stability of the prepared AuNR formulations. Figure 5 shows the mean hydrodynamic diameter of CTAB-coated AuNRs before and after different rounds of washing treatment. A slight decrease (6 to 7 nm) in the overall hydrodynamic diameter of the nanoparticles formulation was observed after an additional round of washing. This indicates that a fraction of CTAB molecules was removed from the surface of the AuNRs with every round of washing by centrifugation. In general, we observed that AuNRs became less stable in the aqueous phase and formed aggregates after two to three rounds of washing. We observed that the mean hydrodynamic diameter of AuNRs increases slightly when the concentration of PEO–PPO–PEO and PEG-SH in the reaction mixture is increased (Figure 6). According to TEM analysis the hydrodynamic sizes of the AuNRs functionalized

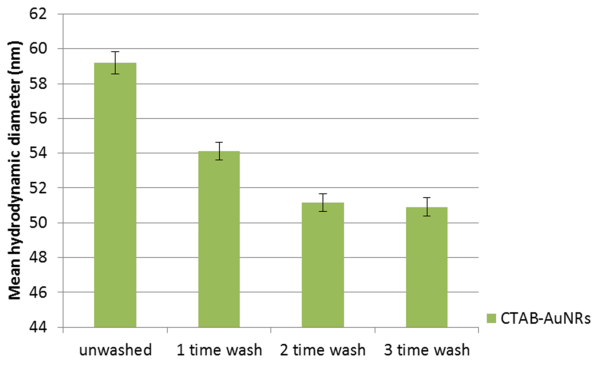

Figure 5: Mean hydrodynamic diameters of as-synthesized AuNRs (unwashed) and AuNRs washed three times by centrifugation. The hydrodynamic diameter is inferred from the diameter of the outermost encapsulation layer on a particle.

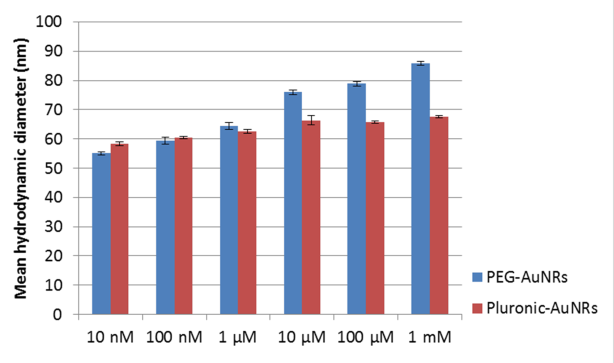

Figure 6: Mean hydrodynamic diameter of AuNRs encapsulated with different concentrations of PEG-SH or Pluronic.

with PEG-SH or PEO–PPO–PEO are found to be larger than those of AuNRs. This is mainly due to the solvated polymer layers of PEO–PPO–PEO or PEG-SH on the AuNRs surface. In our study, only AuNRs which underwent three washing treatments were used for functionalization with polymer molecules. The hydrodynamic diameter of the AuNRs was determined to be 55 and 58 nm after passivating their surface with PEO–PPO–PEO and PEG-SH molecules.

For in vitro imaging study, OSCC cells were treated with AuNRs functionalized with either PEG-SH or PEO–PPO–PEO molecules for evaluating their biocompatibility. In accordance with the cell viability results in Figure 4, three concentrations of PEG-SH (10 nM, 1 µM, 1 mM) and Pluronic (10 nM, 100 µM, 1 mM) were used to passivate AuNRs, and these formulations were employed for in vitro dark-field imaging. Figure 7 shows dark-field images of OSCC cells with the encapsulated AuNRs synthesized in this study. The bright red and orange scattered spots located within the cells suggest that the AuNRs were internalized into the cells by non-specific cellular uptake since no biomolecules were attached to our gold formulations. Huang et al. performed a similar experiment where AuNRs were also observed to be internalized by malignant oral epithelial cell lines and the extinction spectra analysis confirmed that the scattering colors within the cells was caused by nanoparticles [7].

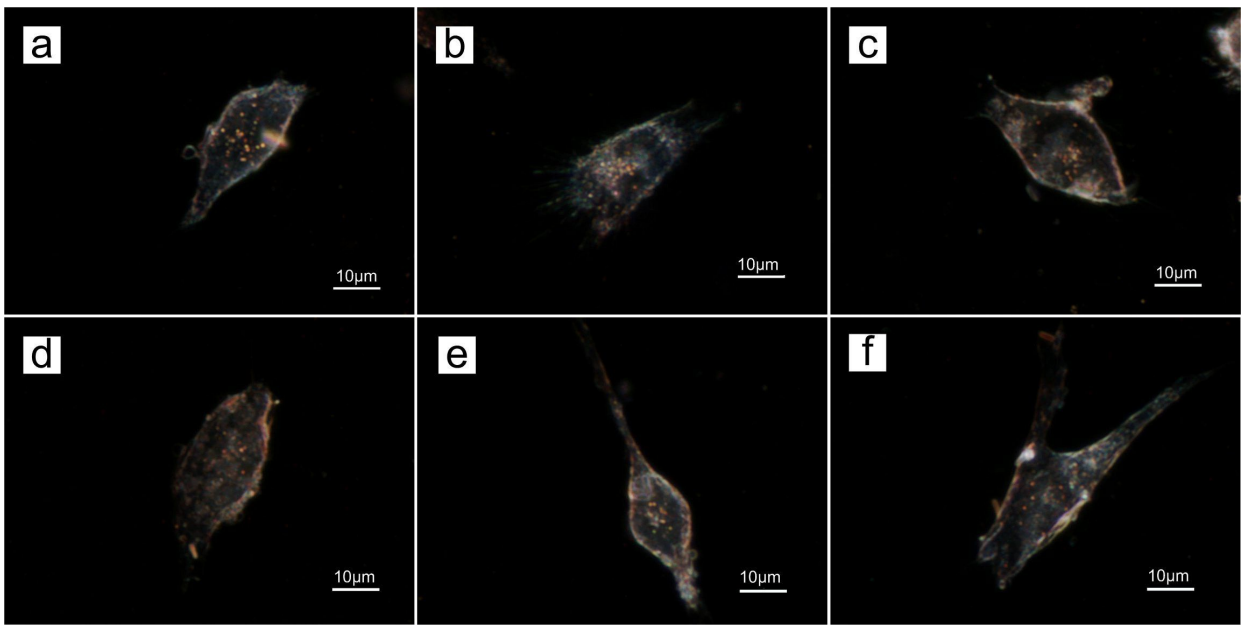

Figure 7: Dark-field images of OSCC cells with AuNRs encapsulated with (a) 10 nM, (b) 1 µM, (c) 1 mM of PEG-SH and (d) 10 nM, (e) 100 µM (f) 1 mM of Pluronic F127.

Thus, the coupling of the inherent scattering property of AuNRs with the use of polymer-based encapsulation further facilitates the use of AuNRs as biocompatible in vivo probes.

Conclusion

In this work, we studied the cytotoxicity, colloidal stability and optical property of AuNRs before and after functionalizing them with PEG-SH and PEO–PPO–PEO molecules. The as-synthesized AuNR surfaces are functionalized with CTAB molecules. This formulation is highly toxic and not suitable to be used for any biological applications. To employ the AuNRs for biological studies, the surface of AuNRs needs to be passivated with a biocompatible polymer coating. The encapsulation of AuNRs with PEG-SH or PEO–PPO–PEO molecules produces biocompatible AuNRs formulations. These formulations lead to stable colloidal solutions and can be readily used for dark-field imaging of cancer cells. We believe that this work provides useful insight for developing new protocols for preparing biocompatible AuNRs for applications ranging from cell imaging to targeted in vivo drug delivery.

Supporting Information

Supporting Information File 1

Chemical formula of PEG-SH and Pluronic (PEO–PPO–PEO).
[http://www.beilstein-journals.org/bjnano/content/supplementary/2190-4286-5-64-S1.pdf]

References

1. Eustis, S.; El-Sayed, M. A. *Chem. Soc. Rev.* **2006,** *35,* 209–217. doi:10.1039/b514191e
2. Jain, P. K.; Lee, K. S.; El-Sayed, I. H.; El-Sayed, M. A. *J. Phys. Chem. B* **2006,** *110,* 7238–7248. doi:10.1021/jp057170o
3. Huang, X.; El-Sayed, I. H.; El-Sayed, M. A. Applications of Gold Nanorods for Cancer Imaging and Photothermal Therapy. In *Cancer Nanotechnology;* Grobmyer, S. R.; Moudgil, B. M., Eds.; Methods in Molecular Biology, Vol. 624; Humana Press, 2010; pp 343–357. doi:10.1007/978-1-60761-609-2_23
4. Yu, C.; Irudayaraj, J. *Anal. Chem.* **2007,** *79,* 572–579. doi:10.1021/ac061730d
5. Prescott, S. W.; Mulvaney, P. *J. Appl. Phys.* **2006,** *99,* 123504. doi:10.1063/1.2203212
6. Nikoobakht, B.; El-Sayed, M. A. *Chem. Mater.* **2003,** *15,* 1957–1962. doi:10.1021/cm020732l
7. Huang, X.; El-Sayed, I. H.; Qian, W.; El-Sayed, M. A. *J. Am. Chem. Soc.* **2006,** *128,* 2115–2120. doi:10.1021/ja057254a
8. Dickerson, E. B.; Dreaden, E. C.; Huang, X.; El-Sayed, I. H.; Chu, H.; Pushpanketh, S.; McDonald, J. F.; El-Sayed, M. A. *Cancer Lett.* **2008,** *269,* 57–66. doi:10.1016/j.canlet.2008.04.026
9. Wijaya, A.; Schaffer, S. B.; Pallares, I. G.; Hamad-Schifferli, K. *ACS Nano* **2009,** *3,* 80–86. doi:10.1021/nn800702n
10. Nikoobakht, B.; El-Sayed, M. A. *J. Phys. Chem. A* **2003,** *107,* 3372–3378. doi:10.1021/jp026770+
11. Nikoobakht, B.; Wang, J.; El-Sayed, M. A. *Chem. Phys. Lett.* **2002,** *366,* 17–23. doi:10.1016/S0009-2614(02)01492-6
12. Johnson, C. J.; Dujardin, E.; Davis, S. A.; Murphy, C. J.; Mann, S. *J. Mater. Chem.* **2002,** *12,* 1765–1770. doi:10.1039/b200953f
13. Gao, J.; Bender, C. M.; Murphy, C. J. *Langmuir* **2003,** *19,* 9065–9070. doi:10.1021/la034919i
14. Murphy, C. J.; Gole, A. M.; Stone, J. W.; Sisco, P. N.; Alkilany, A. M.; Goldsmith, E. C.; Baxter, S. C. *Acc. Chem. Res.* **2008,** *41,* 1721–1730. doi:10.1021/ar800035u
15. Alkilany, A. M.; Nagaria, P. K.; Hexel, C. R.; Shaw, T. J.; Murphy, C. J.; Wyatt, M. D. *Small* **2009,** *5,* 701–708. doi:10.1002/smll.200801546
16. Huang, X.; El-Sayed, I. H.; Qian, W.; El-Sayed, M. A. *Nano Lett.* **2007,** *7,* 1591–1597. doi:10.1021/nl070472c
17. Oyelere, A. K.; Chen, P. C.; Huang, X.; El-Sayed, I. H.; El-Sayed, M. A. *Bioconjugate Chem.* **2007,** *18,* 1490–1497. doi:10.1021/bc070132i
18. Agarwal, A.; Mackey, M. A.; El-Sayed, M. A.; Bellamkonda, R. V. *ACS Nano* **2011,** *5,* 4919–4926. doi:10.1021/nn201010q
19. Gibson, J. D.; Khanal, B. P.; Zubarev, E. R. *J. Am. Chem. Soc.* **2007,** *129,* 11653–11661. doi:10.1021/ja075181k
20. Niidome, T.; Yamagata, M.; Okamoto, Y.; Akiyama, Y.; Takahashi, H.; Kawano, T.; Katayama, Y.; Niidome, Y. *J. Controlled Release* **2006,** *114,* 343–347. doi:10.1016/j.jconrel.2006.06.017
21. Green, H. N.; Martyshkin, D. V.; Rodenburg, C. M.; Rosenthal, E. L.; Mirov, S. B. *J. Nanotechnol.* **2011,** *2011,* 631753. doi:10.1155/2011/631753
22. Li, J. L.; Day, D.; Gu, M. *Adv. Mater.* **2008,** *20,* 3866–3871. doi:10.1002/adma.200800941
23. Gong, T.; Olivo, M.; Dinish, U. S.; Goh, D.; Kong, K. V.; Yong, K.-T. *J. Biomed. Nanotechnol.* **2013,** *9,* 985–991. doi:10.1166/jbn.2013.1603
24. Dubois, L. H.; Nuzzo, R. G. *Annu. Rev. Phys. Chem.* **1992,** *43,* 437–463. doi:10.1146/annurev.pc.43.100192.002253
25. Clarke, P. Reports: Globalfoundries hints at $10-bn fab location, 2013.
26. Iqbal, M.; Chung, Y.-I.; Tae, G. *J. Mater. Chem.* **2007,** *17,* 335–342. doi:10.1039/b610761c
27. Goh, D.; Gong, T.; Dinish, U. S.; Maiti, K. K.; Fu, C. Y.; Yong, K.-T.; Olivo, M. *Plasmonics* **2012,** *7,* 595–601. doi:10.1007/s11468-012-9347-3
28. Smith, D. K.; Korgel, B. A. *Langmuir* **2008,** *24,* 644–649. doi:10.1021/la703625a
29. Pérez-Juste, J.; Pastoriza-Santos, I.; Liz-Marzán, L. M.; Mulvaney, P. *Coord. Chem. Rev.* **2005,** *249,* 1870–1901. doi:10.1016/j.ccr.2005.01.030
30. Sakai, T.; Alexandridis, P. *Chem. Mater.* **2006,** *18,* 2577–2583. doi:10.1021/cm051757y
31. Sakai, T.; Alexandridis, P. *Langmuir* **2004,** *20,* 8426–8430. doi:10.1021/la049514s
32. van Oss, C. J. Stability Versus Flocculation of Aqueous Particle Suspensions. In *The Properties of Water and their Role in Colloidal and Biological Systems;* van Oss, C. J., Ed.; Interface Science and Technology, Vol. 16; Elsevier: Amsterdam, Netherlands, 2008; pp 113–130.
33. Dunn, S. E.; Brindley, A.; Davis, S. S.; Davies, M. C.; Illum, L. *Pharm. Res.* **1994,** *11,* 1016–1022. doi:10.1023/A:1018939521589
34. Wang, S.; Lu, W.; Tovmachenko, O.; Rai, U. S.; Yu, H.; Ray, P. C. *Chem. Phys. Lett.* **2008,** *463,* 145–149. doi:10.1016/j.cplett.2008.08.039

Beilstein Journal of Nanotechnology

Towards precise defect control in layered oxide structures by using oxide molecular beam epitaxy

Federico Baiutti, Georg Christiani and Gennady Logvenov*

Review

Open Access

Address:
Max-Planck Institute for Solid State Research, Heisenbergstrasse 1, D-70569, Stuttgart, Germany

Email:
Gennady Logvenov* - g.logvenov@fkf.mpg.de

* Corresponding author

Keywords:
artificial superlattices; complex oxides; defect chemistry; interface effects; molecular beam epitaxy

Beilstein J. Nanotechnol. **2014,** *5,* 596–602.
doi:10.3762/bjnano.5.70

Received: 19 December 2013
Accepted: 10 April 2014
Published: 08 May 2014

This article is part of the Thematic Series "Physics, chemistry and biology of functional nanostructures II".

Guest Editor: A. S. Sidorenko

Abstract

In this paper we present the atomic-layer-by-layer oxide molecular beam epitaxy (ALL-oxide MBE) which has been recently installed in the Max-Planck Institute for Solid State Research and we report on its present status, providing some examples that demonstrate its successful application in the synthesis of different layered oxides, with particular reference to superconducting La_2CuO_4 and insulator-to-metal $La_{2-x}Sr_xNiO_4$. We briefly review the ALL-oxide MBE technique and its unique capabilities in the deposition of atomically smooth single-crystal thin films of various complex oxides, artificial compounds and heterostructures, introducing our goal of pursuing a deep investigation of such systems with particular emphasis on structural defects, with the aim of tailoring their functional properties by precise defects control.

Introduction

The progress in the synthesis of layered complex oxide compounds with high precision has been stimulated by the research on the many functional properties, from electrical to magnetic and optical, and on the multitude of structural and electronic phases that pertain to these strongly correlated materials [1]. Together with this, a major field of investigation is represented by interface effects occurring in oxides heterostructures [2]. In the last decades, their study has revealed the presence of unexpected properties, such as superconductivity [3,4], metallicity [5,6] and magnetism [7], which cannot be ascribed to any of the constituent phases taken singularly. Many, sometimes contradictory, mechanisms have been proposed in order to explain interface effects, including cationic intermixing [8], electronic reconstruction [9,10] and extrinsic doping [11,12], witnessing the complexity of the phenomena.

In order to achieve further progress in the study of complex oxides, there is an urgent need for a synergetic cross-fertiliza-

tion of the chemistry and physics approaches. Recognizing this, researchers at the Max-Planck Institute for Solid State Research (MPI-FKF) have pursued a long-standing program to synthesize and investigate epitaxial metal oxide thin films and heterostructures based on the ALL-oxide MBE technique, which allows for the synthesis of structures of the best quality, together with the possibility to operate a compositional control at the most accurate level, possibly down to the single atomic layer [13]. The purpose is to provide new insights in the mechanisms underlying complex oxides and interfaces properties and to synthetize novel compounds and devices, giving particular importance to the role of defect chemistry in the definition of the functionalities and to the possibility of tuning them through a control of defects concentration and distribution.

Oxide MBE

The MBE deposition technique is characterized by the evaporation of the elements constituting the desired compound from metal sources, followed by their recombination on the substrate surface. This provides the lowest kinetic energy of the incoming species, ensuring low undesired intermixing of different atoms or phases. Moreover, given the low deposition rate (few Ångstroms/minute), one can use appropriate monitoring tools to control the growth process very accurately. These two aspects represent major developments in comparison with the other most common oxide thin films deposition techniques, pulsed laser deposition (PLD) and sputtering. On the other hand, obvious limitations to the thickness of the samples and uncertainties in the deposition rates of each element, which eventually result in an off-stoichiometric growth, need to be taken into account. Indeed, at the present day there is no in-situ or ex-situ characterization method that can provide a control of the stoichiometry with an accuracy better than 1%. This makes the MBE method very uncertain, and only producing a large amount of samples ensures feasibility and reproducibility.

For the growth of complex oxides, one can use an MBE system whose construction is derived from the standard systems used for the synthesis of semiconducting heterostructures. The first modification required is the addition of a strong oxidation source. That is because one needs to work at low gas pressure ($<10^{-4}$ Torr) in the growth chamber in order to maintain the "MBE regime" conditions characterized by a ballistic path of the atoms from the metal source to the deposition surface, while having at the same time the possibility to oxidize the evaporated metals to the desired valence state in a temperature range (usually between 600 °C and 700 °C), which is suitable for the growth of a highly crystalline structure. The feasibility of using ozone as a source for the successful growth of complex oxides and in particular high-T_c superconductors was demonstrated by several groups led by H. Mooij, A. Goldman, J. Eckstein, I. Bozovic, D. Schlom, M. Naito, T. Kawai, H. Koinuma, J.-P. Locquet and some others, and now the ozone delivery systems are commercially available and commonly implemented.

The specific conditions needed for the growth of complex oxides also require some further modifications. Since all parts operate under severe working conditions (high temperature, strongly oxidizing atmosphere), the materials for each component must be chosen extremely carefully. Materials such as molybdenum or PBN, which are often used in standard MBE, are not applicable in the oxide MBE given their tendency to form volatile oxides. Moreover, in order to synthesize a complex oxide, one needs an adequate number of evaporation sources. A modular design with vacuum gates between each source and the growth chamber is desired, enabling the opening of a source for the replacement of the material or for maintenance without venting the main growth chamber. Typically, two types of evaporation sources are used: thermal effusion cells (or Knudsen cell) and electron-beam sources. Thermal effusion cells can be heated up to 2000 °C and provide an extremely stable temperature and evaporating atomic flux. Electron-beam sources can be used for the evaporation of metals that require higher temperature (typically refractory metals), but in this case the atomic fluxes are less stable.

In the field of oxide MBE, a major development was represented by the layer-by-layer deposition scheme, called ALL-oxide MBE, introduced by the Varian group [14-16], which enables an extremely accurate control of the growth process and therefore a rational material design at various levels. In contrast to a standard MBE, in which all the constituents of the grown compound are evaporated together (codeposition), in this case the sources shutters are sequenced in a way that the correct number and species of atoms forming each atomic layer is placed on the growing surface at the right time, so that each of them is deposited singularly and in a sequence defined by the operator. Key tool for the ALL-MBE technique is the reflection high-energy electron diffraction (RHEED) system, which allows the in-situ characterization of the growth process, giving information about the morphology and the crystal structure of the film surface [17]. According to these, one can optimize the synthesis process, e.g., carry out corrections in the stoichiometry or in the growth conditions and control the sequence of the atomic layers.

In semiconductors MBE, the ALL-MBE method is used to deposit so called "delta doped" structures [18], where the dopants are confined to a single atomic plane. Extending this approach to the field of oxide MBE, one can do "single atomic layer engineering", precisely defining the composition of each atomic layer, omitting or adding single layers to a given struc-

ture, stacking layers that belong to different compounds and designing artificial and metastable multilayers. A milestone in the ALL-oxide MBE technique was represented by the study of interface superconductivity between non-superconducting metallic $La_{1.55}Sr_{0.45}CuO_4$ and insulating La_2CuO_4 layers, in which the replacement of a small amount of Cu by Zn in a single CuO_2 plane allowed to localize the CuO_2 plane responsible for this interface effect [19]. The ALL-oxide MBE technique has been recently used by A. Bhattacharya et al. to tailor the magnetic exchange interaction in $LaMnO_3$–$SrMnO_3$ [20], where magnetic properties of these superlattices were tuned between ferromagnetic and antiferromagnetic metallic states by inserting extra single-unit-cell layers of $LaMnO_3$ and $SrMnO_3$, respectively.

The ALL-oxide MBE at the Max-Planck Institute for Solid State Research

The oxide MBE system that has been recently acquired by our institute is addressed to the atomic layer-by-layer growth of complex oxides and is equipped with two growth chambers, which are identical in construction and can work in parallel without interference, allowing us to increase the number of growth experiments and to reduce the time needed for the growth optimization. Designing and building were performed by DCA Instruments (Turku, Finland) according to the demands based on the experience achieved by of one of the authors during his work on the prototype ALL-oxide MBE systems at Oxxel GmbH (Bremen, Germany) and later in the Brookhaven National Laboratory (USA) [21]. The system has a cluster tool configuration. It is equipped with one ultra-high vacuum central distribution chamber (CDC) for the transfer of the samples. The CDC has eight connection ports: four of these are occupied by the two growth chambers, a load lock and a storage chamber, leaving four spare ports for a future expansion of the system. It will be possible to attach, for example, spectroscopic tools such as angular resolved photoemission spectroscopy (ARPES), time-of-flight ion scattering and recoil spectroscopy (TOF-ISARS), X-ray photoelectron spectroscopy (XPS) or any other, according to demands. Each chamber has a vertical design, which allows for the substrate transfer system to be fully automated. The substrate transfer between the load lock, the storage and each growth chamber is controlled by a PC-based logic controller. A photo of the MBE system is shown in Figure 1.

The schematic view of a growth chamber is presented in Figure 2. It is equipped with ten water cooled spools, each of whom houses an elemental source, a computer-controlled linear-motion shutter, a gate valve and two ports for the future installation of an atomic absorption spectroscopy system to measure the deposition rates during the film growth process. The effusion cell ports are positioned symmetrically around the chamber center line. In addition, each growth chamber is equipped with a four pockets electron-beam evaporator directly located below the substrate position. The growth chamber is provided with an internal liquid nitrogen cooled cryogenic panel surrounding the substrate area, and its geometry is optimized for a maximum substrate size of 3″. The substrate manipulator has motorized rotation and vertical translation. Pumping is provided by a corrosive gas version of a turbo-pump with a scroll-type backing pump and by an ion-pump. A differential pumping module is used as a common chamber, connected to all effusion cells and the electron gun differential pumping lines. This way, each source can be opened for service and replacement of a source element without venting the growth chamber within a short period of time, even during the film growth. The differential pumping module is also used to pump the electron gun of

Figure 1: Photo of the dual chamber ALL-oxide MBE system installed in the Max-Planck Institute for Solid State Research.

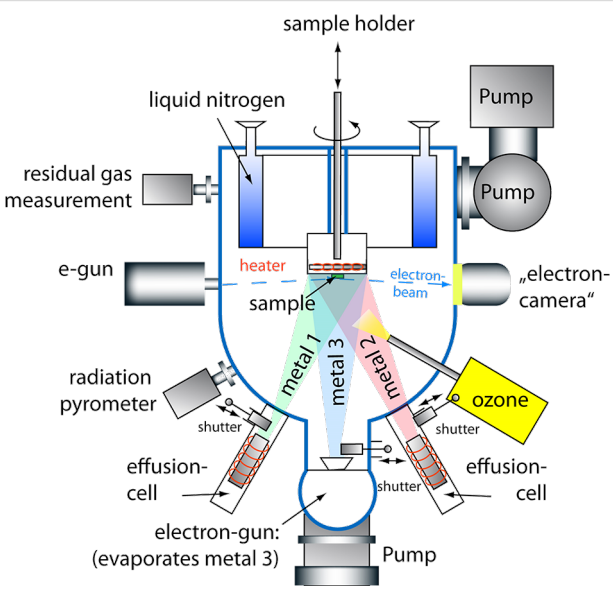

Figure 2: Sketch of the growth chamber.

the RHEED system and the load locked quartz crystal monitor (QCM) head. The QCM, which is mounted on a linear bellows assembly and is separated from the growth chamber by a gate valve, is used to calibrate the absolute deposition rates for each source before starting the process, while the RHEED system allows for the in-situ monitoring of the growth in real time. The oxygen resistive heater provides a maximum temperature of the heater element up to 1200 °C and the substrate temperature is controlled by a radiation pyrometer. The oxidation during the film growth is ensured by the delivery of pure ozone. Distilled ozone is collected from an ozone generator system and stored in an insulated still, where it is absorbed by silica gel spheres. The still temperature is adjusted by means of liquid nitrogen cooling and a heating element in order to control the evaporation rate of ozone, which is delivered to the growth chamber. The typical pressure in the growth chamber during a deposition is 10^{-6} to 10^{-5} Torr. The accurate layer-by-layer deposition control is enabled by electro-pneumatic linear shutters positioned in front of each source, which accurately control the amount of atoms deposited for each species and each layer. The shuttering system is implemented in a controlling software system that allows the operator to write recipes defining the composition of each atomic layer, to modify them during the film growth and to adjust the stoichiometry according to the RHEED pattern.

Results and Discussion

Using our ALL-oxide MBE system we can deposit a broad range of thin single phase oxide films and heterostructures. During the system optimization phase, we have experimented with $La_{2-x}Sr_xCuO_4$ and $La_{2-x}Sr_xNiO_4$ with different doping levels (x), $LaNiO_3$, $LaAlO_3$, $LaSrAlO_4$ and several other complex oxides. In particular, we have deposited superlattices with ultrathin layers, down to one unit cell thick. In most cases, such films and heterostructures have good cristallinity, smooth surfaces and interfaces. The crystallographic structure of our films is determined by high-resolution X-Ray diffraction (XRD) using a 4 circles X-ray machine by Bruker, while surface morphology is measured by a multimode atomic force microscope (AFM) by Veeco. In Figure 3 and Figure 4 we show AFM images for 25 nm thick La_2NiO_4 on $SrTiO_3$ (STO) substrate and for La_2CuO_4 on $LaSrAlO_4$ (LSAO) grown in our system, that suggest how our films are free from secondary phases outgrows and that layer-by-layer growth mode is achieved. The STO substrate was TiO_2 terminated by etching in buffered HF acid and a following annealing at 950 °C in oxygen flow. The LSAO substrate was simply cleaned in an ultrasonic bath with aceton and following isopropanol without special treatment for surface termination. Thus, we suppose that the LSAO substrate has a mixed termination of LaSrO and AlO_2 layers. The root mean square roughness is in both cases R_{ms} = 0.4 nm over a scanning area of 25 μm^2. In the former image, one can see clear atomic terraces, about 300 nm wide, with 0.5 unit cell tall steps due to the slight miscut angle of the STO substrate (<0.1°). The AFM image of the La_2CuO_4 film on LSAO does not clearly exhibit such atomic terraces first because, according to specifications, the miscut angle is less than 0.01°, which would lead to an atomic terraces width larger than 1.2 μm, secondarily because the mixed termination of the substrate can act in the direction of smearing these terraces given the fact that the surface roughness of each of the terraces is

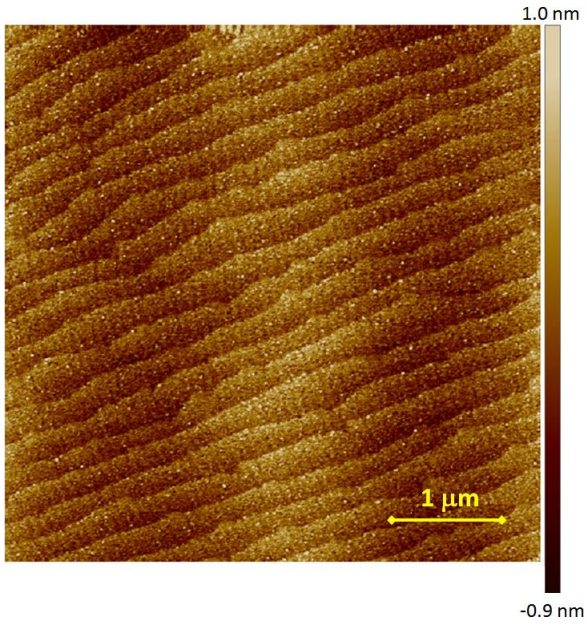

Figure 3: AFM image of 25 nm thick La_2NiO_4 film on STO substrate.

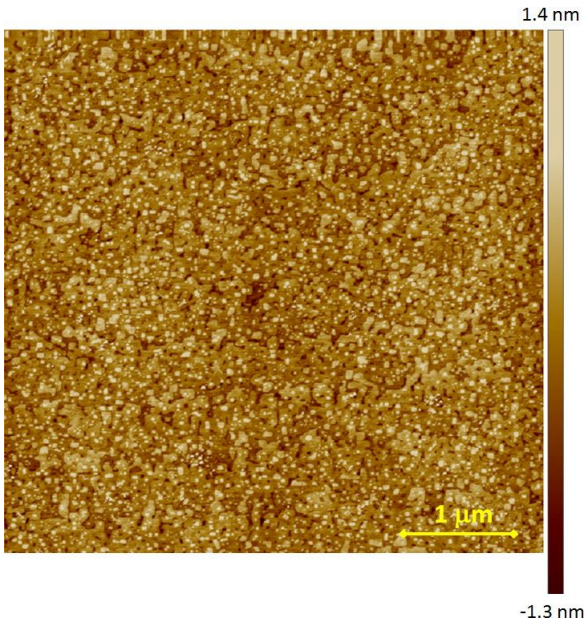

Figure 4: AFM image of 25 nm thick La_2CuO_4 film on LSAO substrate.

comparable to half of the La_2CuO_4 molecular layer size of about 0.65 nm.

The XRD θ–2θ scan for a La_2NiO_4–La_2CuO_4 bi-layer is shown in Figure 5. The high quality crystal structure of the epitaxial layers is confirmed by the observation of pronounced separate peaks from La_2NiO_4 and La_2CuO_4 layers up to (00 14) Bragg reflections, by the presence of Laue fringes around the main diffraction peaks (left inset) and by the X-ray reflectance (XRR) oscillations observed at low grazing angle (right inset). No XRR modulations deriving from the bilayer structure are expected, given the similar density of the constituent layers (7.22 g/cm^3 for LCO and 7.14 g/cm^3 for LNO).

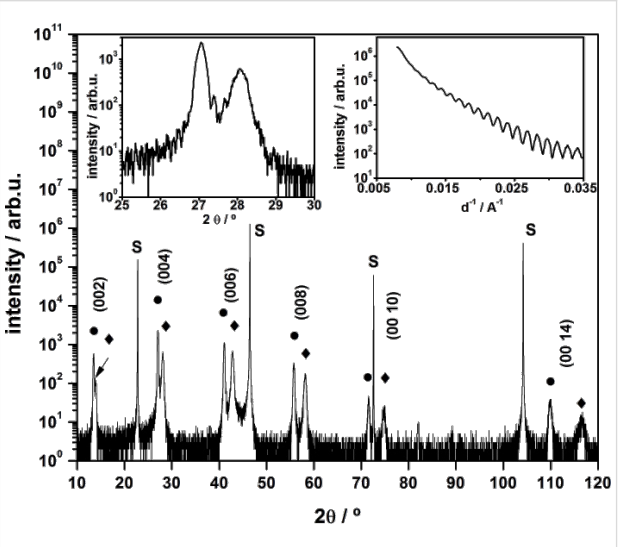

Figure 5: XRD θ–2θ scan of a bilayer heterostructure La_2NiO_4 (diamonds)–La_2CuO_4 (circles) on a STO(100) substrate (S). The thickness of the La_2NiO_4 and La_2CuO_4 is 26 nm and 40 nm respectively, according to the number of RHEED oscillations recorded during the growth. In the left inset: magnification of the (004) diffraction peak; in the right inset: XRR scan.

A crucial parameter for the growth of complex oxides is the system oxidation power. The oxidation state of the transition metals in the ozone-assisted MBE strongly depends on the ozone concentration in the growth chamber, that is, the efficiency of the ozone delivery, as the ozone molecules lifetime is in the range of some seconds. To our knowledge, one of the most demanding tests to check if the optimal concentration of ozone is reached is the synthesis of superconducting cuprates thin films [22]. To realize this test we tried to synthesize superconducting La_2CuO_4 epitaxial films. This parent compound for the $La_{2-x}Sr_xCuO_4$ family is an antiferromagnetic insulator that can be converted to superconducting $La_2CuO_{4+\delta}$, with $T_c \approx$ 40 K, upon annealing in ozone atmosphere due to the introduction of interstitial oxygen [23]. In Figure 6, we present resistivity versus temperature curves for two La_2CuO_4 films grown in our lab, carried out by using a four-probe method with Pt contacts deposited by sputtering on the corners implemented in a custom-built DC measurements setup. Both films were grown under the same conditions: substrate temperature 620 °C and chamber pressure $2.5 \cdot 10^{-5}$ Torr. The difference was in the cooling process after the growth. The insulating film was cooled down to 200 °C with a cooling rate of 30 °C/min and then the ozone delivery was stopped and the film was cooled down to room temperature in vacuum (10^{-9} Torr), and shows a resistivity curve that is an exponential function of temperature, while the second one, cooled down to room temperature at an increased ozone pressure of $5 \cdot 10^{-5}$ Torr, shows a superconducting transition around 40 K. This way we found that, in our growth conditions, (i) copper is oxidized to the maximum valence state Cu^{2+}, which is the first prerequisite to form the La_2CuO_4 phase and (ii) the ozone partial pressure in our deposition system is adequate to provide the optimal doping level.

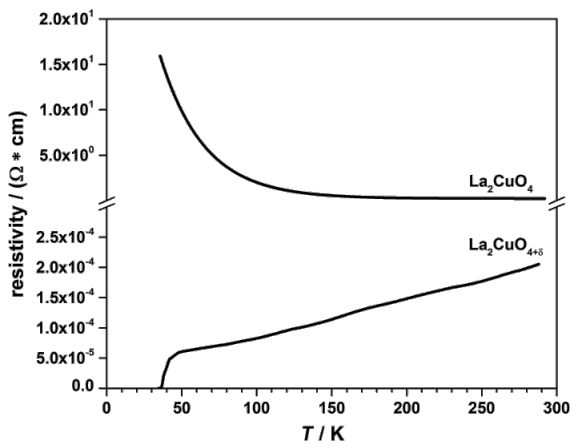

Figure 6: Resistivity versus temperature for the parent compound La_2CuO_4 and for the superconducting $La_2CuO_{4+\delta}$.

Using our ALL-oxide MBE system, we also focused on the growth of lanthanum nickelate $La_{2-x}Sr_xNiO_4$ with different Sr doping levels (x). This class of oxides is interesting because it is, under many aspects of crystal chemistry, similar to the superconducting $La_{2-x}Sr_xCuO_4$. The transition metal Nickel (Ni) can have several valence states, Ni^{1+}, Ni^{2+} and Ni^{3+}. Since La_2NiO_4 is one of the Ruddlesden–Popper phases $A_{n+1}B_nO_{3n+1}$ with n = 1, it is challenging to grow it as a single phase without the intergrowth of other phases. Here we report that, by using our ALL-oxide MBE, we synthesized atomically smooth $La_{2-x}Sr_xNiO_4$ epitaxial films with $0 \leq x \leq 1.4$. Diffraction measurements show that our films are c-axis oriented single phases, as can be seen in Figure 7, where the XRD θ–2θ scan for a composition with the nominal doping level x = 1 is shown. In the right inset, we report the calculated c-axis values for the different grown compositions: they exhibit a monotonical decrease for increasing

doping content. The in-plane resistivity versus temperature for $La_{2-x}Sr_xNiO_4$ with different Sr doping level is shown in Figure 8. The resistivity value systematically decreases with increasing Sr content. All the experimental data are in good agreement with those reported previously for $La_{2-x}Sr_xNiO_4$ epitaxial thin films grown by PLD [24]. Further analyses of films crystal structure, including high-resolution transmission electron microscopy (HR-TEM) and transport properties and will be presented elsewhere [25].

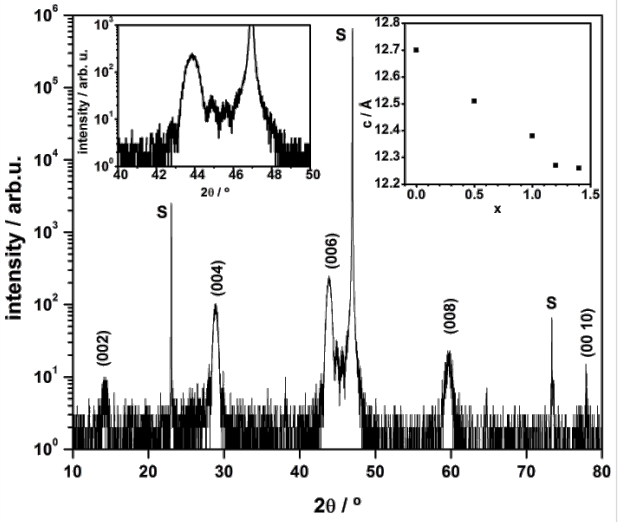

Figure 7: XRD θ–2θ scan of 13 nm thick $La_1Sr_1NiO_4$ on LSAT(100) (S). Laue fringes can be seen in the left inset, magnification around the (006) diffraction peak. In the right inset, the c-axis value, obtained by applying the Bragg equation for each peak position and subsequent refinement with the Nelson–Riley function, for thin films of $La_{2-x}Sr_xNiO_4$ epitaxially grown on LSAT(100) substrate.

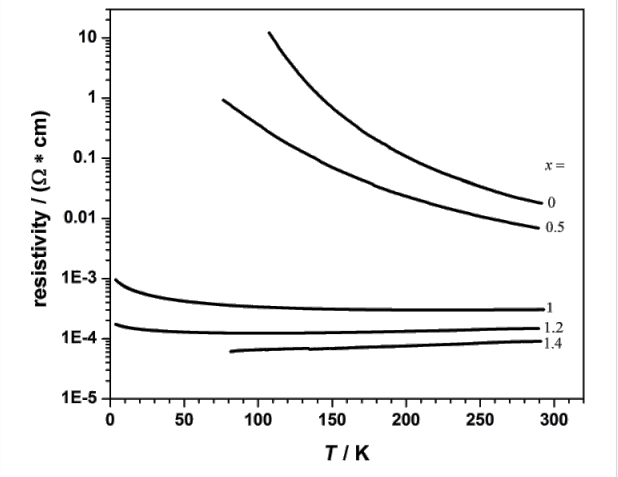

Figure 8: Resistivity versus temperature for $La_{2-x}Sr_xNiO_4$ with different doping levels.

Conclusion

We described our ALL-oxide MBE system, equipped with the state-of-art technology, a high level of automation and modularity and we showed some of its capabilities in the growth of different complex oxides and heterostructures. No alternative deposition techniques can provide a comparable level of flexibility and control at the sub-unit cell level, and we aim to take advantage of it when synthesizing various combinations and sequences of different layered oxides, trying to induce novel ground states in the interfaces or in the oxides blocks and to define innovative model systems for physical and chemical investigations. As previously mentioned, though, limitations occur, including for example the range of metal sources that can be evaporated, the oxidation power of the system and the control of stoichiometry during the growth process.

Besides these, other aspects have to be considered. First to be cited is the presence of the substrate whose roughness is in the best of the cases maintained, not smoothed, during the growth process, and which acts affecting layers morphology and interface abruptness. In addition, heteroepitaxy between substrate and film induces a strain state, which is responsible for the modification of the functional properties of the compound. By using the ALL-oxide MBE capabilities, in combination with advanced ex-situ investigation tools such as HR-TEM, we could deeper investigate how the epitaxial strain state, both in single phase films and in superlattices, is localized and how it is related to the functional and the structural properties. Another crucial point is given by thermodynamical limitations. Indeed, one should consider that the synthesis of artificial compounds or interfaces can lead to structural instabilities due, for instance, to solubility limits or to the tendency of atoms intermixing at interfaces resulting in cationic redistribution or intergrowth of secondary phases. Moreover, how do charge compensation mechanisms act at interfaces? What is the result of the “polar discontinuity” and of the presence of interfacial space charge zones? Together with electronic and cationic rearrangement, one should consider the major role which can be played by oxygen defects, which can easily be formed and migrate in the structure.

Taking all this into account, our approach will be based on the careful investigation of the aspects related to defects formation and distribution, with the aim to put in evidence their crucial role in the definition of the functionalities of complex oxide heterostructures. Taking advantage of this investigation, we aim to move from the idea of a “perfect sample”, which resembles theoretical models with minimized presence of imperfections, to the concept of precise defects control, based on the fine tuning of defects concentration and distribution. Its application to the “layer by layer engineering” by ALL-oxide MBE, could allow

us to develop new methods for the fabrication of layered oxides and heterostructures with novel functional properties.

Acknowledgements

We acknowledge Prof. Dr. J. Maier and Dr. G. Gregori for the insightful and continuous discussions.

References

1. Tsymbal, E. Y.; Dagotto, E. R. A.; Eom, C.-B.; Ramesh, R., Eds. *Multifunctional oxide heterostructures;* Oxford University Press: Oxford, U.K., 2012. doi:10.1093/acprof:oso/9780199584123.001.0001
2. Hwang, H. Y.; Iwasa, Y.; Kawasaki, M.; Keimer, B.; Nagaosa, N.; Tokura, Y. *Nat. Mater.* **2012,** *11,* 103. doi:10.1038/NMAT3223
3. Reyren, N.; Thiel, S.; Caviglia, A. D.; Kourkoutis, L. F.; Hammerl, G.; Ricter, C.; Schneider, C. W.; Kopp, T.; Rüetschi, A. S.; Jaccard, D.; Gabay, M.; Muller, D. A.; Mannhart, J. *Science* **2007,** *317,* 1196. doi:10.1126/science.1146006
4. Gozar, A.; Logvenov, G.; Kourkoutis, L. F.; Bollinger, A. T.; Giannuzzi, L. A.; Muller, D. A.; Bozovic, I. *Nature* **2008,** *455,* 782. doi:10.1038/nature07293
5. Ohtomo, A.; Hwang, H. Y. *Nature* **2004,** *427,* 423. doi:10.1038/nature02308
6. Bhattacharya, A.; May, S. J.; te Velthuis, S. G. E.; Warusawithana, M.; Zhai, X.; Jiang, B.; Zuo, J. M.; Fitzsimmons, M. R.; Bader, S. D.; Eckstein, J. N. *Phys. Rev. Lett.* **2008,** *100,* 257203. doi:10.1103/PhysRevLett.100.257203
7. Takahashi, K. S.; Kawasaki, M.; Tokura, Y. *Appl. Phys. Lett.* **2001,** *79,* 1324. doi:10.1063/1.1398331
8. Willmott, P. R.; Pauli, S. A.; Herger, R.; Schlepütz, C. M.; Martoccia, D.; Patterson, B. D.; Delley, B.; Clarke, R.; Kumah, D.; Cionca, C.; Yacoby, Y. *Phys. Rev. Lett.* **2007,** *99,* 155502. doi:10.1103/PhysRevLett.99.155502
9. Wu, J.; Pelleg, O.; Logvenov, G.; Bollinger, A. T.; Sun, Y.-J.; Boebinger, G. S.; Vanević, M.; Radović, Z.; Božović, I. *Nat. Mater.* **2013,** *12,* 877. doi:10.1038/nmat3719
10. Nakagawa, N.; Hwang, H. Y.; Muller, D. A. *Nat. Mater.* **2006,** *5,* 204. doi:10.1038/nmat1569
11. Kalabukhov, A.; Gunnarsson, R.; Börjesson, J.; Olsson, E.; Claeson, T.; Winkler, D. *Phys. Rev. B* **2007,** *75,* 121404. doi:10.1103/PhysRevB.75.121404
12. Di Castro, D.; Salvato, M.; Tebano, A.; Innocenti, D.; Aruta, C.; Prellier, W.; Lebedev, O. I.; Ottaviani, I.; Brookes, N. B.; Minola, M.; Moretti Sala, M.; Mazzoli, C.; Medaglia, P. G.; Ghiringhelli, G.; Braicovich, L.; Cirillo, M.; Balestrino, G. *Phys. Rev. B* **2012,** *86,* 134524. doi:10.1103/PhysRevB.86.134524
13. Schlom, D. G.; Haeni, J. H.; Lettieri, J.; Theis, C. D.; Tian, W.; Jiang, J. C.; Pan, X. Q. *Mater. Sci. Eng., B* **2001,** *87,* 282. doi:10.1016/S0921-5107(01)00726-7
14. Eckstein, J. N.; Bozovic, I. *Annu. Rev. Mater. Sci.* **1995,** *25,* 679. doi:10.1146/annurev.ms.25.080195.003335
15. Bozovic, I.; Eckstein, J. N.; Klausmeier-Brown, M. E.; Virshup, G. F. *J. Supercond.* **1992,** *5,* 19. doi:10.1007/BF00617991
16. Chaiken, A.; Wall, M. A.; Howell, R. H.; Bozovic, I.; Eckstein, J. N.; Virshup, G. F. *J. Mater. Res.* **1996,** *11,* 1609. doi:10.1557/JMR.1996.0202
17. Bozovic, I.; Eckstein, J. N. *MRS Bull.* **1995,** *20* (5), 32.
18. Schubert, E. F. *J. Vac. Sci. Technol., A* **1990,** *8,* 2980. doi:10.1116/1.576617
19. Logvenov, G.; Gozar, A.; Bozovic, I. *Science* **2009,** *326,* 699. doi:10.1126/science.1178863
20. Santos, T. S.; Kirby, B. J.; Kumar, S.; May, S. J.; Borchers, J. A.; Maranville, B. B.; Zarestky, J.; te Velthuis, S. G. E.; van den Brink, J.; Bhattacharya, A. *Phys. Rev. Lett.* **2011,** *107,* 167202. doi:10.1103/PhysRevLett.107.167202
21. Logvenov, G.; Bozovic, I. *Physica C* **2008,** *468,* 100. doi:10.1016/j.physc.2007.08.013
22. Schlom, D. G.; Marshall, A. F.; Sizemore, J. T.; Chen, Z. J.; Eckstein, J. N.; Bozovic, I.; Von Dessonneck, K. E.; Harris, J. S., Jr.; Bravman, J. C. *J. Cryst. Growth* **1990,** *102,* 361. doi:10.1016/0022-0248(90)90393-Y
23. Bozovic, I.; Logvenov, G.; Belca, I.; Narimbetov, B.; Sveklo, I. *Phys. Rev. Lett.* **2002,** *89,* 107001. doi:10.1103/PhysRevLett.89.107001
24. Shinomori, S.; Okimoto, Y.; Kawasaki, M.; Tokura, Y. *J. Phys. Soc. Jpn.* **2002,** *71,* 705. doi:10.1143/JPSJ.71.705
25. Baiutti, F. et al. To be published.

License and Terms

Beilstein Journal of Nanotechnology

Cyclodextrin-poly(ε-caprolactone) based nanoparticles able to complex phenolphthalein and adamantyl carboxylate

Daniela Ailincai[1] and Helmut Ritter[*2]

Full Research Paper

Open Access

Address:
[1]Centre of Advanced Research in Bionanoconjugates and Biopolymers, "Petru Poni" Institute of Macromolecular Chemistry of Romanian Academy, 41A Aleea Grigore Ghica Voda, 700487 Iasi, Romania and [2]Heinrich-Heine-Universität, Institut für Organische Chemie und Makromolekulare Chemie, Geb. 26.33, Eb. 00, Universitätsstr. 1, 40225 Düsseldorf, Germany

Email:
Helmut Ritter[*] - h.ritter@uni-duesseldorf.de

* Corresponding author

Keywords:
click reaction; complexation; cyclodextrin; encapsulation; nanoparticles

Beilstein J. Nanotechnol. **2014,** *5,* 651–657.
doi:10.3762/bjnano.5.76

Received: 10 January 2014
Accepted: 14 April 2014
Published: 16 May 2014

This article is part of the Thematic Series "Physics, chemistry and biology of functional nanostructures II".

Guest Editor: A. S. Sidorenko

Abstract

A new compound composed of poly(ε-caprolactone) and β-cyclodextrin (β-CD) was synthesized by click chemistry. This compound was used to obtain stable nanoparticles, which have been proven to be able to complex phenolphthalein and adamantyl carboxylate. The nanoparticles are characterized by a distinct morphology, i.e., a hydrophobic core formed by the polyester chain and a shell containing the CD part. Moreover, the formed nanoparticles have been proven to encapsulate umbelliferone in the polyester phase, which may serve as an example for the uptake of a drug. The formed nanoparticles were characterized in terms of sizes and morphology by both DLS and TEM.

Introduction

The development of new nanoscale systems for the encapsulation of drugs or imaging agents, which could be used in the treatment, localization or diagnosis of diseased tissues, represents one of the most interesting aims for researchers working in the realm of biochemistry. A lot of such systems have been reported in the past years, including nanovesicles based on natural macromolecular compounds, liposomes formed by autoassemble of phospholipids in aqueous medium [1], and nanovesicles formed by the autoassemble of synthetic amphiphilic copolymers, polymersomes [2]. There is a broad variety of conditions which have to be met, both for nanoparticles and for the macromolecular compounds that underlie their formation [3].

The existence of various barriers present at different levels of the human body, necessitates the use of nano-level carriers. Regarding the requirements for the macromolecular compounds used to form nanoparticles, among the most important

are biocompatibility, biodegradability and nontoxicity [4,5]. The aliphatic polyesters combine the requirements above mentioned. Consequently, they had a huge impact on the biomedical field and are used in surgical sutures, tissue scaffolding and for bone screws [6]. Between them, one of the most studied and used is poly(ε-caprolactone), a linear aliphatic polyester, obtained by ring-opening polymerization of ε-caprolactone.

Poly(ε-caprolactone) was used in several combinations, including click reaction products. Functionalized polyester was obtained, which was further used for grafting β-CD on it. The final product has been proven to exhibit a host–guest ability with different compounds [7]. Pseudo-polyrotaxanes based on propargyl functionalized poly(ε-caprolactone) and mono-(6-azido-6-desoxy)-ß-CD have been successfully obtained [8].

Here, we propose to obtain an amphiphilic behavior by using poly(ε-caprolactone), which is known for its high hydrophobicity. To obtain an amphiphilic behavior requires the presence of a hydrophilic compound, which also has to comply with the biocompatibility, biodegradability and nontoxicity requirements. Copper catalyzed click chemistry became a very important tool for the synthesis of new polymeric structures over the past years [9] and represents an attractive method for bonding a polyester chain with a hydrophilic compound [10].

The use of propargylic alcohol as an initiator leads to a polyester with an acetylenic end group, which allows its use as a click reaction precursor. The chemical modification of CD, consisting of the selective substitution of the C6-hydrogen with an azidic group, permits its use as a click reaction partner for the modified poly(ε-caprolactone). CDs are cyclic oligosaccharides composed of α-(1-4)-linked α-D-glucosyl units [11]. They have a hydrophobic cavity in their interior, whereas the exterior part is hydrophilic. Drugs with adequate sizes can be complexed by the internal hydrophobic part of the CDs, while macromolecular drugs are only partially included [12]. Host–guest interactions between a monoacrylated CD and *N*-isopropylacrylamide based copolymer have been reported [13]. The characterization and the morphology of a complex based on fish oil encapsulated in CD with the use of polycaprolactone have also been reported [14,15]. Furthermore, CD inclusion complexes with different essential oils and their potential application for antimicrobial delivery have been described [16].

The aim of this study was to develop a β-CD-poly-ε-caprolactone compound by click chemistry, which is able to form nanoparticles in water. Once obtained, the nanoparticles were used for host–guest behavior studies with different hydrophobic compounds, including phenolphthalein and adamantyl carboxylate. The ability of the click reaction product to complex umbelliferone was also investigated, based on its structural similarity with other hydrophobic compounds previously described in the literature as guests for CD.

Experimental

Materials, general remarks

β-CD was obtained from Wacker Chemie GmbH, Burghausen, Germany and was used after being dried overnight with a vacuum oil pump over P4O10. *N*,*N*-Dimethylformamide (DMF) was purchased from Fluka, Germany. Dimethyl sulfoxide-d_6 (99.9 atom % D) and deuterium oxide. ε-Caprolactone was purchased from Acros, dried over calcium hydride, distilled under reduced pressure, and stored over 0.4 nm molecular sieves. Sodium ascorbate (AppliChem) and copper(II) sulfate (Carl Roth GmbH) were used as received. Commercially available reagents and solvents were used without further purification.

Measurements

^{1}H NMR spectra were recorded on a Bruker Avance DRX 600 at 20 °C by using DMSO-d_6 or $CDCl_3$ (99.9%) as solvents. Chemical shifts referenced to the solvent value δ = 2.5 ppm for DMSO-d_6 and δ = 7.26 ppm for $CDCl_3$. SEC-MALS measurements were carried out on a combined system comprising the following elements: refractive-index detector Optilabrex (Wyatt Technologies, laser wavelength 658 nm), three-angle light-scattering detector miniDawn TREOS (Wyatt Technologies, laser wavelength 658 nm, detector angles at 43.5°, 90.0° and 136.5°), UV detector Waters 486 (Waters), column set of HEMAbio 300 and HEMAbio 100 (MZ-Analysentechnik), pump, degasser and autosampler (Agilent 1200, Agilent technologies). The eluent was ultrapure water at a flow rate of 1 mL/min. The molecular weight was calculated with Astra5 software from static-light-scattering data by using the Zimm model. Dynamic light scattering (DLS) experiments were carried out with a Malvern Zetasizer Nano ZS ZEN 3600 at a temperature of 25 °C. The particle size distribution is derived from a deconvolution of the measured intensity autocorrelation function of the sample by a general purpose method, i.e., the non-negative least squares algorithm, included in the DTS software. The TEM images have been obtained with a TEM Zeiss 902.

Synthesis

Synthesis of alkyne-functionalized polyester

The strategy for the synthesis of functionalized aliphatic polyester bearing a propargyl end-group relies on the Sn(Oct)-mediated ring-opening polymerization (ROP) of ε-caprolactone by using the propargylic alcohol as an initiator. A 10 mL round bottom flask was heated and purged with argon. 5 g

(43.806 mmol, 10 Eg) of ε-caprolactone and 608.86 mg of propargylic alcohol was added to the round-bottom flask and heated at 120 °C. When the temperature is reached, 88.72 mg (0.219 mmol) of $Sn(Oct)_2$, 0.5 mol % with respect to the monomer, is added. Argon was purged into the reaction flask. The reaction mixture was stirred for 24 h. After this, the product was cooled at room temperature and a solid is formed. The product was dissolved in CH_2Cl_2, separated through precipitation in a large excess of hexane, and dried under vacuum (91% mass yield). The reaction product was characterized in terms of molecular weight and dispersity by GPC and the obtained values were 4600 for the Mw and 1,164 for the dispersity index. The structure was proved by NMR. ^{1}H NMR (600 MHz, $CDCl_3$): 1.15 (H from acetylenic group), 1.3 (H-e), 1.6 (H-d), 2.3 (H-c), 3.6 (H-g'), 4 (H-g).

Synthesis of the CD endgroup containing poly(ε-caprolactone) by a “click” reaction

Mono-(6-azido-6-desoxy)-ß-CD has been obtained following the published procedure [7]. In a similar manner as described before [8] the click reaction was successfully realized by adding mono-(6-azido-6-desoxy)-ß-CD to a solution of polyester in DMF (0.6% w/w). To the reaction mixture were added 10 mol % sodium ascorbate and 5 mol % copper(II) sulfate pentahydrate. The flask was immersed in an oil bath at 95 °C for 24 h. The solvent was removed at the rotatory evaporator and the product was dried under vacuum.

^{1}H NMR (600 MHz, C_2D_6SO) 3.32 (H-2,4), 3.6–3.84 (H-3,5,6), 4.44–4.6 (OH-6), 4.85 (H-1), 5.73 (OH-2, 3) from the β-CD rest and 1.15 (H), 1.3 (H-e), 1.6 (H-d), 2.3 (H-c), 3.6 (H-g'), 4 (H-g) from the polyester. The melting point was 77 °C.

The success of the click reaction between the poly(ε-caprolactone) with an acetylenic final group and the modified β-CD was also proved by FTIR analysis. The polyester presented one peak at 2096 cm^{-1} corresponding to the acetylenic group, while the modified β-CD presented two peaks, one at 2040 cm^{-1} and one at 2100 cm^{-1}, corresponding to the azidic group. The click reaction product had no peaks in these region since all reactive groups (acetylenic and azidic) have been consumed during the reaction (Figure 1).

Preparation of nanoparticles

A solution of the click reaction compound (Figure 1, (3)) was prepared by dissolving 100 mg compound into 1 mL of DMF. Small amounts from this solution were added to a large excess of water (35 mL) under an ultrasonifier treatment. The formation of aggregates was proved by means of DLS measurements.

Phenolphthalein and adamantyl carboxylate complexation by the formed nanoparticles

A suspension of the nanoparticles (A) was obtained as previously described. A solution of phenolphthalein in water was prepared, to which trace amounts of NaOH were added to increase the pH and obtain a pinkish solution (B). A was added to B, while stirring (C). To C, a solution of adamantly-carboxylate in water was added, while vigorously stirring.

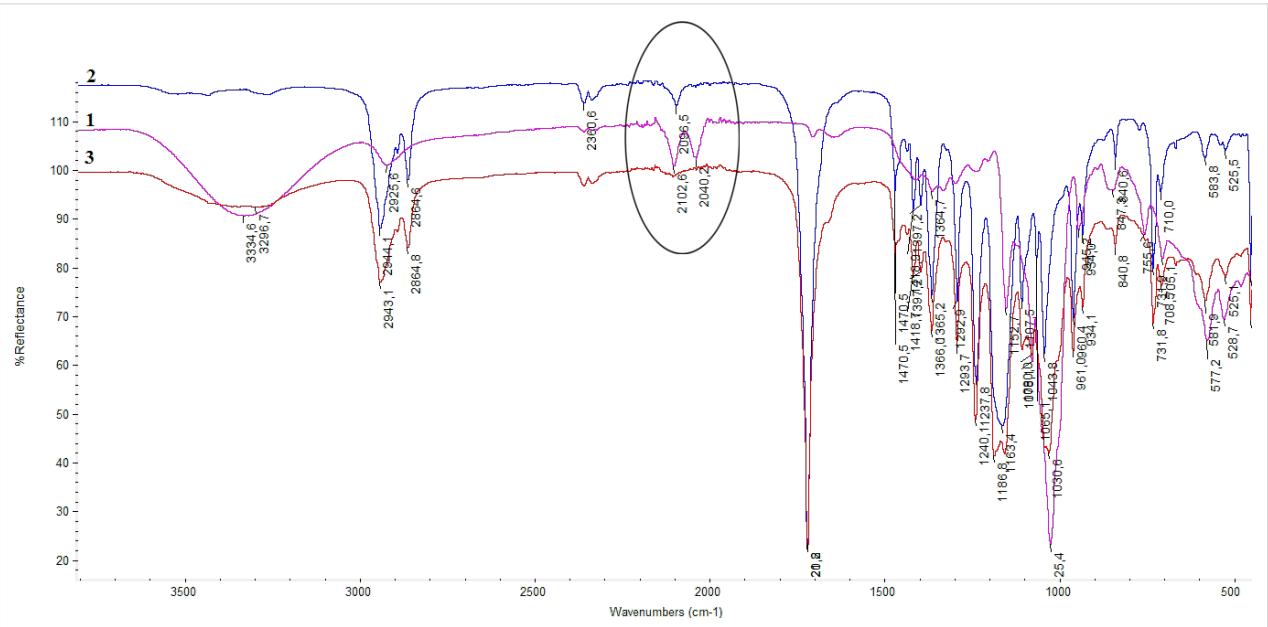

Figure 1: The FTIR spectra for (1) the mono-6-azido-CD, (2) the alkyne compound of poly(ε-caprolactone), and (3) the click reaction product.

Results and Discussion

Previously synthesized mono-6-azido-β-CD (**1**) was "clicked" with an alkyne compound of poly(ε-caprolactone) (**2**) (Scheme 1). The reaction was catalyzed by copper(I), obtained in situ by the reduction of $CuSO_4$ with sodium ascorbate. DMF was used as a solvent due its high boiling point and its ability to solubilize both starting materials. The click reaction product was characterized by using ^{1}H NMR and FTIR spectroscopy.

The properties of **3** in water were investigated by DLS measurements. We observed that the higher the concentration of the copolymer the greater the sizes of the nano-aggregates. These nano-aggregates are quite stable in water as DLS measurements of the suspension, performed after 8 days, shows an increase of the nano-aggregates' diameter of ≈35% (Figure 2).

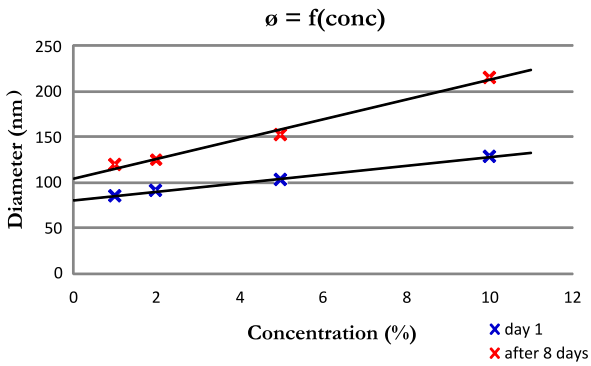

Figure 2: The dependency between the nanoparticles' diameter (formed by **3** in water) as a function of the concentration.

The nanoparticles were prepared by adding small amounts of a solution of **3** in DMF to a solution of umbelliferone in ultrapure water (35 mL). The amount of the added umbelliferone was varied in this experimental protocol. We observed that the diameter of the nanoparticles increased with an increasing umbelliferone concentration (Figure 3). Moreover, the diameter of the nanoparticles encapsulating umbelliferone was bigger than the diameter of the nanoparticles without umbelliferone. The increase of the diameter of the nanoparticles formed in the umbelliferone solution can be explained by the entrapment of umbelliferone, a highly hydrophobic compound, in the hydrophobic core of the nanoparticles.

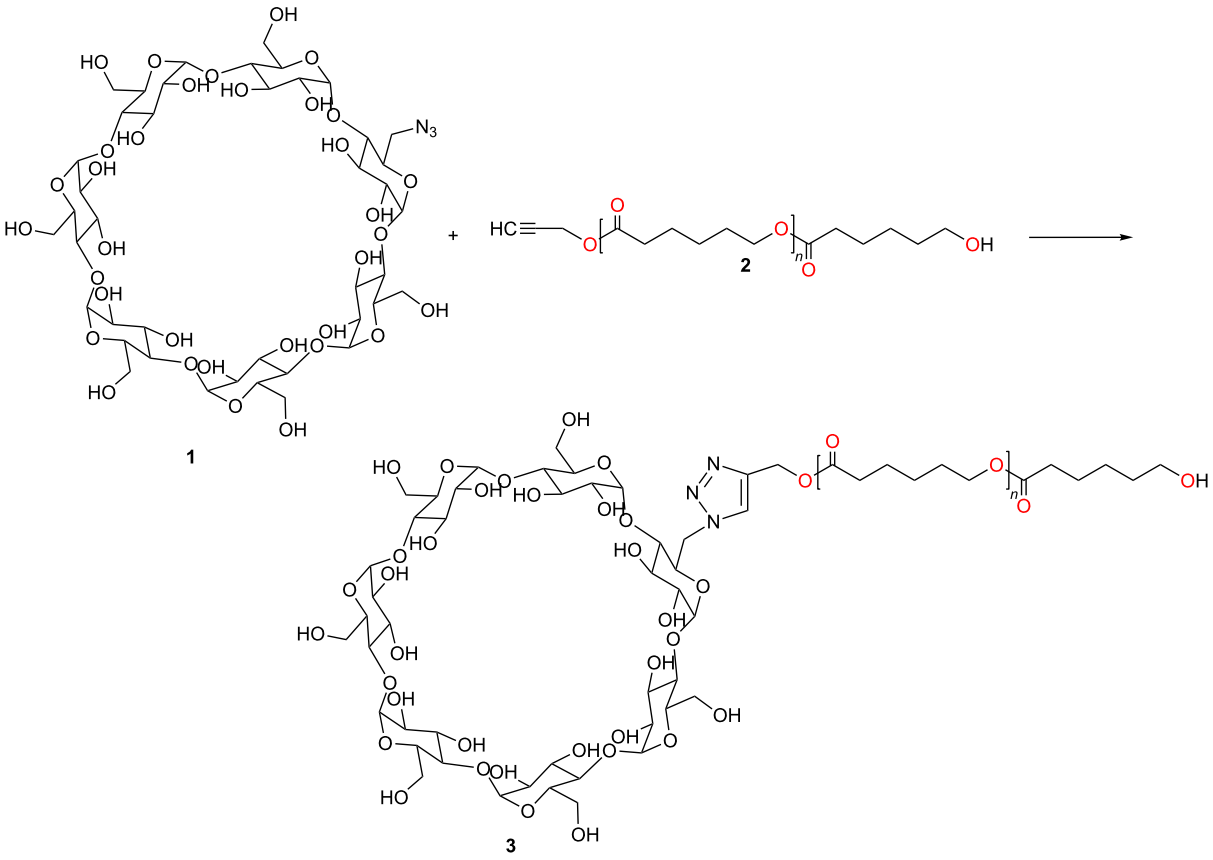

Scheme 1: Click reaction between mono-6-azido-CD (**1**) and the alkyne compound of poly(ε-caprolactone) (**2**).

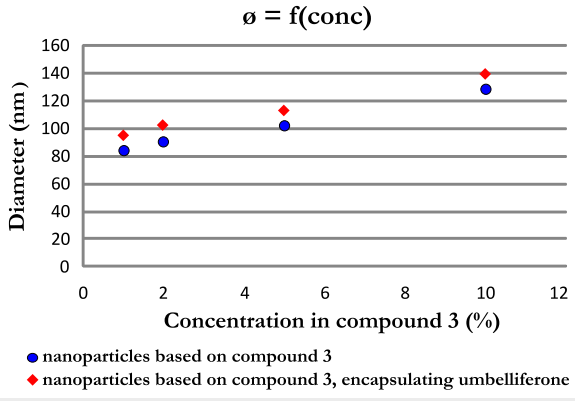

Figure 3: Diameter of the nanoparticles based on compound **3**, with and without umbelliferone.

To investigate the morphology of the formed nanoaggregates, TEM analysis was performed. The microscope images show the formation of nanoparticles the sizes of which are in agreement with the DLS measurements. TEM images of nanoparticles obtained with two different concentrations are presented in Figure 4 (A: concentration 1%, B: concentration 2%).

We also tested the ability of the formed nanoparticles to complex phenolphthalein and adamantyl carboxylate. Furthermore, this study also aimed for establishing the exact morphology of the nanoparticles. Pictures were taken of the phenolphthalein solution in water at pH > 7, the nanoparticles suspension added to the phenolphthalein solution, and the adamantyl carboxylate added to the previous phase (Figure 5).

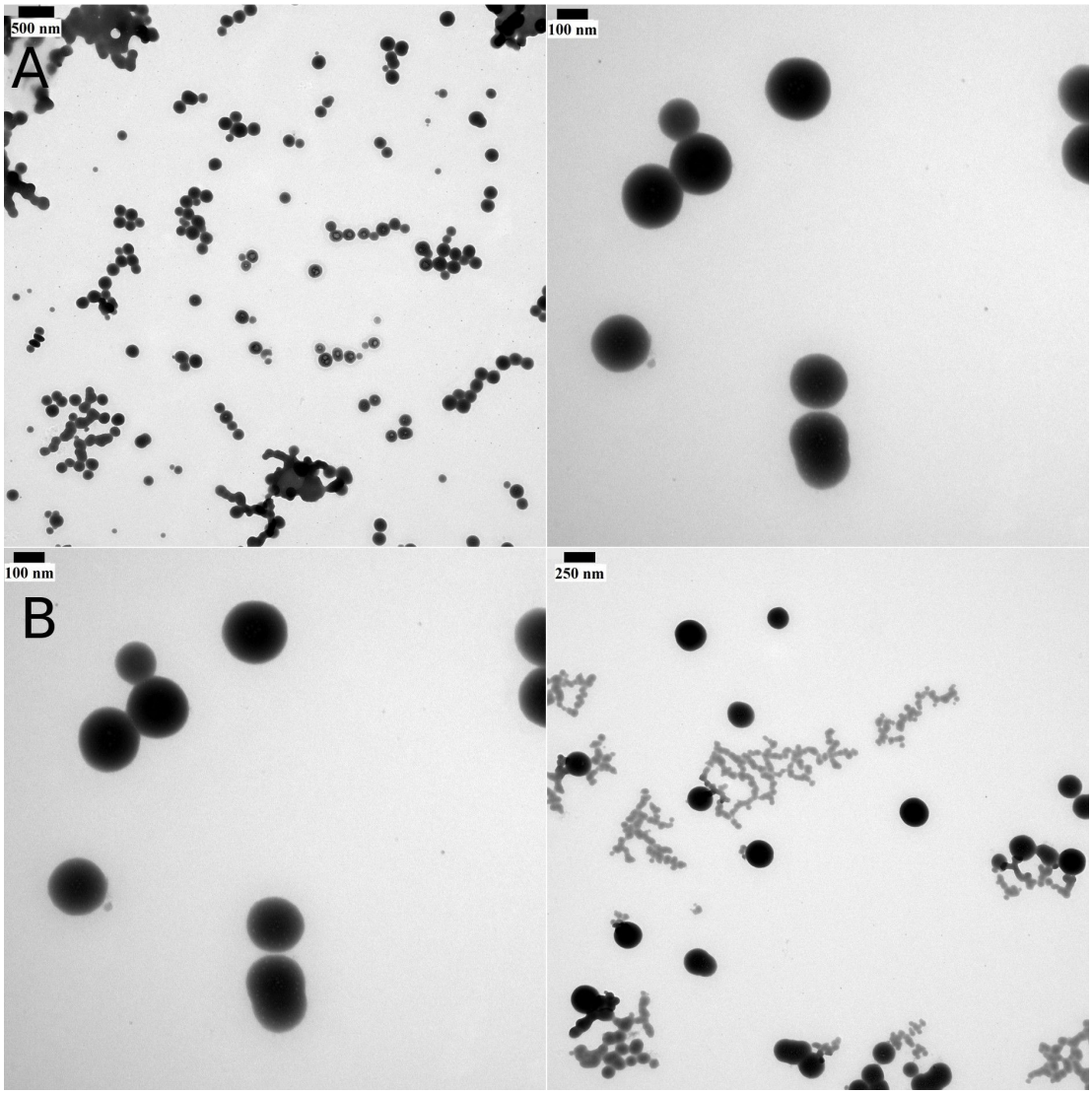

Figure 4: TEM images for the nanoparticles based on **3**. The nanoparticles were obtained by dispersing the click reaction product (**3**) in water. with a concentration of 1% (A) and 2% (B).

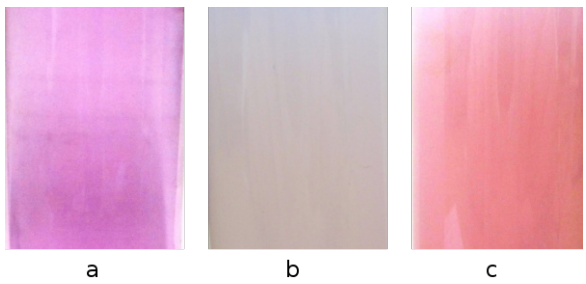

Figure 5: The color during the complexation with phenolphthalein and adamantyl carboxylate. (a) Phenolphthalein solution in water at pH > 7, (b) nanoparticles suspension added to the phenolphthalein solution, (c) nanoparticles suspension in phenolphthalein solution after the addition of adamantyl carboxylate.

Based on the ability of the nanoparticles to complex phenolphthalein and adamantyl carboxylate we propose the morphology shown in Figure 6.

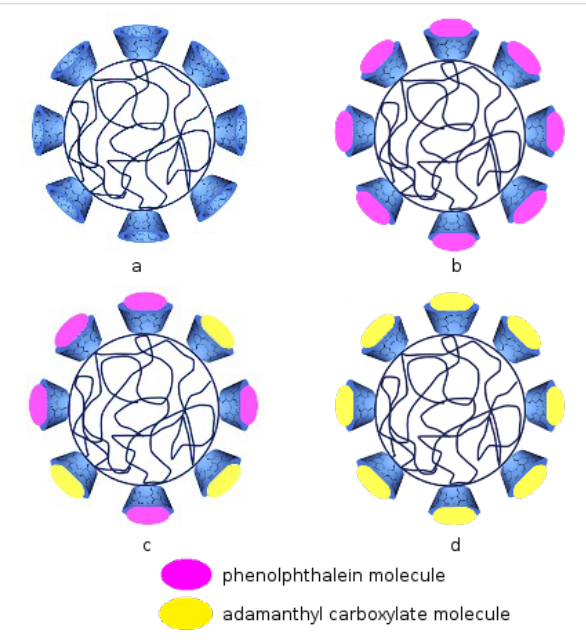

Figure 6: Schematic representation of the CD based nanoparticles morphology. (a) In water at pH > 7, (b) in phenolphthalein solution, (c) after small amounts of adamantyl carboxylate were added to the phenolphthalein solution, (d) after a large amount of adamantyl carboxylate was added to the phenolphthalein solution.

Presumably, the interior is formed by the hydrophobic poly(ε-caprolactone) chain, while the β-CD part is located on the exterior (Figure 6a). When the nanoparticles suspension is added to the phenolphthalein solution (pH > 7) the phenolphthalein is included in the hydrophobic cavity of β-cyclodextrin (Figure 6b) and the suspension changes its color from pink in white (Figure 5). The affinity of adamantyl carboxylate to β-cyclodextrin is higher than of phenolphthalein to β-cyclodextrin. Thus, the addition of adamantyl carboxylate results in phenolphthalein leaving the β-cyclodextrin cavity and adamantyl carboxylate entering it so that the suspension changes its color back to pink (Figure 5).

Conclusion

In conclusion, we successfully prepared nanoparticles in water by nano-precipitation of a solution of poly(ε-caprolactone) tailored with the addition of β-CD as an endgroup. We proved that the formed nanoparticles are able to complex phenolphthalein and adamantyl carboxylate, respectively, due to their distinct morphology. They consist of a hydrophobic core composed of the polyester chain and a shell, to which the β-CD part is covalently attached. The nanoparticles have been characterized in terms of morphology and diameter by both DLS measurements and TEM. Umbelliferone, a hydrophobic molecule, was not included in the cavity of the CD moiety according to ROESY NMR measurements. However, the encapsulation of umbelliferone in the hydrophobic part of the nanoparticles was demonstrated by the increased diameter of nanoparticles obtained in a solution with umbelliferone compared to nanoparticles obtained in pure water.

References

1. Bangham, A. D. *Biophys. J.* **1994,** *67,* 1358–1359. doi:10.1016/S0006-3495(94)80607-1
2. Seok, J. L.; Jan, F. *J. Controlled Release* **2012,** *161,* 473–483. doi:10.1016/j.jconrel.2011.10.005
3. Petros, R. A.; DeSimone, J. M. *Nat. Rev. Drug Discovery* **2010,** *9,* 615–627. doi:10.1038/nrd2591
4. Mohanraj, V. J.; Chen, Y. *Trop. J. Pharm. Res.* **2006,** *5,* 561–573. doi:10.4314/tjpr.v5i1.14634
5. Wang, A. Z.; Langer, R.; Farokhzad, O. C. *Annu. Rev. Med.* **2012,** *63,* 185–198. doi:10.1146/annurev-med-040210-162544
6. Ikada, Y.; Tsuji, H. *Macromol. Rapid Commun.* **2000,** *21,* 117–132. doi:10.1002/(SICI)1521-3927(20000201)21:3<117::AID-MARC117>3.0.CO;2-X
7. Jazkewitsch, O.; Ritter, H. *Macromolecules* **2011,** *44,* 375–382. doi:10.1021/ma102456n
8. Jazkewitsch, O.; Mondrzyk, A.; Staffel, R.; Ritter, H. *Macromolecules* **2011,** *44,* 1365–1371. doi:10.1021/ma1027627
9. Munteanu, M.; Choi, S.; Ritter, H. *Macromolecules* **2008,** *41,* 9619–9623. doi:10.1021/ma8018975
10. Sinnwell, S.; Inglis, A. J.; Stenzel, M. H.; Barner-Kowollik, C. Blocks, Stars and Combs: Complex Macromolecular Architecture Polymers via Click Chemistry. In *Click Chemistry for Biotechnology and Material Science;* Lahann, J., Ed.; John Wiley & Sons: Chichester, UK, 2009; pp 89–117. doi:10.1002/9780470748862.ch6
11. Tomasik, P.; Schilling, C. H. Complexes of starch with organic guests. *Advances in carbohydrate chemistry and biochemistry;* Academic Press: San Diego, CA, USA, 1998; pp 345–426.
12. Davis, M. E.; Brewster, M. E. *Nat. Rev. Drug Discovery* **2004,** *3,* 1023–1035. doi:10.1038/nrd1576

13. Choi, S.; Munteanu, M.; Ritter, H. *J. Polym. Res.* **2009,** *16,* 389–394. doi:10.1007/s10965-008-9240-0
14. Choi, M.-J.; Ruktanonchai, U.; Min, S.-G.; Chun, J.-Y.; Soottitantawat, A. *Food Chem.* **2010,** *119,* 1694–1703. doi:10.1016/j.foodchem.2009.09.052
15. Choi, M.-J.; Ruktanonchai, U.; Soottitantawat, A.; Min, S.-G. *Food Res. Int.* **2009,** *42,* 989–997. doi:10.1016/j.foodres.2009.04.019
16. Hill, L. E.; Gomes, C.; Taylor, T. M. *LWT-Food Sci. Technol.* **2013,** *51,* 86–93. doi:10.1016/j.lwt.2012.11.011

License and Terms

Beilstein Journal of Nanotechnology

An analytical approach to evaluate the performance of graphene and carbon nanotubes for NH_3 gas sensor applications

Elnaz Akbari[1], Vijay K. Arora[*2,3], Aria Enzevaee[4], Mohamad. T. Ahmadi[5], Mehdi Saeidmanesh[5], Mohsen Khaledian[5], Hediyeh Karimi[1,6] and Rubiyah Yusof[1,6]

Full Research Paper

Open Access

Address:
[1]Centre for Artificial Intelligence and Robotics (CAIRO), Universiti Teknologi Malaysia, Kuala Lumpur, Malaysia, [2]Faculty of Electrical Engineering, Universiti Teknologi Malaysia, Johor Bahru, Malaysia, [3]Department of Electrical Engineering and Physics, Wilkes University, Wilkes-Barre, PA 18766, USA, [4]Faculty of Mechanical Engineering, Universiti Teknologi Malaysia, Johor Bahru, Malaysia, [5]Computational Nanoelectronic Research Group Faculty of Electrical Engineering, Universiti Teknologi Malaysia, Johor Bahru, Malaysia and [6]Malaysia–Japan International Institute of Technology (MJIIT), Universiti Teknologi Malaysia, Kuala Lumpur, Malaysia

Email:
Vijay K. Arora* - vijay.arora@wilkes.edu

* Corresponding author

Keywords:
carbon nanotube (CNT); conductance; FET-based gas sensor; graphene

Beilstein J. Nanotechnol. **2014,** *5,* 726–734.
doi:10.3762/bjnano.5.85

Received: 27 November 2013
Accepted: 29 April 2014
Published: 28 May 2014

This article is part of the Thematic Series "Physics, chemistry and biology of functional nanostructures II".

Associate Editor: A. Gölzhäuser

Abstract

Carbon, in its variety of allotropes, especially graphene and carbon nanotubes (CNTs), holds great potential for applications in variety of sensors because of dangling π-bonds that can react with chemical elements. In spite of their excellent features, carbon nanotubes (CNTs) and graphene have not been fully exploited in the development of the nanoelectronic industry mainly because of poor understanding of the band structure of these allotropes. A mathematical model is proposed with a clear purpose to acquire an analytical understanding of the field-effect-transistor (FET) based gas detection mechanism. The conductance change in the CNT/graphene channel resulting from the chemical reaction between the gas and channel surface molecules is emphasized. NH_3 has been used as the prototype gas to be detected by the nanosensor and the corresponding current–voltage (*I*–*V*) characteristics of the FET-based sensor are studied. A graphene-based gas sensor model is also developed. The results from graphene and CNT models are compared with the experimental data. A satisfactory agreement, within the uncertainties of the experiments, is obtained. Graphene-based gas sensor exhibits higher conductivity compared to that of CNT-based counterpart for similar ambient conditions.

Introduction

There is a rapid growth in the development of sensors both in research and commercial applications. Our daily lives can be noticeably influenced by the development and advancement of miniature and/or portable gas sensors capable of accurately detecting analytes in real-time. Sensors with higher sensitivity and selectivity as well as faster response time are desired. Portability, remote operability and cost effectiveness are some of the features receiving considerable attention because of the ease of their implementation. Rapid advancement in nanoengineering as well as the production of faster and more compact integrated electronic components allow for these goals to be reached [1-6]. Nanotechnology is the study and application of materials with at least one dimension of the order of 1 to 100 nanometers, which is comparable to the de Broglie wavelength of carriers. Novel applications [7-9] are possible by exploiting the quantum waves in operation of these low-dimensional devices. New materials are being discovered in building novel sensors that can operate on the nanometer scale. Examples of these include graphene and carbon nanotubes (CNTs), as well as various semi-conductive nanowires and nanotubes [10,11]. Arora, Tan, and Gupta [12] have studied the carrier statistics of graphene and response of carriers to high electric fields. Arora and Bhattacharyya [13] have combined the carrier statistics of CNTs and discussed the band structure and its applications to quantum transport. In a recent paper [14], Chin et. al show how nanoelectronic parameters can be extracted from quantum conductance. In the next section, we advance these thoughts as we design the sensor made out of graphene and CNT.

Carbon nanotubes and graphene

CNTs were first discovered by Sumio Iijima in 1991 [15] and have been extensively studied ever since. A single-walled carbon nanotube (SWCNT) is formed by rolling up a honeycomb lattice of a single atomic carbon sheet, i.e., graphene along a specific axis [16], known as chiral direction. The diameter of a typical CNT is around a few nanometers and its length can be over a micrometer, making it distinctly one-dimensional (1D) in its conductance with propagating quantum waves in the quasi free direction along the length of tube. Standing quantum waves are formed in the periphery of the tube forming the cylinder. A CNT is known to have a very high electrical and thermal conductivity as well as a high Young's modulus giving it the mechanical strength. The applications of CNTs are broad due to their compact structure and include transistors, sensors, solar cells, fuel cells, etc. [17].

Andre Geim and Konstantin Novoselov [18] discuss several applications of graphene, as one of the allotropes of carbon, which can be described as a single atomic layer of graphite. In this material, a two-dimensional honeycomb structure of sp^2-bonded carbon atoms is tightly packed in a lattice structure [18]. Due to its zero bandgap energy, graphene has a high electron mobility at room temperature. The electron transfer in graphene is 100 times faster than that in silicon. A zero band gap with massless Dirac fermions makes graphene theoretically lossless, making it a perfect two-dimensional (2D) semiconductor [19-21]. Due to the abovementioned outstanding characteristics, graphene and CNT are being used as possible candidates for high performance gas sensors. When integrated in the sensor circuit and exposed to an analyte gas as illustrated in Figure 1, the detection signals are obtained through the changes in the *I–V* characteristics of graphene/CNT. Operational amplifiers amplify these signals that can be converted to digital format for digital signal processing.

FET-based structure

As presented in Figure 2, the structure of the proposed gas sensors that use CNT/graphene as the conducting channel looks quite similar to the conventional metal-oxide semiconductor field effect transistor (MOSFET), which comprises source and drain electrodes with the gate insulator inducing the channel of carriers and a silicon back gate [22,23] to augment the carrier density or adjust the threshold voltage. A CNT/graphene channel connects the source and the drain electrodes, and the gate is separated from the channel by a dielectric barrier layer. In most studies, silicon is used as the back gate while SiO_2 is employed to act as a dielectric layer [23,24]. When gas molecules are in contact with the surface of CNT/graphene, the carrier concentration will change due to the variability of the current in the drain and the source, which is a measurable pa-

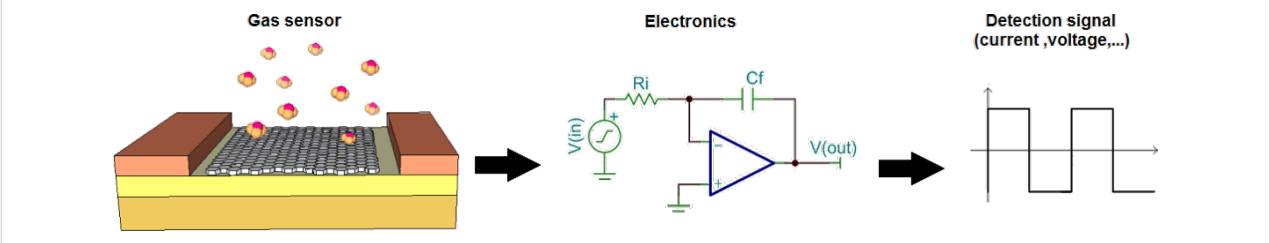

Figure 1: Schematic of a gas sensor.

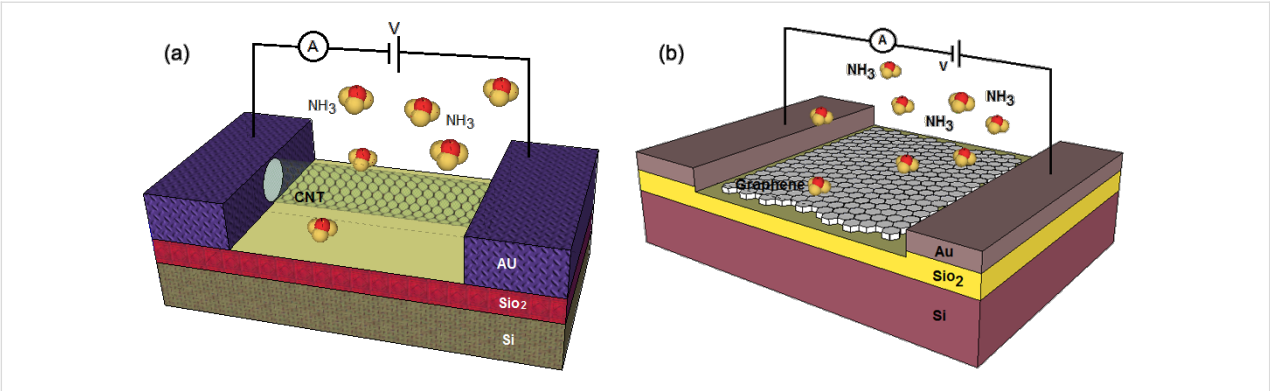

Figure 2: FET-based structure for gas sensor with (a) CNT channel and (b) graphene channel.

rameter [5,25-29]. The best gas sensor has a high sensitivity and is capable of sensing even one atom or molecule of gas [3,30]. Numerous recent theoretical studies on gas molecular adsorption on CNT/graphene have been reported for NO_2, H_2O, NH_3, CO, and NO molecules that are physically adsorbed on pristine CNT/graphene [31,32].

Figure 3 illustrates a schematic representation of CNTs when electron-donating NH_3 gas molecules are in the atmosphere around the sensor. Under such conditions, NH_3 molecules are adsorbed on the surface of the CNT channel and donate electrons to it. This process causes a quite significant change in the electrical properties of the CNT. These strong adsorption effects stem from the inherent properties of gas molecules and the bonding characteristics between these molecules and the CNT [33,34]. It is always important to obtain p-type and/or n-type semiconducting CNT to incorporate them in a complementary logic. A p–n junction is a result of this complementarity. n-Type and p-type nanoscale field effect transistors can be formed for implementation by applying positive or negative gate voltage and can be useful from the application perspective [35].

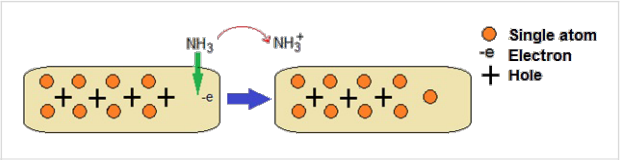

Figure 3: Schematic of the NH_3 sensing mechanism based on the gas adsorption phenomenon.

Gas molecules can modulate the electronic structure of graphene in diverse ways. The adsorption of CO_2 and O_2 converts the system to p-type semiconductor while the adsorption of NH_3 leads to n-type behavior. Similar to CNTs, these rich adsorption effects are caused by the intrinsic property of the gas molecules and the bonding characteristics between gas molecules and graphene [36]. The resulting p-type and n-type semiconducting behavior might be detected in experiment by applying and modulating gate voltage. Among all gas molecules considered, obviously NH_3 molecule adsorption can greatly enhance the conductance [32,36].

Proposed model for CNTs

We attempt to model the CNT conductance by considering the energy dispersion relation, and deriving the final model by using the Taylor series expansion near the Fermi points, as follows [37,38]:

$$E(k) = \pm\frac{t3a_{C\text{-}C}}{2}\sqrt{\left(\frac{2}{3d}\right)^2 + k_x^2} \quad (1)$$

where the (±) sign has been included to account for the valence and conductance bands. $a_{C\text{-}C}$ = 0.142 nm represents carbon–carbon bond length, d denotes CNT diameter and t = 2.7 eV is the nearest neighbour C–C tight binding overlap energy. For the first band gap energy we can simply write $E_G = (2a_{C\text{-}C}\cdot t/d) = 0.8$ eV·nm/d (nm). In addition, since the band structure is parabolic near the k = 0 points, we can write for the energy:

$$E(k) \approx \frac{E_G}{2} + \frac{\hbar^2 k_x^2}{2m^*} \quad (2)$$

where $\hbar$ is the reduced Planck's constant, k_x represents the longitudinal wave vector component along the length of the tube and m^* denotes the effective mass of the CNT effective mass depending on the tube diameter [39,40]. The number of conduction channels can be written as:

$$M(E) = 2\frac{\Delta E}{\Delta k\, L} = \frac{3a_{C\text{-}C}t}{L}\left(\frac{4E}{3a_{C\text{-}C}t} - \frac{8}{9d^2}\right)^{1/2} \quad (3)$$

where L denotes the channel length. Two major factors contribute to the conductance effect on large channels, enabling it to follow the Ohmic scaling law based on the Landauer formula. The first factor, which is independent of length, is the interface resistance. The second one results from the fact that the relation between the conductance and the width is nonlinear and is dependent upon the number of modes in the conductor. However, these modes are the quantized parameters in the Landauer formula in which both factors are interrelated as demonstrated below [41]:

$$G = \frac{2q^2}{h}\int_{-\infty}^{+\infty} M(E)T(E)\left(-\frac{df}{dE}\right)dE \tag{4}$$

where h is the Planck's constant, q denotes the electron charge and T is the transmission probability of an electron injected through the channel approximated as $T(E) = 1$ in ballistic channels [42]. $f(E)$ is the Fermi–Dirac distribution with df/dE exploding to a delta function near the Fermi energy for degenerate statistics. The conductance can be obtained as follows [43]:

$$G = \frac{2q^2}{h}\frac{3a_{\text{c-c}}t}{L}\left(\frac{4}{3a_{\text{c-c}}t}\right)^{1/2} \times\int_{-\infty}^{+\infty}\left(E-\frac{2a_{\text{c-c}}t}{3d^2}\right)^{\frac{1}{2}} d\left(\frac{1}{1+e^{(E-E_{\text{F}})/k_{\text{B}}T}}\right) \tag{5}$$

Equation 5 can be re-written as:

$$G = \frac{4q^2}{hL}\left(3a_{\text{c-c}}t\pi k_{\text{B}}T\right)^{\frac{1}{2}} \times\left[\int_0^{+\infty}\frac{x^{-1/2}}{1+e^{x-\eta}}dx+\int_0^{+\infty}\frac{x^{-1/2}}{1+e^{x+\eta}}dx\right] \tag{6}$$

where $x = (E - E_{\text{G}})/k_{\text{B}}T$ and the normalized Fermi energy is given by $\eta = (E_{\text{F}} - E_{\text{G}})/k_{\text{B}}T$. This equation can be numerically solved by applying the partial integration method [44-46]. The general model for the conductance of carbon nanotube-based gas sensor can be derived similar to that of silicon-based model proposed by Gunlycke [47].

$$G = \frac{4q^2}{hL}\left(3a_{\text{c-c}}t\pi k_{\text{B}}T\right)^{\frac{1}{2}}\left[\mathcal{I}_{-\frac{1}{2}}(\eta)+\mathcal{I}_{-\frac{1}{2}}(-\eta)\right] \tag{7}$$

$\mathcal{I}_j(\eta)$ is the Fermi–Dirac integral of the order j. The conductance characteristic demonstrates the performance of NH_3 gas sensor based on a CNT nanostructure. It has been revealed that when the CNT gas sensor is exposed to NH_3, the conductance changes [48]. We have proposed a model based on the reported experimental data and the relationship between conductance, gas concentration and temperatures as follows [49]:

$$G_{\text{wg}} = G_{\text{wog}} + G_{\text{wgT}} + G_{\text{wgF}} \tag{8}$$

When the sensor is exposed to the gases in different temperatures, we can define three components for conductance, namely G_{wog}, $G_{\text{wg}\mathbf{T}}$ and G_{wgF}. The first component G_{wog}, is the conductance without the presence of gas. $G_{wg\boldsymbol{T}}$ is defined as the conductivity changes in the presence of gas depending on the temperature and the last component, G_{wgF}, is based on different values of gas concentration at a constant temperature [49]. The conductance changes with temperature and various concentrations when CNT gas sensor is exposed to NH_3. E_{G} is dependent on temperature and gas concentration. Consequently, we can write:

$$\left\{\begin{matrix}E_{\text{G}}\propto F\\ E_{\text{G}}\propto T\end{matrix}\right\}\Rightarrow E_{\text{G}} = \delta T + \lambda F \tag{9}$$

Writing $\eta = (E_{\text{F}} - E_{\text{G}})/k_{\text{B}}T$ explicitly, we obtain

$$G_{\text{wog}} = \frac{4q^2}{hL}\left(3a_{\text{c-c}}t\pi k_B T\right)^{\frac{1}{2}} \times\left[\mathcal{I}_{-\frac{1}{2}}\left(\frac{E_{\text{F}}-E_{\text{G}}}{k_{\text{B}}T}\right)+\mathcal{I}_{-\frac{1}{2}}\left(\frac{E_{\text{G}}-E_{\text{F}}}{k_{\text{B}}T}\right)\right] \tag{10}$$

Equation 9 and Equation 10 are combined to obtain the conductance of gas sensor as:

$$G_{\text{wg}} = \frac{4q^2}{hL}\left(3a_{\text{c-c}}t\pi k_{\text{B}}T\right)^{\frac{1}{2}} \times\left[\mathcal{I}_{-\frac{1}{2}}\left(\frac{E_{\text{F}}-\delta T-\lambda F}{k_{\text{B}}T}\right)+\mathcal{I}_{-\frac{1}{2}}\left(\frac{\delta T+\lambda F-E_{\text{F}}}{k_{\text{B}}T}\right)\right] \tag{11}$$

The Fermi–Dirac integral plays a significant role in the modeling of the behavior of the semiconductor. So, the following expansion of the Fermi–Dirac integral is taken into consideration:

$$\mathcal{I}_j\left(\eta_F\right)=2\eta_F^{j+1}\sum_{n=0}^{\infty}\frac{t_{2n}}{\Gamma(j+2-2n)\eta_F^{2n}}+\cos(\pi j)\sum_{n=1}^{\infty}\frac{(-1)^{n-1}e^{-n\eta_F}}{n^{j+1}} \tag{12}$$

where $t_0 = 1/2$, $t_n=\sum_{\mu=1}^{\infty}(-1)^{\mu-1}/\mu^n=(1-2^{1-n})\zeta(n)$, and $\zeta(n)$ is the Riemann Zeta function. In the degenerate limit ($\eta >> 0$), which is the operation regime for the nanometer-scale devices, the expressions for the Fermi–Dirac integral can be obtained from Equation 12 as $\mathcal{I}_j\left(\eta_F\right)\to\eta_F^{j+1}/\Gamma\left(j+2\right)$. Accordingly, the Fermi–Dirac integral of order –1/2 can be simplified as [50]:

$$\mathcal{I}_{-\frac{1}{2}}\left(\eta_F\right)\to\frac{2\eta_F^{1/2}}{\sqrt{\pi}} \tag{13}$$

Based on the current–voltage characteristic of graphene-based FET devices, the gas sensor performance can be evaluated through Equation 14. Assuming that the source and substrate terminals are kept in ground potential, by applying a small voltage between source and drain (V_{DS}), the channel region experiences a flow of electrons. Moreover, the relationship between current and conductance can be replaced by Fermi–Dirac integral of the general conductance model of SWCNT as:

$$I=\frac{4q^2}{hL}\left(3a_{\text{c-c}}t\pi k_{\text{B}}T\right)^{\frac{1}{2}}\left[\mathcal{I}_{-\frac{1}{2}}\left(\frac{E_{\text{F}}-\delta T-\lambda F}{k_{\text{B}}T}\right)+\mathcal{I}_{-\frac{1}{2}}\left(\frac{\delta T+\lambda F-E_{\text{F}}}{k_{\text{B}}T}\right)\right]\cdot\left(V_{\text{gs}}-V_{\text{t}}\right) \tag{14}$$

where V_{gs} is the gate–source voltage and V_t is the threshold voltage.

Proposed model for graphene

The underlying operational principle in MOSFET is based on the electron flow between the source and drain electrodes, which can be controlled by the gate voltage. According to Landauer formula, there is a direct proportionality between conductance G and the transmission probability T of carriers from one electrode to another demonstrated by [41]:

$$G=\frac{2q^2}{h}T \tag{15}$$

Taylor expansion is used to investigate a parabolic relationship involving energy and wave vector [51]:

$$E(k)\approx\frac{E_{\text{G}}}{2}+\frac{E_{\text{G}}}{4\beta^2}k_x^2 \tag{16}$$

where β is the quantized wave vector given in [52]. The wave vector in the parabolic part of the band energy can be extracted as:

$$k=\sqrt{\frac{4E}{3a_{\text{c-c}}t}-2\beta^2} \tag{17}$$

The conductance on large channel following the Ohmic scaling law based on Landauer formula can then be obtained as:

$$G=\frac{6q^2}{hL}\left(a_{\text{c-c}}t\pi k_{\text{B}}T\right)^{\frac{1}{2}}\times\left[\int_0^{+\infty}\frac{x^{-1/2}}{1+e^{x-\eta}}dx+\int_0^{+\infty}\frac{x^{-1/2}}{1+e^{x+\eta}}dx\right] \tag{18}$$

where $x = (E - E_G)/k_BT$ and the normalized Fermi energy is $\eta = (E_F - E_G)/k_BT$. The performance of NH_3 gas sensor based on graphene nanostructure is demonstrated by its conductance characteristic. It has been shown that the conductance changes when the graphene gas sensor is exposed to NH_3 [53].

The corresponding formula equating the *I–V* characteristic of the graphene channel can then be written as:

$$I=\frac{6q^2}{hL}\left(a_{\text{c-c}}t\pi k_{\text{B}}T\right)^{\frac{1}{2}}\left[\mathrm{I}_{-\frac{1}{2}}\left(\frac{E_{\text{F}}-\delta T-\lambda F}{k_{\text{B}}T}\right)+\mathrm{I}_{-\frac{1}{2}}\left(\frac{\delta T+\lambda F-E_F}{k_{\text{B}}T}\right)\right]\times\left(V_{\text{gs}}-V_{\text{t}}\right) \tag{19}$$

Results and Discussion

Figure 4 illustrates the assessments of the gas sensor performance based on CNT and graphene nano-structures by considering their current–voltage characteristics when they are exposed to NH_3 [53]. Also shown is the experimental data [53]. The agreement is good except near the minimum, for which the Dirac point is shifted to positive gate voltage.

Charge transfer is involved within the sensing mechanism of graphene and CNT-based gas sensors. This occurs during the interaction of gas molecules with the graphene and CNT surfaces. The conductivities of both channel media are modified through this interaction. The phenomenon is likely to occur as a result of the interaction of NH_3 molecules with the carbon

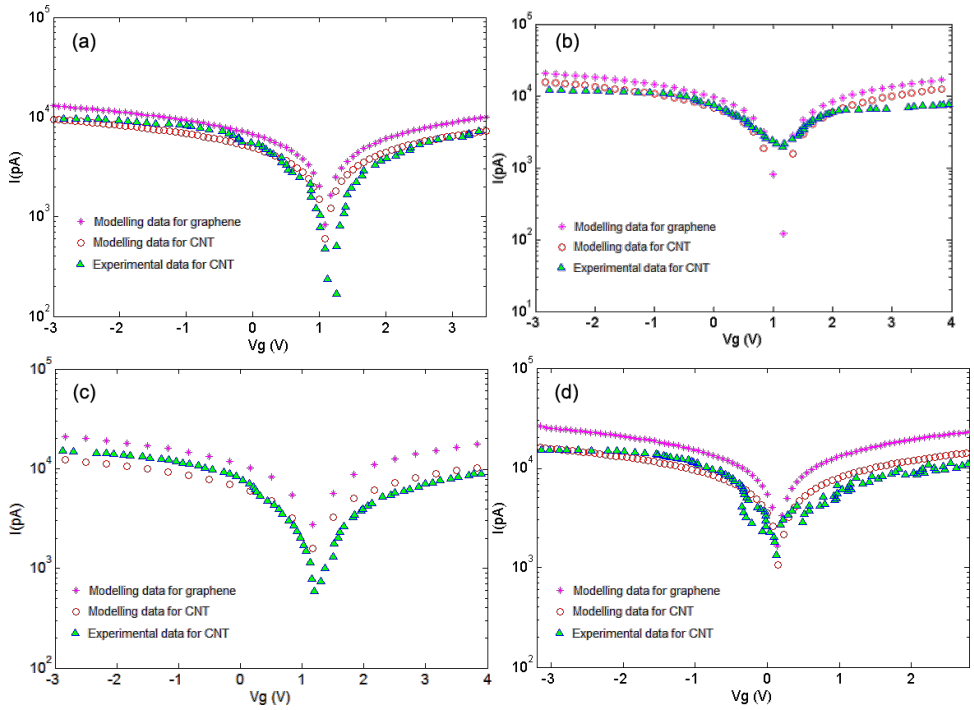

Figure 4: *I–V* characteristics of graphene and CNT after exposure to NH_3 under F = 500 ppm at (a) T = 25 °C, (b) T = 50 °C, (c) T = 100 °C, (d) T = 150 °C.

on the surface of graphene/CNT. Thus, electrons move from NH_3 molecules to these materials. Figure 4 illustrates the *I–V* characteristics of the graphene/CNT gas sensors corresponding to temperatures of 25, 50, 100, and 150 °C, respectively. At the first three temperatures, for the minimum values of current, there have not been significant changes in the gate voltage. This can imply that at temperatures below 150 °C, the gas is reluctant to be adsorbed on graphene/CNT. However, the currents corresponding to each gate voltage value have risen at higher temperatures in all these four cases. Also, as shown in Figure 4d, at 150 °C the gate voltage becomes more negative. NH_3 is an electron donating agent and it leaves electrons on the channel. This causes the graphene/CNT Fermi level to move toward their conduction band edges, making the threshold voltage V_{th} more negative. Thus, it can be said that this shift toward negative gate voltage is caused by the adsorption of NH_3 on the graphene/CNT channel at this temperature.

Figure 5 illustrates the *I–V* characteristics of the proposed models for graphene and CNT in comparison with results for a CNT based experiment. An increase in the current can be associated with the charge transfer between NH_3 molecules and graphene/CNT where the NH_3 molecules operate as the donor. This phenomenon is also known as chemical doping by gas molecules. The sensitivity can be observed from the response of graphene/CNT-based gas sensors under 100 ppm, 200 ppm and 500 ppm NH_3. A decreasing trend in the gate voltage similar to that for 150 °C can be seen at 200 °C. It can be concluded that at temperatures above 150 °C, the NH_3 adsorption and the consequent electron donating behavior increases, which causes a further shift of the gate voltage toward negative values. The figure gives a clear illustration of the fact that there is a good agreement between the proposed models and extracted data [53]. In the suggested models, different values of temperature and gas concentration are demonstrated in the terms of the parameters δ and λ, respectively, as presented in Table 1.

Table 1: Different temperature and concentration values with respective parameters δ and λ.

T (°C)	F (ppm)	δ	λ
25	500	−3.65	0.027
50	500	−2.35	0.027
100	500	−1.45	0.027
150	500	−0.95	0.027
200	100	−0.7	0.005
200	200	−0.7	0.012
200	500	−0.7	0.027

Referring to the analytical models, δ has been introduced as the temperature control parameter obtained by iteration. The analyt-

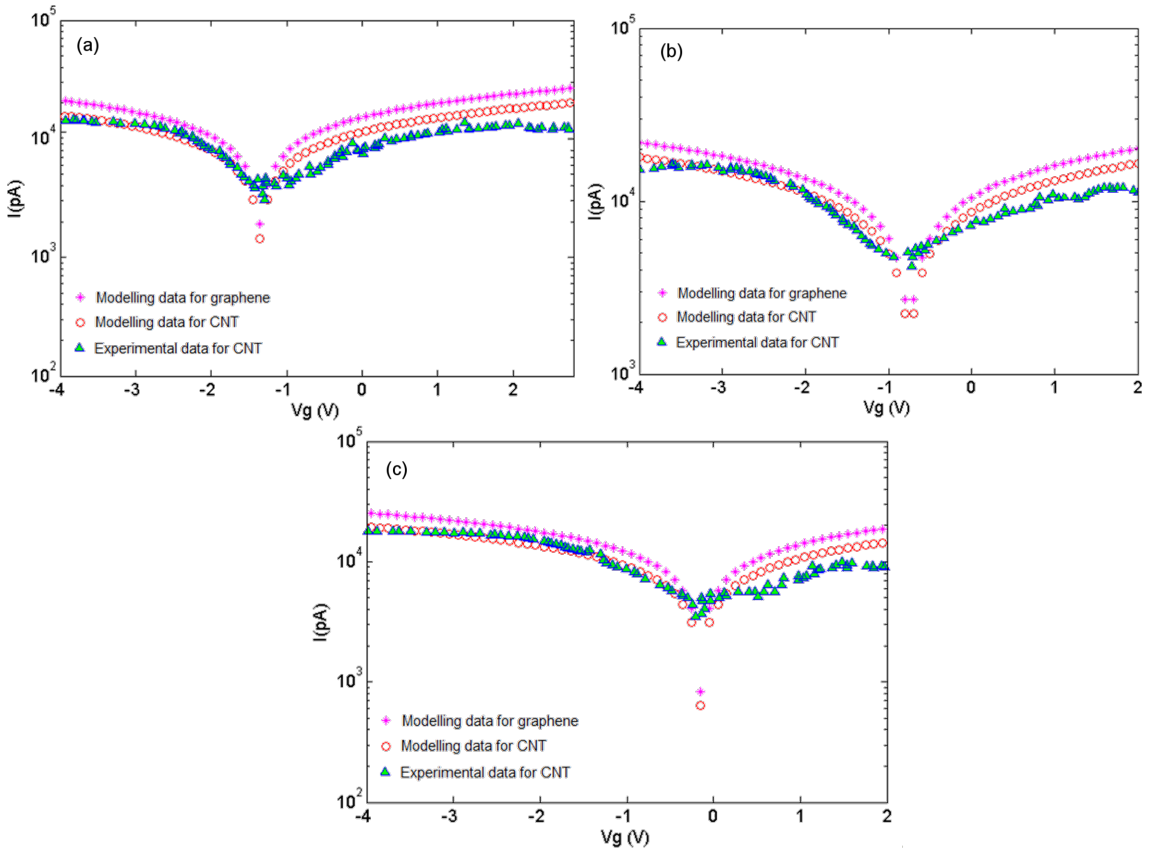

Figure 5: *I–V* characteristics after exposure to NH_3 for graphene and CNT at T = 200 °C and under (a) F = 100 ppm, (b) F = 200 ppm, (c) F = 500 ppm.

ical models in our study show that the rate of changes in conductivity depending on temperature can be expressed by the following equation:

$$\delta = aLn(T) - b \tag{20}$$

Here, parameters a and b are calculated to be a = 0.0138 and b = 0.0595. The parameter λ has been defined as a control parameter of gas concentration also calculated by iteration and shows that the rate of changes in conductivity depends on gas concentration, for which the equation can be written as:

$$\lambda = cLn(F) - d \tag{21}$$

where the constants are calculated in the same manner to be c = 1.4129 and d = 8.0494.

Conclusion

Outstanding properties such as high sensitivity as well as remarkable carrier transport features make both graphene and CNTs promising candidates for use in nanosensors. It has been observed that these materials experience a measureable change in conductance levels when exposed to NH_3. This interesting feature has been suggested to be employed in gas detection systems. Two control parameters, i.e., the temperature control parameter (δ) and gas concentration control parameter (λ) have been introduced. A comparative analysis between the FET-based models for graphene/CNT sensor structures has been carried out, in which the latter has been validated by an experimental work by Peng et al. [53]. Aiming to minimize the error, the coefficients δ and λ are calculated by iteration. The *I–V* characteristics of the gas sensors are considered for the comparative study under exposure to different NH_3 concentrations and temperatures. Finally, the comparison between the *I–V* characteristics of graphene and CNTs under similar conditions shows that graphene exhibits a higher conductivity than CNTs.

Acknowledgements

VKA thanks the Universiti Teknologi Malaysia (UTM) for an award of a distinguished visiting professorship and UTM Research University Grant (GUP) Q.J130000.2623.04H32 of the Ministry of Education (MoE).

References

1. Xu, K.; Tian, X.; Wu, C.; Liu, J.; Li, M.; Sun, Y.; Wei, F. *Sci. China, Ser. E: Technol. Sci.* **2013,** *56,* 32–35. doi:10.1007/s11431-012-5054-8
2. Rahmani, M.; Ahmadi, M. T.; Karimi, H. F. A.; Kiani, M. J.; Akbari, E.; Ismail, R. *Sens. Lett.* **2013,** *11,* 270–275. doi:10.1166/sl.2013.2742
3. Kiani, M. J.; Ahmadi, M. T.; Akbari, E.; Karimi, H.; Che Harun, F. K. *Key Eng. Mater.* **2013,** *553,* 7–11. doi:10.4028/www.scientific.net/KEM.553.7
4. Amiri, I. S.; Ali, J. *Nanosci. Nanotechnol. Lett.* **2013,** *5,* 850–856. doi:10.1166/nnl.2013.1636
5. Amiri, I. S.; Ahsan, R.; Shahidinejad, A.; Ali, J.; Yupapin, P. P. *Commun., IET* **2012,** *6,* 2671–2675. doi:10.1049/iet-com.2011.0773
6. Amiri, I. S.; Rahim, F. J.; Arif, A. S.; Ghorbani, S.; Naraei, P.; Forsyth, D.; Ali, J. *Life Sci. J.* **2013,** *10,* 904–910.
7. Yang, E. H. *Proc. SPIE* **2010,** *7679,* 767902. doi:10.1117/12.851012
8. Akbari, E.; Ahmadi, M. T.; Kiani, M. J.; Feizabadi, H. K.; Rahmani, M.; Khalid, M. *J. Comput. Theor. Nanosci.* **2013,** *10,* 1301–1304. doi:10.1166/jctn.2013.2846
9. Akbari, E.; Yusof, R.; Ahmadi, M. T.; Enzevaee, A.; Kiani, M. J.; Karimi, H.; Rahmani, M. *J. Nanomater.* **2014,** *2014,* No. 534105. doi:10.1155/2014/534105
10. Das, S.; Lahiri, I.; Kang, C.; Choi, W. *Proc. SPIE* **2011,** *8031,* 80311K. doi:10.1117/12.883743
11. Kiga, N.; Takei, Y.; Inaba, A.; Takahshi, H.; Matsumoto, K.; Shimoyama, I. CNT-FET gas sensor using a functionalized ionic liquid as gate. IEEE 25th International Conference on Micro Electro Mechanical Systems (MEMS), 2012, Paris, France, Jan 29–Feb 2, 2012; pp 796–799. doi:10.1109/MEMSYS.2012.6170306
12. Arora, V. K.; Tan, M. L. P.; Gupta, C. *J. Appl. Phys.* **2012,** *112,* 114330. doi:10.1063/1.4769300
13. Arora, V. K.; Bhattacharyya, A. *Nanoscale* **2013,** *5,* 10927–10935. doi:10.1039/c3nr03814a
14. Chin, H. C.; Bhattacharyya, A.; Arora, V. K. *Carbon* **2014,** in press. doi:10.1016/j.carbon.2014.04.055
15. Iijima, S. *Nature* **1991,** *354,* 56–58. doi:10.1038/354056a0
16. Karamdel, J.; Amadi, M. T.; Majlis, B. Y.; Dee, C. F.; Ismail, R. Formulation and Simulation for Electrical Properties of a (5,3) Single Wall Carbon Nanotube. IEEE International Conference on Semiconductor Electronics, 2008. ICSE 2008, Johor Bahru, Malaysia, Nov 25–27, 2008; IEEE, 2008; pp 545–548. doi:10.1109/SMELEC.2008.4770384
17. Salvetat, J.-P.; Bonard, J.-M.; Thomson, N. H.; Kulik, A. J.; Forró, L.; Benoit, W.; Zuppiroli, L. *Appl. Phys. A: Mater. Sci. Process.* **1999,** *69,* 255–260. doi:10.1007/s003390050999
18. Mousavi, H. *Commun. Theor. Phys.* **2011,** *56,* 373–376. doi:10.1088/0253-6102/56/2/30
19. Yang, L.; Park, C.-H.; Son, Y.-W.; Cohen, M. L.; Louie, S. G. *Phys. Rev. Lett.* **2007,** *99,* 186801. doi:10.1103/PhysRevLett.99.186801
20. Son, Y.-W.; Cohen, M. L.; Louie, S. G. *Phys. Rev. Lett.* **2006,** *97,* 216803. doi:10.1103/PhysRevLett.97.216803
21. Amiri, I. S.; Afroozeh, A.; Bahadoran, M. *Chin. Phys. Lett.* **2011,** *28,* No. 104205. doi:10.1088/0256-307X/28/10/104205
22. Heller, I.; Janssens, A. M.; Männik, J.; Minot, E. D.; Lemay, S. G.; Dekker, C. *Nano Lett.* **2008,** *8,* 591–595. doi:10.1021/nl072996i
23. Sivasathya, S.; Thiruvadigal, D. J. *Asian J. Chem.* **2013,** *25,* S411–S413.
24. Uchida, K.; Saitoh, M.; Kobayashi, S. Carrier transport and stress engineering in advanced nanoscale transistors from (100) and (110) transistors to carbon nanotube FETs and beyond. IEEE International Electron Devices Meeting, 2008. IEDM 2008, San Francisco, CA, USA, Dec 15–17, 2008; IEEE, 2008; pp 1–4. doi:10.1109/IEDM.2008.4796753
25. Ding, L.; Wang, S.; Zhang, Z.; Zeng, Q.; Wang, Z.; Pei, T.; Yang, L.; Liang, X.; Shen, J.; Chen, Q.; Cui, R.; Li, Y.; Peng, L.-M. *Nano Lett.* **2009,** *9,* 4209–4214. doi:10.1021/nl9024243
26. Zhang, J.; Zhang, R.; Wang, X.; Feng, W.; Hu, P.; O'Neill, W.; Wang, Z. *J. Micromech. Microeng.* **2013,** *23,* 095031. doi:10.1088/0960-1317/23/9/095031
27. Amiri, I. S.; Nikoukar, A.; Shahidinejad, A.; Anwar, T.; Ali, J. *Life Sci. J.* **2013,** *10,* 391–400.
28. Wang, Y.; Huang, B.-C.; Zhang, M.; Woo, J. C. S. *Microelectron. Reliab.* **2012,** *52,* 1602–1605. doi:10.1016/j.microrel.2011.09.036
29. Amiri, I. S.; Ali, J. *Quantum Matter* **2013,** *2,* 484–488. doi:10.1166/qm.2013.1086
30. Ding, W.; Hayashi, R.; Suehiro, J.; Zhou, G.; Imasaka, K.; Hara, M. *IEEE Trans. Dielectr. Electr. Insul.* **2006,** *13,* 353–361. doi:10.1109/TDEI.2006.1624280
31. Cho, T. S.; Lee, K.-J.; Kong, J.; Chandrakasan, A. P. The design of a low power carbon nanotube chemical sensor system. 45th ACM/IEEE Design Automation Conference, 2008, Anaheim, CA, USA, June 8–13, 2008; IEEE, 2008; pp 84–89.
32. Nguyen, L. Q.; Phan, P. Q.; Duong, H. N.; Nguyen, C. D.; Nguyen, L. H. *Sensors* **2013,** *13,* 1754–1762. doi:10.3390/s130201754
33. Arakelyan, V. M.; Aleksanyan, M. S.; Hovhannisyan, R. V.; Shahnazaryan, G. E.; Aroutiounian, V. M.; Hernadi, K.; Nemeth, Z.; Forro, L. *J. Contemp. Phys. (Arm. Acad. Sci.)* **2013,** *48,* 176–183. doi:10.3103/S1068337213040063
34. Xie, H.; Sheng, C.; Chen, X.; Wang, X.; Li, Z.; Zhou, J. *Sens. Actuators, B* **2012,** *168,* 34–38. doi:10.1016/j.snb.2011.12.112
35. McEuen, P. L.; Fuhrer, M. S.; Park, H. *IEEE Trans. Nanotechnol.* **2002,** *1,* 78–85. doi:10.1109/TNANO.2002.1005429
36. Huang, B.; Li, Z.; Liu, Z.; Zhou, G.; Hao, S.; Wu, J.; Gu, B.-L.; Duan, W. *J. Phys. Chem. C* **2008,** *112,* 13442–13446. doi:10.1021/jp8021024
37. Ahmadi, M. T.; Ismail, R.; Tan, M. L. P.; Arora, V. K. *J. Nanomater.* **2008,** 769250. doi:10.1155/2008/769250
38. Dresselhaus, M. S.; Dresselhaus, G.; Eklund, P. C.; Rao, A. M. Carbon nanotubes. In *The Physics of Fullerene-Based and Fullerene-Related Materials;* Andreoni, W., Ed.; Physics and Chemistry of Materials with Low-Dimensional Structures, Vol. 23; Springer: Dordrecht, The Netherlands, 2000; pp 331–379. doi:10.1007/978-94-011-4038-6_9
39. Ahmadi, M. T.; Johari, Z.; Amin, N. A.; Mousavi, S. M.; Ismail, R. Carbon nanotube conductance model in parabolic band structure. IEEE International Conference on Semiconductor Electronics (ICSE), Melaka, Malaysia, June 28–30, 2010; IEEE, 2010; pp 256–259. doi:10.1109/SMELEC.2010.5549582
40. Anantram, M. P.; Léonard, F. *Rep. Prog. Phys.* **2006,** *69,* 507. doi:10.1088/0034-4885/69/3/R01
41. Ahmadi, M. T.; Johari, Z.; Amin, N. A.; Fallahpour, A. H.; Ismail, R. *J. Nanomater.* **2010,** No. 753738. doi:10.1155/2010/753738
42. Datta, S. *Electronic Transport in Mesoscopic Systems;* Cambridge University Press: Cambridge, UK, 2002.
43. Peres, N. M. R.; Neto, A. H. C.; Guinea, F. *Phys. Rev. B* **2006,** *73,* 195411. doi:10.1103/PhysRevB.73.195411
44. Dingle, R. B. *Asymptotic expansions: their derivation and interpretation;* Academic Press: London, 1973.

45. Zaharah, J.; Ahmadi, M. T.; Chek, D. C. Y.; Amin, N. A.; Ismail, R. *J. Nanomater.* **2010,** No. 909347. doi:10.1155/2010/909347
46. Kažukauskas, V.; Kalendra, V.; Bumby, C. W.; Ludbrook, B. M.; Kaiser, A. B. *Phys. Status Solidi C* **2008,** *5,* 3172–3174. doi:10.1002/pssc.200779193
47. Gunlycke, D.; Areshkin, D. A.; White, C. T. *Appl. Phys. Lett.* **2007,** *90,* 142104. doi:10.1063/1.2718515
48. Yoon, H. J.; Jun, D. H.; Yang, J. H.; Zhou, Z.; Yang, S. S.; Cheng, M. M.-C. *Sens. Actuators, B* **2011,** *157,* 310–313. doi:10.1016/j.snb.2011.03.035
49. Xia, J.; Chen, F.; Li, J.; Tao, N. *Nat. Nanotechnol.* **2009,** *4,* 505–509. doi:10.1038/nnano.2009.177
50. Kim, R.; Lundstrom, M. arXiv:0811.0116 [cond-mat.mes-hall] **2008**.
51. Berger, C.; Song, Z.; Li, X.; Wu, X.; Brown, N.; Naud, C.; Mayou, D.; Li, T.; Hass, J.; Marchenkov, A. N.; Conrad, E. H.; First, P. N.; de Heer, W. A. *Science* **2006,** *312,* 1191–1196. doi:10.1126/science.1125925
52. Brey, L.; Fertig, H. A. *Phys. Rev. B* **2006,** *73,* 235411. doi:10.1103/PhysRevB.73.235411
53. Peng, N.; Zhang, Q.; Chow, C. L.; Tan, O. K.; Marzari, N. *Nano Lett.* **2009,** *9,* 1626–1630. doi:10.1021/nl803930w

License and Terms

Beilstein Journal of Nanotechnology

Designing magnetic superlattices that are composed of single domain nanomagnets

Derek M. Forrester*[1], Feodor V. Kusmartsev[1] and Endre Kovács[2]

Full Research Paper

Open Access

Address:
[1]Department of Physics, School of Science, Loughborough University, Leicestershire, LE11 3TU United Kingdom and [2]Department of Physics, University of Miskolc, H-3515 Miskolc, Hungary

Email:
Derek M. Forrester* - d.m.forrester@lboro.ac.uk

* Corresponding author

Keywords:
hysteresis; nanoparticles; magnetic phases; superlattices

Beilstein J. Nanotechnol. **2014,** *5,* 956–963.
doi:10.3762/bjnano.5.109

Received: 09 February 2014
Accepted: 16 June 2014
Published: 03 July 2014

This article is part of the Thematic Series "Physics, chemistry and biology of functional nanostructures II".

Guest Editor: A. S. Sidorenko

Abstract

Background: The complex nature of the magnetic interactions between any number of nanosized elements of a magnetic superlattice can be described by the generic behavior that is presented here. The hysteresis characteristics of interacting elliptical nanomagnets are described by a quasi-static method that identifies the critical boundaries between magnetic phases. A full dynamical analysis is conducted in complement to this and the deviations from the quasi-static analysis are highlighted. Each phase is defined by the configuration of the magnetic moments of the chain of single domain nanomagnets and correspondingly the existence of parallel, anti-parallel and canting average magnetization states.

Results: We give examples of the phase diagrams in terms of anisotropy and coupling strength for two, three and four magnetic layers. Each phase diagrams character is defined by the shape of the magnetic hysteresis profile for a system in an applied magnetic field. We present the analytical solutions that enable one to define the "phase" boundaries between the emergence of spin-flop, anti-parallel and parallel configurations. The shape of the hysteresis profile is a function of the coupling strength between the nanomagnets and examples are given of how it dictates a systems magnetic response. Many different paths between metastable states can exist and this can lead to instabilities and fluctuations in the magnetization.

Conclusion: With these phase diagrams one can find the most stable magnetic configurations against perturbations so as to create magnetic devices. On the other hand, one may require a magnetic system that can easily be switched between phases, and so one can use the information herein to design superlattices of the required shape and character by choosing parameters close to the phase boundaries. This work will be useful when designing future spintronic devices, especially those manipulating the properties of CoFeB compounds.

Introduction

The development of highly ordered superlattices is of significant importance from a practical perspective as well as for discovering new collective properties. The cumulative magnetic effects associated with the interaction of many nanomagnets can be witnessed as giving rise to unique-phase transitional behaviors. This is especially true for thin elliptical cylinder nanomagnets that have high shape anisotropies [1]. A nanomagnet with high shape anisotropy must have some kind of modulation in order to reduce the height of the anisotropy energy barrier. This is typically done through doping in order to reduce the saturation magnetization of the nanomagnet. In recent years amorphous ferromagnetic materials have been successfully doped (with, for example, vanadium or chromium [2]) to lower the saturation magnetization of the compound. In doing so the energy barrier between stable states of the magnetization remains at a surmountable level. This is of high significance for designing magnetic logic elements and magnetic sensors because changing the geometry of the nanomagnet and levels of doping allows one to change the magnetic properties in a controllable way. Superlattices with magnetic elements of amorphous magnetic alloys, such as $Co_{60}Fe_{20}B_{20}$ [3] and $Fe_{65}Co_{35}B_{12}$ [4], have been developed due to their excellent room temperature magnetoresistance properties. Indeed, these bromide alloys are prime candidates for creating functional magnetic field sensors and magnetic random access memory devices. Recent work has even focused on controlling the nucleation and propagation of topological magnetic solitons through CoFeB/Ru superlattice stacks [5]. With their excellent magnetic properties and soft magnetic character, amorphous magnetic materials will continue to be used in future devices. Thus, we investigate the generic magnetic response of nanomagnets that are composed of amorphous magnetic materials that have low random anisotropy.

In this work we study the magnetic response of linear arrays of nanomagnets to an oscillating magnetic field that is applied at a slight angle from parallel to the longest axis of an individual nanomagnet. A small perturbing magnetic field is also introduced that enables the system to locate the metastable states that exist in the energy landscape. The size of the shape anisotropy energy barrier is a function of the saturation magnetization, the geometry of the nanomagnet and its demagnetization factors.

These demagnetization factors, $N_{x,y,z}$, are defined by length scales associated with the x, y and z axes of a nanomagnet. To a reasonable degree of accuracy, given the high accuracy of modern fabrication technologies, each of the N magnetic layers in the superlattice can be taken as having the same demagnetization factors. Each nanomagnet in the system, each given an index $i = 1,2...,N$, has lengths $l_{x,y,z}$. The nanomagnets in the superlattice, each of which is a thin elliptical cylinder of volume V, have dimensionless magnetization vectors associated with them: $\mathbf{m}_i = (m_{xi},m_{yi},m_{zi}) = (\cos\varphi_i \sin\theta_i,\sin\varphi_i \sin\theta_i,\cos\theta_i)$. Here, we focus primarily upon structures that have antiferromagnetic coupling between nanomagnets. Ferromagnetic coupling invariably leads to magnetization hysteresis profiles that depict parallel magnetizations of equal magnitude and direction for all the constituent nanomagnets. In artificial superlattice structures the thickness of the interlayer is manipulated to enforce an antiferromagnetic coupling. In all superlattices the lattice period of the layers is of crucial importance to defining its purpose and physical properties [6,7].

The properties of the spacer layers (composed of MgO or Ru, for example) between the nanomagnets, and the resulting interfacial exchange coupling, usually leads to magnetization saturation fields in superlattices that are smaller than those of individual magnetic layers [8]. The coupling energy is a function of the thickness of the interlayer. Experimentally, it has been found that creating a ruthenium interlayer of 1.2–1.5 nm between CoFeB nanomagnets has the consequence of generating an antiferromagnetic coupling, whereas with a larger thickness ferromagnetic coupling will ensue [9]. We investigate the changes in the hysteresis profiles that become apparent in systems of antiferromagnetically coupled nanomagnets when the coupling strength is altered.

It is important to note that the interaction of magnetic disks in a stack may have a dipolar character. For example, if we consider two small elliptical magnetic particles in a vacuum, separated by large distances from each other so that each particle will have a large magnetic moment, then these particles will primarily have only dipolar interaction. However, when the distance between these particles decreases, the inter-particle interaction will be modified. The latter depends on the specific media separating the particles. If this is a metal then there appears the RKKY interaction, which is mediated by the electrons of the surrounding metal. Depending on the distance between particles it may have both antiferromagnetic and ferromagnetic character. However if the media between the particles is not metallic and say, a dielectric, then at each magnetic particle there may be induced higher multipoles which add additional contributions into the overall interaction.

Thus, the resulting interaction between the particles depends on the relative interaction between them, so that the shape anisotropy will play a key role. Recently, Serantes et al. [10]

produced a methodology that is based upon a very powerful computational Monte Carlo technique to study the magnetic ordering in a system of dipolarly interacting magnetic nanoparticles distributed along 1D chains. They studied in detail the very interesting issue of the interplay between the nanoparticles magnetostatic dipolar interaction and magnetic anisotropy [10]. The separation distance for dipole–dipole interactions also determines whether the system has an affinity for an antiferromagnetic or ferromagnetic interaction. Therefore, in their work two different cases, non- and collinear, are considered [10]. So, in the present paper we have considered the case when the particles are packed into the stack. Here the magnetic moments are oriented perpendicular to the stack (or chain of particles). Due to this form of construction the inter-particle dipolar interaction has primarily the antiferromagnetic character (which, in the next section, we will describe by the constant of inter-particles interaction, J).

Thus, our approach is consistent with the studies [10-13], which found by computational Monte Carlo techniques that the magnetization of the dipolarly interacting magnetic nanoparticles is well described by the Curie–Weiss law. Moreover, Serantes et al. [10] obtained in the mean-field approximation that even non-interacting particles are described by the Curie–Weiss law where the critical parameter, an ordering temperature, stands for the antiferromagnetic order. Because of that fact the general conclusion of these papers was that a mean-field treatment is not adequate to study magnetic nanoparticle systems [10-13]. Therefore, in the present paper we developed a microscopic approach which is based on considering the dynamical behavior of magnetic nanoparticles with the use of coupled micromagnetic equations. The results we obtain are consistent both with a macroscopic Curie–Weiss type fitting and the microscopic calculations of Serantes and co-workers [10], which point to the primary importance of the shape anisotropy of nanoparticles and the resulting magnetic properties of these systems.

Results

The superlattice magnetic energies and magnetic fields

By lowering the saturation magnetization (M_s) of magnetic compounds such as CoFeB by doping [2] one can extend the elongation of each nanomagnet without creating too high an energy barrier between the stable states of the superlattice [14,15]. This is important for creating magnetic logic or memory devices, so as to enable switching between different orientations of the magnetic moments in moderate magnetic fields. The height of the energy barrier is reduced by doping and in order to compensate for the resulting off-set in the height of the barrier a higher aspect ratio nanomagnet has to be designed. The shape anisotropy is given by [15],

$$E_{sh} = -\mu_0 V \sum_{i=1}^{N} \left(N_x M_{xi}^2 + N_y M_{yi}^2 + N_z M_{zi}^2 \right). \quad (1)$$

In this work we define the longest axis of each nanomagnet to be in the x-direction and so the smallest shape anisotropy is associated with this x-coordinate (tending to zero the more stretched a magnet becomes). A superlattice composed of interspersed nanomagnets can be created by balancing the aforementioned energy concerns to create a robust system against thermal instabilities (shaped as an elliptical stack). The protection of magnetic information can be achieved due to the increase in magnetic volume and the reduced switching current density [16]. The energy equations for the system of N nanomagnets are,

$$E = E_e + E_{in} + E_{ze} + E_{sh} \,, \quad (2)$$

where the interaction energies between the end and next nearest to the end nanomagnets (one nearest neighbor) are given by E_e

$$E_e = -\mu_0 V \left(J_{1,2} \mathbf{M}_1 \cdot \mathbf{M}_2 + J_{N,N-1} \mathbf{M}_N \cdot \mathbf{M}_{N-1} \right), \quad (3)$$

the inner interaction energies (two nearest neighbors) E_{in} are,

$$E_{in} = -\mu_0 V \sum_{i=2}^{N-1} \left(J_{i,i-1} \mathbf{M}_i \cdot \mathbf{M}_{i-1} + J_{i,i+1} \mathbf{M}_i \cdot \mathbf{M}_{i+1} \right), \quad (4)$$

and the Zeeman energies E_{ze} are

$$E_{ze} = -\mu_0 V \sum_{i=1}^{N} \left(\mathbf{H} \cdot \mathbf{M_i} \right). \quad (5)$$

Later, we will define all the coupling energies equal, with J being a dimensionless coupling parameter. When J is negative the coupling is antiferromagnetic for certain interlayer thicknesses. The nature of the coupling changes according to the mechanisms of Ruderman–Kittel–Kasuya–Yosida (RKKY) interaction theory [17-19]. The field applied to the superlattices is $\mathbf{H} = M_s \mathbf{h} = M_s \{h_x, h_y, h_z\}$ (with $M_s = 0.5 \times 10^6$ A/m) and we reintroduce the notation $\{e,a,b\} = 2\{N_x, N_y, N_z\}$ from [15]. Now, the dynamical equations for the magnetization are derived from the Landau–Lifshitz–Gilbert (LLG) equation ([15,20,21]),

$$\frac{\partial \mathbf{M}_i}{\gamma \partial t} = [\mathbf{M}_i \times \mathbf{H}_{\text{eff},i}] - \frac{\alpha}{M_s} [\mathbf{M}_i \times \left[\mathbf{M}_i \times \mathbf{H}_{\text{eff},i} \right]], \quad (6)$$

where $\mathbf{H}_{\text{eff},i}$ is an effective field and γ is the gyromagnetic ratio. In the last term, the Gilbert damping, with damping parameter α, is incorporated into the model. Equation 6 is expanded as in [22] to find the evolution of the magnetization angles in each nanomagnet. A resulting dimensionless form is found by dividing by M_s^2 and writing time as $t = \tau/\gamma M_s$. The dimensionless parameters used here (J, e, a, b, and $h_{x,y,z}$), have also been divided by N_x throughout [15]. The magnetizations are defined through $\partial\varphi_i/\partial\tau$ and $\partial\theta_i/\partial\tau$. The resulting $2N$ coupled first-order differential equations are then solved with a numerical algorithm based upon adaptive Runge–Kutta–Cash–Karp techniques. The oscillating magnetic field is directed along the x-axis of the superlattice, i.e., the longest axis, with a frequency of 1 GHz.

The response of nanomagnets to an applied magnetic field

Throughout we use the damping parameter equal to α = 0.01 and a large value of b (about 390) to confine the magnetic moments to move in the x–y-plane. We investigated nanomagnets with semi-major to semi-minor elliptical cross-sections of $l_x/l_y \approx 10$. The external magnetic field in the x and y components,

$$h_x(\tau) = h_a \cos f\tau \cos\beta, \quad h_y(\tau) = h_a \cos f\tau \sin\beta + \lambda \quad (7)$$

is applied with frequency $f_{\text{applied}} = f\gamma M_s$ and amplitude $H_a = M_s h_a$. The angle of deviation between the applied field and the x-axis of the superlattice is β, and λ is a small time-dependent perturbation in h_y with amplitude 0.02 (the perturbation has its origin in a thermally assisted magnetization reversal, as discussed on page 6 of [15] and in [23]). In the stretched elliptical disks or nanowires the perturbation in h_x has an insignificant effect and hence can be neglected. The h_z component of the field is taken to be zero.

We define the phases by the shape of the magnetic hysteresis curves of magnetization as a function of the applied magnetic field strength. There are two phases involving spin-flop states: $AF1$ and $AF2$. These phases have characteristic Barkhausen jumps from scissored states into anti-parallel states of the relative orientations of the magnetic moments of each nanomagnet in a superlattice. Anti-parallel states occur when the magnetic moments point with opposite polarity along the easy-axes and are shown by a series of plateaus, in between saturation states (a parallel phase P occurs when there are no AP or AF states and is usually typical of ferromagnetically coupled systems). An AP phase exists when there are no scissored states. An index (j = 1,..) is applied to signify the number of distinct plateaus that are present in a hysteresis loop, e.g., $AF1_j$. In the $AF1$ phase there is a change of state from the scissored one into a parallel one. The $AF2$ phase does not have this transition. Both the $AF1$ and $AF2$ phases, however, have transitions that go from parallel states into scissored states [15]. The AF phases are quite robust at the levels of damping that occur in most CoFeB systems (α ≈ 0.01). The balance between the coupling strength J and anisotropy parameter a is shown through the phase diagram of Figure 1a for the two coupled nanomagnets systems that were also considered in [15].

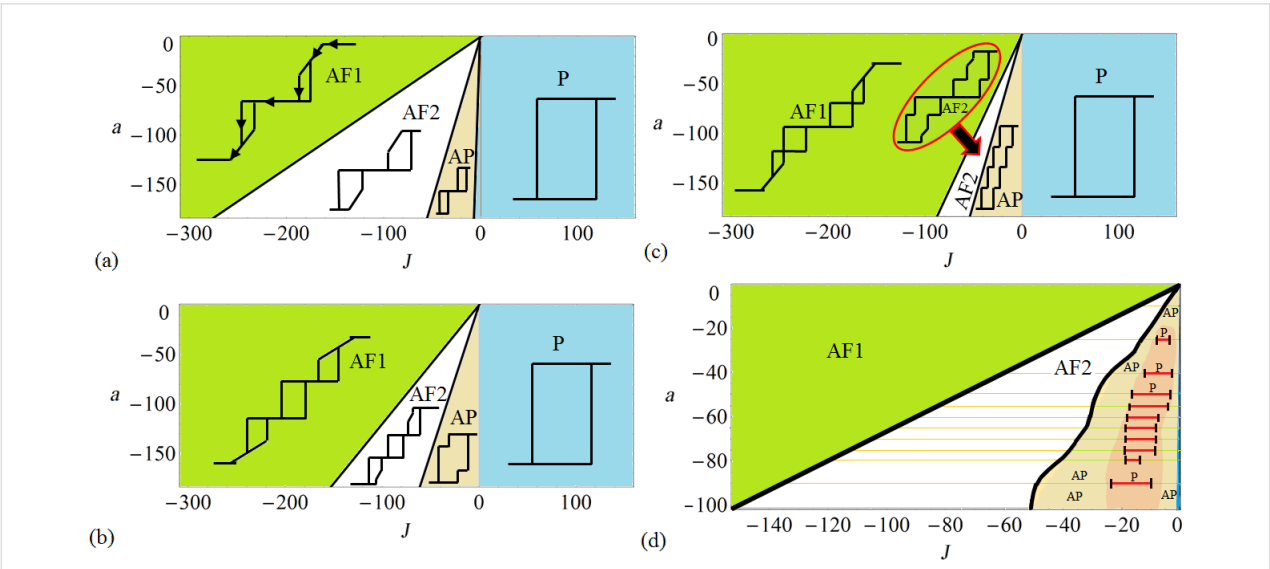

Figure 1: The magnetic phase diagrams of anisotropy, a, as a function of coupling strength J. In (a) N = 2, (b) N = 3, (c) N = 4 the phase diagrams are found through a quasi-static analysis. In (d) the dynamical results by using Equation 6 for N = 2 are shown. One can see that in the AP phase the hysteresis alternates between an AP and P phase, indicating that the AP phase is the least stable.

In this phase diagram the *AF*1 phase occurs when [15]

$$\left(0 < a \leq 2J/3\right)_{N=2}. \tag{8}$$

In this system the average magnetization, that evolves with the application of an external magnetic field, has a defining Barkhausen jump that emerges from an anti-parallel alignment of the magnetic moments into a scissoring spin-flop condition (the *AF*1 phase). Again, to reiterate the findings of the two nanomagnet systems [15] before increasing N we now state the limits of the *AF*2 phase to be,

$$\left(2J/3 < a \leq 2J\right)_{N=2}. \tag{9}$$

The *AP* phase exists predominantly when $a > 2J$. In Figure 1a the Barkhausen jump between an antiparallel state straight into a parallel one occurs, which is the nature of the *AF*2 phase. In each region of the phase diagrams of Figure 1a–c, a schematic of the shape of the magnetization versus applied magnetic field curve for the pertinent phase is shown.

The phase diagrams in Figure 1a–c are found through the use of the quasi-static techniques described in [15]. The fourth phase diagram, Figure 1d, is found from the dynamical analysis by using the LLG equations (Equation 6). From Figure 1d one can see that the *AP* phase is the least stable, with large breakdown to a *P* state within the analytically found *AP* region – compare to Figure 1a. This indicates that spin-flop phases *AF*1 and *AF*2 are more durable for logic operations. The *AP* phase, in the range of damping for CoFeB compounds around $\alpha = 0.01$, is most stable for high anisotropies and high coupling strengths |J|. The analytically found (through the quasi-classical method [15]) phase boundary between the *AP* and *AF*2 phases holds with some degree of fluctuation for the fully dynamical analysis. However, the *AF*2–*AF*1 phase boundary corresponds completely with the analytically found solutions.

In Figure 1b, the phase diagram for three coupled nanomagnets is shown. Again there are *AF* (1,2), *AP*, and *P* regimes. When the anisotropy is in the range

$$\left(0 < a \leq 3J/4\right)_{N=3}, \tag{10}$$

there is an *AF*1 spin-flop phase. Whereas, when the system of three nanomagnets is designed with anisotropies in the range,

$$\left(3J/4 < a \leq 3J\right)_{N=3} \tag{11}$$

the *AF*2 phase is dominant. Beyond $a = 3J$ the *AP* phase takes form. For $N = 4$, the phases are separated under the conditions that for the *AF*1 regime,

$$\left(0 < a \leq (5+3\sqrt{2})J/7\right)_{N=4} \tag{12}$$

The *AF*2 phase for four layers of nanomagnets occurs in the range,

$$\left((5+3\sqrt{2})J/7 < a \leq \left(9+4\sqrt{2}\right)J/7\right)_{N=4} \tag{13}$$

In Figure 2, the resulting hysteresis evolution as a function of |J| is shown for four coupled nanomagnets. It demonstrates that by changing the interlayer spacing and the coupling strength, completely different magnetic phases are found. Figure 2 shows the evolution of the hysteresis profile as J is altered. The results are obtained from a full dynamical analysis, using Equation 6, and compared to the analytically obtained phase diagram of a against |J| where J is always taken as an antiferromagnetic coupling. In Figure 2 one can see that there are clear magnetization plateaus that characterize the nature of the hysteresis (plateaus of the same value of $\langle m \rangle$ are given the same index). When $2 \leq |J| \leq 9$, there are $j = 3$ plateaus and an *AP* phase. The dynamical analysis reveals that for very small coupling strengths, $|J| \leq 2$, a *P* phase exists that has a hysteresis curve that is similar to that of a single nanomagnet in an applied field. For greater values of |J|, there are $j = 5$ plateaus in the *AP* and subsequent *AF* phases, i.e., AP_5, $AF1_5$ and $AF2_5$.

Figure 2 has four coupled nanomagnets each of dimensions $l_x = 186$ nm, $l_y = 20$ nm, and $l_z = 1.5$ nm (with $N_x = 0.00454$ and $N_z = 0.88269$). With the inclusion of a thermally induced fluctuation, λ (see [15]) the number of plateaus can be variable. The small perturbation to the system can result in metastability and the magnetic field should be cycled many times in order to obtain all possible Barkhausen jumps, in accordance with the energy balances of the system under investigation. It is a subtle balance that exists in these energy landscapes. For example, in Figure 3 (for the anisotropy level of $a = -50$ and increasing the coupling strength steadily) there are $j = 3$–7 plateaus within the different phases. The last image in this figure shows that extra plateaus can emerge upon repeatedly cycling the magnetic field hundreds of times if the energy balance is precarious enough to allow the opportunity for finding extra metastable states. It is not, however, always the case that extra plateaus emerge. Thus, near the critical points of stability [24], at the boundaries marking phase transitions, thermally induced fluctuations in the magnetization can alter the whole nature of the magnetic evolution. Thus, the phase diagrams can be used to find the arrange-

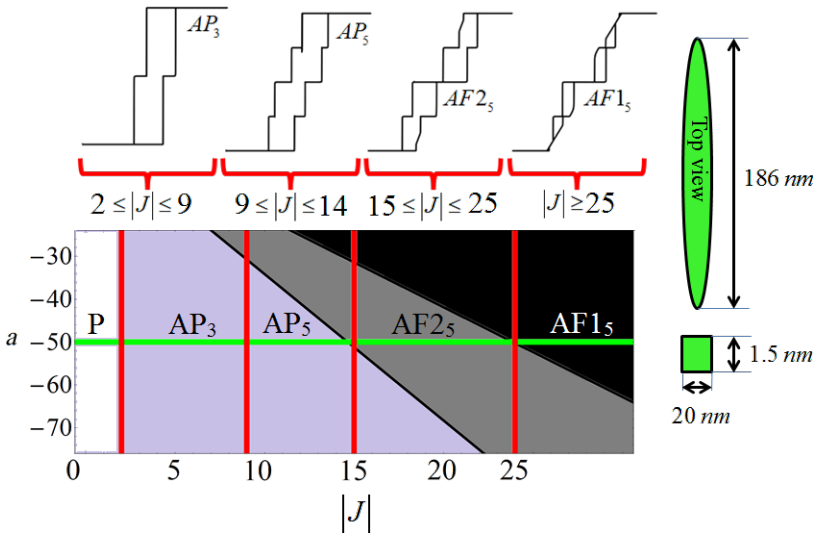

Figure 2: The evolution of four nanomagnets with constant anisotropy and varying interaction strength. Along the top of the plot the shape of the hysteresis, for magnetization against applied field, in a range of J is shown schematically. The anisotropy parameter is taken as $a = -50$ (with $N_x = 0.00454$). The green line intersecting the bottom phase diagram represents this constant value of anisotropy. The hysteresis occurs with j plateaus of differing values of $\langle m \rangle$, which is the meaning of the subscript of AP_j, $AF1_j$, and $AF2_j$ (plateaus of the same value of $\langle m \rangle$ are given the same index). The hysteresis profiles have been obtained by using a full dynamical analysis using the LLG equations, Equation 6, and compared to the analytically obtained phase diagram that is similar to Figure 1. The plateaus occur at $\langle m \rangle = 0, \pm 1/2, \pm 1$. When $\langle m \rangle = 0$, $(\varphi_1,\varphi_2,\varphi_3,\varphi_4) = (0,\pi,0,\pi)$ or $(\pi,0,\pi,0)$. For the saturation magnetized states, all the φ are equal. In the cases of $\langle m \rangle = 1/2$ the azimuthal angles take the form $(\pi,0,0,0)$ etc. and vice versa for $\langle m \rangle = -1/2$, e.g., $(\pi,\pi,\pi,0)$. Each of the nanomagnets has dimensions l_x= 186 nm, l_y = 20 nm, and l_z = 1.5 nm. The top and front view geometry and sizes are shown schematically.

ment of nanomagnets that is most robust against perturbations. This is important for creating optimized computational and logic devices.

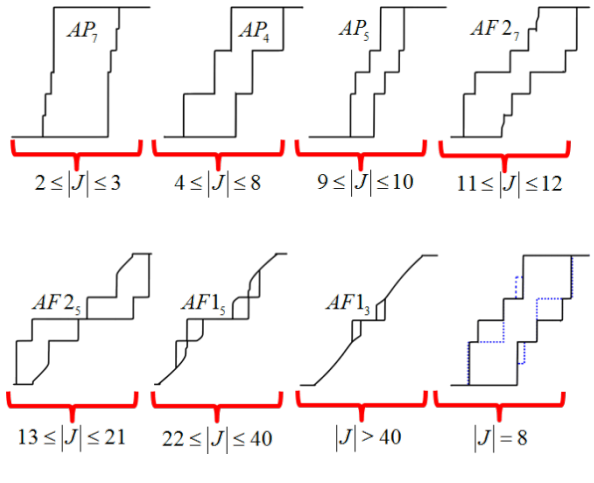

Figure 3: The hysteresis profiles for $N = 6$. There are fluctuating levels of magnetization plateaus as the energy balances of the system shift between metastable states. The magnetic field has to be cycled a number of times to obtain all of the possible Barkhausen jumps. For example, the last hysteresis loop shown will only display the black lines for many cycles. However, for this case of $J = -8$, further cycles reveal the dashed (blue) plateaus.

Discussion and Conclusion

In these systems of single domain nanomagnets the macro-spin approximation holds and the internal degrees of freedom can be analyzed by using classical dynamics. We have used the dynamical Landau–Lifshitz–Gilbert equations in complement to a quasi-static analysis of the complicated energy landscapes of the interacting nanomagnets. In doing so we combine analytical solutions, obtained through quasi-classical methods [15], with numerical solutions found through a full dynamical analysis. The result is a design ethic for creating superlattice structures composed of elliptically shaped and regularly patterned magnetic particles. The quasi-static model has been used to identify possible regimes of the many particle system. Naturally the low frequency limit of the applied magnetic field must reproduce the magnetostatic approach, as it does. However we found that even in the high frequency limit, even to the gigahertz or terahertz frequency range of the applied magnetic field, that the regimes of the behavior identified within the static model still stand. The reason for this correspondence between the high and low frequency limits or static phases is due to the substantial damping, that removes the high probability for the creation of chaos in these systems. Indeed, we have found that chaos emerges within certain limits of the energy balances in the system, particularly for less elongated nanomagnets and those less damped. In our future publication we plan to address the issue of the chaos which may arise in the chains of magnetic

particles. But the chaos is suppressed when the damping is suitably high, the case which we are considering here. With the emergence of new devices such as the magnetic ratchet for spintronic memory and logic in three-dimensions [25] and recent results for multisegmented nanowires [26] (where the shape anisotropy provides the preferential orientation of segmented magnetic moments along the nanowire), understanding the magnetic phases has never been more timely. Indeed, by the experimental studying of the magnetic hysteresis of these nanosized stacks the different magnetic regimes described herein can be observed. This may shed light on the complexity of the behavior of these unique and extremely interesting magnetic systems. Also, hybrid structures of ferromagnetic superlattices, combined with two-dimensional materials such as graphene and silicene have the potential to revolutionize spin-injection and detection devices for spintronics [27-30]. The ferromagnetic materials are ideal contacts for creating these spintronic devices on, for example, a single layer of graphene [29]. A magnetic ratchet device could be used to inject, at room temperature, a reservoir of spin-polarized electrons for propagation through a graphene spin barrier and avoid conductivity mismatch. The understanding of the macrospin dynamics of the superlattices can enable the design of such devices, with the spin-up/down electrons injected into the graphene for differing tunnel-transmission probabilities. Indeed, the magnetic superlattice can also be a very sensitive detector of magnetic fields, and may be used for biodetection as in [31]. Thus, these methods, discussed herein, for understanding the magnetization dynamics as a function of coupling energy and applied magnetic fields, can be used as the basis for creating novel nanomagnetic devices for magnetoresistance experiments and the creation of hybrid structures. The stability of the phases was also strongly indicated as being a function of the coupling strength between the nanomagnets for the case of a system composed of two nanomagnets. In the cases of N nanomagnet superlattices the phase boundaries have been highlighted by way of example by using analytical results derived from a quasi-static approach for $N = 3$ and $N = 4$. The results of the quasi-static analytics were then compared to a full dynamical analysis and it was found that a very good correspondence between them exists. Taking superlattices that are composed of N nanomagnets with the same geometry, i.e., l_x = 186 nm, l_y = 20 nm, and l_z = 1.5 nm, and varying the coupling strength between them gave illuminating results. As the coupling strength is altered for larger systems of nanomagnets, $N > 2$, one can find that there are sub-phases within the main phases that are characterized by different numbers of plateaus in the hysteresis profiles. These plateaus are related to the orientations of each single-domains magnetic moments. For example, in Figure 2 there are $2^N = 16$ possible configurations of the magnetic moments for four coupled nanomagnets. In the hysteresis profile there are a possible $N + 1$ magnetization plateaus: those of the two saturated states, those of complete anti-parallel alignment (or with pairs of equal azimuthal angles, e.g., $(0,0,\pi,\pi)$), and also those when there is one nanomagnet out of phase with the rest by π radians. It was seen that for the case of four nanomagnets the AP phase can occur with $j = 3$ or 5 depending upon the coupling strength. As the number of nanomagnets in the superlattice is extended there exist many more metastable states and paths between energy minima in the system. In the example of Figure 3, for $N = 6$ coupled nanomagnets, this was demonstrated. In various coupling strength regimes there are sub-phases within each of the main AF and AP phases that exist with different numbers of plateaus emerging. Before a cross-over from one sub-phase into the next, e.g., Figure 3 with $J = -8$, the system is again unstable and upon cycling the applied magnetic field many times all $N + 1$ possible levels of magnetization plateaus can emerge. Thus, when designing the nanomagnetic structures, one needs to carefully investigate these sub-phases too, as the anisotropy/coupling balance strongly dictates the resulting hysteresis profile within the phase. Experiments to test for these phases and sub-phases should be designed by creating the superlattices with different inter-layer thicknesses. In doing so we hope that this will lead to greater clarity in the design process of larger, $N > 2$, arrays of nanomagnets, which will be very important in the future for creating stable magnetic devices.

Acknowledgements

DMF thanks the EPSRC for funding under KTA grant - “Developing prototypes and a commercial strategy for nanoblade technology”. EK thanks the TAMOP-4.2.1.B-10/2/KONV-2010-0001 project in the framework of the New Hungarian Development Plan.

References

1. Imre, A.; Csaba, G.; Ji, L.; Orlov, A.; Bernstein, G. H.; Porod, W. *Science* **2006,** *311,* 205–208. doi:10.1126/science.1120506
2. Kubota, H.; Fukushima, A.; Yakushiji, K.; Yakata, S.; Yuasa, S.; Ando, K.; Ogane, M.; Ando, Y.; Miyazaki, T. *J. Appl. Phys.* **2009,** *105,* 07D117. doi:10.1063/1.3068484
3. Wu, K.-M.; Huang, C.-H.; Wang, Y.-H.; Kao, M.-J.; Tsai, M.-J.; Wu, J.-C.; Horng, L. *J. Appl. Phys.* **2007,** *101,* 09B503. doi:10.1063/1.2712317
4. Hashimoto, A.; Saito, S.; Omori, K.; Takashima, H.; Ueno, T.; Takahashi, M. *Appl. Phys. Lett.* **2006,** *89,* 032511. doi:10.1063/1.2234294
5. Fernández-Pacheco, A.; Petit, D.; Mansell, R.; Lavrijsen, R.; Lee, J.-H.; Cowburn, R. P. *Phys. Rev. B* **2012,** *86,* 104422. doi:10.1103/PhysRevB.86.104422
6. Dediu, V. I.; Kabanov, V. V.; Sidorenko, A. S. *Phys. Rev. B* **1994,** *49,* 4027–4032. doi:10.1103/PhysRevB.49.4027
7. Lee, K. C.; Erb, U. *Beilstein J. Nanotechnol.* **2013,** *4,* 292–299. doi:10.3762/bjnano.4.32

8. Hu, W.; Wilson, R. J.; Koh, A.; Fu, A.; Faranesh, A. Z.; Earhart, C. M.; Osterfeld, S. J.; Han, S.-J.; Xu, L.; Guccione, S.; Sinclair, R.; Wang, S. X. *Adv. Mater.* **2008,** *20,* 1479–1483. doi:10.1002/adma.200703077
9. Huang, J. C. A.; Hsu, C. Y.; Chen, S. F.; Liu, C. P.; Liao, Y. F.; Lin, M. Z.; Lee, C. H. *J. Appl. Phys.* **2007,** *101,* 123923. doi:10.1063/1.2748860
10. Serantes, D.; Baldomir, D.; Pereiro, M.; Hernando, B.; Prida, V. M.; Sánchez-Llamazares, J. L.; Zhukov, A.; González, J. *J. Phys. D: Appl. Phys.* **2009,** *42,* 215003. doi:10.1088/0022-3727/42/21/215003
11. Vargas, P.; Altbir, D.; Knobel, M.; Laroze, D. *Europhys. Lett.* **2002,** *58,* 603–609. doi:10.1209/epl/i2002-00438-4
12. Prida, V. M.; Vega, V.; Serantes, D.; Baldomir, D.; Ilyn, M.; Zhukov, A. P.; González, J.; Hernando, B. *Phys. Status Solidi A* **2009,** *206,* 2234–2239. doi:10.1002/pssa.200881731
13. Serantes, D.; Baldomir, D.; Pereiro, M.; Arias, J. E.; Mateo-Mateo, C.; Buján-Núñez, M. C.; Vázquez-Vázquez, C.; Rivas, J. *J. Non-Cryst. Solids* **2008,** *354,* 5224–5226. doi:10.1016/j.jnoncrysol.2008.07.040
14. Roy, K.; Bandyopadhyay, S.; Atulasimha, J.; Munira, K.; Ghosh, A. W. *arXiv:1107.0387v2 [cond-mat.mes-hall]* **2011**.
15. Forrester, D. M.; Kusmartsev, F. V.; Kovács, E. *Phys. Rev. B* **2013,** *87,* 174416. doi:10.1103/PhysRevB.87.174416
16. Kong, Y. C.; Lim, S. H.; Lee, K.-J. *J. Korean Phys. Soc.* **2009,** *54,* 1630. doi:10.3938/jkps.54.1630
17. Ruderman, M. A.; Kittel, C. *Phys. Rev.* **1954,** *96,* 99. doi:10.1103/PhysRev.96.99
18. Kasuya, T. *Prog. Theor. Phys.* **1956,** *16,* 45–57. doi:10.1143/PTP.16.45
19. Yosida, K. *Phys. Rev.* **1957,** *106,* 893. doi:10.1103/PhysRev.106.893
20. Lai, R.; Sievers, A. *J. Appl. Phys.* **1998,** *81,* 3972. doi:10.1063/1.364910
21. Chen, A. P.; Zhukov, A.; González, J.; Domínguez, L.; Blanco, J. M. *J. Appl. Phys.* **2006,** *100,* 083907. doi:10.1063/1.2362760
22. Forrester, D. M.; Kusmartsev, F. V. *Phys. Status Solidi A* **2014,** *211,* 884–889. doi:10.1002/pssa.201330122
23. Ostler, T. A.; Barker, J.; Evans, R. F. L.; Chantrell, R. W.; Atxitia, U.; Chubykalo-Fesenko, O.; El Moussaoui, S.; Le Guyader, L.; Mengotti, E.; Heyderman, L. J.; Nolting, F.; Tsukamoto, A.; Itoh, A.; Afanasiev, D.; Ivanov, B. A.; Kalashnikova, A. M.; Vahaplar, K.; Mentink, J.; Kirilyuk, A.; Rasing, T.; Kimel, A. V. *Nat. Commun.* **2012,** *3,* 666. doi:10.1038/ncomms1666
24. Forrester, D. M.; Kürten, K. E.; Kusmartsev, F. V. *Phys. Rev. B* **2007,** *76,* 134404. doi:10.1103/PhysRevB.76.134404
25. Lavrijsen, R.; Lee, J.-H.; Fernández-Pacheco, A.; Petit, D. C. M. C.; Mansell, R.; Cowburn, R. P. *Nature* **2013,** *493,* 647–650. doi:10.1038/nature11733
26. Prida, V. M.; García, J.; Iglesias, L.; Vega, V.; Görlitz, D.; Nielsch, K.; Díaz-Barriga-Castro, E.; Mendoza-Reséndez, R.; Ponce, A.; Luna, C. *Nanoscale Res. Lett.* **2013,** *8,* 263. doi:10.1186/1556-276X-8-263
27. Tsai, W.-F.; Huang, C.-Y.; Chang, T.-R.; Lin, H.; Jeng, H.-T.; Bansil, A. *Nat. Commun.* **2013,** *4,* 1500. doi:10.1038/ncomms2525
28. Maassen, J.; Ji, W.; Guo, H. *Nano Lett.* **2011,** *11,* 151–155. doi:10.1021/nl1031919
29. van 't Erve, O. M. J.; Friedman, A. L.; Cobas, E.; Li, C. H.; Robinson, J. T.; Jonker, B. T. *Nat. Nanotechnol.* **2012,** *7,* 737–742. doi:10.1038/nnano.2012.161
30. El Mel, A.-A.; Duvail, J.-L.; Gautron, E.; Xu, W.; Choi, C.-H.; Angleraud, B.; Granier, A.; Tessier, P.-Y. *Beilstein J. Nanotechnol.* **2012,** *3,* 846–851. doi:10.3762/bjnano.3.95
31. Kurlyandskaya, G. V.; Sánchez, M. L.; Hernando, B.; Prida, V. M.; Gorria, P.; Tejedor, M. *Appl. Phys. Lett.* **2003,** *82,* 3053. doi:10.1063/1.1571957

License and Terms

Beilstein Journal of Nanotechnology

Methods for rapid frequency-domain characterization of leakage currents in silicon nanowire-based field-effect transistors

Tomi Roinila*[1], Xiao Yu[2], Jarmo Verho[1], Tie Li[2], Pasi Kallio[1], Matti Vilkko[1], Anran Gao[2] and Yuelin Wang[2]

Full Research Paper

Open Access

Address:
[1]Department of Automation Science and Engineering, Tampere University of Technology, Tampere, Finland and [2]Shanghai Institute of Microsystem and Information Technology, Chinese Academy of Sciences, Shanghai, China

Email:
Tomi Roinila* - tomi.roinila@tut.fi

* Corresponding author

Keywords:
admittance spectroscopy; excitation design; frequency characterization; frequency response; silicon nanowire

Beilstein J. Nanotechnol. **2014,** *5,* 964–972.
doi:10.3762/bjnano.5.110

Received: 28 February 2014
Accepted: 10 June 2014
Published: 04 July 2014

This article is part of the Thematic Series "Physics, chemistry and biology of functional nanostructures II".

Guest Editor: A. S. Sidorenko

Abstract

Silicon nanowire-based field-effect transistors (SiNW FETs) have demonstrated the ability of ultrasensitive detection of a wide range of biological and chemical targets. The detection is based on the variation of the conductance of a nanowire channel, which is caused by the target substance. This is seen in the voltage–current behavior between the drain and source. Some current, known as leakage current, flows between the gate and drain, and affects the current between the drain and source. Studies have shown that leakage current is frequency dependent. Measurements of such frequency characteristics can provide valuable tools in validating the functionality of the used transistor. The measurements can also be an advantage in developing new detection technologies utilizing SiNW FETs. The frequency-domain responses can be measured by using a commercial sine-sweep-based network analyzer. However, because the analyzer takes a long time, it effectively prevents the development of most practical applications. Another problem with the method is that in order to produce sinusoids the signal generator has to cope with a large number of signal levels. This may become challenging in developing low-cost applications. This paper presents fast, cost-effective frequency-domain methods with which to obtain the responses within seconds. The inverse-repeat binary sequence (IRS) is applied and the admittance spectroscopy between the drain and source is computed through Fourier methods. The methods is verified by experimental measurements from an n-type SiNW FET.

Introduction

Recent development in sensing biochemical molecules has been rapid. Among many sensing technologies, silicon nanowire (SiNW)-based field-effect transistors (FETs) [1] are one of the most promising building blocks for the next generation of electrical circuits in recognizing a wide range of biological and chemical targets. They have been successfully used in the detection of DNA [2], pH [3], protein [4], glucose [5], virus [6], and vapor [7]. Despite significant developments, underlying detection mechanism and dynamics of the SiNW FETs are not well-defined, and hence, further studies and methods are required [8].

Due to the large surface-to-volume ratio, one-dimensional nanostructures are one of the best candidates for ultra-sensitive sensors. The most typical configuration applies a nanowire as the essential building block, bonding two ends of the nanowire to a solid substrate to create a SiNW FET. Figure 1 shows the structure of a typical SiNW FET. The thin SiNW body is electrically isolated from the silicon substrate by a buried oxide (box) layer. Back-gate contact is used to control the conductivity of the SiNW with the box layer. When applying a threshold voltage on the silicon substrate, SiNW conductivity varies rapidly with small changes in the potential of the nanowire surface, which are induced by the molecules (detection targets) adsorbed on the surface oxide of the nanowire. The conductivity change is seen as a change in the voltage–current behavior (V_{ds}–I_{ds} behavior) between the drain and source. Some current, known as leakage current, flows between the gate and drain of the transistor, and affects I_{ds}. Recent studies by the authors indicate that the leakage current is likely to be frequency-dependent. Accurate measurements of such frequency-dependent characteristics can be used to validate the functionality of the SiNW FETs and to determine their most effective operation ranges. In addition, the measurements could possibly be advantageous in developing new detection technologies utilizing SiNW FETs.

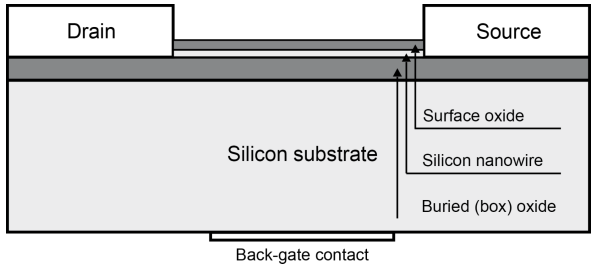

Figure 1: Conceptual diagram of a SiNW FET.

Based on an extensive literature review, the leakage current has not been previously measured or characterized in the frequency domain, with the exception of the work of the authors. The number of studies considering frequency-domain measurements of SiNW FETs is very low. The authors in [9] applied low-frequency noise spectroscopy (LFNS), and characterized generation–recombination centers in silicon nanowires grown by using chemical vapor deposition. Their aim was to demonstrate the potential of the LFNS in characterizing deep levels in nanowires. The authors in [10] presented a novel protein-detection methodology based on frequency-domain electrical measurements. They demonstrated that the power spectral density of voltage from a current-biased SiNW FET showed 1/*f*-dependence in the frequency domain in the presence of protein not specific to the antibody receptor. However, in the presence of protein recognized by the SiNW FET, the spectral density of the voltage exhibited a Lorentzian shape with a frequency of several kilohertz. The authors in [11] demonstrated by simulations that nanowires exhibited an AC-transfer function that resembled that of a high-pass filter. They showed that the corner frequency of the filter decreases as more molecules, corresponding to a higher net charge, attached to the nanowire and displaced more charge carriers in the nanowire channel. The results provided the means to build a low-cost frequency-based detection system when applying the SiNW FET.

Despite the impressive results of past studies, frequency-domain analysis of the SiNW FETs has not gained much popularity. One of the main reasons is that efficient frequency-response-measurement techniques are not well known. All the measurements in these studies were performed by using a sine-sweep-based network analyzer. Although the method usually yields reliable and accurate responses, it suffers from a number of drawbacks. The most important of these is the length of time required for the measurement. Responses are measured separately at various frequencies by applying single sinusoids. Consequently, one measurement cycle usually takes several minutes, which makes the method inefficient for most practical applications. Another problem with the method is that in order to produce sinusoids the signal generator has to cope with a large number of signal levels. This may become challenging in developing low-cost applications. Instead of using single sinusoids, an excitation signal with a broadband spectrum can be generated to gather all the spectral information in one measurement. There exists a multitude of such signals. The authors in [12] listed ten different signals in their survey. One special class of these signals is the maximum-length binary sequence (MLBS). The sequence is one class of periodic pseudo-random multi-frequency signals. The MLBS has energy at several frequencies. This makes it possible to simultaneously measure a frequency response at those frequencies through Fourier methods [13]. Therefore, instead of measuring a response sepa-

rately at each frequency, all the required information can be captured within one measurement. This drastically reduces the measurement time from several minutes to few seconds. The short measurement time has many advantages in the presented application. For example, the possible heating effect during the measurement procedure can be minimized. In addition, the fast measurement technique has significant advantages over the slow method for practical applications such as detecting chemical targets.

In this paper, the inverse-repeat binary sequence (IRS) is applied as an excitation injection. The IRS is used to characterize linear dynamics from nonlinear systems [14]. The sequence is generated from the conventional MLBS by doubling the MLBS and toggling every other bit of the doubled sequence. Because the sequence has a binary form, it can be easily generated by a low-cost application. The efficiency of the IRS excitation has been demonstrated in numerous applications, such as chemical process systems [15], analysis of a reservoir pipeline-valve system [16], and in frequency-response measurement of switched-mode power supplies [17].

This paper presents fast frequency-domain methods with which to measure and characterize the leakage current in SiNW FETs. The primary aim of the work is to present a cost-effective implementation to obtain the leakage current in the frequency domain. The work is an extended and revised version of the results in [18]. The measurement technique is further improved by applying the IRS excitation instead of the MLBS. In addition, the applied device is described more in detail, and the measurement results are more comprehensive. The theoretical backgrounds of the methods are introduced, followed by the experimental results from an n-type SiNW FET.

Methods

Consider the system $g(t)$ shown in Figure 2 as a linear time-invariant system for small disturbances. According to basic control theory, the system can be fully characterized by its impulse response(s), which can be transformed into frequency domain and presented by the frequency-response function (FRF) [19]. The excitation $x(t)$ is injected into the system and the output response $y(t)$ is obtained. The input and output noises ($e(t)$ and $r(t)$) disturb the measurements that can be now denoted by $x_e(t)$ and $y_r(t)$.

The frequency-response function of the device can be denoted as

$$G(j\omega) = \frac{Y(j\omega)}{X(j\omega)} \tag{1}$$

where $Y(j\omega)$ and $X(j\omega)$ denote the Fourier transforms of the corresponding time-domain signals $y(t)$ and $x(t)$. In the presence of external noise the noise-affected frequency-response function $G_n(j\omega)$ can be denoted as

$$G_n(j\omega) = \frac{Y_r(j\omega)}{X_e(j\omega)} \tag{2}$$

where $X_e(j\omega)$ and $Y_r(j\omega)$ denote the Fourier transforms of $x_e(t)$ and $y_r(t)$. Denoting the error signals $e(t)$ and $r(t)$ by their Fourier transforms $E(j\omega)$ and $R(j\omega)$, $G_n(j\omega)$ becomes

$$G_n(j\omega) = G(j\omega)\frac{1+\left[R(j\omega)/Y(j\omega)\right]}{1+\left[E(j\omega)/X(j\omega)\right]} \tag{3}$$

Clearly, in the presence of noise at the input and output signals, the measured transfer function obtained by Equation 3 may significantly differ from the real frequency-response function $G(j\omega)$. To avoid the problem, the cross-correlation technique has been often applied [20]. In this method, a cross-correlation is computed between the perturbation and sensed output after which the frequency response is obtained by Fourier transform. The method tends to cancel out the effect of external noise in

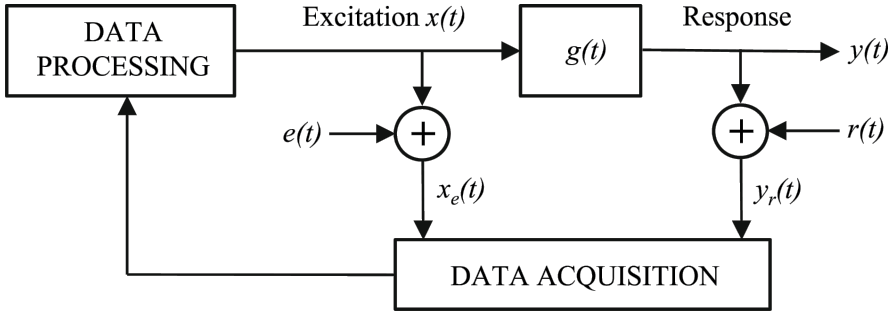

Figure 2: Typical measurement system.

output provided that the excitation resembles ideal white noise. The method requires, however, that the measured perturbation is noise free. Considering a system shown in Figure 2, the ideal perturbation is not measured and used in the computation. Hence the cross-correlation technique fails and both random and bias error will be present. Even in the case of ideal perturbation, the cross-correlation technique reduces the effect of noise only from the output side. In the presence of noise both at input and output, the logarithmic averaging procedure [21] is proposed as

$$G_{\log}\left(j\omega\right)=\left(\prod_{k=1}^{P}\frac{U_{rk}\left(j\omega\right)}{I_{ek}\left(j\omega\right)}\right)^{1/P} \tag{4}$$

where P denotes the number of injected excitation periods. In the method, the measurements from both input and output sides are segmented and Fourier transformed after which Equation 4 is applied. As the conventional cross-correlation method requires that the excitation resembles ideal white noise (or more specifically, the auto correlation of the excitation resembles Dirac delta function), the logarithmic averaging procedure does not have this requirement. The method tends to cancel out the effect of uncorrelated noise both from input and output sides, and hence, the frequency response is obtained more accurately [21].

Inverse-repeat binary sequence

The MLBS is an efficient excitation sequence for various frequency-domain analysis [22]. However, an assumption with MLBS is, that the process under consideration is linear. It may be obvious that practical transistors and related measurement systems are always affected by some nonlinearities, such as the quantization effect. The nonlinear phenomena should be minimized to increase the accuracy of the measurements. There are basically two methods to model systems that exhibit nonlinearities. The first and more difficult method is to identify a model that includes all the system nonlinearities. The second and more practical method is to identify only the linear part of the model. One the most convenient way to minimize the effect of nonlinearities is to carefully select the excitation injection.

The inverse-repeat binary sequence (IRS) has been a popular excitation signal for nonlinear systems to characterize the linear part. The sequence is generated from the MLBS by doubling the MLBS and toggling every other bit of the doubled sequence. By using an adequately long signal length and a sufficiently short clock cycle, the spectral and auto-correlation properties of the IRS are very close to the corresponding properties of a pure white noise. The sequence has the lowest possible peak factor, which means that the signal energy is very high in relation to the signal amplitude [23]. Another advantage of the signal is that it can be generated with a low-cost application, the output of which can only cope with a small number of signal levels. Furthermore, leakage in the frequency-response calculation can be avoided because the sequence is periodic. The IRS is a highly acceptable alternative to be applied with (4) due to its capability to suppress the undesired effect of nonlinear phenomena. As an example, the power spectrum of the IRS generated by a five-bit length shift register [24] is shown in Figure 3. The power drops towards zero at half of the generation frequency of $1/2\Delta t$ and its harmonics.

It should be emphasized that signal energy in the IRS is divided into a number of frequency harmonics, as shown in Figure 3. The FRF may become difficult to obtain under high signal-to-noise (SNR) requirements if the excitation amplitude cannot be increased due to system sensitivities. Furthermore, the IRS may not make significant improvements in the FRF measurements compared to the results of the MLBS in the case of a system with strong odd-order nonlinearities [17]. A straightforward IRS design procedure is well documented. The authors in [17] considered the frequency-response measurements of switched-mode power supplies, and applied the IRS to analyze the output impedance. The design steps of the excitation sequence can also be applied for the application in this paper.

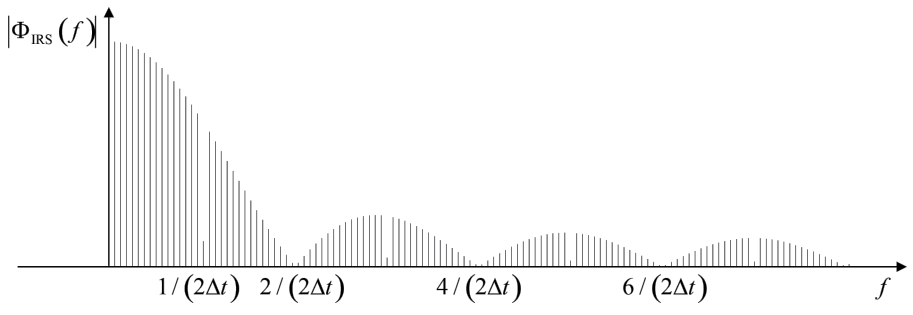

Figure 3: Shape of the power spectrum of IRS from 5-bit length shift register.

Results and Discussion

The presented methods were applied, and the leakage current was characterized from a SiNW FET. An n-type SiNW FET device was fabricated by using a silicon-on-insulator (SOI) wafer with a top-down method. A full description of the fabrication process is given in [25]. The structure of the device is schematically shown in Figure 4, where G, S, and D denote the gate, source, and drain, respectively.

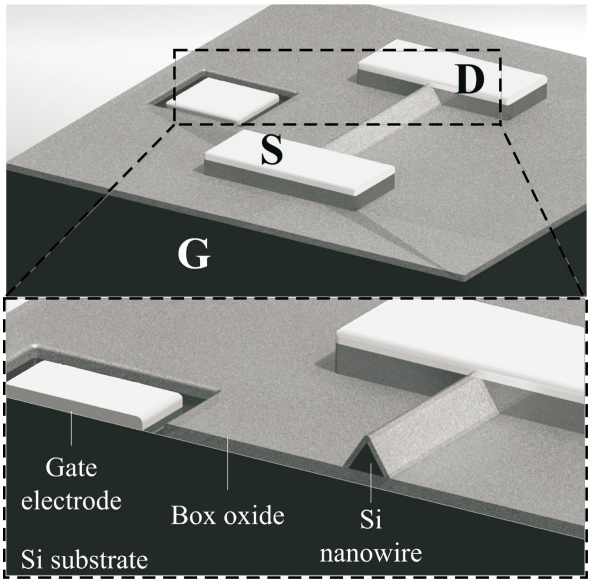

Figure 4: Schematic of the applied SiNW FET device.

A scanning electron microscope (SEM) image of the device is shown in Figure 5. The source and drain regions are heavily doped with boron, while the nanowire channel has a low-doping concentration of phosphorous. The contacts were doped by different dopants in order to form an off-state channel while there was no gate voltage applied on it thus saving energy. The cross-section of the SiNW is a triangle, with bottom width of 50 nm, and height of 65 nm. The length of the SiNW is 10 µm. The doping concentration is $3{\cdot}10^{15}/cm^3$. The DC measurements (I_{ds}–V_{ds} and I_{ds}–V_g) of the device are shown in Figure 6 and Figure 7.

Figure 8 shows the measurement setup. The gate voltage of the SiNW FET is controlled by U_G. The interface board communicating between the computer and the device under test is National Instruments USB-6251 measurement card (MC). The maximum sampling frequency of the card is 1 MHz (aggregate), and the maximum digital-to-analog converting frequency (maximum generation frequency of the excitation) is 2.8 MHz. The measured data is digitized by a 16-bit analog-to-digital (A/D) converter. The measurement card is controlled by a Matlab/Data Acquisition toolbox.

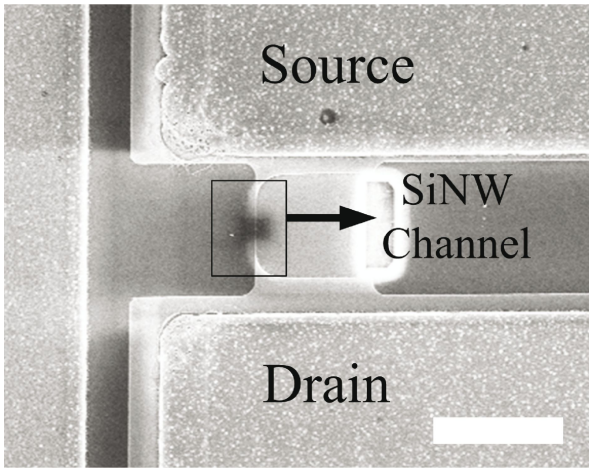

Figure 5: SEM image of the SiNW FET device. The scale bar is 20 µm.

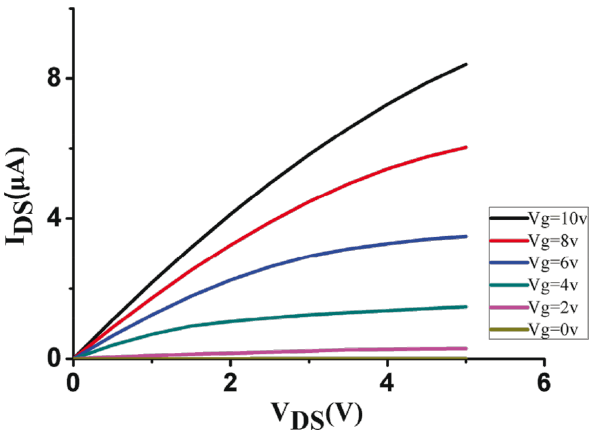

Figure 6: I_{ds}–V_{ds} DC measurement results.

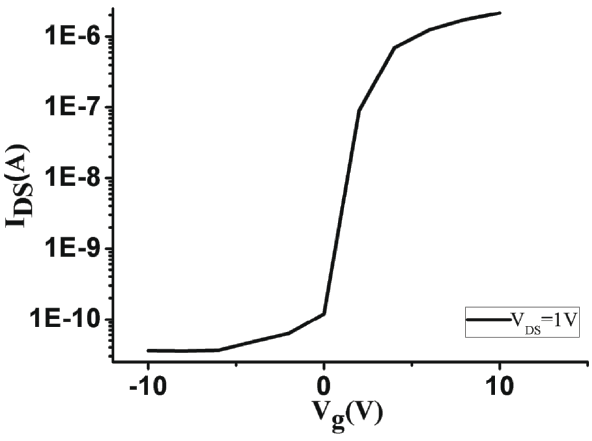

Figure 7: I_{ds}–V_g DC measurement results.

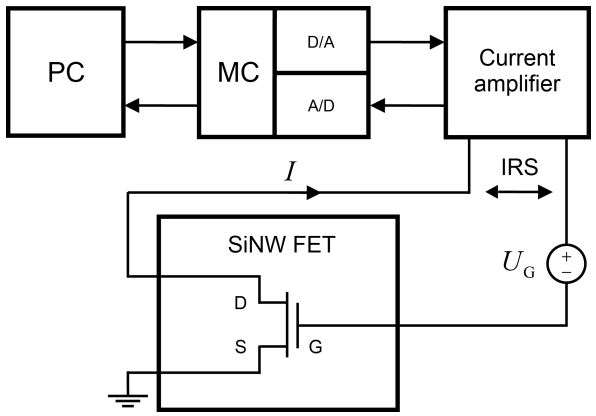

Figure 8: Conceptual diagram of the measurement setup.

Because the measurement card was not directly suitable for measuring very small currents, an amplifier was designed to interface with the measurement setup. The amplifier can measure currents in the range of 1–1000 nA (at an excitation voltage level of ±1 mV). Figure 9 shows a simplified schematic of the amplifier. The upper operational amplifier in the schematic works as an excitation voltage buffer, which drives the ground-referred unknown impedance Z_x through a current sense resistor R_{sense}. The measured current causes a voltage drop in this resistor, which is then amplified with the lower instrumentation amplifier. C_c and R_c are added to prevent oscillation in case Z_x is highly capacitive. Excitation voltage scaling, power supplies, filtering, and additional amplifier stages are not included. The amplifier has a selectable gain of −1.1 mV/nA or −4.5 mV/nA. The bandwidth depends on the impedance to be measured, and varies in the range from 10 to 100 kHz.

The IRS was synthesized by an eight-bit length shift register [24]. The measurable bandwidth was limited by the current amplifier, and was approximately 70 kHz. The generation frequency of the measurement card was set to 100 kHz to

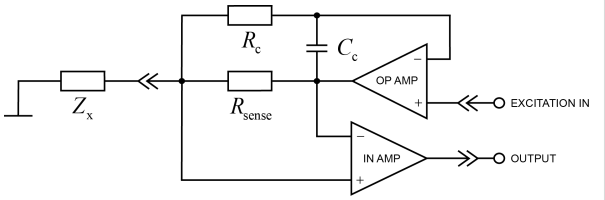

Figure 9: Simplified schematic of the measurement amplifier.

provide enough energy to the whole frequency band. Because the measured signal levels were extremely low, a large number of excitation periods and averaging were used to reduce the effect of noise. Two hundred periods were used in the experiment. The total length of the excitation signal was $L = 200 \cdot 2 \cdot (2^8 - 1) = 102{,}000$. With these parameters, the lowest frequency harmonic was 100 kHz/510 ≈ 196 Hz. The sampling frequency f_o was set to four times the generation frequency (400 kHz) to provide reasonable multi-sampling [17]. Table 1 summarizes the parameters used in the experiment.

Table 1: Parameters used in the experiment.

parameter	value	unit
excitation signal length, P	510	bits
generation frequency, f_{gn}	100	kHz
number of excitation periods, R	200	
excitation amplitude, A	1	mV
sampling frequency, f_o	400	kHz

The designed IRS was then injected into the SiNW FET through the current amplifier. Figure 10a shows a sample of the generated IRS in the time domain. Figure 10b shows the (scaled) power spectra. The voltage between the gate and drain was measured, together with the corresponding current. The device was assumed to maintain approximately the constant operating point during multiple excitations. The total amount of collected

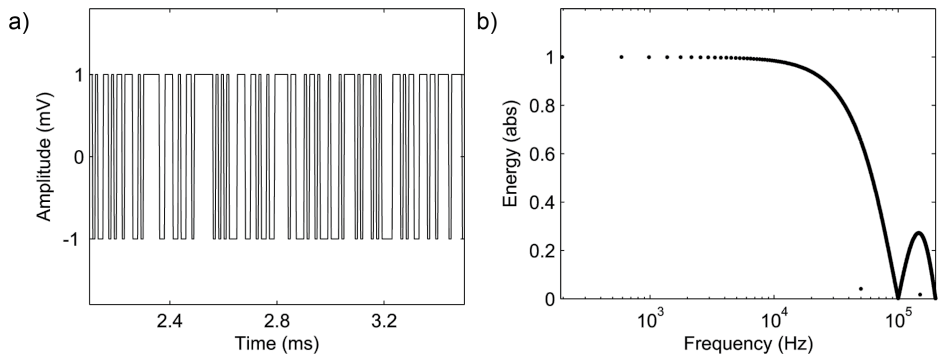

Figure 10: Generated excitation sequence; a) sample in the time domain, and b) (scaled) energy content.

data was 408,000 samples. The process of collecting the data took $4L/f_o$ = 1.02 s. The collected data was divided into segments, each with a length of one full multi-sampled excitation period (4·510 = 2,040). The logarithmic averaging procedure (Equation 4) was then applied to each data period.

Figure 11 shows the computed frequency responses (admittance spectroscopy) when the gate voltage was changed from 1.0 V to 3.0 V. The figure shows an almost linear drop in the gain curve when the gate voltage is below 2.0 V. When the gate voltage drops from 2.5 V to below 2.0 V, I_{ds} drops quickly because it reaches the threshold voltage (2.0 V) that turns the channel to an off-state (while it was on-state at 2.5 V). Figure 12 shows the admittance spectroscopies for the gate voltages around the threshold value where the dynamics change rapidly.

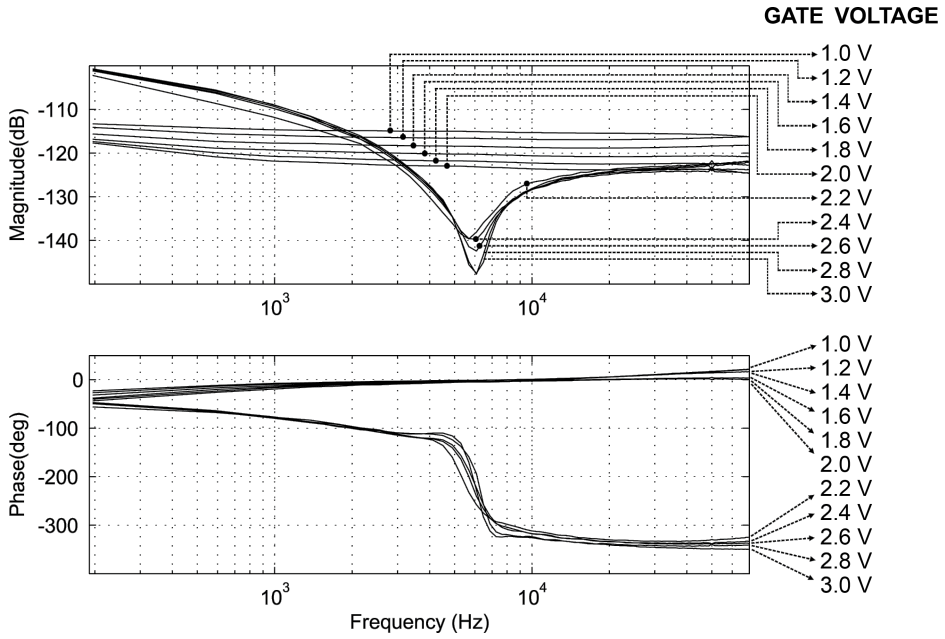

Figure 11: Admittance spectroscopy for gate voltages from 1.0 V to 3.0 V.

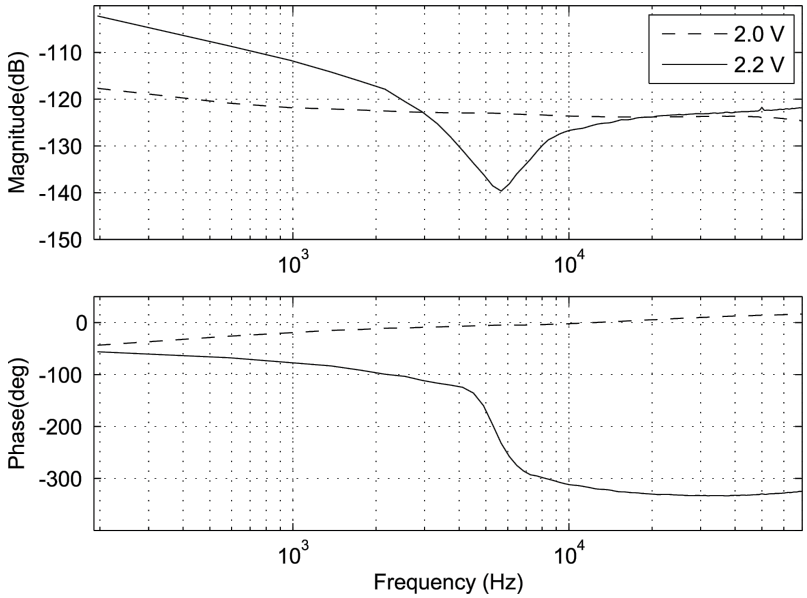

Figure 12: Admittance spectroscopy for gate voltages of 2.0 V and 2.2 V.

Conclusion

Silicon nanowire-based field-effect transistors (SiNW FETs) have been experimentally used for direct, label-free, highly selective, real-time detection of biological and chemical targets at very low concentrations. Most SiNW FET detectors are fabricated with SOI wafers, in which the back-gate contact is used to control the conductivity of the SiNW with the box layer. The molecules (detection targets) vary the surface potential of the transistor surface oxide. The leakage currents in those oxide layers affect the current between the source and drain. Recent studies indicate that the leakage current is frequency dependent. Measuring such characteristics can provide valuable tools to validate the functionality of the used transistors, and possibly have advantages in developing new frequency-domain-based detection technologies utilizing SiNW FETs.

This paper has presented fast frequency-domain methods with which to measure and characterize the leakage current. The inverse-repeat binary sequence (IRS) was applied, and the characterizing frequency responses were measured through Fourier methods. The experimental results showed that the leakage current strongly changes its frequency-domain properties at a certain gate voltage. This voltage value corresponds to the threshold voltage of the device.

The presented methods can be implemented cost-effectively, and provide responses within a few seconds. The applied techniques can also be used for measuring frequency responses other than the leakage current. The methods can be applied, for example, in analyzing the impedance of the nanowire in SINW FETs. This will be one part of the future work of the authors. Other future work will include further analysis of the leakage current, studying alternative excitation signals, implementing fully automated measurement systems, and designing new frequency-domain-based detection technologies.

References

1. Wan, Y.; Sha, J.; Chen, B.; Fang, Y.; Wang, Z.; Wang, Y. *Recent Pat. Nanotechnol.* **2009,** *3,* 1–9. doi:10.2174/187221009787003348
2. Gao, Z.; Agarwal, A.; Trigg, A.; Singh, N.; Fang, C.; Tung, C.; Buddharaju, K. Silicon Nanowire Arrays for Ultrasensitive Label-Free Detection of DNA. In *Solid-State Sensors, Actuators and Microsystems Conference, 2007. TRANSDUCERS 2007. International,* IEEE, 2006; pp 2003–2006.
3. Antohe, V. A.; Radu, A.; Mátéfi-Tempfli, M.; Attout, A.; Yunus, S.; Bertrand, P.; Duțu, C. A.; Vlad, A.; Melinte, S.; Mátéfi-Tempfli, S.; Piraux, L. *Appl. Phys. Lett.* **2009,** *94,* 073118. doi:10.1063/1.3089227
4. Zheng, G.; Patolsky, F.; Cui, Y.; Wang, W. U.; Lieber, C. M. *Nat. Biotechnol.* **2005,** *23,* 1294–1301. doi:10.1038/nbt1138
5. Wang, X.; Chen, Y.; Gibney, K. A.; Erramilli, S.; Mohanty, P. *Appl. Phys. Lett.* **2008,** *92,* 013903. doi:10.1063/1.2832648
6. Patolsky, F.; Zheng, G.; Hayden, O.; Lakadamyali, M.; Zhuang, X.; Lieber, C. M. *Proc. Natl. Acad. Sci. U. S. A.* **2004,** *101,* 14017–14022. doi:10.1073/pnas.0406159101
7. Kamins, T. I.; Sharma, S.; Yasseri, A. A.; Li, Z.; Straznicky, J. *Nanotechnology* **2006,** *17,* S291–S297. doi:10.1088/0957-4484/17/11/S11
8. Wang, Y.; Li, G. Simulation of a Silicon Nanowire FET Biosensor for Detecting Biotin/Streptavidin Binding. In *Nanotechnology (IEEE-NANO), 2010 10th IEEE Conference on,* IEEE, 2010; pp 1036–1039.
9. Motayed, A.; Krylyuk, S.; Davydov, A. V. *Appl. Phys. Lett.* **2011,** *99,* 113107. doi:10.1063/1.3637049
10. Zheng, G.; Gao, X. P. A.; Lieber, C. M. *Nano Lett.* **2010,** *10,* 3179–3183. doi:10.1021/nl1020975
11. Nguyen, T. C.; Qiu, W. Z.; Skafidas, E. *IEEE Trans. Biomed. Eng.* **2012,** *59,* 213–218. doi:10.1109/TBME.2011.2170424
12. Schoukens, J.; Pintelon, R.; van der Ouderaa, E.; Renneboog, J. *IEEE Trans. Instrum. Meas.* **1988,** *37,* 342–352. doi:10.1109/19.7453
13. Godfrey, K. R. Introduction to Binary Signals Used in System Identification. In *Proc. International Conference on Control,* 1991; pp 161–166.
14. Godfrey, K. *Perturbation Signals for System Identification;* Prentice Hall: New York, NY, USA, 1993.
15. Srinivasan, R.; Rengaswamy, R. *Ind. Eng. Chem. Res.* **1999,** *38,* 3420–3429. doi:10.1021/ie980761z
16. Gong, J.; Lambert, M.; Zecchin, A.; Simpson, A. Frequency response measurement of pipelines by using the inverse-repeat binary sequence. In *Proc. International Conference on Computing and Control for the Water Industry,* 2011.
17. Roinila, T.; Vilkko, M.; Suntio, T. *IEEE Trans. Power Electron.* **2010,** *25,* 2179–2187. doi:10.1109/TPEL.2010.2043688
18. Roinila, T.; Yu, X.; Gao, A.; Li, T.; Verho, J.; Vilkko, M.; Kallio, P.; Wangy, Y.; Lekkala, J. Characterizing Leakage Current in Silicon Nanowire-Based Field-Effect Transistors by Applying Pseudo-Random Sequences. In *Proc. International Conference on Manipulation, Manufacturing and Measurement on the Nanoscale,* 2012.
19. Ljung, L. *System Identification-Theory for the User;* Prentice Hall: New York, NY, USA, 1999.
20. Barkley, A.; Santi, E. *IEEE Trans. Power Electron.* **2009,** *24,* 2021–2031. doi:10.1109/TPEL.2009.2020588
21. Pintelon, R.; Schoukens, J. *System Identification - A Frequency Domain Approach;* Institute of Electrical and Electronics Engineers, Inc.: New York, NY, USA, 2001.
22. Roinila, T.; Vilkko, M.; Suntio, T. *IEEE Trans. Power Electron.* **2009,** *24,* 2746–2755. doi:10.1109/TPEL.2009.2027706
23. Godfrey, K. R. *Comput. Control. Eng. J.* **1991,** *2,* 187–195. doi:10.1049/cce:19910049
24. Golomb, S. *Shift Register Sequences;* Holden-Day: San Fransisco, CA, USA, 1967.
25. Gao, A.; Lu, N.; Dai, P.; Li, T.; Pei, H.; Gao, X.; Gong, Y.; Wang, Y.; Fan, C. *Nano Lett.* **2011,** *11,* 3974–3978. doi:10.1021/nl202303y

BEILSTEIN JOURNAL OF NANOTECHNOLOGY

Nanoforging – Innovation in three-dimensional processing and shaping of nanoscaled structures

Andreas Landefeld* and Joachim Rösler

Letter

Open Access

Address:
Institut für Werkstoffe, Technische Universität Braunschweig, Langer Kamp 8, 38106 Braunschweig, Germany

Email:
Andreas Landefeld* - a.landefeld@tu-bs.de

* Corresponding author

Keywords:
forging; manipulation; nanoforging; plastic deformation; tungsten

Beilstein J. Nanotechnol. **2014,** *5,* 1066–1070.
doi:10.3762/bjnano.5.118

Received: 02 April 2014
Accepted: 25 June 2014
Published: 16 July 2014

This article is part of the Thematic Series "Physics, chemistry and biology of functional nanostructures II".

Guest Editor: A. S. Sidorenko

Abstract

Background: This paper describes the shaping of freestanding objects out of metallic structures in the nano- and submicron size. The technique used, called nanoforging, is very similar to the macroscopic forging process.

Results: With spring actuated tools produced by focused ion beam milling, controlled forging is demonstrated. With only three steps, a conical bar stock is transformed to a flat- and semicircular bent bar stock.

Conclusion: Compared with other forming techniques in the reduced scale, nanoforging represents a beneficial approach in forming freestanding metallic structures, due to its simplicity, and supplements other forming techniques.

Findings

The macroscopic world offers a large variety of three-dimensional forming processes, for example casting, forging or cutting. Producing three-dimensional mechanical resilient structures in the submicron- and nanoscale is a very challenging task. Generally, when size is reduced it becomes more and more difficult to position nanoobjects and to control their geometry in three individual dimensions. Adhesive effects become dominant and forces such as gravity are negligible. Other macroscopical versatile processes like casting or cutting are not reproducible to the nanoscale, at the moment. For example, studies on chip formation in the nanoscale are a wide field of research at present [1,2]. But three dimensional cutting in the nanoscale is still unexplored. Casting is also limited in its nano-applicability. The mold filling depends on the mold temperature and the filling pressure [3] and is also limited by the surface tension of the cast-material. Some complex three dimensional shapes were

realized by casting of metal with a low melting temperature [3,4]. Dimensions of cast details are in the submillimeter- and microscale, and due to the mentioned limitations, applications in the submicron- and nanoscale do not seem to be feasible. For electromechanical and optical application numerous patterning techniques were developed. Only a few are applicable for patterning metals. An example is imprinting. This techniques uses a macroscopic stamp with structures in the micro- and nano-range. By pressing it into a substrate the structure of the stamp is replicated as imprint. Polymers [5], but also metallic glasses [6], are used as substrate material for this surface patterning process. It is less applicable for three-dimensional forming of individual objects than for structuring of large and plain surfaces. Another example is electrodeposition [7]. This technique enables three dimensional patterning in the nano-range by deposition of metals electrochemically. Like imprinting, electrodeposition is less suitable for direct and individual shaping of freestanding structures.

Recently Landefeld et al. [8] and Schloesser et al. [9] showed that forging has a great potential to form miniaturized freestanding objects. In their studies cubic single crystalline Ni_3Al-particles were compressed, investigating the true strain-true stress response of the freestanding nanoparticles. High degrees of deformation (true strain $\varphi > 1$) were observed without any signs of cracking [8,10,11]. The measured yield strengths of 2500 MPa to 5000 MPa are a significant portion of the theoretical strength [8]. Landefeld and Rösler [12] successfully produced defined forged shapes out of the single crystalline cubic Ni_3Al-particles. They used lithographically etched dies as a mold for open die forging. Other techniques like free forming were also studied on these particles. This only shows a small part of shapes forging enables.

It turned out that it is helpful to simplify processes when scaled down. In this respect forging is an attractive forming process where complex three-dimensional structures can be realized with simple tools. In the most elementary way a bar stock is forged between two rams which move towards each other. The shaped surfaces are small in nanoforging. High forces sometimes set boundaries in macroscopic forging, which is not an issue when microscopic material volumes are formed. As mentioned above, the small volume of the used material also yields mechanical properties which are not achievable in macroscopic forging. Consequently high degrees of deformation, good mold filling as well as complex shapes can be more readily achieved. Single crystalline silicon, processed by focused ion beam milling, is used for durable spring actuated forging tools. Furthermore, high strength metals can be processed and high deformation degrees of the bar stock can be realized without heating. This is notably interesting for structural components and when magnetic or electrical properties of metals are desired. Due to forging in the vacuum of a scanning electron microscope (SEM) the unwanted oxidation can be minimized.

The experiments were done in a DualBeam microscope (FEI Helios NanoLab^{TM} 650). A system of two micromanipulators (MM3A-EM from Kleindiek Nanotechnik) was mounted on the stage and at the door of the microscope in a angle of 90° to each other. Regarding nanoforging, the positioning accuracy is 3.5 nm and 5 nm, respectively, in the two rotational axes and 0.25 nm in the linear axis [13]. The forging tools were machined by focused ion beam milling at the corner of a single crystalline Si-substrate. Varying tools in different positions were produced to allow several forging steps after each other (Figure 1).

All of these tools are based on a spring principle similar to so called spring swages which were known in historic blacksmith shops. The upper spring arm moves down when pressing straight on it, consequently the upper and the lower arm come closer, resulting in shaping of the bar stock between the forging surfaces. After load relief the upper spring arm moves in its

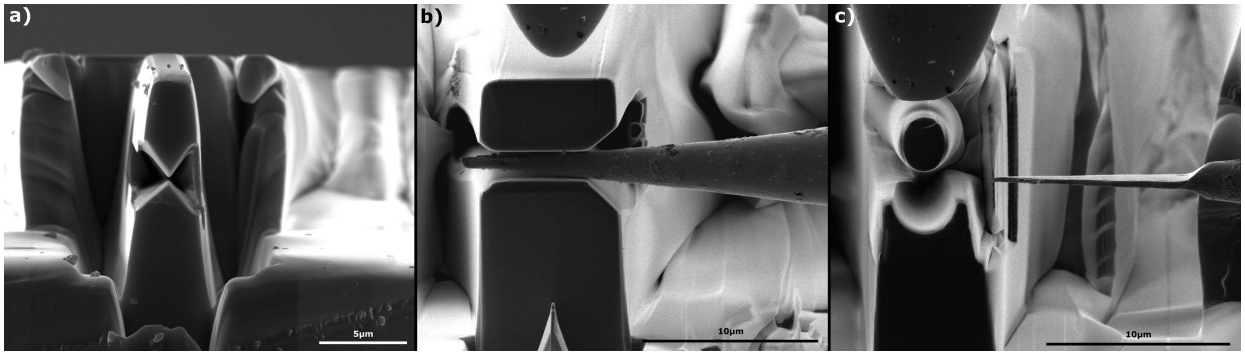

Figure 1: Scanning electron microscope images of different forging tools. Image a) shows a cutting tool, b) a freeforming tool and c) a bending tool.

initial position. This principle allows fast and precise forging between both forming surfaces (video Supporting Information File 2). The bar stock was produced from a 0.5 mm drawn polycrystalline tungsten wire with a purity of 99.995%. Tungsten can be relatively easy machined electrochemically. It is often used for tough and sharp probes in scanning probe microscopy. An electrochemical process described in [12] is applied here to produce the essentially conical bar stock, having a diameter of 100 to 300 nm at the tip and 1000 to 4000 nm at the forging tail.

Figure 2b illustrates a possible installation where the flat punch (a) actuates the forging tool (b) and shapes the bar stock (c) between the forging surfaces (d). The forging tools can be arranged in a staggered way, so that different forging steps can be done after each other without the need of time and effort of tool changing. The geometries of the forging tools were varied to show exemplary three different possibilities of nanoforging. A cutting tool, a freeforming tool and a bending tool is shown in Figure 1. The function of the three forging tools is described below.

i) Trimming via shearing-off is used when the tip of the bar stock needs to be cut to length. In this demonstration, the forging tool is designed with two sharp symmetrical wedges (Figure 2a) and a wedge angle of 30° and 40°. The intersecting angle of the cutting surface is consequently similar to the wedge angle. The video Supporting Information File 1 shows a cut on a tungsten bar stock exemplarily.

ii) Forging between even surfaces is a free forming process also common in macroscopic forging processes. Basically there are two different kinds, the stretch forging and the spread forging. The grade of stretching and spreading can be influenced in the following ways. First the bar stock can be rotated by 90° after each forging step resulting in a stretched workpiece. Second the bite ratio s_B/w_0 influences the material flow. It is defined as ratio of the bite s_B and the width w_0. The lower the bite ratio, the higher the grade of stretching (Figure 3) [14]. For example, when a bite ratio s_B/w_0 of 0.2 and a reduction of height h_0/h_1 by a factor of 1.21 is choosen, the bar stock is stretched by a factor of $l_1/l_0 = 1.16$ and spread by a factor of $w_1/w_0 = 1.04$. The video Supporting Information File 2 shows a tungsten bar stock flattened by forging between even surfaces. Figure 1c shows a flattened bar stock before it was bent in the next step. In this demonstration the initial thickness of 680–1800 nm of the conical bar stock was reduced to 200–300 nm. Still, there is potential to reduce the thickness below 100 nm. An correlation of the material flow between macroscopic forging and nanoforging was found. In this study the bite ratio was about 2.2, thus the bar stock was as expected more spread than stretched. However, due to the conical geometry of the bar stock, it was not possible to give an exact comparison between Figure 3 and the results of nanoforging.

iii) The third forging tool allows the bending of a flat bar to a semicircle. A semicircular forging die and a cylindrical upper spring arm defines the contour of the flat bar. The lower side is stretched and the upper side is compressed resulting in a semicircle geometry of the flat bar. Figure 4a and video Supporting Information File 3 shows how the flat bar is formed into the lower die. When lifted out it can be seen that the upper bending arm is broken, due to a too high chosen distance between the upper and the lower arm of the forging tool.

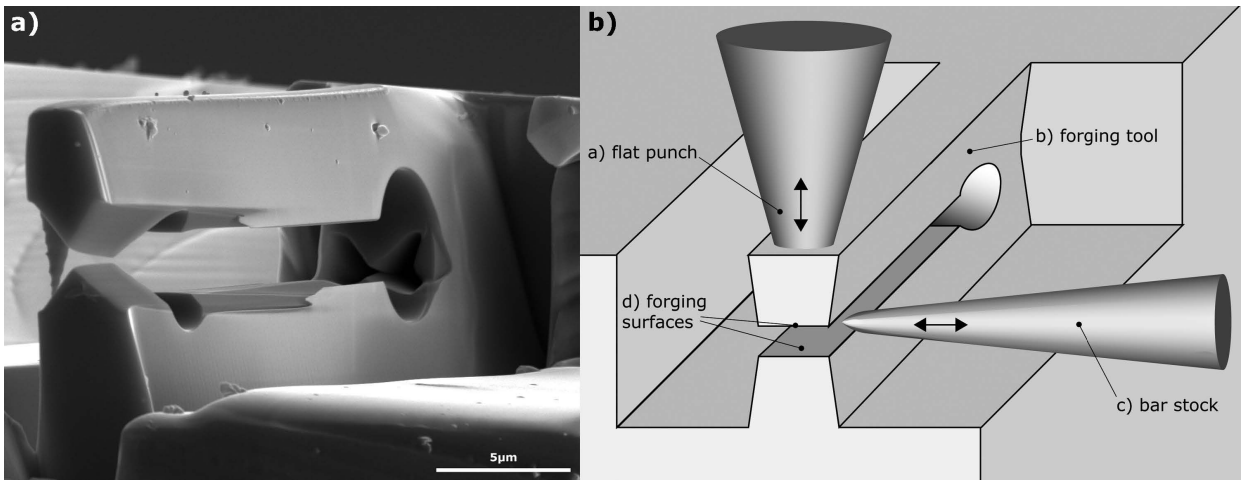

Figure 2: Spring principle of a cutting tool on the left (a). Installation schematically on the right (b). The upper bending arm of the forging tool moves down when pressing on it with the flat punch. It moves in its initial position while load release due to the elastic force. The bar stock is moved between the forging surfaces.

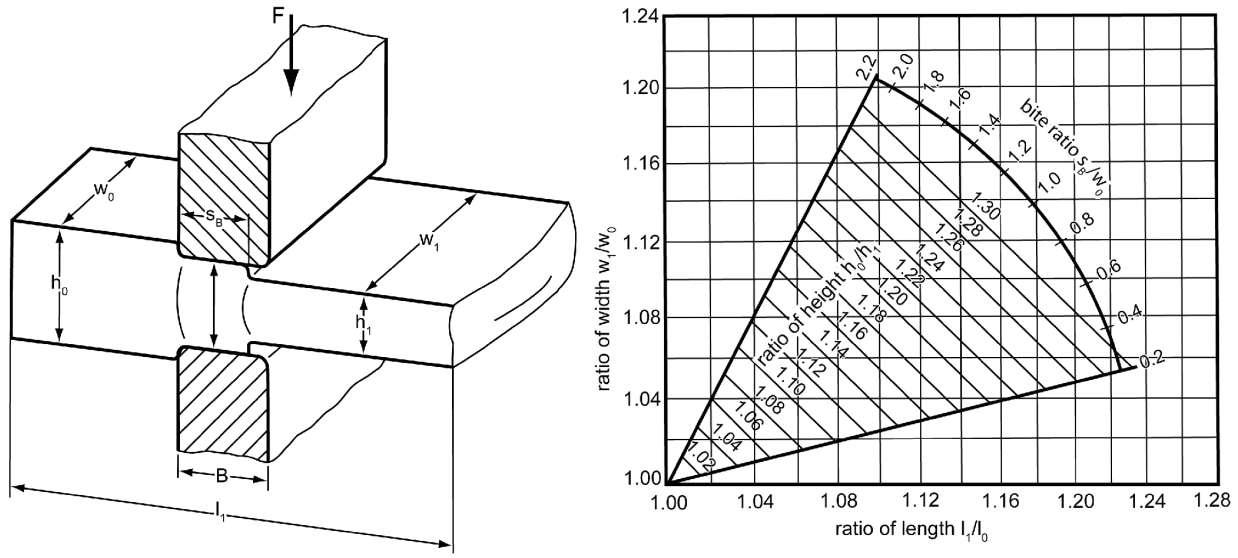

Figure 3: The grade of stretching and spreading is influenced by the bite ratio s_B/w_0. Illustrations after Spur and Stöferle [14].

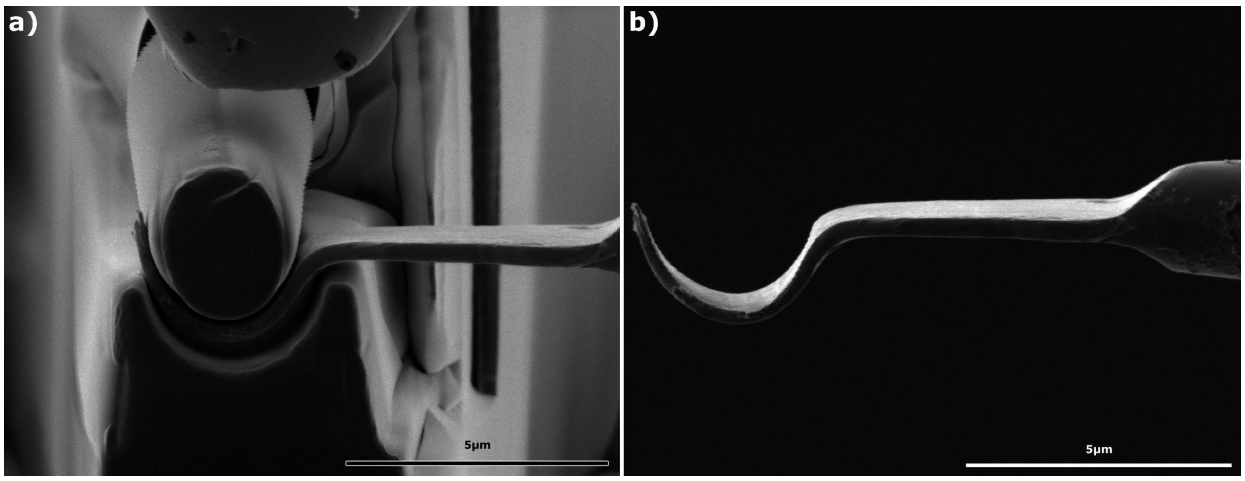

Figure 4: SEM images of the bending process. The flat bar is forged in the lower forging die and adapted its outer geometry. The inner shape is given by the cylindrical upper bending arm.

Nevertheless a smooth and clear geometry is reproduced (Figure 4b).

In summary we have given an overview of the forging process in the submicron- and nanoscale. A tungsten bar stock with a taper diameter of 2 µm at the forging end was first cut, than stretched and broadened and finally bent to a semicircle. On the basis of these three techniques it is exemplary shown that forging offers a great potential in shaping of three-dimensional structures in the submicron- and nano-range. The forging tools, produced here by focused ion beam milling of a single crystalline silicon wafer, can be individually designed and adjusted to the needs. Therefore, forging parts with a great variety of shapes are possible. With little constraint much of the macroscopic forging technique is realizable in the nanoscale. Typical parts produced by forging could be axle-shafts, discs, flat or spiral springs. Furthermore, bending and cutting of nano wires could be also possible applications of nanoforging. In contrast to structures produced by ion- or electron beam induced deposition, homogenous metallic structures can be manufactured with a high mechanical load capacity. Nanoforging plays out its strength when a small quantity and flexible and individual control of shape is required as well as mechanical properties of metals are of interest.

Supporting Information

Supporting Information File 1

Tungsten bar stock trimmed by a cutting tool.
[http://www.beilstein-journals.org/bjnano/content/supplementary/2190-4286-5-118-S1.avi]

Supporting Information File 2

Tungsten bar stock flattened by forging between even surfaces.
[http://www.beilstein-journals.org/bjnano/content/supplementary/2190-4286-5-118-S2.avi]

Supporting Information File 3

Tungsten flat bar bent to a semicircle geometry.
[http://www.beilstein-journals.org/bjnano/content/supplementary/2190-4286-5-118-S3.avi]

License and Terms

The definitive version of this article is the electronic one which can be found at:
doi:10.3762/bjnano.5.118

References

1. Nowag, K. Deformation mechanisms of hard to machine metal alloys at the microscale. Ph.D. Thesis, Technische Universität Braunschweig, Germany, 2013.
2. Islam, S.; Ibrahim, R.; Khandoker, N. The mechanics of single crystal Cu machining at nanoscale. *11th International Conference on the Mechanical Behavior of Materials (ICM11);* 2011; pp 2369–2374.
3. Yang, C.; Li, B. S.; Ren, M. X.; Fu, H. Z. *Int. J. Adv. Manuf. Technol.* **2010,** *46,* 173–178. doi:10.1007/s00170-009-2098-4
4. Baumeister, G.; Buqezi-Ahmeti, D.; Glaser, J.; Ritzhaupt-Kleissl, H.-J. *Microsyst. Technol.* **2011,** *17,* 289–300. doi:10.1007/s00542-011-1237-7
5. Guo, L. J. *Adv. Mater.* **2007,** *19,* 495–513. doi:10.1002/adma.200600882
6. Saotome, Y.; Fukuda, Y.; Yamaguchi, I.; Inoue, A. *J. Alloys Compd.* **2007,** *434–435,* 97–101. doi:10.1016/j.jallcom.2006.08.126
7. Schwarzacher, W. *Electrochem. Soc. Interface* **2006,** *15,* 32–35.
8. Landefeld, A.; Mook, M. W.; Rösler, J.; Michler, J. *ISRN Nanomater.* **2012,** No. 890486. doi:10.5402/2012/890486
9. Schloesser, J.; Rösler, J.; Mukherji, D. *Int. J. Mater. Res.* **2011,** *102,* 532–537. doi:10.3139/146.110504
10. Rösler, J.; Mukherji, D.; Schock, K.; Kleindiek, S. *Nanotechnology* **2007,** *18,* 125303. doi:10.1088/0957-4484/18/12/125303
11. Maaß, R.; Meza, L.; Gan, B.; Tin, S.; Greer, J. *Small* **2012,** *8,* 1869–1875. doi:10.1002/smll.201102603
12. Landefeld, A.; Rösler, J. Fabrication of Metallic Nanocomponents by Forging of Ni_3Al-Nanoparticles. 2012 MRS Fall Meeting; 2012; mrsf11–1412.
13. *MM3A-EM, MM3A-UHV, MM3A-LT Inspection Sheet*; Kleindiek Nanotechnik GmbH, 2007.
14. Spur, G.; Stöferle, T. *Handbuch der Fertigungstechnik, Band 2/2 Umformen;* Carl Hanser Verlag : München, Wien, 1984.

BEILSTEIN JOURNAL OF NANOTECHNOLOGY

Nanocavity crossbar arrays for parallel electrochemical sensing on a chip

Enno Kätelhön[1], Dirk Mayer[2], Marko Banzet[2], Andreas Offenhäusser[2,3] and Bernhard Wolfrum[*2,3]

Full Research Paper

Open Access

Address:
[1]Institute of Bioelectronics (PGI-8/ICS-8) and JARA-Fundamentals of Future Information Technology, Forschungszentrum Jülich, 52425 Jülich, Germany. Current address: Department of Chemistry, Physical and Theoretical Chemistry Laboratory, Oxford University, South Parks Road, Oxford, OX1 3QZ, United Kingdom, [2]Institute of Bioelectronics (PGI-8/ICS-8) and JARA-Fundamentals of Future Information Technology, Forschungszentrum Jülich, 52425 Jülich, Germany and [3]Institute of Physics, RWTH Aachen University, 52074 Aachen, Germany

Email:
Bernhard Wolfrum* - b.wolfrum@fz-juelich.de

* Corresponding author

Keywords:
electrochemical imaging; nanoelectrochemistry; redox cycling

Beilstein J. Nanotechnol. **2014,** *5,* 1137–1143.
doi:10.3762/bjnano.5.124

Received: 26 February 2014
Accepted: 25 June 2014
Published: 23 July 2014

This article is part of the Thematic Series "Physics, chemistry and biology of functional nanostructures II".

Guest Editor: A. S. Sidorenko

Abstract

We introduce a novel device for the mapping of redox-active compounds at high spatial resolution based on a crossbar electrode architecture. The sensor array is formed by two sets of 16 parallel band electrodes that are arranged perpendicular to each other on the wafer surface. At each intersection, the crossing bars are separated by a ca. 65 nm high nanocavity, which is stabilized by the surrounding passivation layer. During operation, perpendicular bar electrodes are biased to potentials above and below the redox potential of species under investigation, thus, enabling repeated subsequent reactions at the two electrodes. By this means, a redox cycling current is formed across the gap that can be measured externally. As the nanocavity devices feature a very high current amplification in redox cycling mode, individual sensing spots can be addressed in parallel, enabling high-throughput electrochemical imaging. This paper introduces the design of the device, discusses the fabrication process and demonstrates its capabilities in sequential and parallel data acquisition mode by using a hexacyanoferrate probe.

Introduction

Redox cycling represents a powerful method for the detection of analytes that can participate in repeated redox reactions [1-8]. Sensors typically use two electrodes that are located in close proximity to each other and can be biased individually. During operation one electrode is set to a potential above the redox potential E_0 of the analyte under investigation, while the other electrode is set below this potential. Molecules can repeatedly participate in subsequent redox reactions at the electrodes, hence forming a current across the gap. This current can then be measured externally and allows one to draw conclusions

regarding a variety of analytes or reaction characteristics such as the electrode kinetics or the analyte concentration.

A distinct advantage of this technique over conventional amperometry, using a single working electrode, is given by the increased Faradaic current caused by the redox cycling effect. A single molecule entering the sensor does not only contribute with an individual charge transfer to the Faradaic current but participates in multiple reactions that each result in a charge transfer to the working electrode. Sensitivity differs among sensor designs and is mainly determined by the collection efficiency of the sensor and the average time a molecule requires for passing one redox cycle. In recent years, a variety of on-chip redox cycling devices has been implemented. Hereby, the highest sensitivity per electrode area was reported for nanofluidic redox cycling sensors. These sensors feature micron-sized electrodes that are arranged in parallel to each other and the wafer surface, being separated by a nano-scaled gap [9-11]. The current per molecule obtained with such a sensor featuring the inter electrode distance h is directly proportional to h^{-2}. Therefore, small inter-electrode distances can significantly amplify the electrochemical signal [12,13]. Amplification factors can be calculated via comparison to a single electrode of the same size and may reach several orders of magnitudes, allowing very low detection limits; Recently, Lemay's group reported the ultimate detection limit by sensing at molecular resolution inside a nanofluidic redox cycling device [14-16]. Besides the advantages of electrochemical amplification, redox cycling sensors allow for the formation of large, dense arrays of electrochemical sensors that are highly desirable for applications such as on-chip parallel biosensing or the detection of chemical communication in a neuronal network. This can be achieved via the organization of feed lines in a perpendicular arrangement. Individual sensors are then located at each of the feed line intersections. Redox cycling is enabled at the intersection by setting the potentials of two orthogonal feed lines to values above and below the redox potential of an analyte. Even though faradaic currents may also occur at all other electrodes that are connected to the biased feed lines and are exposed to redox-active molecules, their individual contribution to the overall measured current is comparably small due to the strong amplification by the redox cycling effect. Hence, individual sensors can be easily read out by this method.

Addressable redox cycling electrode arrays have been pioneered by the group of Matsue since 2008 and various designs have been reported since then. Implementations include systems, which consist of two wafers of parallel bar electrodes that are glued face-to-face to each other [17,18], arrays of ring–ring-based sensors with orthogonal feed lines [19], and designs featuring interdigitated electrodes at the intersections [20]. Reported applications include gene-function analysis [18], electroluminescence detection [21], mapping of cell topographies [22], detection of cellular enzyme secretion [19,23], detection of DNA hybridization [24], and evaluation of embryoid bodies [25].

This paper describes the design and fabrication of a crossbar-based nanocavity redox cycling sensor array that combines the advantages of the two approaches: crossbar architecture and nanocavity sensors. The large redox cycling amplification of the nanocavity sensors allows such arrays to be operated in a parallel readout for high-throughput applications. The redox cycling response during electrochemical imaging using parallel data acquisition is demonstrated and different modes of operation for its future use in mapping neurochemical events in cell culture are discussed.

Results and Discussion

Our sensors offer two different modes of operation: The sequential and the parallel readout mode. During sequential data acquisition, each crossing point on the sensor is addressed individually one after the other, while the electrochemical image of the sensor surface is assembled afterwards. As it can be seen in Figure 1a, two electrodes that are arranged perpendicular to each other are set to potentials above and below the redox potential, while all other electrodes remain unbiased. Redox

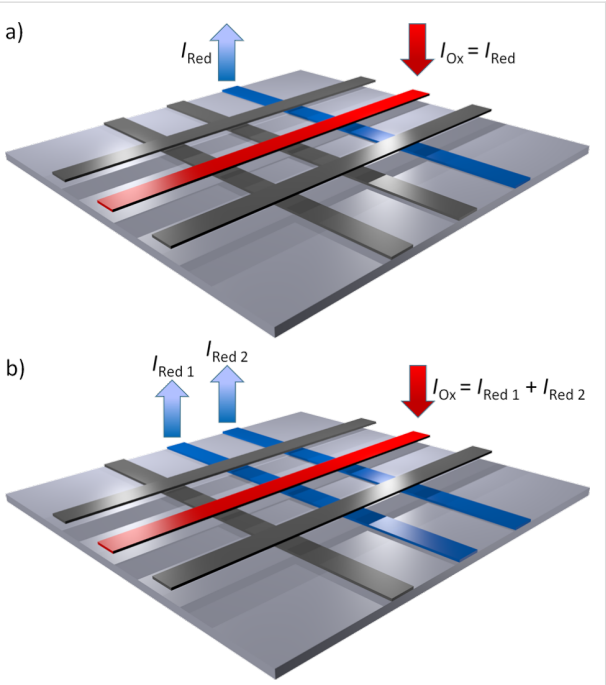

Figure 1: Illustration of the two modes of operation: a) Sequential data acquisition: Each intersection is read out sequentially. b) Parallel data acquisition: Intersections are read out simultaneously in a row-wise fashion.

cycling is then enabled at the corresponding intersection and the respective redox-cycling current can be detected at both electrodes. In parallel acquisition mode, however, two or more electrodes that are arranged perpendicular to the one oxidizing electrode are biased to reducing potentials. Hence, redox cycling is enabled at each intersection between a reducing electrode and the oxidizing electrode, thus, resulting in a row-wise read-out. As sketched in Figure 1b, the individual redox-cycling currents of each intersection can be measured at the reducing electrodes, while the current at the oxidizing electrode amounts to the sum of all other redox cycling currents.

Figure 2 compares data of the sensor during operation in both acquisition modes in presence of 1 mM hexacyanoferrate.

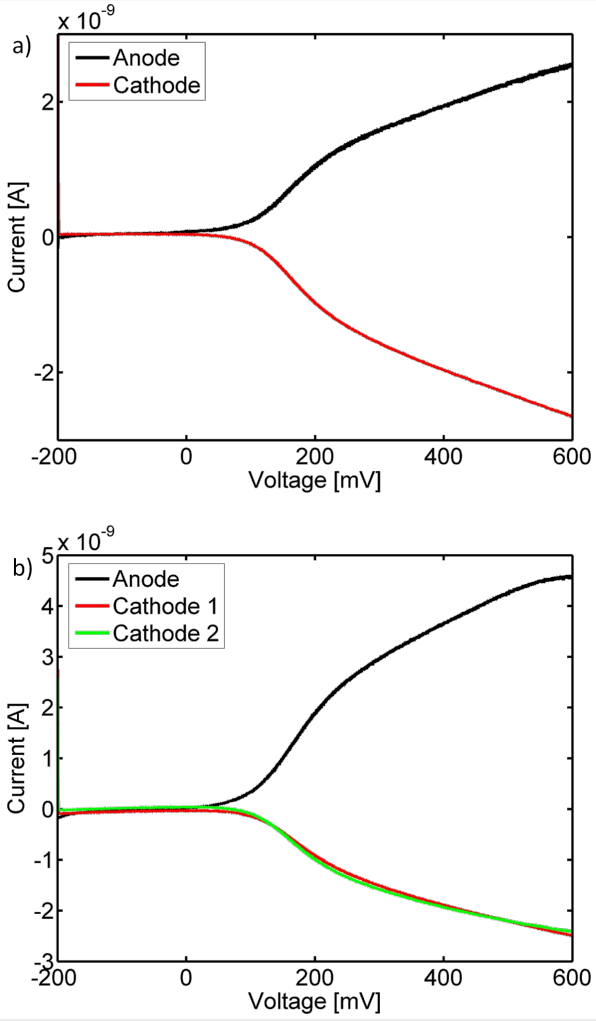

Figure 2: Redox cycling currents: a) Cyclic voltammogram detected in sequential data acquisition mode at a single intersection. b) Cyclic voltammograms recorded at two intersections during parallel acquisition. Both data sets were recorded in 1 mM potassium hexacyanoferrate in PBS and filtered via a Butterworth filter. Furthermore, the data were offset corrected and traces recorded in a single electrode setup were subtracted from the anodic currents in order to isolate the respective redox cycling currents.

Hereby, both graphs exhibit some characteristics in common: Below the redox potential, which can be found around 180 mV, the current does not increase with the anodic voltage. However, above the redox potential there is a fast increase in current, which is due to the now enabled redox cycling. Nevertheless, the current does not reach the expected diffusion-limited steady state at high overpotentials. This effect can be attributed to kinetic limitations that may be caused by impurities on the electrode surfaces that remain from the fabrication process. Furthermore, in both cases the anodic and the sum of the cathodic currents equal. Thus, redox cycling inside the sensor is highly efficient.

Figure 3 demonstrates the concentration dependency of an individual sensor. Hereby, a single intersection was characterized at varied concentrations of potassium hexacyanoferrate in sequential acquisition mode. As it can be seen in the plot the redox cycling current scales approximately linearly with the concentration. The slope of the sensor response was obtained via a linear regression yielding a sensitivity of $2.4 \pm 0.2 \times 10^4$ A·m^{-2}·M^{-1} in the overlapping electrode area (1.68×10^{-12}·m^2). Figure 4 shows a typical sensor response but the array exhibits a large variance in sensitivity making it necessary to calibrate individual sensors for quantitative imaging. The largest current responses obtained were in the range of 1.7×10^5 A·m^{-2}·M^{-1}, which is still significantly less than the theoretically expected diffusion-limited value for the devices in case of a one-electron process if we neglect kinetic limitations

$$\frac{I}{c \cdot A} = \frac{1000 \cdot D \cdot F}{h} = 9.5 \times 10^5 \, \frac{\mathrm{A \cdot L}}{\mathrm{m^2 mol}}. \qquad (1)$$

Here, c is the concentration in (mol/L), A the overlapping electrode area in m^2, $D = 0.64 \times 10^{-9}$ m^2/s the diffusion coefficient, F = 96485 C/mol the Faraday constant, and h = 65 nm the nanocavity height. Deviations between expected and recorded current responses in nanocavity devices have been observed previously and are thought to depend on fabrication inhomogeneities and residues as well as adsorption effects limiting the electrode kinetics.

In order to demonstrate parallel electrochemical recording at the nanocavity crossbar array, we monitor concentration fluctuations at the chip surface induced by the dissolution of a hexacyanoferrate crystal [26]. For this purpose, all but one electrode are biased to a reducing potential of −200 mV, while the one electrode is biased to an oxidizing potential of 600 mV. In this operation mode, redox cycling is simultaneously enabled at all 16 sensors along the oxidizing electrode and the respective sensor signal can be read out at the corresponding perpendicular cathodes. The device is then calibrated in plain 100 mM

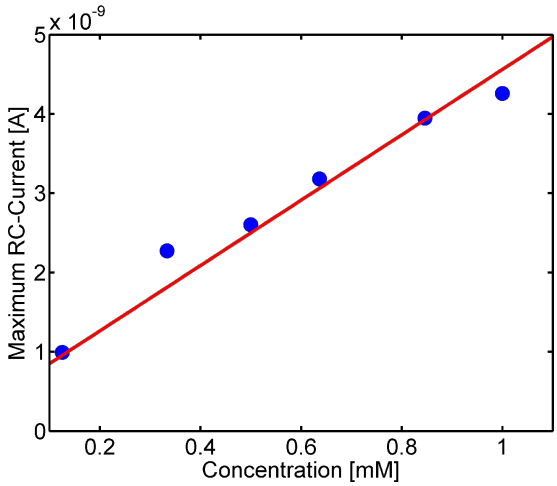

Figure 3: Concentration dependency of an intersection in sequential data acquisition. Data was recorded during cyclic voltammograms at different concentrations of potassium hexacyanoferrate in 100 mM KCl and represents the absolute difference between the cathodic peak current and a measurement using only the background electrolyte.

KCl solution as well as in a 1 mM potassium hexacyanoferrate solution in order to linearly interpolate the response curve for the individual sensors. After adding the 1 mM potassium hexacyanoferrate solution, three sensors that are located next to each other (the yield of functional sensors is approximately 40%) are chosen and a potassium hexacyanoferrate crystal is added to the solution. The so obtained electrochemical image of its dissolution after background subtraction can be seen in Figure 4. The parallel readout of the crossbar array allows the chemical concentration to be mapped at all active sensors simultaneously with a millisecond temporal resolution, which is sufficient for resolving fast dissolution processes. The sensitivity is determined by the height of the nanocavities (65 nm) while the spatial resolution relies on the sensor array density (ca. 244/mm^2). When using the current fabrication process, the sensor density is limited by the low yield of functional intersections, which is probably related to stability issues with the passivation layer. Solving this problem would in principle allow for high-density mapping in the range of 10000/mm^2 for reasonable cross bar pitches of 10 µm as obtainable by conventional optical lithography.

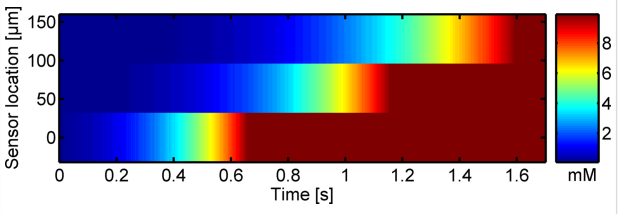

Figure 4: Electrochemical recording of the change in concentration during dissolution of a potassium haxacyanoferrate crystal above the sensor surface.

Conclusion

We introduced the design and fabrication of a novel device for the electrochemical on-chip imaging of redox molecules by redox cycling. The presented chip was fabricated with standard cleanroom technology and features nanocavity redox cycling devices in a crossbar architecture for sensitive electrochemical detection at a high sensor density. Measurements in potassium hexacyanoferrate solution are shown and different modes of operation are demonstrated: the sequential readout of individual sensors and the parallel readout mode, which allows for the spatiotemporal sensing along one feed line.

It can be assumed that the presented technique, which combines high-density sensing of electrochemical species with redox cycling amplification in the nanofluidic cavities, will be advantageous for electrochemical imaging methods and electrochemical biological assays. Particularly, one may expect that the detection or mapping of neutrotransmitter secretion (such as the redox-active molecule dopamine [13]) in neuronal networks will be one of the most interesting applications [27-37]. In this case, the sensor array is exposed to fast fluctuations in the neurotransmitter concentration. By biasing the two parallel sets of bar-electrodes to reducing and oxidizing potentials, one can then correlate the electrochemical signals at orthogonal electrodes, hence recording data from all sensors simultaneously (see Figure 5). Overall, we expect a wide range of applications for high-density nanocavity sensors and remain looking forward to see their implementation in future imaging systems.

Experimental

Sensor design

Our device features two orthogonal sets of 16 parallel bar electrodes, each. These electrodes are 14 µm wide, separated by 64 µm (center to center), and fabricated in parallel to the wafer surface. At each intersection, the electrodes are separated by an about 65 nm wide gap, while the arrangement is stabilized by a thick passivation layer that covers the whole device. The interelectrode area is connected to the bulk reservoir via small access channels that interpenetrate the passivation layer and enable diffusive access to a bulk reservoir. An illustration of the sensor array and a top view microscopic image as well as cross sections of the nanocavity sensor, cut by a focused ion beam (FIB), can be found in Figure 6.

Fabrication

Devices are structured by means of optical lithography and are processed in class-100 cleanroom facilities. Nanocavities at the intersections between platinum electrodes are formed via the

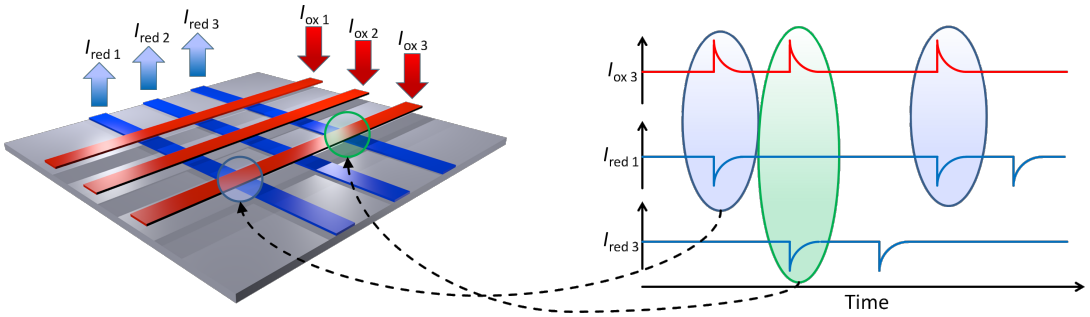

Figure 5: Illustration of a future electrochemical setup for parallel spike recording on-chip. By correlation of individual spike events at anodic and cathodic electrodes, all electrodes intersections can be read out simultaneously.

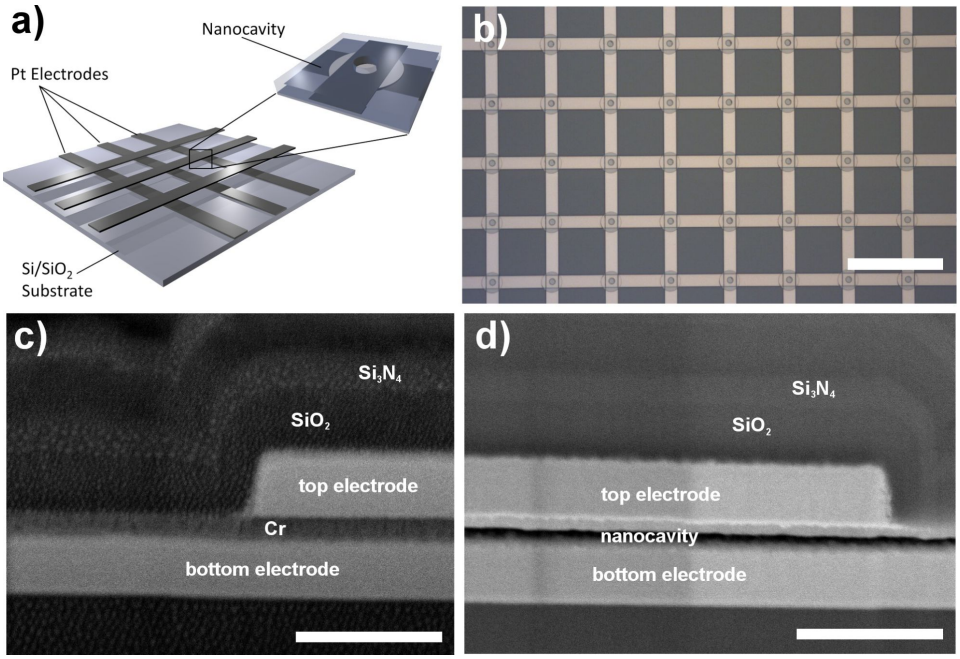

Figure 6: Nanocavity array chip: a) Illustration of a sensor array. The inset sketches a nanocavity sensor that can be found at each feed-line intersection. The light grey spherical layer represents the nanocavity, while the hole in the top electrode and in the passivation layer is the access channel that connects the bulk reservoir on the chip surface to the nanocavity. b) Microscopic top view of a part of the array. c,d) Scanning electrochemical microscope images of FIB-induced cross sections of a nanocavity sensor before (c) and after (d) removal of the sacrificial chromium layer. The scale bars for the images in (b), (c), and (d) are 100 µm, 400 nm, and 400 nm, respectively.

deposition of a sacrificial layer followed by an isotropic etch. The full device is stabilized by a silicon oxide/silicon nitride stack that covers the full device and is solely opened trough access holes above each crossbar intersection. Since the whole device is covered by the passivating layer, electrodes can only be accessed from within cavity, while a connection to the bulk reservoir is only enabled through the access channels.

The sensor is fabricated on a thermally oxidized silicon substrate while all structures are formed via lift-off processes or reactive ion etching. Electrodes are fabricated by depositing a titanium/platinum/chromium stack that features the thicknesses 7/50/7 nm by using electron beam evaporation. In the next step, 50 nm thick chromium sacrificial layers are deposited at the positions of the future intersections. These layers define the geometric features of the nanocavities. Afterwards, the top electrodes are fabricated from an electron-beam evaporated stack of chromium/platinum/titanium stack of the thicknesses 7/50/7 nm. Subsequently, a passivation composed of alternating layers. $SiO_2/Si_3N_4/SiO_2$ is deposited via plasma enhanced chemical vapor deposition [38]. In the next step, access holes are etched through the passivation directly down

onto the chromium sacrificial layer by reactive ion etching. The chromium is then fully removed in an isotropic wet etch using chrome etch solution.

Electrochemical methods

Electrochemical characterization is either performed via cyclic voltammetry or amperometry. Cyclic voltammograms were recorded using an EPC 10 patch clamp system (HEKA Elektronik Dr. Schulze GmbH, Lambrecht, Germany) and the corresponding software Patch Master. Hereby, one bar electrode is swept from −200 mV to 600 mV and then sweept reverse from 600 mV to −200 mV at a rate of 80 mV/s, while the corresponding other electrode(s) remain at a reducing potential of −200 mV. Parallel redox cycling amperometric measurements for electrochemical imaging are performed by using a custom-built amplifier system (picoAmp64) [36]. The electrodes are set to constant potentials of either −200 mV or 600 mV. All measurements are performed after a equilibration time of 10 s, while the potential of the solution is controlled through an Ag/AgCl reference electrode.

Acknowledgements

We gratefully acknowledge funding by the Helmholtz Young Investigators program.

References

1. Sanderson, D. G.; Anderson, L. B. *Anal. Chem.* **1985,** *57,* 2388–2393. doi:10.1021/ac00289a050
2. Aoki, K.; Morita, M.; Niwa, O.; Tabei, H. *J. Electroanal. Chem.* **1988,** *256,* 269–282. doi:10.1016/0022-0728(88)87003-7
3. Fan, F.-R. F.; Bard, A. J. *Science* **1995,** *267,* 871–874. doi:10.1126/science.267.5199.871
4. Niwa, O. *Electroanalysis* **1995,** *7,* 606–613. doi:10.1002/elan.1140070702
5. Neugebauer, S.; Müller, U.; Lohmüller, T.; Spatz, J. P.; Stelzle, M.; Schuhmann, W. *Electroanalysis* **2006,** *18,* 1929–1936. doi:10.1002/elan.200603612
6. Goluch, E.; Wolfrum, B.; Singh, P. S.; Zevenbergen, M. A. G.; Lemay, S. G. *Anal. Bioanal. Chem.* **2009,** *394,* 447–456. doi:10.1007/s00216-008-2575-x
7. Lewis, P. M.; Sheridan, L. B.; Gawley, R. E.; Fritsch, I. *Anal. Chem.* **2010,** *82,* 1659–1668. doi:10.1021/ac901066p
8. Aggarwal, A.; Hu, M.; Fritsch, I. *Anal. Bioanal. Chem.* **2013,** *405,* 3859–3869. doi:10.1007/s00216-013-6738-z
9. Rassaei, L.; Singh, P. S.; Lemay, S. G. *Anal. Chem.* **2011,** *83,* 3974–3980. doi:10.1021/ac200307n
10. Lemay, S. G.; Kang, S.; Mathwig, K.; Singh, P. S. *Acc. Chem. Res.* **2013,** *46,* 369–377. doi:10.1021/ar300169d
11. Kätelhön, E.; Wolfrum, B. *Rev. Anal. Chem.* **2012,** *31,* 7–14. doi:10.1515/revac-2011-0031
12. Wolfrum, B.; Zevenbergen, M.; Lemay, S. *Anal. Chem.* **2008,** *80,* 972–977. doi:10.1021/ac7016647
13. Kätelhön, E.; Hofmann, B.; Lemay, S. G.; Zevenbergen, M. A. G.; Offenhäusser, A.; Wolfrum, B. *Anal. Chem.* **2010,** *82,* 8502–8509. doi:10.1021/ac101387f
14. Zevenbergen, M. A. G.; Singh, P. S.; Goluch, E. D.; Wolfrum, B. L.; Lemay, S. G. *Nano Lett.* **2011,** *11,* 2881–2886. doi:10.1021/nl2013423
15. Singh, P. S.; Kätelhön, E.; Mathwig, K.; Wolfrum, B.; Lemay, S. G. *ACS Nano* **2012,** *6,* 9662–9671. doi:10.1021/nn3031029
16. Kang, S.; Nieuwenhuis, A. F.; Mathwig, K.; Mampallil, D.; Lemay, S. G. *ACS Nano* **2013,** *7,* 10931–10937. doi:10.1021/nn404440v
17. Lin, Z.; Takahashi, Y.; Kitagawa, Y.; Umemura, T.; Shiku, H.; Matsue, T. *Anal. Chem.* **2008,** *80,* 6830–6833. doi:10.1021/ac801389d
18. Lin, Z.; Takahashi, Y.; Murata, T.; Takeda, M.; Ino, K.; Shiku, H.; Matsue, T. *Angew. Chem., Int. Ed.* **2009,** *48,* 2044–2046. doi:10.1002/anie.200805743
19. Takeda, M.; Shiku, H.; Ino, K.; Matsue, T. *Analyst* **2011,** *136,* 4991–4996. doi:10.1039/c1an15620a
20. Ino, K.; Saito, W.; Koide, M.; Umemura, T.; Shiku, H.; Matsue, T. *Lab Chip* **2011,** *11,* 385–388. doi:10.1039/c0lc00437e
21. Lin, Z.; Ino, K.; Shiku, H.; Matsue, T.; Chen, G. *Chem. Commun.* **2010,** *46,* 243–245. doi:10.1039/B915871E
22. Lin, Z.; Ino, K.; Shiku, H.; Matsue, T. *Chem. Commun.* **2010,** *46,* 559–561. doi:10.1039/B915212A
23. Ino, K.; Goto, T.; Kanno, Y.; Inoue, K. Y.; Takahashi, Y.; Shiku, H.; Matsue, T. *Lab Chip* **2014,** *14,* 787–794. doi:10.1039/C3LC51156A
24. Zhu, X.; Ino, K.; Lin, Z.; Shiku, H.; Chen, G.; Matsue, T. *Sens. Actuators, B* **2011,** *160,* 923–928. doi:10.1016/j.snb.2011.09.004
25. Ino, K.; Nishijo, T.; Arai, T.; Kanno, Y.; Takahashi, Y.; Shiku, H.; Matsue, T. *Angew. Chem., Int. Ed.* **2012,** *51,* 6648–6652. doi:10.1002/anie.201201602
26. Macpherson, J. V.; Unwin, P. R. *J. Phys. Chem.* **1995,** *99,* 3338–3351. doi:10.1021/j100010a052
27. Wightman, R. M. *Science* **2006,** *311,* 1570–1574. doi:10.1126/science.1120027
28. Berberian, K.; Kisler, K.; Fang, Q.; Lindau, M. *Anal. Chem.* **2009,** *81,* 8734–8740. doi:10.1021/ac900674g
29. Zachek, M. K.; Takmakov, P.; Park, J.; Wightman, R. M.; McCarty, G. S. *Biosens. Bioelectron.* **2010,** *25,* 1179–1185. doi:10.1016/j.bios.2009.10.008
30. Liu, X.; Barizuddin, S.; Shin, W.; Mathai, C. J.; Gangopadhyay, S.; Gillis, K. D. *Anal. Chem.* **2011,** *83,* 2445–2451. doi:10.1021/ac1033616
31. Lin, Y.; Trouillon, R. I.; Svensson, M. I.; Keighron, J. D.; Cans, A.-S.; Ewing, A. G. *Anal. Chem.* **2012,** *84,* 2949–2954. doi:10.1021/ac3000368
32. Schulte, A.; Nebel, M.; Schuhmann, W. *Methods Enzymol.* **2012,** *504,* 237–254. doi:10.1016/B978-0-12-391857-4.00012-4
33. Kim, B. N.; Herbst, A. D.; Kim, S. J.; Minch, B. A.; Lindau, M. *Biosens. Bioelectron.* **2013,** *41,* 736–744. doi:10.1016/j.bios.2012.09.058
34. Takahashi, Y.; Shevchuk, A. I.; Novak, P.; Babakinejad, B.; Macpherson, J.; Unwin, P. R.; Shiku, H.; Gorelik, J.; Klenerman, D.; Korchev, Y. E.; Matsue, T. *Proc. Natl. Acad. Sci. U. S. A.* **2012,** *109,* 11540–11545. doi:10.1073/pnas.1203570109
35. Alivisatos, A. P.; Andrews, A. M.; Boyden, E. S.; Chun, M.; Church, G. M.; Deisseroth, K.; Donoghue, J. P.; Fraser, S. E.; Lippincott-Schwartz, J.; Looger, L. L.; Masmanidis, S.; McEuen, P. L.; Nurmikko, A. V.; Park, H.; Peterka, D. S.; Reid, C.; Roukes, M. L.; Scherer, A.; Schnitzer, M.; Sejnowski, T. J.; Shepard, K. L.; Tsao, D.; Turrigiano, G.; Weiss, P. S.; Xu, C.; Yuste, R.; Zhuang, X. *ACS Nano* **2013,** *7,* 1850–1866. doi:10.1021/nn4012847
36. Yakushenko, A.; Kätelhön, E.; Wolfrum, B. *Anal. Chem.* **2013,** *85,* 5483–5490. doi:10.1021/ac4006183
37. Wang, J.; Trouillon, R.; Lin, Y.; Svensson, M. I.; Ewing, A. G. *Anal. Chem.* **2013,** *85,* 5600–5608. doi:10.1021/ac4009385

38. Schmitt, G.; Schultze, J.-W.; Faßbender, F.; Buß, G.; Lüth, H.; Schöning, M. J. *Electrochim. Acta* **1999,** *44,* 3865–3883. doi:10.1016/S0013-4686(99)00094-8

BEILSTEIN JOURNAL OF NANOTECHNOLOGY

Electron-beam induced deposition and autocatalytic decomposition of $Co(CO)_3NO$

Florian Vollnhals, Martin Drost, Fan Tu, Esther Carrasco, Andreas Späth, Rainer H. Fink, Hans-Peter Steinrück and Hubertus Marbach*

Full Research Paper

Open Access

Address:
Lehrstuhl für Physikalische Chemie II and Interdisciplinary Center for Molecular Materials (ICMM), Friedrich-Alexander-Universität Erlangen-Nürnberg, Egerlandstr. 3, 91058 Erlangen, Germany

Email:
Hubertus Marbach* - hubertus.marbach@fau.de

* Corresponding author

Keywords:
autocatalytic growth; cobalt tricarbonyl nitrosyl; electron-beam induced deposition; nanofabrication; scanning transmission X-ray microscopy

Beilstein J. Nanotechnol. **2014,** *5,* 1175–1185.
doi:10.3762/bjnano.5.129

Received: 10 March 2014
Accepted: 30 June 2014
Published: 30 July 2014

This article is part of the Thematic Series "Physics, chemistry and biology of functional nanostructures II".

Guest Editor: A. S. Sidorenko

Abstract

The autocatalytic growth of arbitrarily shaped nanostructures fabricated by electron beam-induced deposition (EBID) and electron beam-induced surface activation (EBISA) is studied for two precursors: iron pentacarbonyl, $Fe(CO)_5$, and cobalt tricarbonyl nitrosyl, $Co(CO)_3NO$. Different deposits are prepared on silicon nitride membranes and silicon wafers under ultrahigh vacuum conditions, and are studied by scanning electron microscopy (SEM) and scanning transmission X-ray microscopy (STXM), including near edge X-ray absorption fine structure (NEXAFS) spectroscopy. It has previously been shown that $Fe(CO)_5$ decomposes autocatalytically on Fe seed layers (EBID) and on certain electron beam-activated surfaces, yielding high purity, polycrystalline Fe nanostructures. In this contribution, we investigate the growth of structures from $Co(CO)_3NO$ and compare it to results obtained from $Fe(CO)_5$. $Co(CO)_3NO$ exhibits autocatalytic growth on Co-containing seed layers prepared by EBID using the same precursor. The growth yields granular, oxygen-, carbon- and nitrogen-containing deposits. In contrast to $Fe(CO)_5$ no decomposition on electron beam-activated surfaces is observed. In addition, we show that the autocatalytic growth of nanostructures from $Co(CO)_3NO$ can also be initiated by an Fe seed layer, which presents a novel approach to the fabrication of layered nanostructures.

Introduction

The fabrication of nanostructures by using focused electron-beam induced processing (FEBIP) techniques, especially electron-beam induced deposition (EBID), has progressed considerably over the last decade [1-5]. In EBID, suitable precursor molecules are dosed onto a surface and then decomposed by the focused electron beam of a scanning electron microscope (SEM) or a transmission electron microscope (TEM). The volatile precursor fragments are pumped off by the vacuum

system, while the non-volatile dissociation products remain on the surface as a deposit. Some materials can be deposited with high purity, e.g., iron from iron pentacarbonyl, $Fe(CO)_5$ [6-9], cobalt from dicobalt octacarbonyl, $Co_2(CO)_8$ [10,11], or Au from Au(CO)Cl [12]. In addition, EBID offers the advantage of very small obtainable structure sizes [13], the possibility of 3D fabrication, e.g., pillars, and rapid prototyping capabilities [14].

A related FEBIP approach is electron-beam induced surface activation (EBISA) [7]. In EBISA, a suitable substrate, e.g., SiO_x [7,15-18], TiO_2 [19], or a thin porphyrin film on Ag(111) [8], is irradiated by the focused electron beam in the absence of a precursor, under high vacuum [15] or ultrahigh vacuum (UHV) conditions [7,8,16-19], resulting in a patterned, chemically activated surface. In a second step, a precursor is introduced into the system and decomposes selectively at the irradiated, i.e., activated, areas. Activated in this context means that the corresponding areas are catalytically active towards the decomposition of certain precursor molecules; thereby, an initial deposit (primary structure) can be selectively formed at the pre-irradiated region. The initial deposit might then autocatalytically grow (AG) upon further exposure to the precursor molecules, which allows to produce nanostructures of desired size (secondary growth). Such autocatalytic growth was also observed for primary structures produced by EBID [7]. Reports indicate that the fabrication of primary structures is more effective for EBID compared to EBISA. This might be due to the differences in precursor decomposition for EBID (i.e., in the presence of impinging electrons) and at the pre-activated sites for EBISA [8].

The EBID and EBISA processes as well as the autocatalytic growth are shown schematically in Figure 1. In addition, the figure introduces a third processing step (c) denoted as "tertiary growth", in which the structure resulting from a secondary growth process is used as a seed layer for the deposition of another layer of different material by using a different precursor. While this process can be interpreted as a "second secondary growth step", we will use the term "tertiary growth" throughout this publication to avoid confusion and highlight the sequential nature of the processes.

Depending on the substrate and the precursor, different activation mechanisms have been proposed [7,8,15,18,19]. To be

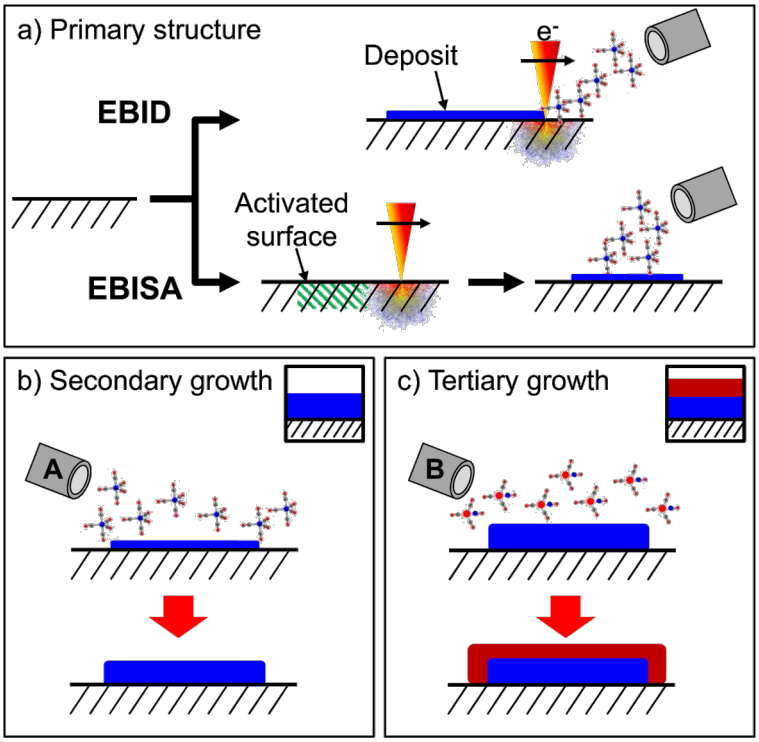

Figure 1: Fabrication and secondary/tertiary growth of nanostructures. The deposits can be fabricated by electron irradiation of a surface in the presence of a precursor (EBID) to form a thin primary deposit (a, top). In the absence of a precursor (a, bottom), some surfaces can undergo selective electron-beam induced surface activation (EBISA), also yielding a primary deposit upon post-exposure to the precursor. If the primary deposits are exposed to the precursor in a successive step, autocatalytic decomposition can lead to further secondary autocatalytic growth of the deposit (b). In the case that a second, different precursor is supplied, another autocatalytic growth process (tertiary growth) can occur, leading to the formation of a layered nanostructure (c). The icons in b) and c) will be used to indicate the respective process throughout this publication.

suitable for EBISA, the precursor is required to be susceptible to decomposition only at activated sites. Furthermore, it has to exhibit autocatalytic decomposition in order to facilitate the subsequent growth (also denoted as secondary growth) on top of the primary structure.

Most of the previous EBISA studies as well as some EBID studies used $Fe(CO)_5$ as precursor, which yields practically pure, (poly-)crystalline Fe on different substrates [7,8,16-19]. In addition, $Co_2(CO)_8$ was also identified as a suitable precursor for EBISA in experimental work on silica surfaces in a high-vacuum environment [15]. Since other precursors may show a similar behavior, we investigated one relevant candidate concerning autocatalytic growth, namely cobalt tricarbonyl nitrosyl, $Co(CO)_3NO$, in more detail. This precursor is more stable and easier to handle than the related $Co_2(CO)_8$. Cobalt tricarbonyl nitrosyl was studied before concerning its ionization properties in the gas phase [20,21], the electron induced decomposition under surface science conditions in UHV [22], and the fabrication and characterization of EBID nanostructures under high vacuum conditions [23-25].

In the gas phase, the decomposition proceeds through direct ionization or dissociative electron attachment depending on the kinetic energy of the involved electrons. Dissociative electron attachment is mainly observed for low-energy secondary electrons (<10 eV) and yields incompletely decomposed fragments, mostly $[Co(CO)_2NO]^-$. Direct ionization occurs for $E > 10$ eV and results in smaller fragments like Co^+ or $[CoCO]^+$ [20,21]. It was suggested that the direct ionization route leads to the deposition of incompletely dissociated precursor molecules, which in turn influences the content of non-metallic contaminants in the deposit [21].

Based on the irradiation of cold (105 K) $Co(CO)_3NO$ films of about 2.5 nm thickness on amorphous carbon and Au substrates with 500 eV electrons under UHV conditions, the following decomposition mechanism was proposed [22]: At a low electron dose ($<5 \times 10^{16}$ e^-/cm^2), one or two CO molecules are released and the NO ligand decomposes, yielding an adsorbed $(CO)_xOCoN$ species. Upon further electron irradiation at low temperatures, decomposition of CO ligands is observed, yielding carbon-rich $(CoO_yN)C_{ads}$. If instead the initially produced $(CO)_xOCoN$ species is annealed above 244 K, the thermally unstable CO ligands desorb without decomposition, yielding carbon free CoO_yN [22].

At room temperature, EBID using $Co(CO)_3NO$ in a standard high-vacuum SEM setup yields deposits consisting of about 40–50 atom % Co, 25–35 atom % O, 10–15 atom % N and 10–15 atom % C as determined by energy-dispersive X-ray spectroscopy (EDX) [23-25]. The composition is almost independent of the applied beam current and energy, apart from a slight increase in oxygen content for increasing beam power [23]. The deposition yield decreases for higher electron energy, and increases strongly above 403 K substrate temperature [23]. A more detailed study addressed the temperature dependence for various precursors. For $Co(CO)_3NO$ and $Co_2(CO)_8$ three distinct regimes were proposed: (1) EBID only, (2) seeded growth, i.e., enhancement of deposition rate and autocatalytic growth, and (3) spontaneous decomposition and film growth, i.e., chemical vapor deposition (CVD) [24]. For $Co(CO)_3NO$, EBID was found up to about 393 K, followed by seeded growth up to about 403 K and spontaneous decomposition at higher temperatures. In the EBID regime, increasing the temperature from 293 to 323 K lowered the carbon content by a factor of three. In addition, the oxygen content decreased and the nitrogen content increased with temperature, while the cobalt content remained almost constant. In the seeded and spontaneous growth regimes, the composition remained constant at about 50 atom % Co, 20–25 atom % O and N, and a few atom % C.

In the present study, the autocatalytic growth of nanostructures by using $Co(CO)_3NO$ at room temperature is investigated and compared to that using $Fe(CO)_5$. EBID structures prepared from $Co(CO)_3NO$ in a UHV environment are exposed to additional $Co(CO)_3NO$ to induce autocatalytic growth; the resulting deposits are characterized by SEM and scanning transmission X-ray microscopy (STXM). STXM allows for the non-destructive quantitative spectromicroscopic characterization of the individual layers with nanoscale resolution and high contrast due to the possibility of resonant imaging [26]. The EBID deposits are compared to deposits produced by EBISA with $Co(CO)_3NO$, and to deposits prepared by autocatalytic growth of $Co(CO)_3NO$ on iron seed layers, which were prepared beforehand by EBID with $Fe(CO)_5$. The latter process opens up a novel approach for the localized fabrication of arbitrarily shaped bilayer and even multilayer nanostructures.

Results and Discussion

EBID plus autocatalytic growth

EBID structures were deposited from $Co(CO)_3NO$ on native SiO_x on Si(100) and 100 nm Si_3N_4 membranes, and on commercially available, thermal 300 nm SiO_2 on Si(100). The beam energy was 15 keV at a beam current of 400 pA; the step size was 6.2 nm. Figure 2 displays SEM images of square structures (1×1, 2×2 and 4×4 μm^2) on the native oxide on Si_3N_4, which were irradiated with primary electron (PE) doses ranging from 0.02 to 0.5 C/cm^2, at a precursor pressure of approx. 9×10^{-6} mbar. The irradiation of each individual structure was performed by successively sweeping the same area 10 times

(rather than in a single sweep). This procedure enhances the uniformity of the fabricated structures, which otherwise shows a pronounced asymmetry due to proximity effects (see Figure S1 in Supporting Information File 1 for details). In Figure 2 the electron dose increases from left to right, and the size from top to bottom. The structures were written sequentially, left-to-right and row-by-row in one experimental run: The EBID process lasted 32 min, and thereafter, the precursor pressure was maintained to induce autocatalytic growth. The deposition process, including the EBID step, lasted 230 min, which corresponds to an accumulated precursor dose of about 9.3×10^4 Langmuir ($1\ L = 10^{-6}$ Torr·s $\approx 1.33 \times 10^{-6}$ mbar·s). Since EBID of the individual deposits was performed sequentially, the respective times for autocatalytic growth after EBID varied from 230 min for the low dose structures on the top left corner (exposed first) to 198 min for the high dose structures on the bottom right (exposed last). The structures appear brighter for higher doses: While below 0.05 C/cm^2 no structure can be unequivocally identified, a dose of 0.5 C/cm^2 marks the start of observable proximity effects in the form of fringes around the structures. Closer inspection of the structures shows that, despite the same electron dose was applied per surface area, larger squares are brighter and more defined compared to the smaller ones, which points to a deposition that is influenced by proximity effects [2].

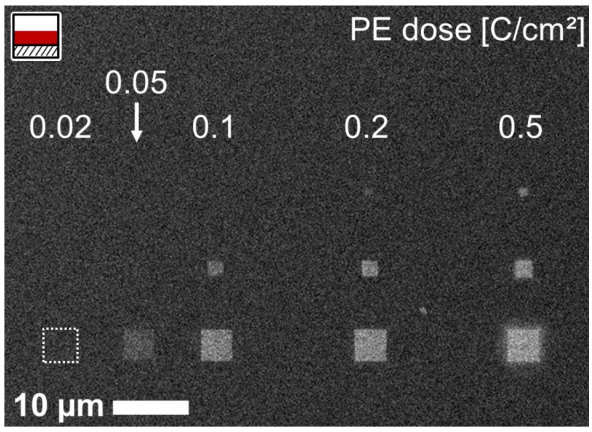

Figure 2: SEM micrograph of square EBID structures of different sizes and primary electron doses (as indicated), prepared on a 100 nm Si_3N_4 membrane using $Co(CO)_3NO$. The structures were prepared in one experimental run, from left to right, top to bottom. After the EBID step, the precursor was further supplied to allow for autocatalytic growth. The total growth time increases from 198 min (bottom right structure) to 230 min (top left structure). The minimum electron dose for detectable deposition is about 0.05 C/cm^2, while a dose of 0.5 C/cm^2 marks the start of proximity effect-induced loss of structure definition (fringe surrounding bottom right structure).

In addition to the dose dependence, the growth time-dependent appearance of the structures was investigated. Figure 3 compares SEM images of square deposits fabricated by EBID and autocatalytic growth, using $Co(CO)_3NO$ as precursor. The growth time, t_G, was varied from 25 to 160 min. In each of the six images (a–f), the two squares in the right column were irradiated with a primary electron dose of 0.2 C/cm^2, and the square in the left column with 0.1 C/cm^2. The inset in each case shows the morphology of the respective structures at 44× higher magnification.

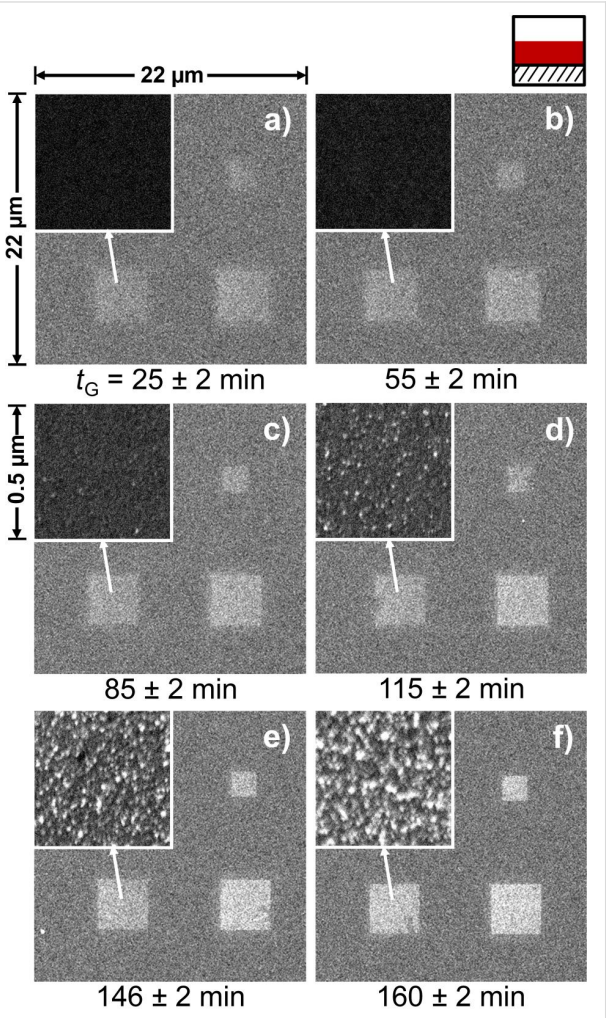

Figure 3: Nanostructures prepared by EBID plus autocatalytic growth using $Co(CO)_3NO$ on Si_3N_4 with different growth times, as indicated below the images. The electron dose during EBID was 0.2 C/cm^2 for the structures in the right column of every image; the dose of the lower left square was 0.1 C/cm^2. The insets show higher magnification images of the respective structures directly below. With increasing growth time the images appear brighter, and the granular nature of the deposits is more pronounced.

The data in Figure 3 shows a direct correlation between the brightness of the structures in SEM and the applied growth time, indicating an increased material deposition. The brighter appearance of the deposited structures at larger growth times is attributed to an enhanced yield of backscattered electrons (BSE) and thereby induced secondary electrons. Indeed, Monte-Carlo simulations using the software CASINO (v. 2.42) [27] show an

increase in the BSE emission coefficient by more than 20% for a 5 nm layer of $Co_{0.51}O_{0.24}N_{0.14}C_{0.11}$ (composition reported by Gazzadi et al. [23]) and by over 40% for a 5 nm layer of pure Co compared to the bare 100 nm Si_3N_4 membrane. The high-magnification insets in Figure 3 reveal the formation of a strongly corrugated, granular deposit, which can be interpreted as the growth of small clusters of material. Both the increase in the brightness of the deposits and the cluster growth mode are in line with the autocatalytic growth of EBID deposits upon dosage of additional $Co(CO)_3NO$.

The samples were further characterized at the PolLux soft X-ray STXM beamline [28] at the Swiss Light Source using a zone plate with a nominal resolution of 30 nm and a photomultiplier tube (PMT) behind the specimen for X-ray detection in transmission mode. The STXM was operated under high-vacuum conditions (low 10^{-6} mbar range) to reduce contamination from the decomposition of residual gases. In Figure 4, Co L-edge spectra of deposits prepared by EBID (0.2 C/cm^2) and autocatalytic growth with $Co(CO)_3NO$ are presented for different growth times. The left panel (a) shows an overview of the Co $L_{2/3}$ region; the right panel (b) an enlargement of the L_3 region along with the spectrum of a layer of pure cobalt (grey) that was produced by physical vapor deposition (PVD).

The comparison of the Co peak positions (maxima) of the metallic cobalt film prepared by PVD (779.9 eV, Co^0) and the structures prepared by EBID plus autocatalytic growth (780.4 eV) reveals a chemical shift of approx. 0.5 eV, which is indicative of cobalt in an oxidized state ([29] and references [8] and [9] therein). This suggests a composition in the form of $CoO_xN_y(C_z)$, in line with previous reports for comparable EBID structures by Gazzadi et al. [23,25] and Mulders et al. [24].

The observed intensities in Figure 4 are a direct measure of the layer thickness of the deposits on the Si_3N_4 membrane. In transmission X-ray microscopy or NEXAFS spectroscopy in transmission mode, the absorbance (or optical density, OD) is derived from:

$$\mathrm{OD} = \mu(E) \times d = -\ln(I/I_0) = \ln(I_0/I), \qquad (1)$$

with I_0 and I being the incident and the transmitted intensities, respectively, d represents the sample thickness and $\mu(E)$ the photon energy dependent linear absorption coefficient. The peak shape and the energy of the resonant Co L_3 transition are similar for all deposits, which supports a common attenuation coefficient for this energy. The spectral intensities in Figure 4 also indicate that the layer thickness increases with growth time. As the analysis is based on the Co L_3 signal, this increase is unequivocally related to the growth of a layer of Co-containing material by autocatalytic decomposition of $Co(CO)_3NO$.

In order to quantify the absorption of the deposits, images were recorded at the resonant transition peak at 780.4 eV. The resonant transition yields the strongest element-specific absorption and thus maximizes the image contrast for ease of evaluation.

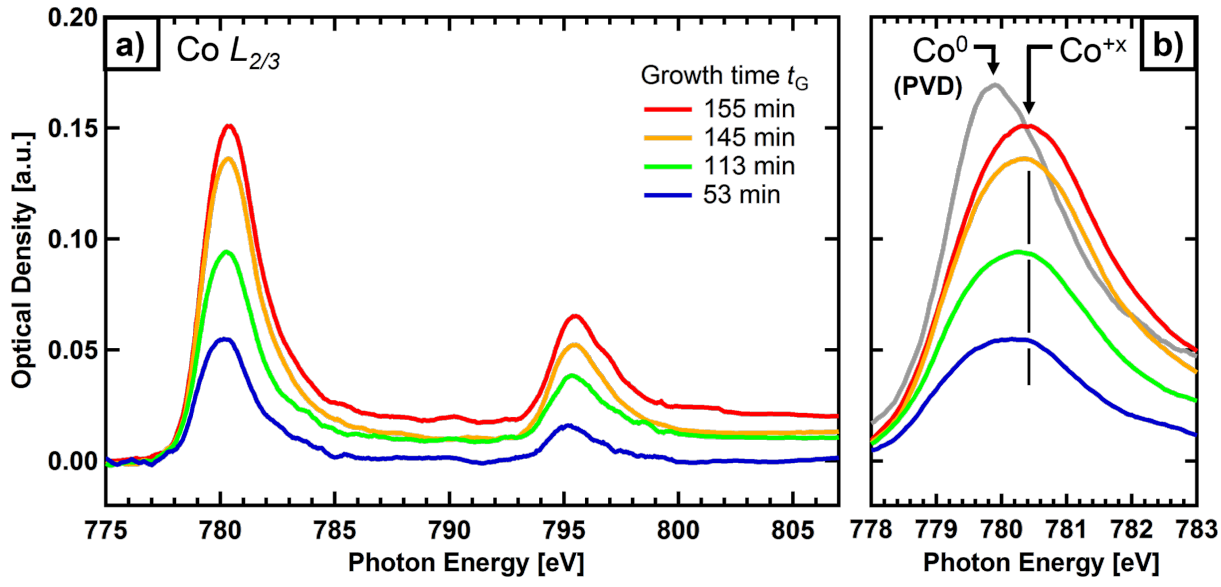

Figure 4: (a) Co L-edge X-ray absorption spectra of deposits prepared on a Si_3N_4 membrane by EBID (0.2 C/cm^2) plus autocatalytic growth using $Co(CO)_3NO$, with different growth times (indicated by colors); the spectra were vertically shifted to a common pre-edge baseline. (b) L_3 edge of the deposits at an enlarged photon energy scale, along with the spectrum of a Co layer produced by PVD as reference (grey).

The optical density of the structures was calculated by averaging the signal over the area of the respective structure (in the STXM micrograph) and referencing the signal to the background, i.e., the signal of the pristine membrane near the deposit. The granular structure of the deposits, which was observed in SEM (cf. Figure 3), could not be observed in STXM due to the limited resolution of the applied zone plate of approx. 30 nm.

As the exact chemical composition of the deposit is not known, the linear absorption coefficient of the deposited material, $\mu_{deposit}$, is also unknown. As an approximation, we use the value of pure Co, μ_{Co}, instead and denote the derived thickness value as apparent cobalt thickness, d_A, which is calculated by using Equation 1. Since the oxygen, nitrogen and carbon contributions are small compared to resonant Co L_3 signals, d_A is considered a meaningful value, reflecting the nominal thickness of a pure Co layer. The real thickness of the deposit is certainly underestimated, but since the composition of the different EBID deposits is very likely the same, a comparison of the deposits obtained with different growth times is possible (see section Experimental for more details).

Figure 5 summarizes the thickness analysis for several deposits produced by EBID plus autocatalytic growth as a function of the primary electron dose during EBID and the growth time, t_G, during which $Co(CO)_3NO$ was continually supplied. The 3D plot in Figure 5a shows the optical density (left vertical axis) and apparent Co layer thickness (right vertical axis) vs growth time and primary electron dose (log scale), and Figure 5b and Figure 5d show the detailed plots against the latter two parameters. The STXM micrograph (transmitted intensity) in Figure 5c

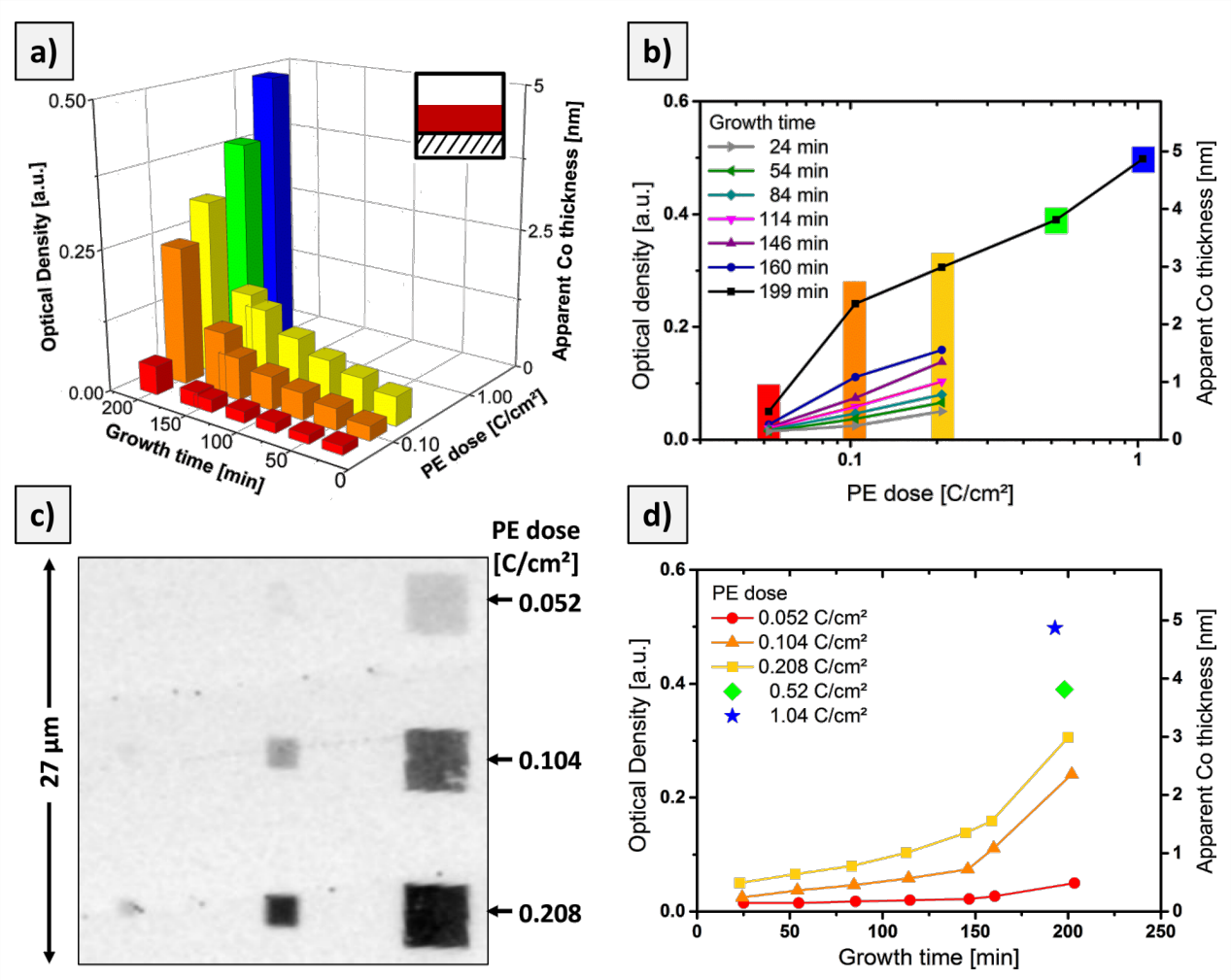

Figure 5: Evaluation of the X-ray absorption data for the growth of Co-containing deposits by EBID plus autocatalytic growth upon $Co(CO)_3NO$ dosage. a) Optical density (left vertical axis) and apparent Co thickness (right vertical axis) of 4 × 4 µm^2 squares vs growth time and PE dose during EBID. b) and d) detailed graphs of the observed growth behavior; the color code identifies the respective data set. c) STXM micrograph (transmitted intensity) of a set of deposits prepared with different PE doses, but the same growth time of about 160 min obtained at a photon energy of 780.4 eV. See text for the definition of the apparent Co thickness.

displays a set of square deposits fabricated with the indicated primary electron doses and a growth time of about 160 min. The data in Figure 5 are in line with our previous observations: The optical density increases with both electron dose and autocatalytic growth time. The dependence on the primary electron dose in Figure 5b can be linearly extrapolated to zero, in order to obtain the minimum dose required for direct EBID, yielding a value of 0.03 ± 0.01 C/cm^2 or 1.8 ± 0.6 × 10^3 electrons per nm^2. The dependency of the optical density on the growth time in Figure 5d (for a given primary electron dose) initially exhibits an almost linear behavior, but for t_G > 150 min a strong nonlinear increase is apparent. The morphology of the deposits in Figure 3 indicates that the growth proceeds in a granular fashion and not by homogeneous layer-by-layer growth. For this complex growth process, during which the number of available sites, the (local) precursor concentration or both may vary, a nonlinear behavior is to be expected.

EBISA plus autocatalytic growth

The susceptibility to decomposition by an electron beam-activated surface or via an autocatalytic process is a prerequisite for the successful application of a precursor for EBISA-based fabrication of nanostructures. In order to study the suitability of $Co(CO)_3NO$, a number of test patterns were irradiated on different surfaces under UHV conditions and subsequently exposed to $Co(CO)_3NO$. The investigated surfaces were SiO_x layers on Si(100) and Si_3N_4, both of which are suitable substrates for EBISA using $Fe(CO)_5$ [7,16]. On these surfaces, electron stimulated desorption of oxygen and the thereby created oxygen vacancies were identified as the active sites for the initial decomposition of $Fe(CO)_5$ [7,18]. However, the corresponding experiments with $Co(CO)_3NO$ as a precursor in EBISA were not successful, i.e., deposition of material on the activated surfaces was not observed (data not shown). We thus have to conclude that $Co(CO)_3NO$ is not suitable as precursor for the fabrication of nanostructures by using EBISA on silicon oxide surfaces.

An alternative approach could be to use different substrates for EBISA: It was shown recently by our group that it is possible to activate thin layers of large organic molecules (2*H*-tetraphenyl porphyrin) on metal single crystals for $Fe(CO)_5$ decomposition [8]. The proposed activation mechanism involves the electron-beam induced formation of reactive organic moieties, which might be reactive also towards the initial decomposition of $Co(CO)_3NO$. Such investigations are, however, out of the scope of the present study.

Autocatalytic growth on iron seed layers

In addition to the experiments described before, the fabrication of layered nanostructures by EBID using both $Fe(CO)_5$ and $Co(CO)_3NO$ was explored. In the course of these experiments, we observed that $Co(CO)_3NO$ does not only decompose autocatalytically on Co-containing deposits (such as the EBID deposits discussed before), but also on high purity Fe nanostructures. The latter can be prepared from $Fe(CO)_5$ by EBID or EBISA, plus successive autocatalytic growth.

The iron structures are typically composed of very pure (>90–95 atom %) cubic crystallites, as a result of the autocatalytic growth process [7,8,16-19]. The morphology ranges from scattered clusters for low electron doses and shorter growth times, to fused, polycrystalline patches of cubic crystallites for high electron doses and long growth times [7,8,16-19]. After preparation of the Fe deposits with $Fe(CO)_5$, $Co(CO)_3NO$ was introduced into the chamber for a given growth time that was identical for all Fe seed deposits. Thereafter, the samples were investigated by SEM (not shown) and STXM. For the STXM analysis, images were acquired at the Fe L_3 and Co L_3 absorption edges. To determine the thickness of the Co layer, the absorption by the Fe layer underneath has to be considered: Whereas the absorption by Co at the Fe L_3 edge (708.7 eV) is negligible, the absorption by Fe at the Co L_3 edge (780.4 eV) is considerable. By comparison of the optical density (OD) of pure iron deposits at both energies, a contribution of (25 ± 5)% of the Fe intensity at the Fe L_3 edge is determined for the Co L_3 edge, i.e.,

$$\begin{aligned} \mathrm{OD_{Co}}\left(\mathrm{Co\ L_3}\right) &= \mathrm{OD_{total}}\left(\mathrm{Co\ L_3}\right) - \mathrm{OD_{Fe}}\left(\mathrm{Co\ L_3}\right) \\ &= \mathrm{OD_{total}}\left(\mathrm{Co\ L_3}\right) - 0.25\ \mathrm{OD_{Fe}}\left(\mathrm{Fe\ L_3}\right) \end{aligned}$$

This correction was taken into account to determine the apparent thickness of the Co contribution in the $CoO_xN_yC_z$/Fe bilayer.

As the first step, the autocatalytic growth of the iron structures was investigated. Figure 6 shows an overall linear increase of the optical density (left vertical axis) and the average thickness (right vertical axis) with autocatalytic growth time for the Fe L_3 edge. For electron doses above 0.05 C/cm^2, the data for different PE doses are very similar. This indicates that the Fe layer thickness is mainly determined by the autocatalytic growth time, with an autocatalytic growth rate of 0.5 ± 0.1 Å per minute (approx. 1.3 × 10^{-3} Å/Langmuir). The observation that for electron doses of 0.05 C/cm^2 and below only reduced thicknesses are obtained indicates that the threshold for creating a homogenously reactive initial deposit by EBID is not yet reached. Thus, only for electron doses exceeding 0.05 C/cm^2, the number of catalytically active sites per area approaches a saturation value. This induction period is followed by a constant rate of autocatalytic precursor decomposition, which results in

constant height growth. It is likely that the deposit formed in the induction period is a closed layer of iron on the surface. These results confirm that continued deposition of Fe is possible on the initial layer prepared by EBID with comparatively low electron doses and thus short fabrication times, as was observed before [7,8,16-19].

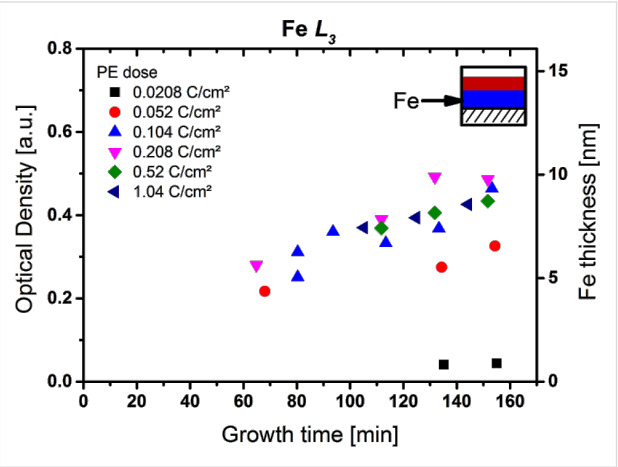

Figure 6: Optical density at the Fe L_3 edge at 708.7 eV (left vertical axis) and average thickness of the iron layer (right vertical axis) of various $CoO_xN_yC_z$/Fe nanostructures versus autocatalytic growth time for $Fe(CO)_5$. The different symbols indicate different primary electron (PE) doses. Above 0.05 C/cm^2, the thickness/optical density increases linearly with the growth time at a rate of 0.5 ± 0.1 Å/min irrespective of the applied PE dose. Lower PE doses (red, black) exhibit reduced thickness.

In a next step, the high purity Fe structures are exposed to $Co(CO)_3NO$. This results in the deposition of a layer of material containing cobalt on top of the Fe structure in a tertiary growth process. The deposition is selective, i.e., the Co-containing layer is only observed on the Fe structures while the pristine membrane remains uncovered. The composition of the Co-containing layers is most likely again $CoO_xN_yC_z$, which is supported by the shift of the Co L_3 peak to higher energy, and by Auger electron spectroscopy of comparable structures on SiO_x/Si(100) (not shown); note that severe charging prevents Auger electron spectroscopy on the Si_3N_4 membrane samples.

Figure 7 shows the optical density (left vertical axis) at the Co L_3 edge and average apparent Co thickness d_A (right vertical axis) of $CoO_xN_yC_z$ layers grown on iron seed layers of increasing thickness (corresponding to the layers in Figure 6). In all cases the same total growth time (210 min) using $Co(CO)_3NO$ was applied. On top of an Fe layer thicker than 4 nm, a comparable optical density of 0.76 ± 0.08 is observed for the autocatalytically grown $CoO_xN_yC_z$ layers, independent of the thickness of the initial Fe layers. This can be interpreted as being due to very similar starting conditions for the tertiary growth process on all investigated Fe layers. It is reasonable to assume that the Fe deposits are closed layers of Fe, which provide identical densities of active sites for the initial decomposition of $Co(CO)_3NO$. The nature of the active site cannot be deduced from the available data, but we assume that upon adsorption of the $Co(CO)_3NO$ precursor on the clean Fe film the immediate dissociation of the precursor takes place. In order to gain more insight into the underlying reaction(s), chemically more sensitive methods like XPS and IR spectroscopy may be helpful.

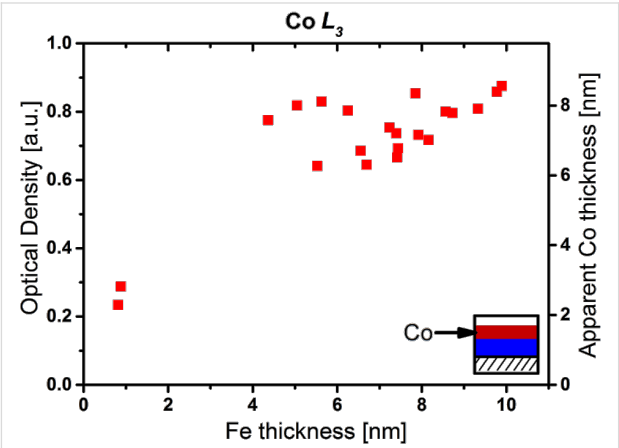

Figure 7: Optical density at the Co L_3 edge and apparent cobalt thickness of $CoO_xN_yC_z$ layers grown autocatalytically from $Co(CO)_3NO$ on Fe layers plotted against the Fe layer thickness. The Fe layers were prepared by EBID and autocatalytic growth by using $Fe(CO)_5$. In a second step, $Co(CO)_3NO$ was dosed for 210 min to produce the $CoO_xN_yC_z$ layers via (auto-)catalytic decomposition. The optical density and thickness are corrected to account for the absorption of the Fe deposit underneath (see text). The OD of the $CoO_xN_yC_z$ layer is almost independent of the Fe layer thickness for Fe layers thicker than 4 nm.

The apparent cobalt thickness observed on the thick Fe seed layers is 7.4 ± 0.8 nm; the average growth rate is 0.35 ± 0.05 Å/min. It is likely, however, that the growth on Fe seeds exhibits non-linear behavior, as was observed above for the autocatalytic growth on the cobalt seed layer (cf. Figure 5).

Comparing the growth behavior of $Co(CO)_3NO$ and $Fe(CO)_5$, the presented data (Figure 6 vs Figure 5d) suggest two very different growth modes for the different precursors under otherwise identical reaction conditions. On the one hand, the autocatalytic decomposition of $Fe(CO)_5$ proceeds at a constant rate and produces high purity Fe deposits, which (above a threshold) are almost independent of the applied PE dose. On the other hand, the autocatalytic decomposition of $Co(CO)_3NO$ exhibits pronounced non-linear, possibly even exponential behavior and is strongly influenced by the applied primary electron dose during the initial EBID step. In contrast to $Fe(CO)_5$, the decomposition yields an oxygen-, nitrogen- and carbon-rich $CoO_xN_yC_z$ deposit instead of pure cobalt. Besides the involved

chemistry, which is likely to be quite different, yet difficult to study with the available techniques, the deposits structure seems to have a strong influence on the growth behavior. As was already reported before [7,8,16-19], iron structures fabricated by EBID/EBISA plus autocatalytic growth are composed of cubic crystallites of α-Fe(bcc). These crystallites are quite regular, and their vacuum interfaces consist mainly of low index {100} faces of these cubes. A representative structure is presented in Figure S2 of Supporting Information File 1. In the case of $Co(CO)_3NO$, not very well-defined granular structures are observed after the autocatalytic growth step, indicating a rather amorphous and defect rich deposit with a high surface area. Such structures are likely to show different, possibly increased reactivity compared to ordered, flat surfaces. Indeed, the observed decomposition of $Co(CO)_3NO$ on the nominally flat Fe seed layers is less pronounced than on the Co seed layer produced with very high primary electron doses.

Conclusion

We have investigated the electron-beam induced decomposition of $Fe(CO)_5$ and $Co(CO)_3NO$ and the subsequent secondary growth via selective autocatalytic decomposition upon further precursor dosage. The two precursors show very different growth characteristics under the applied reaction conditions. Structure fabrication by using $Co(CO)_3NO$ is strongly affected by the applied electron dose in the EBID step and subsequent autocatalytic growth time. The influence of the electron dose follows a logarithmic trend, while the autocatalytic thickness growth shows non-linear, possibly exponential behavior with growth time. This is explained by the observed granular morphology of the deposits and the associated high surface area, defect rich, and reactive deposit–vacuum interface. The analysis of the chemical composition of the structures prepared from $Co(CO)_3NO$ points to an oxygen-, nitrogen-, and carbon-rich $CoO_xN_yC_z$ composite material, with the Co L_3 peak shifted towards an oxidic state. $Fe(CO)_5$ exhibits a constant growth rate of 0.5 ± 0.1 Å/min, which above a threshold of 0.05 C/cm^2 is almost independent of the electron dose applied during the initial EBID step. The deposits prepared by EBID/EBISA and autocatalytic growth from $Fe(CO)_5$ are composed of polycrystalline, high purity Fe (typically more than 90–95 atom %). While the electron irradiation defines the shape of the deposit, the thickness of the prepared structures is governed mainly by the autocatalytic growth process. The practical separation of shape definition and deposit formation has some advantages, most obviously the reduction of proximity effects due to lower required electron dose as compared to the EBID-only process.

In order to fully understand the underlying mechanism of the autocatalytic decomposition especially of $Co(CO)_3NO$, it is necessary to conduct further studies on model systems using complementary surface science techniques, e.g., X-ray photoelectron spectroscopy (XPS) or infrared absorption spectroscopy (IR/IRAS), and expand the work that has been done on the electron-beam induced decomposition to include the autocatalytic growth.

Our study also shows that the EBISA approach does not work with $Co(CO)_3NO$ as a precursor: While $Fe(CO)_5$ decomposes on activated, i.e., electron pre-irradiated, areas of SiO_x surfaces and forms a deposit, this behavior was not observed for $Co(CO)_3NO$. Interestingly, $Co(CO)_3NO$ decomposes autocatalytically on Fe seed layers, which opens up a number of fabrication possibilities. As the fabrication of Fe structures by EBISA plus autocatalytic growth has been shown to be a successful approach not only on SiO_x surfaces, but also on TiO_2 [19] and on substrates pre-covered with organic layers [8], such Fe layers could be generally considered as seeding layers for precursors that are not susceptible to decomposition by the electron-beam activated surface. Furthermore, the fabrication of layered nanostructures without the necessity for multiple electron beam exposure steps was demonstrated. It is likely that such a seeding concept also works for other precursor combinations. The known autocatalytic growth of high purity Co deposits from $Co_2(CO)_8$ [15] makes that precursor an obvious candidate for the fabrication of layered Co/Fe nanostructures with arbitrary shapes.

Thus, the presented results considerably expand the possibilities of FEBIP-based nanofabrication techniques. We also show that the potential for (auto-)catalytic decomposition of typical EBID precursors needs to be studied in detail. This approach is necessary to gain a deeper understanding of the underlying processes, the consequences of autocatalytic growth for EBID experiments and, subsequently, to develop new or improved methods for the fabrication of FEBIP-based nanostructures.

Experimental

All structures were fabricated in a commercial UHV system (Multiscanlab, Omicron Nanotechnology, Germany) with a base pressure of $p < 2 \times 10^{-10}$ mbar. The system consists of a UHV-compatible electron column (Leo Gemini) for scanning electron microscopy (SEM, nominal resolution better than 3 nm), electron beam based lithography (EBL, EBID), local Auger electron spectroscopy (AES) and scanning Auger microscopy (SAM), with a resolution better than 10 nm using a hemispherical electron energy analyzer. All electron exposures for SEM and lithography were performed at a beam energy of 15 keV and a current of 400 pA. The lithographic processes were controlled through a custom-developed software based on LabVIEW 8.6 (National Instruments) and a high-speed DAC PCIe-card (M2i.6021-exp, Spectrum GmbH, Germany). SEM

images were acquired with *SmartSEM* (Zeiss) and are shown with minor contrast and brightness adjustments only.

The precursors were purchased from ACROS Organics (iron pentacarbonyl, $Fe(CO)_5$) and abcr GmbH & Co. KG (cobalt tricarbonyl nitrosyl, $Co(CO)_3NO$). The purity of the precursor gas was analyzed with a quadrupole mass spectrometer in a dedicated gas analysis chamber (base pressure below 2×10^{-9} mbar).

The precursor gas was dosed onto the sample surface through a nozzle. Based on simulations using GIS Simulator (version 1.5) [30], the local pressure increase on the sample surface was calculated to be a factor of 30. For a fixed background pressure of 3.0×10^{-7} mbar, this corresponds to a local pressure at the surface of about 9×10^{-6} mbar [31].

Si_3N_4 samples (TEM size holder SI frame, 500 µm × 500 µm membrane size, thickness 100 nm) were supplied by Plano GmbH. Si(100) samples were purchased from the Institute of Electronic Materials Technology, Warsaw, Poland.

STXM experiments were performed at the PolLux beamline at the Swiss Light Source (SLS), Paul Scherrer Institut, Villigen (CH) [28]. The standard STXM setup uses high brilliance synchrotron radiation light that is focused on the sample by a Fresnel zone plate. The sample is raster-scanned with interferometric control through the focal spot, while the transmitted photon intensity is recorded by using a photo multiplier tube. Near-edge X-ray absorption fine structure (NEXAFS) spectra were recorded by consecutive scanning of the investigated area with varying photon energy. The lateral resolution in routine operation for the applied zone plate was 30 to 40 nm. The STXM data were analyzed using aXis2000 (http://unicorn.mcmaster.ca/aXis2000.html).

The value for the absorption coefficient at the resonant transition was determined by fitting the spectrum of a PVD Co layer to a theoretical spectrum ("X-ray Form Factor, Attenuation, and Scattering Tables"; NIST [32-34]), which do not account for resonant transitions. The fit is accomplished by scaling the optical density of the measured spectrum of the Co layer to match the pre-edge and post-edge region of the theoretical spectrum of 1 nm thick Co. The scaled spectrum, which contains the resonant transition, then allows to determine $\mu(E)$ values. The linear attenuation coefficient for Co at the resonant transition was found to be $\mu_{Co}(779.9\ eV) = 0.103 \pm 0.02\ nm^{-1}$. For the quantification of the apparent cobalt thickness of the $CoO_xN_yC_z$ deposits, we assume that the absorption coefficient of the resonant peak intensity is comparable for pure Co and $CoO_xN_yC_z$, i.e., $\mu_{Co}(779.9\ eV) \approx \mu_{CoOxNyCz}(780.4\ eV)$.

The absolute thickness of the $CoO_xN_yC_z$ deposits may be three to five times greater than the reported apparent Co thickness according to our estimations. The absorption coefficient $\mu_{Fe}(708.7\ eV) = 0.050 \pm 0.01\ nm^{-1}$ was also determined using the described fitting procedure.

Supporting Information

Supporting Information contains additional SEM images of proximity effects during EBID of $Co(CO)_3NO$ and examples of Fe deposits prepared by EBID/EBISA and autocatalytic growth using $Fe(CO)_5$ as a precursor on native oxide on a silicon nitride membrane.

Supporting Information File 1

Additional SEM images.
[http://www.beilstein-journals.org/bjnano/content/supplementary/2190-4286-5-129-S1.pdf]

Acknowledgements

We thank Benjamin Watts and Jörg Raabe at the Swiss Light Source for experimental assistance during beamtime at PolLux. The PolLux end station was financed by the German Federal Ministry for Education and Research (Bundesministerium für Bildung und Forschung, BMBF) through contracts 05KS4WE1/6 and 05K10WEA.

This work was funded by DFG through grant MA 4246/1-2, and the Excellence Cluster "Engineering of Advanced Materials" granted to the FAU Erlangen-Nürnberg.

FV acknowledges funding from the Studienstiftung des deutschen Volkes; FV and AS acknowledge funding from the Graduate School Molecular Science (GSMS) of the FAU Erlangen-Nürnberg.

This work was conducted within the framework of the COST Action CM1301 (CELINA).

References

1. Utke, I.; Hoffmann, P.; Melngailis, J. *J. Vac. Sci. Technol., B* **2008,** *26,* 1197–1276. doi:10.1116/1.2955728
2. van Dorp, W. F.; Hagen, C. W. *J. Appl. Phys.* **2008,** *104,* 081301–081342. doi:10.1063/1.2977587
3. Botman, A.; Mulders, J. J. L.; Hagen, C. W. *Nanotechnology* **2009,** *20,* 372001. doi:10.1088/0957-4484/20/37/372001
4. Randolph, S. J.; Fowlkes, J. D.; Rack, P. D. *Crit. Rev. Solid State Mater. Sci.* **2006,** *31,* 55–89. doi:10.1080/10408430600930438

5. Huth, M.; Porrati, F.; Schwalb, C.; Winhold, M.; Sachser, R.; Dukic, M.; Adams, J.; Fantner, G. *Beilstein J. Nanotechnol.* **2012,** *3,* 597–619. doi:10.3762/bjnano.3.70
6. Lukasczyk, T.; Schirmer, M.; Steinrück, H.-P.; Marbach, H. *Small* **2008,** *4,* 841–846. doi:10.1002/smll.200701095
7. Walz, M.-M.; Schirmer, M.; Vollnhals, F.; Lukasczyk, T.; Steinrück, H.-P.; Marbach, H. *Angew. Chem., Int. Ed.* **2010,** *49,* 4669–4673. doi:10.1002/anie.201001308
8. Vollnhals, F.; Wintrich, P.; Walz, M.-M.; Steinrück, H.-P.; Marbach, H. *Langmuir* **2013,** *29,* 12290–12297. doi:10.1021/la4028095
9. Gavagnin, M.; Wanzenboeck, H. D.; Belić, D.; Bertagnolli, E. *ACS Nano* **2013,** *7,* 777–784. doi:10.1021/nn305079a
10. Belova, L. M.; Dahlberg, E. D.; Riazanova, A.; Mulders, J. J. L.; Christophersen, C.; Eckert, J. *Nanotechnology* **2011,** *22,* 145305. doi:10.1088/0957-4484/22/14/145305
11. Fernández-Pacheco, A.; De Teresa, J. M.; Córdoba, R.; Ibarra, M. R. *J. Phys. D: Appl. Phys.* **2009,** *42,* 055005. doi:10.1088/0022-3727/42/5/055005
12. Mulders, J. J. L.; Veerhoek, J. M.; Bosch, E. G. T.; Trompenaars, P. H. F. *J. Phys. D: Appl. Phys.* **2012,** *45,* 475301. doi:10.1088/0022-3727/45/47/475301
13. van Dorp, W. F.; van Someren, B.; Hagen, C. W.; Kruit, P.; Crozier, P. A. *Nano Lett.* **2005,** *5,* 1303–1307. doi:10.1021/nl050522i
14. Koops, H. W. P.; Hoinkis, O. E.; Honsberg, M. E. W.; Schmidt, R.; Blum, R.; Böttger, G.; Kuligk, A.; Liguda, C.; Eich, M. *Microelectron. Eng.* **2001,** *57–58,* 995–1001. doi:10.1016/S0167-9317(01)00565-2
15. Muthukumar, K.; Jeschke, H. O.; Valenti, R.; Begun, E.; Schwenk, J.; Porrati, F.; Huth, M. *Beilstein J. Nanotechnol.* **2012,** *3,* 546–555. doi:10.3762/bjnano.3.63
16. Walz, M.-M.; Vollnhals, F.; Rietzler, F.; Schirmer, M.; Kunzmann, A.; Steinrück, H.-P.; Marbach, H. *J. Phys. D: Appl. Phys.* **2012,** *45,* 225306. doi:10.1088/0022-3727/45/22/225306
17. Walz, M.-M.; Vollnhals, F.; Rietzler, F.; Schirmer, M.; Steinrück, H.-P.; Marbach, H. *Appl. Phys. Lett.* **2012,** *100,* 053118. doi:10.1063/1.3681593
18. Walz, M.-M.; Vollnhals, F.; Schirmer, M.; Steinrück, H.-P.; Marbach, H. *Phys. Chem. Chem. Phys.* **2011,** *13,* 17333–17338. doi:10.1039/c1cp20865a
19. Vollnhals, F.; Woolcot, T.; Walz, M.-M.; Seiler, S.; Steinrück, H.-P.; Thornton, G.; Marbach, H. *J. Phys. Chem. C* **2013,** *117,* 17674–17679. doi:10.1021/jp405640a
20. Engmann, S.; Stano, M.; Matejčík, Š.; Ingólfsson, O. *Angew. Chem., Int. Ed.* **2011,** *50,* 9475–9477. doi:10.1002/anie.201103234
21. Engmann, S.; Stano, M.; Papp, P.; Brunger, M. J.; Matejčík, Š.; Ingólfsson, O. *J. Chem. Phys.* **2013,** *138,* 044305. doi:10.1063/1.4776756
22. Rosenberg, S. G.; Barclay, M.; Fairbrother, D. H. *J. Phys. Chem. C* **2013,** *117,* 16053–16064. doi:10.1021/jp404905t
23. Gazzadi, G. C.; Mulders, H.; Trompenaars, P.; Ghirri, A.; Affronte, M.; Grillo, V.; Frabboni, S. *J. Phys. Chem. C* **2011,** *115,* 19606–19611. doi:10.1021/jp206562h
24. Mulders, J. J. L.; Belova, L. M.; Riazanova, A. *Nanotechnology* **2011,** *22,* 055302. doi:10.1088/0957-4484/22/5/055302
25. Gazzadi, G. C.; Mulders, J. J. L.; Trompenaars, P.; Ghirri, A.; Rota, A.; Affronte, M.; Frabboni, S. *Microelectron. Eng.* **2011,** *88,* 1955–1958. doi:10.1016/j.mee.2010.12.031
26. Ade, H.; Hitchcock, A. P. *Polymer* **2008,** *49,* 643–675. doi:10.1016/j.polymer.2007.10.030
27. Drouin, D.; Couture, A. R.; Joly, D.; Tastet, X.; Aimez, V.; Gauvin, R. *Scanning* **2007,** *29,* 92–101. doi:10.1002/sca.20000
28. Raabe, J.; Tzvetkov, G.; Flechsig, U.; Böge, M.; Jaggi, A.; Sarafimov, B.; Vernooij, M. G. C.; Huthwelker, T.; Ade, H.; Kilcoyne, D.; Tyliszczak, T.; Fink, R. H.; Quitmann, C. *Rev. Sci. Instrum.* **2008,** *79,* 113704. doi:10.1063/1.3021472
29. Zheng, F.; Alayoglu, S.; Guo, J.; Pushkarev, V.; Li, Y.; Glans, P.-A.; Chen, J.-I.; Somorjai, G. *Nano Lett.* **2011,** *11,* 847–853. doi:10.1021/nl104209c
30. Friedli, V.; Utke, I. *J. Phys. D: Appl. Phys.* **2009,** *42,* 125305. doi:10.1088/0022-3727/42/12/125305
31. Schirmer, M.; Walz, M.-M.; Papp, C.; Kronast, F.; Gray, A. X.; Balke, B.; Cramm, S.; Fadley, C. S.; Steinrück, H.-P.; Marbach, H. *Nanotechnology* **2011,** *22,* 475304. doi:10.1088/0957-4484/22/47/475304
32. Chantler, C. T.; Olsen, K.; Dragoset, R. A.; Chang, J.; Kishore, A. R.; Kotochigova, S. A.; Zucker, D. S. X-Ray Form Factor, Attenuation and Scattering Tables (version 2.1). http://physics.nist.gov/ffast (accessed Jan 13, 2014).
33. Chantler, C. T. *J. Synchrotron Radiat.* **2001,** *8,* 1124. doi:10.1107/S0909049501008305
34. Chantler, C. T. *J. Phys. Chem. Ref. Data* **1995,** *24,* 71–643. doi:10.1063/1.555974

License and Terms

BEILSTEIN JOURNAL OF NANOTECHNOLOGY

Fringe structures and tunable bandgap width of 2D boron nitride nanosheets

Peter Feng*[1], Muhammad Sajjad[1], Eric Yiming Li[1], Hongxin Zhang[2], Jin Chu[3], Ali Aldalbahi[4] and Gerardo Morell[1]

Full Research Paper

Open Access

Address:
[1]Institute of Functional Nanomaterials and Department of Physics, College of Natural Sciences, University of Puerto Rico, San Juan, PR/USA 00936-8377, [2]Globalfoundrie, 400 Stone Break Road extension, Malta, NY 12020, USA, [3]Chongqing Institute of Green and Intelligent Technology, CAS, Chongqing 400714, China and [4]King Abdullah Institute for Nanotechnology and Department of Chemistry, KSU, Riyadh 11451, Saudi Arabia

Email:
Peter Feng* - peter.feng@upr.edu

* Corresponding author

Keywords:
boron nitride sheets; fringe patterns; functionalization; tunable bandgap width

Beilstein J. Nanotechnol. **2014,** *5,* 1186–1192.
doi:10.3762/bjnano.5.130

Received: 11 March 2014
Accepted: 04 July 2014
Published: 31 July 2014

This article is part of the Thematic Series "Physics, chemistry and biology of functional nanostructures II".

Guest Editor: A. S. Sidorenko

Abstract

We report studies of the surface fringe structures and tunable bandgap width of atomic-thin boron nitride nanosheets (BNNSs). BNNSs are synthesized by using digitally controlled pulse deposition techniques. The nanoscale morphologies of BNNSs are characterized by using scanning electron microscope (SEM), and transmission electron microscopy (TEM). In general, the BNNSs appear microscopically flat in the case of low temperature synthesis, whereas at high temperature conditions, it yields various curved structures. Experimental data reveal the evolutions of fringe structures. Functionalization of the BNNSs is completed with hydrogen plasma beam source in order to efficiently control bandgap width. The characterizations are based on Raman scattering spectroscopy, X-ray diffraction (XRD), and FTIR transmittance spectra. Red shifts of spectral lines are clearly visible after the functionalization, indicating the bandgap width of the BNNSs has been changed. However, simple treatments with hydrogen gas do not affect the bandgap width of the BNNSs.

Introduction

The recent successful investigation of graphene has stimulated interest in atomically thin boron nitride sheets [1,2]. Similar to the method used to produce graphene, BNNSs can be exfoliated from bulk BN crystals by simple mechanical cleavage techniques [3-5]. The problem is that the obtained hBN nanosheets are usually limited by too small size. Therefore, recently most work on synthesis of large BNNSs is based on either chemical-solution-derived method or a chemical vapor deposition (CVD) process. Many excellent results have been reported [6-9]. Systematic and comprehensive reviews of two-

dimensional (2D) boron nitride nanostructures: nanosheets, nanoribbons, nanomeshes, and hybrids with graphene have been presented by Lin [10].

Theoretically, surface treatment can effectively control the band gap of nano BN and plays a crucial role of engineering their electrical and electronic properties. For example for BN nanotubes (BNNT), 50% tube surface coverage with chemisorbed hydrogen atoms would cause the BN band gap (which was computed to be 4.29 eV in pristine BNNT) decreased to 2.01 eV [11]. For BNNSs case the adsorption behavior of a single H atom either on the top site of a B or on the top site of an N atom, or two H atoms adsorbed on adjacent B and N sites are also investigated [12]. Using first-principles computations [13] and hybrid density functional theory calculations with van der Waals correction [14], Chen and Zhang show that polar boron nitride (BN) nanoribbons can be favorably aligned via substantial hydrogen bonding at the interfaces, which induces significant interface polarizations and sharply reduces the band gap of insulating BNNSs.

Based on these research, we have experimentally conducted several experiments on using digitally controlled pulse deposition technique to quick synthesis of BNNSs [15] as well as their applications for gas sensors [16] and electronic devices [17-19]. In the present paper, the focus of studies is on variation of the fringe structures and the hydrogen (H) atoms induced band gap width. Chemically shifted components were observed following H treatment, and clear evidence of tunable bandgap width was found.

Experimental

A pulsed CO_2 laser deposition technique (CO_2-PLD: wavelength: 10.6 μm, pulse width: 1–5 μs, repetition rate: 5 Hz, and pulse energy: 5 J) was used. Detailed description of PLD experimental setup can be found in our previous papers [18,19]. Briefly, the laser beam, focused with a 30 cm focal length of ZnSe lens, was incident at 45 degree relative to a rotated (speed of circa 200 rpm) pyrolytic hexagonal BN target (2.00" diameter × 0.125" thick, 99.99% purity, B/N ratio ≈1.05, density ≈1.94 g/ccm) under high vacuum (2.66×10^{-3} Pa) chamber. The purpose of the use of the long-focal-length lens is to effectively control the laser-produced plasma beams. The diameter of the focus spot of laser beam on the target was about 2 mm and could be varied by shifting focal lens. The power density of the laser on the target was 2×10^8 W/cm^2 per pulse. Molybdenum (Mo) and silicon (Si) wafers (1×1 cm^2) as substrates were used and placed 4 cm away from the target. Substrate temperature was controlled by using a thermocouple and heater. Prior to laser irradiation, substrates were rinsed in acetone and methanol in sequence. The duration for each deposition was few minutes. The as-grown samples were then characterized by using SEM, Raman scattering, X-ray diffraction, and FTIR transmittance, respectively. For studies of the nanoscale morphology of BNNSs, the samples were simply scratched off and then transferred to the grids for TEM measurement.

Results and Discussion

Fringe structures of boron nitride nanosheets

Figure 1 shows TEM images of BNNSs with different magnifications. The sample is prepared at low temperature, around 350 °C. Each as-grown sample normally consists of a large amount of BNNSs that are partially overlapped one another. Average size of each continuous BNNS piece is around a few micrometer squares. The thickness of the BNNS varies from 1 nm to 10 nm. Each BNNS appears highly flat and transparent properties. The well-shaped edge of each BNNS piece is clearly visible as shown in Figure 1a.

Figure 1b shows TEM image with a large magnification, indicating there are many tiny fringes at the edge of the BNNSs. All the fringes have almost the same orientations. Continuing to

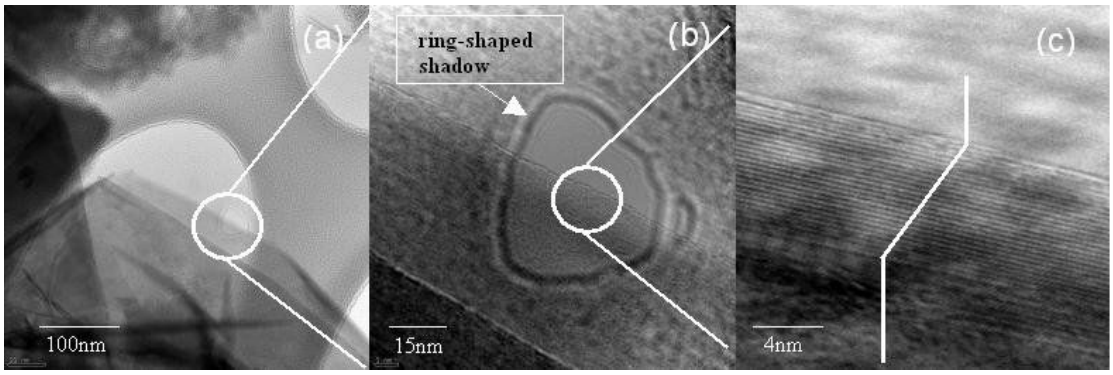

Figure 1: TEM images of BNNSs with different magnifications.

magnify the TEM image, the highly ordered fringe pattern becomes obvious (Figure 1c), where each fringe is related to a single atomic layer, and thickness of the each atomic layer is around 0.33 nm. Accordingly, the thickness of the obtained BNNS can be estimated around 8 nm (total 25 stacked layers).

It has been noticed that in the most case, low-temperature synthesis yields flat BNNS, whereas high temperature (>500 °C) of synthesis yields relatively high density of intrinsic impurities and the most samples appear curved. A basic reason could be due to the sheets' stress caused by temperature.

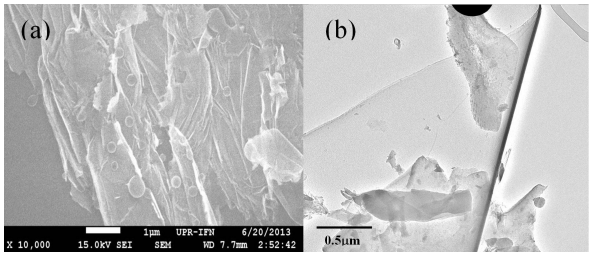

Figure 3: SEM images of BNNSs with (a) curved/wrinkle and (b) folding structure.

With a high-resolution TEM, plenty of rippled structures can be easily observed from the obtained BN samples. Figure 2a shows TEM image of the curved structures. Figure 2b shows TEM image of ellipse-shaped bent structure. Unusual curled structure such as spiraling layer is also observed as shown in Figure 2c that could be related to nanotube in the "parchment model" [20]. Associated with the widths, density or directions of the ripples, in a significant number of cases, we observe various cases, in which two structures of ripples are combined (Figure 2d) because of the random distributions of BNNS pieces. On the other hand, the experimental data above probably suggest that the BNNSs have extremely flexible properties. From SEM images of as-grown BNNSs as shown in Figure 3, ones can easily find that (a) curved/wrinkle and (b) folding structures of BNNSs everywhere. The unique mechanical and electronic properties indicate that the BNNS is a promising material for flexible electronics.

It should be mentioned that a ring-shaped shadow can be identified from the TEM images shown in Figure 1a and 1b. Initially, such shadow is supposed due to the damage of the BNNS. This is because the electron energy used for the electron beam in TEM is usually higher than the knock-on damage threshold [21]. Consequently, the damage of ultra-thin BNNS occurs frequently during TEM measurements in many cases.

Interesting is that the shift of the ring-shaped shadow marked with white spots is also observed from the TEM images of BNNS as shown in Figure 4. Normally, any damage of BNNS would be permanent. It seems rare or not possible for the shift of the damaged area. Hence, we expect that the shadows shown in Figure 1 and Figure 4 be rather related to TEM aberrations than to the damage from the high-energy electron beam in the present case.

Actually, permanent damage of extremely thin BNNSs occurs frequently at the case of long duration of exposure to high-energy electron beams during TEM measurements. Figure 5a and 5b show the dynamics where the beam damage has just started to form small holes, locally reducing the thickness. After some more irradiation, some "holes" can be found within the irradiated regions (Figure 5c and 5d). Since the product of such "holes" was observed in real time, the process could easily be stopped by switching off the electron beam after formation of the first hole or potentially at the first vacancy through the entire sheet. Figure 5b shows the edge of the atomic thin BNNS. Obviously, the vacancy defect "holes" in the edge area was caused by TEM electron beam. In order to avoid the problems above, super-thin BNNSs are always imaged extremely fast with reduced illumination, or the TEM should be operated at low energy of electron beam.

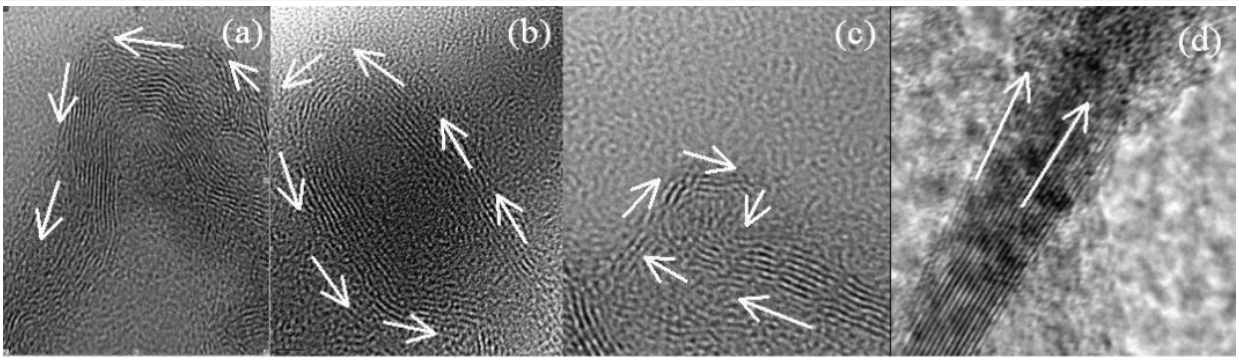

Figure 2: TEM images of BNNSs with a), curved, b), ellipse-shaped bent, c) unusual curled structures, and (d) combination of structures of ripples where tiny ripple construction are related the stacked atomic layers. Width of each ripple/atomic layers is 0.33 nm.

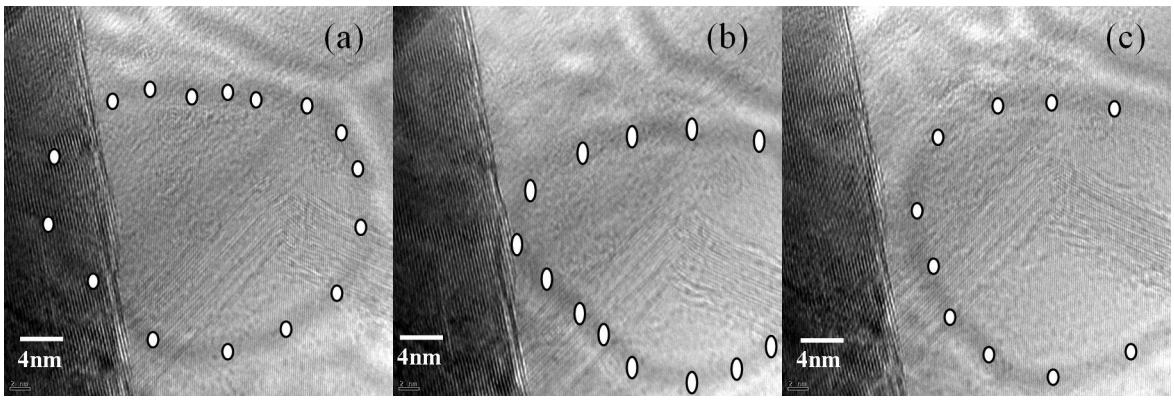

Figure 4: (a–c) TEM images of BNNSs with ring-shaped shadow shifting from the edge. All scale bars are 4 nm.

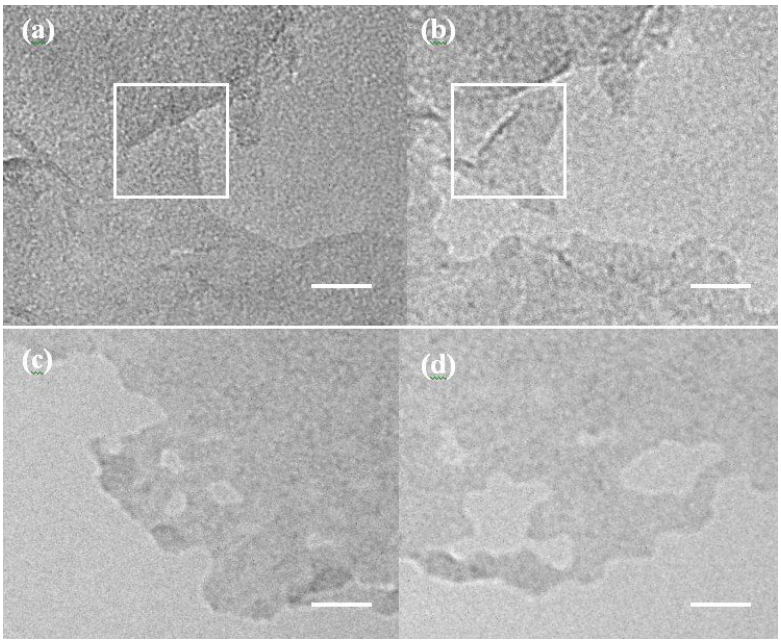

Figure 5: Dynamics in BNNS during TEM measurement a) before and b) after beam. Time between the images is 8 s. Also visible in the sequence is the generation of vacancies within the layer. (c,d) Topological defects are incorporated during this edge reconstruction. On the other edge of the same hole, atoms are removed by the electron beam. Scale bar, 2 nm.

Functionalization for tunable bandgap width of BNNSs

The wide-band gap of BNNS is a serious obstacle for their application in electronics, despite their high thermal and chemical stabilities. In our previous paper [22], we studied the electric behaviors of hydrogenated BNNS and temperature dependences of resistances before and after hydrogen plasma treatment. The present paper addresses on how to produce atomic BNNS with a desirable bandgap width based on material functionalization. Theoretically, the BNNS band gap would decrease following an increase of atomic hydrogen coverage on the surfaces of BNNSs. Therefore, functionalization of the BNNSs is conducted in a special chamber as shown in Figure 6 based on hydrogen atom plasma beam treatments, and then the samples are characterized using Raman scattering spectroscopy, XRD, and FTIR. From these spectral line profiles and shifts we could investigate variations of the bandgap width and crystalline structures.

Figure 7a shows the Raman spectra of the BNNSs using triple monochromator with an excitation wavelength of 514 nm (Ar^+ ion Laser). The microscope focused the laser beam onto the surface of the sample. Comparison of two spectral lines before and after treatment, two phenomena can be identified: 1) typical

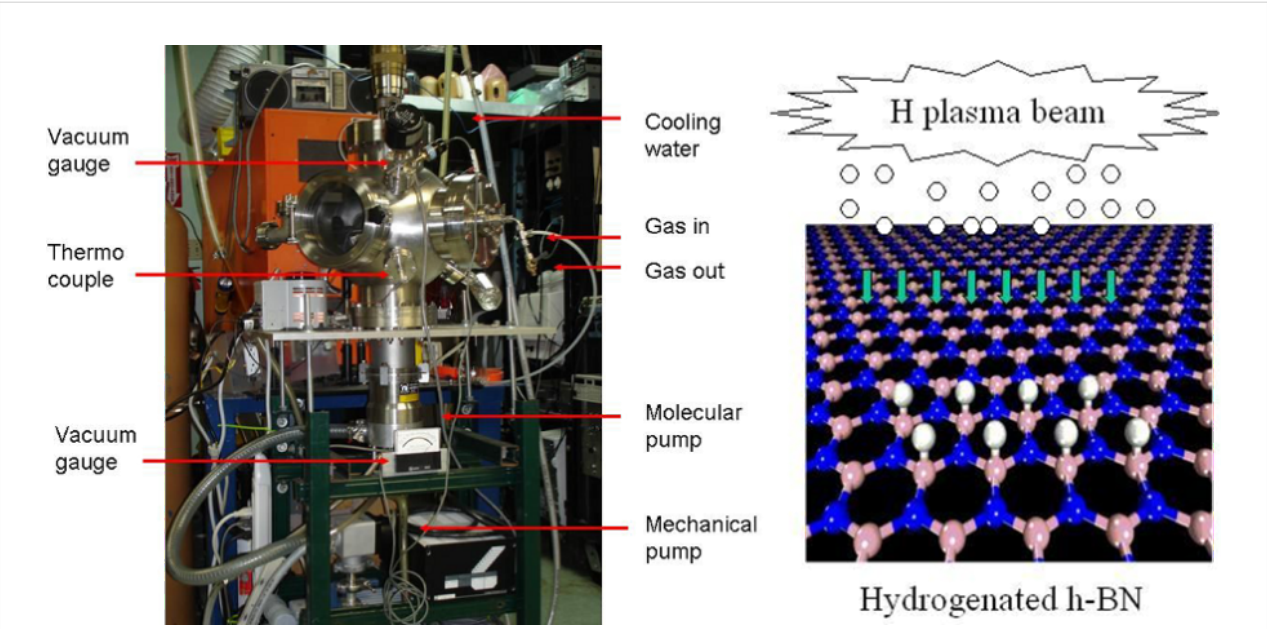

Figure 6: (a) Experimental set up for H plasma functionalization of the BNNSs, and (b) schematic diagram for formation of hydrogenated BNNS.

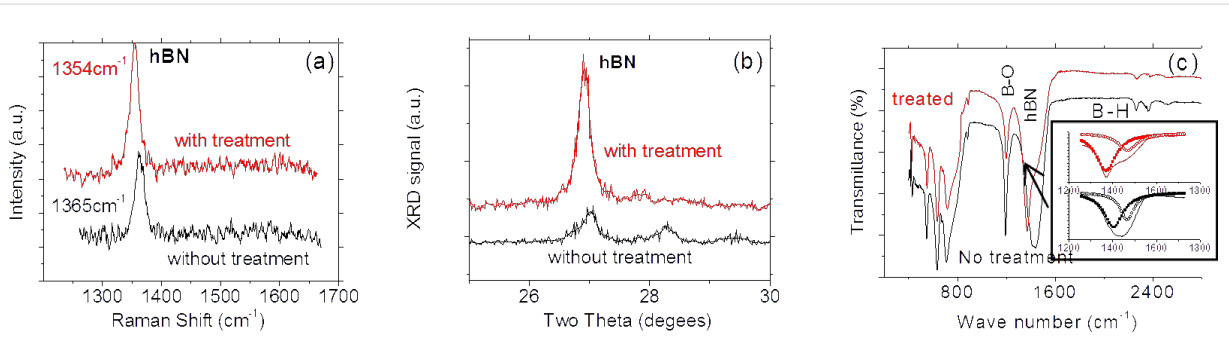

Figure 7: (a) Raman scattering, (b) XRD, and (c) FTIR transmittance spectra of the BNNSs before and after functionalization. Red shifts of all spectral lines is clear visible after functionalization.

Raman active E_{2g} mode of BNNSs with the hexagonal phase shifts from 1365 cm^{-1} to 1354 cm^{-1}. This suggests that the bandgap width of the treated BNNS has been reduced down to 1%, and 2) the width of the spectral line is slightly reduced after the treatment. According to the data from high-resolution TEM and EDX measurements [15,22], we know a pulse deposition technique normally yields high quality of BNNSs where no carbon and other impurities are detected except for a very small amount of oxygen, which is possibly from the residual gas in the chamber. It is expected that the treatment/hydrogenation would cause partial reactions between the hydrogen and oxygen atoms to form water molecules and then evaporation. This process would improve the quality of BNNSs. As a result, the defect concentrations in the treated/hydrogenated BNNSs would decrease, resulting in narrow spectral profile.

Figure 7b shows the XRD pattern of the BNNS sample with and without hydrogenation. The hexagonal structure associated peak shifts from $2\theta \approx 27.02°$ to $2\theta \approx 26.92°$ after the treatment. This indicates that the lattice constant of the BNNS hexagonal structure increases up to 1% according to Bragg formulation of X-ray diffraction. Since the bandgap width or energy normally is inversely proportional to the lattice constant for III–V nitride materials [23], we can easily conclude that hydrogen atoms-based functionalization have caused the bandgap width decreased down to 1%. This is in good agreement with the data obtained from the Raman spectrum of BNNSs. It is noticed that a tiny peak positioned at $2\theta \approx 27.8°$ is related to B_2O_3 content present in the original BNNSs without the treatment. As seen in Figure 7b that the B_2O_3 content greatly decreases after the hydrogenation.

Figure 7c shows the FTIR spectra of BNNSs in the transmission mode. The dotted (red) and solid (black) spectral lines correspond to the samples with and without the treatment, respectively. A peak recorded at about 1429 cm^{-1} is associated with the in-plane E_{1u} B–N bond stretching vibration of sp^2-bonded hBN phase [24,25]. It shifts to low wave number down to 1369 cm^{-1} after the treatment, indicating the width of the band gap changes down to 4.3%. This value is quite larger than the results obtained from the Raman and XRD data. The reason is still not clear but to reexamine the FTIP spectra, it can be found that the FTIR spectra actually is dominated by an intense band peaking at 1370.6 cm^{-1} with a shoulder on the higher energy wing at ≈1469 cm^{-1} and the featureless low intensity background at lower wave number. The FTIR peak at ≈1469 cm^{-1} could be assigned as bands bound by impurities or defects, or a phonon replica of bands. The comparison between the normalized FTIR spectra measured with increased spectral resolution from 1200 cm^{-1} to 1800 cm^{-1} for BNNSs before and after functionalization, respectively, is shown in the inset of Figure 7c. It is easy to identify that the hydrogen atom treatments improve the quality of BNNSs. Evident is that the content of the shoulder peak obviously decreases as shown in the inset of Figure 7c. Furthermore, the content of B_2O_3 mode at 1200 cm^{-1} is also greatly reduced after the treatment. All these phenomena are now in good agreement with the results obtained from the Raman and XRD measurements. After functionalization, the shoulder peaking remains nearly no shift at ≈1469 cm^{-1}, whereas the dominating peak shifts from 1405 to 1370.6 cm^{-1}, from which we can conclude the bandgap width has been reduced down to 2.4%.

Conclusion

Experimental data indicated that low-temperature deposition yields highly flat and transparent BNNSs. The well-shaped edge of BNNS piece is clearly visible, from which the highly ordered fringe patterns can be identified with increased resolution of TEM. Highly ordered fringe structures at the edge are related to atomic layers thickness. In contrast in high-temperature condition, the most samples appear curved. Plenty of unusual curved or curled structures have been observed. These experimental data probably indicate that the BNNSs have extremely flexible mechanic properties.

We conclude that functionalization can be used to realize tunable bandgap width. Red shifts of Raman scattering spectroscopy, XRD, and FTIR transmittance spectral lines confirm that after the treatment, the bandgap width of the BNNSs has been reduced down to 1–2.4%. Furthermore, the treatment/hydrogenation could also cause partial reactions between the hydrogen and oxygen atoms to form water molecules and then evaporation, resulting in decreasing the defect concentrations in treated/hydrogenated BNNSs, and improving the quality of BNNSs.

Acknowledgements

This work is financially supported by NASA-PR-EPSCoR seed grant (NASA Grant Nos: NNX10AM80H, NNX13AB22A) and Army research office/DoD grant (62826-RT-REP), as well as visiting professor program/KSU at KSA. Aldalbahi acknowledges the financial support by King Saud University, Deanship of Scientific Research, College of Science Research Center. We acknowledge Dr. Maxime and staff of Nanoscopy Facility, a user facility at the University of Puerto Rico, sponsored UPR, NSF for TEM measurements.

References

1. Dean, C. R.; Young, A. F.; Meric, I.; Lee, C.; Wang, L.; Sorgenfrei, S.; Watanabe, K.; Taniguchi, T.; Kim, P.; Shepard, K. L.; Hone, J. *Nat. Nanotechnol.* **2010,** *5,* 722. doi:10.1038/nnano.2010.172
2. Lee, C.; Li, Q.; Kalb, W.; Liu, X.-Z.; Berger, H.; Carpick, R. W.; Hone, J. *Science* **2010,** *328,* 76. doi:10.1126/science.1184167
3. Lin, Y.; Williams, T. V.; Connell, J. W. *J. Phys. Chem. Lett.* **2010,** *1,* 277. doi:10.1021/jz9002108
4. Du, M.; Wu, Y.; Hao, X. *CrystEngComm* **2013,** *15,* 1782. doi:10.1039/c2ce26446c
5. Wang, Y.; Shi, Z.; Yin, J. *J. Mater. Chem.* **2011,** *21,* 11371. doi:10.1039/C1JM10342C
6. Shi, Y.; Hamsen, C.; Jia, X.; Kim, K. K.; Reina, A.; Hofmann, M.; Hsu, A. L.; Zhang, K.; Li, H.; Juang, Z.-Y.; Dresselhaus, M. S.; Li, L.-J.; Kong, J. *Nano Lett.* **2010,** *10,* 4134. doi:10.1021/nl1023707
7. Yu, J.; Qin, L.; Hao, Y.; Kuang, S.; Bai, X.; Chong, Y.-M.; Zhang, W.; Wang, E. *ACS Nano* **2010,** *4,* 414. doi:10.1021/nn901204c
8. Song, L.; Ci, L.; Lu, H.; Sorokin, P. B.; Jin, C.; Ni, J.; Kvashnin, A. G.; Kvashnin, D. G.; Lou, J.; Yakobson, B. I.; Ajayan, P. M. *Nano Lett.* **2010,** *10,* 3209. doi:10.1021/nl1022139
9. Kim, K. K.; Hsu, A.; Jia, X.; Kim, S. M.; Shi, Y.; Hofmann, M.; Nezich, D.; Rodriguez-Nieva, J. F.; Dresselhaus, M.; Palacios, T.; Kong, J. *Nano Lett.* **2010,** *12,* 161. doi:10.1021/nl203249a
10. Lin, Y.; Connell, J. W. *Nanoscale* **2012,** *4,* 6908. doi:10.1039/c2nr32201c
11. Han, S. S.; Lee, S. H.; Kang, J. K.; Lee, H. M. *Phys. Rev. B* **2005,** *72,* 113402. doi:10.1103/PhysRevB.72.113402
12. Koswattage, K. R.; Shimoyama, I.; Baba, Y.; Sekiguchi, T.; Nakagawa, K. *J. Chem. Phys.* **2011,** *135,* 014706. doi:10.1063/1.3605497
13. Chen, W.; Li, Y.; Yu, G.; Li, C.-Z.; Zhang, S. B.; Zhou, Z.; Chen, Z. *J. Am. Chem. Soc.* **2010,** *132,* 1699. doi:10.1021/ja908475v
14. Zhang, Z.; Guo, W.; Yakobson, B. I. *Nanoscale* **2013,** *5,* 6381. doi:10.1039/C3NR01180A
15. Sajjad, M.; Ahmadi, M.; Guinel, M. J.-F.; Lin, Y.; Feng, P. *J. Mater. Sci.* **2013,** *48,* 2543. doi:10.1007/s10853-012-7044-4
16. Sajjad, M.; Feng, P. *Mater. Res. Bull.* **2014,** *49,* 35. doi:10.1016/j.materresbull.2013.08.019
17. Feng, P. X.; Sajjad, M. *Mater. Lett.* **2012,** *89,* 206. doi:10.1016/j.matlet.2012.08.053
18. Sajjad, M.; Morell, G.; Feng, P. *ACS Appl. Mater. Interfaces* **2013,** *5,* 5051. doi:10.1021/am400871s

19. Sajjad, M.; Feng, P. X. *Appl. Phys. Lett.* **2011,** *99,* 253109. doi:10.1063/1.3671170
20. Pakdel, A.; Zhi, C.; Bando, Y.; Golberg, D. *Mater. Today* **2012,** *15,* 256. doi:10.1016/S1369-7021(12)70116-5
21. Zobelli, A.; Gloter, A.; Ewels, C. P.; Seifert, G.; Colliex, C. *Phys. Rev. B* **2007,** *75,* 245402. doi:10.1103/PhysRevB.75.245402
22. Zhang, H. X.; Feng, P. X. *ACS Appl. Mater. Interfaces* **2012,** *4,* 30. doi:10.1021/am201435z
23. Collazo, R.; Dietz, N. The Group III-Nitride Material Class: from Preparation to Perspectives in Photoelectrocatalysis. In *Photoelectrochemical Water Splitting;* Lewerenz, H.-J.; Peter, L. M., Eds.; RSC Publishing, 2013; pp 193–222. doi:10.1039/9781849737739-00193
24. Paine, R. T.; Narula, C. K. *Chem. Rev.* **1990,** *90,* 73. doi:10.1021/cr00099a004
25. Chen, Z.-G.; Zou, J.; Liu, G.; Li, F.; Wang, Y.; Wang, L.; Yuan, X.-L.; Sekiguchi, T.; Cheng, H.-M.; Lu, G. Q. *ACS Nano* **2008,** *2,* 2183. doi:10.1021/nn8004922

License and Terms

BEILSTEIN JOURNAL OF NANOTECHNOLOGY

Surface processes during purification of InP quantum dots

Natalia Mordvinova*[1,§], Pavel Emelin[1], Alexander Vinokurov[1], Sergey Dorofeev[1], Artem Abakumov[1,2] and Tatiana Kuznetsova[1]

Full Research Paper

Open Access

Address:
[1]Department of Chemistry, M.V. Lomonosov Moscow State University, 119991, Moscow, Russian Federation and [2]Electron Microscopy for Materials Research (EMAT), University of Antwerp, Groenenborgerlaan 171, B-2020 Antwerp, Belgium

Email:
Natalia Mordvinova* - n.mordvinova@gmail.com

* Corresponding author
§ Phone: +7(495)9393871

Keywords:
cadmium-free material; electrophoresis; luminescence; precipitation; purification; quantum dots; semiconductors

Beilstein J. Nanotechnol. **2014,** *5,* 1220–1225.
doi:10.3762/bjnano.5.135

Received: 09 April 2014
Accepted: 09 July 2014
Published: 06 August 2014

This article is part of the Thematic Series "Physics, chemistry and biology of functional nanostructures II".

Guest Editor: A. S. Sidorenko

Abstract

Recently, a new simple and fast method for the synthesis of InP quantum dots by using phosphine as phosphorous precursor and myristic acid as surface stabilizer was reported. Purification after synthesis is necessary to obtain samples with good optical properties. Two methods of purification were compared and the surface processes which occur during purification were studied. Traditional precipitation with acetone is accompanied by a small increase in photoluminescence. It occurs that during the purification the hydrolysis of the indium precursor takes place, which leads to a better surface passivation. The electrophoretic purification technique does not increase luminescence efficiency but yields very pure quantum dots in only a few minutes. Additionally, the formation of $In(OH)_3$ during the low temperature synthesis was explained. Purification of quantum dots is a very significant part of post-synthetical treatment that determines the properties of the material. But this subject is not sufficiently discussed in the literature. The paper is devoted to the processes that occur at the surface of quantum dots during purification. A new method of purification, electrophoresis, is investigated and described in particular.

Introduction

Colloidal semiconductor nanocrystals (NCs) have been studied extensively for the last two decades due to their unique size-dependent optical properties and their potential applications in the areas of photoluminescent devices, light-emitting diodes, displays, photodetectors, photovoltaic devices, solar cells and biological imaging [1,2]. III–V Nanocrystals are of increasing interest as a replacement for toxic CdSe quantum dots (QDs). Among them, InP QDs attracted the most attention because they are not toxic and have a broad photoluminescence color range in the visible spectrum. There are several methods to synthesize InP NCs. The most popular synthetic route is the reaction of an indium salt with tris(trimethylsilyl)phosphine ($P(TMS)_3$)

in a solvent with a high boiling point at high temperatures [3,4]. This phosphorous precursor has a number of disadvantages and should be replaced with another one, for example PH_3 [5,6].

Right after synthesis, QDs should be purified from byproducts. There are a lot of strategies for the size and shape-selective purification of nanoparticles [7]. Size-selective precipitation is one of the most important separation technique used widely in colloid chemistry. It relies on the fractional precipitation from a "good" solvent by addition of a "bad" one [8]. Another simple and effective method widely used in biological and biochemical research, protein chemistry and pharmacology is electrophoresis [9]. Electrophoretic techniques can separate charged objects in a uniform electric field, but this technique is usually applied to aqueous solutions of QDs [10].

In this paper we compare two methods of InP QDs purification: traditional precipitation and a new electrophoretic technique in an organic solvent and describe the surface processes that occur during purification.

Experimental

Materials and equipment

For synthesis we used high-purity argon, PH_3 (high purity, mixture with argon 1:1), anhydrous indium acetate ($In(OAc)_3$, Aldrich, 99.9%), myristic acid (98%, Fluka). Toluene, acetone and octadecene (ODE, 90%) were used as solvents.

Absorption spectra were measured at room temperature with a Varian Cary 50 spectrophotometer in a 1 cm quartz cuvette. Photoluminescence (PL) spectra were measured at room temperature with an Ocean Optics 4000 USB spectrometer calibrated by using a 2600 K W-lamp. Excitation of PL was carried out by using a 405 nm continuous laser LED (40 mW). Powder X-ray diffraction (XRD) patterns were taken on a Rigaku D/MAX 2500 diffractometer using Cu Kα radiation (λ = 1.540598 Å). Transmission electron microscopy (TEM) was performed on a LEO912 AB OMEGA microscope. High-angle annular dark field scanning transmission electron microscopy (HAADF-STEM) imaging and energy-dispersive X-ray (EDX) analysis have been performed with an aberration-corrected FEI Titan 80-300 "cubed" microscope equipped with a Super-X detector and operated at 200 kV. The TEM specimens were prepared by placing drops of the QD suspension onto a holey carbon grid. IR spectra were taken on a Perkin-Elmer "Frontier" FTIR-spectrometer.

QDs synthesis and purification

Synthesis of InP NCs was performed as described in [5]. Myristic acid was used as a stabilizer. The mixture of precursors (0.1 mmol of $In(OAc)_3$ and 0.3 mmol of myristic acid in 2 mL of ODE) was heated to 260 °C in neutral Ar atmosphere under stirring. After the complete dissolution of precursors about 3 mmol PH_3 was bubbled through the solution. The mixture was maintained at the reaction temperature for 15 min, then rapidly cooled and purified.

To purify the synthesized NCs, we carried out the precipitation with acetone or an electrophoretic technique. NCs precipitated with acetone were separated by centrifugation and re-dissolved in toluene. Electrophoresis was carried out in acetone in an U-shaped quartz tube, the distance between two electrodes is 10 cm. The QDs were placed near the cathode and deposited on the anode made of stainless steel at the voltage of 1 kV and were also re-dissolved in toluene. Purification was performed repeatedly and IR spectra were taken each time, and 30 days after the last purification. TEM was also performed after the final purification of QDs. The reaction mixture and the last fraction of precipitate with acetone were vacuum-sealed in two ampoules to monitor changes in the intensity of luminescence.

Results and Discussion

XRD shows that the QDs are pure InP nanocrystals (Figure 1). Figure 2a shows an overview HAADF-STEM image of the QDs that have a size ranging between 2 and 7 nm. The ring electron diffraction pattern (insert in Figure 2a) shows that the QDs are crystalline with the face-centered cubic InP crystal structure ($a \approx 5.9$ Å). The HAADF-STEM image of a [011]-oriented QD and its Fourier transform in Figure 2b and Figure 2c, respectively, confirm that the QDs have the face-centered cubic InP crystal structure and demonstrate occasional stacking faults related to a replacement of "cubic" layers with "hexagonal" layers. The EDX analysis confirms the presence of both In and P in QDs (Figure 3) and reveals the In:P ratio of

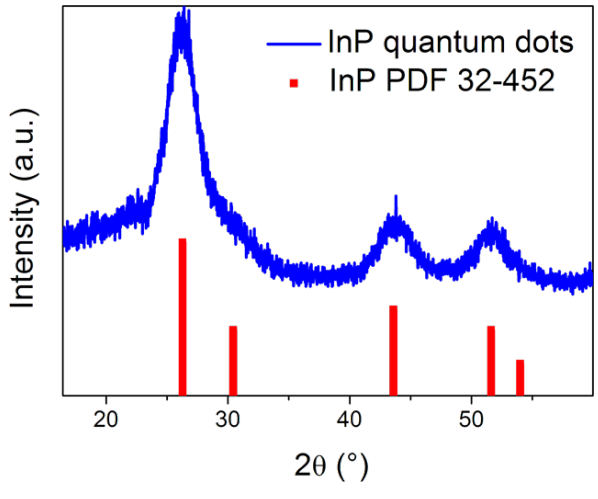

Figure 1: X-ray powder diffraction pattern of the synthesized InP QDs.

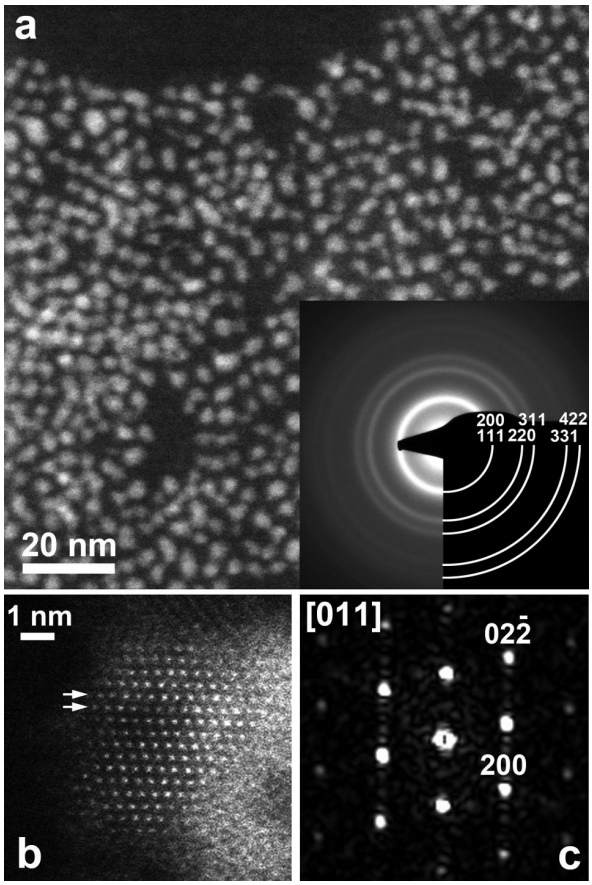

Figure 2: (a) Overview HAADF-STEM image of InP QDs. The ring electron diffraction pattern (insert) is indexed on a face-centered cubic lattice with $a \approx 5.9$ Å. (b) High resolution HAADF-STEM image of the [011]-oriented QD. Planar defects (stacking faults) associated with {111} close-packed planes are marked with arrows. (c) Fourier transform of the HAADF-STEM image in Figure 2b indexed with a face-centered cubic InP unit cell. Weak extra spots along the $[1\bar{1}1]$ reciprocal lattice direction are because of stacking faults.

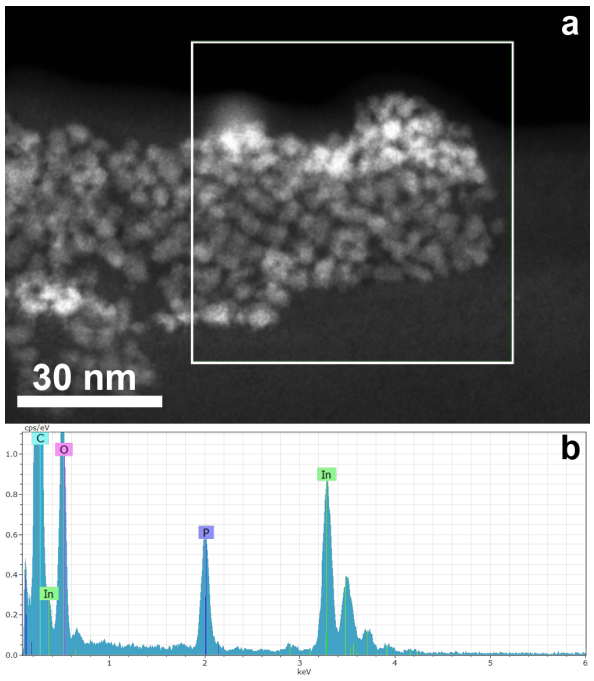

Figure 3: HAADF-STEM image of InP QDs with the area selected for the EDX analysis (a) and the EDX spectrum (b).

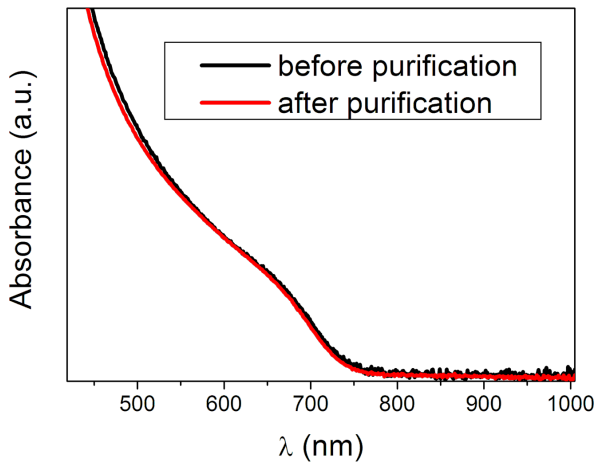

Figure 4: UV–vis absorption spectra of InP QDs before purification and after the last precipitation with acetone.

1.14(2):0.86(2). The EDX spectra reveal that the QDs are noticeably oxidized.

Figure 4 shows the UV–vis absorption spectra of InP QDs before purification and after the last precipitation with acetone. These spectra are the same. The spectrum of the sample purified with electrophoresis completely matches with these spectra. Thus, we can conclude that small as well as large particles could be completely precipitated and the size distribution of NCs is the same for different types of purification. The excitonic peak is diffuse. This indicates that QDs are polydisperse. The size distribution obtained from TEM is shown in Figure 5.

Precipitation with acetone

Figure 6 shows how the IR spectra changes during the precipitation with acetone and after 30 days from the last purification. The IR spectra of the second and the following steps of purification were identical. Therefore, we consider only the second step of precipitation. The assignment of the vibrations of the samples is given in Table 1.

Apparently, the sample after the first precipitation contained a large amount of ODE. Besides, this IR-spectrum shows the presence of COO^- groups in the sample and the absence of C=O and O–H groups. Thus, there was only indium myristate

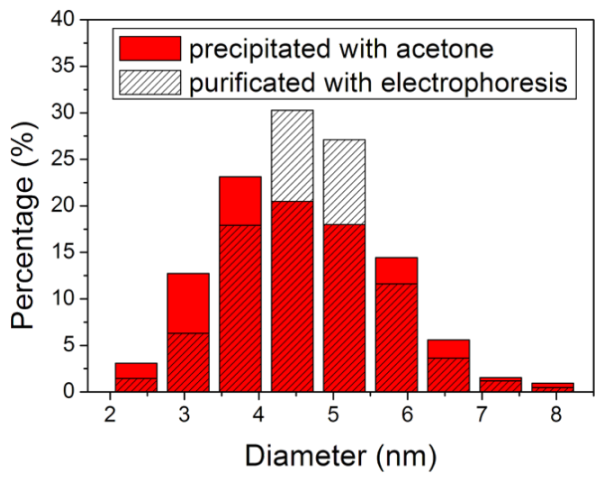

Figure 5: Size distribution of purified InP QDs.

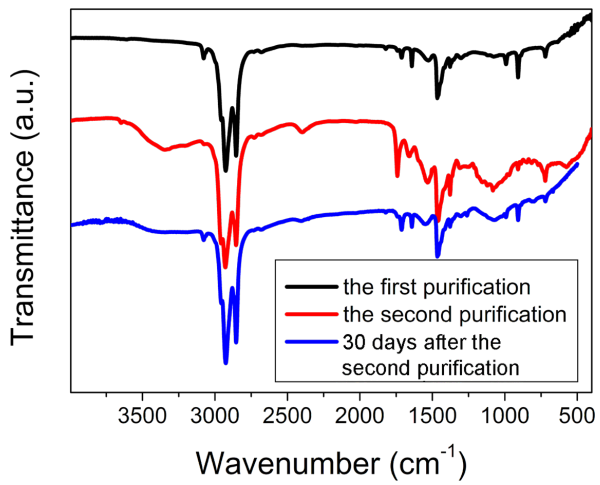

Figure 6: IR spectra of QDs precipitated with acetone.

Table 1: Assignment of the vibrations of the samples.

wavenumber [cm^{-1}][a]	assignments	comments
3600–3000	O–H st	myristic acid
3095–3075	$=CH_2$ st	ODE
3000–2840	C–H st	
2440–2275	P–H st	PH_3
1765–1645	C=O st	myristic acid
1690–1635	C=C st	ODE
1610–1550	(COO^-) st as	
1470–1430	CH_3 δ as or CH_2 δ	
1450–1400	(COO^-) st sy	
1300–800	–OH	myristic acid
1005–985	$CH=CH_2$	ODE
920–900		
770–720	$–(CH_2)_n–$	

[a][11,12].

$(In(MA)_3)$ and no myristic acid (HMA) in the sample. After the second purification peaks, that we have assigned to HMA, appear. Before purification there was some excess of unreacted $In(MA)_3$ in the sample that was almost removed during the first purification, but a small part of $In(MA)_3$ was still dissolved in ODE that covered the surface of the QDs. So, we suppose that after the first precipitation with acetone the QDs are nanocrystals of InP stabilized with the myristate anion and covered with an ODE layer that contains dissolved $In(MA)_3$ (Figure 7a).

During the second precipitation $In(MA)_3$ in the ODE layer is hydrolyzed because of the water contained in acetone according to the following reaction:

$$In(MA)_3 + 3H_2O \rightarrow In(OH)_3 \downarrow + 3HMA.$$

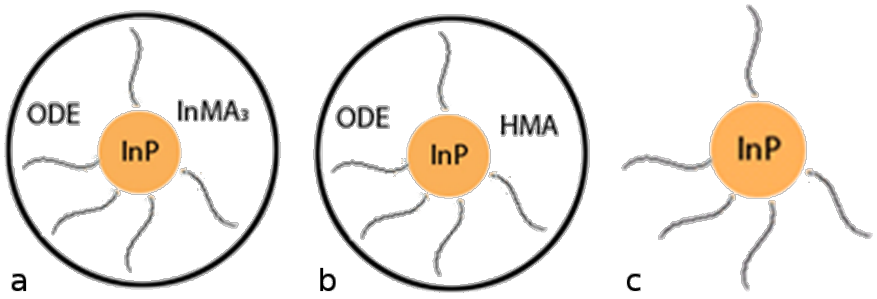

Figure 7: Scheme of QD at different steps of purification. (a) after the first purification, (b) after the second precipitation with acetone, (c) after the second purification with electrophoresis.

$In(OH)_3$ is insoluble in ODE and leaves this layer of the QD. A QD after the second precipitation with acetone is shown in Figure 7b. Myristic acid is formed by the hydrolysis and most probably dissolves the surface of the QD under the formation of PH_3 according to the next reaction:

$$InP + 3HMA \rightarrow In(MA)_3 + PH_3.$$

This hypothesis is confirmed by the IR spectrum of the sample precipitated for the second time, which contains a peak that corresponds to P–H vibrations. After 30 days the quantity of free myristic acid decreases (Figure 6) and the quantum yield (QY) of luminescence increases (reaches more than 1%) as the result of the stabilization on the QDs surface.

It is known that the efficiency of QD luminescence increases a few days after synthesis because of the oxidation of the QDs surface [4]. In order to show that the increasing luminescence intensity is indeed a result of hydrolysis during precipitation, two aliquots (reaction mixture and precipitated samples) were vacuum-sealed. The QY of the reaction mixture did not increase. But the QY of the precipitated QDs increased and reached more than 1% after 30 days.

Electrophoretic technique

The electrophoretic technique enables us to purify QDs from ODE that is dissolved in the stabilizing shell. After the first electrophoretic purification small peaks corresponding to ODE are noticeable in the IR spectrum and after the second purification there are no ODE peaks in the IR spectrum of the sample (Figure 8). Similar to the precipitation with acetone, we consider only the second step of purification with electrophoresis because the properties of the samples obtained after the second purification are identical. During the first purification excess ODE and $In(MA)_3$ are removed from the QDs surface as it happens during the first precipitation with acetone. During the second purification ODE completely leaves the QDs surface and the QDs look as shown in Figure 7c. After 30 days MA^- that stabilizes the QD is hydrolyzed because of traces of water in air (Figure 8). Because of the poor stabilization of the QDs surface the quantum yield of luminescence does not increase and is less than 0.5%.

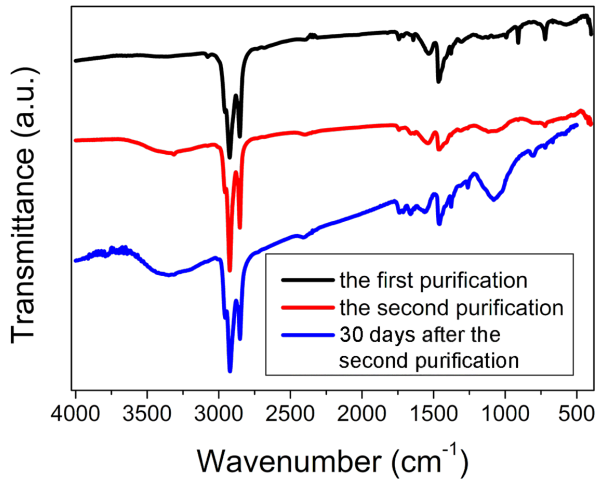

Figure 8: IR spectra of QDs purified with the electrophoresis.

The comparison of the TEM images for two types of purification is shown in Figure 9. QDs purified with electrophoresis are grouped together, the distance between two QDs is about 1–3 nm (Figure 9b). QDs precipitated with acetone are distributed more randomly and are not aggregated because of the ODE layer which prevents the aggregation of particles.

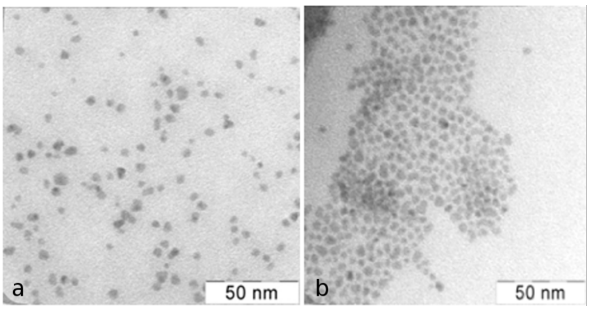

Figure 9: TEM images of InP QDs (a) after the second precipitation with acetone, (b) after the second purification with electrophoresis.

$In(OH)_3$ formation

In our previous paper [5] we described a low-temperature (160–200 °C) synthesis of QDs that is accompanied by the formation of $In(OH)_3$. We supposed that indium acetate, which contains traces of water, causes the formation of $In(OH)_3$. The scheme of purification mentioned above explains this fact by the hydrolysis of unreacted $In(MA)_3$. Actually, solutions of samples stabilized with HMA and synthesized at lower temperatures (160–200 °C) are almost transparent; the concentration of InP QDs is very low. So on the other hand, the concentration of unreacted $In(MA)_3$ is very high. To confirm our suggestion, we performed one additional synthesis. During the synthesis excess PH_3 was bubbled through the precursors solution heated to 160 °C. The solution became dark brown and very saturated. XRD showed that after purification there is only InP and no $In(OH)_3$ in the sample. Our investigations of the reaction at different temperatures enables us to conclude that at lower temperatures the rate of the reaction between $In(MA)_3$ and PH_3 is very low and the hydrolysis of unreacted $In(MA)_3$ during the purification leads to the formation of $In(OH)_3$.

Conclusion

We have compared two methods for the purification of QDs: precipitation with acetone and an electrophoretic technique. Electrophoresis is a fast and efficient technique that enables the purification of QDs from byproducts, including ODE, that contaminate the sample. During the precipitation with acetone ODE admixture could hardly be removed. However, electrophoresis has some limitations: After purification through electrophoresis no luminescence is observed. To increase the quantum yield of QDs purified in such a way a postsynthetic treatment, for example photoetching with HF [13], is required. Luminescence QY of QDs precipitated with acetone increases up to 1% because of the hydrolysis of excess indium myristate, which is dissolved in ODE. We have proposed the structure of QDs after each step of both types of purification and explained the differences between them.

We also explained the formation of $In(OH)_3$ during the low-temperature synthesis by the hydrolysis of unreacted indium myristate during the purification. To prevent the formation of $In(OH)_3$ a greater amount of PH_3 should be bubbled through the precursors solution.

Acknowledgements

This work was supported by the Russian Foundation for Basic Research Grant No. 12-03-00933A and the Russian Presidential Grant No. MK-4778.2013.3. IR experiments were effectuated in the frame of Development Program at User Facilities Center of M.V. Lomonosov Moscow State University supported by Federal Contract 16.552.11.7081.

References

1. Sun, K.; Vasudev, M.; Jung, H.-S.; Yang, J.; Kar, A.; Li, Y.; Reinhardt, K.; Snee, P.; Stroscio, M. A.; Dutta, M. *Microelectron. J.* **2009,** *40,* 644–649. doi:10.1016/j.mejo.2008.06.033
2. Lim, J.; Park, M.; Bae, W. K.; Lee, D.; Lee, S.; Lee, C.; Char, K. *ACS Nano* **2013,** *7,* 9019–9026. doi:10.1021/nn403594j
3. Micic, O. I.; Curtis, C. J.; Jones, K. M.; Sprague, J. R.; Nozik, A. J. *J. Phys. Chem.* **1994,** *98,* 4966–4969. doi:10.1021/j100070a004
4. Guzelian, A. A.; Katari, J. E. B.; Kadavanich, A. V.; Banin, U.; Hamad, K.; Juban, E.; Alivisatos, A. P.; Wolters, R. H.; Arnold, C. C.; Heath, J. R. *J. Phys. Chem.* **1996,** *100,* 7212–7219. doi:10.1021/jp953719f
5. Mordvinova, N.; Vinokurov, A.; Dorofeev, S.; Kuznetsova, T.; Znamenkov, K. *J. Alloys Compd.* **2014,** *582,* 43–49. doi:10.1016/j.jallcom.2013.08.003
6. Vinokurov, A. A.; Dorofeev, S. G.; Znamenkov, K. O.; Panfilova, A. V.; Kuznetsova, T. A. *Mendeleev Commun.* **2010,** *20,* 31–32. doi:10.1016/j.mencom.2010.01.012
7. Kowalczyk, B.; Lagzi, I.; Grzybowski, B. A. *Curr. Opin. Colloid Interface Sci.* **2011,** *16,* 135–148. doi:10.1016/j.cocis.2011.01.004
8. Murray, C. B.; Norris, D. J.; Bawendi, M. G. *J. Am. Chem. Soc.* **1993,** *115,* 8706–8715. doi:10.1021/ja00072a025
9. Westermeier, R. *Electrophoresis in practice;* Wiley-VCH: Weinheim, 2005.
10. Fu, A.; Micheel, C. M.; Cha, J.; Chang, H.; Yang, H.; Alivisatos, A. P. *J. Am. Chem. Soc.* **2004,** *126,* 10832–10833. doi:10.1021/ja046747x
11. Yukhnevich, G. V. *Infrared spectroscopy of water;* Moscow, Nauka, Russia, 1973.
12. Pretsch, E.; Buellmann, P.; Affolter, C. *Structure Determination Of Organic Compounds;* Springer, 2000.
13. Adam, S.; Talapin, D. V.; Borchert, H.; Lobo, A.; McGinley, C.; de Castro, A. R. B.; Haase, M.; Weller, H.; Möller, T. *J. Chem. Phys.* **2005,** *123,* 084706. doi:10.1063/1.2004901

License and Terms

BEILSTEIN JOURNAL OF NANOTECHNOLOGY

Synthesis, characterization, and growth simulations of Cu–Pt bimetallic nanoclusters

Subarna Khanal[1], Ana Spitale[2], Nabraj Bhattarai[1], Daniel Bahena[1], J. Jesus Velazquez-Salazar[1], Sergio Mejía-Rosales[3], Marcelo M. Mariscal[*2] and Miguel José-Yacaman[*1]

Full Research Paper

Open Access

Address:
[1]Department of Physics and Astronomy, University of Texas at San Antonio, One UTSA Circle, 78249, San Antonio, Texas, USA, [2]INFIQC, CONICET, Departamento de Matemática y Física, Facultad de Ciencias Químicas, Universidad Nacional de Córdoba, (XUA5000) Córdoba, Argentina and [3]Center for Innovation and Research in Engineering and Technology, and CICFIM-Facultad de Ciencias Físico-Matemáticas, Universidad Autónoma de Nuevo León, San Nicolás de los Garza, NL 66450, México

Email:
Marcelo M. Mariscal[*] - marcelo.mariscal@conicet.gov.ar;
Miguel José-Yacaman[*] - miguel.yacaman@utsa.edu

* Corresponding author

Keywords:
Cu–Pt clusters; energy dispersive X-ray spectroscopy (EDX); grand-canonical Langevin dynamics; nanoalloys; scanning transmission electron microscopy (STEM)

Beilstein J. Nanotechnol. **2014,** *5,* 1371–1379.
doi:10.3762/bjnano.5.150

Received: 09 May 2014
Accepted: 06 August 2014
Published: 27 August 2014

This article is part of the Thematic Series "Physics, chemistry and biology of functional nanostructures II".

Guest Editor: A. S. Sidorenko

Abstract

Highly monodispersed Cu–Pt bimetallic nanoclusters were synthesized by a facile synthesis approach. Analysis of transmission electron microscopy (TEM) and spherical aberration (C_s)-corrected scanning transmission electron microscopy (STEM) images shows that the average diameter of the Cu–Pt nanoclusters is 3.0 ± 1.0 nm. The high angle annular dark field (HAADF-STEM) images, intensity profiles, and energy dispersive X-ray spectroscopy (EDX) line scans, allowed us to study the distribution of Cu and Pt with atomistic resolution, finding that Pt is embedded randomly in the Cu lattice. A novel simulation method is applied to study the growth mechanism, which shows the formation of alloy structures in good agreement with the experimental evidence. The findings give insight into the formation mechanism of the nanosized Cu–Pt bimetallic catalysts.

Introduction

The study of bimetallic (BM) nanoclusters has received particular interest because of their myriad properties and applications in optics, magnetism, catalysis, and others, mainly because their high tunability and superior features compared with those of their monometallic counterparts [1-6]. Depending on the elements, relative concentrations, and details of the synthesis

method, the BM may form core–shell structures, heterostructures, and alloy nanocrystals, and this diversity potentiates the increase of the mass specific activity (MSA) of the nanoparticle while also minimizing the cost by using precious metals only in the surface of the particles. Thus, in order to attain a better control on shape, size and composition of the BM nanoparticles, it is critically important to understand the correlation between their structures and other properties [7-12]. Features expected for these BM nanostructures include the tuning of physical and chemical interactions among different atoms and phases that lead to novel functions, the changed miscibility and interactions unique to nanometer dimensions, and the morphological variations that are related to new particles [13].

Pt-based nanoparticles are frequently studied because of their high reactivity with organic molecules, which makes them capable of converting them to CO_2 easily, and useful for electrocatalysis in fuel cells. There is an increasing interest in combining morphology engineering with the synergistic effect of adding a second metal to produce Pt-based particles with higher catalytic activities than pure Pt catalysts [14-17]. The stability at high temperatures and resistance against both physical impacts and chemical attacks make the Pt group metals quite distinguishable from other transition metals. Particularly, by combining Pt with secondary metals such as Ni, Co, Cu, Fe or Ti, it has been possible to produce particles with enhanced electrocatalytic performance towards the oxidation of CO [18,19], methanol oxidation reactions (MOR) [20-24], polymer electrolyte membrane fuel cells (PEMFCs) [15,25-28], hydrogen storage [29,30], and detecting hydrogen [31]. For instance, Wu et al. [32] studied a series of Pt-based bimetallic (Pt–Co, Pt–Fe, Pt–Ni, Pt–Pd) nanocrystals with octahedral and cubic shape and examined their facet-dependent catalytic performance for the oxygen reduction reaction (ORR). Guo and co-workers [33] synthesized FePt and CoPt nanowires by organic-phase decomposition and demonstrated that these systems are good catalysts for the ORR. Yun and co-workers [34] developed a unified embedded atom model to investigate the most energetically favorable atomic arrangements of Pd–Pt, Cu–Pt, Au–Pt and Ag–Pt nanoalloys using Monte Carlo simulations, obtaining intermetallic compounds for the Pd–Pt system, onion-like structures for the Cu–Pt system, and core–shell structures for Au–Pt and Ag–Pt. Yu et al. [35] investigated the formation of and dealloying of CuPt bimetallic nanoparticles in presence of hexadecylamine or PVP as capping agents, obtaining different morphologies of nanoparticles depending on their sizes. Recently, several groups have worked on the synthesis of CuPt core–shell and alloys nanoparticles, obtaining morphologies such as nanotubes, cubes, spheres, hollow structures and others [36-39]. These particles exhibit excellent catalytic activities for CO oxidation, methanol oxidation, formic acid electro-oxidation, and ORR, in comparison with other Pt-based nanoparticles [40-42].

In this paper, we describe the synthesis of monodispersed sub-3 nm Cu–Pt BM nanoclusters, and their characterization by spherical aberration (C_s)-corrected scanning transmission electron microscopy (STEM) techniques. The use of high angle annular dark field (HAADF-STEM) images, intensity profiles, and energy dispersive X-ray spectroscopy (EDX) line scans, allowed us to study the atomic positions of Cu and Pt, and to compare the structure of the particles with the results of atomistic simulations. We applied a novel simulation method to study the growth mechanism of CuPt bimetallic nanoclusters; in particular, we explored the attaching of Pt atoms on Cu seeds by using grand-canonical Langevin dynamics (GCLD) simulations, which shows the formation of alloy structures in good agreement with empirical evidence.

Experimental

Chemicals and materials

Reagent-grade chemicals from Sigma-Aldrich such as chloroplatinic acid hydrate ($H_2PtCl_6{\cdot}xH_2O$, 99.9%), copper(I) acetate ($CuCO_2CH_3$, 97%), tetraoctylammonium bromide (TOAB, 99%), hexadecyltrimethylammonium bromide (CTAB), sodium borohydrate ($NaBH_4$), 1-dodecanethiol, toluene and ethanol were used as received without further purification.

Preparation of Cu–Pt bimetallic nanoclusters

In a first step, the $H_2PtCl_6{\cdot}xH_2O$ metal ions were transferred into a toluene solution by a phase transformation process. An aqueous solution of 30 mM of 5 mL Pt precursor was mixed with a 60 mM of 10 mL solution of tetraoctylammonium bromide (TOAB, 99%) by vigorously stirring for 15 min. The organic phase was separated and formed 15 mM concentration stock solution.

In a second step, 0.03 g of copper(I) acetate and 0.240 g of hexadecyltrimethylammonium bromide (CTAB) were added into the 10 mL of toluene, and the mixture was heated at 120 °C under magnetic stirring to form a dark green solution. Afterwards, a freshly prepared sodium borohydrate ($NaBH_4$) (72 μL, 4.6 M) was added under vigorously stirring. The dark green solution changed into dark brown within a minute indicating the formation of Cu nanoparticles. Then 36 μL of 1-dodecanethiol was added to stabilize the Cu nanoparticles. After preparing the Cu nanoparticles, 3 mL of the Pt precursor solution was quickly added into the colloidal solution and after 5 min of waiting $NaBH_4$ (72 μL, 4.6 M) was added and the heating was stopped. The colloidal solution was left for cooling at room temperature, and the product was separated by centrifugation and washed

with ethanol three times. The final product was redispersed in a toluene organic solution.

Electron microscopy characterization

The morphology of the nanoparticles was characterized by transmission electron microscope (TEM) and high resolution transmission electron microscopy (HRTEM) by using a JEOL 2010F operated at 200 kV. The STEM images were recorded in a C_s-corrected JEOL JEM-ARM 200F operated at 200 kV. HAADF STEM images were obtained with a convergence angle of 26 mrad and collection semi-angles from 50 to 180 mrad. The probe size used was about 0.09 nm with the probe current of 22 pA. In addition, bright field (BF) STEM images were recorded by using a collection semi-angle of 11 mrad. Energy dispersive X-ray spectra were obtained by using a probe size of 0.13 nm with a probe current of 86 pA.

Models and simulation method

The simulation method employed is a grand-canonical Langevin dynamics (GCLD). Langevin dynamics is a method that extends molecular dynamics to represent the effect of perturbations caused by friction and eventual collisions occurring due to the presence of a solvent (the molecules in real systems are seldom under vacuum). For doing so, it makes use of stochastic differential equations, adding two terms to Newton's second law to approximate the effects of neglected degrees of freedom. On the other hand, temperature can be controlled, approximating the canonical ensemble. Although it does not fully represent an implicit solvent (electrostatic screening and hydrophobicity), it mimics the viscosity of the medium. The original GCLD method was developed by M. M. Mariscal and co-workers [43,44] to study metallic deposition phenomena on crystalline planar surfaces. Now, the method has been extended to non-planar systems, like clusters and bimetallic nanoparticles (NPs). The simulation cell contains two distinct regions: the NPs region, and a much larger solution region. The solvent is not modeled explicitly, but it is provided as a stochastic bath. Thus, the solution part contains only metal particles that can either be of the same element as the metal atoms of the nanoparticle or different from them. All solution particles move according to Langevin's equation:

$$\frac{d\vec{v}}{dt} = -\frac{d\vec{r}}{dt}\gamma + \vec{F}_{\mathrm{p}} + \vec{F}_{\mathrm{r}}$$

where γ is the friction constant, $\vec{F}_{\mathrm{r}}$ represents the random force acting on each particle and $\vec{F}_p$ represents the force due to the potential interaction between the particles and the NP, as they do not interact with each other. The friction constant γ and the random force $\vec{F}_{\mathrm{r}}$ are related by the fluctuation–dissipation theorem. The Langevin dynamics was implemented by Ermak's algorithm [45]. Specifically, NP atoms interact with each other through potentials calculated from the embedded atom method [46]. To mimic the interaction between the NP atoms and the implicit solvent, they move according to Langevin's equation but with a friction coefficient that decreases as the bond order of the metal atoms increases, since atoms inside the NP (higher coordination number) are not expected to interact with the solvent as much as the atoms in the surface (lower coordination).

Following the experimental evidence, fcc structures were selected as Cu seeds for Pt growing. In particular we have employed the truncated octahedron (TO), the surface of which holds six square (100) faces and eight equilateral hexagonal (111) faces. TO structures of two sizes (n = 201 and n = 586) were used as seeds, which correspond to a diameter of 1.6 and 2.4 nm respectively. The simulations were carried out with our custom-developed code at 393 K (120 °C, as the experimental condition). 1×10^7 LD steps were employed for each production run, giving a total simulation time of 20 ns.

Results and Discussion

Experimental results

Figure 1a shows a representative STEM micrograph of as-synthesized Cu–Pt nanoclusters prepared by using the one-pot sequential reduction process described in a previous section. The inset shows a magnified HAADF-STEM image, illustrating the size and distribution of particles. The Cu–Pt nanoclusters were highly monodispersed and had an average size of 3.0 ± 1.0 nm. The size distribution histogram is presented in Figure 1b.

Figure 2a shows the HAADF-STEM image of Cu–Pt bimetallic nanostructures. The distributions of Cu and Pt in the nanoparticles were studied by EDX using the STEM mode. The EDX technique was applied to obtain 2D elemental mapping and cross-sectional compositional line profile of the nanostructures [47,48]. Here we observe the Cu–Pt bimetallic nanoalloy clusters and the compositional distribution of each element. Figure 2b (and Figure S2 in Supporting Information File 1) shows the EDX line profile of Cu and Pt, measured through the center of an individual nanoparticle (marked by a green line in Figure 2a). Both the Cu and the Pt signals were clearly traced across the entire particle (ca. 3 nm). Furthermore, the EDX spectrum also indicates that Pt atoms are present also in the surface region.

Figure 3a shows a HAADF-STEM micrograph of Cu–Pt nanoparticles, in which we can clearly observe different atomic contrasts, related to the presence of Cu and Pt atoms. The inset of Figure 3a shows the corresponding fast Fourier

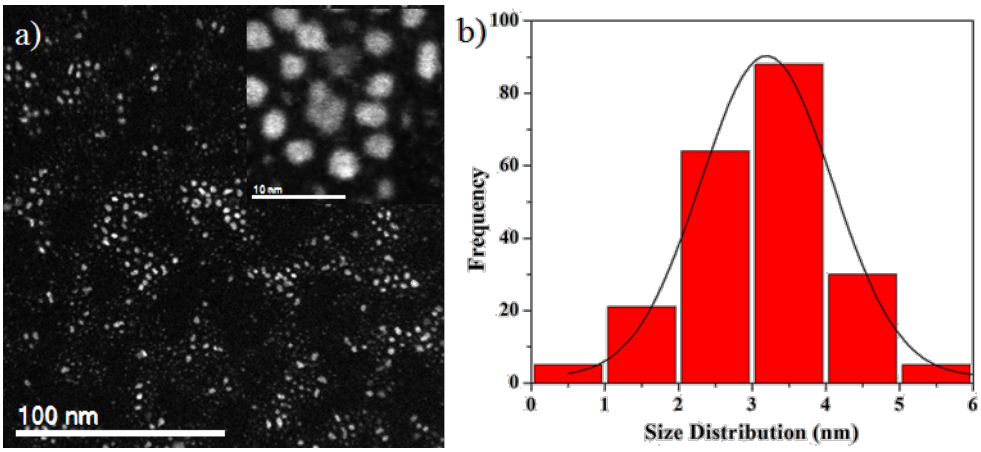

Figure 1: (a) STEM image of Cu–Pt bimetallic nanoparticles. The inset in (a) shows the HAADF-STEM image, and (b) Size distribution histogram, the average diameter is 3.0 ± 1.0 nm.

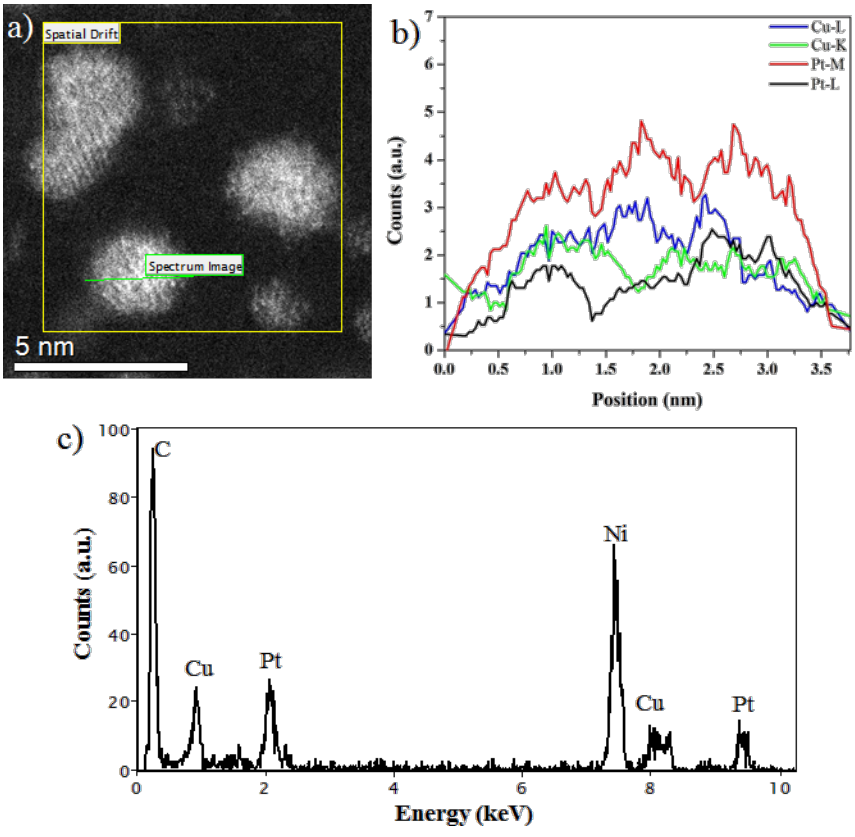

Figure 2: (a) HAADF-STEM image of Cu–Pt bimetallic nanoparticles, (b) Cu and Pt elemental line profiles along the green line across the nanostructure in (a), and (c) energy dispersive X-ray spectroscopy (EDX) spectrum of corresponding Cu–Pt bimetallic nanoparticles.

transform (FFT). From the FFT it can be concluded that the crystal structure is fcc, and the zone axis in this case is [011]. Figure 3b was built considering only (111) reflections, so the fringe spacing corresponds to the interplanar distance for the (111) planes. Figure 3d shows the intensity profile corresponding to the line drawn perpendicular to the planes in Figure 3b. The measured interplanar distance is 0.218 nm, which compares well with the expected spacing of (111) planes

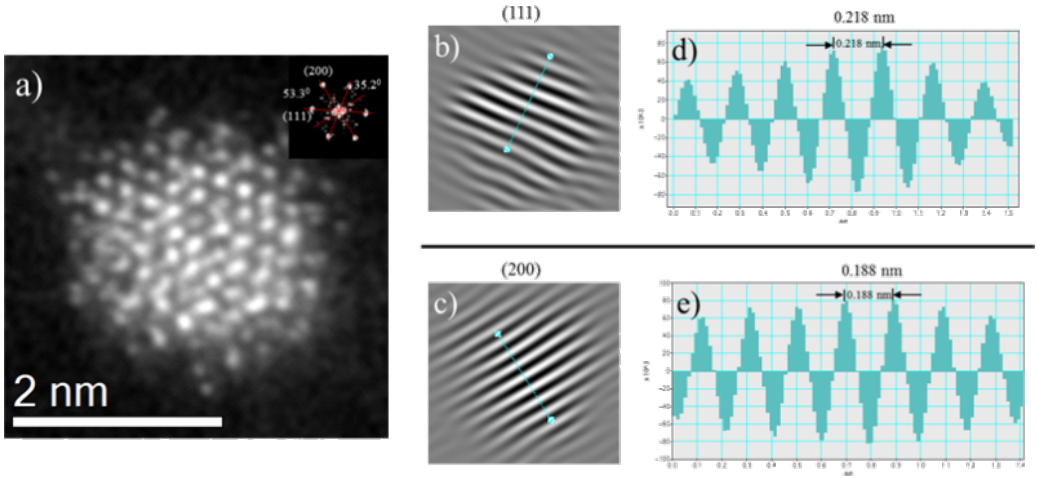

Figure 3: High resolution HAADF-STEM image of (a) Cu–Pt bimetallic nanoparticle; the inset represents the fast Fourier transform (FFT) of the image. The FFT was used to measure the interplanar distances corresponding to (111) (b, d) and (200) (c, e) planes.

of a CuPt alloy (0.219 nm) [35]. Figure 3c represents the filtered image considering only (200) reflections. Here the measured interplanar distance (shown in Figure 3e) was 0.188 nm.

HAADF-STEM imaging can be used to investigate the elemental distribution in bimetallic particles, under the assumption that the height of the atomic columns is fairly uniform, or that the differences in height are known, since the intensity signal depends strongly on the atomic number (Z). Figure 4a shows an atomic resolution STEM image of a Cu–Pt bimetallic nanoparticle oriented along the [011] zone axis, with crystal facets defined by the (111) and (002) planes. It can be easily noted that the intensity of two neighboring columns, likely to have roughly the same height, may have very different intensities. The intensity profile shown in Figure 4b, corresponding to the white line marked in Figure 4a, shows how different these intensities may be. Under the assumption of equal heights, these differences would be due to the local differences in the elemental composition of the atomic columns. As it will be shown in next section, our simulations predict similar intensity profiles.

Simulation results

Several grand-canonical Langevin dynamics (GCLD) simulations were performed in order to explore the growth mechanism of Pt atoms on Cu seeds. Figure 5 shows selected snapshots taken during time evolution of the deposition of Pt atoms on Cu nanoclusters with fcc TO morphology at different sizes. At first view, the simulation results predict structures very similar to those observed in the experiments. For the TO_{201} seed, the final diameter of the CuPt nanoalloys was ca. 1.8 nm, whereas for the TO_{586} seed it was ca. 2.6 nm. Even though this is slightly smaller than the diameters in the experiment

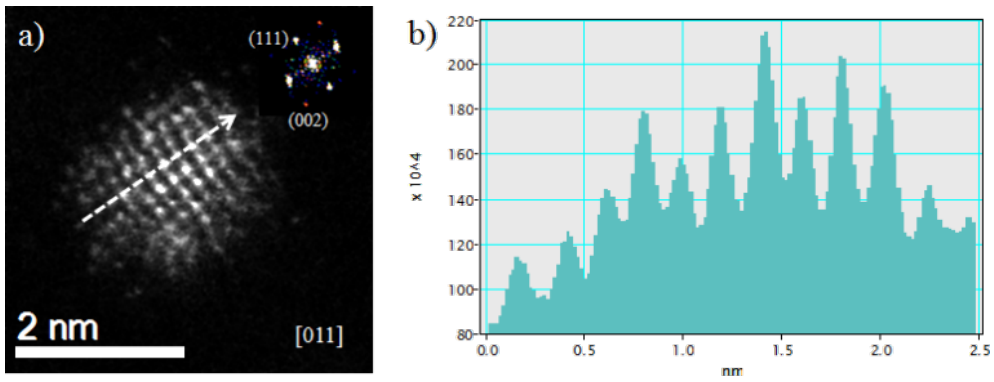

Figure 4: (a) C_s-corrected STEM-HAADF image of a bimetallic Cu–Pt nanoparticle oriented along the [011] zone axis, and (b) intensity profile (in arbitrary units) measured over the white arrow marked in (a). For atomic columns of the same height, the differences in intensities are due to local changes in elemental composition.

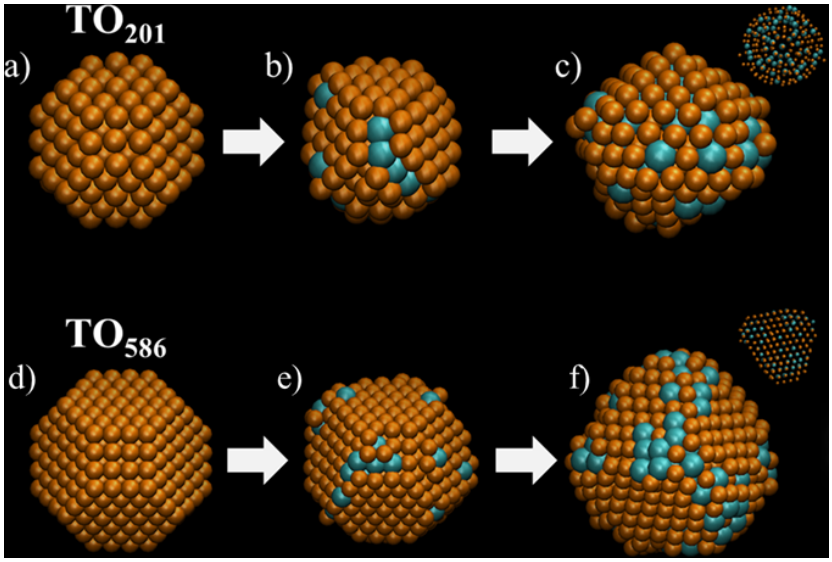

Figure 5: Snapshots taken during time evolution (20 ns) of Pt (cyan) deposition on the Cu NPs (orange) at T = 393 K: (upper panel) TO_{201} seed and (lower panel) TO_{586} seed. Atoms in solution are not shown for clarity.

(ca. 3 nm), it is within the expected value considering that if dynamics are allowed longer time the nanoparticle continues to grow. It is noteworthy that the TO_{201} Cu seed exhibits a structural transition from fcc to an icosahedron after 32–33 Pt atoms were deposited (Figure 5a–c). In the case of the TO_{586} Cu seed, the fcc structure is retained and in both cases CuPt alloys are evident, with an enrichment of Pt in the sub-surface layers. In all cases, the Pt deposition begins preferentially at the (100) faces due to the most favorable adsorption energy on open facets.

The final configurations of the GCLD simulations (Figure 5c,f), were used as input coordinates for the simulation of HAADF-STEM microscopy. For these simulations we used the multi-slice method as implemented in the xHREM package by Ishizuka, that uses an algorithm based on fast Fourier transforms. In Figure 6, the STEM simulation images corresponding to configurations Figure 5c and Figure 5f, respectively, are shown for two different orientations. It can be noted how the Pt-rich region of the nanoparticle brighter due to the Z-contrast feature of STEM. In addition, Figure S3 and Figure S4 in

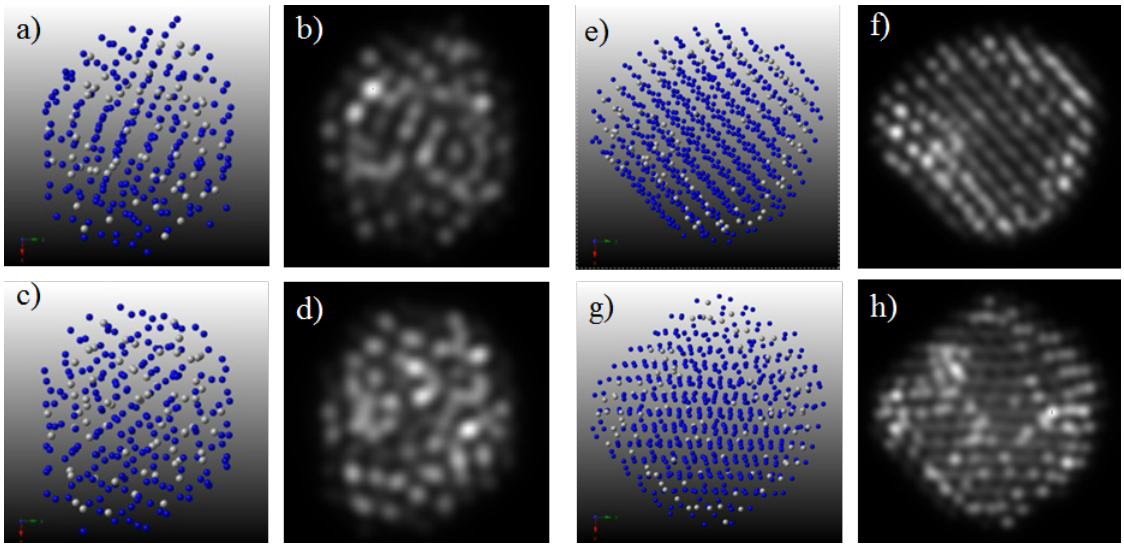

Figure 6: STEM simulated images of the final configurations shown in Figure 5. In (a–c) TO_{201} seed and (e–h) TO_{586} seed. The structures (c, d) and (g, h) were rotated by 30° around the y-axis. Note how the regions enriched in Pt appear brighter.

Supporting Information File 1 show the structures rotated by 30, 60 and 90° around the y- and x-axes, in which the Pt-rich regions appear brighter. These images are in very good agreement with the experimental images taken with the JEOL JEM-ARM 200F microscope.

In order to understand the novel structural transition observed for the Cu TO_{201} seed, the total energy of the nanoalloy was plotted against the number of GCLD steps (i.e., time) and compared with the number of Pt atoms added to the Cu seed (see Figure S5 in Supporting Information File 1). It is remarkable how the potential energy slightly increases just after adding 32–33 Pt atoms. Subsequently, while $N_{Pt} = 33$ constant, the potential energy decreases during the structural transition, a phenomenon itself which merits further research.

To determine the mixing pattern of the obtained nanoalloys, we calculate the relative concentration of each atom type across the nanoalloys, a fingerprint that could be compared directly with the experimental results shown in Figure 2b. Based on the concentration profiles shown in Figure 7, it can be recognized that the resulting structures were alloyed NPs with an enrichment of Pt in the sub-surface layers.

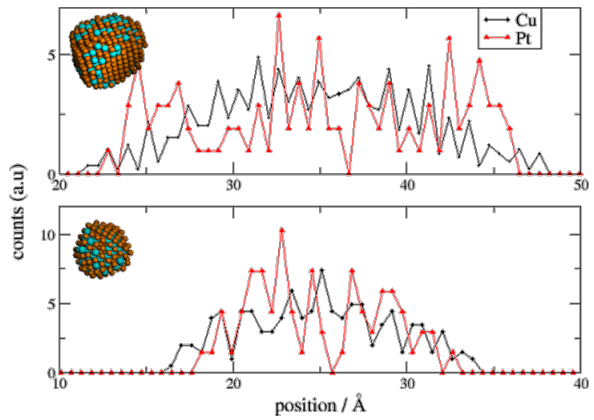

Figure 7: Cu and Pt elemental line profiles across the nanoalloy structure obtained after 20 ns of GCLD simulation, (upper panel) TO_{586} seed and (lower panel) TO_{201} seed.

To elucidate kinetic parameters, the mean square displacement (MSD) of the Pt atoms in the nanoalloy was calculated by taking previous configurations in the recorded trajectory as reference configuration. Moreover, the MSD reflects the relative change of diffusivity of the atoms at different temperatures and the activation energy (E_a) for Pt diffusion in Cu NPs can be calculated, plotting the diffusion constant as a function of $(k{\cdot}T)^{-1}$ [49]. By means of a linear regression fit, an E_a of 0.009 eV/atom was found (Figure S6 in Supporting Information File 1). If we assume the transition state theory to be valid for the problem at hand, we can estimate the waiting time (t_w) for a transition at 393 K to be equal to 1.30 ps. Evidently, this time is small and as a consequence we observe Pt diffusion inside the nanoalloy by means of atom dynamics simulations.

Figure 8 shows the change in the total energy (E_{exc}) of the Cu nanocluster, when a Pt atom is exchanged with a Cu atom from the first, second and third sub-surface layers. The exchange energy was obtained through energy minimizations by using a conjugated gradient algorithm. E_{exc} is a thermodynamic parameter that indicates the stability of one structure with respect to another. Since $E_{exc} < 0$ for the inclusion of Pt atoms, the formation of alloy CuPt NPs is expected from energetic considerations.

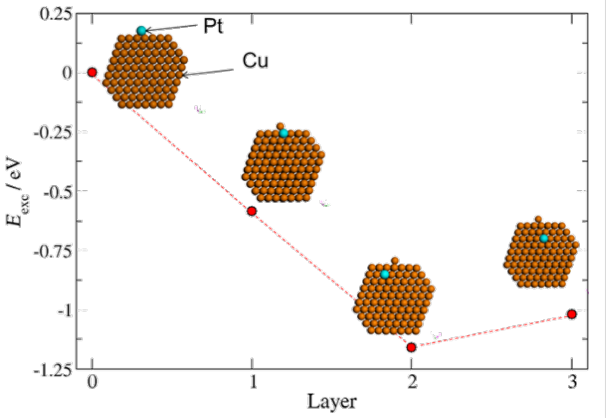

Figure 8: Calculation of exchange energy (E_{exc}) for Pt atom diffusion in different sub-surface layers inside a Cu nanocluster with truncated octahedral geometry.

Conclusion

In summary, monodispersed bimetallic Cu–Pt alloy nanoparticles with highly uniform size and composition were synthesized by using a facile approach. Spherical aberration-corrected STEM, in combination with high resolution spectral and chemical analysis, has allowed us to study the atomic structure of the Cu–Pt bimetallic nanoclusters, and the chemical compositions of the particles were measured by STEM-EDX analysis. HAADF-STEM imaging allowed us to study the distribution of Cu and Pt, and to compare these results against atomistic simulations and simulated STEM images.

By using GCLD simulations, we have been able to study the formation mechanism of Cu–Pt bimetallic nanoclusters. In general terms alloyed nanoclusters were obtained. The enrichment of Pt layers obtained during the dynamic simulations could be easily explained by the activation energy for diffusion of Pt atoms on Cu. Both, thermodynamic and kinetic parameter (exchange energy and activation energy) confirms the existence

of alloyed CuPt nanoparticles. The morphologies obtained with the simulations are in good agreement with the experimental findings.

Supporting Information

Supporting Information File 1

Additional experimental data.
[http://www.beilstein-journals.org/bjnano/content/supplementary/2190-4286-5-150-S1.pdf]

Acknowledgements

This work was supported by grants from the National Center for Research Resources (5 G12RR013646-12) and the National Institute on Minority Health and Health Disparities (G12MD007591) from the National Institutes of Health The authors would like to acknowledge to the NSF for support with grants DMR-1103730, "Alloys at the Nanoscale: The Case of Nanoparticles Second Phase and PREM: NSF PREM Grant # DMR 0934218; "Oxide and Metal Nanoparticles- The Interface Between Life Sciences and Physical Sciences". In addition, the authors would like to acknowledge the support of the Welch Foundation (grant No. AX-1615, "Controlling the Shape and Particles Using Wet Chemistry Methods: The Case of Bimetallic Nanoparticles". MMM wish to thank CONICET PIP 11220110100992, Universidad Nacional de Córdoba, ANPCyT Program BID (PICT 2010-1233) for financial support. SMR acknowledge support from Conacyt, through the CIAM program (project 148967). The authors acknowledge the Texas Advanced Computing Center (TACC).

References

1. Ferrando, R.; Jellinek, J.; Johnston, R. L. *Chem. Rev.* **2008,** *108,* 845–910. doi:10.1021/cr040090g
2. Koh, S.; Leisch, J.; Toney, M. F.; Strasser, P. *J. Phys. Chem. C* **2007,** *111,* 3744–3752. doi:10.1021/jp067269a
3. Lim, B.; Jiang, M.; Camargo, P. H. C.; Cho, E. C.; Tao, J.; Lu, X.; Zhu, Y.; Xia, Y. *Science* **2009,** *324,* 1302–1305. doi:10.1126/science.1170377
4. Gupta, G.; Slanac, D. A.; Kumar, P.; Wiggins-Camacho, J. D.; Wang, X.; Swinnea, S.; More, K. L.; Dai, S.; Stevenson, K. J.; Johnston, K. P. *Chem. Mater.* **2009,** *21,* 4515–4526. doi:10.1021/cm901203n
5. Greeley, J.; Stephens, I.; Bondarenko, A.; Johansson, T. P.; Hansen, H. A.; Jaramillo, T.; Rossmeisl, J.; Chorkendorff, I.; Nørskov, J. K. *Nat. Chem.* **2009,** *1,* 552–556. doi:10.1038/nchem.367
6. Khanal, S.; Casillas, G.; Velazquez-Salazar, J. J.; Ponce, A.; Jose-Yacaman, M. *J. Phys. Chem. C* **2012,** *116,* 23596–23602. doi:10.1021/jp3092418
7. Ding, Y.; Gao, Y.; Wang, Z. L.; Tian, N.; Zhou, Z.-Y.; Sun, S.-G. *Appl. Phys. Lett.* **2007,** *91,* 121901–121903. doi:10.1063/1.2785953
8. Tian, N.; Zhou, Z.-Y.; Sun, S.-G.; Ding, Y.; Wang, Z. L. *Science* **2007,** *316,* 732–735. doi:10.1126/science.1140484
9. Bhattarai, N.; Casillas, G.; Khanal, S.; Salazar, J. J.; Ponce, A.; Jose-Yacaman, M. *J. Nanopart. Res.* **2013,** *15,* 1–13. doi:10.1007/s11051-013-1660-z
10. Khanal, S.; Casillas, G.; Bhattarai, N.; Velázquez-Salazar, J. J.; Santiago, U.; Ponce, A.; Mejía-Rosales, S.; José-Yacamán, M. *Langmuir* **2013,** *29,* 9231–9239. doi:10.1021/la401598e
11. Bhattarai, N.; Casillas, G.; Khanal, S.; Bahena, D.; Velazquez-Salazar, J. J.; Mejia, S.; Ponce, A.; Dravid, V. P.; Whetten, R. L.; Mariscal, M. M.; Jose-Yacaman, M. *MRS Commun.* **2013,** *3,* 177–183. doi:10.1557/mrc.2013.30
12. Khanal, S.; Bhattarai, N.; Velazquez-Salazar, J. J.; Bahena, D.; Soldano, G.; Ponce, A.; Mariscal, M. M.; Mejia-Rosales, S.; Jose-Yacaman, M. *Nanoscale* **2013,** *5,* 12456–12463. doi:10.1039/c3nr03831a
13. Vo-Dinh, T., Ed. *Nanotechnology in biology and medicine: methods, devices, and applications;* CRC Press: Boca Raton: FL, USA, 2007. doi:10.1201/9781420004441
14. Sasaki, K.; Naohara, H.; Cai, Y.; Choi, Y. M.; Liu, P.; Vukmirovic, M. B.; Wang, J. X.; Adzic, R. R. *Angew. Chem., Int. Ed.* **2010,** *49,* 8602–8607. doi:10.1002/anie.201004287
15. Service, R. F. *Science* **2007,** *315,* 172. doi:10.1126/science.315.5809.172
16. Peng, Z.; Yang, H. *Nano Today* **2009,** *4,* 143–164. doi:10.1016/j.nantod.2008.10.010
17. Khanal, S.; Bhattarai, N.; McMaster, D.; Bahena, D.; Velazquez-Salazar, J. J.; Jose-Yacaman, M. *Phys. Chem. Chem. Phys.* **2014,** *16,* 16278–16283. doi:10.1039/C4CP02208D
18. Bianchi, C. L.; Canton, P.; Dimitratos, N.; Porta, F.; Prati, L. *Catal. Today* **2005,** *102–103,* 203–212. doi:10.1016/j.cattod.2005.02.003
19. Li, C.; Yamauchi, Y. *Phys. Chem. Chem. Phys.* **2013,** *15,* 3490–3496. doi:10.1039/c3cp44313b
20. Chen, A.; Holt-Hindle, P. *Chem. Rev.* **2010,** *110,* 3767–3804. doi:10.1021/cr9003902
21. Liu, Y.; Chi, M.; Mazumder, V.; More, K. L.; Soled, S.; Henao, J. D.; Sun, S. *Chem. Mater.* **2011,** *23,* 4199–4203. doi:10.1021/cm2014785
22. Wang, L.; Yamauchi, Y. *J. Am. Chem. Soc.* **2010,** *132,* 13636–13638. doi:10.1021/ja105640p
23. Wang, H.; Xu, C.; Cheng, F.; Zhang, M.; Wang, S.; Jiang, S. P. *Electrochem. Commun.* **2008,** *10,* 1575–1578. doi:10.1016/j.elecom.2008.08.011
24. Li, Y.; Wang, Z. W.; Chiu, C.-Y.; Ruan, L.; Yang, W.; Yang, Y.; Palmer, R. E.; Huang, Y. *Nanoscale* **2012,** *4,* 845–851. doi:10.1039/c1nr11374g
25. Steele, B. C.; Heinzel, A. *Nature* **2001,** *414,* 345–352. doi:10.1038/35104620
26. Long, N. V.; Duy Hien, T.; Asaka, T.; Ohtaki, M.; Nogami, M. *Int. J. Hydrogen Energy* **2011,** *36,* 8478–8491. doi:10.1016/j.ijhydene.2011.03.140
27. Mani, P.; Srivastava, R.; Strasser, P. *J. Power Sources* **2011,** *196,* 666–673. doi:10.1016/j.jpowsour.2010.07.047
28. Marković, N. M.; Ross, P. N. *Electrochim. Acta* **2000,** *45,* 4101–4115. doi:10.1016/S0013-4686(00)00526-0
29. Ward, M. D. *Science* **2003,** *300,* 1104–1105. doi:10.1126/science.1084940
30. Schlapbach, L.; Züttel, A. *Nature* **2001,** *414,* 353–358. doi:10.1038/35104634
31. Lauhon, L. J.; Gudiksen, M. S.; Wang, D.; Lieber, C. M. *Nature* **2002,** *420,* 57–61. doi:10.1038/nature01141

32. Wu, J.; Gross, A.; Yang, H. *Nano Lett.* **2011,** *11,* 798–802. doi:10.1021/nl104094p
33. Guo, S.; Li, D.; Zhu, H.; Zhang, S.; Markovic, N. M.; Stamenkovic, V. R.; Sun, S. *Angew. Chem., Int. Ed.* **2013,** *52,* 3465–3468. doi:10.1002/anie.201209871
34. Yun, K.; Cho, Y.-H.; Cha, P.-R.; Lee, J.; Nam, H.-S.; Oh, J. S.; Choi, J.-H.; Lee, S.-C. *Acta Mater.* **2012,** *60,* 4908–4916. doi:10.1016/j.actamat.2012.05.032
35. Yu, F.; Zhou, W. *Prog. Nat. Sci.* **2013,** *23,* 331–337. doi:10.1016/j.pnsc.2013.04.009
36. Su, L.; Shrestha, S.; Zhang, Z.; Mustain, W.; Lei, Y. *J. Mater. Chem. A* **2013,** *1,* 12293–12301. doi:10.1039/c3ta13097e
37. Xu, D.; Bliznakov, S.; Liu, Z.; Fang, J.; Dimitrov, N. *Angew. Chem.* **2010,** *122,* 1304–1307. doi:10.1002/ange.200905248
38. Xu, D.; Liu, Z.; Yang, H.; Liu, Q.; Zhang, J.; Fang, J.; Zou, S.; Sun, K. *Angew. Chem., Int. Ed.* **2009,** *48,* 4217–4221. doi:10.1002/anie.200900293
39. Mohl, M.; Dobo, D.; Kukovecz, A.; Konya, Z.; Kordas, K.; Wei, J.; Vajtai, R.; Ajayan, P. M. *J. Phys. Chem. C* **2011,** *115,* 9403–9409. doi:10.1021/jp112128g
40. Xu, D.; Bliznakov, S.; Liu, Z.; Fang, J.; Dimitrov, N. *Angew. Chem., Int. Ed.* **2010,** *49,* 1282–1285. doi:10.1002/anie.200905248
41. Xu, D.; Liu, Z.; Yang, H.; Liu, Q.; Zhang, J.; Fang, J.; Zou, S.; Sun, K. *Angew. Chem.* **2009,** *121,* 4281–4285. doi:10.1002/ange.200900293
42. Strasser, P.; Koh, S.; Anniyev, T.; Greeley, J.; More, K.; Yu, C.; Liu, Z.; Kaya, S.; Nordlund, D.; Ogasawara, H. *Nat. Chem.* **2010,** *2,* 454–460. doi:10.1038/nchem.623
43. Mariscal, M.; Leiva, E.; Pötting, K.; Schmickler, W. *Appl. Phys. A* **2007,** *87,* 385–389. doi:10.1007/s00339-007-3915-y
44. Schmickler, W.; Pötting, K.; Mariscal, M. *Chem. Phys.* **2006,** *320,* 149–154. doi:10.1016/j.chemphys.2005.07.005
45. Allen, P.; Tildesley, D. J. *Computer Simulation of Liquids;* Clarendon: Oxford, UK, 1987.
46. Zhou, X.; Johnson, R.; Wadley, H. *Phys. Rev. B* **2004,** *69,* 144113. doi:10.1103/PhysRevB.69.144113
47. Ferrer, D.; Torres-Castro, A.; Gao, X.; Sepúlveda-Guzmán, S.; Ortiz-Méndez, U.; José-Yacamán, M. *Nano Lett.* **2007,** *7,* 1701–1705. doi:10.1021/nl070694a
48. Lim, B.; Wang, J.; Camargo, P. H. C.; Jiang, M.; Kim, M. J.; Xia, Y. *Nano Lett.* **2008,** *8,* 2535–2540. doi:10.1021/nl8016434
49. Brandt, E. *J. Phys.: Condens. Matter* **1989,** *1,* 10003. doi:10.1088/0953-8984/1/50/003

License and Terms

BEILSTEIN JOURNAL OF NANOTECHNOLOGY

Microstructural and plasmonic modifications in Ag–TiO_2 and Au–TiO_2 nanocomposites through ion beam irradiation

Venkata Sai Kiran Chakravadhanula[1,§], Yogendra Kumar Mishra[2], Venkata Girish Kotnur[1,¶], Devesh Kumar Avasthi[3], Thomas Strunskus[1], Vladimir Zaporotchenko[1], Dietmar Fink[4], Lorenz Kienle[5] and Franz Faupel[*1]

Full Research Paper

Open Access

Address:
[1]Chair for Multicomponent Materials, Institute for Materials Science, Christian Albrechts University Kiel, Kaiserstr. 2, Kiel, 24143, Germany, [2]Functional Nanomaterials, Institute for Materials Science, Christian Albrechts University Kiel, Kaiserstr. 2, Kiel, 24143, Germany, [3]Inter University Accelerator Center, Materials Science Group, P.O. Box: 10502, New Delhi, 110067, India, [4]Instituto da Fisica, Universidad Autonoma Metropolitana–Iztapalapa, Av. San Rafael Atlixco No. 186, Col. Vicentina, Delegacion Iztapalapa, Mexico D.F., 09340, Mexico and [5]Synthesis and Real Structure, Institute for Materials Science, Christian Albrechts University Kiel, Kaiserstr. 2, Kiel, 24143, Germany

Email:
Franz Faupel[*] - ff@tf.uni-kiel.de

* Corresponding author
§ Presently at Helmholtz Institute Ulm (HIU) Electrochemical Energy Storage, Albert-Einstein-Allee 11, 89081 Ulm, Germany
¶ Presently at Precision and Microsystems Engineering, Delft University of Technology, Mekelweg 2, 2628 CD DELFT, The Netherlands.

Keywords:
noble metal–titania nanocomposite; surface plasmon resonance; swift heavy ions

Beilstein J. Nanotechnol. **2014,** *5,* 1419–1431.
doi:10.3762/bjnano.5.154

Received: 12 May 2014
Accepted: 01 August 2014
Published: 01 September 2014

This article is part of the Thematic Series "Physics, chemistry and biology of functional nanostructures II".

Guest Editor: A. S. Sidorenko

Abstract

The development of new fabrication techniques of plasmonic nanocomposites with specific properties is an ongoing issue in the plasmonic and nanophotonics community. In this paper we report detailed investigations on the modifications of the microstructural and plasmonic properties of metal–titania nanocomposite films induced by swift heavy ions. Au–TiO_2 and Ag–TiO_2 nanocomposite thin films with varying metal volume fractions were deposited by co-sputtering and were subsequently irradiated by 100 MeV Ag^{8+} ions at various ion fluences. The morphology of these nanocomposite thin films before and after ion beam irradiation has been investigated in detail by transmission electron microscopy studies, which showed interesting changes in the titania matrix. Additionally, interesting modifications in the plasmonic absorption behavior for both Au–TiO_2 and Ag–TiO_2 nanocomposites were observed, which have been discussed in terms of ion beam induced growth of nanoparticles and structural modifications in the titania matrix.

Introduction

Metal nanoparticles embedded in dielectric matrices in the form of nanocomposites have gained significant research interest due their multifunctional properties appropriate for various applications ranging from solar cells to targeted drug delivery [1-4]. The plasmonic properties of the nanocomposite films mainly depend upon the type of nanoparticles (Au or Ag), their morphology and the dielectric constant of the embedding matrix [5,6]. As the dielectric constant in the expression for extinction coefficient (denominator), hence the refractive index of the matrix plays a very important role in surface plasmon resonance (SPR). Several dielectric matrices, such as SiO_2 and polymers have been utilized to fabricate different multifunctional nanocomposites for different applications [7-9]. Generally, the main motivation behind the use of an insulating matrix is to maintain the necessary separation between metal nanoparticles (resulting from differences in surface energy of the individual components), thereby preventing an agglomeration of the metallic nanoparticles. However, further functionalities are added to the nanocomposite system if semiconducting matrices are used, in which the dielectric properties of the matrix allows for a better tunability of SPR. In this regard, the use of semiconducting matrices, such as SnO_2 [10], ZnO [11] and CdS [12] for the embedding of noble metal nanoparticles has shown great potential.

Thin films and nanostructures of TiO_2 are probably one of the most investigated systems for different applications, such as memristors, dye-sensitized solar cells, antibacterial coatings, photocatalysts, and implants [13-18]. The different properties of metal–TiO_2 nanocomposites mainly depend on the metal volume filling fraction and the stoichiometry of the matrix. Generally, once the nanocomposites are prepared their properties are fixed. It is therefore very difficult to further modify the plasmonic response of these already synthesized nanocomposites. An additional fabrication experiment with slightly modified parameters might help. In this regards, the use of swift heavy ions (SHI) in order to modify the properties of the prepared nanocomposites in a controlled manner by selecting appropriate ion energies and fluences is a promising alternative [19]. The use of SHI has already shown its potential for controlling the morphology of the metal nanoparticles embedded in a silica matrix [20-26]. So far, in these experiments the chosen matrix was silica because of the fact that the effect of swift heavy ion irradiation of silica in terms of creating an ion track is well understood [27-29]. To summarize, the nanoparticles grow in size if they are close to each other and their sizes are smaller than the diameter of ion track, whereas if the inter particle distance is larger a size reduction occurs. If the particles are larger than the diameter of ion track, but smaller than a particular size, they elongate along the ion beam direction, resulting in parallel elongated nanoparticles [22,27,30-32]. SHI irradiation can result in reduction, growth, or elongation of nanoparticles in a controlled manner and thereby facilitating the tuning of the SPR wavelength of the nanocomposite system. In the scenario described here, the aim was to study the swift heavy ion irradiation of noble metal nanoparticles embedded in a matrix, in which the formation of ion tracks is not known to occur. Under this premise, we picked a TiO_2 matrix. Unlike silica, SHI irradiation might introduce several other types of structural changes in the TiO_2 matrix, which in turn affect the plasmonic properties of the nanocomposite system [17]. The detailed structural modifications and changes of optical properties of pure titania thin films under SHI irradiations have been already investigated [17,33-37]. Detailed understandings about the modification of metal–SiO_2 and metal–polymer nanocomposites under SHI irradiation have already been reported but such studies about metal–TiO_2 nanocomposites would be very interesting. Titania is a wide band gap semiconductor, and the tuning of the SPR in such a matrix by ion beam irradiation is another aim of the present work. Hence, the effects of swift heavy ion irradiation on metal–TiO_2 nanocomposites at different ion beam fluences has been studied and discussed here.

Results and Discussion

The microstructural morphologies of Au–TiO_2 nanocomposites with metal volume filling fractions (MVF) from 7 to 50% were investigated by transmission electron microscopy (TEM) studies and are shown in Figure 1. With the increase of the Au MVF from 7 to 13%, the average diameter of the Au nanoparticles increased and for an extreme case, in which the Au MVF was about 50%, the growth of extremely large nanoparticles has been observed (Figure 1d). The selected area electron diffraction patterns corresponding to each nanocomposite film are shown below the bright-field TEM images. They demonstrate that the TiO_2 matrix in the nanocomposite film is in an amorphous state.

In similar manner, Ag–TiO_2 nanocomposite thin films with varying Ag MVF (from 15 to 47%) have been synthesized and the corresponding bright-field TEM images are shown in Figure 2. A closer look at all TEM images in Figure 2 reveals the growth of smaller as well as larger Ag nanoparticles during co-sputtering process and the average diameter of Ag nanoparticles increases with increasing Ag metal volume fraction. In fact a deeper look at the TEM images of Au–TiO_2 nanocomposites (Figure 1) also confirmed the growth of smaller Au nanoparticles apart from the clearly visible ones (those with dark contrast in the bright field TEM images). Such type of Ag nanoparticle growth has also been observed in other matrices, e.g., SiO_2

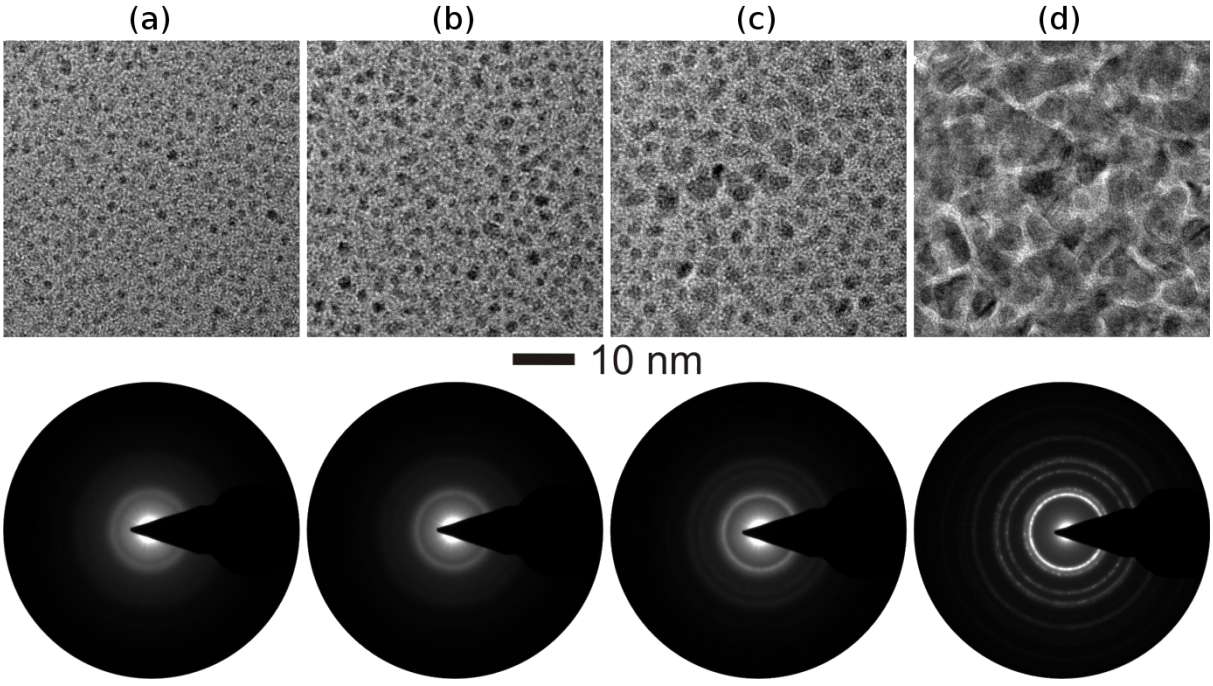

Figure 1: Bright-field TEM images of Au–TiO_2 nanocomposite thin films with different MVFs, (a) 7%, (b) 11%, (c) 13% and (d) 50%. In these bright-field TEM images, dark and bright areas correspond to the Au nanoparticles and the TiO_2 matrix, respectively. The selected area electron diffraction (SAED) patterns corresponding to each MVF composite is shown exactly below each TEM image.

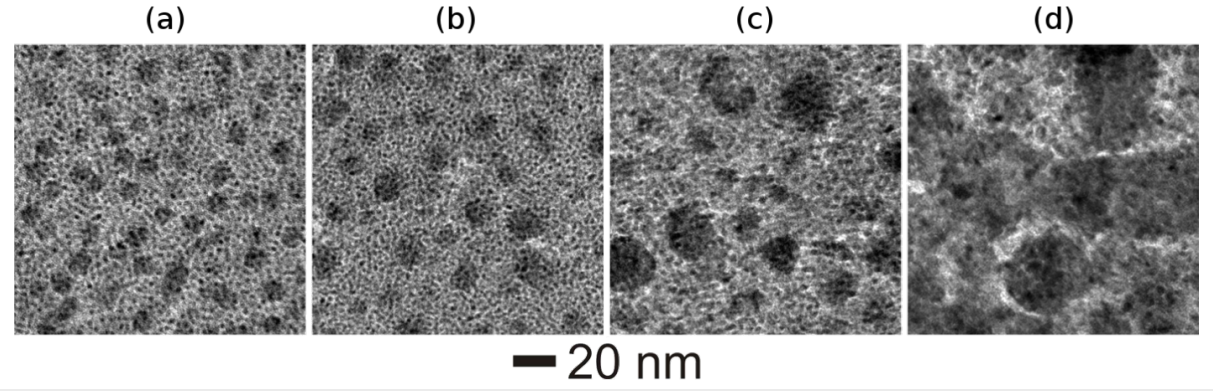

Figure 2: Bright field TEM morphologies of Ag–TiO_2 nanocomposite films with different metal volume filling fractions, (a) 15%, (b) 26%, (c) 34% and (d) 47%.

[38]. The dark and bright contrasts in the TEM image correspond to Ag nanoparticles and TiO_2 matrix, respectively.

Detailed investigations on the particle size distribution of the Ag nanoparticles embedded in a TiO_2 matrix have been performed by 3D-tomography studies [39,40]. Tomography results have confirmed the bimodal distribution of Ag nanoparticles with the presence of larger nanoparticles on top of the surface and smaller nanoparticles embedded inside the matrix.

To investigate the effect of ion irradiation on metal–TiO_2 nanocomposites, the deposited Au–TiO_2 and Ag–TiO_2 nanocomposite films (both with MVF ≈ 15%) were selected. Nanocomposite films with 15% metal volume fraction were intentionally chosen because of the intermediate values of inter-particle separation (IPS) between the metal nanoparticles. Nanoparticle size and inter-particle separation are the two very important parameters responsible for dissolution, growth or elongation of nanoparticles due to SHI irradiation. For a nanocomposite with relatively small nanoparticle diameter (smaller than the ion track diameter) and larger IPS, the dissolution of nanoparticles occurs due to SHI irradiation [22]. However if the IPS distance is very low, a growth of nanoparticles occurs under ion irradiation irrespective of the particle

diameter. Elongation of metal nanoparticles along the ion beam direction in the nanocomposite has been observed mostly for the cases when the average diameter of nanoparticles was equal to or larger than the ion track diameters [25]. The host matrix of the nanocomposite film plays a very important role during swift heavy ion irradiation. Due to unpredictive nature of the TiO_2 matrix, Au–TiO_2 (MVF ≈ 15%) and Ag–TiO_2 (MVF ≈ 15%) nanocomposites were selected for study as in both nanocomposites isolated nanoparticles embedded in TiO_2 matrix can be observed (Figure 1 and Figure 2) and the IPS distances are also not too large.

Bright-field TEM images of 100 MeV Ag^{8+} ion irradiated Au–TiO_2 (MVF ≈ 15%) at different fluences are shown in Figure 3. In a pristine nanocomposite film, Au nanoparticles are well separated (Figure 3a) with average diameter of around 2 nm (see the size distribution corresponding to Figure 3a). An increase of the average diameter of Au nanoparticles from 2 to 7 nm has been observed after irradiation with fluences up to 1×10^{13} ions/cm^2 as can be seen in bright-field TEM images (Figure 3b-d) and the corresponding size distributions.

The TEM image of the Au–TiO_2 nanocomposite irradiated at the lowest fluence (1×10^{12} ions/cm^2, Figure 3b) demonstrates the local growth growth of Au nanoparticles. The average diameter of the nanoparticle did not increase much but the density of nanoparticles has significantly increased. The local growth of the nanoparticle under SHI irradiation is attributed to the fact that the co-sputtered nanocomposite film exhibits a bi-modal distribution of nanoparticles. In the pristine sample along with visible nanoparticles (Figure 3a), single atoms, clusters and small nanoparticles of Au, which could not contribute to the nucleation and growth process, are also present, which could not contribute to nucleation and growth process. The electronic energy deposited by ions is converted into thermal energy, which enhances the process of nucleation and growth of metal nanoparticles in the nanocomposite film and hence more Au nanoparticles can be observed in the bright-field TEM image (in Figure 3b) corresponding to fluence 1×10^{12} ions/cm^2. With an increase in ion fluence to 3×10^{12} ions/cm^2, further growth of Au nanoparticles takes place (Figure 3c). The average diameter of the nanoparticles has not much increased but the particle size distribution has broadened. The diameter of some nanoparticles even exceeds 6 nm, with more nanoparticles (Figure 3c) in the size range from 2 to 6 nm as compared to pristine state (Figure 3a) and those irradiated at 1×10^{12} ions/cm^2 (Figure 3b). It seems that an ion irradiation at about 3×10^{12} ions/cm^{2}initiates the agglomeration of smaller nanoparticles. Thereby, the resultant number of Au nanoparticles having larger diameters has increased as compared to pristine and that irradiated at lower fluences. Since this fluence (about 3×10^{12} ions/cm^2) almost corresponds to the track overlap value that results in the thermalization of the whole nanocomposite film, this kind of agglomeration (growth) behavior of Au nanoparticles in the Au–TiO_2 film can be expected. The bright-field TEM image corresponding to the Au–TiO_2

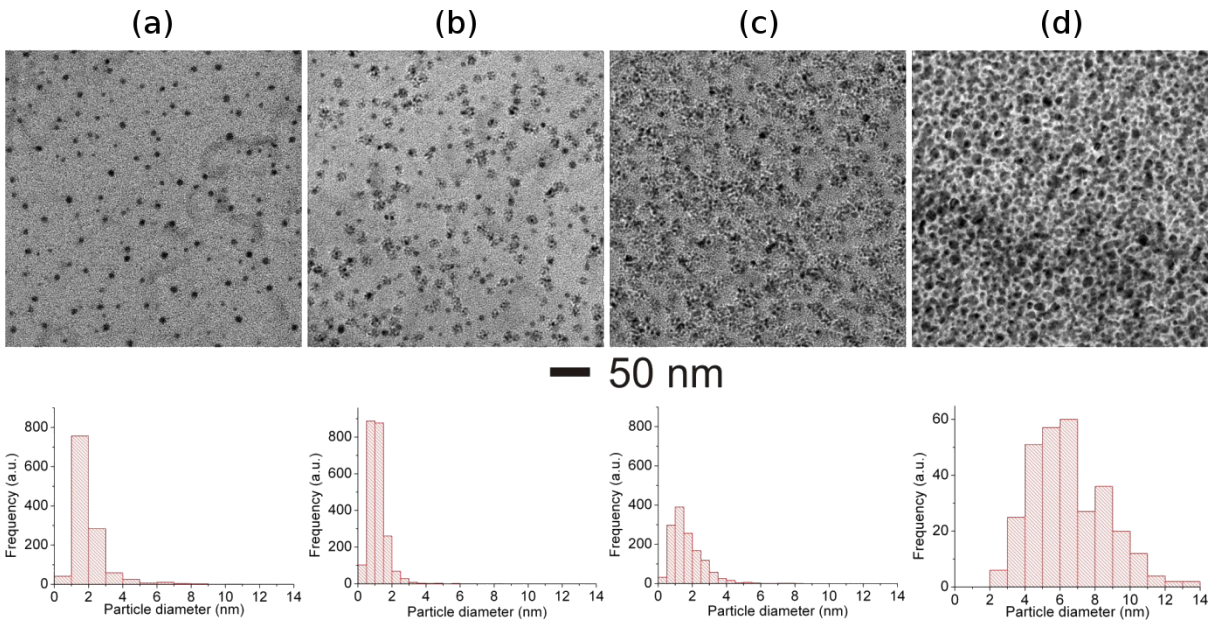

Figure 3: Morphological evolutions in Au–TiO_2 nanocomposite (MVF ≈ 15%) under 100 MeV Ag^{8+} ion irradiation at different fluences; Bright field TEM image of: (a) pristine film, (b) 1×10^{12} ions/cm^2, (c) 3×10^{12} ions/cm^2, (d) 1×10^{13} ions/cm^2. Size distributions corresponding to each TEM image are shown below the images.

nanocomposite (Figure 3d) irradiated at a yet higher fluence (about 1×10^{13} ions/cm^2) confirms the growth of large Au nanoparticles with diameters ranging up to 14 nm (size distribution in Figure 3d). Because of the agglomeration of the nanoparticles due to irradiation at high fluence, the particle density has been significantly reduced. Of course there exists a possibility of the sputtering of some metal nanoparticles from the surface of the nanocomposite due to ion irradiation. But it is very small and can be qualitatively ignored. However, accurate quantitative information requires precise ion beam experiments. It is important to emphasize here that there exists some nanoparticles with larger diameter in the pristine nanocomposite film (Figure 3c) which satisfy the condition of elongation [22]. However no elongation of nanoparticles been has been observed (conventional bright-field TEM image in Figure 3d) after irradiation up to a fluence of about 1×10^{13} ions/cm^2. Despite the fact that condition for elongation (particle size ≥ track size) holds true, no elongation of nanoparticles under ion irradiation has been observed and it is probably due to absence of a latent track formation mechanism because of the semiconducting nature of the matrix as compared to insulating matrices (e.g., SiO_2) in which ion tracks are usually formed [20,28,29,41].

Ion irradiation studies on Ag–TiO_2 nanocomposite (MVF ≈ 15%) film were also performed and corresponding bright-field TEM images are shown in Figure 4. The pristine Ag–TiO_2 nanocomposite sample exhibits Ag nanoparticles with a bi-modal particle size distribution (Figure 4a and the corresponding particle size distribution) [39,40]. After irradiation with 100 MeV Ag^{8+} ions at a fluence of about 1×10^{12} ions/cm^2, the average diameter of the Ag nanoparticles is increased indicating the growth of nanoparticles. A possible nanoparticle growth mechanism already discussed for Au–TiO_2 nanocomposites in the previous section holds true. In contrast to Au–TiO_2 system, the growth of Ag nanoparticles with relatively large diameters (Figure 4band corresponding particle size distribution) has been observed in Ag-TiO_2 nanocomposites after SHI irradiation. After irradiating at a fluence of 3×10^{12} ions/cm^2, a further growth of nanoparticles is observed and the density of the nanoparticles is reduced. This is obvious because smaller nanoparticles are agglomerated into bigger nanoparticles. Irradiation at the highest fluence of ca. 1×10^{13} ions/cm^2 results in the growth of Ag nanoparticles with very large diameters (up to ca. 26 nm) with a broad size distribution (Figure 4dand its particle size distribution). Since the particle size is very large, the effective density of nanoparticles has been significantly decreased because formation of larger nanoparticles occurs only at the expense of smaller nanoparticles. Similar to the Au–TiO_2 nanocomposites, no elongation of Ag nanoparticles in TiO_2 matrix, apart from the large diameters, has been observed even at the highest fluence apart.

The growth of Au and Ag nanoparticles in a TiO_2 matrix after ion irradiation with 100 MeV Ag^{8+} at different fluences has been demonstrated. However, the behavior of the TiO_2 matrix

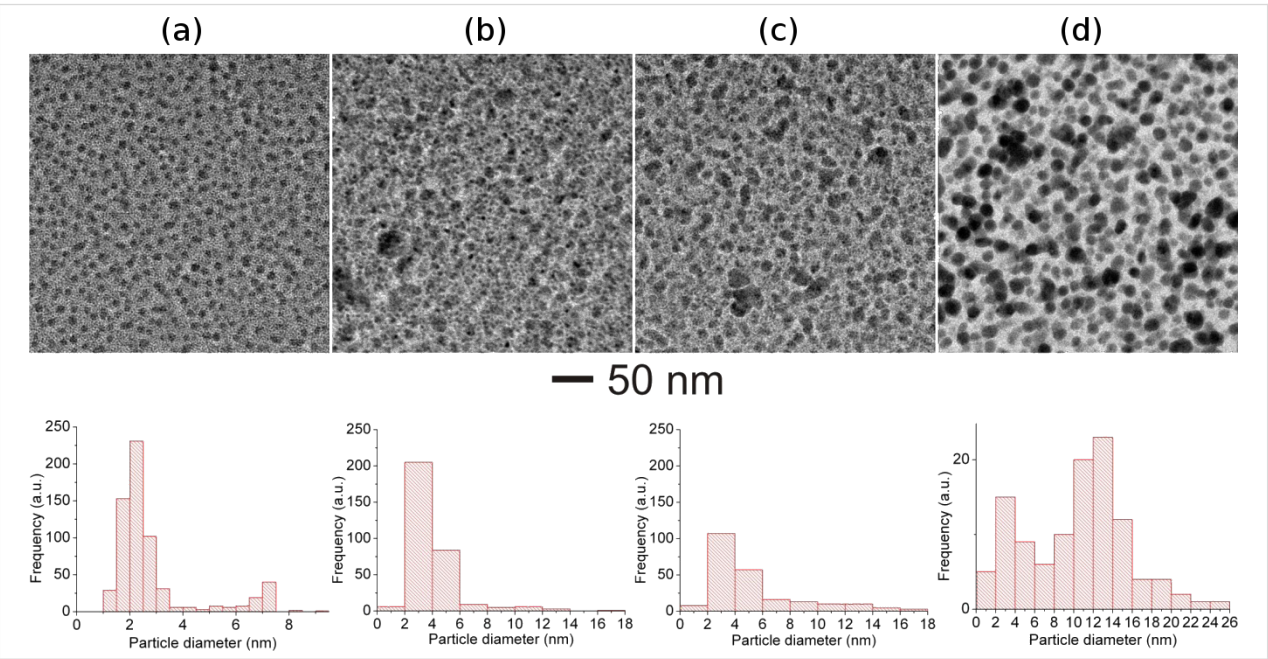

Figure 4: Morphological evolutions in Ag–TiO_2 nanocomposite films (MVF ≈ 15%) under 100 MeV Ag^{8+} ion irradiation at different fluences. Bright-field TEM image of: (a) pristine film, (b) 1×10^{12} ions/cm^2, (c) 3×10^{12} ions/cm^2, (d) 1×10^{13} ions/cm^2. The particle size distributions corresponding to each TEM image are shown below the images.

under ion irradiation is extremely important. In fact the matrix of the nanocomposite film plays a very important role in reduction, growth and elongation of metal nanoparticles by swift heavy ion irradiation. When a swift heavy ion passes through the film, it deposits a large amount of electronic energy, which is instantly converted into thermal energy and thus each ion creates an ion track along its path. The large amount of thermal energy deposited by the ions results in a cylindrical zone along the ion path with very high temperatures. The corresponding temperature profile can be divided in two zones (i) the central zone, i.e., the ion path where the material is molten, and (ii) the surrounding zone where the matrix is not molten but the temperature is still high enough for metal nanoparticles to be in molten state. The formation of ion tracks in insulator matrices, e.g., SiO_2, has been understood in terms of thermal spike and Coulomb explosion models [26,41,42]. But SHI-induced modifications in metal–semiconducting matrices like TiO_2 are still unclear as changes in the matrix strongly affect the response of the metal nanoparticles to the ion irradiation. It is most probable that due to the semiconducting nature of TiO_2, the formation of molten tracks does not occur and, hence, the elongation of nanoparticles is unexpected under SHI irradiation. However the large amount of electronic energy (S_e) deposited by the ions in the nanocomposite film is sufficient for the growth of nanoparticles (Figure 3 and Figure 4) as well as other structural changes in the TiO_2 matrix. In order to understand the SHI-induced effects, detailed microstructural studies of the Ag–TiO_2 nanocomposite (MVF ≈ 15%) film irradiated at different fluences (1×10^{12} to 1×10^{13} ions/cm^2) by using TEM and SAED analysis are shown in Figure 5.

The TiO_2 matrix in the as-deposited (pristine) film is amorphous as revealed by SAED pattern corresponding to bright-field TEM image of Figure 5a. After irradiation at fluences of 1×10^{12}, 3×10^{12} and 1×10^{13} ions/cm^2, an increase of the crystallinity of the TiO_2 matrix (metrics from brookite and rutile structures) has been observed from selected area electron diffraction patterns of Figure 5b–d. In addition, reflections corresponding to the metrics from TiO [43,44] were observed along with large TiO crystals after ion beam irradiation (see below in Figure 8 and Figure 9). Several studies on SHI-induced crystallization of amorphous TiO_2 thin films have been performed and it has been reported that under SHI irradiation, the crystallization evolves through the formation of TiO_2 nanocrystals in rutile and anatase phases [37,45]. In a similar study an increase of the dielectric constant of the TiO_2 film after 100 MeV Ag^{8+} ion irradiation has been reported. This is another evidence for the increasing crystallinity [35,46]. SHI-induced crystallization in nanocomposite films plays indeed a very strong role in the growth behavior of embedded metal nanoparticles in the nanocomposite film.

The optical properties of pristine as well as irradiated Au–TiO_2 nanocomposite films (with an MVF of about 7% and 15%) have

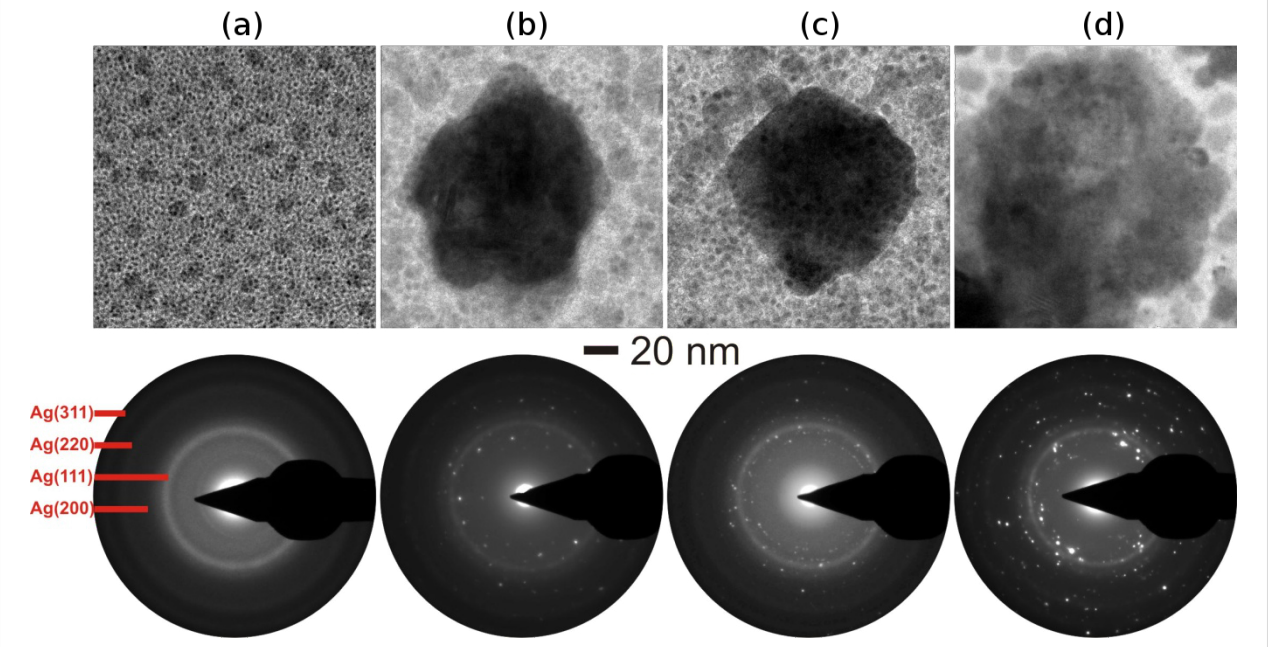

Figure 5: Microstructural changes in the TiO_2 matrix of the nanocomposite film with MVF (Ag) ≈ 15% induced by 100 MeV Ag^{8+} ions. Bright field TEM images corresponding to: (a) pristine film, (b) 1×10^{12} ions/cm^2, (c) 3×10^{12} ions/cm^2, (d) 1×10^{13} ions/cm^2. The selected area electron diffraction patterns with respect to pristine film (a) and different irradiation fluences are shown below. Crystallinity of the TiO_2 matrix has been observed as a result of the reflections corresponding to the metrics from brookite and rutile structures from the SAED patterns from (b) to (d).

been measured by using UV–visible spectroscopy and are discussed here. Figure 6 shows the SPR absorption spectra (a,b) and transmission spectra (c,d) of nanocomposite films with MVF ≈ 7% and 15%, respectively. After irradiation (up to 1×10^{13} ions/cm^2), the UV–visible spectra for both nanocomposites show a red shift of the SPR peak position. The shift of the SPR peak is larger for the nanocomposite film having a higher MVF ($\Delta\lambda \approx 35$ nm for MVF ≈ 7% and $\Delta\lambda \approx 60$ nm for MVF ≈ 15%, respectively). The transmission spectra for irradiated Au–TiO_2 nanocomposite films show that the transmission behavior for both nanocomposite films is only affected in the vicinity of TiO_2 and SPR band-edges. For higher wavelengths (beyond the tail of SPR absorption) the nanocomposites are almost transparent.

A closer look at the spectra in Figure 6a,b suggest that each spectrum mainly consists of two types of information, i.e., i) band-edge at lower wavelength (~320 nm) which is due to TiO_2 matrix and ii) a peak in the visible–near infrared region (from about 580 nm to 650 nm for the different spectra) that arises from surface plasmon resonance absorption due to electron density oscillations in Au nanoparticles induced by electric field vector of light. From Figure 6, it can be clearly observed that SHI irradiations induce significant changes in the Au–TiO_2 nanocomposite. With an increase in ion fluence the band-edge of TiO_2 matrix shifts to lower wavelengths, which indicates an improvement in crystallinity of the matrix. From Tauc plot analyses for both nanocomposites, a shift of ca. 0.1 eV in the band-edge energy of TiO_2 (between pristine and 1×10^{13} ions/cm^2) is observed, which also confirms the structural changes in the TiO_2 matrix. The red shift of the SPR peak, a slight narrowing of full width at half maximum (FWHM) and a simultaneous increase in SPR peak intensity with an increase in ion fluence are clear indications for the growth of Au nanoparticles in the nanocomposite film.

Similar to Au–TiO_2 nanocomposites, detailed UV–visible absorption and transmission studies for SHI-irradiated Ag–TiO_2 nanocomposites (MVF ca. 13% and 27%) at different fluences (1×10^{12}, 3×10^{12} and 1×10^{13} ions/cm^2) were performed and

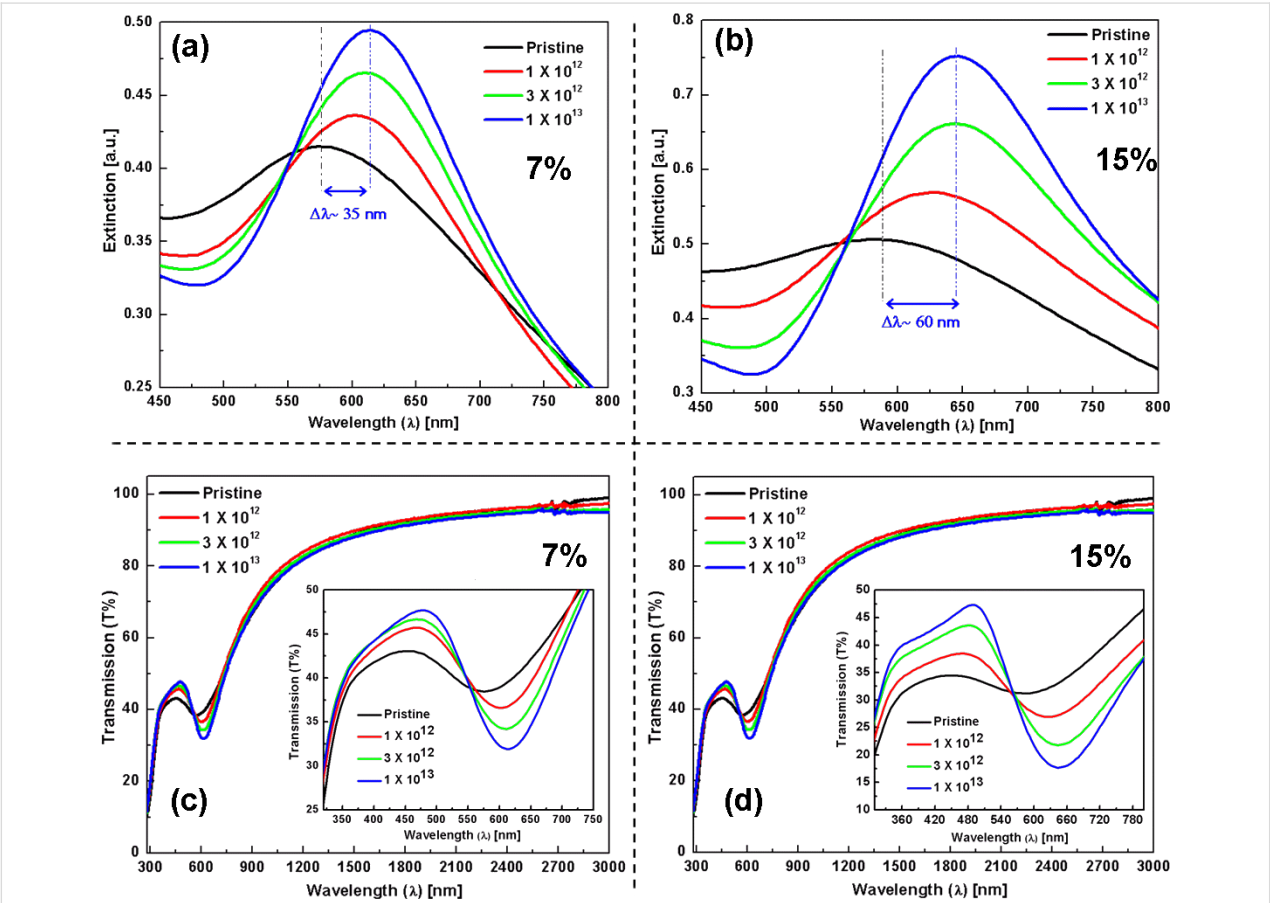

Figure 6: UV–visible absorption and transmission spectra of Au–TiO_2 nanocomposite films (with an MVF of about 7% and 15%, respectively) at different ion beam fluences (1×10^{12}, 3×10^{12} and 1×10^{13} ions/cm^2). (a,b) Variations in SPR absorption as a function of the ion beam fluence. (c,d) Transmission spectra of Au–TiO_2 nanocomposite films (corresponding to a and b) as a function of the ion beam fluence. The inset images (in c and d) show the magnified views from band-edge regions.

the corresponding results are shown in Figure 7. The variation in plasmonic response of these Ag–TiO_2 nanocomposites are shown in Figure 7a,b and a red shift ($\Delta\lambda \approx 45$ nm for 13% and $\Delta\lambda \approx 75$ nm for 27%, respectively) of the SPR peak has been observed after irradiation at 1×10^{13} ions/cm^2 fluence. The optical behaviour of the Ag–TiO_2 nanocomposite system is quite different as compared to Au–TiO_2 in terms of structural changes in the TiO_2 matrix (band-edge shift from Tauc plots are given in Supporting Information File 1, Figure S2 and Figure S3) and SPR peak positions after SHI irradiation. The shift of the band-edge of the TiO_2 matrix is very small and the SPR peaks have broadened (become larger with increase in MVF) after SHI irradiation. The SPR peak intensity for the nanocomposite film with lower volume fraction remains almost unchanged up to a fluence of 3×10^{12} ions/cm^2 and increases (Figure 7a) for the highest fluence. However, for the nanocomposite film with MVF ≈ 27%, a decrease in the SPR peak intensity is observed after ion irradiation. The transmission spectra of the Ag–TiO_2 nanocomposite films are shown in Figure 7c,d and it can be observed that trend is almost similar to that of Au–TiO_2 nanocomposites. However, the behavior in vicinity of the band-edges (TiO_2 and SPR) is quite different. The broadening of the SPR peaks of the Ag nanoparticles also affects the transmission behaviour of these nanocomposites. The change in transmission is almost negligible for the nanocomposite film with MVF ≈ 13%. However, with increase in MVF a reduction can be observed at different ion fluences.

The plasmonic behavior of metallic nanoparticles embedded in the nanocomposite films mainly depends on the following factors: i) morphology, IPS, size distribution of nanoparticles, and ii) the dielectric constant of the host matrix (TiO_2 in present case). It has already been demonstrated that the pristine nanocomposite films (Au–TiO_2 and Ag–TiO_2) in the present case exhibit bimodal particle size distributions [14] and that the TiO_2 matrix is amorphous (evident from SAED patterns). For bimodal particle size distribution, the detailed TEM analysis has demonstrated that big nanoparticles are on top of the surface,

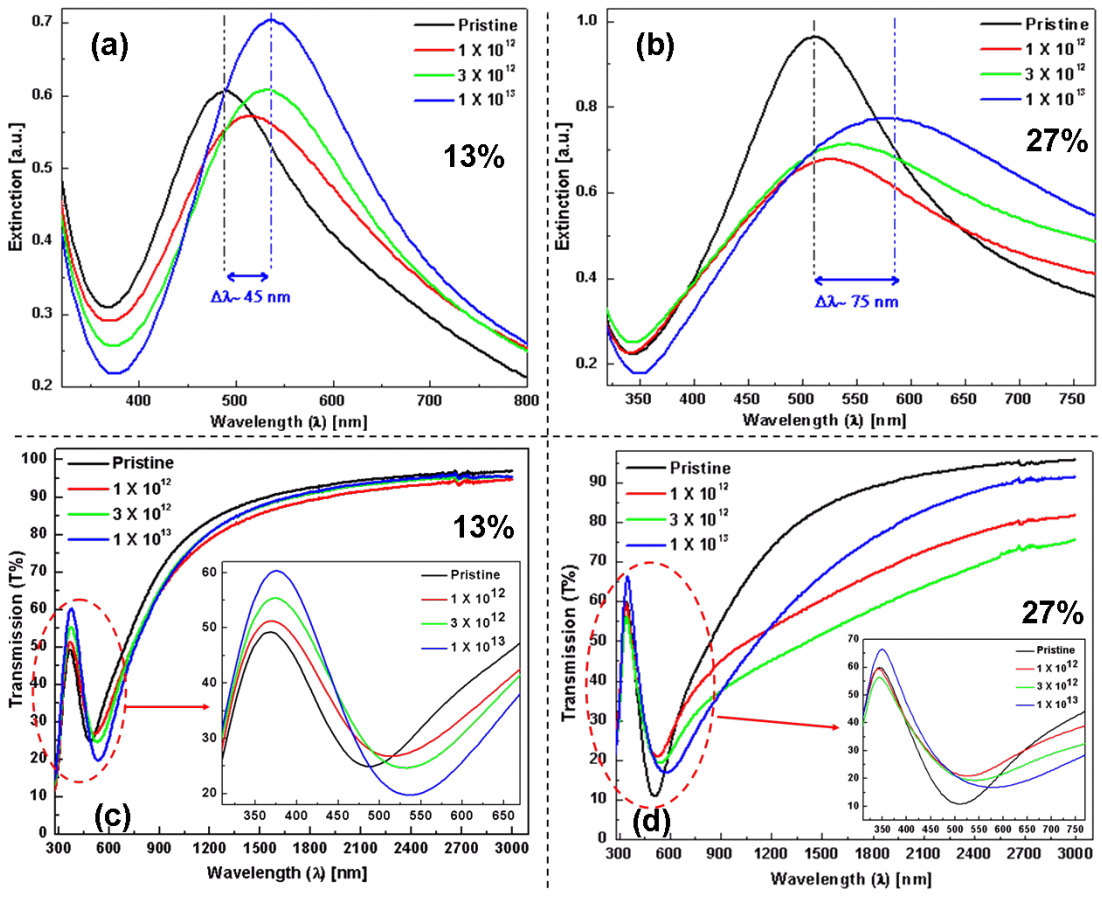

Figure 7: (a, b) UV–visible absorption spectra of Ag–TiO_2 nanocomposite films (MVF ca. 13% and 27%, respectively) as a function of the ion beam fluence (from 1×10^{12} to 1×10^{13} ions/cm^2). A red shift of the SPR peak of about 45 nm and 75 nm (for 13% and 27%, respectively) is observed after irradiation at the highest fluence. (c, d) Transmission spectra of Ag–TiO_2 nanocomposite films as a function of the ion beam fluence. Inset images (in c and d) are the magnified views corresponding to marked regions.

while the smaller ones are embedded inside the nanocomposite film [39,40]. In principle, one should observe a double SPR peak corresponding to the bimodal size distribution of the nanoparticles. But in the case studied here, since the number of larger nanoparticles is very low as compared to that of smaller ones, only one broad SPR peak is observed. It is very important to mention the dependence of the SPR on these parameters because under swift heavy ion irradiation all these parameters (size of nanoparticles, size distribution, and refractive index of TiO_2 matrix) are modified. Earlier studies have demonstrated that swift heavy ion irradiation can result in the reduction or growth of nanoparticles depending upon their size and inter-particle separations in the nanocomposite films [24]. In the Au–TiO_2 and Ag–TiO_2 nanocomposites studied here, the inter-particle separation is relatively small and, hence, the growth of nanoparticles has been observed after SHI irradiation as evident by TEM results and red shifts in SPR peaks. With increasing size of the nanoparticles, the SPR peak shows red shift. But, generally, the peak shift is not very large (Figure 6 and Figure 7). However, an increase in the refractive index of the matrix contributes to a large shift of the SPR peak position of the nanoparticles [47]. Earlier studies about SHI-induced modifications in TiO_2 thin films have reported structural transformations as well an increase of the dielectric constant [35]. The increase of the dielectric constant is a direct consequence of the increase in refractive index of the host matrix and contributes significantly to the red shift of the SPR peak positions. The area under the SPR curve is measure for the total number of nanoparticles present in the nanocomposite film. As mentioned above, there are, apart from nanoparticles visible in TEM, numerous atoms, clusters and smaller nanoparticles in the as-deposited films, which contribute to the further growth of new nanoparticles as well as an increase in the size of already existing nanoparticles. Therefore, after SHI irradiation, the number of nanoparticles is most likely increased which could also be responsible for the enhanced SPR absorption peak (Figure 6a,b and Figure 7a). As long as there are atomic species available to participate in nucleation and growth, the number of nanoparticles in the nanocomposite film will continuously increase with increasing ion beam fluence. When the irradiation fluence is increased beyond a certain threshold (so that almost all metallic species are consumed after irradiation), the resultant number of nanoparticles present in the nanocomposite film might decrease due to agglomeration of smaller nanoparticles into bigger ones as higher fluences directly correspond to a larger amount of thermal energy deposited in the nanocomposite film. For nanocomposite films with higher metal volume fractions, the growth behavior of the nanoparticles under SHI irradiation might be different as observed by the reduction in SPR intensity for the Ag–TiO_2 nanocomposite with MVF ≈ 27% in Figure 7b. When the metal volume fraction is high, there is a high probability for the formation of irregularly shaped Ag nanoparticles with decreased inter-particle distances (a tendency towards percolation). This will enhance the plasmonic coupling between the nanoparticles and lead to a broadening of the SPR peak which can be observed in Figure 7b. It is very important to mention here that for the TEM investigations the specimens were deposited on TEM grids, while for the SPR measurements glass substrates have been used. Therefore it will be difficult to correlate the total number of nanoparticles from the TEM size distribution with the observed SPR enhancements after SHI irradiation at different fluences. Therefore, the observed red-shifts of the SPR positions in the Au–TiO_2 and Ag–TiO_2 nanocomposite films studied here are due to cumulative effects from an increase in particle size, a change in the size distribution and, most significantly, because of structural changes in the host TiO_2 matrix.

During TEM measurements of the Ag–TiO_2 nanocomposite (MVF ≈ 13%) irradiated at 3×10^{12} ions/cm^2, the formation of some large sub-micron sized crystals with various morphologies were observed [48]. In addition, small TiO_x fragments were found at higher fluences. Since growth of Ag nanoparticle with such a large dimension was unexpected, detailed TEM investigations on these large particles were performed and measurements revealed that they were TiOx crystals. The TEM, SAED, and corresponding simulation pattern is shown in Figure 8. The detailed TEM, SAED, and EDAX studies confirmed the formation of crystalline TiO phase after SHI irradiation.

The formed crystals are of the order of 400 nm in size and exhibit a similar *d*-spacing as reported for TiO by Bartkowski et al. [49]. However, there are only very few reports, which describe the formation of TiO nanostructures through various methods [43,44]. Hence the fact that, in the present case, the formation of this phase briefly occurs and then vanishes again with increasing fluence can only be understood by the interaction of two different counteracting mechanisms evolving at different fluences. According to this postulation, at lower fluences, one observes the tendency towards the formation of TiO, with larger unaffected area. At higher fluences, one can see the destruction of the evolved TiO phase into fragments. According to this supposition, the emergence of double or multiple hits signifies phase destruction, the further increase in fluence leads to the destruction of that previously created TiO phase. From the SAED patterns (Figure 8), the [2 −1 −1] zone axis of the TiO phase agrees with the simulated results for TiO by using the JEMS software [50].

In spite of the well-known problems of the light elements' quantification by EDX, test measurements on distinct samples (e.g., amorphous TiO_2) point to a sufficient reliability of the setup for

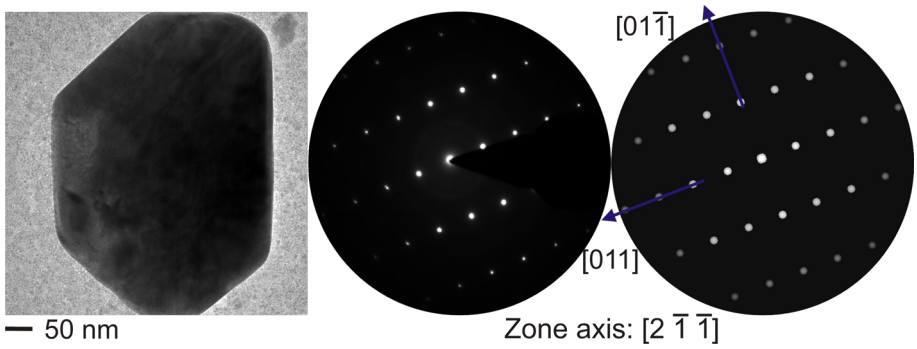

Figure 8: Micron-sized single crystalline TiO with the corresponding experimental SAED pattern and simulated SAED pattern.

a semi-quantitative interpretation. Hence, the EDX-nanoprobe analysis of the TEM (Figure 9) confirms that the ratio of Ti:O in the nanocomposite is 1:2 and that it is 1:1 in the nanocrystal. Interestingly, the desired equimolar ratio of Ti and O is well adjusted even on the nanoscale. But in order to confirm this, further SHI irradiation studies on these nanocomposites are required to be performed in a systematic manner and the same will be planned in future.

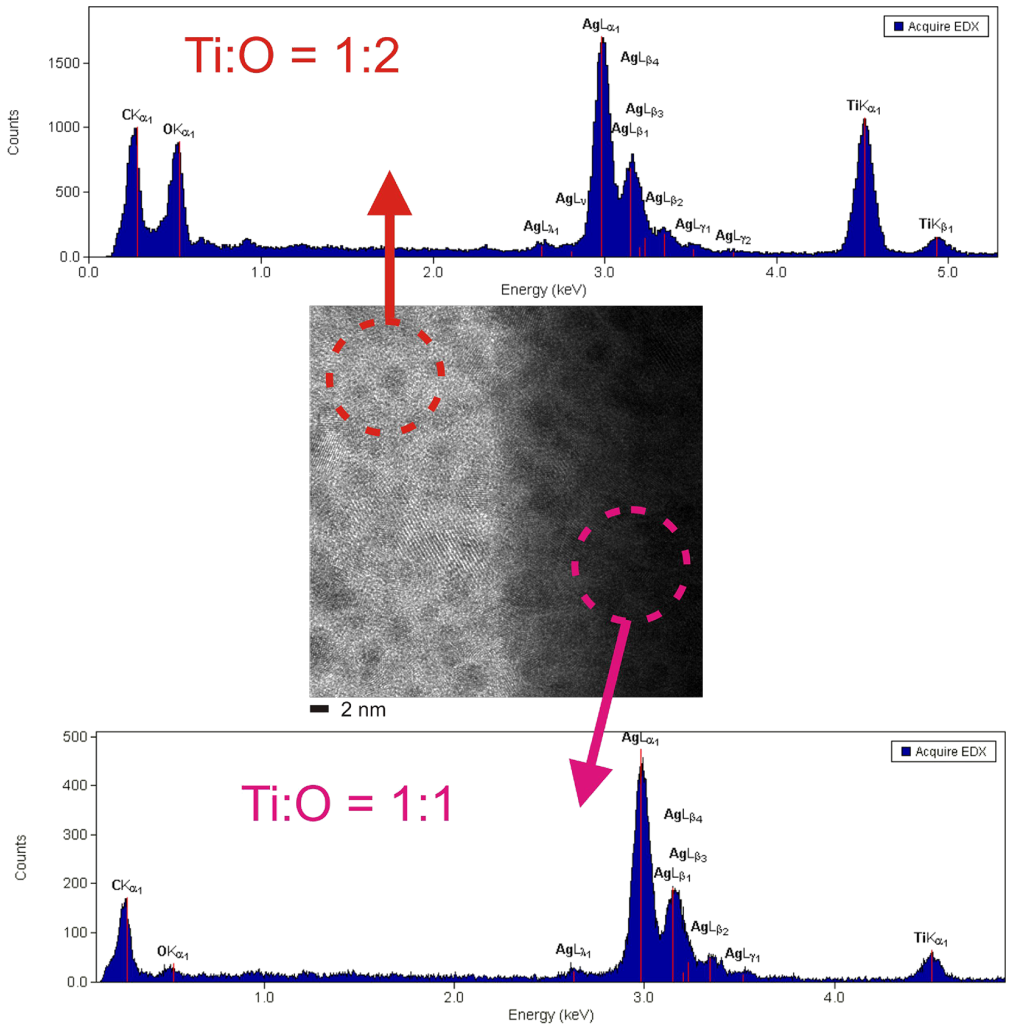

Figure 9: TEM nanoprobe EDX analysis on the TiO crystal and the matrix confirming the ratio of Ti:O in both the areas to be 1:1 and 1:2, respectively.

The formation of TiO nanostructures in the Ag–TiO_2 nanocomposites is only possible by SHI irradiation (this process is far from thermodynamic equilibrium) as compared to conventional heating experiments (in thermodynamic equilibrium) and it was also revealed by a comparative study involving the in situ heating of the Ag–TiO_2 nanocomposites in the TEM. From the in situ TEM heating experiments (Figure 10), crystallization of the matrix with the associated growth of the nanoparticles was observed.

On in situ heating, from room temperature to 500 °C, there is an increase in the size of the nanoparticles due to Ostwald ripening, (also observed after the in situ heating of Au–TiO_2 nanocomposites). In addition, evidence for the changes in the matrix at 500 °C can also be observed in the SAED patterns. Although signatures for the change in the matrix are evident right from 300 °C through the diffuse intensities corresponding to the reflections of the anatase form of TiO_2. At 500 °C, these appear as ring patterns confirming the crystallization of TiO_2 into the anatase type.

Conclusion

In conclusion, we have successfully fabricated Ag–TiO_2 and Au–TiO_2 nanocomposites with desired metal volume fractions in a controlled manner. The microstructural evolutions in the nanocomposite films by detailed TEM analysis revealed the bimodal size distribution of metal nanoparticles in as-deposited nanocomposite films with larger nanoparticles on the surface and smaller nanoparticles embedded inside the nanocomposite film. SHI irradiation of these nanocomposite films at different fluences resulted in an improvement in the crystalline nature of host TiO_2 matrix as well as growth in the average diameter of nanoparticles. Formation of different phases of the host TiO_2 matrix is also observed under SHI irradiation which is most likely due to structural transformations due to large amount of electronic energy deposited into the nanocomposite films. The growth of nanoparticles in the metal–titania nanocomposite films under swift heavy ion irradiation has been discussed in terms of dissolution and growth induced by large electronic energy deposition. The deposited thermal energy is sufficient to promote the growth of nanoparticles and the structural changes in the TiO_2 matrix. With increase in ion beam fluence, the growth of larger nanoparticles has been observed. Plasmonic properties of Au–TiO_2 and Ag–TiO_2 nanocomposite films before and after SHI irradiations always showed a red shift of the SPR peak position after irradiation. The red shift of the SPR peaks in the both nanocomposite films has been explained in terms of growth in size of nanoparticles as well structural transformations in the host TiO_2 matrix.

Experimental

Ag–TiO_2 and Au–TiO_2 nanocomposite thin films were prepared by co-sputtering from two different magnetron sources in a home-made vacuum deposition chamber. The host matrix (TiO_2) and metal (Ag/Au) targets were co-sputtered by using two different magnetron sources, i.e., RF and DC, respectively, in the chamber. The deposition chamber was evacuated to a base pressure of 10^{-7} mbar with the help of a rotary pump (for pre-vacuum) followed by turbo molecular pump (for high vacuum). Metal was deposited by the DC planar magnetron source ION'X 2UHV (Thin Film Consulting). A similar-type RF magnetron source was used for sputtering the copper-bonded titanium dioxide (Williams Advanced Materials) to prevent charging of the target. The deposition rates from both targets were in situ monitored by two independent quartz-crystal monitors. For TiO_2, the deposition rate was varied from 1 to 4 nm/min by varying the RF power, while in the case of Au/Ag, the deposition rates were varied from 0.5 to 3 nm/min

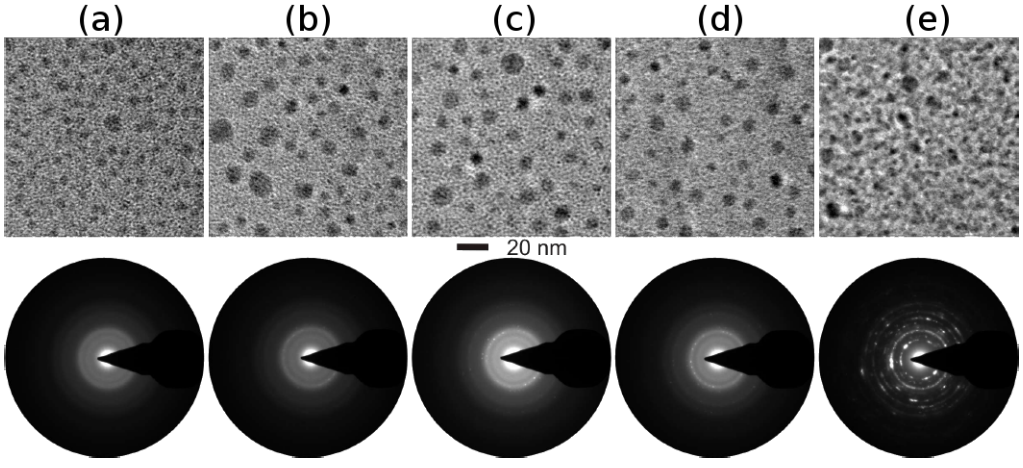

Figure 10: In situ heating of the Ag–TiO_2 nanocomposites at (a) room temperature (b) 150 °C, (c) 300 °C, (d) 400 °C and (e) 500 °C (total time: 3 h).

by changing the DC power. The metal volume fractions of the nanocomposite films were monitored by controlling the deposition rates of metal and matrix, respectively. The sample holder was rotated throughout the deposition process to achieve uniform and homogeneous deposition of all the samples mounted on the sample holder. The thickness of the deposited films was measured by a surface profilometer (Dektak 8000) by depositing the nanocomposite film on a masked silicon wafer. Subsequently, the metal volume fractions in the nanocomposite films were also determined by using energy dispersive X-ray spectrometer (SEM–EDX Philips XL30) with proper calibration. For characterization convenience, these nanocomposite films were simultaneously deposited at different substrates, e.g., glass (for UV–visible absorption), carbon-coated Cu grids (for TEM measurements) and Si substrates for EDX. The deposited Ag–TiO_2 and Au–TiO_2 nanocomposite films with different MVFs (for gold: 7% and 15%, for silver: 13% and 27%) were irradiated by 100 MeV Ag^{8+} ions at different fluences (1×10^{12}, 3×10^{12}, 1×10^{13} ions/cm^2) by using the Pelletron accelerator facility at Inter University Accelerator Centre, New Delhi. The energy of the Ag ions was selected by "Stopping and range of ions in matter (SRIM) 2008" calculations [51]. The values of electronic energy loss (S_e) for 100 MeV Ag^{8+} ions in Au–TiO_2 (MVF ≈ 15%) and Ag–TiO_2 (MVF ≈ 13%) nanocomposites are about 14.9 and 13.9 keV/nm, respectively (Supporting Information File 1, Figure S1). The values of the corresponding nuclear energy losses for both of the cases are very small and can be neglected. Since the nanocomposite film thicknesses are very small, the S_e value can be assumed to be uniform all along the film thickness. To investigate the effect of ion irradiation, detailed characterizations of pristine as well as irradiated nanocomposite films on different substrates have been performed. The microstructural evolution of nanoparticles as well as of the host matrix in the nanocomposite films have been investigated by transmission electron microscopy (Philips Tecnai F30 G^2). Optical extinction studies of the nanocomposite films were carried out by using a UV–vis–NIR spectrophotometer (Perkin Elmer Lambda 900).

Supporting Information

Supporting Information File 1

Additional experimental data
[http://www.beilstein-journals.org/bjnano/content/supplementary/2190-4286-5-154-S1.pdf]

Acknowledgements

The authors acknowledge the discussions with Dr. Tomislav Hrkac and Dr. Andriy Lotnyk. German Science Foundation (DFG) and Department of Science and Technology (DST) are acknowledged towards the funding of the bilateral collaborative work. Special thanks to Prof. S. Cruz–Jimenez, UAM Mexico, for valuable discussions that lead to the postulated model for the formation of TiO. YKM mentions the postdoctoral grant from Alexander von Humboldt Foundation

References

1. Jain, P. K.; Huang, X.; El-Sayed, I. H.; El-Sayed, M. A. *Acc. Chem. Res.* **2008,** *41,* 1578. doi:10.1021/ar7002804
2. Jamali, M.; Hedayati, M. K.; Mozooni, B.; Javaherirahim, M.; Abdelaziz, R.; Zillohu, A. U.; Elbahri, M. *Adv. Mater.* **2011,** *23,* 4243. doi:10.1002/adma.201102353
3. Atwater, H. A.; Polman, A. *Nat. Mater.* **2010,** *9,* 205. doi:10.1038/nmat2629
4. Elbahri, M.; Hedayati, M. K.; Chakravadhanula, V. S. K.; Jamali, M.; Strunskus, T.; Zaporojtchenko, V.; Faupel, F. *Adv. Mater.* **2011,** *23,* 1993. doi:10.1002/adma.201003811
5. Kreibig, U.; Vollmer, M. *Optical properties of metal clusters;* Springer, 1995. doi:10.1007/978-3-662-09109-8
6. Quinten, M. *Optical Properties of Nanoparticle Systems;* Wiley-VCH, 2011. doi:10.1002/9783527633135
7. Caseri, W. *Macromol. Rapid Commun.* **2000,** *21,* 705. doi:10.1002/1521-3927(20000701)21:11<705::AID-MARC705>3.0.CO;2-3
8. Mohapatra, S.; Mishra, Y. K.; Avasthi, D. K.; Kabiraj, D.; Ghatak, J.; Varma, S. *J. Phys. D: Appl. Phys.* **2007,** *40,* 7063. doi:10.1088/0022-3727/40/22/030
9. Takele, H.; Greve, H.; Pochstein, C.; Zaporojtchenko, V.; Faupel, F. *Nanotechnology* **2006,** *17,* 3499. doi:10.1088/0957-4484/17/14/023
10. Wu, W.; Liao, L.; Zhang, S.; Zhou, J.; Xiao, X.; Ren, F.; Sun, L.; Dai, Z.; Jiang, C. *Nanoscale* **2013,** *5,* 5628. doi:10.1039/c3nr00985h
11. Mishra, Y. K.; Chakravadhanula, V. S. K.; Hrkac, V.; Jebril, S.; Agarwal, D. C.; Mohapatra, S.; Avasthi, D. K.; Kienle, L.; Adelung, R. *J. Appl. Phys.* **2012,** *112,* 064308. doi:10.1063/1.4752469
12. Liu, H.; Ye, F.; Ma, X.; Cao, H.; Yang, J. *CrystEngComm* **2013,** *15,* 7740. doi:10.1039/c3ce41187g
13. Lu, Q.; Lu, Z.; Lu, Y.; Lv, L.; Ning, Y.; Yu, H.; Hou, Y.; Yin, Y. *Nano Lett.* **2013,** *13,* 5698. doi:10.1021/nl403430x
14. Khan, M. M.; Ansari, S.; Amal, M. I.; Lee, J.; Cho, M. H. *Nanoscale* **2013,** *5,* 4427. doi:10.1039/c3nr00613a
15. Matsubara, K.; Tatsuma, T. *Adv. Mater.* **2007,** *19,* 2802. doi:10.1002/adma.200602823
16. Chen, X.; Mao, S. S. *Chem. Rev.* **2007,** *107,* 2891. doi:10.1021/cr0500535
17. Marjanović, N.; Vujisić, M.; Stanković, K.; Osmokrović, P. *Radiat. Eff. Defects Solids* **2011,** *166,* 1. doi:10.1080/10420150.2010.533673
18. Sanz, R.; Jensen, J.; Johansson, A.; Skupinski, M.; Possnert, G.; Boman, M.; Hernandez-Vélez, M.; Vazquez, M.; Hjort, K. *Nanotechnology* **2007,** *18,* 305303. doi:10.1088/0957-4484/18/30/305303
19. Fink, D.; Chadderton, L. T. *Braz. J. Phys.* **2005,** *35,* 735. doi:10.1590/S0103-97332005000500003
20. Toulemonde, M.; Trautmann, C.; Balanzat, E.; Hjort, K.; Weidinger, A. *Nucl. Instrum. Methods Phys. Res., Sect. B* **2004,** *216,* 1. doi:10.1016/j.nimb.2003.11.013

21. Ridgway, M. C.; Giulian, R.; Sprouster, D. J.; Kluth, P.; Araujo, L. L.; Llewellyn, D. J.; Byrne, P.; Kremer, F.; Fichtner, P. F. P.; Rizza, G.; Amekura, H.; Toulemonde, M. *Phys. Rev. Lett.* **2011,** *106,* 095505. doi:10.1103/PhysRevLett.106.095505
22. Avasthi, D. K.; Mishra, Y. K.; Singh, F.; Stoquert, J. P. *Nucl. Instrum. Methods Phys. Res., Sect. B* **2010,** *268,* 3027. doi:10.1016/j.nimb.2010.05.033
23. Mishra, Y. K.; Kabiraj, D.; Avasthi, D. K.; Pivin, J. C. *Radiat. Eff. Defects Solids* **2007,** *162,* 207. doi:10.1080/10420150601132883
24. Mishra, Y. K.; Avasthi, D. K.; Kulriya, P. K.; Singh, F.; Kabiraj, D.; Tripathi, A.; Pivin, J. C.; Bayer, I. S.; Biswas, A. *Appl. Phys. Lett.* **2007,** *90,* 073110. doi:10.1063/1.2642824
25. Mishra, Y. K.; Singh, F.; Avasthi, D. K.; Pivin, J. C.; Malinovska, D.; Pippel, E. *Appl. Phys. Lett.* **2007,** *91,* 063103. doi:10.1063/1.2764556
26. Toulemonde, M.; Costantini, J.; Dufour, C.; Meftah, A.; Paumier, E.; Studer, F. *Nucl. Instrum. Methods Phys. Res., Sect. B* **1996,** *116,* 37. doi:10.1016/0168-583X(96)00007-9
27. Rizza, G.; Coulon, P. E.; Khomenkov, V.; Dufour, C.; Monnet, I.; Toulemonde, M.; Perruchas, S.; Gacoin, T.; Mailly, D.; Lafosse, X.; Ulysse, C.; Dawi, E. *Phys. Rev. B* **2012,** *86,* 035450. doi:10.1103/PhysRevB.86.035450
28. Dawi, E.; Vredenberg, M.; Rizza, G.; Toulemonde, M. *Nanotechnology* **2011,** *22,* 215607. doi:10.1088/0957-4484/22/21/215607
29. Afra, B.; Rodriguez, M. D.; Trautmann, C.; Pakarinen, O. H.; Djurabekova, F.; Nordlund, K.; Bierschenk, T.; Giulian, R.; Ridgway, M. C.; Rizza, G.; Kirby, N.; Toulemonde, M.; Kluth, P. *J. Phys.: Condens. Matter* **2013,** *25,* 045006. doi:10.1088/0953-8984/25/4/045006
30. Dufour, C.; Khomenkov, V.; Rizza, G.; Toulemonde, M. *J. Phys. D: Appl. Phys.* **2012,** *45,* 065302. doi:10.1088/0022-3727/45/6/065302
31. Rizza, G.; Attouchi, F.; Coulon, P.-E.; Perruchas, S.; Gacoin, T.; Monnet, I.; Largeau, L. *Nanotechnology* **2011,** *22,* 175305. doi:10.1088/0957-4484/22/17/175305
32. Ruffino, F.; De Bastiani, R.; Grimaldi, M. G.; Bongiorno, C.; Giannazzo, F.; Roccaforte, F.; Spinella, C.; Raineri, V. *Nucl. Instrum. Methods Phys. Res., Sect. B* **2007,** *257,* 810. doi:10.1016/j.nimb.2007.01.090
33. Thakurdesai, M.; Mohanty, T.; John, J.; Gundu Rao, T. K.; Raychaudhuri, P.; Bhattacharyya, V.; Kanjilal, D. *J. Nanosci. Nanotechnol.* **2008,** *8,* 4231. doi:10.1166/jnn.2008.AN32
34. Kumar, A.; Jaiswal, M. K.; Kanjilal, D.; Joshi, R. K.; Mohanty, T. *Appl. Phys. Lett.* **2011,** *99,* 013109. doi:10.1063/1.3608140
35. Trivedi, S. J.; Khan, S. A.; Joshi, U. S. *Radiat. Eff. Defects Solids* **2013,** *168,* 532. doi:10.1080/10420150.2013.778858
36. Singh, A. P.; Kumari, S.; Tripathi, A.; Singh, F.; Gaskell, K. J.; Shrivastav, R.; Dass, S.; Ehrman, S. H.; Satsangi, V. R. *J. Phys. Chem. C* **2010,** *114,* 622. doi:10.1021/jp906725b
37. Thakurdesai, M.; Kanjilal, D.; Bhattacharyya, V. *Semicond. Sci. Technol.* **2009,** *24,* 085023. doi:10.1088/0268-1242/24/8/085023
38. Mishra, Y. K.; Mohapatra, S.; Kabiraj, D.; Mohanta, B.; Lalla, N.; Pivin, J.; Avasthi, D. *Scr. Mater.* **2007,** *56,* 629. doi:10.1016/j.scriptamat.2006.12.008
39. Chakravadhanula, V. S. K.; Hrkac, T.; Zaporojtchenko, V.; Podschun, R.; Kotnur, V. G.; Kulkarni, A.; Strunskus, T.; Kienle, L.; Faupel, F. *J. Nanosci. Nanotechnol.* **2011,** *11,* 4893. doi:10.1166/jnn.2011.3881
40. Chakravadhanula, V. S. K.; Kübel, C.; Hrkac, T.; Zaporojtchenko, V.; Strunskus, T.; Faupel, F.; Kienle, L. *Nanotechnology* **2012,** *23,* 495701. doi:10.1088/0957-4484/23/49/495701
41. Klaumünzer, S. *Nucl. Instrum. Methods Phys. Res., Sect. B* **2004,** *225,* 136. doi:10.1016/j.nimb.2004.05.014
42. Pivin, J. C.; Roger, G.; Garcia, M. A.; Singh, F.; Avasthi, D. K. *Nucl. Instrum. Methods Phys. Res., Sect. B* **2004,** *215,* 373. doi:10.1016/j.nimb.2003.07.002
43. Zribi, M.; Kanzari, M.; Rezig, B. *Thin Solid Films* **2008,** *516,* 1476. doi:10.1016/j.tsf.2007.07.195
44. Enyashin, A. N.; Ivanovskii, A. L. *Russ. J. Inorg. Chem.* **2006,** *51,* 1302. doi:10.1134/S0036023606080171
45. Thakurdesai, M.; Kanjilal, D.; Bhattacharyya, V. *Appl. Surf. Sci.* **2012,** *258,* 7855. doi:10.1016/j.apsusc.2012.04.089
46. Rath, H.; Dash, P.; Som, T.; Satyam, P. V.; Singh, U. P.; Kulriya, P. K.; Kanjilal, D.; Avasthi, D. K.; Mishra, N. C. *J. Appl. Phys.* **2009,** *105,* 074311. doi:10.1063/1.3103333
47. Kelly, K. L.; Coronado, E.; Zhao, L. L.; Schatz, G. C. *J. Phys. Chem. B* **2003,** *107,* 668. doi:10.1021/jp026731y
48. Aumayr, F.; Facsko, S.; El-Said, A. S.; Trautmann, C.; Schleberger, M. *J. Phys.: Condens. Matter* **2011,** *23,* 393001. doi:10.1088/0953-8984/23/39/393001
49. Bartkowski, S.; Neumann, M.; Kurmaev, E. Z.; Fedorenko, V. V.; Shamin, S. N.; Cherkashenko, V. M.; Nemnonov, S. N.; Winiarski, A.; Rubie, D. C. *Phys. Rev. B* **1997,** *56,* 10656. doi:10.1103/PhysRevB.56.10656
50. Stadelmann, P. *Ultramicroscopy* **1987,** *21,* 131. doi:10.1016/0304-3991(87)90080-5
51. James Ziegler - SRIM & TRIM. http://www.srim.org/ (accessed May 11, 2014).

License and Terms

BEILSTEIN JOURNAL OF NANOTECHNOLOGY

Probing the electronic transport on the reconstructed Au/Ge(001) surface

Franciszek Krok[1], Mark R. Kaspers[2], Alexander M. Bernhart[2], Marek Nikiel[1], Benedykt R. Jany[1], Paulina Indyka[3], Mateusz Wojtaszek[1], Rolf Möller[2] and Christian A. Bobisch[*2]

Full Research Paper

Open Access

Address:
[1]Smoluchowski Institute of Physics, Jagiellonian University, Reymonta 4, 30-059 Krakow, Poland, [2]Faculty of Physics, Center for Nanointegration Duisburg-Essen, University of Duisburg-Essen, 47048 Duisburg, Germany and [3]Faculty of Chemistry, Jagiellonian University, Ingardena 3, 30-060, 30-059 Krakow, Poland

Email:
Christian A. Bobisch* - christian.bobisch@uni-due.de

* Corresponding author

Keywords:
Au on Ge(001); electronic transport; multi probe STM; scanning tunnelling potentiometry

Beilstein J. Nanotechnol. **2014,** *5,* 1463–1471.
doi:10.3762/bjnano.5.159

Received: 16 May 2014
Accepted: 14 August 2014
Published: 05 September 2014

This article is part of the Thematic Series "Physics, chemistry and biology of functional nanostructures II".

Guest Editor: A. S. Sidorenko

Abstract

By using scanning tunnelling potentiometry we characterized the lateral variation of the electrochemical potential μ_{ec} on the gold-induced Ge(001)-c(8 × 2)-Au surface reconstruction while a lateral current flows through the sample. On the reconstruction and across domain boundaries we find that μ_{ec} shows a constant gradient as a function of the position between the contacts. In addition, nanoscale Au clusters on the surface do not show an electronic coupling to the gold-induced surface reconstruction. In combination with high resolution scanning electron microscopy and transmission electron microscopy, we conclude that an additional transport channel buried about 2 nm underneath the surface represents a major transport channel for electrons.

Introduction

Structures consisting of single atoms represent the lower spatial limit for electronic circuits. On such a small scale, the electronic structure is dominated by quantum phenomena, i.e., the electronic conduction crucially relies on the electronic states. Recently, many studies focus on self-organized Au atom wires on the Ge(001) surface, which show Tomonaga–Luttinger liquid properties, i.e., represent a one-dimensional electronic system [1-3]. In contrast to other nanowire structures, e.g., in atoms on Si(111) [4] or Au on Si(557) [5], the Au/Ge(001) wires are rather robust against a Peierls distortion [6], so that the Au/Ge(001) surface offers the unique opportunity to study a Tomonaga–Luttinger liquid. In addition, such atomic scale wires may be used as atomic scale leads to contact, e.g., small atomic structures or molecules. The anisotropic transport properties of this surface structure have triggered controversial discussions within the scientific community [7-9]. However, to access the anisotropic transport properties, a significant electron current needs to be coupled to the atomic wires. At neigh-

bouring terraces, the Au/Ge(001) wire structure is rotated by 90° and then a single layer step represents a domain boundary. Simultaneously, also the correlated electronic structure is rotated. Thus, the coupling between adjacent terraces can be probed by applying a lateral current through the reconstructed surface. Even though the metallic contacts to the Au/Ge(001) surface may be farther apart, a local sensitive probe can study the electronic properties in the vicinity of the domain boundaries. We know from previous experiments that the Au/Ge(001) surface exhibits a two dimensional conductance channel on a micrometre-scale averaging across several Au-reconstructed 1D domains [10].

Scanning tunnelling microscopy (STM) and various STM-based methods are excellent tools to study the topographic structure, the electronic structure, and electron transport phenomena of conducting surfaces at the limit of lateral resolution. By performing scanning tunnelling potentiometry (STP) [11] we tried to study the lateral variation of the electrochemical potential μ_{ec} (called potential in the following) at the boundary between two rotated Au wire-like domains while a lateral current was flowing through the Au/Ge(001) sample (see also the scheme in Figure 1a below). By using a multiprobe STM setup (Omicron Nanoprobe) individually controlled STM tips are used to establish well defined electric contacts to the reconstructed surface. We applied a voltage between two contacts leading to a current flow across the surface. Thus, if the main contribution of the total current is flowing through the Au reconstructed 1D domains, the impact of the predicted conductance anisotropy should be observed as a variation of the electrochemical potential in the vicinity of the domain boundaries.

Experimental

The germanium substrate is cut from a wafer of a n-type Ge(001) crystal with a resistivity of about 30 Ω·cm. The cleaning procedure of the substrate consists of a few cycles of 600 eV Ar^+ ion sputtering at a sample temperature of 1040 K (as measured by a pyrometer). After this procedure, the STM imaging proves that the Ge(001) surface exhibits atomically flat terraces with a lateral extension of 30–50 nm and a mixed (2 × 2)/c(4 × 2)-two domain reconstruction pattern as checked by low energy electron diffraction (LEED).

We deposited 6 monolayers (MLs) of Au on the reconstructed Ge(001) from a resistively heated crucible. The deposition rate of 0.2 ML/min is monitored by using a quartz crystal microbalance and the substrate temperature during the deposition of Au is kept at 150 K. After the deposition, no ordered structure is observed until the sample is annealed. After annealing to 770 K for about 10 min the Au-induced wire-like Ge(001)-c(8 × 2)-Au structure emerges [1,3]. The excess amount of Au aggregates into Au clusters. We intentionally deposited this excess amount of Au since the Au clusters may serve as metallic leads to contact the surface structure by STM tips [12,13]. In Figure 1b an overview of the sample surface is provided by a high resolution SEM image exhibiting several Au clusters together with the terrace edges. The Au clusters are of about 150 nm size and they are of an asymmetric octagonal shape at their base (see Figure 1b and Figure 1c). A high resolution STM image of the area between the Au clusters exhibits Au reconstructed terraces separated by single layer steps, exemplarily shown in Figure 1d. At most step edges the wire structure is rotated by 90° resulting from the reconstructed Ge(001) substrate. The domains exhibit some structural defects within the atomic wires. For the struc-

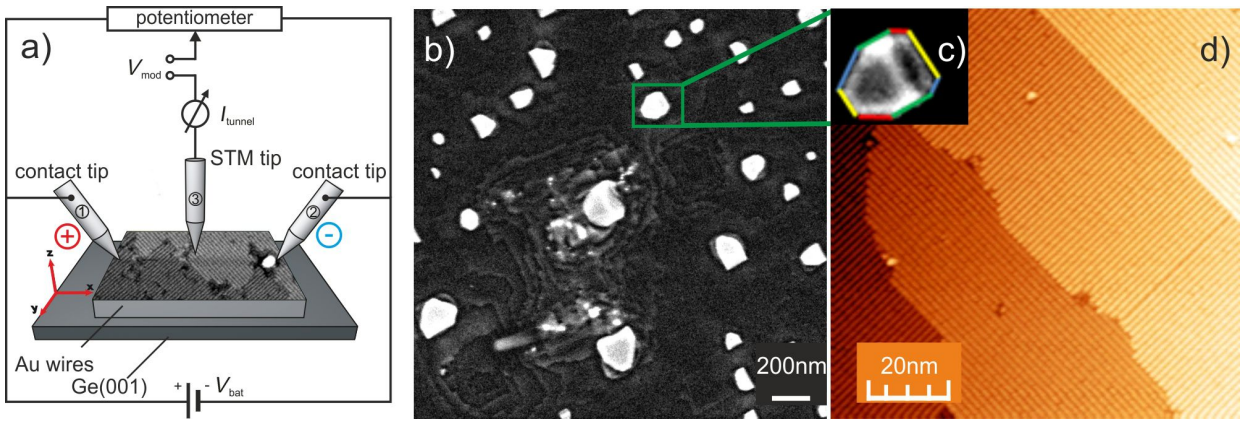

Figure 1: a) Scheme of the potentiometry setup using a multiprobe STM. Two STM tips (1 and 2) in contact with the sample surface are used to drive a lateral current. The third STM tip (3) simultaneously images the topography and the electrochemical potential of the surface. b) HRSEM image of the 6 ML Au/Ge(001) sample surface exhibiting the Au clusters and some terrace edges. Most clusters are of asymmetric octagonal shape as depicted by the colour contour in c). d) HRSTM image of an area between the Au clusters showing two differently oriented domains of the Au induced wires (I_T = 200 pA, V_{sample} = −2 V).

tural and electronic analysis of the samples two different experimental techniques were applied:

We use a multiprobe scanning tunnelling microscope (Nanoprobe by Omicron) to analyse the lateral variation of the potential caused by a current parallel to the surface. The mechanical stability and performance of the commercial STM setup was improved in order to provide atomic resolution, e.g., on the Si(111)-(7 × 7) surface or the Bi(111) surface [12]. During the scanning tunnelling potentiometry (STP) experiments, two tips contact the surface and drive a lateral current. A third STM tip simultaneously measures the topography and the potential of the surface between the contacts [13-15]. The STP experiments were carried out at a base pressure below 3×10^{-10} mbar for various sample temperatures between 130 K and 300 K. In order to establish smooth contacts to the surface, electrochemically etched Au tips were gently pressed against the Au/Ge(001) surface by sub-sequentially using the z-piezo drive of the STM unit for different course approach tip/sample separations. The contact formation is monitored for a bias voltage of 1 V between tip and substrate by the appearance of a contact current in the microampere regime. The lateral position of the STM tips is monitored by using a scanning electron microscope. The scheme of the STP measurement is depicted in Figure 1a: Two tips (1 and 2) contact the sample and apply a voltage V_{bat} leading to a transverse current I_{trans} through the surface while the third tip measures the STM topography and the potential, simultaneously. Therefore, a feedback loop adjusts the dc tunnelling voltage such that the dc tunnelling current becomes zero. Thus, for each lateral tip position the applied dc tunnelling voltage corresponds to the potential underneath the STM tip. This allows us to map the potential with atomic precision. To maintain a tunnelling distance between the STM tip and the sample surface, we additionally apply a small alternating tunnelling voltage (V_{mod}) such that the tip/sample distance can be controlled by the corresponding ac component of the tunnelling current. Further experimental details can be found elsewhere [12,16]. The contact tips are placed such that the direction of the applied lateral current is mainly oriented orthogonal to the main direction of the germanium surface steps originating from the miscut of the Ge(001) sample. The contact area between the Au tips and the surface is relatively large, so we assume that both, the Au-induced wire-like Ge(001)-c(8 × 2)-Au structure and the Au islands are contacted by the tips simultaneously. All image acquisition was done by using the open source software GSxM [17] and data processing was done by using WxSM [18].

For the transmission electron microscope (TEM) measurements lamellas of the Au/Ge(001) of the very same sample were prepared with the use of an FEI Quanta 3D FEG scanning electron microscope equipped with a 30 keV Ga^+ focused ion beam gun (FIB). In order to preserve the surface of the Au/Ge sample against the standard FIB operation during the lamella preparation, the sample surface at first was covered (capped) with a 20 nm layer of thermally evaporated carbon. Then, on top of the cap layer, a platinum layer was deposited using a gas injection system by the electron beam and the FIB beam was used to cut out the lamella. The high resolution (HR) TEM and high angle annular dark field (HAADF) scanning TEM images together with energy dispersive X-ray spectroscopy (EDX) analysis of the sample were obtained by the FEI Tecnai Osiris transmission electron microscope operated at 200kV electron beam.

Results

Figure 2a shows a large scale STM image of the Au/Ge(001) surface. Several surface steps and Au clusters are observed. The terraces exhibiting the Au wire-like structure are about 100 nm wide. In Figure 2a, for two of the terraces the corresponding directions of the wires are indicated by white lines. Due to the contact geometry the electrons are flowing in the direction indicated by the arrow in b). Hence, the current is oriented either approximately parallel or orthogonal to the wire-like structure, depending on the orientation of the domain. To ensure the best resolution for the potentiometry across (8 × 2) domain boundaries, i.e., step edges, the fast scan direction is chosen in parallel to the direction of the current.

A double-tip scan artefact is observed for the Au clusters. However, it can be well identified by the topography so that the corresponding potential was analysed accordingly. The potential shown in Figure 2b exhibits a gradient on the reconstructed terraces. In contrast, the potential on the Au clusters is rather constant at a value corresponding to a value of the surrounding terrace. The gradient of the potential of various STP images is determined to be about $\Delta V = 20$ μV/nm for an estimated local average current density j of 11 A/m. The latter is estimated from the total transverse current I_{trans} and the contact geometry. In the middle of the connecting line between the contact tips, j can be written as [19]:

$$j = \frac{2}{\pi \cdot d} I_{\text{trans}} ,$$

where $d = 170 \pm 20$ μm is the distance between the contact tips and $I_{trans} = 3$ mA is the total transverse current. With these results and assuming an isotropic conductivity we can determine the conductivity $\sigma = (j/\Delta V)$ of the terraces' area at room temperature to be about 0.55 mS.

Figure 2c exemplarily shows line profiles of the potential and the corresponding topography as marked in Figure 2a and

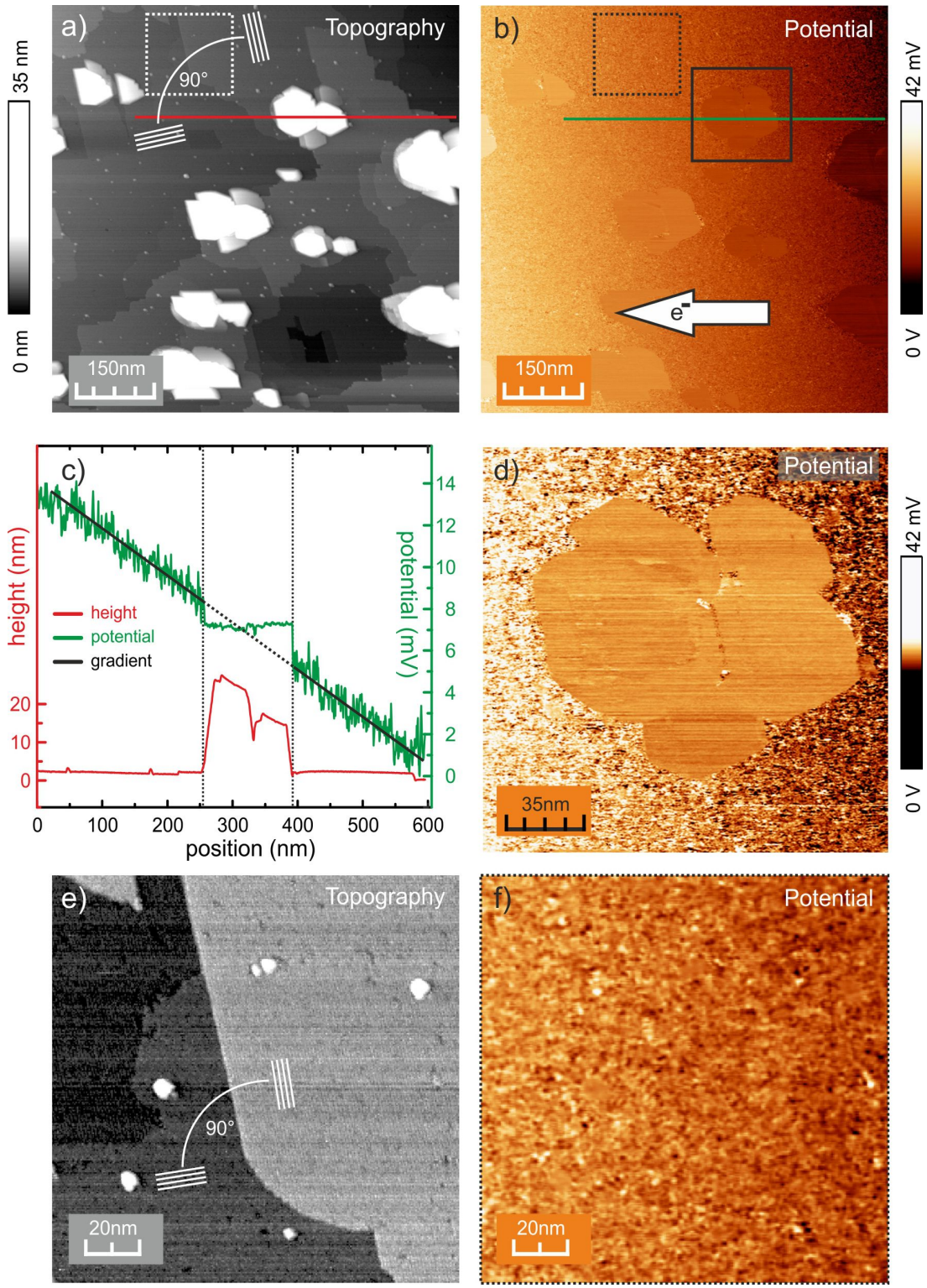

Figure 2: a) STM image of the Au/Ge(001) surface showing both different types of Au wire-like domains and several Au clusters. b) Corresponding image of the potential, exhibiting a constant gradient on the terraces (Au wire-like domains). The Au clusters appear with constant potential and rather sharp transitions at their borders. c) Line profiles of the topography (red) and potential (green) as marked in a) and b). As a guide to the eye a linear function was fitted to the overall gradient of the potential. d) Potential near a Au cluster. Sharp transitions of the potential at the perimeter of the cluster are easily recognized. e) and f) show the topography and the corresponding potential for a small area near a step edge, i.e., domain boundary. The directions of the atomic wires are marked by white lines in a) and e) (V_{bat} = 9 V, I_{trans} = 3 mA).

Figure 2b. On the reconstructed surface the potential exhibits strong fluctuations (±2.5 mV) but no direct correlation to steps in the topography. The potential on the Au clusters appears rather flat and smooth, only limited by the resolution of our STP setup (±5 μV) and is constant within the experimental error. At the edge of the Au clusters a discontinuity of the potential occurs. The resistivity, i.e., the corresponding gradient of the potential on the terraces scales about linearly as a function of the absolute sample temperature (Figure 3) indicating that the measured conductivity for the present Au/Ge(001) system is metallic. Although it may be assumed that the transverse current may heat the Ge sample, we do not see any indications for this in our data. As sample heating would result in a temperature difference between the tunnelling tip and the sample, a thermovoltage in the tunnelling gap would occur. This voltage would also be measured by our STP setup and would be independent of the polarity of the transverse current. Since we do not observe this effect, heating of the sample seems to be negligible.

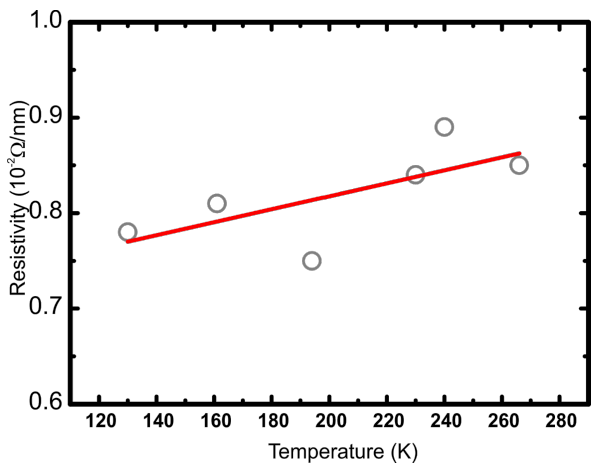

Figure 3: Resistivity, as evaluated from the gradient of the potential in the STP images, as a function of the temperature of the sample.

In order to study the depth profile of the Au/Ge(001) samples, thin lamellas cut from the Au/Ge(001) sample were further analysed by means of high resolution TEM measurements. Figure 4 shows the corresponding TEM data. The contrast in the TEM image (Figure 4a) exhibits that the Au cluster (dark) is not only growing on top of the Ge surface, but also a large part of the cluster is digged into the Ge(001) substrate. The top surface of the cluster is not parallel to the Ge(001) substrate surface and is tilted by about 5° with respect to the substrate. This is common for all observed clusters. Furthermore, the measured angle between the side and top planes of the clusters (compare Figure 4a) is about 144.2 ± 1.6° which is very close to value of 144.8° corresponding to the angle between the [110] and [111] faces for a face-centred cubic crystal symmetry. These observations show that the excess amount of Au forms clusters of [110]-orientation, in agreement to previous STM studies of the same system by Wang et al. [20]. Also, HRTEM images with atomic resolution show that the Au clusters are crystalline.

Apart from that, in Figure 4a, a thin layer exhibiting the similar dark contrast as the gold cluster is also observed. This layer is extending from the cluster at both sides and is found about 2 nm below the apparent sample surface [21]. As a guide to the eye the apparent sample surface is marked by the black arrows in Figure 4a and determines the position where the grey contrast (Ge) changes into bright (capping carbon layer). The HAADF HRSTEM image (Figure 4c) through the Au/Ge lamella taken along the indicated line in a) and its corresponding EDX line profile show that this thin layer is enriched with Au. The occurrence of carbon throughout the whole observed lamella surface is due to the measurement process and only reflects the deposition and adsorption probability of C onto the different exposed materials along the surface of the lamella.

Discussion

We find an abrupt transition of the potential between Au clusters and the reconstructed Au/Ge surface which indicates that the clusters are not electrically coupled to the conducting channels of the Au-induced reconstructed Ge(001) surface. We have carefully checked that the discontinuity is not only caused by the double tip artefact. The abrupt transition from the linear slope on the terrace to the constant potential on the Au cluster appears for all observed Au clusters and at the perimeter of almost the whole cluster. A careful inspection reveals that there exists one direction, along which the potential on the cluster matches the potential on the surrounding terrace. Since the potential on the Au clusters is constant for the whole area of the cluster the potential on the Au clusters is not caused by a tip artefact. It may be possible that the variation of the potential for the flat surface and the Au clusters occurs on a scale which is much smaller than the topographic and potential resolution of the experimental setup. Also in this case an abrupt variation of potential would be observed. However, we explain our findings by a two dimensional conducting layer underneath the surface which is electronically coupled to both, the Au atomic wires and the Au clusters while the Au clusters and the Au atomic wires at the surface are not coupled to each other. Our HRTEM data supports this assumption. In Figure 5, an atomically resolved HRTEM image of the interface between the Au cluster and the substrate surface is shown. In image a), on the right side the substrate surface level is indicated by a dashed line. It is clearly seen that the substrate surface region does not prop-

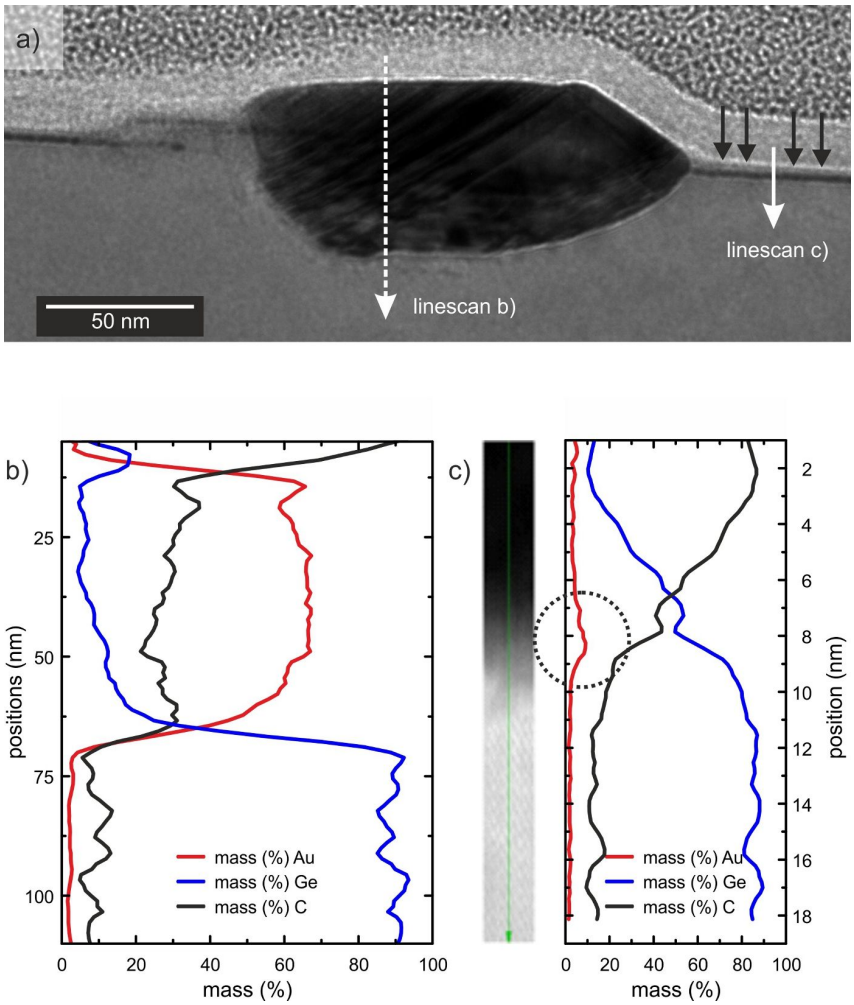

Figure 4: a) Exemplary TEM image of a lamella of Au grown on Ge(001) after the deposition of 6 ML of Au and annealing at 770 K. The apparent sample surface is exemplarily marked by black arrows on the right hand side of the image. b) EDX line scan analysis through the Au cluster. The Au cluster is reaching far into the Ge substrate. The non-zero Ge signal from the Au cluster is due to secondary fluorescence (excitations of "bulk" Ge caused by the X-ray emission from Au), which is a well-known effect (artefact) in the EDX spectroscopy. c) HAADF HRSTEM image through the Au/Ge lamella taken along the line on the right hand side in a). The results of the line scan EDX analysis are also shown. The Au concentration is found to reach its maximum of approx. 10% underneath the apparent sample surface (see circle). On the lower side of the image the atomic structure of Ge(001) bulk is visible.

agate with crystalline order to the Au cluster. A discontinuity region (about 2 nm wide), called in the image "cavity", may either be a substrate depletion filled with carbon or disordered germanium. In both cases, this results in a weak electrical connection between the cluster and the reconstructed Au/Ge terraces.

The occurrence of such a Au-enriched layer is not unexpected since Au is known to segregate into Ge bulk [22] especially at elevated temperatures. Therefore, we conclude that the subsurface layer emerges upon preparation of the Au/Ge(001) sample. By applying a voltage between the contacts to the surface, the current can also flow through the buried Au-enriched layer. Since the step edges, i.e., domain boundaries are expected to be scattering centres for the current, some contrast in the potential similar to surface transport in Si(111)-$\sqrt{3} \times \sqrt{3}$:Ag [13] and thin Bi(111) films on silicon [12,16] would be expected. However, the maps of the potential show no fine-structure related to the step edges or other surface defects so we conclude that the main current is not carried by the surface, i.e., the Au atomic wires, but by the subsurface layer. Thus, the corresponding conductivity of the buried layer is higher than the conductivity along the sample surface including the Au atomic wire structure, the Au wire domain boundaries and the interface between the Au clusters and the Au wire domains. A simple model for the Au/Ge structure is shown in Figure 5b. In addition, a line profile of the potential across a Au cluster and an idealized profile for the depicted simple wiring scheme is shown.

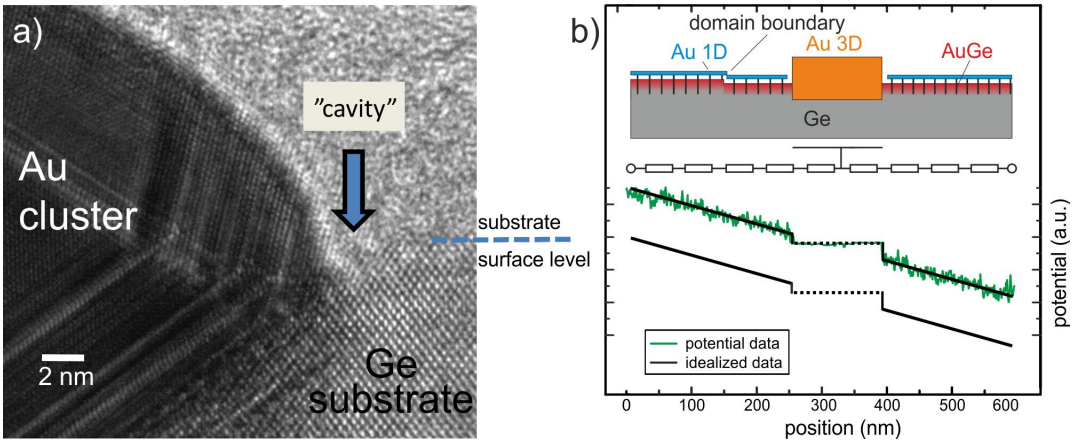

Figure 5: a) An atomically resolved HRTEM image of the interface between the Au cluster and the surrounding substrate surface. The substrate surface level is indicated with the dashed line. The arrow points to the discontinuity region ("cavity") between the crystalline substrate surface region and the Au cluster. b) Scheme of the Au/Ge(001) sample structure. The Au cluster is electronically decoupled from the Au atomic wires but is coupled to a buried Au-enriched layer. The Au atomic wires are also coupled to this buried subsurface layer. The simplified wiring diagram is shown in the middle and a potential profile from original data and its simplified form is also shown.

To test our hypothesis we performed a simple finite elements simulation for a comparable conductive structure by using FEMLAB [23]. Figure 6 shows two simulated images of the potential which show that the sharp transition at the Au clusters can be simulated if a highly conductive cluster is placed on a lower conductive material. If no metallic contacts are present at the perimeter of the cluster and only a single point contact underneath the cluster (Figure 6a) is active, a sharp transition similar to the findings in our potentiometry data is found. As a guide to the eye, equipotential lines are plotted which show the impact of the cluster on the potential in its vicinity.

Our potentiometry data correspond quite well to Figure 6a, which corroborates our assumption for the sample structure as depicted in Figure 5b. If instead the cluster is placed onto the low conductive material with a planar contact a smoother transition occurs and the potential bends towards the cluster edges (see Figure 6b). Line profiles for both cases are shown in Figure 6c.

Conclusion

In conclusion, we find that the electronic transport properties of the system Au/Ge(001) are not only given by the atomic wire-

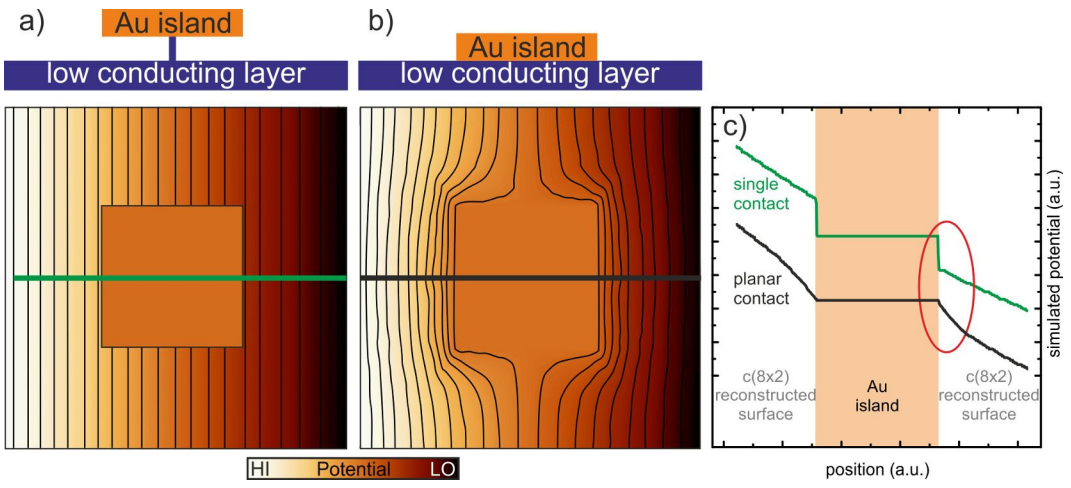

Figure 6: a) Finite elements simulation for the potential if one single path connects a highly conductive cluster to a low conducting substrate while the borders of the cluster are not connected to the substrate (single point contact). b) Simulated potential if the highly conductive cluster is placed directly on top of a low conducting substrate (planar contact). The colour palette represents the potential variation. As a guide to the eye equipotential lines are superimposed. A side view of the corresponding contact geometry is shown above each simulation. c) Line profiles for both contact geometries in a) and b); the upper graph/profile exhibits a sharp transition, while the lower graph exhibits a bending of the potential in the proximity of the cluster.

like surface structure exhibiting a Tomonaga–Luttinger behavior, but also by a 2D conductive layer underneath the surface. Upon contacting the Au/Ge(001) sample surface, we contact the surface structure and the subsurface layer which both carry the resulting electric current. Since no lateral variations of the potential are observed in the vicinity of domain boundaries at the Au induced wire-like Ge(001)-c(8 × 2)-Au structure, we conclude that the subsurface layer appears to be the major transport channel for this contact geometry. Rather sharp transitions of the potential at embedded Au islands suggest a decoupling of the Au islands from the surface layer. From in depth-profile analysis we can conclude that the Au islands contact the Au enriched subsurface layer which carries the lateral current. Therefore, the peculiar electronic structure of the Au/Ge(001) surface is not accessible even if micrometre-sized point contacts to the Au/Ge surface are used. These findings are of major importance if the Au/Ge(001) atomic wire structure shall be contacted by metallic leads to access its one-dimensional transport properties. The appropriate choice of electric leads appears to be a crucial parameter for passing electric currents through the one-dimensional electronic structure of Ge/Au. This may have wider impact, since segregation needs to be considered for other atomic wire-like surface structures as well. Whenever surface structures are engineered by adsorbing material, in depth profile analysis may unravel buried electronic channels which can prevent to access to the electronic system of the surface.

Acknowledgements

The authors gratefully acknowledge financial support from the Deutsche Forschungsgemeinschaft under the program "SFB616: Energy Dissipation at Surfaces" and the Polish National Science Center, grant no. DEC-2012/07/B/ST5/00906. Part of the research was carried out with equipment purchased with financial support from the European Regional Development Fund in the framework of the Polish Innovation Economy Operational Program (Contract No. POIG.02.01.00-12-023/08).

References

1. Haldane, F. D. M. *J. Phys. C* **1981,** *14,* 2585. doi:10.1088/0022-3719/14/19/010
2. Schäfer, J.; Blumenstein, C.; Meyer, S.; Wisniewski, M.; Claessen, R. *Phys. Rev. Lett.* **2008,** *101,* 236802. doi:10.1103/PhysRevLett.101.236802
3. Blumenstein, C.; Schäfer, J.; Mietke, S.; Meyer, S.; Dollinger, A.; Lochner, M.; Cui, X. Y.; Patthey, L.; Matzdorf, R.; Claessen, R. *Nat. Phys.* **2011,** *7,* 776. doi:10.1038/nphys2051
4. Yeom, H. W.; Takeda, S.; Rotenberg, E.; Matsuda, I.; Horikoshi, K.; Schaefer, J.; Lee, C. M.; Kevan, S. D.; Ohta, T.; Nagao, T.; Hasegawa, S. *Phys. Rev. Lett.* **1999,** *82,* 4898–4901. doi:10.1103/PhysRevLett.82.4898
5. Segovia, P.; Purdie, D.; Hengsberger, M.; Baer, Y. *Nature* **1999,** *402,* 504–507. doi:10.1038/990052
6. Blumenstein, C.; Schäfer, J.; Morresi, M.; Mietke, S.; Matzdorf, R.; Claessen, R. *Phys. Rev. Lett.* **2011,** *107,* 165702. doi:10.1103/PhysRevLett.107.165702
7. Heimbuch, R.; Kuzmin, M.; Zandvliet, H. J. W. *Nat. Phys.* **2012,** *8,* 697–698. doi:10.1038/nphys2414
8. Nakatsuji, K.; Komori, F. *Nat. Phys.* **2012,** *8,* 174. doi:10.1038/nphys2240
9. Blumenstein, C.; Schäfer, J.; Mietke, S.; Meyer, S.; Dollinger, A.; Lochner, M.; Cui, X. Y.; Patthey, L.; Matzdorf, R.; Claessen, R. *Nat. Phys.* **2012,** *8,* 174. doi:10.1038/nphys2241
10. Wojtaszek, M.; Kolmer, M.; Godlewski, S.; Budzioch, J.; Such, B.; Krok, F.; Szymonski, M. Multi-Probe Characterization of 1D and 2D Nanostructures Assembled on Ge(001) Surface by Gold Atom Deposition and Annealing. In *Atomic Scale Interconnection Machines;* Joachim, C., Ed.; Advances in Atom and Single Molecule Machines; Springer Verlag: Berlin, Germany, 2012; pp 141–152. doi:10.1007/978-3-642-28172-3_11
11. Muralt, P.; Pohl, D. W. *Appl. Phys. Lett.* **1986,** *48,* 514. doi:10.1063/1.96491
12. Bannani, A.; Bobisch, C. A.; Möller, R. *Rev. Sci. Instrum.* **2008,** *79,* 083704. doi:10.1063/1.2968111
13. Homoth, J.; Wenderoth, M.; Druga, T.; Winking, L.; Ulbrich, R. G.; Bobisch, C. A.; Weyers, B.; Bannani, A.; Zubkov, E.; Bernhart, A. M.; Kaspers, M. R.; Möller, R. *Nano Lett.* **2009,** *9,* 1588. doi:10.1021/nl803783g
14. Druga, T.; Wenderoth, M.; Homoth, J.; Schneider, M. A.; Ulbrich, R. G. *Rev. Sci. Instrum.* **2010,** *81,* 083704. doi:10.1063/1.3469809
15. Muralt, P.; Meier, H.; Pohl, D. W.; Salemink, H. W. M. *Appl. Phys. Lett.* **1987,** *50,* 1352. doi:10.1063/1.97853
16. Bobisch, C. A.; Möller, R. *Chimia* **2012,** *66,* 23–30. doi:10.2533/chimia.2012.23
17. Zahl, P.; Bierkandt, M.; Schröder, S.; Klust, A. *Rev. Sci. Instrum.* **2003,** *74,* 1222. doi:10.1063/1.1540718
18. Horca, I.; Fernández, R.; Gómez-Rodríguez, J. M.; Colchero, J.; Gómez-Herrero, J.; Baro, A. M. *Rev. Sci. Instrum.* **2007,** *78,* 013705. doi:10.1063/1.2432410
19. Ji, S.-H.; Hannon, J. B.; Tromp, R. M.; Perebeinos, V.; Tersoff, J.; Ross, F. M. *Nat. Mater.* **2012,** *11,* 114. doi:10.1038/nmat3170
20. Wang, J.; Li, M.; Altman, E. I. *Surf. Sci.* **2005,** *596,* 126. doi:10.1016/j.susc.2005.09.009
21. To ensure a correct estimation of the buried layer depth we did also EFTEM (energy filtered TEM) and EELS measurements; all data support that the Au layer is buried around 2 nm below the Ge sample surface.
22. Dornath-Mohr, M. A.; Cole, M. W.; Lee, H. S.; Wrenn, C. S.; Eckart, D. W.; Fox, D. C.; Yerke, L.; Chang, W. H.; Lareau, R. T.; Jones, K. A.; Cosandy, F. *MRS Online Proc. Libr.* **1990,** *181,* 369. doi:10.1557/PROC-181-369
23. FEMLAB. http://www.math.chalmers.se/Math/Research/Femlab/ (accessed May 15, 2014).

BEILSTEIN JOURNAL OF NANOTECHNOLOGY

Growth evolution and phase transition from chalcocite to digenite in nanocrystalline copper sulfide: Morphological, optical and electrical properties

Priscilla Vasthi Quintana-Ramirez[1], Ma. Concepción Arenas-Arrocena[*2,§], José Santos-Cruz[3], Marina Vega-González[4], Omar Martínez-Alvarez[5], Víctor Manuel Castaño-Meneses[6], Laura Susana Acosta-Torres[2] and Javier de la Fuente-Hernández[2]

Full Research Paper

Open Access

Address:
[1]Posgrado en Ciencia e Ingeniería de Materiales, Centro de Física Aplicada y Tecnología Avanzada, Universidad Nacional Autónoma de México, 76230, Querétaro, México, [2]Escuela Nacional de Estudios Superiores Unidad León, UNAM, Boulevard UNAM No. 2011 Predio el Saucillo y el Potrero, 36969, León Guanajuato, México, [3]Facultad de Química, Materiales Universidad Autónoma de Querétaro, 76010, Querétaro, México, [4]Centro de Geociencias, UNAM, 76230, Querétaro, México, [5]Departamento de Ingeniería en Energía, Universidad Politécnica de Guanajuato, 38483, Guanajuato, México and [6]Departamento de Ingeniería Molecular de Materiales, CFATA, UNAM, 76230, Querétaro, México

Email:
Ma. Concepción Arenas-Arrocena[*] - carenas@enes.unam.mx

* Corresponding author
§ Phone: + 52 - 477 1943418

Keywords:
abundant materials in the crust of Earth; electrical resistance; nanocrystals; nanodisks; non-toxic semiconductors; optical band gap; phase transition; photocurrent

Beilstein J. Nanotechnol. **2014,** *5,* 1542–1552.
doi:10.3762/bjnano.5.166

Received: 08 May 2014
Accepted: 26 August 2014
Published: 15 September 2014

This article is part of the Thematic Series "Physics, chemistry and biology of functional nanostructures II".

Guest Editor: A. S. Sidorenko

Abstract

Copper sulfide is a promising p-type inorganic semiconductor for optoelectronic devices such as solar cells, due its small band gap energy and its electrical properties. In this work nanocrystalline copper sulfide (Cu_xS), with two stoichiometric ratios (x = 2, 1.8) was obtained by one-pot synthesis at 220, 230, 240 and 260 °C in an organic solvent and amorphous Cu_xS was obtained in aqueous solution. Nanoparticle-like nucleation centers are formed at lower temperatures (220 °C), mixtures of morphologies (nanorods, nanodisks and nanoprisms) are seen at 230 and 240 °C, in which the nanodisks are predominant, while big hexagonal/prismatic crystals are obtained at 260 °C according to TEM results. A mixture of chalcocite and digenite phases was found at 230 and 240 °C, while a clear transition to a pure digenite phase was seen at 260 °C. The evolution of morphology and transition of phases is consistent to the electrical, optical, and morphological properties of the copper sulfide. In fact, digenite $Cu_{1.8}S$ is less resistive (346 Ω/sq)

and has a lower energy band gap (1.6 eV) than chalcocite Cu_2S (5.72×10^5 Ω/sq, 1.87 eV). Low resistivity was also obtained in Cu_xS synthesized in aqueous solution, despite its amorphous structure. All Cu_xS products could be promising for optoelectronic applications.

Introduction

Metallic chalcogenides based on cadmium, such as cadmium telluride, CdTe, or cadmium sulfide, CdS, have been widely investigated regarding their application in the optoelectronic field, mainly in photovoltaic devices due to the semiconducting, electronic and optical properties [1-5]. Cadmium is a toxic heavy metal, which limits its applications in the optoelectronic area. In fact, the current trend is to develop environment-friendly nanometric semiconductors with adequate optoelectronic properties for solar cells. It is well known that all properties (physical, chemical, magnetic) of nanometric materials differ from the bulk semiconductor due to the quantum effects [6]. Among the non-toxic nanomaterials with a small energy band gap that are promising for photovoltaic devices are: iron sulfide (FeS_2), tungsten sulfide (WS_2) and copper sulfide (Cu_2S) [7]. The last is a terrestrially abundant and interesting semiconductor due to its stoichiometric variety usually depicted as Cu_xS. Copper-rich sulfides (Cu_2S), Cu_xS with $x = 0.03$, 0.2, 0.25, and CuS are widely reported [8-27]. The stoichiometric ratio can be tailored by changing the concentration of copper or sulfide precursors, the reaction parameters and the kind of solvents. The following phases were obtained: djurleite ($Cu_{1.97}S$), digenite ($Cu_{1.8}S$) or analite ($Cu_{1.75}S$) [8-29]. These crystalline phases are stable p-type compounds, which could be used as absorber materials in solar cells [30-32]. However, the exact identification of the crystalline structure is controversial due to the stock of 86 XRD patterns for Cu_xS, some of which have reflections with narrowly spaced positions (see Table 1). This proximity makes it difficult to clearly assign diffraction patterns to certain crystalline phases.

On the other hand, the control of size, shape, distribution and stoichiometry of Cu_xS is an essential challenge nowadays, because these parameters are dependent on several factors [12,13,15,18,21]. For example, the reaction temperature modified the shape, size and optical properties of monodisperse Cu_2S obtained from a simple one-pot route [15]. In fact, there exists wide research about the synthesis of copper sulfide nanostructures obtaining different Cu/S ratios [9,11,16,20,23-26]. However, the lack of knowledge about the growth evolution and the phase transitions of copper sulfide is the motivation of this work.

In this work, the growth evolution and the phase transition of copper sulfide in the temperature range from 220 to 260 °C in an organic solvent is reported. The full electrical, morphological and optical properties of these crystalline samples synthesized in the organic solvent were compared with the amorphous Cu_xS obtained from aqueous solution.

Results and Discussion

Structural properties from X-ray diffraction

The structural properties of the copper sulfide samples (Cu_xS) depend on the synthesis and the reaction temperature (Figure 1). A fully amorphous product is obtained from aqueous solution according to the X-ray diffraction pattern (Figure S1 in Supporting Information File 1). However, the crystallinity of organic products is dependent on the temperature reaction. At 220 °C, Cu_xS presents three peaks with low intensity at $2\theta = 38$, 46.5 and 49° corresponding to the chalcocite structure (JCPDS 31-0482) (Figure 1a). Above a temperature of 230 °C, the Cu_xS product is more crystalline. There are four peaks with broadening and better intensity at $2\theta = 37.84$, 46.5, 48.82, and 54.94°, which match both to the chalcocite (JCPDS 31-0482) phase and djurleite phase (JCPDS 20-0365). At 240 °C (Figure 1b), well defined peaks of the digenite phase ($Cu_{1.8}S$, JCPDS 47-1748) appear at 28.26, 30.02, 32.66, 42.42, 46.62, 52.32, and 55.12 corresponding to the rhombohedral structure, which is consistent to the literature [19]. Small peaks of chalcocite can be seen, which are indicative of a mixture of phases. The X-ray pattern of Cu_xS synthesized at 260 °C presents sharp peaks at $2\theta = 27.84$, 32.22, 32.66, 46.24, 55.12, and 67° of the digenite phase.

Three shapes of unit cells of Cu_2S chalcocite phase can be presented: monoclinic (low chalcocite), hexagonal (high chalcocite), and cubic (cubic chalcocite) [30]. It is well known that the transformation from monoclinic (α,γ-Cu_2S) to hexagonal (β-Cu_2S) occurs at 103.5 °C and 101.8 °C for bulk and nanostructure chalcocite, respectively [33]. According to Machani et al. [34] the monoclinic phase changes to djurleite in ambient air and the real phase obtained is djurleite instead of chalcocite, even though, the chalcocite phase is usually reported [8,12-15]. In fact, the djurleite phase is obtained in ambient air [18], while chalcocite is obtained under argon atmosphere [14]. So, the products reported here obtained at 220 °C and 230 °C really are the chalcocite phase despite some peaks which match with djurleite. In fact, the Cu_xS products maintained the crystalline phases after we stored them for one year at room temperature, which is indicative of a good stability of the Cu_2S chalcocite and $Cu_{1.8}S$ digenite phases (results not shown here).

Table 1: Crystalline phases of copper sulfide from copper-rich (Cu_2S) to the lower concentration of copper (CuS) prepared in organic and aqueous media reported in the literature [8-27].

JCPDS	crystalline structure	morphology	position of reflections in [2θ, °] (respective crystallographic planes)	band gap energy E_g (eV)	solution/reference
84-0209	β-Cu_2S	bulk crystals	37.5 (1 0 2); 45.5 (1 1 0); 48 (1 0 3); 54 (0 0 4); 54.5 (2 0 1)	1.22	organic/[8]
232-0961	ortho. α-Cu_2S	films	27.5 (1 8 0); 33 (0 4 4); 47 (2 13 1); 51 (5 9 3); 57 (6 0 5)	2.48[a]	aqueous/[9]
02-1294	ortho. α-Cu_2S	hexagonal nanodisks	≈38; ≈46; ≈48.5; ≈61		organic/[10]
84-1770	Cu_2S	films	27.5 (1 1 1); 32.3 (2 0 0); 46 (2 2 0); 54.5 (3 1 1)		aqueous/[11]
00-0649	Cu_2S	hexagonal nanodisks	≈37.5; ≈45.5; ≈48.5; ≈54.5		organic/[12]
26-1116	hex. β-Cu_2S	14-facets polyhedra	37.5 (1 0 2); 45.5 (1 1 0); 48 (1 0 3); 54 (1 1 2)	1.35–1.56[b]	organic/[13]
26-1116	hex. β-Cu_2S	hexagonal nanocrystals	34.5 (1 0 1); 44 (1 0 2); 54 (1 1 0); 57 (1 0 3); 64.5 (0 0 4)		organic/[14]
26-1116	hex. β-Cu_2S	hexagonal nanodisks	37.5 (1 0 2); 45.5 (1 1 0); 48 (1 0 3); 54 (1 1 2)	1.36–1.53[b]	organic/[15]
26-1116	hex. β-Cu_2S	hexagonal nanodisks	37.5 (1 0 2); 45.5 (1 1 0); 48 (1 0 3); 54.5 (0 0 4); 56 (2 0 1)		water–organic/[16]
26-1116	hex. β-Cu_2S	nanorods	26.5 (0 0 2); 30 (1 0 1); 37.5 (1 0 2); 46 (1 1 0); 48.5 (1 0 3); 59 (2 0 0)	2.48[a]	water–organic/[17]
29-0578	tet. $Cu_{1.96}S$	films	27.5 (1 0 2); 32.5 (1 0 3); 39 (1 0 4); 48.5 (2 0 2)	1.4	aqueous/[9]
04-0842	digenite $Cu_{1.8}S$	spherical nanoparticles	≈28; ≈32.5; ≈46.5		organic/[12]
47-1748	digenite $Cu_{1.8}S$	irregular nanoparticles	≈28; ≈32; ≈46.5		aqueous/[18]
47-1748	digenite $Cu_{1.8}S$	irregular nanoparticles	≈28; ≈32; ≈46.5; ≈55		water–organic/[19]
24-0061	digenite $Cu_{1.8}S$	films	28 (1 1 1); 32 (2 0 0); 46 (2 2 0)	1.55	aqueous/[20]
23-0960	cub. digenite $Cu_{1.76}S$	films	28 (6 6 2); 32 (8 6 0); 47 (10 10 0); 55 (15 7 1)	2.11[a]	aqueous/[9]
00-0833	CuS	spherical nanoparticles	≈29.5; ≈32.5; ≈48.5		organic/[12]
79-2321	CuS	irregular nanoparticles	29.5; 32; 48; 59		aqueous/[18]
01-1281	hex. CuS	clusters of nanoparticles	29 (1 0 2); 32 (1 0 3); 48 (1 1 0); 52.5 (1 0 4);		aqueous/[21]
03-0724	hex. CuS	nanoflowers	27.6 (1 0 1); 29.5 (1 0 2); 31.6 (1 0 3); 47.6 (1 1 0); 52.5 (1 0 8); 59 (1 1 6)		aqueous/[22]
85-0620	CuS	films based on nanorods	44 (1 0 6); 45 (0 0 8); 51 (1 0 8); 54 (1 1 6); 65 (2 1 6); 75 (2 0 8)		aqueous/[23]
06-0464	hex. CuS	films	29 (1 0 2); 31.5 (1 0 3); 32.5 (0 0 6); 48 (1 1 0); 52.5 (1 0 8)	1.72[a]	aqueous/[9]
06-0464	hex. CuS	films	29 (1 0 2); 31.5 (1 0 3); 32.5 (0 0 6); 48 (1 1 0)	1.55	aqueous/[20]
06-0464	hex. CuS	films	32 (1 0 3); 39.5 (1 0 5); 43.5 (1 0 6); 48 (1 1 0); 53 (1 0 8); 59.5 (1 1 6); 74.5 (2 0 8)	2.8	organic/[24]
06-0464	CuS	films based on polycrystals	28 (1 0 1); 29 (1 0 2); 32 (1 0 3) 34 (0 0 6); 48 (1 1 0); 59 (1 1 6); 59.2 (1 0 6) 52 (1 0 8)	2[a]; 2.58[b]	aqueous/[25]
06-0464	hex. CuS	nanoflowers	27.6 (1 0 1); 29.5 (1 0 2); 31.6 (1 0 3); 48 (1 1 0); 52.5 (1 0 8); 59 (1 1 6)		ethanol/[26]
06-0464	hex. CuS	irregular nanoparticles	28 (1 0 1); 29 (1 0 2); 32 (1 0 3); 48 (1 1 0); 52 (1 0 8); 59 (1 1 6)		water–oil/[27]

[a]Direct band gap; [b]indirect band gap.

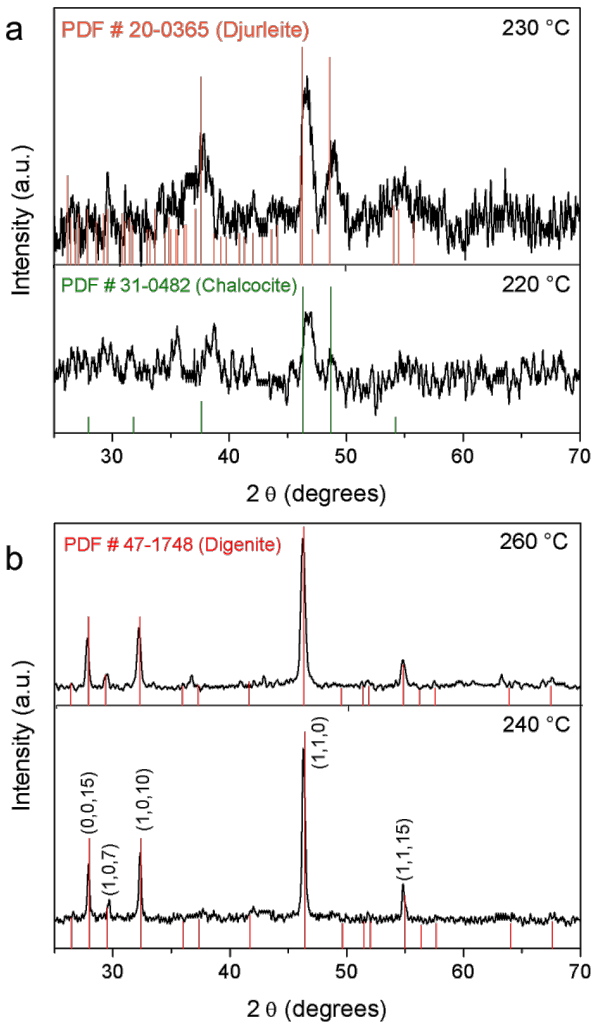

Figure 1: X-ray patterns of copper sulfide synthesized in organic solution at a) 230 and 220 °C, the chalcocite phase is obtained and at b) 240 and 260 °C, the predominant phase is the digenite.

The grain size and stress of the crystalline copper sulfide samples from organic synthesis at 230–260 °C were obtained from the full widths at a half maximum (FWHM) of the diffraction peaks and the linear combination of the following equation [35]:

$$\frac{\beta\cos(\theta)}{\lambda} = \frac{1}{D} + \frac{\varepsilon\sin(\theta)}{\lambda},$$

where β is the FWHM measured in radians, θ the Bragg angle of the peaks, λ the XRD wavelength, in our case in nanometers (λ = 0.154 nm), D is the effective crystallite size, and ε is the effective strain. A plot of β cos(θ)/λ versus sin(θ)/λ for all the samples gives the grain size and the strain, as shown in Figure S2 in Supporting Information File 1. The intercept is the inverse of the grain size and the slope is the strain, respectively. The grain size increases as the temperature increases (24.5 to 28.3 nm), the effective strain decreases in the samples shown that the least stress was at 260 °C (-8.26×10^{-5}) and the highest was at 230 °C (-2.73×10^{-3}).

Morphology from TEM and HRTEM

TEM images revel that amorphous Cu_xS from aqueous solution is constituted of nanometric particles with undefined shape that are agglomerated into clusters (See Figure S3 in Supporting Information File 1), which is in concordance with Cu_xS obtained in similar aqueous systems [21].

The morphology of Cu_xS samples from organic solution depends on the reaction temperature, for example irregular particles below 10 nm can be observed for Cu_xS obtained at 220 °C (Figure 2a). At 230 °C short chains of stacked nanorods with lengths (l) and width (w) of about 13.97 ± 2.7 × 5.86 ± 1.09 nm (from 260 particles), are seen in Figure 2b. Some hexagonal nanodisks of about 20–40 nm and prisms of about 50 nm are also observed. At 240 °C (Figure 2c) aligned nanorods are seen with similar dimensions (13.55 ± 1.86 × 5.91 ± 0.75 nm from 130 particles) to those seen at 230 °C. The size of the Cu_xS crystals at the higher temperature is not significantly different. However, the amount of crystals with a prism geometry is increased. These two types of morphology are consistent to the mixture of phases that were shown in the X-ray results. Big crystals with different sizes (25–80 nm) are observed for the samples of Cu_xS synthesized at 260 °C (Figure 2d) and a fewer nanorods of about 17.35 ± 3.70 × 6.59 ± 1.27 nm (from 30 particles) are also seen in Figure S4 in Supporting Information File 1. The average aspect ratios (l/w) of the Cu_xS nanorods are about 2.38 (230 °C), 2.29 (240 °C), and 2.63 (260 °C) taken from the data of size distribution (Figure S5 in Supporting Information File 1). The change and evolution of the morphology is consistent to the transition of phase, from chalcocite to digenite.

In order to verify the full transition of the digenite phase an HRTEM analysis of the crystals was made. The distance between the lines in the HRTEM image (Figure 3) is approximately 0.32 nm. This corresponds to the (0015) plane spacing of the digenite phase, which matches the peak of 46% of intensity in the XRD pattern shown in Figure 1b. The diffraction pattern of electrons obtained by the Fourier transformation (inset of Figure 3) shows an interplanar distance of about 0.197 nm, close to the value 0.19644 nm for the (110) spacing of the digenite phase (the peak for 100% intensity in the XRD pattern).

From TEM images, it can be observed that the phase transformation occurs from 220 to 260 °C and involves three stages: the

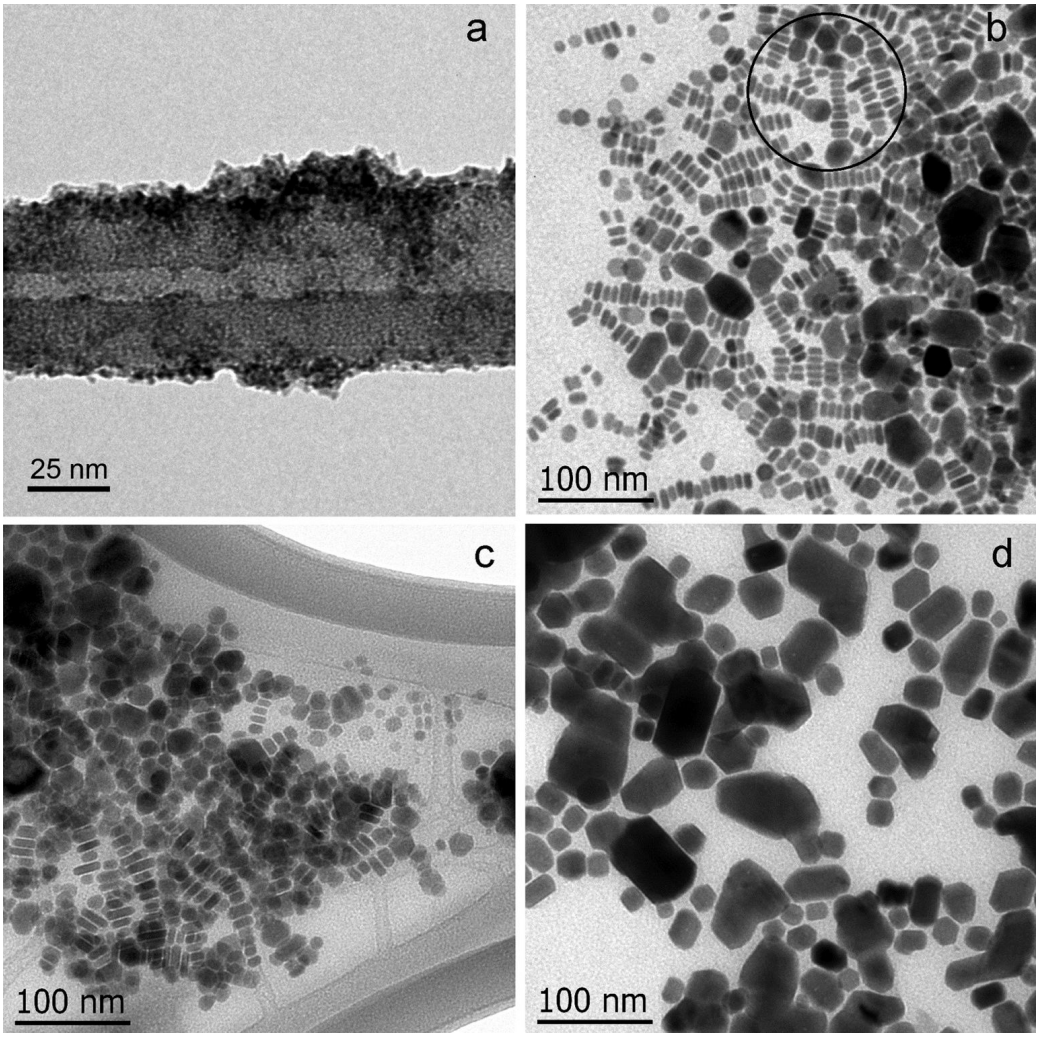

Figure 2: TEM images of copper sulfide synthesized in organic solution at a) 220, b) 230, c) 240 and d) 260 °C. The morphology of the Cu_xS change from irregular nanoparticles to nanoprisms with increasing temperature. The encircled area shows an alignment of the nanorrods (b).

nucleation, the shape evolution of the chalcocite crystals and the transition of the chalcocite to the digenite phase. Nanoparticles are formed in the first stage at 220 °C, which are the nuclei to the formation of a mixture of morphologies, i.e., nanodisks (25–40 nm) and irregularly shaped prisms (50–100 nm). The movement of the nanodisks results in the formation of the digenite phase through fusion of the nanodisks.

Cu/S ratio from EDS

The EDS patterns shows two peaks at 0.9 and 8.0 keV attributed to Cu Kα and Cu Lα emission, while a third peak at 2.3 keV is due to the S Kα emission. Table 2 displays the average of Cu/S ratios calculated from the atomic percentage of each element from at least three measurements. The amorphous copper sulfide synthesized in an aqueous solution has a Cu/S ratio of 1.48 ± 0.03, close to the 1:1 ratio of CuS [18]. The organic Cu_xS samples show the following Cu/S ratios: 1.58 ± 0.02 for the sample at 220 °C, 1.92 ± 0.05, and 1.83 ± 0.08 for crystalline chalcocite/digenite at 230 and 240 °C, respectively, and 1.69 ± 0.05 for the digenite phase (at 260 °C). These values are similar to the chalcocite Cu_2S and digenite $Cu_{1.8}S$ phases, respectively.

Optical properties

The optical absorbance spectra of the Cu_xS are shown in Figure 4. Both, the amorphous sample from aqueous synthesis and the chalcocite Cu_xS from organic synthesis at 220 °C, present a weak and broad absorption band at approximately 500 nm. However, crystalline Cu_xS samples show a well-defined absorbance band between 490 to 600 nm. In fact, a red shift of about 40 to 60 nm is presented from the chalcocite (Cu_2S) to the digenite phases ($Cu_{1.8}S$), which is in agreement to the increment of crystal size. This phenomenon is related to the free charges due to the copper deficiency in the samples. For

Table 2: Summary of the morphological, optical, and electrical properties of Cu_xS samples.

samples/temperature (°C)	crystalline phase	nanorod dimensions $l \times w$ (nm)	Cu/S ratio	maximum absorbance peak (nm)	direct E_g (eV)	resistance (Ω/sq)
A[a]/100	amorphous	—	1.48 ± 0.03	530	2.20	461.50
O[b]/220	chalcocite	—	1.58 ± 0.02	—	1.57	8.66×10^6
O/230	chalcocite/ digenite	13.97 ± 2.7 × 5.86 ± 1.09	1.92 ± 0.05	440	1.87	5.72×10^5
O/240	chalcocite/ digenite	13.55 ± 1.8 × 5.91 ± 0.75	1.83 ± 0.08	480	1.76	7.29×10^7
O/260	digenite	17.35 ± 3.7 × 6.59 ± 1.27	1.69 ± 0.05	540	1.60	346.45

[a]Samples from aqueous solution; [b]samples from organic solution.

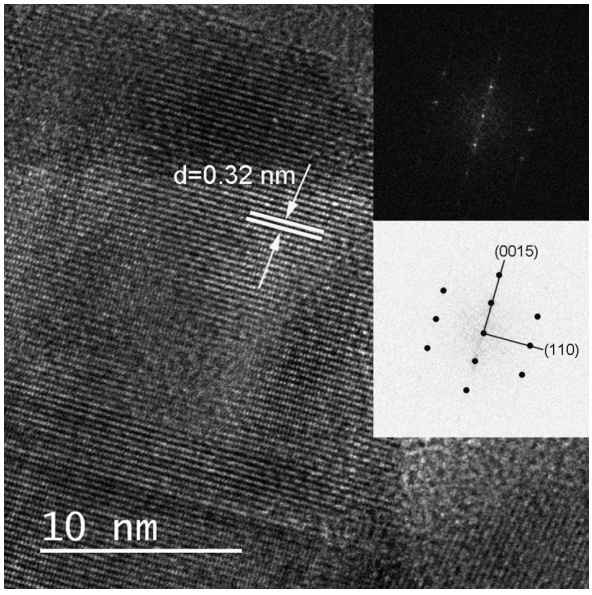

Figure 3: HRTEM image of copper sulfide obtained from synthesis in an organic solvent. The inset figures display the crystallographic planes (0015) and (110), respectively, of the digenite phase.

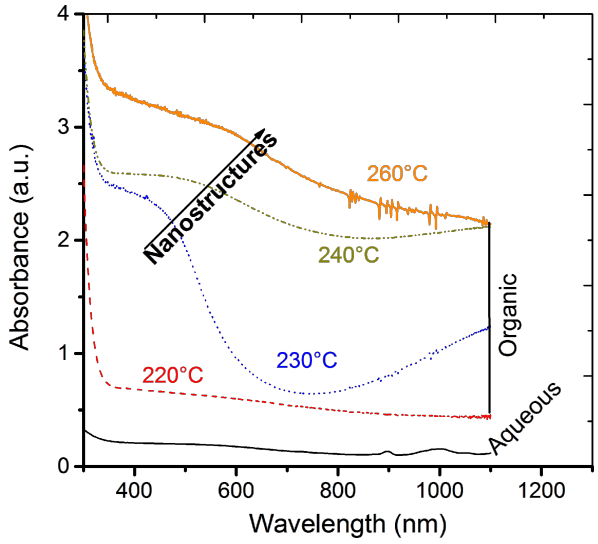

Figure 4: Absorbance of copper sulfide nanocrystals synthesized in an aqueous solution and in an organic solvent. A clear shift towards low energies is observed in the Cu_xS samples synthesized in the range from 230 to 260 °C.

example, the maximum absorbance band has been reported at 450 nm for Cu_2S, while it is observed at longer wavelength (950 nm) for CuS [36]. It is clear, that the deficiencies of copper generate a displacement or shift of the optical absorption, which is consistent to the transition of the phases.

The energy band gaps of the samples were computed by the Tauc plot for direct transition (Figure 5). The indirect plot (inset) did not present a satisfactory straight-line region for all samples. The Cu_xS sample prepared in aqueous solution shows an E_g about 2.2 eV for the direct and 2.0 eV for the indirect transition, respectively (see inset of Figure 5). This is coherent with the value of 2.3 eV reported for crystalline or amorphous CuS covellite thin films from an aqueous solution [25,37].

On the other hand, the direct E_g values of the Cu_xS samples prepared in the organic solvent are in the range of 1.57–1.87 eV. These values are adequate for an optical absorption in the visible region, which makes the samples very promising materials for solar cell applications. In Table 2 we observe a clear decrease of E_g from 1.87 to 1.60 eV from crystalline chalcocite to the digenite phase, which is in agreement to the increasing crystal size observed with TEM. These values are slightly smaller to those reported for bulk copper sulfide (1.7 and 2.0 eV) [38], so, it is consistent to the size of the nanostructures. On the other hand, an effect was found for chalcocite crystals, namely a shift into the UV region was observed and consequently, large E_g values were obtained at high deposition times without modifying the chalcocite phase [13].

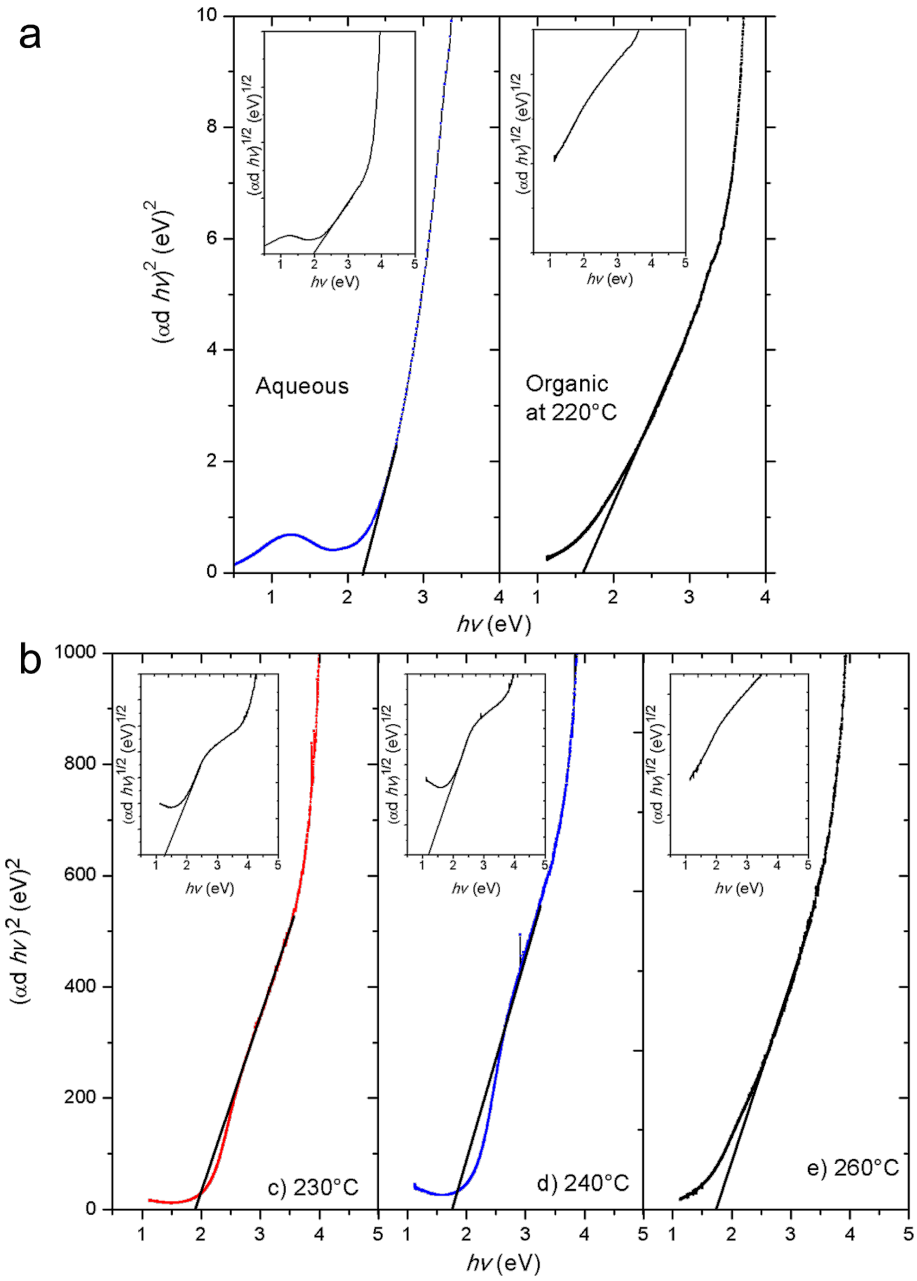

Figure 5: Direct band gaps of copper sulfide in a) amorphous phase obtained by aqueous synthesis and b) crystalline phases from organic media. Indirect band gap plots are included as an inset in all plots. The clear slopes in the graphics show the direct band gap energy.

Electrical properties

The Cu_xS films prepared in aqueous solution are amorphous with undefined morphology. They exhibit a low square electrical resistivity (about 10^3 Ω/sq) as shown in Figure 6. Chalcocite Cu_xS from organic solution has a resistance of the order of 10^5–10^6 Ω/sq, while crystalline Cu_xS has a resistivity of about 10^7 Ω/sq at 240 °C and 10^2 Ω/sq at 260 °C, respectively. In fact, the samples obtained at 230 and 240 °C, which consist of a mixture of chalcocite and digenite phases, are more resistive than the digenite phase (sample at 260 °C). This means that the copper deficiency improves the conductivity of the Cu_xS, which is consistent to the reports in the literature [20]. Deficient copper structures like anaite ($Cu_{1.75}S$) have been grown onto the surface of CuS thin films, which improved their conductivity [28].

The time–photo-current response of Cu_xS is reported for the first time (Figure 7). It is clear that the amorphous Cu_xS presents a low photosensitivity in contrast to the crystalline Cu_xS samples obtained from organic solution, which are

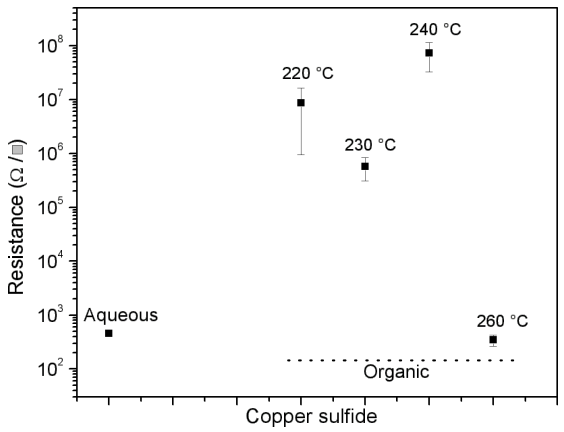

Figure 6: Square resistance of copper sulfide films synthesized in an aqueous solution (left) and in organic solution (right). The samples with low electrical resistance are amorphous Cu_xS obtained from aqueous solution and crystalline Cu_xS synthesized at 260 °C.

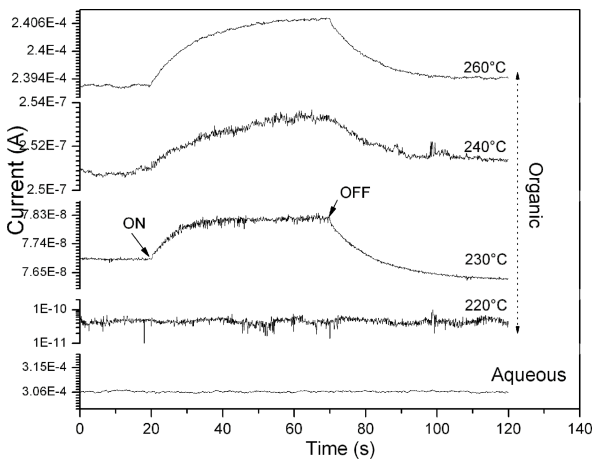

Figure 7: Photoconductivity of copper sulfide films, synthesized in both aqueous and organic media. Only the organic samples show photoconductivity.

slightly photosensible, suggesting a photo-generation of carrier charges. The current increases gradually as a function of the time exposed to the light, this is attributed to the recombination of charges due to the superficial states in the Cu_xS samples.

Mechanism of the formation and phase transition

According to the results presented above, a formation mechanism of the growth and the phase transition from chalcocite to digenite is proposed (Figure 8). It is clear that the nucleation of the crystals begins at 220 °C. It is a key to ensure the growth of nanoparticles at initial stages of the reaction. Above this temperature chains of aligned nanorods are formed and other crystals, nanodisks and prisms, grow. The chains of nanorods are predominant at 230 °C while nanodisks and prisms are the main morphology at 240 °C. A full phase transition from chalcocite to digenite is obtained at 260 °C.

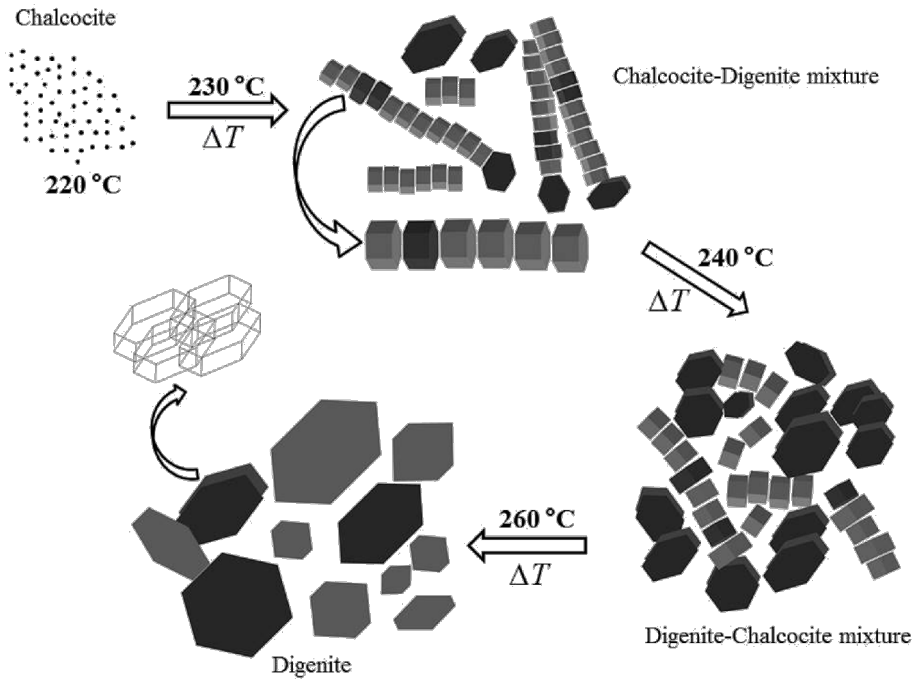

Figure 8: Scheme of the phase-transition mechanism from chalcocite to digenite and the formation of the respective nanocystals of the Cu_xS samples as a function of the temperature. The growth of the crystalline digenite begins with the formation the nanoparticles at 220 °C and it ends at 260 °C.

Wang et al. obtained nanodisks of chalcocite Cu_2S at 220 °C [15]. But, in our case, this temperature is the first stage to the phase transformation from the chalcocite to the digenite phase. According to Wang et al., the growth and rearrangement of the nanodisks are dependent on the concentration of precursors, amount of surfactant, the reaction temperature, and the reaction time. We found that this rearrangement of nanodisks is necessary for the transition of the digenite phase and it is induced only by the temperature.

On the other hand, the amorphous structure of Cu_xS prepared from aqueous solution is consistent to its synthesis at low temperatures [37], during which the CuS crystalline covellite phase can be formed above 200 °C [24,25], and the tailoring of the Cu/S stoichiometric ratio and the phase transformation had been reached at temperatures between 230 to 700 °C [21]. Grozdanov and Najdoski found that the electrical sheet resistance decreases as the copper content decreased [25]. This is consistent with our results.

Conclusion

Copper sulfide with 2 and 1.8 of Cu/S ratio were synthesized successfully from chemical synthesis in an organic solvent at 220–260 °C. Amorphous Cu_xS was also obtained from aqueous solution at low temperatures with a low electrical resistance, indicative of a high conductivity. The evolution growth, formation of nanostructures, and phase transition were completely described in a scheme based on the TEM images. The full phase transition from chalcocite to digenite is obtained at 260 °C in an organic media. It is clear that the optical and electrical properties are suitable for optoelectronic applications, such as solar cells.

Experimental

Crystalline copper sulfide nanostructures were obtained by one-pot synthesis in an organic solvent while raising the reaction temperature from 220 to 260 °C. Amorphous copper sulfide was also synthesized by a chemical reaction in aqueous solution at 40 °C. Films, colloid and powder products were obtained from both reactions.

Reagents

For the organic reaction: copper(I) acetate ($C_2H_3CuO_2$, Sigma-Aldrich, 97%), tri-*n*-octylphosphine oxide ($OP(C_8H_{17})_3$, TOPO Sigma-Aldrich, ≥98%), 1-dodecanethiol ($C_{12}H_{25}SH$, Aldrich, ≥98%), and dichlorobenzene ($C_6H_4Cl_2$, Sigma-Aldrich 99%) were used as received.

The aqueous reaction: deionized water (10 MΩ·cm), thiourea (H_2NCSNH_2, Aldrich ≥99%), copper(II) sulfate pentahydrate ($CuSO_4{\cdot}5H_2O$, Baker 99.3%), triethanolamine (TEA, $C_6H_{15}NO_3$, Baker 99.8%), and sodium acetate ($NaCOOCH_3$, Baker, 99.5%)

Synthesis of nanocrystalline copper sulfide from organic solvent

It consisted of a one-pot colloidal process previously reported by Wang et al. [15] with slight modifications. In this reaction, $C_2H_3CuO_2$ was the copper precursor and $C_{12}H_{25}SH$ the sulfur precursor. In brief, 1g of TOPO and 0.0488 g of $C_2H_3CuO_2$ were mixed with 30 mL of $C_{18}H_{36}$ in a three-neck flask. Argon was flowed into the system for 30 min to keep the reaction under an inert atmosphere. Then, the solution was heated to 160 °C and 1 mL of $C_{12}H_{25}SH$ was injected quickly under vigorous stirring. The mixture reacted at constant temperature (220, 230, 240 or 260 °C) during 120 min. The colloidal brown products were washed three times with dichlorobenzene by centrifugation (20,000 rpm, 20 min) and were re-dispersed in dichlorobenzene. The organic products were cast on a Corning glass substrate and dried at 60 °C in an electric grill in order to form films.

Synthesis of amorphous copper sulfide from aqueous solution

In this reaction thiourea and copper(II) sulfate pentahydrate ($CuSO_4{\cdot}5H_2O$) were the sulfur and copper precursors, respectively, and the TEA ligand was an intermediary in the reaction. The synthesis proceeded as follows: A three-necked reactor containing 440 mL of deionized water was placed on a hot plate with magnetic stirring at 40 °C for 30 min. Clean Corning glass substrates were immersed inside the reactor in order to obtain the films by in situ deposition. Subsequently 1.3389 g of $CuSO_4{\cdot}5H_2O$, previously dissolved in 20 mL of deionized water (1.3389 g/20 mL), 0.4354 g/14.5 mL of $NaCOOCH_3$ and, 5.18 mL/20 mL of TEA. Finally, 0.2 g/31 mL of H_2NCSNH_2 was added in three aliquots each for 25 min. The substrates were withdrawn from the reactor and rinsed with deionized water. The precipitated products were washed with deionized water three times, immediately they were centrifuged and dried at room temperature. Both films and powder products, received a thermal treatment at 100 °C in air in a stove during 1 h.

Characterization

Powders of two syntheses, aqueous and organic, respectively, of Cu_xS were re-dispersed in isopropanol and toluene. One aliquot from these solutions was placed on carbon-coated copper grids for characterization by TEM, in a JEOL JEM-1010 at 80 kV of acceleration potential. Additionally, thin films of aqueous and organic syntheses of Cu_xS were characterized by X-ray diffraction (Rigaku, MiniFlex, Cu Kα 1.54 Å and 2θ from 10 to 70°, rate 2°/min each 0.02 s), electrically by the four-points-probe technique, by UV–vis spectroscopy (Thermo Scientific Genesys

10S UV–vis spectrophotometer in the range of 200 to 1100 nm) in order to determine, the structural phase, the electrical resistance and optical absorbance spectra, respectively. The photoresponse measurements were made by applying a potential of 1 V at the sample: 20 s in darkness, 50 s under illumination and another 50 s in darkness. For this, two rectangular metallic contacts (0.5 × 0.2 cm) were painted on the surface of the films with silver paint in a square sample of 0.5 cm^2.

Energy dispersive X-ray spectroscopy (EDS) was carried out in a JSM-6060LV SEM at 20 keV by using KBr pellets containing granules of Cu_xS powder to make the punctual analysis.

Supporting Information

Supporting Information File 1

Additional Figures.
[http://www.beilstein-journals.org/bjnano/content/supplementary/2190-4286-5-166-S1.pdf]

Acknowledgements

This work was financed by CONACyT-México (CB176450, CB154787) and SENER-CONACyT (CeMIE-Sol project No. 27). The authors are grateful for the technical support received from Domingo Rangel, Beatriz Millán, Alicia del Real, Lourdes Palma (INB-UNAM) and Gabriel Nava (INB-UNAM). Thank to Marcela Ovalle Marroquín for her appreciable helps in HRTEM.

References

1. Xie, Y.-L. *Electrochim. Acta* **2013,** *105,* 137–141. doi:10.1016/j.electacta.2013.04.157
2. Kosyachenko, L.; Toyama, T. *Sol. Energy Mater. Sol. Cells* **2014,** *120,* 512–520. doi:10.1016/j.solmat.2013.09.032
3. Arenas, M. C.; Mendoza, N.; Cortina, H.; Nicho, M. E.; Hu, H. *Sol. Energy Mater. Sol. Cells* **2010,** *94,* 29–33. doi:10.1016/j.solmat.2009.04.013
4. Salinas, O. H.; López-Mata, C.; Hu, H.; Nicho, M. E. *Sol. Energy Mater. Sol. Cells* **2006,** *90,* 2421–2428. doi:10.1016/j.solmat.2006.03.015
5. Mathew, X.; Cruz, J. S.; Coronado, D. R.; Millán, A. R.; Segura, G. C.; Morales, E. R.; Martínez, O. S.; Garcia, C. C.; Landa, E. P. *Sol. Energy* **2012,** *86,* 1023–1028. doi:10.1016/j.solener.2011.06.024
6. Alivisatos, A. P. *Science* **1996,** *271,* 933–937. doi:10.1126/science.271.5251.933
7. Wadia, C.; Alivisatos, A. P.; Kammen, D. M. *Environ. Sci. Technol.* **2009,** *43,* 2072–2077. doi:10.1021/es8019534
8. Zhao, F.; Chen, X.; Xu, N.; Lu, P.; Zheng, J.-G.; Su, Q.; Wu, M. *J. Phys. Chem. Solids* **2006,** *67,* 1786–1791. doi:10.1016/j.jpcs.2006.02.020
9. Bagul, S. V.; Chavhan, S. D.; Sharma, R. *J. Phys. Chem. Solids* **2007,** *68,* 1623–1629. doi:10.1016/j.jpcs.2007.03.053
10. Tang, A.; Qu, S.; Li, K.; Hou, Y.; Teng, F.; Cao, J.; Wang, Y.; Wang, Z. *Nanotechnology* **2010,** *21,* 285602. doi:10.1088/0957-4484/21/28/285602
11. Lu, Y.; Yi, G.; Jia, J.; Liang, Y. *Appl. Surf. Sci.* **2010,** *256,* 7316–7322. doi:10.1016/j.apsusc.2010.05.072
12. Bera, P.; Seok, S. I. *Solid State Sci.* **2012,** *14,* 1126–1132. doi:10.1016/j.solidstatesciences.2012.05.027
13. Li, Y.; Zhang, L.; Yu, J. C.; Yu, S.-H. *Prog. Nat. Sci.* **2012,** *22,* 585–591. doi:10.1016/j.pnsc.2012.12.001
14. Wu, Y.; Wadia, C.; Ma, W.; Sadtler, B.; Alivisatos, A. P. *Nano Lett.* **2008,** *8,* 2551–2555. doi:10.1021/nl801817d
15. Wang, Y.; Hu, Y.; Zhang, Q.; Ge, J.; Lu, Z.; Hou, Y.; Yin, Y. *Inorg. Chem.* **2010,** *49,* 6601–6608. doi:10.1021/ic100473e
16. Zhang, P.; Gao, L. *J. Mater. Chem.* **2003,** *13,* 2007–2010. doi:10.1039/B305584A
17. Larsen, T. H.; Sigman, M.; Ghezelbash, A.; Doty, R. C.; Korgel, B. A. *J. Am. Chem. Soc.* **2003,** *125,* 5638–5639. doi:10.1021/ja0342087
18. Zhao, Y.; Pan, H.; Lou, Y.; Qiu, X.; Zhu, J.; Burda, C. *J. Am. Chem. Soc.* **2009,** *131,* 4253–4261. doi:10.1021/ja805655b
19. Leidinger, P.; Popescu, R.; Gerthsen, D.; Lünsdorf, H.; Feldmann, C. *Nanoscale* **2011,** *3,* 2544–2551. doi:10.1039/c1nr10076a
20. Nair, M. T. S.; Guerrero, L.; Nair, P. K. *Semicond. Sci. Technol.* **1998,** *13,* 1164–1169. doi:10.1088/0268-1242/13/10/019
21. Kristl, M.; Hojnik, N.; Gyergyek, S.; Drofenik, M. *Mater. Res. Bull.* **2013,** *48,* 1184–1188. doi:10.1016/j.materresbull.2012.12.020
22. Ding, T.-Y.; Wang, M.-S.; Guo, S.-P.; Guo, G.-C.; Huang, J.-S. *Mater. Lett.* **2008,** *62,* 4529–4531. doi:10.1016/j.matlet.2008.08.031
23. Dhasade, S. S.; Patil, J. S.; Han, S. H.; Rath, M. C.; Fulari, V. J. *Mater. Lett.* **2013,** *90,* 138–141. doi:10.1016/j.matlet.2012.09.013
24. Maji, S. K.; Mukherjee, N.; Dutta, A. K.; Srivastava, D. N.; Paul, P.; Karmakar, B.; Mondal, A.; Adhikary, B. *Mater. Chem. Phys.* **2011,** *130,* 392–397. doi:10.1016/j.matchemphys.2011.06.057
25. Grozdanov, I.; Najdoski, M. *J. Solid State Chem.* **1995,** *114,* 469–475. doi:10.1006/jssc.1995.1070
26. Zou, J.; Jiang, J.; Huang, L.; Jiang, H.; Huang, K. *Solid State Sci.* **2011,** *13,* 1261–1267. doi:10.1016/j.solidstatesciences.2011.03.019
27. Jiang, D.; Hu, W.; Wang, H.; Shen, B.; Deng, Y. *Colloids Surf., A* **2011,** *384,* 228–232. doi:10.1016/j.colsurfa.2011.03.053
28. Liufu, S.-C.; Chen, L.-D.; Yao, Q.; Huang, F.-Q. *J. Phys. Chem. C* **2008,** *112,* 12085–12088. doi:10.1021/jp805029w
29. Pattrick, R. A. D.; Mosselmans, J. F. W.; Charnock, J. M.; England, K. E. R.; Helz, G. R.; Garner, C. D.; Vaughan, D. J. *Geochim. Cosmochim. Acta* **1997,** *61,* 2023–2036. doi:10.1016/S0016-7037(97)00061-6
30. Xu, Q.; Huang, B.; Zhao, Y.; Yan, Y.; Noufi, R.; Wei, S.-H. *Appl. Phys. Lett.* **2012,** *100,* 061906. doi:10.1063/1.3682503
31. Isac, L.; Duta, A.; Kriza, A.; Manolache, S.; Nanu, M. *Thin Solid Films* **2007,** *515,* 5755–5758. doi:10.1016/j.tsf.2006.12.073
32. Lu, Y.; Hou, Y.; Wang, Y.; Feng, Z.; Liu, X.; Lü, Y. *Synth. Met.* **2011,** *161,* 906–910. doi:10.1016/j.synthmet.2011.02.023
33. Wang, S.; Guo, L.; Wen, X.; Yang, S.; Zhao, J.; Liu, J.; Wu, Z. *Mater. Chem. Phys.* **2002,** *75,* 32–38. doi:10.1016/S0254-0584(02)00026-3
34. Machani, T.; Rossi, D. P.; Golden, B. J.; Jones, E. C.; Lotfipour, M.; Plass, K. E. *Chem. Mater.* **2011,** *23,* 5491–5495. doi:10.1021/cm2022196
35. Quadri, S. B.; Skeleton, E. F.; Hsu, D.; Dinsmore, A. D.; Yang, J.; Gray, H. F.; Ratna, B. R. *Phys. Rev. B* **1999,** *60,* 9191–9193. doi:10.1103/PhysRevB.60.9191

36. Solanki, J. N.; Sengupta, R.; Murthy, Z. V. P. *Solid State Sci.* **2010,** *12,* 1560–1566. doi:10.1016/j.solidstatesciences.2010.06.021
37. Güneri, E.; Kariper, A. *J. Alloys Compd.* **2012,** *516,* 20–26. doi:10.1016/j.jallcom.2011.11.054
38. Liu, G.; Schulmeyer, T.; Brötz, J.; Klen, A.; Jaegermann, W. *Thin Solid Films* **2003,** *431–432,* 477–482. doi:10.1016/S0040-6090(03)00190-1

License and Terms

BEILSTEIN JOURNAL OF NANOTECHNOLOGY

Growth and structural discrimination of cortical neurons on randomly oriented and vertically aligned dense carbon nanotube networks

Christoph Nick[1,§], Sandeep Yadav[2,§], Ravi Joshi[2], Christiane Thielemann[*1] and Jörg J. Schneider[*2]

Full Research Paper

Open Access

Address:
[1]University of Applied Sciences Aschaffenburg, Department of Engineering, BioMEMS lab, Würzburger Strasse 45, 64743 Aschaffenburg, Germany and [2]Technische Universität Darmstadt, Fachbereich Chemie, Eduard-Zintl-Institut für Anorganische und Physikalische Chemie, Alarich-Weiss-Str. 12, 64287 Darmstadt Germany

Email:
Christiane Thielemann[*] - christiane.thielemann@h-ab.de;
Jörg J. Schneider[*] - joerg.schneider@ac.chemie.tu-darmstadt.de

* Corresponding author
§ Equal contributors

Keywords:
carbon nanotube; chemical vapour deposition; interface; neuron; scaffold

Beilstein J. Nanotechnol. **2014,** *5,* 1575–1579.
doi:10.3762/bjnano.5.169

Received: 08 May 2014
Accepted: 02 September 2014
Published: 17 September 2014

This article is part of the Thematic Series "Physics, chemistry and biology of functional nanostructures II".

Guest Editor: A. S. Sidorenko

Abstract

The growth of cortical neurons on three dimensional structures of spatially defined (structured) randomly oriented, as well as on vertically aligned, carbon nanotubes (CNT) is studied. Cortical neurons are attracted towards both types of CNT nano-architectures. For both, neurons form clusters in close vicinity to the CNT structures whereupon the randomly oriented CNTs are more closely colonised than the CNT pillars. Neurons develop communication paths via neurites on both nanoarchitectures. These neuron cells attach preferentially on the CNT sidewalls of the vertically aligned CNT architecture instead than onto the tips of the individual CNT pillars.

Findings

Biochemically functionalised carbon nanotubes (CNTs) are attractive for various sensing and electronic applications. These include, but are not limited to, gas sensors [1], mechanical sensors [2], biosensors (e.g., for glucose or DNA) [3,4], and vertical interconnect access (vias) applications based on CNT bundles [5]. CNTs have also sparked interest in the biomedical community since they have outstanding potential as a substrate for growing different cell type materials [6-8]. Due to their very

good electrical conductivity they are a promising substrate for neuron growth as well as for biocompatible electrode materials to record and/or stimulate neural activity. CNTs do have a high capacity and low impedance, e.g., compared to IrO_2 which is widely used as electrical interface for cells, as has been manifested by cyclic voltammetry and impedance spectroscopy [9]. Thus CNTs allow to minimise the stimulation voltage as well as the electrode sizes while maintaining a good performance in signal recording [10]. This subject has been of strong interdisciplinary interest over the last decade [9,11,12]. Mainly unordered randomly deposited CNTs and dense carbon nanotube fibres (CNF) have been studied as growth substrate for cells. It was found that both carbon based materials can boost neural activity, most likely due to short circuiting the cells and thus increasing excitatory input [13-15]. Furthermore, due to their 1D morphology, the topography of CNTs may resemble the extracellular matrix, therefore increasing the adhesion of neurons [16]. In addition, chemical functionalization [17] and surface charges [18] influence neurite outgrowth and network formation. CNT islands can serve as scaffolds for neurons due to their well-known capability to guide neural growth [9,19-21]. Since CNTs offer a high intrinsic surface area and thus a high charge injection capability they have proven their ability as electrode material for the recording and the stimulation of neurons. For this purpose randomly oriented CNTs have been synthesized and transferred to suitable substrates involving techniques as stamping/printing and in-place growth. The use of vertically aligned CNTs for the design of 3D electrodes was proposed [22]. The interface between dense vertically aligned carbon nanofibers and neurons derived from the rat pheochromocytoma (PC12 cell line) was also studied [10]. However, although vertically grown CNTs have been proposed as stimulating electrodes for neurons, the growth of primary neurons on these nanostructures has not yet been studied in depth and may present a substantial step along these lines. Herein, we report on the in vitro growth of cortical neurons on islands of randomly oriented CNT as well as on islands of vertically aligned up to 500 μm in length CNT structures. For the fabrication of both types of CNTs a water-assisted catalytically driven chemical vapour deposition (CVD) growth process was employed [23]. Two different morphologies of CNT arrays were grown depending on the CVD conditions applied (i.e., Si and Au substrate, metal catalyst, gas volume). Subsequently both types of spatial arrays, randomly oriented and ordered vertically aligned 3D CNT architectures were studied towards their interaction towards cultured neurons (general growth behaviour, preferential growth).

Islands of randomly oriented and vertical aligned CNTs were structured by using a photo-lithography process as depicted in Figure 1 [24]. A photosensitive resist (AZ 701 mir, Micro-

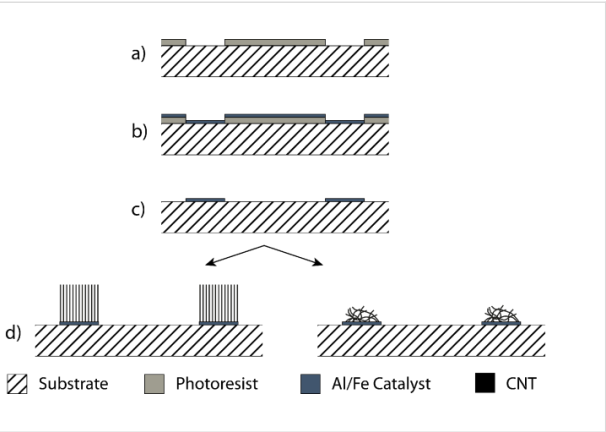

Figure 1: General scheme for the fabrication of spatially deposited CNT islands. (a) A photoresist is lithographically structured; b) defined aluminium and iron layers were evaporated onto the substrate. After removing the photoresist the catalyst islands of bimetallic Al/Fe are spatially structured on the silicon substrate. (d) The follow up growth of CNTs proceeds selectively on these spatially defined catalyst islands in a vertically aligned fashion on the Si substrate (left side), or in a randomly oriented fashion on an Au substrate (right side).

Chemicals GmbH, Ulm, Germany) was spin-coated onto a respective substrate and structured by exposure through a mask and subsequent development. A thin film bimetallic catalyst layer (10–12 nm Al and 1.0–1.4 nm Fe) was first deposited by using electron beam evaporation onto the substrate following by a removal of the resist. This left spatially deposited islands of catalyst behind. Catalyst annealing and CNT synthesis was subsequently carried out in a quartz tube furnace at atmospheric pressure. Typical growth conditions are 780 °C under an argon/hydrogen/ethene/water atmosphere for 2–3 minutes. After heating the substrates to the growth temperature under a steady flow of hydrogen (400 sccm), argon (600 sccm), and ethene (75 sccm) together with a controlled amount of water vapour was introduced into the CVD reactor by streaming a small amount of carrier gas through a water bubbler (150–200 ppm by dew point sensor measurement). Randomly oriented CNT islands were synthesised on silicon substrates covered with a thin (100 nm) layer of gold. This assures a random CNT growth. In contrast, for the growth of the aligned CNT arrays, the growth substrate was silicon and the growth temperature was set to 800 °C with an ethylene flow of 100 sccm (all other conditions being the same as above). The CNTs obtained in this process are mainly double-walled as characterized and described earlier by us [23].

Neural cell culturing was performed by using cryo-conserved embryonic cortical rat neurons (E18 and E19) (Lonza Ltd, Basel, Switzerland). The substrates with CNT islands were sterilized under UV-light [25]. Cell culture medium was prepared according to the following protocol: L-glutamine (2 mM) and 2% NSF-1 were added to the PNBM basal medium. NSF-1, a

supplement supporting neuronal growth and survival, was aliquoted, frozen and added to the medium immediately before each use. Neurons were thawed and cultured with a density of approximately 500,000 cells/mm^2 onto each substrate and incubated in a humidified atmosphere for 4 h. Finally, petri dishes were filled with approximately 3 mL culture medium. Half the medium was replaced twice a week and completely replaced every second week.

In the cell culture protocol no coating (e.g., laminin or poly-D-lysine) prior to cell cultivation was performed. The cell growth behaviour in vitro was studied by scanning electron microscopy (SEM) on pristine vertically aligned CNT arrays and compared to growth of cortical neurons on islands of randomly oriented CNTs under the same conditions. The cells had to be fixed and finally dried before being sputter coated with 5 nm PtPd for SEM investigation. For doing so, the cell culture medium was removed from the substrates and replaced by 2.5% glutaraldehyde. After 2.5 h glutaraldehyde was removed and all substrates were washed in DI-water three times for 20 min each. After this fixation cells were dried in ethanol (10%, 30%, 50%, 70%, 90%, 99.6% for 20 min each). Finally, ethanol was replaced by hexamethyldisilazane (HMDS) that was left to dry in air [26,27]. The obtained samples were subsequently studied by SEM (Philips XL 30 FEG at 15–20 kV). It is obvious that neurons are strongly attracted by the randomly oriented CNT islands and adhere exclusively onto the nanostructured areas (see Figure 2). The cells form dense networks around the islands and also inter-island connections consisting of neurits and cells.

Cell motility and network formation of neurons cultured on islands of vertically aligned CNTs were studied for a time period of 14 days after cultivation (Figure 3). After 4 h of cultivation, the neurons already formed dense clusters in the vicinity of individual CNT pillars (Figure 3a). Occasionally connections between cell clusters were formed (Figure 3a, marked by the arrows). Nevertheless, cells in the interspace region between CNT pillars on the silicon substrate are visible, connecting the pillars. After 2 days in vitro, these “cell bridges” had disappeared but originally formed clusters had attracted even more cells and thus appeared larger. Cells that were initially attached to the silicon substrate disappeared and significantly fewer cells are observed in the interspace between the CNT pillars. After 7 days in vitro the majority of the cells in the interspaces, however, have disappeared and dense cell clusters around the CNT were then pronounced.

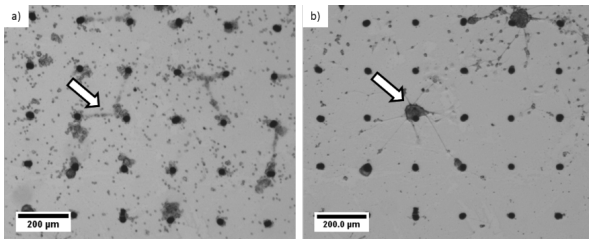

Figure 3: Growth of cortical neurons cultured on islands of vertically aligned CNT architectures. a) Formation of neuron clusters after 4 h and b) after 14 days in vitro. Each CNT pillar is 30 µm in diameter and the distance between two pillars is 200 µm (centre to centre).

Every second day single non-aggregated cells in more than ten interspaces were counted and averaged. Four hours after seeding 49 ± 15 neural cells could be observed in an interspace area of (200 µm × 200 µm – π·(15 µm)^2) = 0.393 mm^2. This number dropped to 9 ± 6 from day 12 onwards. Figure 4 summarizes the development of the number of neurons in the interspaces. At the same time the clusters around the CNT structures appeared darker representing an increased density of cells in the z-axis. This shows that cells grew into three dimensional networks around the CNT islands. Neural connections between CNT pillars could also be observed and became clearly visible after 14 days in vitro (Figure 3b arrow marked).

Neurons accumulate in dense networks around the vertical pillars of CNT and form connections via neurites and in some

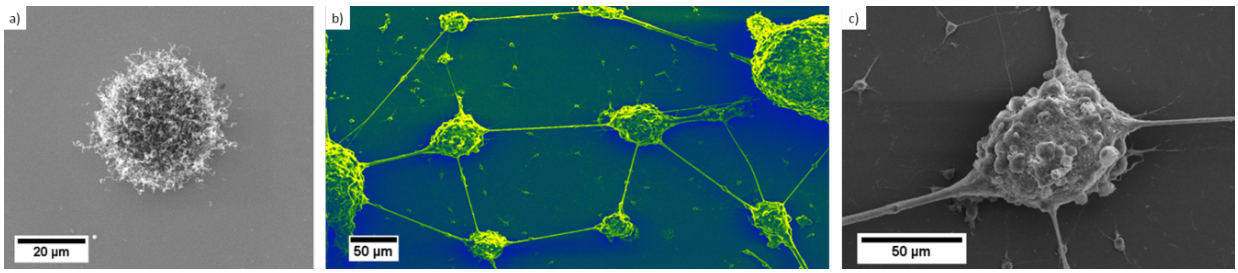

Figure 2: SEM images of neurons cultured on randomly oriented CNT islands. Panel a) depicts a single CNT island with a diameter of ca. 30 µm. In b) and c) after 21 days neurons have accumulated in vitro onto those CNT islands. Neuron cells prefer to grow and adhere onto the CNT islands, forming intimate clusters around individual CNT islands with strong interconnections between the islands (the distance from CNT centre to CNT centre is 200 µm).

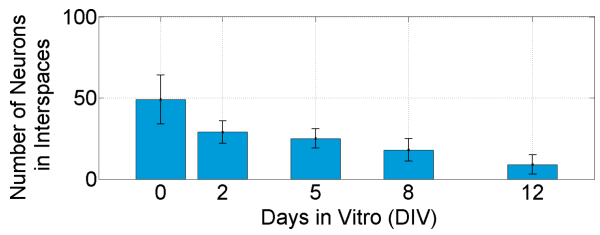

Figure 4: Development of the number of neurons in the interspace regions of the spatially oriented CNTs.

cases also through some cell bodies between the aggregated networks. These results are in line with the results after using micro-stamped structures of carbon nanotubes, which led to the self-assembly of neural networks [28] and to the formation of neural networks on islands of unordered CNTs [12].

After 21 days in vitro the neural network is considered mature and the neurons are observed (see SEM, Figure 5). Cells clearly prefer the CNT sidewalls over the tips and only very few cells grow on top of the vertically aligned CNT structures. The majority of cells follow the given pre-structured linear arrangement of the vertical CNTs, indicating that the neurons are strongly attracted towards the sidewall of the CNT pillars. Cells seem to be able to "climb" onto 3D CNT structures having several 100 µm in height. However, they seem to avoid on purpose a colonisation of the tips of these CNT structures. We could verify this behaviour in parallel experiments by modifying size and shape of the CVD grown micro-structured vertically aligned CNT. Neurons are indeed strongly attracted by the micro-shape and especially by the sidewalls of the aligned nanotubes arrangements (see Supporting Information File 1 for details). With the very recently reported ability to tailor the hydrophilicity and hydrophobicity of such 3D aligned CNT structures over a wide range from superhydrophilic to superhydrophobic [29] the directional cell growth on such structures should be possible and would thus allow understanding these observed preferences from a surface chemistry viewpoint in future work.

In conclusion, pristine randomly and vertically aligned CNTs architectures were studied with respect their use as substrates for neuron cell growth. Both CNT architectures are unique hierarchical structures to direct and control neural cell growth. To the best of our knowledge it is reported for the first time that neuron cells prefer sidewalls of high aspect ratio carbon CNT arrangements over the tips of such structures. Neurons grow all the way from the bottom to the top of these CNT architectures. This finding is crucial for the future design of novel scaffolds and guidance systems for cells.

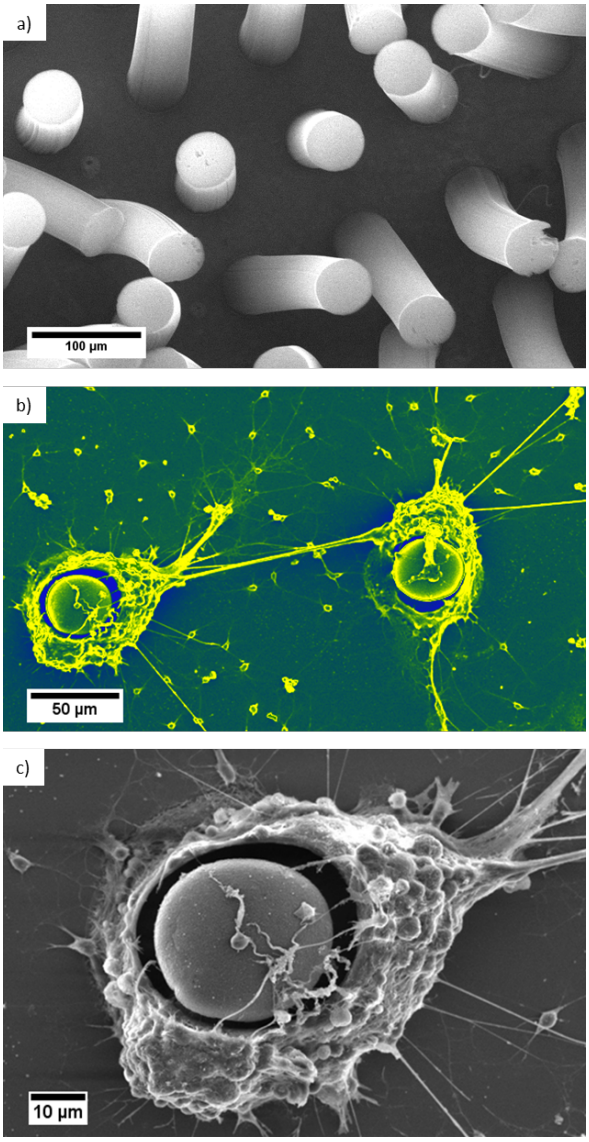

Figure 5: SEM images of a) typical size and arrangement of CNT pillars to be obtained by a WACVD process b) False colour image of two selected CNT pillar architectures with cultured cortical neurons (same dimensions as in Figure 3, height about 400 µm). Note: the distance of the virgin CNT pillars in a) is 100 µm whereas in b) we have deliberately chosen for the neuron growth a substrate with a larger distance of about 200 µm between individual CNT pillars to exemplify the strong attraction even over such macroscopic dimensions. c) Close up view of the vicinity of the vertical aligned CNT structure and the neurons.

Supporting Information

Supporting Information File 1

Additional growth studies through SEM.
[http://www.beilstein-journals.org/bjnano/content/supplementary/2190-4286-5-169-S1.pdf]

Acknowledgements

CN is grateful to the Studienstiftung des Deutschen Volkes, Bonn, Germany, for supporting his research. JJS acknowledges partial financial support through the LOEWE-STT (Sensors Towards Terahertz) project funded within the frame work program LOEWE of the State of Hesse.

References

1. Li, J.; Lu, Y.; Ye, Q.; Cinke, M.; Han, J.; Meyyappan, M. *Nano Lett.* **2003,** *3,* 929–933. doi:10.1021/nl034220x
2. Dharap, P.; Li, Z.; Nagarajaiah, S.; Barrera, E. V. *Nanotechnology* **2004,** *15,* 379. doi:10.1088/0957-4484/15/3/026
3. Li, J.; Ng, H.; Cassell, A.; Fan, W.; Chen, H.; Ye, Q.; Koehne, J.; Han, J.; Meyyappan, M. *Nano Lett.* **2003,** *3,* 597–602. doi:10.1021/nl0340677
4. Lin, Y.; Lu, F.; Tu, Y.; Ren, Z. *Nano Lett.* **2004,** *4,* 191–195. doi:10.1021/nl0347233
5. Hoenlein, W.; Kreupl, F.; Duesberg, G. S.; Graham, A. P.; Liebau, M.; Seidel, R. V.; Unger, E. *IEEE Trans. Compon. Packag. Technol.* **2004,** *27,* 629–634. doi:10.1109/TCAPT.2004.838876
6. Zanello, L.; Zhao, B.; Hu, H.; Haddon, R. *Nano Lett.* **2006,** *6,* 562–567. doi:10.1021/nl051861e
7. Malarkey, E. B.; Fisher, K. A.; Bekyarova, E.; Liu, W.; Haddon, R. C.; Parpura, V. *Nano Lett.* **2009,** *9,* 264–268. doi:10.1021/nl802855c
8. Fung, A. O.; Tsiokos, C.; Paydar, O.; Chen, L. H.; Jin, S.; Wang, Y.; Judy, J. W. *Nano Lett.* **2010,** *10,* 4321–4327. doi:10.1021/nl1013986
9. Bareket-Keren, L.; Hanein, Y. *Front. Neural Circuits* **2013,** *6,* 122. doi:10.3389/fncir.2012.00122
10. Nguyen-Vu, T. D. B.; Chen, H.; Cassell, A. M.; Andrews, R.; Meyyappan, M.; Li, J. *Small* **2006,** *2,* 89–94. doi:10.1002/smll.200500175
11. Galvan-Garcia, P.; Keefer, E. W.; Yang, F.; Zhang, M.; Fang, S.; Zakhidov, A. A.; Baughman, R. H.; Romero, M. I. *J. Biomater. Sci., Polym. Ed.* **2007,** *18,* 1245–1261. doi:10.1163/156856207782177891
12. Sorkin, R.; Greenbaum, A.; David-Pur, M.; Anava, S.; Ayali, A.; Ben-Jacob, E.; Hanein, Y. *Nanotechnology* **2009,** *20,* 015101. doi:10.1088/0957-4484/20/1/015101
13. Lovat, V.; Pantarotto, D.; Lagostena, L.; Cacciari, B.; Grandolfo, M.; Righi, M.; Spalluto, G.; Prato, M.; Ballerini, L. *Nano Lett.* **2005,** *5,* 1107–1110. doi:10.1021/nl050637m
14. Gheith, M. K.; Pappas, T. C.; Liopo, A. V.; Sinani, V. A.; Shim, B. S.; Motamedi, M.; Wicksted, J. P.; Kotov, N. A. *Adv. Mater.* **2006,** *18,* 2975–2979. doi:10.1002/adma.200600878
15. McKnight, T. E.; Ericson, M. N.; Jones, S. W.; Melechko, A. V.; Simpson, M. L. Vertically Aligned Carbon Nanofiber Arrays: An Electrical and Genetic Substrate for Tissue Scaffolding. In *Engineering in Medicine and Biology Society, 2007. EMBS 2007,* 29th Annual International Conference of the IEEE, Lyon, Aug 22–26, 2007; IEEE, 2007; pp 5381–5383. doi:10.1109/IEMBS.2007.4353558
16. Firkowska, I. Carbon nanotube substrates for tissue engineering applications - analysis of surface nanotopography cellular adhesion, and elasticity. Ph.D. Thesis, Rheinische Friedrich-Wilhems-University, Bonn, Germany, 2009.
17. Mattson, M. P.; Haddon, R. C.; Rao, A. M. *J. Mol. Neurosci.* **2000,** *14,* 175–182. doi:10.1385/JMN:14:3:175
18. Hu, H.; Ni, Y.; Montana, V.; Haddon, R. C.; Parpura, V. *Nano Lett.* **2004,** *4,* 507–511. doi:10.1021/nl035193d
19. Li Fan, L.; Feng, C.; Zhao, W.; Qian, L.; Wang, Y.; Li, Y. *Nano Lett.* **2012,** *12,* 3668–3673. doi:10.1021/nl301428w
20. Béduer, A.; Seichepine, F.; Flahaut, E.; Loubinoux, I.; Vaysse, L.; Vieu, C. *Langmuir* **2012,** *28,* 17363–17371. doi:10.1021/la304278n
21. Ben-Jacob, E.; Hanein, Y. *J. Mater. Chem.* **2008,** *18,* 5181–5186. doi:10.1039/b805878b
22. Wang, K.; Fishman, H. A.; Dai, H.; Harris, J. S. *Nano Lett.* **2006,** *6,* 2043–2048. doi:10.1021/nl061241t
23. Joshi, R.; Engstler, J.; Houben, L.; Bar Sadan, M.; Weidenkaff, A.; Mandaliev, P.; Issanin, A.; Schneider, J. J. *ChemCatChem* **2010,** *2,* 1069–1073. doi:10.1002/cctc.201000037
24. Nick, C.; Joshi, R.; Schneider, J. J.; Thielemann, C. *Biointerphases* **2012,** *7,* 58–64. doi:10.1007/s13758-012-0058-2
25. Nick, C.; Quednau, S.; Sarwar, R.; Schlaak, H. F.; Thielemann, C. *Microsyst. Technol.* **2013**. doi:10.1007/s00542-013-1958-x
26. Bray, D. F.; Bagu, J.; Koegler, P. *Microsc. Res. Tech.* **1993,** *26,* 489–495. doi:10.1002/jemt.1070260603
27. Braet, F.; De Zanger, R.; Wisse, E. *J. Microsc. (Oxford, U. K.)* **1997,** *186,* 84–87. doi:10.1046/j.1365-2818.1997.1940755.x
28. Gabay, T.; Jakobs, E.; Ben-Jacob, E.; Hanein, Y. *Physica A* **2005,** *350,* 611–621. doi:10.1016/j.physa.2004.11.007
29. Babu, D. J.; Varanakkottu, S. N.; Eifert, A.; de Koning, D.; Cherkashinin, G.; Hardt, S.; Schneider, J. J. *Adv. Mater. Interfaces* **2014,** 1. doi:10.1002/admi.201300049

BEILSTEIN JOURNAL OF NANOTECHNOLOGY

Mechanical properties of sol–gel derived SiO_2 nanotubes

Boris Polyakov*[1], Mikk Antsov[2,3], Sergei Vlassov[1], Leonid M Dorogin[2,3,4], Mikk Vahtrus[2,3], Roberts Zabels[1], Sven Lange[2,3] and Rünno Lõhmus[2,3]

Full Research Paper

Open Access

Address:
[1]Institute of Solid State Physics, University of Latvia, Kengaraga st. 8, LV-1063, Riga, Latvia, [2]Institute of Physics, University of Tartu, Ravila 14c, 50412, Tartu, Estonia, [3]Estonian Nanotechnology Competence Centre, Ravila 14c, 50412, Tartu, Estonia and [4]ITMO University, Kronverkskiy pr., 49, 197101, Saint Petersburg, Russia

Email:
Boris Polyakov* - boriss.polakovs@cfi.lu.lv

* Corresponding author

Keywords:
atomic force microscopy (AFM); nanomechanical tests; scanning electron microscopy (SEM); silica nanotubes

Beilstein J. Nanotechnol. **2014,** *5,* 1808–1814.
doi:10.3762/bjnano.5.191

Received: 22 April 2014
Accepted: 30 September 2014
Published: 20 October 2014

This article is part of the Thematic Series "Physics, chemistry and biology of functional nanostructures II".

Guest Editor: A. S. Sidorenko

Abstract

The mechanical properties of thick-walled SiO_2 nanotubes (NTs) prepared by a sol–gel method while using Ag nanowires (NWs) as templates were measured by using different methods. In situ scanning electron microscopy (SEM) cantilever beam bending tests were carried out by using a nanomanipulator equipped with a force sensor in order to investigate plasticity and flexural response of NTs. Nanoindentation and three point bending tests of NTs were performed by atomic force microscopy (AFM) under ambient conditions. Half-suspended and three-point bending tests were processed in the framework of linear elasticity theory. Finite element method simulations were used to extract Young's modulus values from the nanoindentation data. Finally, the Young's moduli of SiO_2 NTs measured by different methods were compared and discussed.

Introduction

Hybrid silica core–shell and empty-shell nanomaterials were intensively investigated in recent time [1]. The sol–gel technology for the synthesis of silica nanomaterials is well established, flexible and cost-effective [2,3]. One-dimensional silica nanostructures have plenty of potential applications due to their optical and chemical properties. These include the chemical protection of environmentally sensitive materials [4,5], biological and biosensing applications [6-8], waveguide optics and photonics [9-12]. However, only a few publications were dedicated to the investigation of the mechanical properties of one-dimensional silica nanostructures, and even less to the ones prepared by sol–gel synthesis. Dikin et al. and Ni et al. studied SiO_2 nanowires (NWs) grown at high temperature with the vapor–liquid–solid method, by using resonance and the three-point bending methods, respectively [13,14]. Houmadi et al. investigated the mechanical properties of SiO_2 nanotubes (NTs), which were prepared by sol–gel synthesis using organic NT templates, by using three point bending [15]. The differences of the values of the Young's modulus measured by the listed methods were approximately 40%, which can probably be attributed to peculiarities of the measurement techniques. The effect of the experimental technique on the measured values of

the Young's modulus was demonstrated by Rohlig et al. for ZnO NWs by comparing the resonant technique, nanoindentation, bending of bridges, and tensile and compressive strain tests [16].

In the case of SiO_2 NTs it is also important to consider structural peculiarities of the material itself. Silicon dioxide in the form of quartz as well as amorphous silica, is a compound with covalent bonds, which at room temperature is rather brittle and does not allow plastic deformation. In studies dedicated to the mechanical characterization of SiO_2 NTs and NWs, the material was treated as purely elastic without any plastic yield. However, in recent years plastic deformation of nanomaterials with covalent bonds was demonstrated and investigated by several research teams [17-19]. For instance, when thermally produced silica NWs are irradiated by a moderately intense electron beam (e-beam, 10^{-2} A/cm^2) in transmission electron microscope (TEM), radiation defects can be induced enabling significant plastic deformations in tensile tests, as was shown by Zheng et al. [20].

In this work, we compared several different nanomechanical testing methods applied to thick-walled SiO_2 NTs in order to get a deeper insight into the mechanical properties of this promising material. First, in situ SEM cantilever beam bending tests were carried out on half-suspended SiO_2 NTs. Then AFM was used to perform nanoindentation and three point bending tests. Analytical solutions based on elasticity theory were used to process cantilever-beam and three-point-bending tests data, while the data from nanoindentation experiments were fitted by using finite element method (FEM) simulations and compared with the analytical models (thin shell or membrane model and Hertz model). The problem of indentation of thick-walled elastic NTs was addressed and discussed. To the best of our knowledge, no in situ SEM bending tests, as well as AFM nanoindentation experiments were performed on sol–gel silica NTs previously.

Experimental

Ag/SiO_2 core–shell NWs were synthesized by coating Ag NWs (diameter 60–140 nm, Blue Nano) with SiO_2 by using a well-established sol–gel method [5,6,21]. According to the synthesis procedure silica NTs are expected to be amorphous [5,22]. The empty silica shells (SiO_2 NTs) were obtained by etching the silver core with nitric acid. Silica shells were deposited from solution on an AFM calibration grating (TGXYZ03, Mikromasch), dried and then washed with deionized water.

First, half-suspended NTs were bent inside a high resolution SEM (HRSEM) FEI Helios Nanolab by using a polar coordinate manipulator (MM3A-EM, Kleindiek) without force registration to study the general flexural behavior of SiO_2 NTs. Standard contact AFM cantilevers (ATEC-CONT) were used as the sharp probes. No special procedures were needed for fastening the NTs to the substrate. The static friction between the NT and the substrate was high enough to keep the adhered part of the NT in place during the bending.

Cantilever beam bending technique [23,24] was applied to half-suspended NTs inside a TESCAN Vega-II SBU SEM equipped with a x,y,z-nanomanipulator (SLC-1720-S, SmarAct) and a force sensor. The force sensor was made by gluing an AFM cantilever with a sharp tip (ATEC-CONT cantilevers, Nanosensors, C = 0.2 N/m) to one prong of a commercially available quartz tuning fork (QTF, ELFA). The tip of the ATEC-CONT cantilevers is tilted about 15 degrees relative to the cantilever, which makes the tip visible from the top. In experiments the QTF was driven electrically by an AC voltage at its resonance frequency in amplitude modulation regime. The signal was enhanced by a lock-in amplifier (SR830, Stanford Research Systems) and recorded together with the data of the displacement sensors of the nanomanipulator. The measurements of the Young's modulus consisted of a one-directional in-plane bending of half-suspended NT. In all experiments the tip oscillated parallel to the surface of the sample (shear mode) and normal to the NTs. The amplitude signal of the QTF (proportional to the applied force) and the sequence of SEM images of the gradually bent NT were recorded simultaneously during the experiment. More details including the QTF calibration procedure can be found in Supporting Information File 1 or in our previous work [24]. After the experiment the sample was studied in HRSEM in order to determine outer and inner diameter of every measured SiO_2 NTs.

Nanoindentation and three-point bending tests were done by AFM (Dimension Edge, Bruker) under ambient conditions by using tapping mode cantilevers (PPP-NCH, Nanosensors). The built-in software force–distance spectroscopy routine was used both for nanoindentation and three-point bending tests. Radius of the AFM tip, as well as outer and inner diameters of SiO_2 NTs were measured in HRSEM.

Theory

Cantilever beam bending, three-point beam bending and nanoindentation tests were employed to measure the Young's modulus of SiO_2 NTs (Figure 1). Each method required different theoretical approaches for analysis and is described in more detail in the following sections.

Cantilever beam bending

The Young's modulus of an elastically bent NT can be obtained by applying the equation for the equilibrium of a bent elastic

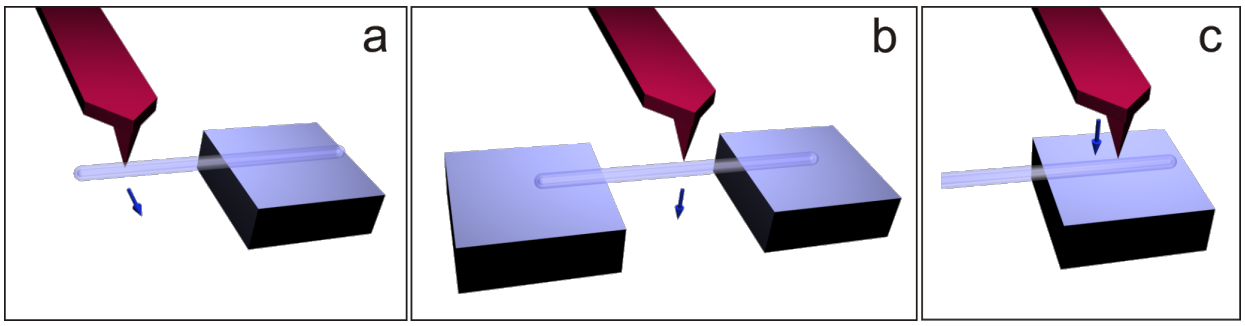

Figure 1: Schematics of mechanical tests performed on SiO_2 NTs. Cantilever (half-suspended) beam bending inside SEM by using a nanomanipulator equipped with a QTF force sensor (a). Three-point beam bending (b) and nanoindentation (c) by using ambient AFM. The arrows indicate the direction of force loading.

beam with Young's modulus E and area moment of inertia I loaded by a point force F at its end. The area moment of inertia I for a cylindrical shell with outer radius R_S and inner radius R_C is given as $I=(\pi/4)\left(R_S^4-R_C^4\right)$. The force–displacement dependence that accounts for the elastic bending and the tensile strain of an isotropic material can be expressed [25]:

$$F=\frac{3EI}{L^3}\delta, \tag{1}$$

where L is the length of the beam, δ is the displacement of the NT end. The knowledge of the geometry of the NT and its force–displacement response is sufficient for determining Young modulus:

$$E=k_{BT}\frac{L^3}{3I}, \tag{2}$$

where $k_{BT} = F/\delta$ is the stiffness of the beam measured during the bending test.

Three-point beam bending

The elastic beam theory is commonly applied for the analysis of the three-point bending tests in the elastic regime [26]. The force–displacement dependence that accounts for the elastic bending and the tensile strain of an isotropic material can be expressed as

$$F=\frac{192EI}{L^3}\delta\left(1+\frac{A}{24I}\delta^2\right), \tag{3}$$

where δ is the displacement of the middle point and A is the area of the cross section of the beam. For a cylindrical shell with an outer radius of R_S and an inner radius of R_C one gets $I=(\pi/4)\left(R_S^4-R_C^4\right)$ and $A=\pi\left(R_S^2-R_C^2\right)$, respectively.

In the linear regime at small displacements the expression for the Young's modulus can be reduced to:

$$E=k_{BT}\frac{L^3}{192I}. \tag{4}$$

We decoupled raw AFM F–δ curves data into the corresponding deformation of the cantilever and of the beam by using the previously measured sensitivity of the cantilever. It enabled us to find the stiffness of the beam, k_{BT}, and calculate the Young's modulus with Equation 4.

Nanoindentation

The analysis of nanoindentation test is more complicated and lacks analytical solutions. The existing model for NT indentation is limited to the thin-shell or membrane case [27]. Therefore, for the case of thick shells studied in this work, we employed finite element method (FEM, COMSOL Multiphysics) models instead, where all geometric parameters can be taken into account. The *Solid Mechanics* module was used, where the thick shell NTs on a SiO_2 plane were indented with a spherical Si tip. All geometrical parameters of each individual shell studied experimentally were used to build the geometry for each separate FEM simulation. The model used the elastic parameters of the silicon tip: Young's modulus E_1 = 160 GPa and Poisson ratio ν_1 = 0.22; and the shell: Young modulus E_2 is to be found and Poisson ν_2 = 0.17 [28]. For a reference we have also applied the thin-shell and Hertz models. The thin-shell approach allows one to neglect the indentation of the surface and the tip geometry by taking into account only the membrane-like compression of the shell. The force–displacement relationship for the thin-shell approximation is commonly written as follows:

$$F\cong CE\frac{t^{5/2}}{R_S{}^{3/2}}\delta, \tag{5}$$

where thickness of the shell $t = R_S - R_C$ and C is a prefactor that depends on the particular boundary conditions with the typical value of $C = 1.2$ [22]. Equation 5 is only applicable within 1% error over the range $0.002 < t/R < 0.1$.

On the contrary, the Hertz model [29] describes only the tip indentation and does not take into account possible membrane-like deformation of the shell. A sphere on a half-space is governed by the following force–displacement relationship:

$$F = \frac{4}{3} E^* R^{1/2} \delta^{3/2} , \qquad (6)$$

where $E^* = \left((1-\nu_1^2)/E_1 + (1-\nu_2^2)/E_2\right)^{-1}$ is the reduced Young's modulus and R is the effective tip radius. The Young's modulus E_1 of the shells found from the Hertz model is underestimated since the shell allows additional elastic relief.

Results and Discussion

Silica NTs deposited from a solution were randomly distributed over the substrate surface, and many NTs were suspended between neighboring substrate structures, with some NTs being half-suspended (Supporting Information File 1, Figure S1). The NTs appeared semitransparent in the SEM images (at 10–15 kV), which enabled the measurement of both outer and inner diameters of the NTs.

Bending tests inside the HRSEM revealed a limited elasticity and high resistance to fracture of the half-suspended SiO_2 NTs. A typical bending experiment is shown in Figure 2. The tip approaches the NT and pushes it near its end (Figure 2a,b). Only negligible elastic shape restoration was observed after tip retraction (Figure 2c,d). Typically, no fracture was observed even at large bending angles (more than 90°). In very few cases, the NTs collapsed during bending (Supporting Information File 1, Figure S2). However fracture was often observed for NTs suspended between two surfaces and pushed in the center.

Cantilever beam bending measurements with force registration were performed on 12 NTs. (A typical measurement is shown in Supporting Information File 1, Figure S3; the results are summarized in Supporting Information File 1, Table S1.) The value of the Young's modulus was numerically fitted to the experimental force–displacement curve registered by the QTF by using Equation 2. The average value of the Young's modulus was 24.5 ± 11.1 GPa.

In AFM measurements the built-in optical microscope was used to find appropriate SiO_2 NTs for the three-point bending and the nanoindentation tests. Prior to the three-point bending test an AFM image of a NT suspended over a trench was taken in tapping mode at low magnification (typically 10 × 10 μm, Figure 3a). In order to ensure proper tip positioning during

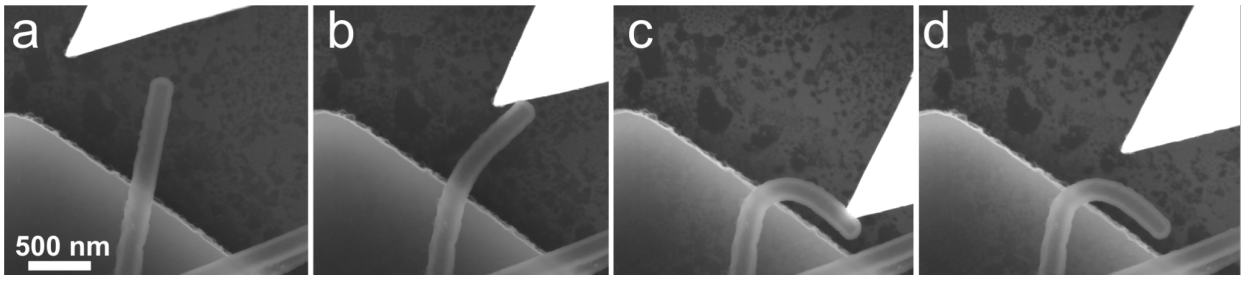

Figure 2: HRSEM images of in situ bending of silica NT. Intact NT (a), slightly bend NT (b), significantly bend NT (c), NT after tip removal (d). Radius of curvature 225 nm.

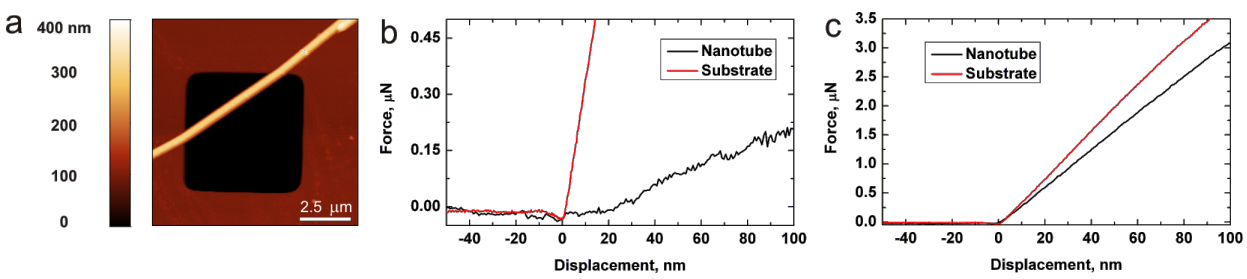

Figure 3: Three-point bending test and nanoindentation. AFM image of suspended silica NT (a); force–distance curve taken on the suspended part of the NT (b); nanoindentation force–distance curve taken on adhered part of the same NT (c).

force spectroscopy a NT was scanned sequentially at a higher magnification (typically 3 × 3 and 1 × 1 μm). Several force–distance curves were taken in the center of a suspended NT. The curves were linear, and the loading and unloading curves coincide, which indicates an elastic response of the NT. A force–distance curve taken on a hard oxidized silicon substrate is shown for comparison (Figure 3b). Values of Young's modulus were calculated by using Equation 3 and Equation 4. Fitting results are shown in Figure 4. The initial region, i.e., the region of displacement below the characteristic inner radius of NT, was used for fitting since the high load region would be invalid due to non-linearity and plastic deformation effect. Measurements were performed on five NTs and results are summarized below in Table 1.

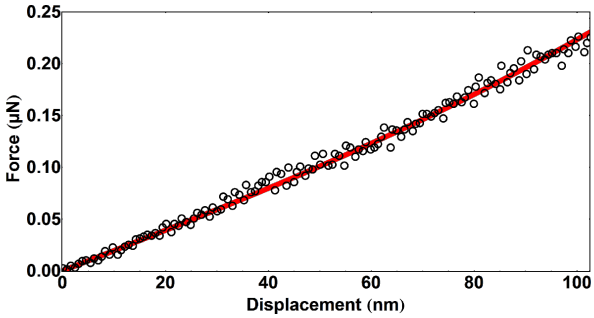

Figure 4: Fitting of three-point bending test of silica NT in AFM.

Nanoindentation experiments were performed on the same NTs that were used in the three-point bending experiments. A selected area of a NT on the substrate (3 × 3 and 1 × 1 μm) was scanned sequentially prior and after nanoindentation. Several force–distance curves (usually three curves) were taken on a NT with an interval of about 1 μm. Typical force–distance curve shown at Figure 3c. Only the initial linear region was used for analysis.

The experimental nanoindentation data was processed by using FEM simulations. A constant indentation depth of 5 nm was applied to the shell. This was done due to the fact that in indentation experiments, for small indentation depths, the initial part of the loading curve corresponds to the elastic regime of material response and therefore the experimental values can be compared to the fully elastic result from FEM simulations. A parametric sweep over the Young modulus of the shell was used to calculate the elastic force acting on the indentation tip and was then compared to the experimental force–displacement curve. Geometrical parameters of indenter and each individual shell were determined from HRSEM images (tip radius 25 nm). An example of a FEM simulation of indentation is shown in Figure 5. Additionally, the thin-shell and Hertz models were used for comparison. The thin-shell model allows to neglect the shape of the indenter and consider only the membrane-like deformation of the NT. The Hertz model, on the contrary, describes the indentation of a spherical tip into a flat substrate only and ignores the possible elastic compressing of a NT. According to FEM simulations, in case of nanoindentation of thick-walled SiO_2 NTs there are both compression and indentation present. Thus, both models underestimate the Young modulus as can be seen from Table 1.

The average values of the Young' modulus measured by half-suspended beam bending, AFM three-point bending and nanoindentation tests (processed by using FEM simulation) were 24.5 ± 11.1 GPa, 41.3 ± 5.8 GPa and 20.1 ± 7.5 GPa, respectively. Our results are in a good agreement with the ones obtained by Dikin et al. (46.5 GPa, [13]). They applied the resonance method on SiO_2 NWs (diameter 80–100 nm) inside an SEM to determine the Young's modulus. However, our values are lower than those obtained by Ni et al. (76.6 GPa for 50–90 nm NWs) and Houmadi (73.3 GPa for 35 nm NTs) by using the three-point bending method [14,15]. The difference in Young's modulus values of SiO_2 NTs and NWs can be attributed to the size effect and the parameters of the chemical reac-

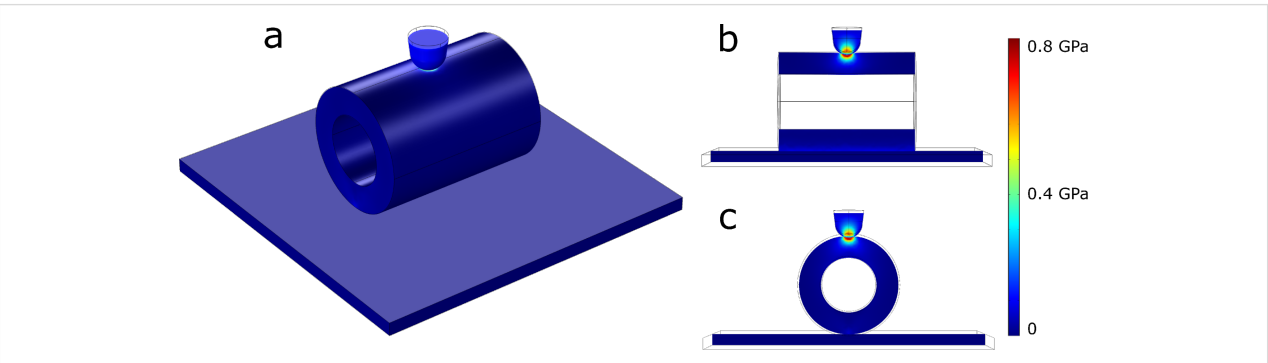

Figure 5: FEM simulation of a SiO_2 NT nanoindentation. Perspective view (a), longitudinal cross section (b), transversal cross section (c). The colors correspond to the von Mises stress.

Table 1: Young's moduli of NTs measured by three-point bending and nanoindentation methods by AFM.

nr.	R_o, outer radius, nm	R_i, inner radius, nm	E_{TPB}, three-point bending, GPa	E_{shell}, nanoindent., GPa	E_{hertz}, nanoindent., GPa	E_{FEM}, nanoindent., GPa
1	91	56	42.3	6.1	5.4	22.0
2	86	50	37.0	11.6	5.9	29.0
3	87	45	41.8	10.0	5.9	21.5
4	115	62	36.5	6.3	2.6	16.8
5	91	41	48.5	5.6	3.0	11.3

tion. It is well-known, that mechanical properties of silica gels strongly depends on post-treatment procedures (aging time and annealing temperature). With an increase of annealing temperature, the density of macroscopic samples of silica gel is increasing as are its hardness and Young's modulus, approaching values of fused silica at ca. 1000 °C [30]. High values of the Young's modulus of sol–gel derived silica NTs [15] even without annealing can be explained by the size effect, which facilitates an effective evaporation of chemical reaction residuals and shrinking of NTs.

We would like to note some peculiarities of the methods used in our study for the characterization of SiO_2 NTs (taking into account the specific properties of this material). The in situ SEM cantilever beam bending method benefits from visual guidance of the bending process, and can be applied to brittle materials or to metals with a well-pronounced elastic-to-plastic transition [24,31]. Since the bending profile of the test object is registered visually by SEM, the smaller the deformation, the higher the error. In SEM, SiO_2 NTs demonstrated limited elasticity and enhanced plasticity, caused by the e-beam promoted generation of defects and their enhanced mobility as it was demonstrated by Zheng et al. for amorhous silica NPs and NWs [20]. It can lead to softening and plastic deformation of the material at large bending angles. Thus, the in situ SEM cantilever beam bending method can give an underestimated Young's modulus for SiO_2 NTs.

The procedure of AFM nanoindentation is rather simple. However, in case of thick-walled nanotubes data processing is complicated and requires FEM simulations and separate HRSEM characterization of the inner and outer diameters. Hertz and membrane models, commonly used for nanoindentation of solid and tubular objects, are inappropriate in case of thick-walled NTs. Moreover, the nanoindentation method is sensitive to local defects and applicable only in the case of a highly homogeneous structure.

Three-point bending test of NTs also suffers from the need of separate electron microscope characterization. However even small displacement of the AFM tip, and thus small deformation of suspended tube, can be measured with high accuracy at small applied force. The experimental data can be easily processed by using simple analytical equations. In our opinion, three-point bending is the most appropriate method for mechanical characterization of thick-walled NTs with limited elasticity.

Conclusion

In this work we measured the Young's modulus of SiO_2 nanotubes by using three different methods. Half-suspended bending tests were carried out inside a SEM by using a nanomanipulator equipped with force sensor. The average value of the Young modulus was found to be 24.5 ± 11.1 GPa. Unexpectedly, significant plasticity was observed. Nanoindentation and three-point bending tests were performed on the same set of NTs under ambient conditions, resulting in values of 20.1 ± 7.5 GPa and 41.3 ± 5.8 GPa, respectively. Three-point bending tests were found to be the most appropriate method for measuring the Young's modulus of sol–gel synthesized SiO_2 NTs.

Supporting Information

Supporting Information File 1

Additional SEM images of broken and collapsed SiO_2 NTs; additional information on in situ SEM bending; some details on FEM simulations; QTF force sensor calibration procedure.
Additional experimental data.
[http://www.beilstein-journals.org/bjnano/content/supplementary/2190-4286-5-191-S1.pdf]

Acknowledgements

The work was supported by the ESF project Nr. 2013/0202/1DP/1.1.1.2.0/13/APIA/VIAA/010, ETF grants 8420, 9007, Estonian Nanotechnology Competence Centre (EU29996), ERDF "TRIBOFILM" 3.2.1101.12-0028, "IRGLASS" 3.2.1101.12-0027, "Nano-Com" 3.2.1101.12-0010 and IUT2-25 project "Structure sensitive interaction mechanisms in func-

tional materials at nanoscale". The authors are also grateful for partial support by COST Action MP1303, the Estonian Science Foundation (grant JD162), and European Union through the European Regional Development Fund (Centre of Excellence "Mesosystems: Theory and Applications", TK114). The support from ITMO International Research Laboratory Program is acknowledged..

References

1. Cheong, K. Y.; Chiew, Y. L. Advances of SiOx and Si/SiOx Core-Shell Nanowires. In *Nanowires Science and Technology;* Lupu, N., Ed.; Intech: India, 2010; pp 131–150.
2. Ciriminna, R.; Fidalgo, A.; Pandarus, V.; Béland, F.; Ilharco, L. M.; Pagliaro, M. *Chem. Rev.* **2013,** *113,* 6592–6620. doi:10.1021/cr300399c
3. Sakka, S., Ed. *Handbook of Sol-Gel Science and Technology;* Kluwer Academic Publisher: New York, NY, USA, 2005.
4. Hu, J.-Q.; Meng, X.-M.; Jiang, Y.; Lee, C.-S.; Lee, S.-T. *Adv. Mater.* **2003,** *15,* 70–73. doi:10.1002/adma.200390014
5. Yin, Y.; Lu, Y.; Sun, Y.; Xia, Y. *Nano Lett.* **2002,** *2,* 427–430. doi:10.1021/nl025508+
6. Sioss, J. A.; Stoermer, R. L.; Sha, M. Y.; Keating, C. D. *Langmuir* **2007,** *23,* 11334–11341. doi:10.1021/la7019846
7. Liu, Y.-H.; Tsai, Y.-Y.; Chien, H.-J.; Chen, C.-Y.; Huang, Y.-F.; Chen, J.-S.; Wu, Y.-C.; Chen, C.-C. *Nanotechnology* **2011,** *22,* 155102. doi:10.1088/0957-4484/22/15/155102
8. Mitchell, D. T.; Lee, S. B.; Trofin, L.; Li, N.; Nevanen, T. K.; Söderlund, H.; Martin, C. R. *J. Am. Chem. Soc.* **2002,** *124,* 11864–11865. doi:10.1021/ja027247b
9. Tong, L.; Gattass, R. R.; Ashcom, J. B.; He, S.; Lou, J.; Shen, M.; Maxwell, I.; Mazur, E. *Nature* **2003,** *426,* 816–819. doi:10.1038/nature02193
10. Elliman, R. G.; Wilkinson, A. R.; Kim, T.-H.; Sekhar, P. K.; Bhansali, S. *J. Appl. Phys.* **2008,** *103,* 104304. doi:10.1063/1.2924420
11. Han, W. S.; Kang, Y.; Lee, S. J.; Lee, H.; Do, Y.; Lee, Y.-A.; Jung, J. H. *J. Phys. Chem. B* **2005,** *109,* 20661–20664. doi:10.1021/jp0547156
12. Jang, J.; Yoon, H. *Adv. Mater.* **2004,** *16,* 799–802. doi:10.1002/adma.200306567
13. Dikin, D. A.; Chen, X.; Ding, W.; Wagner, G.; Ruoff, R. S. *J. Appl. Phys.* **2003,** *93,* 226–230. doi:10.1063/1.1527971
14. Ni, H.; Li, X.; Gao, H. *Appl. Phys. Lett.* **2006,** *88,* 043108. doi:10.1063/1.2165275
15. Houmadi, S.; Dedovets, D.; Si, S.; Tamoto, R.; Oda, R.; Delville, M. H.; Bergaud, C. *Appl. Phys. Lett.* **2013,** *102,* 151904. doi:10.1063/1.4801760
16. Röhlig, C.-C.; Niebelschütz, M.; Brueckner, K.; Tonisch, K.; Ambacher, O.; Cimalla, V. *Phys. Status Solidi B* **2010,** *247,* 2557–2570. doi:10.1002/pssb.201046378
17. Zhai, T.; Yao, J. *One-Dimensional Nanostructures: Principles and Applications;* John Wiley & Sons: Hoboken, New Jersey, USA , 2012. doi:10.1002/9781118310342
18. Han, X.-D.; Zheng, K.; Zhang, Y. F.; Zhang, X. N.; Zhang, Z.; Wang, Z. L. *Adv. Mater.* **2007,** *19,* 2112–2118. doi:10.1002/adma.200602705
19. Smith, D. A.; Holmberg, V. C.; Korgel, B. A. *ACS Nano* **2010,** *4,* 2356–2362. doi:10.1021/nn1003088
20. Zheng, K.; Wang, C.; Cheng, Y.-Q.; Yue, Y.; Han, X.; Zhang, Z.; Shan, Z.; Mao, S. X.; Ye, M.; Yin, Y.; Ma, E. *Nat. Commun.* **2010,** *1,* No. 24. doi:10.1038/ncomms1021
21. Vlassov, S.; Polyakov, B.; Dorogin, L. M.; Vahtrus, M.; Mets, M.; Antsov, M.; Saar, R.; Romanov, A. E.; Löhmus, A.; Löhmus, R. *Nano Lett.* **2014,** *14,* 5201–5205. doi:10.1021/nl5019063
22. Gao, C.; Lu, Z.; Yin, Y. *Langmuir* **2011,** *27,* 12201–12208. doi:10.1021/la203196a
23. Silva, E. C. C. M.; Tong, L.; Yip, S.; van Vliet, K. J. *Small* **2006,** *2,* 239–243. doi:10.1002/smll.200500311
24. Vlassov, S.; Polyakov, B.; Dorogin, L. M.; Antsov, M.; Mets, M.; Umalas, M.; Saar, R.; Lõhmus, R.; Kink, I. *Mater. Chem. Phys.* **2014,** *143,* 1026–1031. doi:10.1016/j.matchemphys.2013.10.042
25. Gere, J.; Goodo, B. *Mechanics of Materials, Brief edition, SI version;* Cengage Learning: Stamford, CT, USA, 2012.
26. Heidelberg, A.; Ngo, L. T.; Wu, B.; Phillips, M. A.; Sharma, S.; Kamins, T. I.; Sader, J. E.; Boland, J. J. *Nano Lett.* **2006,** *6,* 1101–1106. doi:10.1021/nl060028u
27. de Pablo, P. J.; Schaap, I. A. T.; MacKintosh, F. C.; Schmidt, C. F. *Phys. Rev. Lett.* **2003,** *91,* 098101. doi:10.1103/PhysRevLett.91.098101
28. Kim, M. T. *Thin Solid Films* **1996,** *283,* 12–16. doi:10.1016/0040-6090(95)08498-3
29. Hertz, H. R. 1882, Ueber die Beruehrung elastischer Koerper (On The Contact Between Elastic Bodies). *Gesammelte Werke (Collected Works);* Leipzig, Germany, 1895; Vol. 1.
30. Adachi, T.; Sakka, S. *J. Mater. Sci.* **1990,** *25,* 4732–4737. doi:10.1007/BF01129933
31. Polyakov, B.; Dorogin, L. M.; Vlassov, S.; Antsov, M.; Kulis, P.; Kink, I.; Lõhmus, R. *Eur. Phys. J. B* **2012,** *85,* No. 366. doi:10.1140/epjb/e2012-30430-6

License and Terms

BEILSTEIN JOURNAL OF NANOTECHNOLOGY

A reproducible number-based sizing method for pigment-grade titanium dioxide

Ralf Theissmann*, Manfred Kluwig and Thomas Koch

Full Research Paper

Open Access

Address:
Research Services / Analytical Intelligence, KRONOS INTERNATIONAL, Inc., Peschstrasse 5, 51373 Leverkusen, Germany

Email:
Ralf Theissmann* - ralf.theissmann@kronosww.com

* Corresponding author

Keywords:
electron microscopy; particle size; pigment; sizing; titanium dioxide

Beilstein J. Nanotechnol. **2014,** *5,* 1815–1822.
doi:10.3762/bjnano.5.192

Received: 30 April 2014
Accepted: 20 August 2014
Published: 21 October 2014

This article is part of the Thematic Series "Physics, chemistry and biology of functional nanostructures II".

Guest Editor: A. S. Sidorenko

Abstract

A strong demand for reliable characterization methods of particulate materials is triggered by the prospect of forthcoming national and international regulations concerning the classification of nanomaterials. Scientific efforts towards standardized number-based sizing methods have so far been concentrated on model systems, such as spherical gold or silica nanoparticles. However, for industrial particulate materials, which are typically targets of regulatory efforts, characterisation is in most cases complicated by irregular particle shapes, broad size distributions and a strong tendency to agglomeration. Reliable sizing methods that overcome these obstacles, and are practical for industrial use, are still lacking. By using the example of titanium dioxide, this paper shows that both necessities are well met by the sophisticated counting algorithm presented here, which is based on the imaging of polished sections of embedded particles and subsequent automated image analysis. The data presented demonstrate that the typical difficulties of sizing processes are overcome by the proposed method of sample preparation and image analysis. In other words, a robust, reproducible and statistically reliable method is presented, which leads to a number-based size distribution of pigment-grade titanium dioxide, for example, and therefore allows reliable classification of this material according to forthcoming regulations.

Introduction

Titanium dioxide is among the ten most abundant materials on the Earth [1]. In the form of a fine powder, it is used as white pigment in many application systems such as paints, plastics, paper and building materials. It is also used in cosmetics, foods and pharmaceuticals. Its superior properties as white pigment are based on its high refractive index, leading to maximum whiteness and opacity, if its particle size distribution is optimized for best scattering efficiency according to Mie's theory [2,3]. The most common industrial processing routes are the sulfate process and the chloride process. In the sulfate process, for example, ilmenite ore is dissolved in sulfuric acid, iron and titanium are separated by controlled precipitation, and colouring transition metals are removed in a bleaching process prior to calcination. In the chloride process, rutile in the form of sand or

slag, for example, is treated with gaseous chlorine to form titanium tetrachloride. The titanium tetrachloride is purified by distillation and then transformed into solid TiO_2 in a combustion process. After both processes, the resulting powders are de-agglomerated by standard milling procedures and then subjected to a finishing process, which is generally followed by a final de-agglomeration step. In the ideal case, the size (distribution) of the final products is optimised for the optical pigment properties, which are described by using Mie's theory. Mie's theory states that the optimum particle size for refracting light is just about half the wavelength it is meant to interact with. Speaking of visible light, a mean wavelength of 500 nm is reasonable to assume. Therefore, a mean pigment size of 250 nm is close to what the titanium dioxide makers are producing.

The calcination temperature, as the final step of the powder synthesis of the sulfate process, gives the choice of producing either the low-temperature crystallographic phase, anatase, or the high-temperature crystallographic phase, rutile. The chloride process leads to formation of rutile phase particles due to the high temperatures of the combustion process. Both phases have a number of advantages and disadvantages, which lead to their typical applications. Preferred fields of application for rutile pigments are coatings, paints, plastics and building materials, whereas anatase pigments are mainly used in cosmetics, pharmaceuticals or food. One of the most important properties of titanium dioxide is its UV absorption, which protects human skin against sunburn and skin cancer. Optically transparent TiO_2 is the most important ingredient of any commercially available sun cream. The most common way of achieving a transparent, highly UV-absorbent sun cream is to use intentionally manufactured nano-sized titanium dioxide.

An urgent demand for reliable methods for the characterization of particulate materials is triggered by the prospect of forthcoming national and international regulations concerning the classification of nanomaterials [3-6]. Scientific efforts to establish standardized methods for determining number-based size distributions have so far been focused on model systems, such as spherical gold particles, spherical latex particles or spherical silica particles [7-10]. The typical obstacles in the characterization of industrial materials, such as irregular particle shapes [11], a broad size distribution [12] and strong aggregation and agglomeration effects [13,14], have not been addressed successfully. But as industrial materials are the goal of all regulatory efforts, robust, reproducible and reliable methods for the determination of the number-based size distributions for a wide range of industrial materials are urgently needed [3].

This study focuses on two commercially available pigments, KRONOS K2360 and KRONOS K1171. The former is a pigment with a rutile structure for use in coatings and paints, while the latter is a food-grade pigment with an anatase structure. We decided to develop a procedure that requires a minimum of subjective, user-based decisions. The major task to tackle on the way is to prepare a sample suitable for automated particle detection. Since automated detection routines are primarily based on grey-value thresholding, overlapping particles are a serious problem, which is illustrated in Figure 1. As an example, Figure 1 shows five different projections of one agglomerate found in K2360. The number of obviously visible primary particles varies for the different projections, as well as the size of the projected area, which is generally evaluated. These TEM tomogram-based data illustrate the fundamental problem associated with number-based particle size measurements: A true size distribution of the pigment will only be obtained if the full, three-dimensional shape of the particles is evaluated, e.g., as the equivalent sphere diameter or a minimum 3D Feret diameter. All known evaluation methods based on the evaluation of projections or slices contain systematic deviations [15-18]. As for every particle sizing method, besides the physical principles applied, the decision as to how to measure the particle size and its distribution is somewhat arbitrary and generally restricted by practicality aspects.

As the first selective decision, the present study uses polished sections in which overlapping particles are ruled out. As a consequence, the measurement used here does not correspond

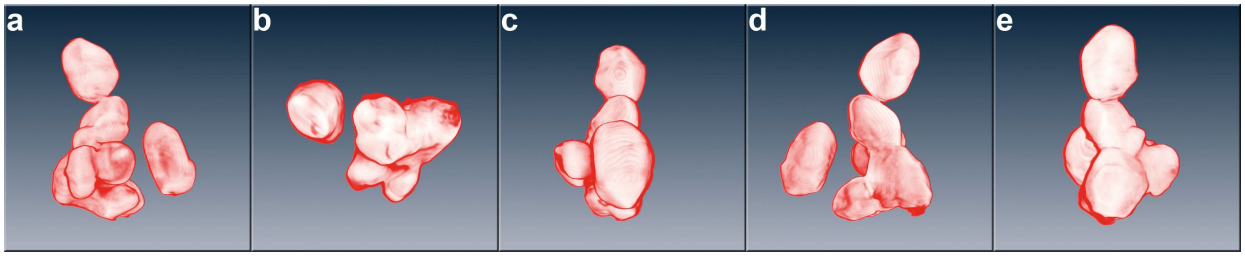

Figure 1: Schematic view of five different projections of one agglomerate found in KRONOS 2360, reproduced from an electron tomogram. The images (a) through (e) demonstrate that the projected area of the pigments varies greatly, depending on viewing direction. Moreover, they illustrate the difficulty with particle detection in projection images in the event of overlapping particles.

to a projected area of the particles, but to a section through the particles. The correlation between a measured size distribution and the "real" size distribution is the subject of so-called stereologic correction: Based on the assumption of a common, known particle shape, stereologic corrections may be used to estimate the "real" size distribution, either from the measured projection sizes or from the measured section sizes [15,19,20]. It is a fact that there is nothing like a common or known particle shape for titanium dioxide pigments. The presence of arbitrary shapes in industrially produced titanium dioxide makes stereologic correction impractical, both for the evaluation of projections and for the evaluation of sections. Consequently, the choice of the measuring technique is somewhat arbitrary. The technique presented in this study was chosen because of its high degree of automation and reproducibility. The effect of lacking stereologic correction, if significant, leads to a result which is slightly smaller than the "real" particle size. Therefore, the uncorrected section-size distributions presented in this publication give lower estimates of the real particle size distributions of the analysed pigments. For the intended purpose, i.e., classification of the material according to the recommendation of the European Commission [4], the method gives a conservative estimate of the particle size distribution.

Results and Discussion

In order to establish the proposed method, especially for the sizing of pigment-grade titanium dioxide, the reproducibility of the method was primarily tested. Each pigment was prepared several times according to the procedure described in the experimental section. The first preparation run included four samples, labelled Ra01 through Ra04 for the rutile pigment and Aa01 trough Aa04 for the anatase pigment. A second preparation run was done several days later. It included the rutile samples Rb05 through Rb10 and the anatase samples Ab05 through Ab08. The first measurement of each sample is labelled M1; the second measurement was performed by a different operator and is labelled M2. The measured results in terms of minimum Feret diameter and equivalent circle diameter (ECD) are summarised in Tables 1 to 4. The first column gives the number of detected primary particles, followed by mean and standard deviation. Meaningful quantiles (d_{10}, d_{16}, d_{25}, d_{50} and d_{84}) are given in the next columns. The data of the different samples are treated without any assumption of a model for the distribution function. Consequently, no standard error based on the standard deviation and the number of particles counted is given. Instead, the standard error is calculated as the standard deviation of the repeated measurements, as done for the mean and all evaluated quantiles. The standard error is used to calculate the 95% confidence interval.

The high reproducibility of the measurement, which leads to a standard error below 2 nm for all evaluated measurements, justifies use of the non-parametric rank sum test of Siegel and Tukey [21] to test whether the measured distribution can be attributed to the same population. The comparison of all measured samples proves that this is the case, both for KRONOS K2360 and for KRONOS K1171. No significant differences between the standard errors for the ECD and minimum Feret diameter measurements are obtained for the rutile pigment. For the anatase pigment, lower standard

Table 1: Evaluation of the primary particle sizes of KRONOS K2360 in terms of the equivalent circle diameter (ECD); all values given in nm.

ECD	# particles	mean	std. dev.	d_{10}	d_{16}	d_{25}	d_{50}	d_{84}
Ra01_M1	9763	**188.5**	58	114.1	130.4	149.3	**183.4**	246.5
Ra02_M1	9912	**187.5**	57.6	113.7	129.9	148.6	**182.3**	245.1
Ra03_M1	8753	**183.3**	56.3	111.2	127	145.3	**177.6**	239.5
Ra04_M1	9729	**189.2**	56.4	116.9	132.8	151.1	**183.7**	245.6
Rb05_M1	9056	**186.7**	57.4	113.1	129.3	148	**182.1**	244.1
Rb05_M2	*8684*	***188.9***	*57.9*	*114.7*	*131*	*149.8*	***181.7***	*246.8*
Rb06_M1	8430	**186.4**	58.2	111.8	128.2	147.1	**181.6**	244.6
Rb06_M2	*9629*	***186.6***	*58.1*	*112.2*	*128.6*	*147.5*	***181.7***	*244.7*
Rb07_M1	8362	**186.7**	57.3	113.2	129.4	148	**181.1**	244.1
Rb08_M1	6909	**187.3**	57.2	114	130.1	148.7	**182.9**	244.5
Rb09_M1	9013	**187.5**	58.5	112.6	129	148.1	**183.2**	246
Rb10_M1	9023	**185.0**	57.7	111	127.3	146.1	**180.9**	242.7
mean		**187.0**	**57.6**	**113.2**	**129.4**	**148.1**	181.8	**244.5**
std. error		**1.6**	**0.7**	**1.6**	**1.6**	**1.6**	**1.6**	**1.9**
confidence level (95%)	lower limit	**183.9**		110.1	126.3	145	**178.7**	240.8
	upper limit	**190.1**		116.3	132.5	151.2	**184.9**	248.2

Table 2: Evaluation of the primary particle sizes of KRONOS K2360 in terms of the minimum Feret diameter; all values given in nm.

min. Feret	# particles	**mean**	std. dev.	d_{10}	d_{16}	d_{25}	**d_{50}**	d_{84}
Ra01_M1	9763	**171.8**	53.2	103.7	118.7	136	**166.2**	225
Ra02_M1	9912	**171.2**	52.7	103.6	118.4	135.6	**166.2**	223.9
Ra03_M1	8753	**167.3**	51.7	101.1	115.7	132.5	**161.9**	219
Ra04_M1	9729	**172.9**	51.6	106.8	121.3	138.1	**167.9**	224.4
Rb05_M1	9056	**170.2**	52.6	102.7	117.5	134.7	**166**	222.8
Rb05_M2	*8684*	***172.1***	*53.3*	*103.8*	*118.8*	*136.2*	***166.1***	*225.3*
Rb06_M1	8430	**169.7**	53.3	101.4	116.4	133.8	**165.1**	222.9
Rb06_M2	*9629*	***170.7***	*53.3*	*102.4*	*117.4*	*134.7*	***166.2***	*224*
Rb07_M1	8362	**170.2**	52.5	102.9	117.7	134.8	**165.3**	222.6
Rb08_M1	6909	**170.5**	52.4	103.4	118.2	135.2	**166.2**	222.9
Rb09_M1	9013	**170.8**	53.5	102.2	117.3	134.7	**166.2**	224.4
Rb10_M1	9023	**168.6**	52.9	100.8	115.7	132.9	**163.7**	221.5
mean		**170.5**	**52.7**	**102.9**	**117.7**	**134.9**	**165.6**	**223.2**
std. error		**1.5**	**0.6**	**1.6**	**1.5**	**1.5**	**1.5**	**1.7**
confidencelevel (95%)	lower limit	**167.6**		99.8	114.8	132	**162.7**	219.9
	upper limit	**173.4**		106	120.6	137.8	**168.5**	226.5

Table 3: Evaluation of the primary particle sizes of KRONOS K1171 in terms of the equivalent circle diameter (ECD); all values given in nm.

ECD	# particles	**mean**	std. dev.	d_{10}	d_{16}	d_{25}	**d_{50}**	d_{84}
Aa01_M1	5766	**152.2**	49.6	88.5	102.5	118.7	**146.4**	201.8
Ab01_M2	*6073*	***151.8***	*49*	*89.1*	*102.9*	*118.8*	***146.7***	*200.8*
Aa02_M1	6205	**150.6**	47.6	89.5	102.9	118.4	**144.4**	198.2
Ab02_M2	*5743*	***153.5***	*49.2*	*90.4*	*104.3*	*120.3*	***147.8***	*202.7*
Aa03_M1	5906	**152.7**	48.6	90.4	104.1	119.9	**146.3**	201.3
Aa04_M1	6280	**150.2**	47.9	88.8	102.3	117.9	**144**	198.1
Ab05_M1	5250	**149.9**	50.1	85.7	99.8	116.1	**144.6**	200.1
Ab06_M1	5565	**152.7**	49	89.9	103.7	119.7	**147**	201.8
Ab07_M1	5808	**150.2**	49	87.4	101.2	117.2	**144.2**	199.2
Ab08_M1	5901	**151.6**	48.7	89.2	102.9	118.8	**146.1**	200.4
mean		**151.5**	**48.9**	**88.9**	**102.7**	**118.6**	**145.7**	**200.4**
std. error		**1.3**	**0.7**	**1.4**	**1.3**	**1.3**	**1.3**	**1.6**
confidence level (95%)	lower limit	**149.1**		86.1	100	116.1	**143.1**	197.4
	upper limit	**154**		91.7	105.3	121	**148.4**	203.5

Table 4: Evaluation of the primary particle sizes of KRONOS K1171 in terms of the minimum Feret diameter; all values given in nm.

min. Feret	# particles	**mean**	std. dev.	d_{10}	d_{16}	d_{25}	**d_{50}**	d_{84}
Aa01_M1	5766	**139.2**	45.3	81.2	93.9	108.7	**133.3**	184.6
Ab01_M2	*6073*	***138.9***	*44.6*	*81.7*	*94.2*	*108.8*	***133.7***	*183.5*
Aa02_M1	6205	**137.9**	43.6	82	94.2	108.5	**132.6**	181.5
Ab02_M2	*5743*	***140.4***	*45*	*82.8*	*95.4*	*110.1*	***135.1***	*185.4*
Aa03_M1	5906	**139.5**	44.4	82.6	95.1	109.6	**133.7**	183.9

Table 4: Evaluation of the primary particle sizes of KRONOS K1171 in terms of the minimum Feret diameter; all values given in nm. (continued)

Aa04_M1	6280	**137.7**	43.8	81.6	93.9	108.2	**132.4**	181.5
Ab05_M1	5250	**137.5**	45.6	79	91.8	106.7	**132.5**	183.1
Ab06_M1	5565	**139.9**	44.8	82.4	95	109.6	**133.9**	184.7
Ab07_M1	5808	**137.9**	44.8	80.4	93	107.6	**132.5**	182.7
Ab08_M1	5901	**139**	44.4	82.1	94.6	109.1	**133.7**	183.4
mean		**138.8**	**44.6**	**81.6**	**94.1**	**108.7**	**133.3**	**183.4**
std. error		**1.0**	**0.6**	**1.2**	**1.1**	**1.0**	**0.8**	**1.3**
Confidence level (95%)	lower limit	**136.8**		79.3	92	106.7	**131.7**	180.9
	upper limit	**140.8**		83.8	96.2	110.6	**135**	186

errors are found for the minimum Feret diameter. This is attributed to a less regular shape as a consequence of the production process.

The data prove that the method presented for primary particle sizing of pigmentary titanium dioxide is highly robust and reproducible. This is the consequence of a rigorous procedure, which primarily targets reliability: a representative, macroscopic amount of sample to start with, preparation that eliminates the possibility of overlapping particles, defined standard operating procedures for sample preparation, measurement and evaluation, and a minimum influence of operator-based uncertainties. The result is an obtained standard error of less than 2 nm and a relative coefficient of variation below 1.6% for all measured quantities.

However, the method has several limitations, which also need to be addressed and discussed here. First of all, the procedure was developed for pigment-grade titanium dioxide prepared as a cross-section. An adjustment of the method may possibly be needed for its application to other particulate materials with other size distributions. The presented results are, accurately speaking, the distribution of ECD and minimum Feret diameter of the pigment sections. Stereologic correction has not been performed, and is not feasible for this application [15,20]. Errors introduced by stereologic effects may gain importance if the size of the measured objects is large compared to the penetration depth of the electron beam. The size distributions measured from polished sections can be expected to differ from those of projected areas. However, the high reproducibility of the proposed method will certainly allow comparison with any other sizing method, as long as a reference or standard for this purpose is present.

Conclusion

A highly reproducible, statistically tested method for the sizing of pigment-grade rutile and anatase is established. The standard error of the method is shown to be below 2 nm for all measured quantities, the relative coefficient of variation being below 1.6%. The presence of a systematic bias due to the lack of stereologic correction cannot be verified for the time being, since a certified standard for titanium dioxide is still lacking. The reproducibility of the method is based on the use of a representative, macroscopic amount of sample material, a high degree of automation, the elimination of detection errors due to overlapping particles and a transparent filtering procedure for detected particles. As a consequence, the method presented is well suited to classifying pigment-grade titanium dioxide according to the recommendation of the EU Commission of 18 October 2011 on the definition of particulate nanomaterial, or for other forthcoming regulations in the future.

Experimental

The experimental procedures described below are in full agreement with the practical guide for particle size characterization published by NIST [22].

Sample preparation

A well-prepared sample is the basis for reliable evaluation of the size distribution of a pigment. The limited quantity of samples used in electron microscopy emphasises this point. Starting with approximately 10 g pigment, which is assumed to be a representative sample, the following steps are taken:

1. The "cone and quartering" method is repeatedly used to divide the sample in half until a quantity of 2 g is left.
2. The 2 g of pigment are thoroughly mixed with 4 g hot-mounting resin and 22.5 g ZrO_2 milling beads. Mixing is done for 4 min at a moderate frequency of 20 Hz, using a Retsch Mixer Mill MM400. The milling beads are removed after the mixing process.
3. The mixture is then hot-mounted by using a Struers Citopress under standard conditions of 180 °C and 3 bar pressure.

4. A five-step polishing process, with active oxide polishing as the final step, leads to a smooth, scratch-free section through the embedded pigments.
5. As the final step before SEM investigation, an 8 nm Au/Pd conductive layer is deposited on top of the sample surface.

The sample preparation procedure summarised above leads to a sample with a high pigment density and allows imaging of several thousand pigments within a set of approx. 50 images. The "cone and quartering" method ensures that the embedded sample is representative. A macroscopic amount is taken for the mixing and embedding procedure. Since the whole representative amount is embedded, effects of flushing are ruled out and the low viscosity of the resin ensures that sedimentation is not a problem. The section finally analysed can therefore be reasonably assumed to be representative. The high area density of the pigment in all images ensures that constant conditions for the automated post-processing and detection procedure are assured.

Measurement, pigment detection and size analysis

A working distance of 7 mm and an acceleration voltage of 5 kV with an Everhart–Thornley detector are chosen as the standard imaging conditions for SEM imaging. The microscope used is a Leo 1530VP SEM. A magnification of 20.000× (5.7 nm/pix) is chosen for the rutile sample, which displays a larger primary particle size, and a magnification of 30.000× (3.8 nm/pix) for the anatase sample, which has a significantly smaller primary particle size. In both cases, this corresponds to approx. 20 pixels for the equivalent circle diameter (ECD) of the 10% quantile d_{10} [23]. A silicon wafer with etched structures is used for calibration of the instrument. The size of the structures is certified by the PTB under Serial No. IMS-HR 08 3641-01 490 and the calibration mark 44049 11 PTB. An automated protocol (macro) for image post-processing and particle detection was developed. The procedure was realised with the commercial software package "analysis" from Olympus-SIS. All filters used are standard filters implemented in the software. The detailed settings are defined in the standard operating procedure and are listed below. This allows maximum transparency of the procedure and maximum comparability and reproducibility of the results, e.g., when dealing with regulatory authorities or their contracting measuring partners.

The full procedure includes unification of the grey values, masking of the unified image, particle detection and filtering of the results, as shown in the images of Figure 2. The first step ensures comparability, not only within the set of images of one sample, but also between different samples or even between samples measured on different instruments with varying detector settings or noise levels. The comparability is sufficient, as long as the penetration depth of the electrons, which is determined by the acceleration voltage, remains constant. In the second step, the images are binarised by using automated grey-value threshold determination [22]. A morphological particle separation filter, the watershed transform, is applied to the binary image. The resulting binary image with the separated particles is used as a mask for the unified image. The final detection of the primary particles is done on the masked unified image, which allows for the detection of the particles, including their grey values. The grey values of the particles are important for the subsequent filtering of the results obtained. It is used in order to remove particles that are located below the polished surface, but give rise to an increased intensity compared to the background. In general, these falsely detected particles show the lowest detected intensities and, therefore, also the lowest standard deviations. A combination of both values has proven adequate for grey-value filtering. Additional filtering is based on the pigment shape. As for the grey values, combined filtering of two shape characteristics has proven advantages, namely the so-called convexity and the shape factor:

1. Unifying the grey values as the basis for final pigment detection (Figure 2b)

- automated contrast and brightness adjustment
- median filter for noise suppression
- rank filter for noise suppression with a size of 5 pixels and a rank of 50%
- multiplicative shading correction for a size of 255 × 255 pixels and a cut-off level of 10%

2. Preparing and applying a mask image, followed by particle detection (Figure 2c,d)

- automated grey-value thresholding and binarisation
- repeated removal of pixels connecting only to three or less neighbouring pixels, using the connectivity filter
- applying the watershed transform in order to separate aggregated or adjacent particles (Figure 2c)
- pixel-by-pixel multiplication of the unified image with the mask image (Figure 2d)
- automated grey-value thresholding and particle detection

3. Morphological and grey-value filtering of the detected particles to extract the primary particles (Figure 2a)

- removing 10% of the particles with the lowest mean grey value of all detected particles
- removing 10% of the particles with the lowest standard deviation of the grey value of all detected particles

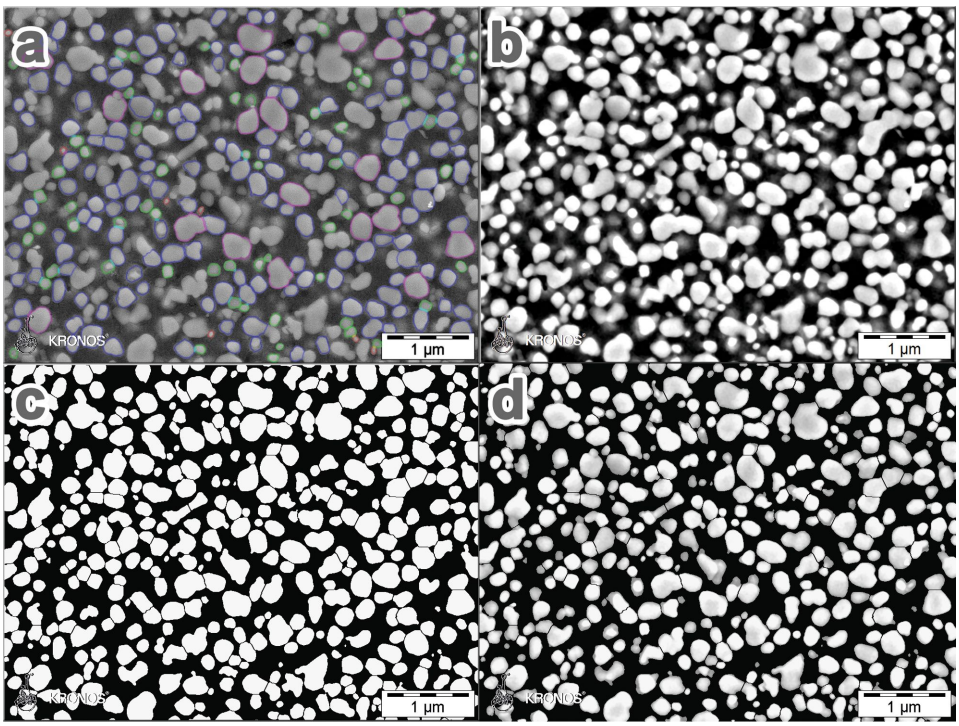

Figure 2: Imaging conditions and image post-processing for pigment sizing for a rutile pigment; a) original image superimposed with the outlines of the finally evaluated particle sections after grey-value and shape filtering; b) unified image after noise reduction and shading correction; c) binarised image after application of a watershed transform and connectivity filter; d) filtered image (b) masked with binarised image (c); automated detection applied to image d.

- removing all particles with a "shape-factor" below 0.86 as non-primary particles
- removing all particles with a convexity of less than 0.90 as non-primary particles

Figure 3 visualises the particle detection characteristics that are intrinsic to the analysis of a polished section. The section through the particles can in principle be located close to the centre of mass, in which case the section gives the maximum

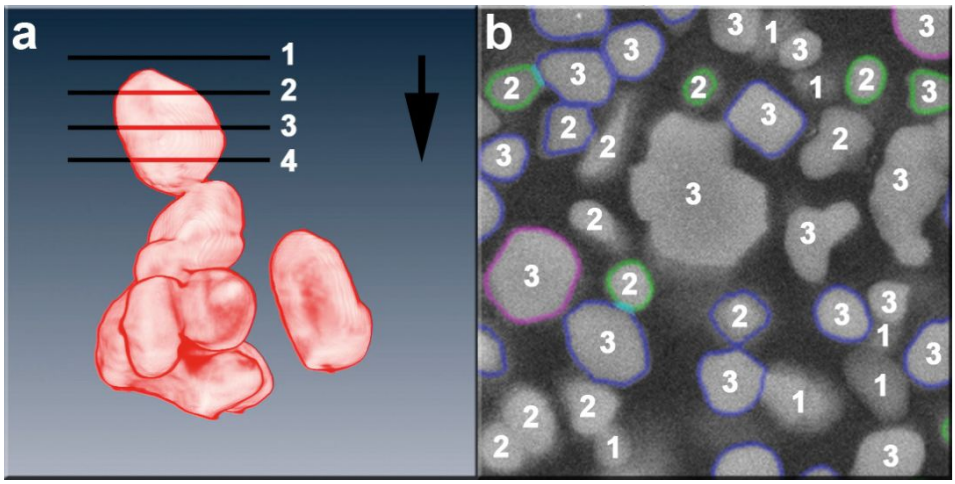

Figure 3: Visualisation of the systematic challenges in the detection of sectioned particles; a) principal possibilities for sectioning a particle; the viewing direction is indicated by the black arrow; lines 1 to 4 indicate section planes through the particle shown; b) a representative electron micrograph of a polished section; the numbers given correspond to the sections given exemplarily in part (a); the particles with a coloured envelope are the ones finally detected after grey-value and morphologic filtering.

area along the viewing direction for a convex particle (plane 3 in Figure 3a). But it can also be directed above the particle (plane 1 and 2 in Figure 3a) or below the centre of mass with respect to the viewing direction (plane 4 in Figure 3a), which leads to a smaller detected area. The cases of planes 3 and 4 in Figure 3 are essentially indistinguishable – they provide sharp particle edges. The cases of planes 1 and 2 give rise to a rim of lower intensities at the particle edges. Figure 3b shows how the different cases look in the SEM image, the numbers given corresponding to the section planes in Figure 3a. Only the particles with a coloured boundary are the ones finally detected after applying all filters. It can be seen that grey-value filtering effectively filters those particles that are located fully below section plane 1. Particles sectioned above the centre of mass, labelled with a 2, are only partially filtered out. The boundaries are detected reasonably well for the counted particles. The detection of particles sectioned close to the centre of mass or below the centre of mass is precise, both cases are labelled with a 3 in Figure 3b, since they are indistinguishable in the SEM image. Uncounted particles labelled with a 3 are filtered out as non-primary particles due to their shape.

Acknowledgements

G. Reifer, M. Krüger and H. Purwin are gratefully acknowledged for their untiring efforts in preparing and measuring numerous samples in order to establish the method presented.

References

1. Wedepohl, K. H. *Geochim. Cosmochim. Acta* **1995,** *59,* 1217–1232. doi:10.1016/0016-7037(95)00038-2
2. Mie, G. *Ann. Phys.* **1908,** *330,* 377–445. doi:10.1002/andp.19083300302
3. Theissmann, R.; Kluwig, M.; Koch, T. A reliable method for sizing constituent particles in pigment-grade titanium dioxide. In *Proceedings of the Microscopy Conference,* Aug 25–30, 2013; EPrints: Regensburg, Germany, 2013; pp 373–374.
4. European Commision. *Off. J. Eur. Communities: Legis.* **2011,** *L 275,* 38–40. doi:10.3000/19770677.L_2011.275.eng
5. Auffan, M.; Rose, J.; Bottero, J.-Y.; Lowry, G. V.; Jolivet, J.-P.; Wiesner, M. R. *Nat. Nanotechnol.* **2009,** *4,* 634–641. doi:10.1038/nnano.2009.242
6. Brown, S. C.; Boyko, V.; Meyers, G.; Voetz, M.; Wohlleben, W. *Environ. Health Perspect.* **2013,** *121,* 1282–1291. doi:10.1289/ehp.1306957
7. Klein, T.; Buhr, E.; Johnsen, K.-P.; Frase, C. G. *Meas. Sci. Technol.* **2011,** *22,* 094002. doi:10.1088/0957-0233/22/9/094002
8. Yoshida, H.; Mori, Y.; Masuda, H.; Yamamoto, T. *Adv. Powder Technol.* **2009,** *20,* 145–149. doi:10.1016/j.apt.2008.05.002
9. Stubbs, J. M.; Sundberg, D. C. *Polymer* **2005,** *46,* 1125–1138. doi:10.1016/j.polymer.2004.11.079
10. Mori, Y.; Yoshida, H.; Masuda, H. *Part. Part. Syst. Charact.* **2007,** *24,* 91–96. doi:10.1002/ppsc.200601048
11. Naito, M.; Hayakawa, O.; Nakahira, K.; Mori, H.; Tsubaki, J. *Powder Technol.* **1998,** *100,* 52–60. doi:10.1016/S0032-5910(98)00052-7
12. Ferraris, C. F.; Hackley, V. A.; Avilés, A. I. *Cem., Concr., Aggregates* **2004,** *26,* 71–81. doi:10.1520/CCA11920
13. Hayakawa, O.; Nakahira, K.; Naito, M.; Tsubaki, J. *Powder Technol.* **1998,** *100,* 61–68. doi:10.1016/S0032-5910(98)00053-9
14. Linsinger, T.; Roebben, G.; Gilliland, D.; Calzolai, L.; Rossi, F.; Gibson, P.; Klein, C. *Requirements on measurements for the implementation of the European Commission definition of the term 'nanomaterial';* Publications Office of the European Union: Luxembourg, 2012.
15. Kötzer, S. *Image Anal. Stereol.* **2006,** *25,* 63–74. doi:10.5566/ias.v25.p63-74
16. Sahagian, D. L.; Proussevitch, A. A. *J. Volcanol. Geotherm. Res.* **1998,** *84,* 173–196. doi:10.1016/S0377-0273(98)00043-2
17. Exner, H. E. *Image Anal. Stereol.* **2004,** *23,* 73–82. doi:10.5566/ias.v23.p73-82
18. Wejrzanowski, T.; Lewandowska, M.; Kurzydłowski, K. J. *Image Anal. Stereol.* **2010,** *29,* 1–12. doi:10.5566/ias.v29.p1-12
19. Hobolth, A.; Jensen, E. B. V. *Image Anal. Stereol.* **2002,** *21,* S23–S29. doi:10.5566/ias.v21.pS23-S29
20. Payton, E. J. *J. Miner. Mater. Charact. Eng.* **2012,** *11,* 221–242.
21. Sachs, L. *Angewandte Statistik;* Springer Verlag: Berlin, Germany, 1984. doi:10.1007/978-3-662-05748-3
22. Jillavenkatesa, A.; Lum, L.-S. H.; Dapkunas, S. *NIST Recommended Practice Guide: Particle Size Characterization;* U.S. Government Printing Office: Washington, USA, 2001.
23. Wedd, M. *Part. Part. Syst. Charact.* **2010,** *27,* 71–75. doi:10.1002/ppsc.201100023

License and Terms